Visible Light-Driven C–H Functionalization Reactions: Methodology Design and Development of a Droplet Microfluidics Screening Platform

by

Alexandra Carol Sun

A dissertation submitted in partial fulfillment
of the requirements for the degree of
Doctor of Philosophy
(Chemistry)
in the University of Michigan
2020

Doctoral Committee

Professor Corey Stephenson, Chair
Professor Stephen Maldonado
Professor Anna Mapp
Professor Melanie Sanford

Alexandra Carol Sun

suna@umich.edu

ORCID iD: 0000-0002-5583-8068

DEDICATION

For my great-grandfather, Dr. Shih-Liang Chien -
You were my first role model in Chemistry and will always be an inspiration to me.

ACKNOWLEDGEMENTS

During my graduate studies at the University of Michigan, I am incredibly grateful to have received the impactful mentorship and unwavering support of many who have guided me along my scientific journey. I am especially indebted to my advisor, Prof. Corey Stephenson, whose invaluable mentorship has continuously nurtured my growth as a scientist while solidifying my passion for pursing scientific research. Since the first day of my summer rotation in his group, Corey has supported my professional development holistically by giving me opportunities to pursue cutting edge, interdisciplinary research, encouraging me to attend a multitude of national conferences, and introducing me to the unparalleled joy of leading scientific outreach programs. I am tremendously grateful for Corey's steadfast advocacy in trusting me to co-lead and transform a seed idea into a highly collaborative and dynamic research program. I am inspired by Corey's intrepid scientific vision and creativity, as well as his dedication to mentoring and training coming generations of young scientists. His mentorship has continuously challenged and motivated me to become the best chemist that I can be and has set me on the course to pursuing the scientific career of my dreams.

I am very grateful to my dissertation committee members, Prof. Anna Mapp, Prof. Melanie Sanford, and Prof. Stephen Maldonado for the valuable guidance they have provided to me over the past five years. I truly appreciate the insight, feedback, and generous support that they have given me during every step of my graduate career. I am especially grateful to Prof. Anna Mapp and Prof. Melanie Sanford for personally inspiring me and setting shining examples of being highly successful women scientific leaders and pioneers. I am also thankful to Prof. Stephen

Maldonado for sharing his infectious passion for electrochemistry, solar cells, and chemical education with me throughout my graduate research, coursework, and outreach. I would also like thank Prof. Robert Kennedy for his incredible support and mentorship as a project collaborator. He has been an invaluable resource and role model to me over the past few years, serving as a professional reference letter writer and helping me develop a strong interest in droplet microfluidics.

I have had the rewarding opportunity to work with a phenomenal group of dedicated, intelligent, and inspirational co-workers in the Stephenson lab. In addition to being incredible mentors and role models, the Stephenson lab members I've worked with throughout the years have become my closest friends and support network. Postdocs: Dr. James Douglas, Dr. Verner Lofstrand, Dr. Xu Zhu, Dr. Markus Kaerkaes, Dr. Irene Bosque-Martinez, Dr. Dirk Alpers, Dr. Daryl Staveness, Dr. Logan Combee, Dr. Madison Sowden. Graduate Students: Dr. Bryan Matsurra, Dr. Mitch Keylor, Dr. Joel Beatty, Dr. Timothy Monos, Dr. Gabriel Magallanes, Martin Sevrin, Theresa Williams, Rory McAtee, Taylor Sodano, Kevin Romero, Edward McClain, Matthew Galliher, James Collins, Anthony Allen, Efrey Noten, Cheng Yang, Beca Rolden, and Alexander Harmata. I would especially like to thank Dr. Joel Beatty and Dr. Tim Monos for their influential mentorship at the start of my graduate studies. Dr. Joel Beatty was an invaluable first-year mentor, who helped me develop a strong sense of independence and tenacity early on, by believing in me and setting a solid example of the scientist I've worked towards becoming. Dr. Tim Monos has been a fantastic mentor and project collaborator since my summer rotation. His patience, perseverance, and devotion to mentoring younger students has been a constant source of inspiration to me. I owe a special thank you to my project collaborators and co-authors: Theresa Williams, Dr. Rory McAtee, Edward McClain, James Collins, and Anthony Allen. I would

especially like to thank my classmates, Dr. Rory McAtee, Taylor Sodano, and Kevin Romero for their friendship and support. I am so grateful to have shared this journey with them, and I continue to be inspired by their dedication, drive, and audacity in the face of scientific challenges. I would also like to express my gratitude to the "Girls' Bay" (especially Theresa Williams, Dirk Alpers, Rory McAtee, James Collins, Anthony Allen, Xiaotong Wu, and Maddie Sowden) for brightening up even the longest days in lab with constant encouragement, positivity, sage advice, and upbeat music.

I am fortunate to have received invaluable mentorship from, as well as built lasting friendships with, many others within the Michigan Chemistry Department. I would like to express my gratitude to my project collaborators and mentors: Dr. Amanda Dewyer (Zimmerman Lab), Dr. Hyungjun Kim (Zimmerman Lab), Dr. Daniel Steyer (Kennedy Lab), and Dr. Ren Wiscons (Matzger Lab). I would like to thank my Michigan Chemistry friends and role models, who have supported me throughout my journey and made my grad school experience the best that it could be. I also owe a special thank you to the student organization, F.E.M.M.E.S. (Women+ Excelling More in Math, Engineering, and the Sciences), for giving me the tremendous honor of connecting with so many exceptional women across the university, as well as the opportunity to make a difference outside of lab.

I am incredibly grateful to my early scientific mentors who have nurtured my interest in STEM and inspired me to pursue a scientific research career. I would like to thank Dr. Albert Shaw for first introducing me to scientific research early on in my childhood by giving me a memorable tour of his lab at Yale University and for being an impactful mentor to me ever since. I would also like to thank my high school Chemistry teacher, Mr. Gary Fadden, for sparking my interest in Chemistry through highly engaging lectures and vivid demos, as well as helping me find self-

confidence in STEM. I owe much gratitude to Dr. Jwu-Ting Chen at the National Taiwan University for giving me the unparalleled opportunity of conducting research in his lab for three consecutive summers as a high school student. Dr. Chen's commitment to scientific education has deeply inspired me, and his influential mentorship laid the foundation for my interest in pursuing chemistry research as a career. As an undergraduate student at Brandeis University, I have had the incredible opportunity to learn from dedicated educators including Dr. Christine Thomas, Dr. Bruce Foxman, Dr. Barry Snider, and Dr. Jason Pontrello, all of whom have further nurtured my interest in Chemistry. I would like to express my gratitude to my undergraduate research advisor, Dr. Christine Thomas, for being one of my biggest role models as a fearless leader, highly accomplished scientist, and devoted working mom. Her invaluable mentorship and guidance helped me solidify my goal to pursue graduate research in Chemistry. During the summer of my junior year, I had the rewarding opportunity to participate in a summer internship at Merck Research Laboratories. I am incredibly thankful to my many Merck mentors, especially my project supervisor, Dr. Joshua Close, for introducing me to research in photoredox catalysis and helping me see myself pursue a research career in the pharmaceutical industry, which I am now beyond thrilled to embark on.

I am indebted to my entire family for their love, belief, and support starting from day one. Every opportunity, success, and aspiration I have been fortunate to have along my academic journey was made possible by my parents' resolute commitment to investing in my education. Mom and Dad, thank you both for sacrificing so much to give me and my siblings the most well-rounded, impactful, and life-changing educational journeys that will set us up for success in our future careers. Mom, thank you for devoting your career to raising the three of us and inspiring us to become driven, hardworking, optimistic, compassionate, and generous individuals through your

own stellar example. Dad, thank you for teaching us the value and importance of family, while instilling in us a strong work ethic, as you've personally exemplified by pursuing a demanding career and being the rock of our family. I am also immensely grateful to my siblings, Katherine Sun and William Sun, who are the best friends, partners in crime, and younger role models that I could ask for. Thank you both for giving me a remarkable childhood and for making my adulthood even more adventurous, inspiring, and rewarding with your companionship. I also owe a special thank you to my grandparents and relatives who have contributed tremendously to giving me an invaluable education, memorable life experiences, and a loving family every step of the way. Thank you, Yieh-Yieh, Nai-Nai, Gong-Gong, and Pei-Pei, for your unconditional love, belief in me, and for being my biggest advocates. Finally, I would like to thank my late great-grandfather, Dr. Chien Shih-Liang, for whom this thesis is dedicated to. While I have never had the opportunity to meet you in person, I continue to feel the impact of your legacy in your success as a chemist, leader, and educator, and most importantly, in the family you've built that I am blessed to call mine.

TABLE OF CONTENTS

LIST OF FIGURES

LIST OF TABLES

LIST OF ABREVIATIONS

[O]	oxidant
°C	degree Celsius
Ac	acetyl
AIBN	azobisisobutyronitrile
aq	aqueous
Ar	aryl
BEt_3	triethylborane
Bn	benzyl
Boc	*tert*-butoxycarbonyl
bpy	2,2‘-bipyridine
bpz	2,2‘-bipyrazine
Bu_3SnH	tributyltin hydride
CF_3	trifluoromethyl
CFL	compact fluorescent lightbulb
cm	centimeter
CV	cyclic voltammetry
Cy	cyclohexyl
d	doublet
DCM	dichloromethane
$dF(CF_3)ppy$	2-(2,4-difluorophenyl)-5-(trifluoromethyl)pyridine
DFT	density functional theory
DMF	dimethylformamide
DMSO	dimethylsulfoxide
d.r.	diastereomeric ratio
dtbbpy	4,4'-di-tert-butyl-2,2'-bipyridine
EGFR	epidermal growth factor receptor
equiv	equivalents
*E*red	reduction potential
ESI	electrospray ionization
Et	ethyl
$E_{1/2}$	half-wave potential
Fac	facial
Fc	ferrocene
g	grams
h	hours
hν	light
Het	heteroarene
HOMO	highest occupied molecular orbital
HRMS	high resolution mass spectroscopy

HTE	high throughput experimentation
Hz	hertz
IR	infrared
Ir	iridium
ISC	intersystem crossing
J	coupling constant
L	liters
LED	light emitting diode
Li	lithium
LUMO	lowest occupied molecular orbital
M	molar concentration
m	multiplet
Me	methyl
MeCN	acetonitrile
Mes	mesityl
mg	milligrams
MHz	megahertz
min	minutes
mL	milliliters
MLCT	metal to ligand charge transfer
mm	millimeters
mmol	millimoles
mol	moles
mol%	mole percent
MW	molecular weight
nL	nanoliters
nm	nanometers
NMR	nuclear magnetic resonance
ns	nanosecond
O_2	oxygen
PC	photocatalyst
PCET	proton coupled electron transfer
Pd	palladium
PF_6	hexafluorophosphate anion
PFA	perfluoroalkoxy
PFD	perfluorodecalin
Ph	phenyl
phen	1,10-phenanthroline
PNO	pyridine *N*-oxide
ppm	parts per million
ppy	2-phenylpyridine
ps	picoseconds
py or pyr	pyridine
q	quartet
rt or RT	room temperature
Ru	ruthenium

s	singlet
SET	single electron transfer
SCE	saturated calomel electrode
t	triplet
TFA	trifluoroacetic acid
TFAA	trifluoroacetic anhydride
THF	tetrahydrofuran
TRIP	3,3′-Bis(2,4,6-triisopropylphenyl)-1,1′-binaphthyl-2,2′-diylhydrogenphosphate
UV	ultraviolet
V	volts
W	watt
δ	chemical shift in parts per million
λ_{max}	maximum wavelength
μL	microliters

ABSTRACT

The use of visible light for promoting chemical reactivity has far-reaching implications in providing access to otherwise challenging bond constructions in drug discovery, as well as minimizing the environmental impact of industrial pharmaceutical production. Along with harnessing a more sustainable energy source (e.g. sunlight), photocatalysis presents a means to circumvent the use of toxic reagents and hazardous conditions classically employed for promoting free radical chemistry in the synthesis of biologically active compounds. This thesis focuses on the development of visible light-mediated methods for the late-stage functionalization of heterocyclic drug scaffolds, as well as the design of a droplet microfluidics platform for the high-throughput optimization of photocatalytic reactions.

Chapter 1 provides a detailed summary of visible light-driven methodology that have been developed to enable the C–H alkylation of biologically relevant (hetero)arenes. The application of photoredox catalysis for alkyl radical generation has given rise to a multitude of methods that feature enhanced functional group tolerance, generality, and operational simplicity. This chapter will highlight examples of visible light-driven Minisci alkylation strategies that represent key advancements in this area of research. The scope and limitation of these transformations will be discussed, with a focus on examining the underlying pathways for alkyl radical generation.

Chapter 2 focuses on a method for the photoredox (perfluoro)alkylation of heteroarenes using alkyl carboxylic acid derivatives. Late-stage introduction of alkyl and perfluoroalkylated groups onto unfunctionalized positions on a drug scaffold holds significant potential for accelerating the drug discovery process. As such, the development of a visible light-driven heteroarene alkylation

strategy, including optimization studies, elucidation of scope, and mechanistic studies, is described.

Chapter 3 describes our efforts in developing a droplet microfluidics-based, nanoelectrospray ionization-mass spectrometry (nESI-MS) platform for screening photoredox catalysis reactions. Both the time and resource-efficient principles governing this technology underscore its anticipated impact on providing accelerated access to an array of diversified drug scaffolds using sustainable, visible light-driven synthetic methods. Application of this system towards the high-throughput late-stage diversification of complex pharmaceutical scaffolds is established in this chapter.

Chapter 4 continues to explore the utility of droplet microfluidics as a platform for screening photoredox reactions in continuous flow. Here, we describe the development of a droplet microfluidic photoreactor setup that combines ESI-MS analysis to enable high-throughput reaction discovery on picomole scale. This platform is anticipated to enable the direct optimization of flow reaction parameters (e.g. flow rate, residence time) and in turn, expedite the translation of discovery scale flow conditions to pilot scale continuous flow operations.

Chapter 5 discusses a microwave heating strategy for streamlining the synthesis and diversification of $Ir(III)^{+}$ polypyridyl complexes for applications in photoredox catalysis. This method is envisioned to help accelerate future developments in visible-light mediated chemistry. Additionally, the synthesis of novel nanohoop ligand-bearing $Ir(III)^{+}$ polypyridyl complexes is described, along with the photophysical and electronic characterization of these complexes.

Chapter 1: Photoredox Catalysis in (Hetero)arene Alkylation

* Portions of this chapter have been published in Sun, A. C.; McAtee, R. C.; McClain, E. J.; Stephenson, C. R. J. Advancements in Visible Light-Enabled Radical C(sp)^2–H Alkylation of (Hetero)arenes; *Synthesis* **2019**, *51*(5), 1063–1072.

1.1 Introduction: Photocatalysis Background and Design Principles

Since the first reported synthesis of tris(bipyridine)ruthenium(II) chloride ($Ru(bpy)_3Cl_2$) in 1936,[1] visible light-active metal complexes have been extensively investigated for applications in water splitting,[2] photovoltaic cells,[3] and energy storage.[4] Until 2008, these complexes had only been employed sporadically as photocatalysts for radical processes in organic synthesis. In the past decade, however, a renewed interest in photoredox catalysis across the synthetic organic chemistry community has led to the development of a diverse array of novel synthetic methodologies.[5,6] In addition to enabling unprecedented bond constructions and new modes of reactivity, visible light photoredox catalysis offers significant benefits over traditional methods for redox chemistry. For example, photoredox catalysis provides an optimal platform for performing redox neutral reactions, as both oxidants and reductants can be transiently generated in the same reaction vessel.

The photochemical processes pertaining to the excited state species of iridium and ruthenium photocatalysts have been extensively studied (**Figure 1.1A**).[7,8,9] Upon the complex's absorption of a photon in the visible region (λ_{max}=375–455 nm), a metal-to-ligand charge transfer (MLCT) event occurs, followed by intersystem crossing to generate the lowest-energy and longer-lived triplet excited state species. This species is "bipolar" in nature, having the ability to either undergo a single-electron reduction (reductive quenching) or a single-electron oxidation (oxidative

quenching). Additionally, the species resulting from either oxidative or reductive quenching are

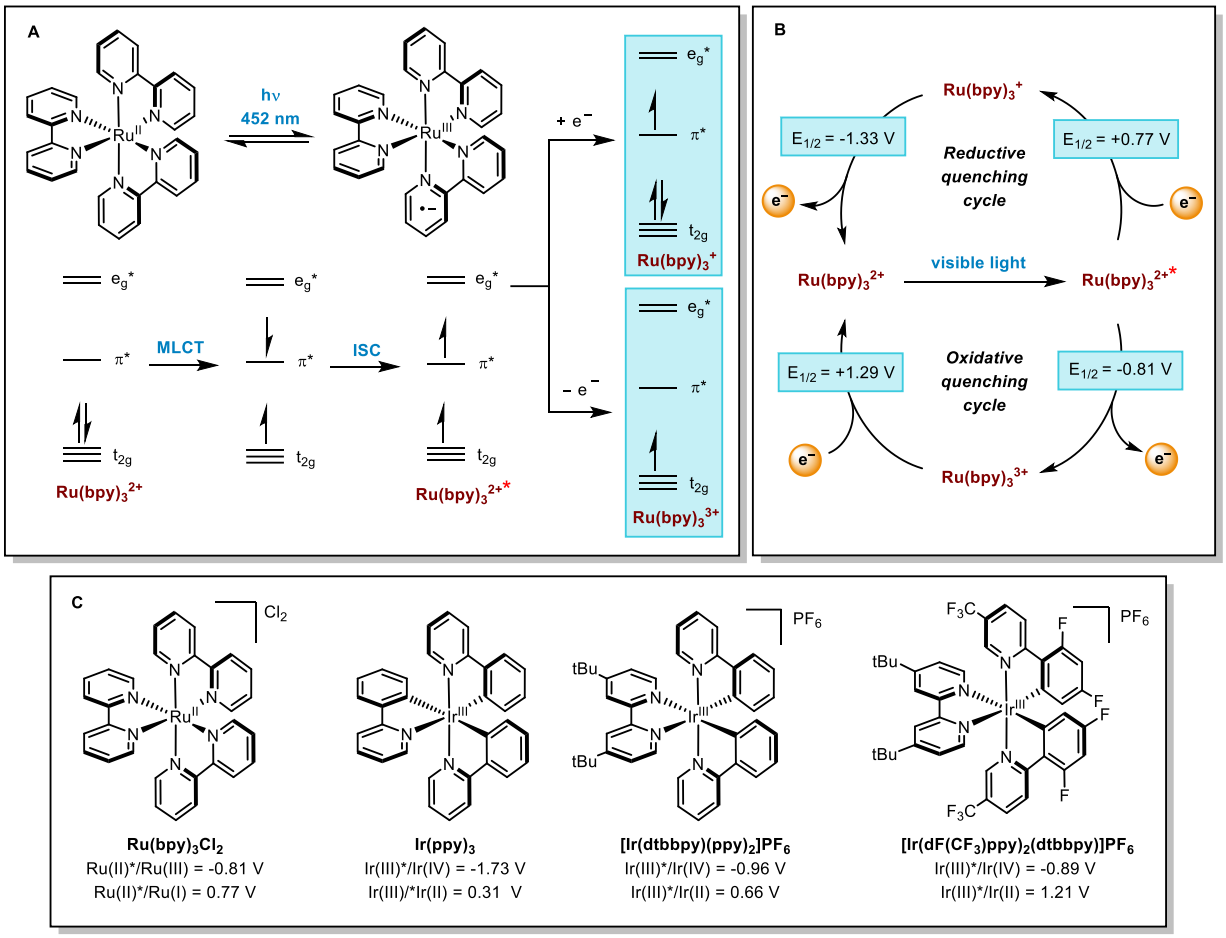

Figure 1.1. Simplified molecular orbital depiction of $Ru(bpy)_3^{2+}$ photochemistry

themselves strong oxidants and reductants, respectively (**Figure 1.1B**). Upon altering the electronic properties of the redox-active pyridyl/bipyridyl ligands, the redox potentials of these photocatalysts can also be fine-tuned (**Figure 1.1C**) to mediate the reduction/oxidation of a variety of organic substrates.

The use of visible light for promoting chemical reactivity has far-reaching implications in minimizing the environmental impact of the chemical industry. While traditional photochemistry has generally utilized ultraviolet light as chemical energy, visible light is a more desirable energy source due to an increased level of selectivity and control of reactivity. Visible light is absorbed

by relatively few organic molecules and can be used to selectively activate specific molecules or even transient species in solution. In addition to the promise of reduced waste streams, the use of a more sustainable energy source (e.g. sunlight), and the avoidance of the hazardous and/or toxic reagents classically-employed for carbon-centered radical formation (e.g. AIBN, Bu_3SnH, BEt_3/O_2), photoredox catalysis has gained meaningful traction due to its ability to integrate with continuous flow technology.[10-13] The enhanced light penetration available in flow can lead to order(s) of magnitude improvements in material throughput, and the applicability of these combined strategies will only increase as methods for in-line manipulation of material continue to improve.[10] Importantly, photoredox catalysis is already exerting a significant influence on industrial chemistry by enabling otherwise infeasible bond disconnections and aiding sustainability efforts. Given the ever-increasing industrial investment (e.g. Merck[10,11] Eli Lilly,[13-17] AbbVie[10]), photoredox catalysis promises to be the most enabling synthetic technology since Pd-based cross-coupling, which happens to be the *only* methodology invented in the last few *decades* to dramatically impact industrial synthesis.[18]

1.2 Radical Functionalization of Unactivated Heteroarenes

Nitrogen-containing heterocycles constitute the backbone of natural products, medicinally valuable small molecules and agrochemicals (**Figure 1.2A**).[19,20] Methodologies for the direct C–H alkylation and perfluoroalkylation of *N*-heteroarenes enable both the late-stage modification of clinical leads and rapid diversification of drug-like libraries.[21,22] These strategies allow for expedient access to unexplored chemical space and circumvent conventional *de novo* chemical syntheses.[23] Notably, the medicinal chemistry community has placed growing interest on late-stage functionalization technologies, as they allow for rapid modulation of drug metabolism and pharmacokinetic profiles of lead compounds.[21-23] Thus, synthetic approaches which are not

dependent on strong oxidants/reductants, high reaction temperatures, or pre-functionalized substrates are of high-value to both academic and industrial sectors.

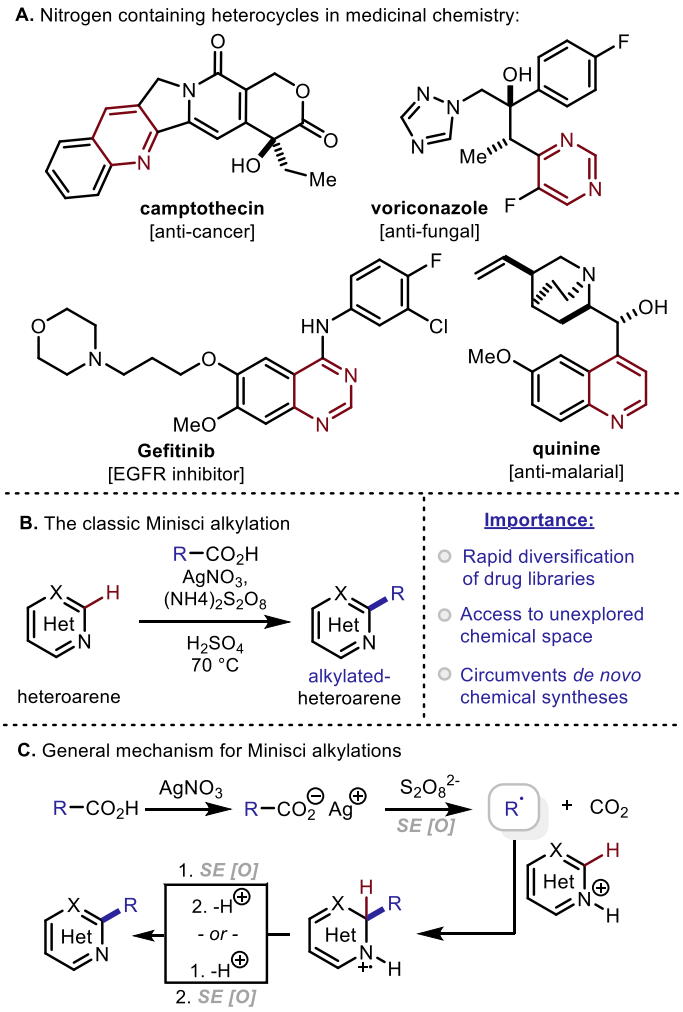

Figure 1.2. The Minisci alkylation of *N*-heteroarenes

The addition of open-shell alkyl and perfluoroalkyl radical intermediates to heteroarenes is referred to as the Minisci reaction (**Figure 1.2B**).[24-27] Minisci's original protocol relied on free radical formation from carboxylic acids via formation of their corresponding silver salts, followed by oxidative decarboxylation upon treatment with a persulfate oxidizing agent. Addition of an alkyl radical intermediate onto a protonated heteroarene, followed by rearomatization, yields the desired alkylated heterocyclic product (**Figure 1.2C**). Based on Studer and Curran's mechanistic

studies, rearomatization is proposed to occur via deprotonation and sequential single electron oxidation of the functionalized heteroarene upon radical addition.[28] Since Minisci's seminal contributions, this reactive paradigm for the alkylation of (hetero)arenes has been a stalwart foundation for modern drug discovery and development.[29] Furthermore, renewed interest in the mild and operationally simple generation of radical intermediates has spurred rapid evolution in the area of (hetero)arene alkylation.[30-32] In part, the driving inertia for this interest has been the emergence of visible light-mediated photoredox catalysis, which facilitates exceptionally mild single electron transfer (SET) events with organic substrates.[33-35] Importantly, the pharmaceutical industry has recognized the transformative impact of photoredox catalysis,[36,37] as it has far reaching implications in harnessing sustainable energy sources, reducing waste streams, and avoiding hazardous and/or toxic reagents classically employed for carbon-centered radical formation (e.g. Bu_3SnH, BEt_3/O_2).

1.3 *N*-Heteroarene Functionalization with Carboxylic Acids and Carboxylic Acid Derivatives

Alkyl carboxylic acids are versatile feedstock chemicals that are ubiquitous throughout nature and have been widely used as chemical building blocks.[38,39] Owing to their low cost, stability, minimal toxicity, and commercial availability, alkyl carboxylic acids have been widely utilized across a variety of synthetic transformations and represent preeminent building blocks for combinatorial chemistry (e.g. amide bond formation). In recent years, the radical decarboxylation of aliphatic carboxylic acids and their activated derivatives has emerged as a powerful strategy for the Minisci functionalization of bioactive organic molecules.

A broad selection of methods has been developed to promote the decarboxylation of alkyl carboxylic acid derivatives through a reductive pathway. In the context of photoredox catalysis, the formation of alkyl radicals via a reductive pathway would enable a net redox neutral catalytic

cycle, thereby eliminating the need for a terminal oxidant. At the same time, a reductive alkylation strategy has the potential to expand upon the scope of alkylation reagents, allowing access to compounds with significantly higher oxidation potentials.[40] Pioneering studies on the reductive decarboxylative generation of alkyl radicals were conducted by Barton and co-workers in the 1960s.[41,42] Barton et al. utilized *N*-hydroxypryidine-2-thione in the reductive activation of carboxylic acids for applications such as carbonyl reduction and reductive halogenation. In 1991, Oda and Okada disclosed the use of *N*-(acyloxy)phthalimides (NAP) as redox auxiliaries to enable the decarboxylative generation of alkyl radicals upon single electron reductive fragmentation ($E_{1/2}$ = -1.26 to -1.39 V vs. SCE (saturated calomel electrode)), using visible light-mediated photoredox catalysis.[43]

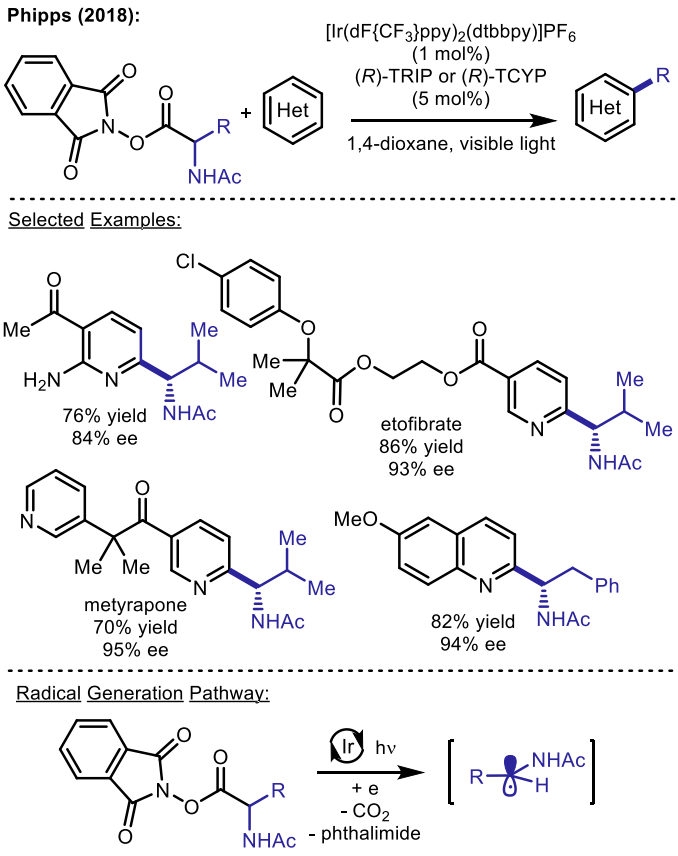

Figure 1.3. Enantioselective synthesis of α-heterocyclic amines using a Brønsted acid/photoredox catalytic platform

Since 2017, NAP esters have been employed in several visible light-driven Minisci alkylation protocols to promote reductive alkyl radical generation.[44-48] Notably, Phipps and co-workers have reported an enantioselective variant of the Minisci reaction (**Figure 1.3**) which utilizes a combination of asymmetric Brønsted acid catalysis and photoredox catalysis.[46] The use of a chiral phosphoric acid catalyst provides both stereo- and regiocontrol in the direct addition of prochiral α-amino alkyl radicals to the 2-position of a variety of pyridine and quinoline-based substrates. This strategy elegantly facilitates the synthesis of enantioenriched α-heterocyclic amines through an efficient late-stage functionalization approach. Jiang and co-workers have also designed an alternative, organocatalytic approach for constructing α-isoquinoline-substituted secondary amines in an enantioselective manner.[47] Nonetheless, the use of NAP esters for photoredox Minisci alkylations typically necessitates a separate isolation step following ester formation, resulting in an overall two-step procedure. In 2018, Sherwood and co-workers at Bristol-Meyers Squibb developed an operationally simple, one-pot protocol for the *in situ* generation of NAP esters, which obviates the need for isolating the pre-functionalized alkyl partner and facilitates the rapid generation of analog libraries.[48]

With the goal of designing a Minisci alkylation strategy for the late-stage functionalization of advanced pharmaceutical intermediates, DiRocco and co-workers at Merck disclosed the innovative use of stable organic peroxides as alkylating reagents under photoredox conditions (**Figure 1.4**).[49] Reaction parameters were optimized using a high-throughput experimentation platform, and the use of cyclometallated $Ir(III)^{+}$ photocatalysts $[Ir(dF\{CF_3\}ppy\}_2(dtbbpy)]PF_6$ and $[Ir(ppy)_2(dtbbpy)]PF_6$ provided access to methyl, ethyl and cyclopropyl radical intermediates from bench-stable and inexpensive alkyl peracetates. The methodology was shown to be amenable to the late-stage alkylation of an array of complex medicinal and agrochemical agents bearing both

6- and 5-membered heterocyclic scaffolds. Most importantly, the transformation proceeded smoothly in the presence of functionalities such as basic amines, alcohols, amides, and esters, without the need for protecting groups. With respect to methyl radical generation, the authors propose a mechanistic pathway involving the activation of *tert*-butylhydroperoxide through a reductive proton-coupled electron transfer (PCET) process. The resulting α-peroxy radical subsequently undergoes homolytic O–O bond cleavage to afford acetic acid and a *tert*-butoxy radical species. The authors hypothesize that methyl radical formation arises from β-scission of the *tert*-butoxy radical, thereby producing acetone as a byproduct.

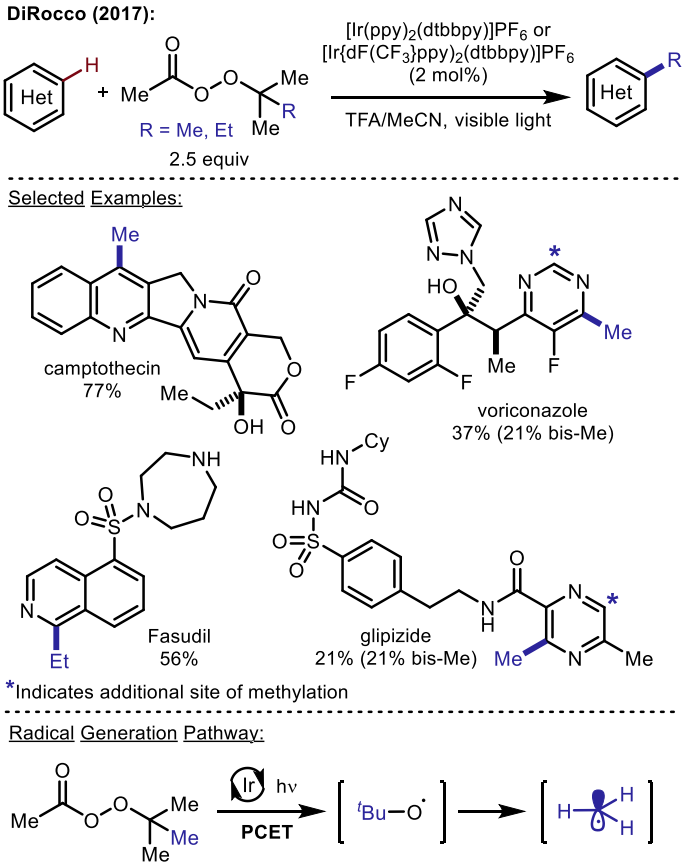

Figure 1.4. Late-stage functionalization of biologically active heterocycles using alkyl peracetates

In 2014, MacMillan et al. reported the first use of photoredox catalysis for the oxidative decarboxylation of alkyl carboxylic acids in the arylation of α-amino acids.[50] In 2017, Glorius and

co-workers disclosed a Minisci alkylation strategy that enables access to alkyl radical intermediates through the oxidative decarboxylation of carboxylic acids.[51] Sodium persulfate is used as an external oxidant to mediate alkyl radical formation, as well as facilitate photocatalyst turnover. The authors propose that the generation of desired alkyl radicals occurs through a hydrogen-atom transfer (HAT) event between a reduced sulfate radical anion species and a carboxylic acid precursor, resulting in oxidative decarboxylation. This reaction manifold enables the expedient functionalization of heterocyclic scaffolds, including pyridine, quinoline, and quinazoline cores. A range of primary, secondary, and tertiary alkyl radicals could be accessed from their corresponding alkyl carboxylic acid and amino acid precursors. The following year, Genovino and Frenette disclosed a separate visible light-driven Minisci alkylation protocol using hypervalent iodine reagents and organophotocatalysis to facilitate alkyl radical generation from carboxylic acids.[52]

1.4 *N*-Heteroarene Functionalization with Alkyl Boronic Acids

Over the past decade, aryl/alkyl-boron reagents have been identified to serve as radical precursors for C−C bond forming processes via oxidative C−B bond cleavage.[53-60] In 2016, Chen and coworkers disclosed the Minisci C–H alkylation of *N*-heteroarenes with primary and secondary alkyl boronic acids using the photocatalyst $Ru(bpy)_3Cl_2$ and acetoxybenziodoxole as a sacrificial oxidant (**Figure 1.5**). Diversely substituted primary and secondary boronic acids (e.g., alkyl bromide, aryl iodide, ester, amide, carbamate, terminal alkyne, and benzyl chloride) were well tolerated. Pyridines, pyrimidines, and a purine riboside substrate were all efficiently functionalized. It should be noted that more electron-rich heteroarenes, including benzothiazole and benzoimidazole, could also be successfully alkylated. The authors propose that the reaction is initiated by a single-electron reduction from the photoexcited Ru(II)* to acetoxybenziodoxole,

providing an oxygen-centered radical intermediate. This radical species is then proposed to react with the alkyl boronic acid reagent to form the desired alkyl radical via a radical "ate" transition state. DFT calculations support that this is a facile and highly exothermic process at room temperature.

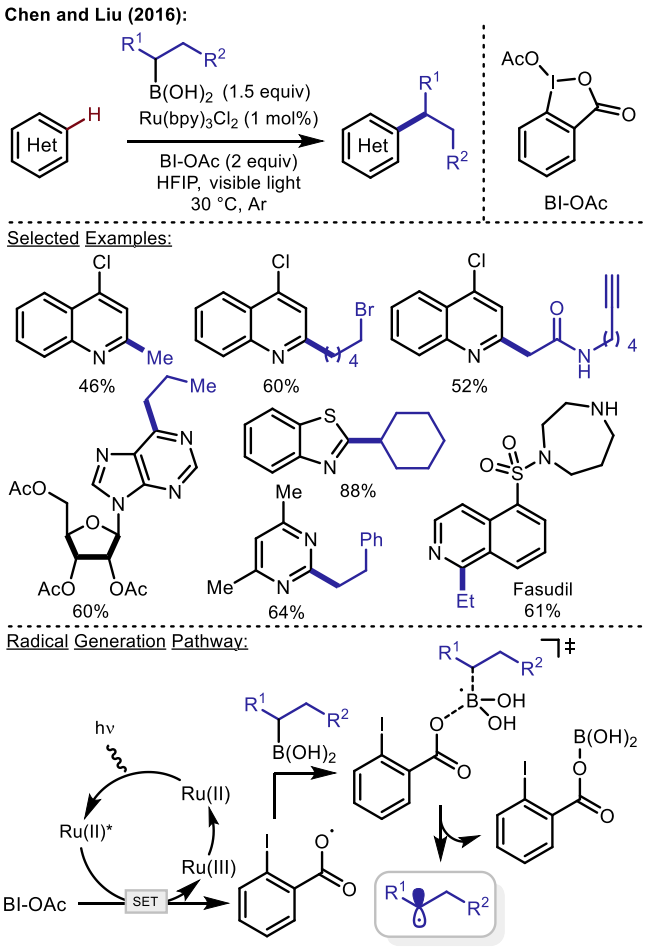

Figure 1.5. Photoredox Minisci alkylation using boronic acid alkylating reagents

1.5 *N*-Heteroarene Functionalization with Alkyl- and Alkoxymethyltrifluoroborates

Potassium organotrifluoroborates are considerably more attractive radical precursors than their corresponding boronic acids, given their lack of an empty *p*-orbital, which increases their overall stability and robustness toward harsh reaction conditions.[61,62] In 2011, Molander and coworkers reported the first use of potassium alkyl- and alkoxymethyltrifluoroborates as radical precursors

in the direct C−H alkylation of (hetero)arenes employing manganese(III) acetate as an oxidant in the presence of trifluoroacetic acid.[63,64] Under the optimized reaction conditions, the authors were able to functionalize several nitrogen-containing heterocycles all in good to excellent yields.

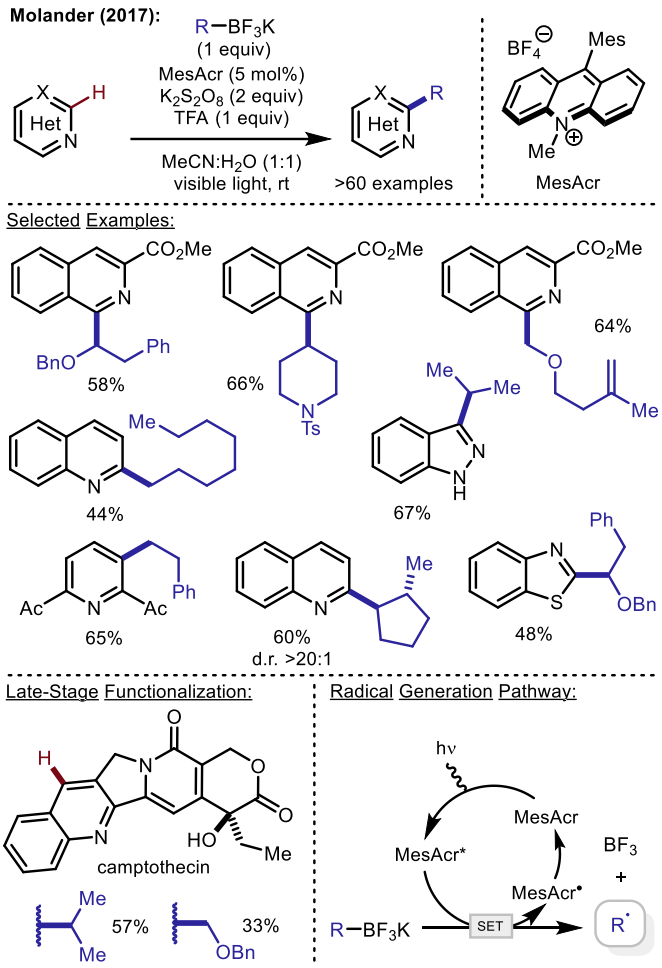

Figure 1.6. Organophotocatalytic Minisci alkylation using alkyltrifluoroborate radical precursors

In 2017, the Molander group reported an impressive advance from their earlier manganese(III) acetate-mediated Minisci chemistry by showcasing that alkyltrifluoroborates (many of which are commercially available) can be activated by an inexpensive, sustainable organophotocatalyst (**Figure 1.6**).[65] Following reaction optimization, the authors found the utility of a mesityl acridinium photocatalyst, potassium persulfate (as a sacrificial oxidant), and trifluoroacetic acid to be the optimal reagent combination for the C–H functionalization of heteroarenes. Under the title

reaction conditions, medicinally important cores including quinolines, isoquinolines, indazoles, pyridines, and quinazolinones, could all be functionalized with an impressive scope of primary, secondary, and tertiary alkyltrifluoroborates in good to excellent yields. As expected, electron-rich cores such as benzimidazole, were unreactive toward these Minisci alkylation conditions. These conditions proved tolerant of a diverse array of functional groups including aryl halides, unprotected amines, thioethers, and amides. Notably, quinine, which features a free alcohol, terminal alkene, and a tertiary amine (which has a known propensity for competitive photocatalytic oxidation) was efficiently (54% yield) and selectively (C2-) functionalized. To showcase the late-stage functionalization utility of their developed protocol, the authors successfully functionalized camptothecin, an anti-cancer drug candidate, at the C7-position. Mechanistically, the authors propose single electron oxidation of the alkyltrifluoroborate reagent, which leads to generation of the desired alkyl radical intermediate and BF_3.

1.6 *N*-Heteroarene Functionalization with Alkyl Halides

Alkyl halides are among the most widely used materials in organic chemistry. However, their application as radical precursors has been hindered because of the harsh conditions required for radical generation, such as the use of highly toxic trialkyltin hydrides.[66] The advent of modern photoredox catalysis provided a solution to this problem, as photoredox catalysts can be readily employed for the reductive dehalogenation of alkyl halides, resulting in the formation of free alkyl radicals. In 2010, the Stephenson group reported the seminal application of photoredox catalysis for the intramolecular alkylation of heteroarenes through reductive dehalogenation of activated alkyl bromides (**Figure 1.7A**).[67] This report represented a significant milestone, as it was the first Minisci alkylation that was promoted by photoredox catalysis. The authors' proposed mechanism involved generation of a Ru(I) species through reductive quenching of the excited state

photocatalyst. This Ru(I) species could then reduce malonyl bromides to produce a carbon-centered radical; subsequent trapping of the radical intermediate by electron rich indoles and pyrroles afforded the functionalized products. Following this initial report, the Stephenson group extended this methodology to access intermolecular C–H alkylations,[68] as well as the intermolecular construction of quaternary centers (**Figure 1.7B**).[69]

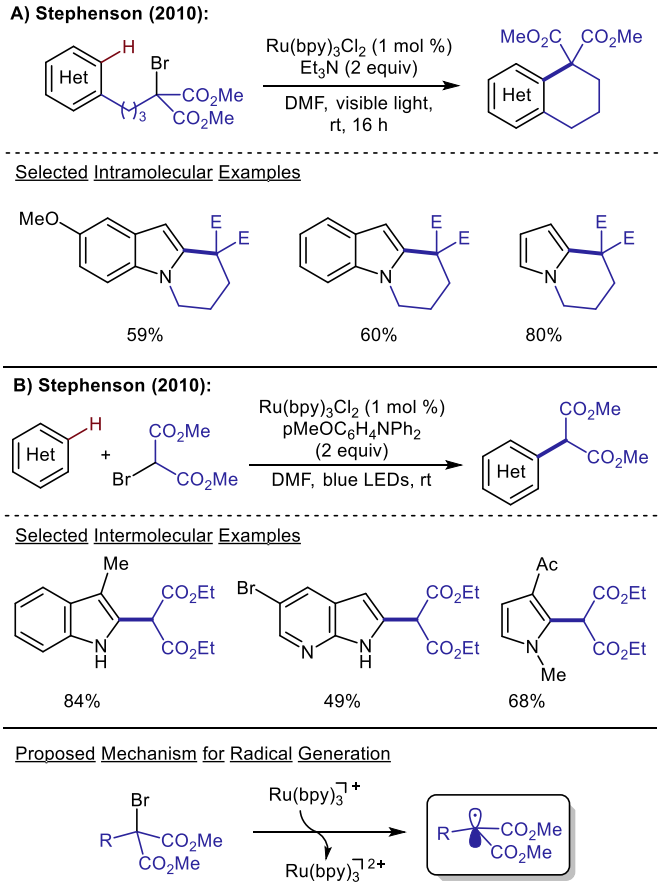

Figure 1.7. Visible light-driven dehalogenative alkylation of heteroarenes

Two recent reports have highlighted the continued expansion of Minisci protocols featuring dehalogenative radical generation. First, a group at Vertex Pharmaceuticals demonstrated the ability to predictably access C3- and C5-functionalized products by performing the Minisci reaction under basic conditions.[70] This report featured the reductive dehalogenation of unactivated alkyl iodides and demonstrated the ability to predict the site of alkylation based upon the

electronics of a heteroaryl substrate. Additionally, the Wang group has reported a separate Minisci alkylation protocol which utilizes a halogen atom abstraction event to promote radical generation.[71] This work was enabled through the adaptation of conditions concurrently reported by the Stephenson[72] and MacMillan[73] groups for visible light-mediated bromide atom abstraction from alkyl and aryl bromides, facilitated by a tris(trimethylsilyl)silane radical [$(Me_3Si)_3Si\bullet$] species generated *in situ*. The use of a halogen atom abstraction approach allowed Wang and co-workers to access a diverse scope of alkyl halides and heteroarenes.

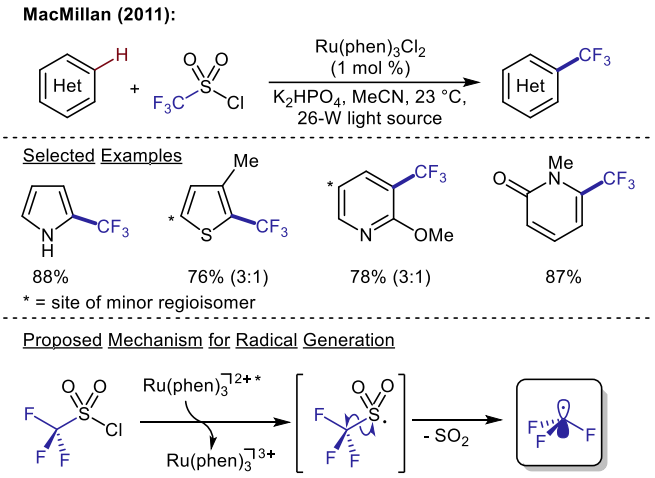

Figure 1.8. Photoredox trifluoromethylation of unactivated (hetero)arenes

The incorporation of trifluoromethyl groups onto (hetero)arenes represents an important transformation in medicinal chemistry applications. As such, dehalogenative Minisci alkylations have also been expanded upon to include the trifluoromethylation of heteroarenes. In 2011, the MacMillan group developed the first reported method for the visible light-driven radical trifluoromethylation of (hetero)arenes (**Figure 1.8**). [74] In this report, reduction of trifluoromethanesulfonyl chloride by a ruthenium photocatalyst induced the loss of sulfur dioxide, affording the reactive trifluoromethyl radical species. This species could be effectively trapped by a number of (hetero)arenes, resulting in C–H trifluoromethylation. This method demonstrated the applicability of photoredox catalysis in medicinal chemistry, as a number of trifluoromethylated

pharmacophores could be easily accessed. Following this report, a collaborative effort by the Fukuzumi, Cho, and You groups described the use of a platinum(II)acetylacetonate (acac) photosensitizer for the reduction of trifluoromethyl iodide. The resultant trifluoromethyl radical was utilized in the subsequent C–H trifluoromethylation of heteroarenes.[75]

In the aforementioned examples, catalysis is promoted by engaging the photosensitizer in outer sphere electron transfer events. At the same time, dehalogenative radical generation has also been demonstrated to be driven by non-canonical photocatalysts that engage the halide substrate through inner sphere electron transfer or direct halogen atom abstraction events. In 2015, the Barriault group described the use of gold photoredox catalysis for the application of unactivated alkyl bromides to the alkylation of *N*-heteroarenes through an intramolecular cyclization (**Figure 1.9**).[76] This methodology was extended to intermolecular radical additions in 2016. In this more recent study, the Barriault group proposed a mechanistic pathway involving an excited state exciplex which could undergo an inner-sphere electron transfer to furnish the alkyl radical species (**Figure 1.9**).[77] The development of these methods has provided mild conditions for accessing primary alkyl radical fragments. Recently, a group from Pfizer reported the use of manganese decacarbonyl (Mn_2CO_{10}) for the alkylation of heteroarenes utilizing simple alkyl iodides as substrates.[78] The authors proposed that the Mn_2CO_{10} catalyst undergoes Mn–Mn bond homolysis upon irradiated with blue light. The resultant $(CO)_5Mn\bullet$ radical species can then abstract an iodine atom from the alkyl iodide reagent to enable alkyl radical generation.

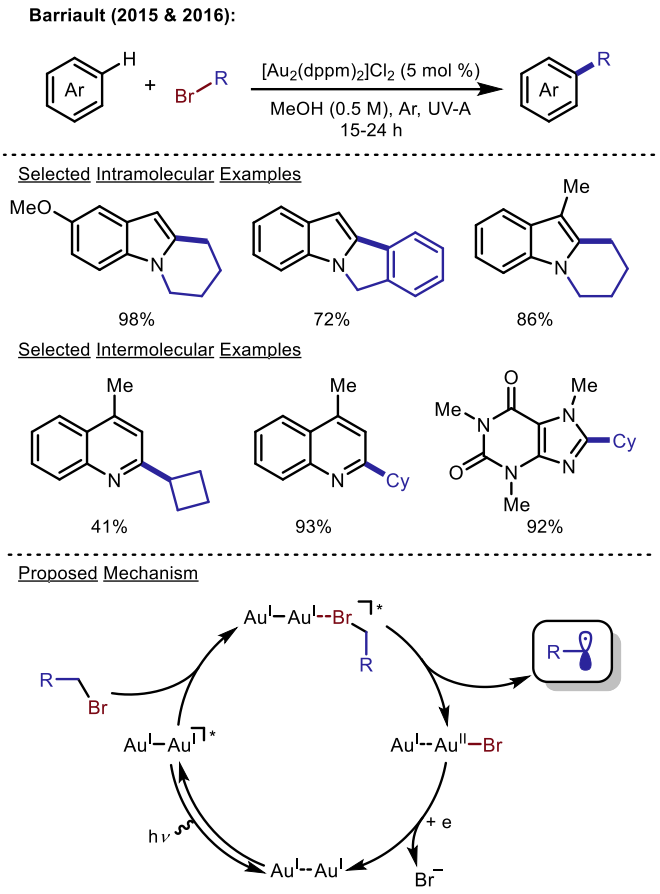

Figure 1.9. Dehalogenative alkylation using gold photoredox catalysis

1.7 *N*-Heteroarene Functionalization with Alcohols and Ethers

The late-stage incorporation of oxygenated functionality into complex molecules can have a significant impact on the physical properties (e.g. solubility) of a compound. For drug discovery, the optimization of these properties for a lead compound is vital to the development of clinical candidates.[79] Thus, the development of methods for the installation of simple oxygenated fragments, such as those derived from alcohols and ethers, is an important point of development for the Minisci reaction.

The application of alcohols in the visible light-driven Minisci alkylation of heteroarenes was first reported in 2015 by the MacMillan group (**Figure 1.10**).[80] The authors proposed that the methylation of heteroarenes could be achieved through the initial addition of a carbon-centered

hydroxymethyl radical onto a heteroarene substrate. The hydroxymethyl group could then be converted to the desired methyl fragment through a spin-center shift induced by the concomitant loss of water. The subsequent benzylic radical species was proposed to be reduced and protonated to furnish the final methylated product. Importantly, the proposed hydroxymethyl radical intermediate in this report was generated through C–H abstraction of methanol with a thiol co-catalyst. This method provided a general manifold for accessing Minisci reactivity, as a variety of alcohols, pyridines, quinolines, and isoquinolines were amendable to these alkylation conditions.

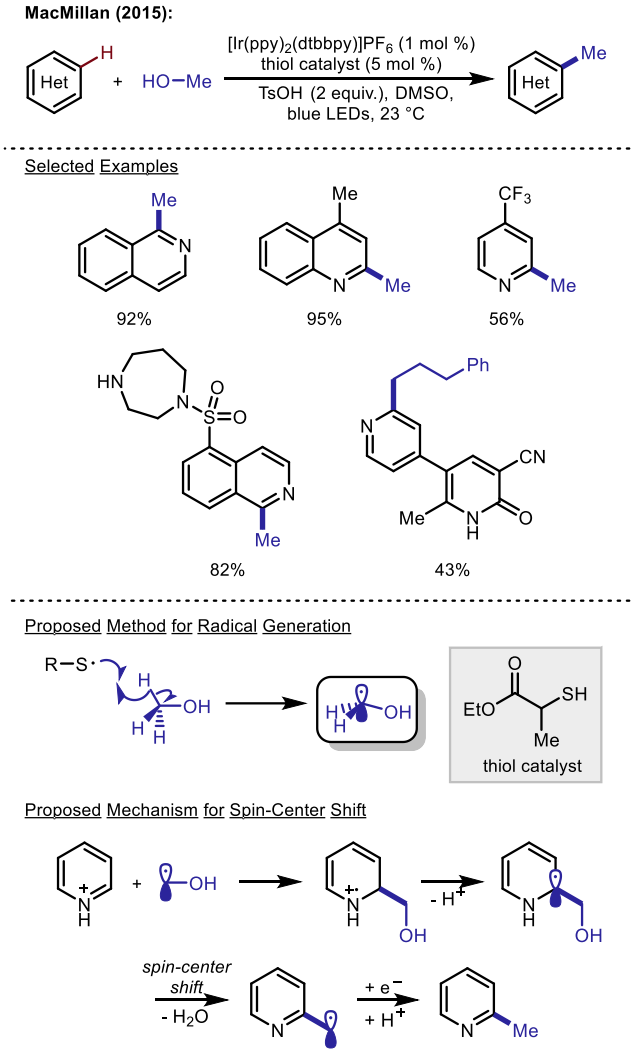

Figure 1.10. Visible light-driven Minisci alkylation reaction using alcohols as alkylating agents

Following this report, in 2016, DiRocco and co-workers utilized a radical relay reaction to promote the visible light-mediated hydroxymethylation of heteroarenes with methanol.[81] This reaction was proposed to proceed through the generation of a phenyl radical species from the Ir(III)-catalyzed reductive decomposition of benzoyl. The phenyl radical intermediate then undergoes hydrogen atom abstraction from methanol, thereby generating the active hydroxymethyl radical species, which could be trapped by a variety of heteroarenes. This hydroxymethylation protocol allows for the late-stage functionalization of an array of pharmacophores. While the above two examples utilize iridium photocatalysts to promote reactivity, Minisci reactions featuring alkyl alcohol reagents have also been reported in the absence of photocatalysts. In 2017, the groups of Li [82] and Barriault [83] independently reported the application of near UV irradiation to promote the methylation of heteroarenes.

In 2014, the MacMillan group reported the first application of ethers in conjunction with photoredox catalysis for Minisci reactivity.[84] The developed method utilized persulfate salts as both an oxidant and C–H abstraction reagent. From a mechanistic standpoint, oxidative quenching of the photocatalyst by the persulfate salt generates an equivalent of sulfate radical anion, which readily abstracts a hydrogen atom from the ethereal substrate. This seminal report demonstrates the impact of photoredox catalysis on broadening the scope of Minisci reaction protocols, as both cyclic and acyclic ethers could be innovatively used as radical alkylating reagents under mild conditions. In 2017, the Ryu group described the use of a polyoxometalate potocatalyst tetrabutylammonium decatungstate (TBADT) for a visible light-driven Minisci alkylation reaction.[85] In its excited state, the TBADT photcatalyst enabled the selective, oxidative generation of radical intermediates through the direct abstraction of electron-rich hydrogen atoms present across ether, alkane, and amide substrates. It is noteworthy that Minisci reactions enabled by the

C–H abstraction of saturated molecules are not limited to oxygenated substrates, as this mechanistic paradigm has also been reported with the employment of protected amines[86] and alkanes.[85,87]

1.8 Conclusion

As exemplified in this chapter, the utility of photoredox catalysis for the Minisci alkylation reaction provides synthetic chemists with a myriad of opportunities to utilize inexpensive, commercially abundant alkylating reagents (e.g. carboxylic acids, alcohols, alkyltrifluoroborates, alkyl halides, etc.) for the direct, C–H alkylation of heteroarenes. Notably, visible light-driven Minisci alkylation reactions have been demonstrated to proceed under mild reaction conditions and are tolerant of a variety of complex functionalities. In particular, these strategies have been shown to hold significant value for late-stage functionalization efforts in drug discovery. The continued development of photoredox Minisci alkylation reactions that are amenable to a broader scope of complex heterocyclic compounds, while providing improved regioselectivity, is vital to enhancing the synthetic utility and impact of this transformation. Furthermore, demonstrating the scalability of photoredox Minisci alkylation protocols (e.g. using continuous flow systems) may offer valuable opportunities for bridging drug discovery efforts with process development needs.

Chapter 2: Visible Light-Driven Strategies for the Decarboxylative (Perfluoro)alkylation of Pharmaceutically Relevant Compounds

*Portions of this chapter have been published in Alexandra C. Sun, Edward J. McClain, Joel W. Beatty, Corey R. J. Stephenson, *Org. Lett.* **2018**, *20*(12), 3487-3490.

2.1 Introduction

2.1.1 Trifluoromethylation of (Hetero)arenes and Late-Stage Alkylation

Fluorinated compounds are the subject of powerful interest within the context of agrochemical and pharmaceutical development, as the incorporation of fluorine onto an organic scaffold can greatly alter pharmacokinetic properties such as metabolic stability, membrane permeability, and solubility.[88] Fluorine atoms can be found in over 200 approved pharmaceuticals to date,[89] and in this context fluorinated moieties such as the trifluoromethyl group (CF_3) have found fundamental, widespread utility (**Figure 2.1A**). Industrially, commodity trifluoromethyl derivatives are produced through direct halogen-fluoride exchange in anhydrous hydrogen fluoride at elevated temperatures (**Figure 2.1B**);[90] while this method is inexpensive to employ, its application is limited to thermally and oxidatively robust molecular architectures, and thus not amenable to complex molecule synthesis. In other instances, multi-step fluorination protocols are employed. For example, a reported synthesis of the ORL-1 antagonist **2** (**Figure 2.1C**) accomplished the benzylic fluorination of the spirocyclic furan **3** through a lengthy 5-step sequence;[91] while scalable, this route relied upon the use of 23.9 kg of bis(2-methoxyethyl)aminosulfur trifluoride—a fuming reagent which produces HF and reacts violently with water—as well as 1.2 kg of shock-sensitive AIBN.

Due to the immense importance of the trifluoromethyl group to pharmaceutical synthesis, a large number of reagents prepossessing C–F bonds has been developed to avoid the forceful, hazardous, and/or circuitous requirements of C–F bond formation (**Figure 2.2**).

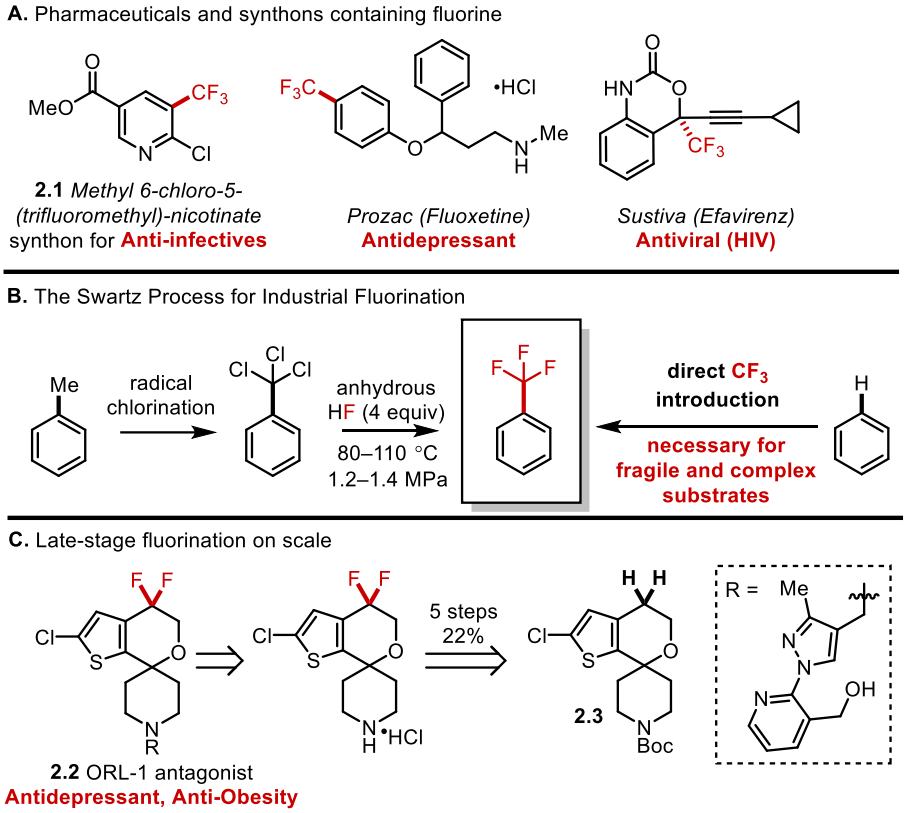

Figure 2.1. Fluorinated pharmaceuticals and intermediates

While the breadth of effective trifluoromethylation reagents is impressive, the relative cost and availability of these reagents varies greatly with complexity and molecular weight–a feature which is largely ignored in the context of academic methodology development. Conversely, in consideration of scalable, financially feasible, and industrially relevant trifluoromethylation methodologies, reagent choice is far more limited. A recent discussion in the context of the synthesis of the (trifluoromethyl)-nicotinate **2.1** (**Figure 2.1A**) places this issue in perspective: On large scale, "applications of Ruperts reagent (R_3SiCF_3) are most prominent. However, the large-scale availability of CF_3SiMe_3 and higher alkyl variants is still limited, and their cost can be

prohibitive for use in commercial pharmaceutical manufacture."[92] In addition, despite the apparent variety of trifluoromethylation reagents, the range of starting-materials used for their preparation is strikingly limited (**Figure 2.2**). Bromotrifluoromethane ($BrCF_3$) is the most commonly utilized fluorinated material for reagent synthesis, and is a well-known promoter of ozone-depletion with a half-life of 110 years in the troposphere.[93] $BrCF_3$ is produced from the greenhouse gas fluoroform (HCF_3, atmospheric lifetime = 254 yr),[94] and the two constitute the original source of CF_3 for a large number of reagents including CF_3I,[95] $TMSCF_3$,[96] CF_3SO_2Na,[97] $Zn(SO_2CF_3)_2$,[98] **2.4**,[99] and **2.5** (**Figure 2.2**).[100,101] The remaining alternative CF_3 reagents are obtained as derivatives of triflic or trifluoroacetic acid, which are produced avoiding the use of environmentally harmful gases directly through the electrochemical fluorination of either methanesulfonyl fluoride or acetyl fluoride, respectively.[90] The sulfinate reagents CF_3SO_2Na and $Zn(SO_2CF_3)_2$ in particular have garnered significant popularity for medicinal chemistry in industry; however, it should be mentioned that beyond their cost and limited availability, the use of these reagents requires an excess of both sulfinate (2-6 equiv.) and *tert*-butyl hydroperoxide (3-10 equiv.), and occasionally requires multiple additions of reagent.[102,103]

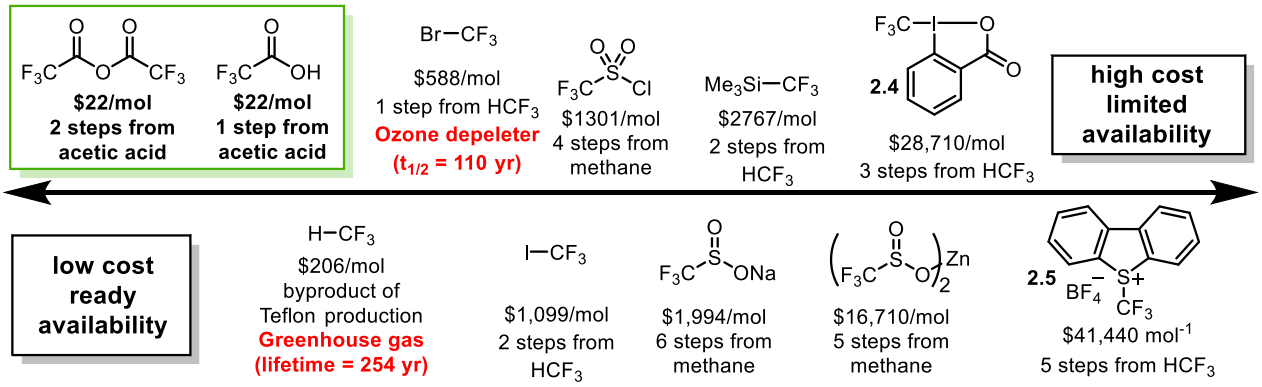

Figure 2.2. Cost per mole and sourcing of popular trifluoromethylation reagents (Sigma-Aldrich at largest quantity available)

2.1.2 Perfluoroalkylation Using Electronically Tuned *N*-Oxides

In consideration of all relevant factors including safety, environmental impact, material availability, ease of handling, and lastly reagent price,[104] TFA and its derivatives undeniably constitute the ideal source of CF_3 in all respects. A particular challenge preventing the widespread use of TFA for trifluoromethylation chemistry is the large energetic cost of C–C bond cleavage, which can be accomplished thermally in a 2 e^- pathway in the presence of copper salts at or above 140 ˚C.[92] Direct oxidative decarboxylation of trifluoroacetate has thus far been shown to be incompatible with electron-rich and electron-neutral substrates, as the potentials required for this reactivity will oxidize many common organic solvents (F_3CO_2Na, $E_{1/2}^{ox}$ = >2.4 V vs. SCE in MeCN) (**Figure 2.3A**).[105]

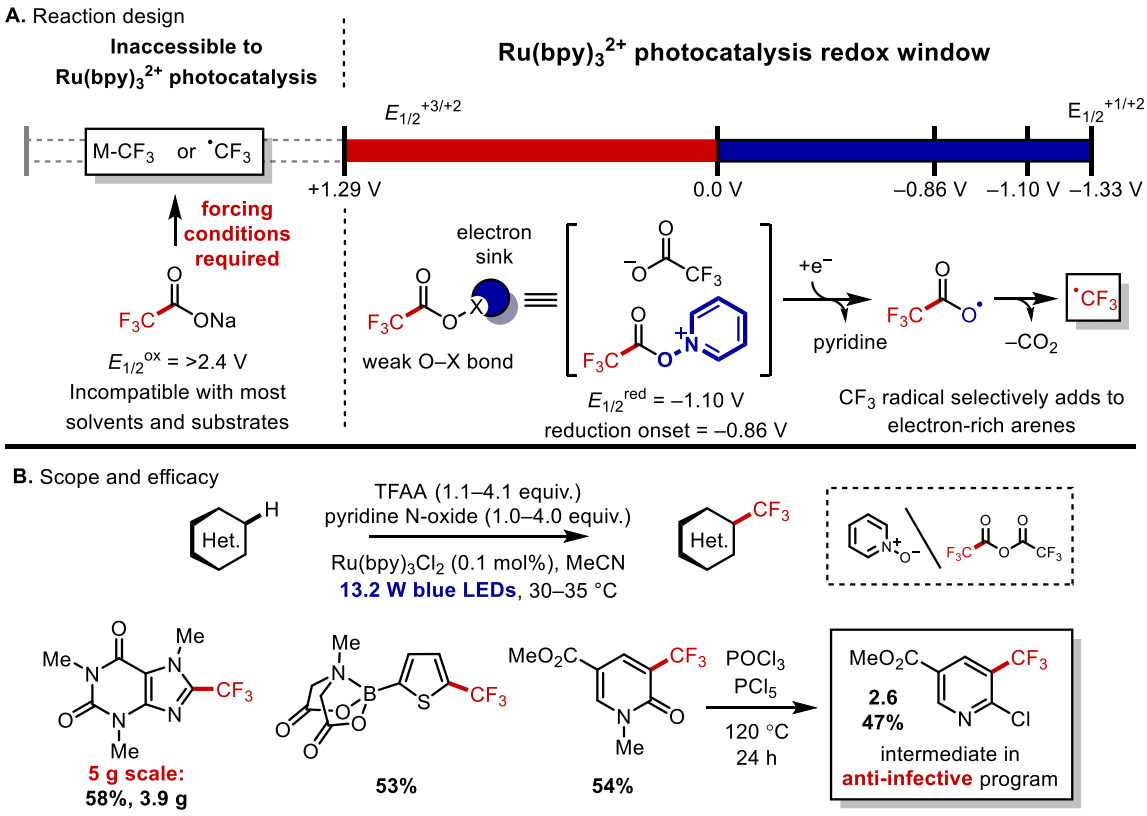

Figure 2.3. Mild photochemical trifluoromethylation with TFAA

The convergence of these factors has resulted in the use of TFA as a CF_3 source only in very limited contexts of thermal [106] or oxidative [107] substrate stability, often in the presence of stoichiometric or superstoichiometric metal promoters.[92] A direct oxidation of TFA is not feasible with photocatalysis, and so the Stephenson group has designed an activation method to promote decarboxylation of its anhydride (TFAA) through an initial reaction with pyridine *N*-oxide (PNO). The strategic use of PNO: **(1)** nucleophilically activates the acid through acylation **(2)** presents a weak N–O bond and low-lying LUMO for facile single-electron reduction **(3)** produces pyridine as an endogenous base necessary to avoid acid buildup and **(4)** avoids trifluoromethylation of the pyridine itself due to poor electronic matching with the electron-poor CF_3 radical (**Figure 2.3A**). Mixing of TFAA with one equivalent of PNO results in the formation of a putative adduct which undergoes *reduction* at mild potentials ($E_{red}^{1/2}$ = –1.10 V vs SCE in MeCN), forming the CF_3 radical within the redox-window of $Ru(bpy)_3^{2+}$. Our group has demonstrated the efficacy of this design in the C–H trifluoromethylation of a number of electron-rich heterocyclic and aromatic substrates, a selection of which are shown in **Figure 2.3B**. This chemistry is compatible with a number of Lewis-basic functionalities, and a number of heterocycles with functionality useful for further cross-coupling reactions have been trifluoromethylated. Significantly, the utility of this chemistry has been demonstrated in the synthesis of intermediates such as chloropyridine **2.6**, an intermediate of significant interest to Boeringher-Ingelheim for an anti-infective program.[92]

2.1.3 Perfluoroalkylation Using Electronically Tuned *N*-Oxides

The reductive decarboxylation of acid derivatives using heterocyclic *N*-oxides offers many opportunities for customizability, including choice of photocatalyst, *N*-oxide, and reagent counter ion. Of these factors, *N*-oxide substitution offers the most control over the reaction outcome. Among the issues encountered in the activation of TFAA with PNO, we identified the reduction potential of the TFAA adduct ($E_{1/2}^{red}$ = –1.10 V vs SCE) as potentially problematic as the reducing power of photoexcited $Ru(bpy)_3Cl_2$ ($E_{red}^{1/2}$ = –0.81 V vs SCE) is too positive for efficient reduction of this species.[108] Of the wide array of pyridines available for investigation, 4-phenylpyridine *N*-oxide (4-Ph-PNO) was expected to both stabilize the immediate product of reduction through additional conjugation, as well as present a lower LUMO due to the electron-withdrawing nature of the phenyl substituent (**Figure 2.4A**).

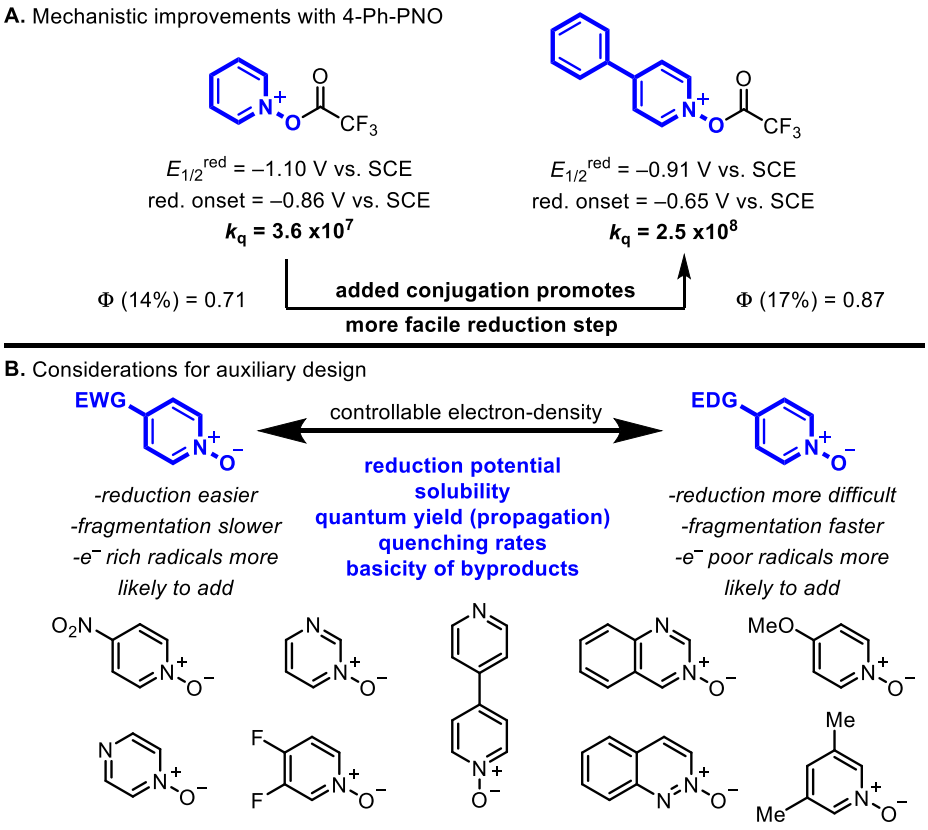

Figure 2.4. Tunable *N*-oxide properties for decarboxylative photochemistry

Indeed, reduction of the 4-Ph-PNO/TFAA adduct was shifted 200 mV in the positive direction ($E_{red}^{1/2}$ = –0.91 V vs SCE) as compared to the reduction of PNO/TFAA, suggesting that this alteration of *N*-oxide electronics is capable of promoting the decarboxylation of TFAA under even more mild conditions. Electron transfer from photoexcited $Ru(bpy)_3Cl_2$ (as indicated by fluorescence quenching) is accomplished roughly 7 times faster with the 4-Ph-PNO adduct, and the observed quantum yield (Φ, yield of product per incident photon)[109] is also increased (**Figure 2.4A**). Significantly improved yields of trifluoromethylation products were obtained for an array of electron-rich substrates, many of which display significant further utility in the context of cross-coupling and unnatural amino acid synthesis (**Figure 2.5**).

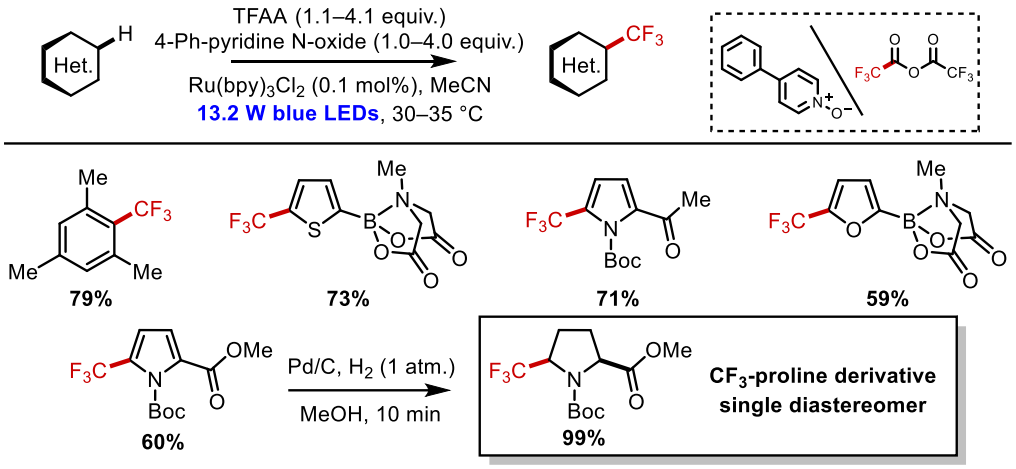

Figure 2.5. Select scope of photoredox (hetero)arene trifluoromethylation

The efficacy of 4-Ph-PNO in this manner represents a clear proof of principal for the importance of *N*-oxide functionalization. Much in the same way that ligand design is understood to influence the efficacy of transition-metal mediated cross-coupling reactivity, pyridine identity in this decarboxylation chemistry can have a significant effect on reaction mechanism and outcome (**Figure 2.4B**). The mechanistic underpinnings of the effects of pyridine substitution will result in more effective reagent choice, resulting in improved yields and reaction efficiencies. Beyond improved yields of trifluoromethylated products, this understanding of *N*-oxide reactivity will

contribute to the generality and efficiency of our method for cross-coupling of heterocycles with a variety of carboxylate radical precursors.

We have investigated this cross-coupling strategy in the context of the synthesis of alternative fluorinated derivatives due to the associated interest in these fluorinated materials by the pharmaceutical industry. Without the need for multi-step reagent synthesis, our method offers inexpensive, scalable, operationally-simple C–H functionalization chemistry which dramatically reduces the environmental footprint of reagent preparation. In our initial studies, we have accomplished the perfluoroethylation (**Fig. 2.6A**) and perfluoropropylation (**Fig. 2.6B**) of a number of electron rich heterocycles and arenes.

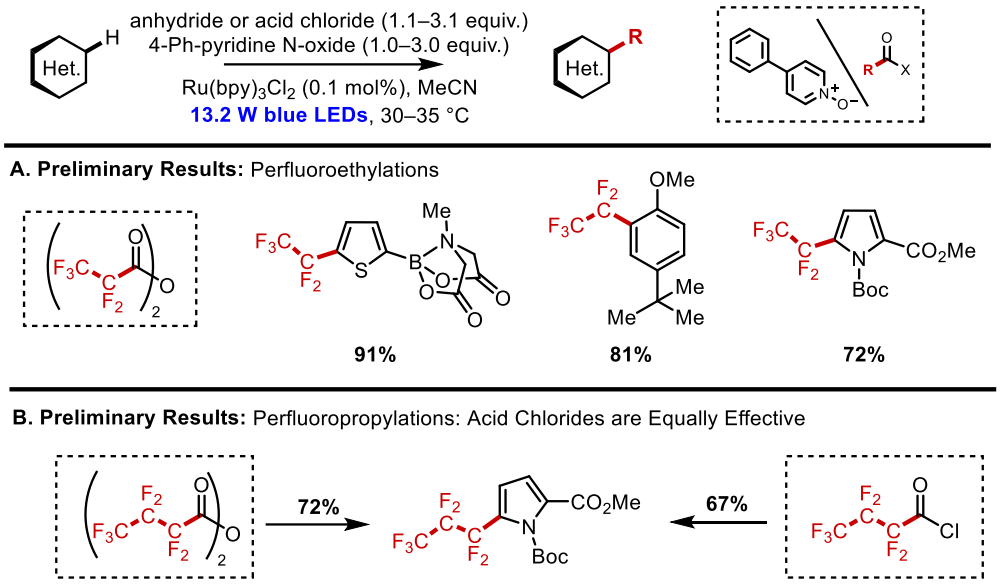

Figure 2.6. Coupling of electron-poor perfluoroalkyl radicals with unfunctionalized heteroarenes

Current methods available for performing these transformations are limited, while the corresponding acid derivatives are readily available for investigation.[110] The generality of this process is cause for optimism, as the yields are good to excellent for electron rich substrates. As the acid-derivative coupling partner increases in size, the use of symmetrical anhydrides becomes less desirable, and acid chlorides have been found to provide equally good yields of product. It

should be noted that the industrial process of fluoride-halogen exchange used to synthesize trifluoromethylated arenes (**Fig. 2.1B**) cannot be applied for the synthesis of these functionalities, and these products are generally constructed through cross-coupling methods often requiring super-stoichiometric copper.[111]

Despite early success with these electron-poor radical precursors, a number of challenges present themselves in the expansion of substrate scope and utility. In particular, subtle electronic changes to the intermediate radical can have a dramatic effect on reaction outcome; for example, switching from the per-halogenated acid derivatives above to difluoroacetic anhydride changes the radical character (CF_2H radical) from purely electrophilic to significantly more nucleophilic.[112] The above insight into direct difluoromethylation reactivity has served as early validation of our design principles for **Phase 2** of our cross-coupling methodology, as the more nucleophilic character of the difluoromethyl radical results in preferential addition to electron-poor pyridine in solution.

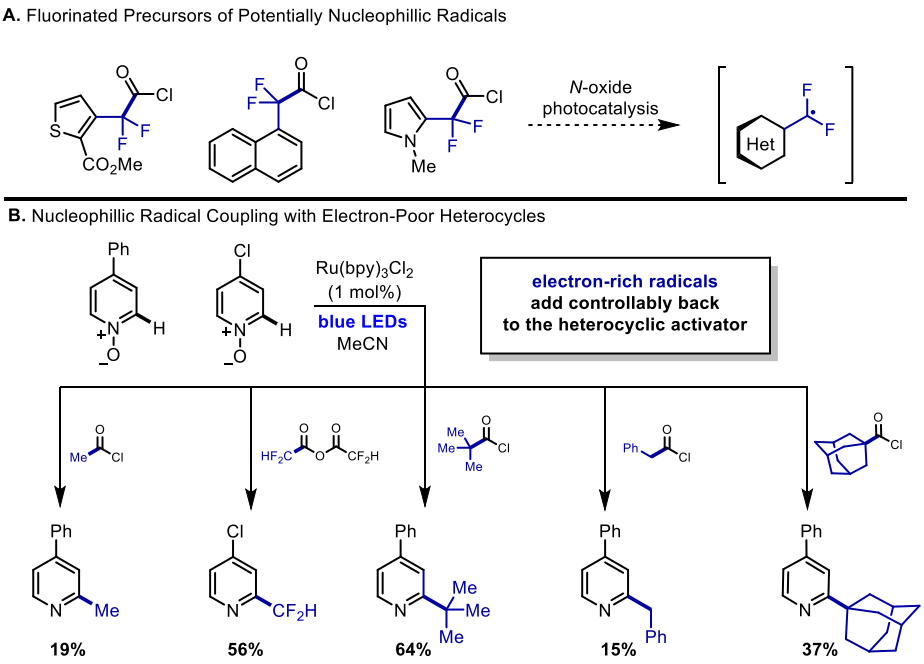

Figure 2.7. Coupling of electron-rich alkyl radicals with heteroarenes

One of the ultimate goals for this cross-coupling chemistry is to apply it to complex, high-value fluorinated acid derivatives such as outlined in **Figure 2.7A**, which may display ambiphillic radical character upon decarboxylation. In order to fully realize this goal, further understanding of reactivity for more simple systems will be needed. The decarboxylation of electron-rich acid anhydrides and chlorides through reduction of electron-poor *N*-oxides forms an electronically matched pair of reactants, which can combine and provide coupled products in a selective fashion. We have extrapolated from these results to accomplish the difluoromethylation of 4-chloropyridine *N*-oxide, where the *N*-oxide acts as both redox trigger and heterocyclic coupling partner (**Figure 2.7B**).

2.1.4 Photochemical Cross Coupling of Acid Derivatives and Heterocycles

An estimated 25% of all reactions performed in the pharmaceutical industry are cross-coupling transformations, a large portion of which are Suzuki couplings.[113] These reactions constitute the backbone of medicinal chemistry methods; however, required pre-functionalization of the starting materials—particularly the boronic acid subunit—is a step-intensive process with associated synthetic challenges and waste streams.[114] Numerous methods exist for the synthesis of boronic acid derivatives,[115] and many boronic acids are produced as (or converted to) the corresponding ester to improve chemical stability and compatibility with chromatography.[116] Associated issues include widespread difficulties in the separation of cleaved diol byproducts—particularly pinacol—from subsequent reaction mixtures.[117,118] As a consequence of these factors, a move away from the use of prefunctionalized materials is currently underway in the chemical community;[119] within this context, the prospective utility of the *N*-oxide acylation/reduction process for pharmaceutical synthesis is high, as it involves readily available starting materials and results in C–H functionalization of a corresponding heterocyclic coupling partner with few byproducts

(**Figure 2.8**). We have formally conceptualized this goal into two phases of orthogonal selectivity. The first, phase, is centered on the coupling of electron-poor radicals with electron-rich heterocycles, for which our group has demonstrated significant proof-of-principal through our trifluoromethylation methodology. Phase 2 involves the heterocyclic substrate itself acting as the coupling partner and transient redox-trigger for activation of the carboxylic acid counterpart. Through the use of this strategy, waste production is significantly decreased by minimizing synthetic operations,[8] and the mutual substrate activation through acylation limits the number of required additives for inherent reactivity. Cleaved heterocycles act as endogenous base, the reactive radical intermediates can be controlled based upon the electronics of the reagents in the system.

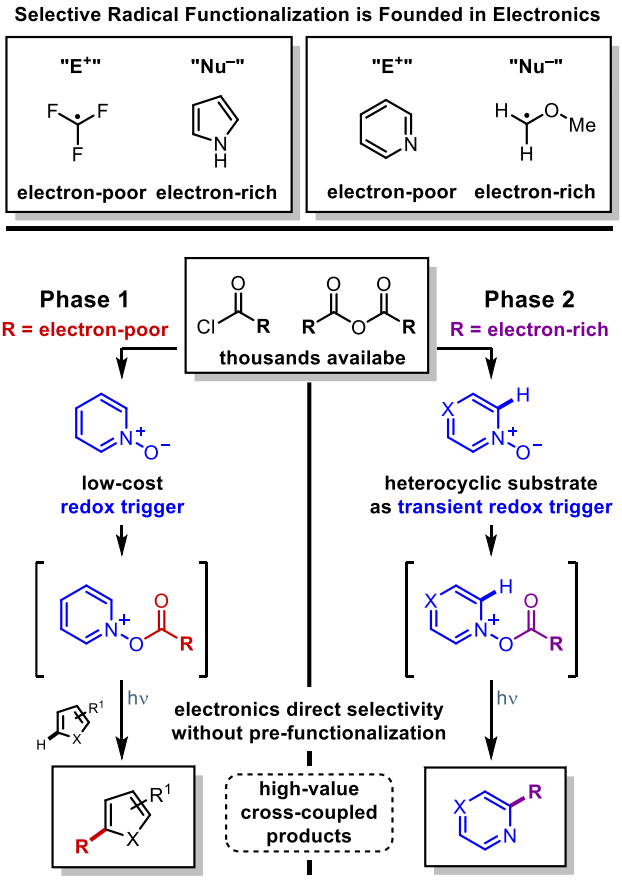

Figure 2.8. Direct, selective cross coupling strategy

We envisioned the immediate applicability of this reaction paradigm (**Figure 2.9A**) towards the design of a facile Minisci alkylation reaction. The Minisci reaction (**Figure 2.9B**), which involves the direct C–H alkylation of heteroarenes by a carbon-centered radical, has garnered much attention and undergone significant development in recent years.[120-122] Minisci's original protocol for the decarboxylative alkylation of heterocycles relied on the use of stoichiometric silver salts, persulfate oxidants, and elevated temperatures.[33a] Since this initial publication, methods for achieving the Minisci alkylation have evolved to incorporate a diverse range of alkylating agents, including trifluoroborate salts,[34a,b] sulfinates,[34c,d] and alcohols.[35a] In particular, the application of photoredox catalysis for Minisci alkylations has led to significant improvements in the sustainability of this transformation, with the development of conditions that require lower reagent loadings and non-oxidative routes for alkyl radical generation.[35]

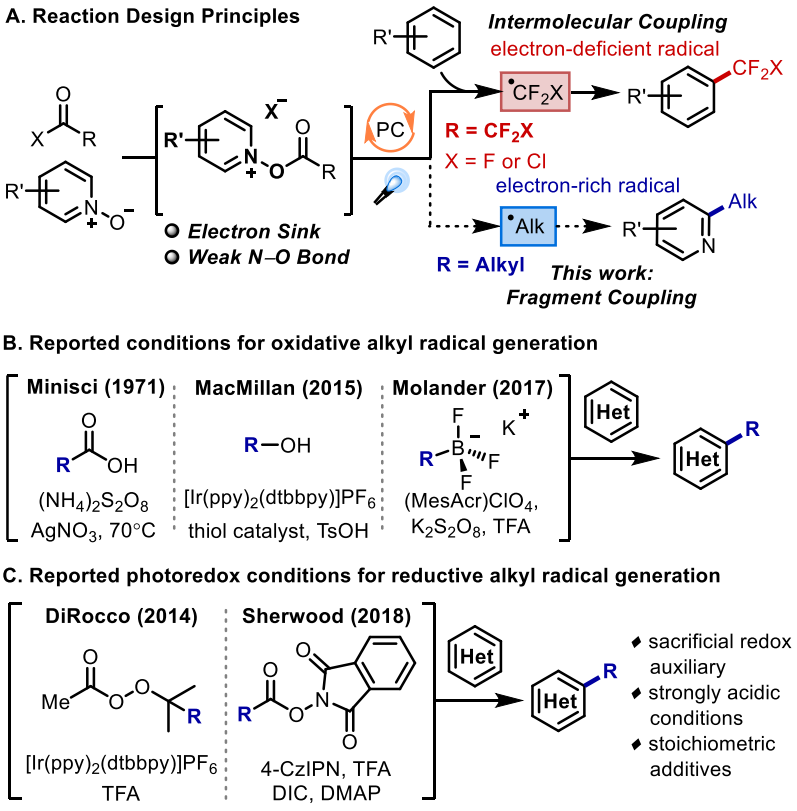

Figure 2.9. Decarboxylative alkylation reaction design principles

While a multitude of protocols have been developed for the oxidative generation of alkyl/fluoroalkyl radicals for Minisci-type transformations, methods that promote the reductive radical alkylation of *N*-heteroarenes are comparatively less established (**Figure 2.9C**).[35b,g] In the context of photoredox catalysis, the formation of alkyl radicals through a reductive pathway would enable a net redox-neutral catalytic cycle, thereby eliminating the need for a stoichiometric terminal oxidant. Notably, in 2014, DiRocco and co-workers reported the photocatalytic alkylation of *N*-heterocycles through the reductive generation of alkyl radicals using perester reagents.[35b] Recently, the groups of Sherwood and Proctor have independently demonstrated the usage of N-(acyloxy)phthalimides for the reductive decarboxylation of alkyl carboxylic acids in Minisci-type transformations.[35g,h] In comparison with previously reported Minisci alkylation methods, the decarboxylative alkylation strategy disclosed herein precludes the use of strongly acidic conditions and a sacrificial redox auxiliary. In using a fragment coupling approach, waste production can be inevitably decreased, as the mutual substrate activation through acylation avoids the use of stoichiometric additives for inherent reactivity. Reduced heterocyclic *N*-oxides can additionally act as endogenous bases, and reactive radical intermediates can be controlled based upon the electronics of reagents in the system.

2.2 Results and Discussion

Pivaloyl chloride and 4-phenylpyridine *N*-oxide were chosen as model substrates for initial pyridine alkylation evaluation. Upon screening several solvents and photocatalysts, we discovered that a combination of acetonitrile and 1 mol% $[Ir(ppy)_2(dtbbpy)]PF_6$ furnished the desired 2-*tert*-butyl-4-phenylpyridine product in 75% yield, as well as the 2,4-di-*tert*-butylated product in 5% yield (**Figure 2.10**). Under the optimized conditions, the scope of decarboxylative alkylations was examined with a number of alkyl carboxylic acid derivatives. Successful methylation (**2.8**) of 4-

phenylpyridine *N*-oxide was achieved, albeit at a lower yield (15%), due to decreased radical stability and nucleophilicity.[123] The importance of the methyl group to drug discovery is vast, as it is a feature which can improve solubility, binding, potency, and a host of other properties.[124] As a consequence, late-stage introduction of the methyl group to un-functionalized positions on a drug scaffold holds significant potential utility. Traditional methods for the Minisci decarboxylation of acetic acid require high temperatures, as well as silver and persulfate as oxidants.[125] Furthermore, the formation of unstable intermediates such as the CH_3 radical is energetically challenging.

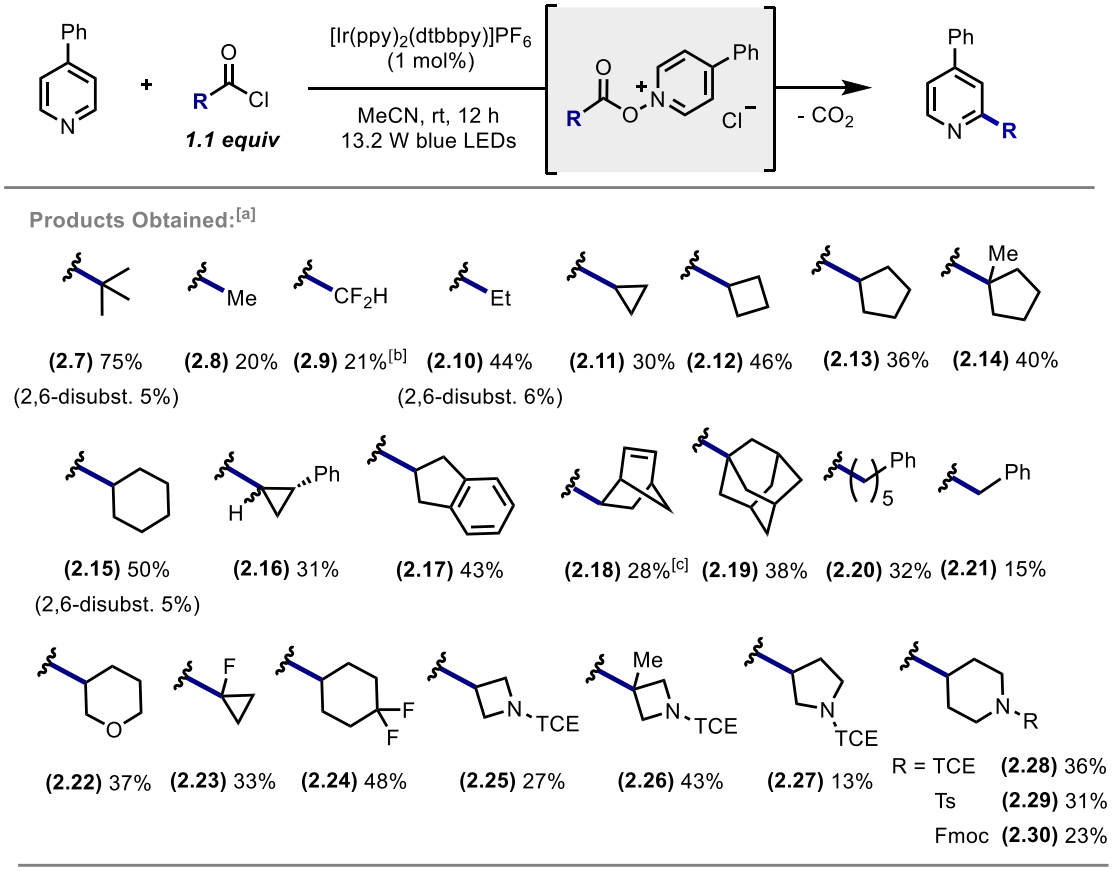

[a] Isolated yields of reactions run on a 0.8 mmol scale with 1.6 mL of acetonitrile (0.5 M) and 1.1 equiv of acid chloride; [b] Run using difluoroacetic anhydride (1.1 equiv); [c] Endo isomer obtained.

Figure 2.10. Alkyl carboxylic acid scope

Scientists at Merck recently reported the generation of such intermediates using photocatalysis *via* the reduction of *tert*-butylperacetate,[126] but to our knowledge this is the only synthetically useful

instance of CH_3 radical generation to date. Our result represents the first photochemical decarboxylation of acetyl chloride at room temperature. Difluoromethylation (**2.9**) was also achieved with the use of difluoromethylacetic anhydride as a source of the CF_2H radical. Moreover, propionic acid could be used for the ethylation (**2.10**) of 4-phenylpyridine in modest yield (50%). This protocol proved amenable to the coupling of 4-phenylpyridine with a wide range of secondary and tertiary cyclic alkanes (**2.11-2.19**), including the cyclohexyl (**2.15**) motif, which has been demonstrated to be a bioisostere of the phenyl functionality.[127] Linear alkyl chains (**2.20**) could also be successfully accessed in modest yields, along with bridged cyclic alkane motifs such as the medicinally relevant norbornene bicycle (**2.12**).[128] In contrast, the benzylation (**2.21**) of 4-phenylpyridine *N*-oxide proceeded with significantly diminished yields. A predominant side reaction that was observed involved the formal decarbonylation of phenylacetyl chloride, yielding 73% formation of benzyl chloride. Furthermore, these conditions enabled the successful appendage of medicinally-relevant fluorinated isosteres[129] onto heteroarenes, including the first example of incorporating the 1-fluorocyclopropane motif (**2.23**) onto a heterocyclic scaffold in one step from its carboxylic acid precursor. A variety of heterocyclic motifs (**2.25-2.30**) successfully underwent cross coupling with 4-phenylpyridine *N*-oxide, including the tetrahydropyranyl (**2.22**) and piperidinyl (**2.28-2.30**) ring systems, which have been used as H-bond donor/acceptor probes in SAR studies.[130] Most notably, we have demonstrated the unique coupling of a tertiary azetidine-derived radical (**2.26**) with an unactivated heteroarene, a transformation otherwise inaccessible to traditional transition metal-mediated cross-coupling methods. Overall, a variety of alkyl substrates, differing in size and electronic properties, have been demonstrated to be successful coupling partners in this transformation. An added benefit to this methodology entails the direct *in situ* formation of non-commercially available acid chloride

reagents from the corresponding carboxylic acid (via oxalyl chloride and catalytic DMF), followed by addition of the heterocyclic *N*-oxide, without the need for any additional purification or isolation steps.

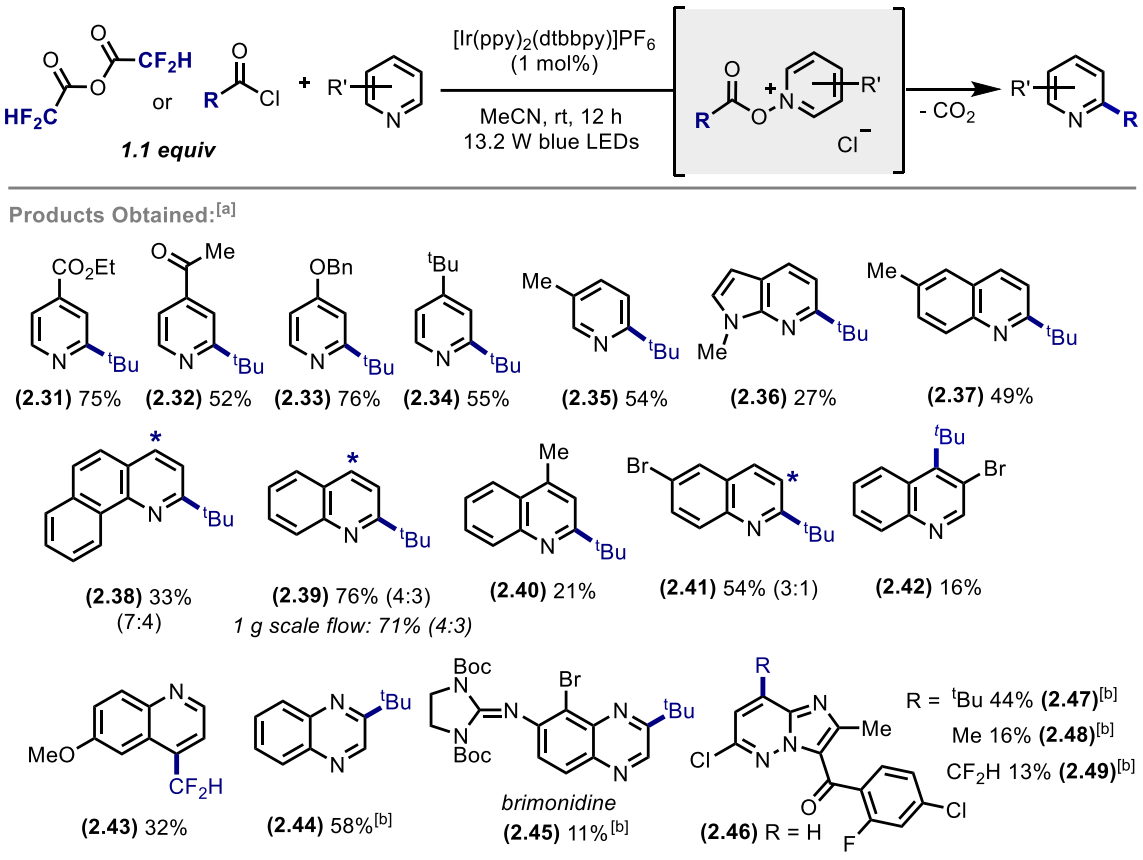

[a] Isolated yields of reactions run on a 0.8 mmol scale with 1.6 mL of acetonitrile (0.5 M) and 1.1 equiv of acid chloride or anhydride reagent; [b] Pyridine N-oxide (5 equiv) and acid chloride or anhydride reagent (5.5 equiv) were used; [c]Asterisks denote additional sites of functionalization.

Figure 2.11. Heteroarene substrate scope

In the next phase of this study, we evaluated a variety of diverse and pharmaceutically relevant heterocyclic motifs (**Figure 2.11**). The *tert*-butylation of mildly electron-deficient pyridine *N*-oxide derivatives, such as ethyl isonicotinate *N*-oxide (**2.31**), as well as 4-acetylpyridine *N*-oxide (**2.32**) proceeded in good yields (75% and 52% respectively). Additionally, our studies showed that electron-rich pyridine *N*-oxides, such as alkylated *N*-oxides and protected alcohols (**2.33-2.35**), could undergo *tert*-butylation in good to modest yields. 7-Azaindole, which can be

considered as a bioisostere of the indole and purine motifs and constitutes an essential subunit of many pharmacophores,[131] could also be functionalized regioselectivity (**2.36**) using this protocol. Quinoline *N*-oxide was successully *tert*-butylated in 76% yield, leading to a 4:3 mixture of regioisomers (**2.39**). Several quinoline *N*-oxide derivatives containing methyl, methoxy, bromo, and chloro substituents, in addition to benzoquinoline, were alkylated in modest yields (**2.37, 2.40-2.42)**. The lower yields observed in the *tert*-butylation of lepidine *N*-oxide (**2.40**) can be attributed to competing deprotonation of the methyl substituent upon generation of the acylated complex, which results in displacement of pivalic acid and precludes reductive alkyl radical generation. Furthermore, difluoromethylation of 6-methoxyquinoline (**2.43**) exclusively resulted in functionalization at the 4-position. While a variety of pyridine and quinoline-based heterocyclic scaffolds could be accessed as coupling partners, functionalization of other five- and six-membered heterocyclic *N*-oxides including benzylimidazole, quinoxaline, pyrimidine, and pyridazine *N*-oxide derivatives could not be achieved using this fragment coupling approach. As is evidenced by the significant recovery of *N*-oxide starting material, the observed lack of reactivity is suspected to be due to the diminished nucleophilicity of the *N*-oxide motif rather than inefficient radical addition.[132] *tert*-Butylation of quinoxaline did proceed successfully, however, in the presence of pyridine *N*-oxide as a redox auxiliary. Furthermore, transitioning from simple heterocyclic substrates to more complicated, biologically relevant molecular scaffolds presents further challenges as both the selective formation of the *N*-oxide functionality and the ability to predict the nucleophilicity of the *N*-oxide increase in complexity. We envisioned that the use of pyridine *N*-oxide as a sacrificial redox auxiliary would be an ideal platform for the alkylation of complex pharmacophore molecules. This concept came to fruition as subjection of brimonidine, a drug molecule used for the treatment of rosacea and open-angle glaucoma, with decarboxylative

alkylation conditions furnished the *tert*-butylated derivative in 11% yield (**2.45**). Additionally, we were able to *tert*-butylate (44% yield) the imidazopyridazine core structure (**2.47**).[133] Further diversification of the scaffold gave rise to the methylated (**2.48**) (16% yield) and difluoromethylated (**2.49**) (13% yield) analogs.

Quantum yield studies indicate that radical chain processes are operative in our system, as evidenced by a ϕ of 1.7. Finally, we have demonstrated the capability to run this decarboxylative alkylation reaction on gram scale both in batch and in flow, suggesting that this methodology may translate beyond discovery scale. Using a 900 μL flow reactor, 1 gram of quinoline N-oxide was *tert*-butylated in an overall 71% yield (relative to 68 % yield on a 1 gram scale in batch), with a residence time of 2.25 min.

2.3 Conclusion

In conclusion, we have reported an operationally simple and visible light-mediated method for the decarboxylative alkylation of heterocyclic *N*-oxides. Most significantly, this protocol offers a platform for the reductive generation of alkyl radicals without the reliance on stoichiometric additives, harsh reagents, and sacrificial redox auxiliaries. We envision this methodology to be of significant utility and practicality for the diversification of heterocyclic scaffolds in a multitude of medicinal applications.

2.4 Experimental Methods and Characterization of Compounds

2.4.1 General Information and Experimental Procedures

Chemicals were either used as received or purified according to the procedures outlined in *Purification of Common Laboratory Chemicals*. Hygroscopic *N*-oxide substrates were dried on a high vaccuum line for 6 h at ambient temperature prior to use. Pyridine N-oxide was dried on a high vacuum line at 60 °C for 12 hours. Thin-layer chromatography (TLC) analysis of reaction

mixtures was performed using Merck silica gel 60 F254 TLC plates and visualized by a dual short wave/long wave UV lamp. Column flash chromatography was performed using 230–400 mesh silica gel or via automated column chromatography.

Nuclear magnetic resonance (NMR) spectra were recorded using an internal deuterium lock on Varian MR400, Varian Inova 500 and Varian Vnmrs 700 spectrometers. Chemical shifts for ^{1}HNMR were reported as δ, parts per million, relative to the signal of $CHCl_3$ at 7.26 ppm. Chemical shifts for ^{13}CNMR were reported as δ, parts per million, relative to the center line signal of the $CDCl_3$ triplet at 77.36 ppm. Multiplicities are reported using the following abbreviations: s = singlet, d = doublet, t = triplet, q = quartet, quint = quintet, m = multiplet, br = broad resonance, dd = doublet of doublet, dt = doublet of triplet, etc. High-resolution mass spectra (ESI) were recorded at the Mass Spectrometry Facility at the Department of Chemistry of the University of Michigan in Ann Arbor, MI, on a Micromass AutoSpec Ultima Magnetic Sector mass spectrometer using electrospray ionization (ESI), positive ion mode. IR spectra were recorded on a Perkin-Elmer Spectrum BX FT-IR spectrometer fitted with an ATR accessory. Actinometry and quantum yield measurements were performed with a Fluoromax-2 fluorimeter equipped with a 150W Xe arc lamp. UV-VIS measurements were obtained on a Shimadzu UV-1601 UV-VIS Spectrometer.

LED lights and the requisite power box and cables were purchased from Creative Lighting Solutions (http://www.creativelightings.com) with the following item codes: CL-FRS5050-12WP-12V (4.4 W blue LED light strip), CL-FRS5050WPDD-5M- 12V-BL (72 W LED strip), CL-PS94670-25W (25 W power supply), CL-PS16020-150W (150 W power supply), CL-PC6FT-PCW (power cord), CL-TERMBL-5P (terminal block). A reaction performed with a 24 W CFL placed 5 cm from the vial provided identical results. Unless stated otherwise, all reactions were run on a 0.8 mmol scale in a 2 dram vial equipped with stir bar and septum. The light apparatuses

used to irradiate the reactions were constructed from test tube racks and wrapped with three 4.4 W blue LED strips. Reactions were run only in slots marked by an X in the picture below so as to keep a moderate distance from the light source (~2.5 cm). At this distance the temperature of the reactions did not exceed 35 ˚C (**Figure 2.12**).

Figure 2.12. Experimental light setup

General Experimental Procedures

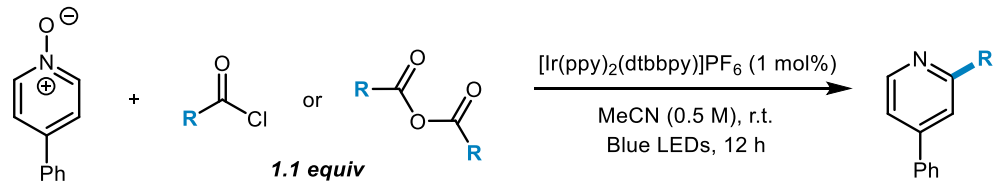

Procedure A. To a 2 dram vial equipped with a stir bar was added heterocyclic N-oxide (0.80 mmol, 1.0 equiv) and $[Ir(ppy)_2(dtbbpy)]PF_6$ (1.0 mol%). The combined materials were dissolved in MeCN (0.5 M, 1.6 mL) and stirred. Upon subsequent addition of the acid chloride or anhydride (0.88 mmol, 1.1 equiv), the resulting solution was stirred for 5 min. The vial was equipped with a screw-on cap with septum, and a 20 gauge needle was placed through the septum for the duration of the reaction. Three 4.4 W LED light strips (positioned 2.5 cm away) were turned on and the reaction was allowed to run for 12-15 hours before the light source was removed. Workup was performed by diluting the reaction with CH_2Cl_2 and washing with saturated $NaHCO_3$ (x1) and then brine (x1). The organic layer was dried over sodium sulfate before filtering and concentrating at

40 ˚C under reduced pressure. The crude residue can then be purified by column chromatography to afford the desired alkylation product(s).

Reaction Optimization: Trimethoxybenzene (0.80 mmol) was added as a stoichiometric internal standard upon completion of the reaction. A sample of the reaction was removed and diluted with $CDCl_3$ for NMR analysis.

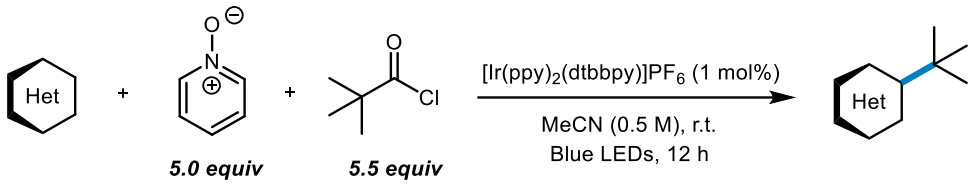

Procedure B. To a 2 dram vial equipped with a stir bar was added the heterocyclic substrate (0.8 mmol), pyridine N-oxide (1.6 mmol, 5.0 equiv), and $[Ir(ppy)_2(dtbbpy)]PF_6$ (1.0 mol%). The combined materials were dissolved in MeCN (0.5 M, 1.6 mL) and stirred. Upon subsequent addition of pivaloyl chloride (1.76 mmol, 5.5 equiv), the resulting solution was stirred for 5 min. The vial was equipped with a screw-on cap with septum, and a 25 gauge needle was placed through the septum for the duration of the reaction. Three 4.4 W LED light strips (positioned 2.5 cm away) were turned on and the reaction was allowed to run for 12-15 hours before the light source was removed. Workup was performed by diluting the reaction with CH_2Cl_2 and washing with saturated $NaHCO_3$ (x1) and then brine (x1). The organic layer was dried over sodium sulfate before filtering and concentrating at 40 ˚C under reduced pressure. The crude residue can then be purified by column chromatography to afford the desired alkylation product(s).

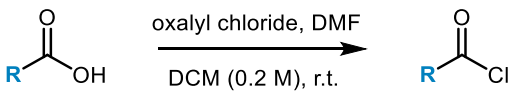

General procedure for acid chloride synthesis. To an oven-dried round bottom flask was added the carboxylic acid substrate (0.96 mmol, 1.0 equiv) and dichloromethane (0.2 M) under a nitrogen atmosphere. To the resulting stirred solution was added oxalyl chloride (1.15 mmol, 1.2

equiv) and 2 drops of DMF. The mixture was stirred at room temperature until all gas evolution ceased (generally 1-5 hours), and reaction progress was monitored by ^{1}H NMR spectroscopy. *Product decomposition may be observed if the solution is stirred for over 5 hours.* Upon reaching >99% conversion, the mixture was concentrated *in vacuo* to remove excess oxalyl chloride, and the crude acid chloride residue was used in the subsequent decarboxylation alkylation step without further purification.

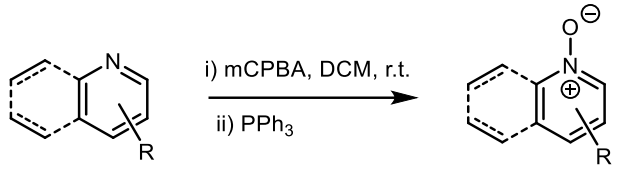

General heterocyclic *N*-oxide synthesis. This procedure was adapted from the work of Herzon and co-workers.[134] 3-Chloroperbenzoic acid (1.0 equiv, 60% w/w) was added in one portion to a solution of the heterocyclic substrate (1.0 equiv) in dichloromethane (0.2 M) at 24 °C. The reaction mixture was stirred for 12 h at 24 °C. PPh_3 (0.5 equiv) was added and the solution was stirred for another 4 h. The product mixture was concentrated to dryness and the residue obtained was purified by flash-column chromatography (eluting with ethyl acetate initially, grading to 10% methanol–ethyl acetate, linear gradient).

Equipment and Procedure for Batch and Flow Processing

A. Equipment and Setup

Figures 2.13-2.15 represent the specific equipment and setup used while performing the decarboxylative *tert*-butylation of quinoline *N*-oxide in continuous flow. This setup was used for both small (200 μmol) and large (6.9 mmol) scale reactions.

The LED assembly was obtained from Luxeon StarLEDs (Model No.: SP-02-V4, consisting of a series of seven LXML-PR02-A900 Royal Blue Luxeon Rebel ES LEDs mounted to a SinkPad-II base; http://www.luxeonstar.com/royal-blue-447.5nm-sinkpad-ii-40mm-7-led-round-led-

1030mw) and was adhered to a heat sink to dissipate heat from the LED (Luxeon, 60 mm round x 45 mm high alpha heat sink; http://www.luxeonstar.com/60mm-round-3.9-degree-cw-alpha-heat-sink). This was powered with a Costway DC power supply (Model No.: EP20570-110V), with both constant current (0-5 A) and constant voltage (0-30 V) capabilities. The light source was operated at 700 mA (unless otherwise noted); the manufacturer lists this as the optimal operating current. Material was pumped through the system with an IPC-04 Ismatec peristaltic pump (Model No.: ISM930C, 4 channel pump) with a range of 32.2 μL/min up to 3.2 mL/min. Material was flowed through Teflon PFA tubing (0.030" inner diameter, 1/16" outer diameter) which was obtained from IDEX Health & Science (Part No.: 1514L; https://www.idex-hs.com/fluidic-connections/dupontr-pfa-tubing-natural-1-16-od-x-030-id-x-50ft.html).

Figure 2.13. Continuous flow processing equipment (Left: Luxeon SP-02-V4 Royal Blue LED mounted to heat sink; Middle: Ismatec peristaltic pump; Right: Costway DC controller)

Figure 2.14 depicts the setup for the gram-scale continuous flow reaction. Beyond the peristaltic pump, the tubing was wrapped around two 18x150 mm borosilicate test tubes and secured in place with tape, generating a 900 μL internal volume reactor. Aluminum foil was taped around the tubing at the points outside of the intended irradiation window as this would define the "reaction vessel". The reaction vessel itself was suspended 1 cm above and below the two light pucks. A back pressure regulator of 20 psi (obtained from IDEX Health & Science; Part No. P-

791) was fitted in between the reactor and the collection flask to control the release of carbon dioxide after the mixture has left the reactor. Finally, the end of the tubing was threaded through a rubber septum which was fitted onto a collection flask with a 20 gauge needle for the dissipation of any pressure build-up from the generation of gaseous byproducts. During each run, a cardboard box lined with aluminum foil (not depicted) was placed over the light source and reaction vessel to minimize irradiation of the starting material vessel or the collection vessel. To get an estimate of the reaction mixture temperature, a thermometer was placed inside one of the borosilicate test tubes. As the light source tends to generate heat even when attached to the heat sink, a stream of compressed air was blown between the LEDs and the tubing to keep the temperature near room temperature. The light source was turned on at least a few minutes before each run to ensure the reaction vessel equilibrated to the steady state temperature (generally 32-35 °C).

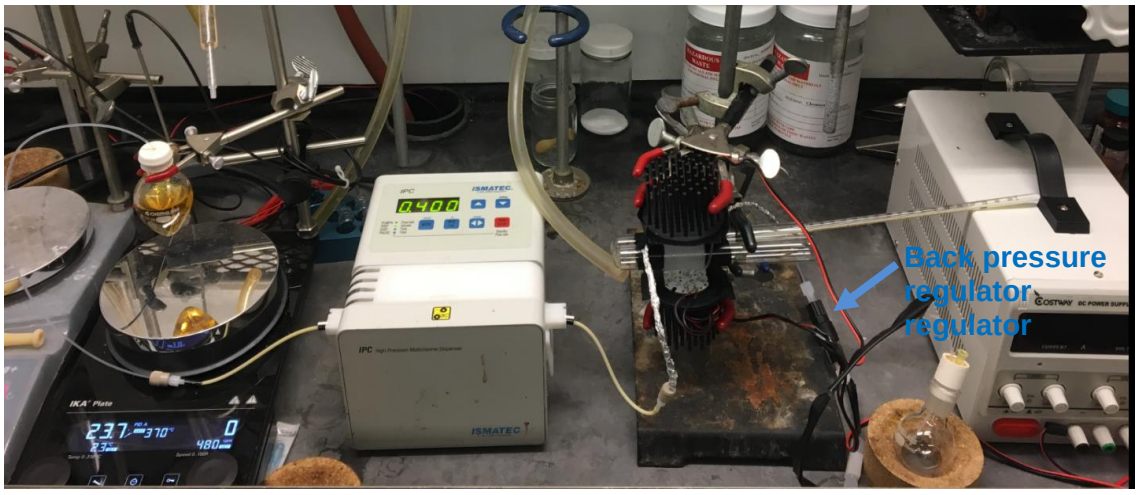

Figure 2.14. Full flow apparatus (direction of flow is from left to right)

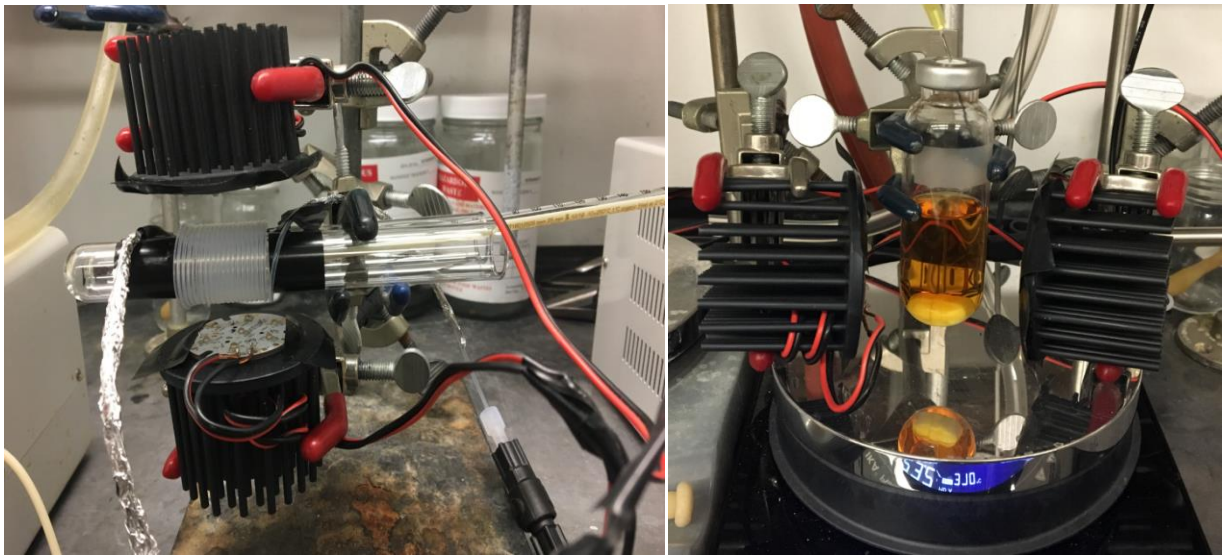

Figure 2.15. Continuous flow and batch reaction vessels (Left: Side view of continuous flow reaction vessel; Right: Gram-scale batch reaction vessel with light sources 1 cm apart on either side of vial)

For the large-scale batch reactions (ca. 1 g, 6.9 mmol of quinoline *N*-oxide), the reaction setup mimicked the flow apparatus. Thus, the reaction vessel was placed in between two light pucks (1 cm distance on each side) and cooled with a stream of compressed air (see Figure 2.15). A 20 gauge needle was inserted into the septum cap to allow for release of carbon dioxide.

B. Optimization of Flow Conditions on Small Scale (200 μmol)

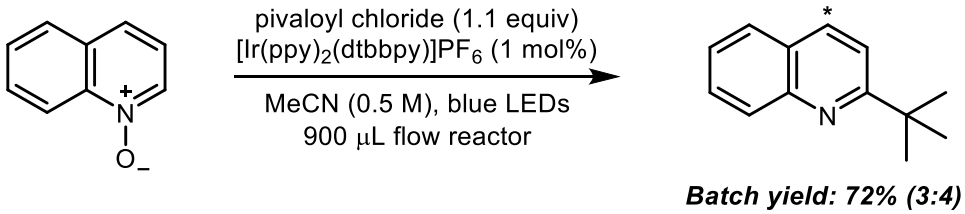

Flow rate (mL/min)	*Residence time (min)*	*^{1}H NMR yield (%)*
0.10	9.0	66 (3:4)
0.25	3.6	70 (3:4)
0.40	**2.25**	**71 (3:4)**
0.50	1.8	66 (3:4)
0.75	1.2	65 (3:4)
1.00	0.9	66 (3:4)

Figure 2.16. Optimization of continuous flow conditions on small scale

General Optimization Procedure. To a 2 dram vial equipped with a stir bar was added anhydrous quinoline N-oxide (0.20 mmol, 1.0 equiv), which had been pre-dried on a high vacuum line for 6 h at ambient temperature. Upon addition of $[Ir(ppy)_2(dtbbpy)]PF_6$ (1.0 mol%), the combined materials were dissolved in MeCN (0.5 M) and stirred. Upon subsequent addition of pivaloyl chloride (0.22 mmol, 1.1 equiv), the resulting solution was stirred for 5 min. The vial was equipped with a septum, through which the reactor tubing had been threaded. The reaction mixture was then flowed through the flow apparatus (see Section A) at various flow rates (see **Figure 2.16**). Trimethoxybenzene (0.20 mmol) was added as a stoichiometric internal standard upon completion of the reaction. A sample of the reaction was removed and diluted with $CDCl_3$ for ^1H NMR analysis.

C. Gram-scale Flow and Batch Reactions

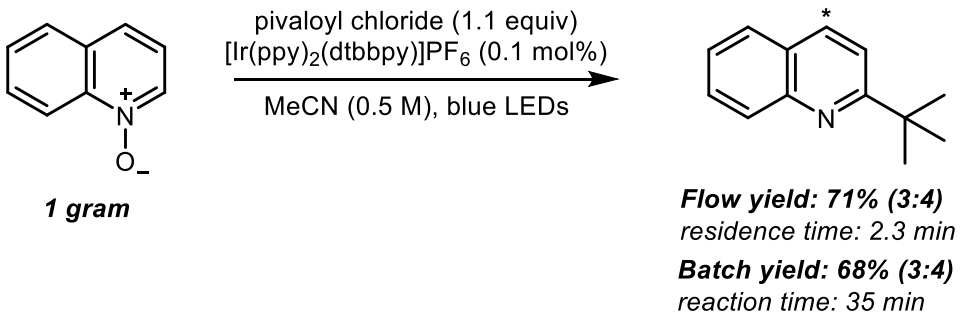

1 gram

Flow yield: 71% (3:4)
residence time: 2.3 min
Batch yield: 68% (3:4)
reaction time: 35 min

General Gram-Scale Flow Procedure. To a 2 dram vial equipped with a stir bar was added anhydrous quinoline N-oxide (6.9 mmol, 1.0 g), which had been pre-dried on a high vacuum line for 6 h at ambient temperature. Upon addition of $[Ir(ppy)_2(dtbbpy)]PF_6$ (0.1 mol%), the combined materials were dissolved in MeCN (0.5 M) and stirred. Pivaloyl chloride (7.59 mmol, 1.1 equiv) was added and the resulting solution was stirred for 5 min. The vial was equipped with a septum, through which the reactor tubing had been threaded. The reaction mixture was then flowed through the flow apparatus (see Section A) at a flow rate of 400 μL/min, providing a residence time of 2.3

min. Workup was performed by diluting the reaction with CH_2Cl_2 and washing with saturated $NaHCO_3$ (x1) and then brine (x1). The organic layer was dried over sodium sulfate before filtering and concentrating at 40 ˚C under reduced pressure. The crude residue was then purified by column chromatography (gradient of 10% ethyl acetate/hexanes to 20% ethyl acetate/hexanes) to afford a 3:4 mixture of 2-*tert*-butyl quinoline and 4-*tert*-butyl quinoline (overall yield: 0.91 g, 71%).

General Gram-Scale Batch Procedure. To a 20 mL microwave vial equipped with a stir bar was added anhydrous quinoline N-oxide (6.9 mmol, 1.0 g), which had been pre-dried on a high vacuum line for 6 h at ambient temperature. Upon addition of $[Ir(ppy)_2(dtbbpy)]PF_6$ (0.1 mol%), the combined materials were dissolved in MeCN (0.5 M) and stirred. Pivaloyl chloride (7.59 mmol, 1.1 equiv) was added and the resulting solution was stirred for 5 min. The vial was sealed with a septum cap, through which was inserted a 20 gauge needle. The reaction mixture was stirred and irradiated for 35 min. Upon completion of the reaction, workup was performed by diluting the reaction with CH_2Cl_2 and washing with saturated $NaHCO_3$ (x1) and then brine (x1). The organic layer was dried over sodium sulfate before filtering and concentrating at 40 ˚C under reduced pressure. The crude residue was then purified by column chromatography (gradient of 10% ethyl acetate/hexanes to 20% ethyl acetate/hexanes) to afford a 3:4 mixture of 2-*tert*-butyl quinoline and 4-*tert*-butyl quinoline (overall yield: 0.87 g, 68%).

2.4.2 Reaction Optimization Data

Preliminary Optimization Data

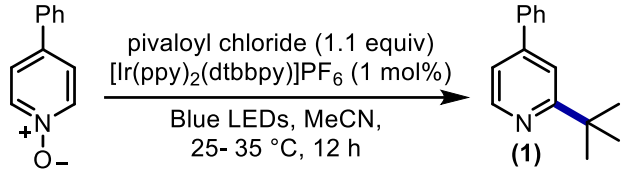

Entry[a]	Alteration from standard	Yield (%)[b]
1	**None**	**71%, 75%[c]**
2	$Ru(bpy)_3(PF_6)_2$	57%
3	$Ir(ppy)_3$	23%
4	$[Ir(dF(CF_3)ppy)_2(dtbbpy)]PF_6$	67%
5	DCM as solvent	57%
6	DMF as solvent	70%
7	0.1 mol% $[Ir(ppy)_2(dttbpy)]PF_6$	60%
8	0.08 M concentration	64%
9	2.0 equiv. pivaloyl chloride	65%

[a] Reactions run on a 0.4 mmol scale with 1.1 equiv of pivaloyl chloride, using 13.2 W blue LEDs. [b] Determined by ^1H NMR spectroscopy with trimethoxybenzene as the internal standard. [c] Isolated yield.

Additional Control Reactions

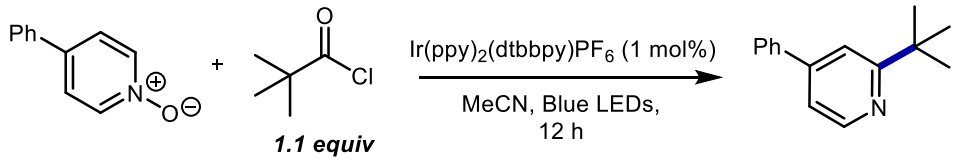

Entry[a]	Alteration from standard	Yield (%)[b]
1	reaction time: 15 min	71
2	pre-sparged reaction with N_2	71
3	No LED lights	0
4	No photocatalyst	0
5	0.25 M concentration	70

[a] Reactions run on a 0.4 mmol scale with 1.1 equiv of pivaloyl chloride, using 13.2 W blue LEDs. [b] Determined by ^1H NMR spectroscopy with trimethoxybenzene as the internal standard.

Lewis Acid Additive Screens

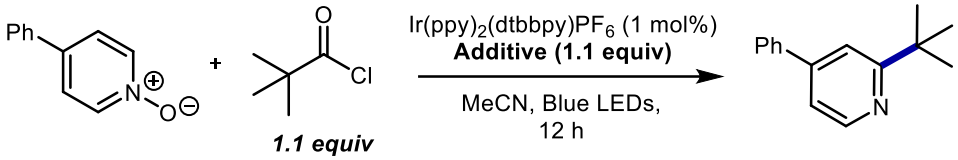

Entry[a]	Additive (1.1 equiv)	Yield (%)[b]
1	$BF_3 \bullet OEt_2$	<10
2	$B(OH)_3$	42
3	TMSCl	62
4	LiCl	64
5	HCl in dioxane	3

[a] Reactions run on a 0.4 mmol scale with 1.1 equiv of pivaloyl chloride, using 13.2 W blue LEDs. [b] Determined by ^{1}H NMR spectroscopy with trimethoxybenzene as the internal standard.

Additional Solvent Screens

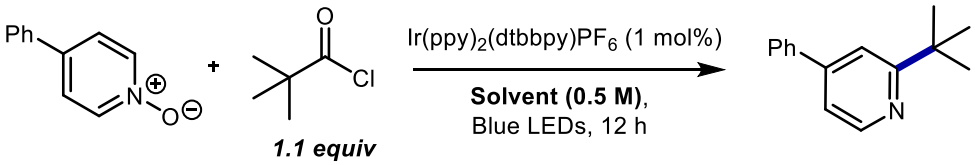

Entry[a]	Solvent (0.5 M)	Yield (%)[b]
1	$MeNO_2$	66
2	DMA	15
3	Chloroform	<10
4	DME	6
5	*t*-Amyl alcohol	33
6	MeCN/DME (1:1)	53
7	$MeNO_2$/DME (1:1)	12
8	MeCN/*t*-BuOH (1:1)	51
9	$MeNO_2$/*t*-BuOH (1:1)	15
10	MeCN/CyOH (1:1)	52
11	$MeNO_2$/CyOH (1:1)	0

[a] Reactions run on a 0.4 mmol scale with 1.1 equiv of pivaloyl chloride, using 13.2 W blue LEDs. [b] Determined by ^{1}H NMR spectroscopy with trimethoxybenzene as the internal standard.

2.4.3 Electrochemical Measurements

As discussed in a previous report[135] by our group, the measurement of reduction potentials for the acylonium salts reported in this manuscript cannot be accurately performed through cyclic voltammetry analysis. The observed signal using cyclic voltammetry is found to have variations in shape and peak potential from run to run, and the peak shape is dependent upon sweep rate. Therefore, differential pulse voltammetry (DPV) was performed to obtain the reduction potentials of the various pyridine N-oxide/acid chloride combinations, and reproducible potentials were obtained through these methods. Measurements were performed with a model CHI660C multi-potentiostat from CH Instruments. DPV pulse parameters were selected based on previous reported methods from our group in measuring reduction potentials for acylated pyridine *N*-oxides.[135] Measurements were performed with a glassy carbon working electrode, Pt auxiliary electrode, Ag/AgCl reference electrode, Bu_4NPF_6 electrolyte (0.1 M in MeCN), and analyte (pyridine-N-oxide/pivaloyl chloride, 1:1, 0.01 M) with the following settings: Incr E (V) = 0.001, Amplitude (V) = 0.005, Pulse Width (sec) = 0.05, Sampling Width (sec) = 0.01, Pulse Period (sec) = 0.5, Quiet Time (sec) = 2, Sensitivity (A/V) = 1 e^{-5}. All voltammograms are reported/displayed after conversion to voltage vs. SCE, where:

$$V_{SCE} = V_{Ag/AgCl} - 0.05\ V$$

Onset potentials are estimated based on the intersection of the baseline and onset slope (shown):

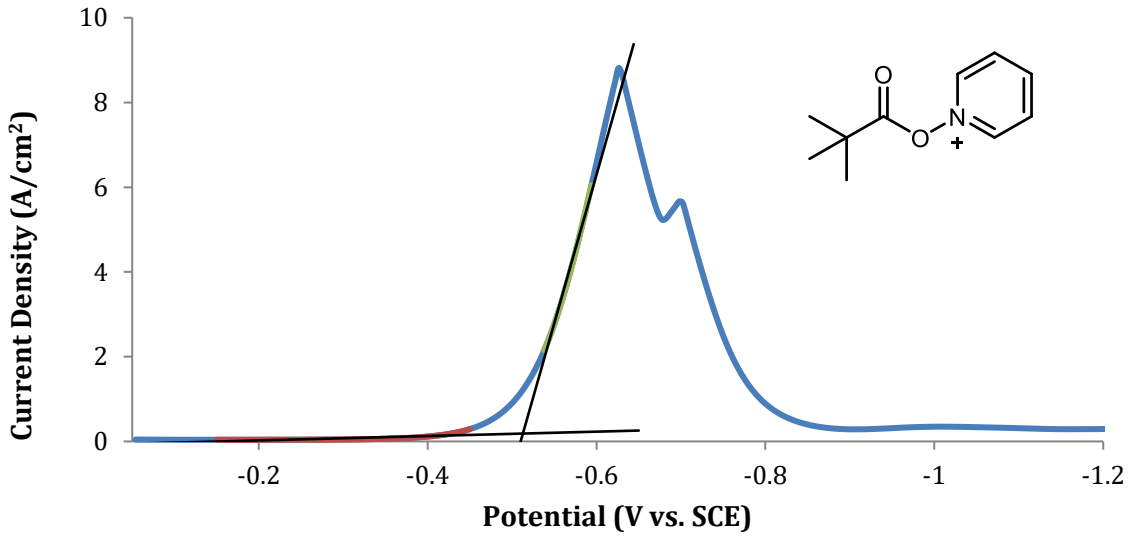

Figure 2.17. DPV of the pivaloyl chloride/pyridine *N*-oxide adduct. Onset reduction potential is observed at –0.51 V vs. SCE. Peak reduction potential is observed at –0.63 V vs. SCE.

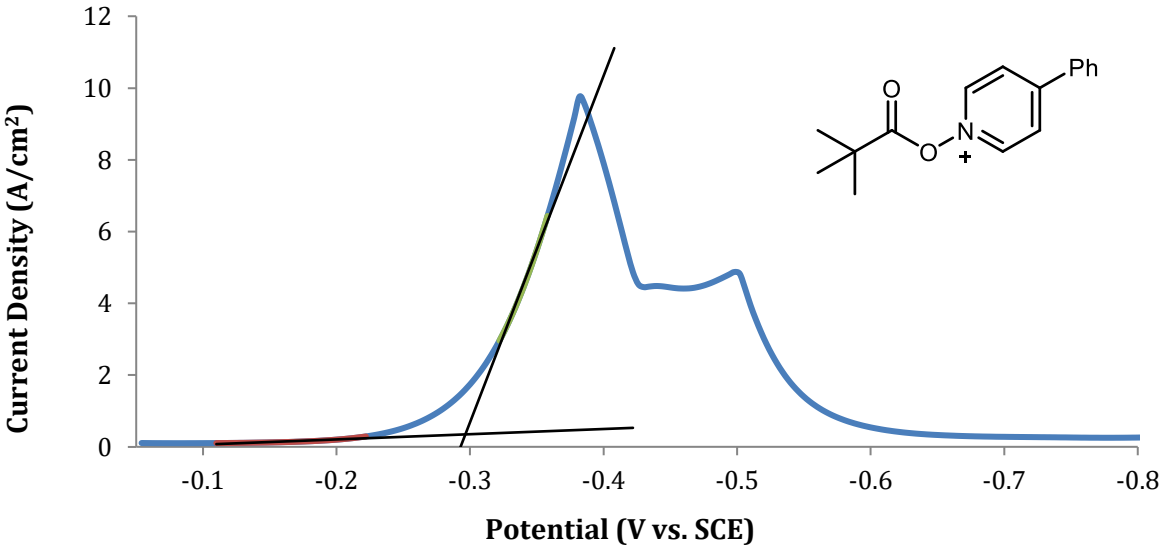

Figure 2.18. DPV of the pivaloyl chloride/4-phenylpyridine *N*-oxide adduct. Onset reduction potential is observed at –0.29 V vs. SCE. Peak reduction potential is observed at –0.38 V vs. SCE.

2.4.4 Quantum Yield Measurements

This experiment closely followed the procedure reported by Cismesia and Yoon.[22] The only modification was the use of a 0.1 cm path length cuvette for the UV/Vis data during the calculation of the photon flux, a modification made during recent investigations into our photochemical radical trifluoromethylation chemistry.[48]

The light source employed was a 150 W Xenon Arc lamp within a Fluoromax-2 Fluorimeter. UV/Vis data was collected on a Shimadzu UV-1601 UV-Vis Spectrometer. The photon flux of this specific fluorimeter had previously been determined within the group to be 5.46×10^{-9} einstein/s at 436 nm (1 einstein = 1 mol photons). The experiment was repeated as is detailed in the Supplementary Information of our recent report[48] to obtain a photon flux of 5.55×10^{-9} einstein/s at 436 nm; this value was used in the following calculations. Specific details for the experimental determination of the quantum yield for the *tert*-butylation of quinoline *N*-oxide are provided below:

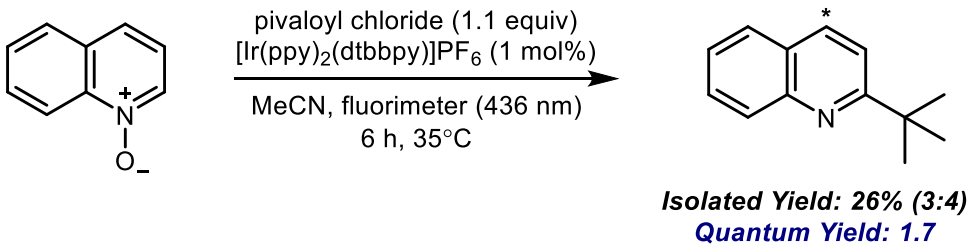

Isolated Yield: 26% (3:4)
Quantum Yield: 1.7

Procedure for Quantum Yield Calculation. In a dark room, anhydrous quinoline N-oxide (0.8 mmol) was added to a dry quartz cuvette (1 cm path length) equipped with a stir bar. Upon addition of $[Ir(ppy)_2(dtbbpy)]PF_6$ (1 mol%), the combined materials were dissolved in MeCN (2 mL) and stirred. Pivaloyl chloride (0.88 mmol) was added and the resulting solution was capped, sealed, and stirred for 5 min. Light exclusion was achieved by wrapping the cuvette in aluminum foil until the reaction was placed in the fluorimeter. The sample holder was pre-equilibrated to 35 °C,

and the reaction sample was allowed to equilibrate to this temperature over 10 minutes. The sample was stirred and irradiated at 436 nm with a 10 nm slit width for 21600 (6 h). After irradiation, workup was performed by diluting the reaction with CH_2Cl_2 and washing with saturated $NaHCO_3$ (x1) and then brine (x1). The organic layer was dried over sodium sulfate before filtering and concentrating at 40 ˚C under reduced pressure. The crude residue was then purified by column chromatography (gradient of 10% ethyl acetate/hexanes to 20% ethyl acetate/hexanes) to afford a 3:4 mixture of 2-*tert*-butylquinoline and 4-*tert*-butylquinoline, with an overall yield of 26% (0.204 mmol).

The quantum yield was calculated as follows (**Equations 1 and 2**), where flux = photon flux; t = time of irradiation (s); f = fraction of light absorbed = $1 - 10^{-A}$, where A = absorbance. As seen in the aforementioned reports, the absorbance of the system is substantial (>3), leading to an f value of approximately 1. For the purposes of this calculation, f is assumed to be equal to 1, implying that all light was absorbed.

$$\text{Quantum Yield} = \Phi = \frac{\text{mol product}}{\text{flux} \cdot t \cdot f} \qquad (1)$$

$$\Phi = \frac{204\ \mu\text{mol}}{(5.55\text{x}10^{-9}\ \text{mol photons/s}\cdot\text{cm}^2) \cdot (21600\ \text{s}) \cdot (1)} = 1.7 \qquad (2)$$

2.4.5 Preparation and Characterization of Substrates and Products

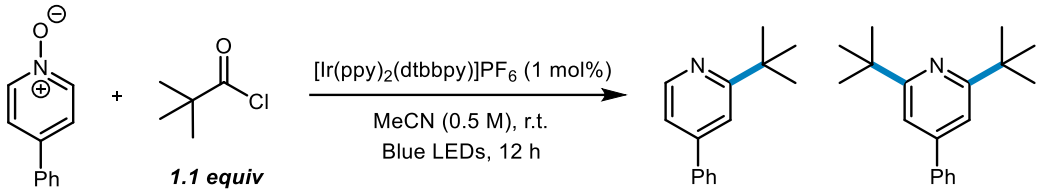

2-*tert*-butyl-4-phenylpyridine (2.7a) and 2,6-di-*tert*-butyl-4-phenylpyridine (2.7b)

The reaction was run according to General Procedure A and was purified by column chromatography (0% to 15% ethyl acetate in hexanes) to afford 2-*tert*-butyl-4-phenylpyridine (118 mg, 71%) and 2,6-di-*tert*-butyl-4-phenylpyridine (6 mg, 3%) as colorless oils. In addition, 4-phenylpyridine (19 mg, 15%) was recovered. The acquired ^{1}H and ^{13}CNMR spectra were identical to those reported in the literature.[136]

2-*tert*-butyl-4-phenylpyridine (2.7a): R_f = 0.75 (ethyl acetate/hexanes 1:4; UV). ^{1}HNMR ($CDCl_3$, 700 MHz): δ 8.61 (d, *J* = 5.1 Hz, 1H), 7.63 (d, *J* = 7.3 Hz, 2H), 7.54 (s, 1H), 7.48 (t, *J* = 7.6 Hz, 2H), 7.43 (t, *J* = 7.3 Hz, 1H), 7.30 (dd, *J* = 5.0, 1.5 Hz, 1H), 1.43 (s, 9H). ^{13}C NMR (176 MHz, $CDCl_3$): δ 170.13, 149.33, 148.95, 139.42, 129.31, 129.03, 127.41, 119.19, 117.52, 37.82, 30.58. HRMS (ESI) m/z $[M + H]^+$ calcd for: $C_{15}H_{17}N$: 212.1434; found: 212.1435.

2,6-di-*tert*-butyl-4-phenylpyridine (2.7b): R_f = 0.88 (ethyl acetate/hexanes 1:4; UV). ^{1}HNMR ($CDCl_3$, 700 MHz): δ 7.64 – 7.59 (m, 2H), 7.47 (t, *J* = 7.7 Hz, 2H), 7.41 (d, *J* = 7.2 Hz, 1H), 7.29 (s, 2H), 1.40 (s, 18H). ^{13}C NMR (176 MHz, $CDCl_3$): δ 168.46, 149.01, 140.74, 129.19, 128.60, 127.61, 114.17, 38.10, 30.58. HRMS (ESI) m/z $[M + H]^+$ calcd for: $C_{19}H_{25}N$: 268.2060; found: 268.2061. IR (neat): v = 2953, 2901, 2864, 1594, 1552, 1498, 1477, 1458, 1400, 1359, 1254, 1167, 1139, 1081.

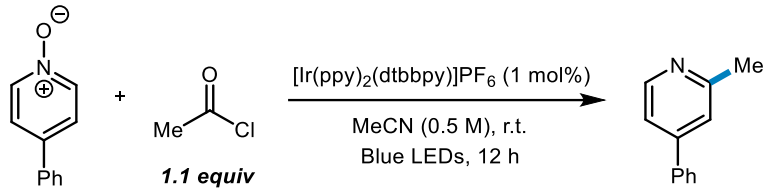

2-methyl-4-phenylpyridine (2.8)

The reaction was run according to General Procedure A and was purified by column chromatography (0% to 15% ethyl acetate in hexanes) to afford the title compound (27 mg, 20 %) in a mixture with 4-phenylpyridine (76 mg, 61%). Rf = 0.25 (ethyl acetate/hexanes 1:4; UV). ^{1}H NMR (700 MHz, $CDCl_3$) δ 8.66 (d, *J* = 5.3 Hz, 2H), **8.54 (d, *J* = 5.1 Hz, 1H)**, 7.66 – 7.59 (m, *J* = 12.2, 7.8 Hz, 4H), **7.53 – 7.39 (m, 9H)**, **7.37 (s, 1H)**, **7.31 (d, *J* = 5.1 Hz, 1H)**, **2.62 (s, 3H)**. ^{13}C NMR (176 MHz, $CDCl_3$) δ **158.82**, 150.23, **149.54**, 148.69, **148.32**, 138.42, **138.12**, 129.10, 129.04, **129.02**, **128.88**, 126.99, **126.98**, 121.63, **121.20**, **118.86**, **24.57**. HRMS (ESI) m/z [M + H]$^+$ calcd for: $C_{12}H_{11}N$: 170.0964; found: 170.0963. The acquired ^{1}H and ^{13}CNMR spectral data corresponding to the mono-methylated product were identical to those reported in the literature.[137]

Note: 2-methyl-4-phenylpyridine and 4-phenylpyridine were inseparable by column chromatography and recrystallization. Attempts to selectivity oxidize 4-phenylpyridine using mCBPA at low temperatures of 0°C and facilitate the isolation of the methylated product were alos unsuccessful.

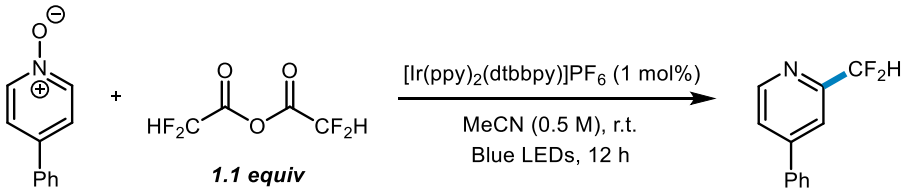

2-difluoromethyl-4-phenylpyridine (2.9)

The reaction was run according to General Procedure A and was purified by column chromatography (0% to 15% ethyl acetate in hexanes) to afford the title compound (34 mg, 21%) as a pale yellow oil and 4-phenylpyridine (78 mg, 63%). R_f = 0.69 (ethyl acetate/hexanes 1:4; UV). ^{1}H NMR (700 MHz, $CDCl_3$) δ 8.70 (d, *J* = 5.1 Hz, 1H), 7.86 (s, 1H), 7.71 – 7.59 (m, 3H), 7.57 – 7.46 (m, 3H), 6.70 (t, *J* = 55.5 Hz, 1H). ^{13}C NMR (176 MHz, $CDCl_3$) δ 153.76 (t, *J* = 25.5 Hz), 150.34, 150.31, 137.73, 129.93, 129.62, 127.43, 123.62, 118.41, 114.37 (t, *J* = 240.5 Hz). ^{19}F NMR (377 MHz, $CDCl_3$) δ -115.86 (d, *J* = 55.5 Hz). HRMS (ESI) m/z $[M + H]^+$ calcd for: $C_{12}H_9F_2N$: 206.0776; found: 206.0778. IR (neat): v = 3034, 1603, 1551, 1450, 1412, 1373, 1206, 1123, 1034.

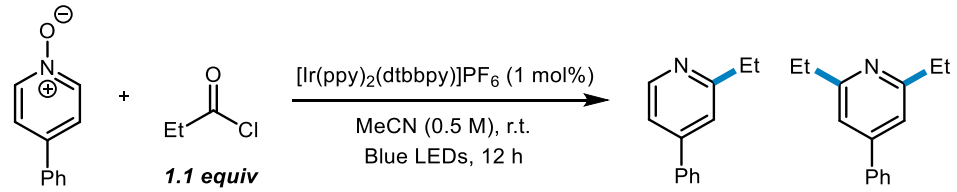

2-ethyl-4-phenylpyridine and 2,6-diethyl-4-phenylpyridine (2.10)

The reaction was run according to General Procedure A and was purified by column chromatography (0% to 15% ethyl acetate in hexanes) to afford 2-ethyl-4-phenylpyridine (65 mg, 44%) and 2,6-diethyl-4-phenylpyridine (10 mg, 6%) as colorless oils and 4-phenylpyridine (41 mg, 33%).

2-ethyl-4-phenylpyridine: R_f = 0.38 (ethyl acetate/hexanes 1:4; UV). ^{1}H NMR (700 MHz, $CDCl_3$) δ 8.57 (d, *J* = 5.1 Hz, 1H), 7.63 (d, *J* = 8.0 Hz, 2H), 7.48 (t, *J* = 7.5 Hz, 2H), 7.43 (t, *J* = 7.3 Hz, 1H), 7.38 (s, 1H), 7.32 (d, *J* = 5.1 Hz, 1H), 2.89 (q, *J* = 7.6 Hz, 2H), 1.36 (t, *J* = 7.6 Hz, 3H). ^{13}C NMR (176 MHz, $CDCl_3$) δ 164.36, 149.96, 149.16, 138.96, 129.37, 129.20, 127.39, 120.38, 119.42, 31.87, 14.35. HRMS (ESI) m/z $[M + H]^+$ calcd for: $C_{13}H_{13}N$: 184.1121; found: 184.1121. The acquired ^{1}H and ^{13} CNMR spectra were identical to those reported in the literature.[138]

2,6-diethyl-4-phenylpyridine: R_f = 0.57 (ethyl acetate/hexanes 1:4; UV). ^{1}H NMR (500 MHz, $CDCl_3$) δ 7.63 (d, *J* = 7.3 Hz, 2H), 7.49 – 7.41 (m, 3H), 7.19 (s, 2H), 2.87 (q, *J* = 7.6 Hz, 4H), 1.34 (t, *J* = 7.6 Hz, 6H). ^{13}C NMR (126 MHz, $CDCl_3$) δ 163.82, 149.59, 139.49, 129.28, 128.98, 127.43, 117.58, 31.98, 14.66. HRMS (ESI) m/z $[M + H]^+$ calcd for: $C_{15}H_{17}N$: 211.1361; found: 211.1353. IR (neat): v = 3060, 2966, 2925, 2850, 1698, 1598, 1554, 1498, 1461, 1406, 1197.

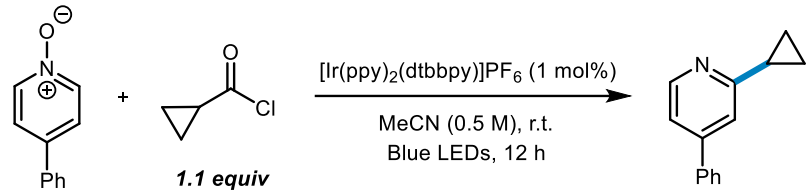

2-cyclopropyl-4-phenylpyridine (2.11)

The reaction was run according to General Procedure A and was purified by column chromatography (0% to 15% ethyl acetate in hexanes) to afford the title compound (47 mg, 30%) as a pale yellow oil and 4-phenylpyridine (50 mg, 40%). R_f = 0.68 (ethyl acetate/hexanes 1:4; UV). ^{1}HNMR ($CDCl_3$, 700 MHz): δ 8.48 (d, *J* = 5.1 Hz, 1H), 7.62 (d, *J* = 7.4 Hz, 2H), 7.47 (t, *J* = 7.6 Hz, 2H), 7.42 (t, *J* = 7.3 Hz, 1H), 7.34 (s, 1H), 7.24 (dd, *J* = 5.1, 1.6 Hz, 1H), 2.13 – 2.06 (m, 1H), 1.11 – 1.06 (m, 2H), 1.02 (ddd, *J* = 10.9, 6.6, 4.0 Hz, 2H). ^{13}C NMR (176 MHz, $CDCl_3$): δ 163.63, 149.98, 148.60, 138.95, 129.31, 129.12, 127.33, 119.65, 118.93, 17.63, 10.15. HRMS (ESI) m/z $[M + H]^+$ calcd for: $C_{14}H_{13}N$: 196.1121; found: 196.1121. The acquired ^{1}H and ^{13}CNMR spectra were identical to those reported in the literature.[139]

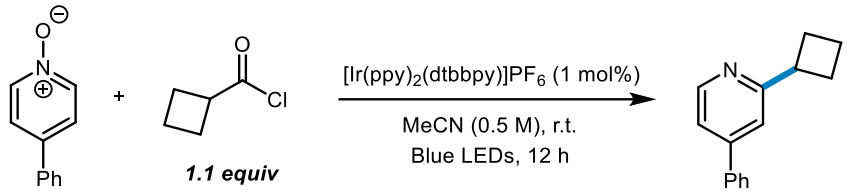

2-cyclobutyl-4-phenylpyridine (2.12)

The reaction was run according to General Procedure A and was purified by column chromatography (0% to 15% ethyl acetate in hexanes) to afford the title compound (70 mg, 42%) as a pale yellow oil and 4-phenylpyridine (43 mg, 35%). R_f = 0.62 (ethyl acetate/hexanes 1:4; UV). ^{1}H NMR (700 MHz, $CDCl_3$): δ 8.61 (d, *J* = 5.1 Hz, 1H), 7.63 (d, *J* = 7.5 Hz, 2H), 7.48 (t, *J* = 7.5 Hz, 2H), 7.43 (dd, *J* = 8.0, 6.5 Hz, 1H), 7.36 (s, 1H), 7.31 (d, *J* = 5.1 Hz, 1H), 3.74 (p, *J* = 8.8 Hz, 1H), 2.44 – 2.35 (m, 4H), 2.14 – 2.03 (m, 1H), 1.98 – 1.87 (m, 1H). ^{13}C NMR (176 MHz, $CDCl_3$) δ 165.52, 149.96, 148.92, 139.00, 129.32, 129.13, 127.35, 119.39, 119.26, 42.47, 28.78, 18.59. HRMS (ESI) m/z $[M + H]^+$ calcd for: $C_{15}H_{15}N$: 210.1277; found: 210.1279. IR (neat): v = 2935, 2864, 1594, 1545, 1499, 1472, 1399, 1243, 1182.

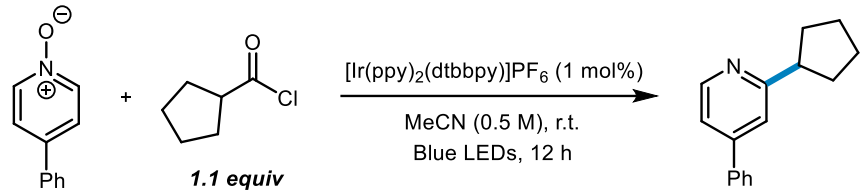

2-cyclopentyl-4-phenylpyridine (2.13)

The reaction was run according to General Procedure A and was purified by column chromatography (0% to 15% ethyl acetate in hexanes) to afford the title compound (70 mg, 39%) as a colorless oil and 4-phenylpyridine (50 mg, 40%). R_f = 0.68 (ethyl acetate/hexanes 1:4; UV). ^{1}H NMR (700 MHz, $CDCl_3$): δ 8.58 (d, *J* = 5.1 Hz, 1H), 7.63 (d, *J* = 7.5 Hz, 2H), 7.48 (t, *J* = 7.5 Hz, 2H), 7.43 (t, *J* = 7.3 Hz, 1H), 7.39 (s, 1H), 7.30 (d, *J* = 5.0 Hz, 1H), 3.30 – 3.18 (m, 1H), 2.17 – 2.08 (m, 2H), 1.90 – 1.80 (m, 4H), 1.73 – 1.70 (m, 2H). ^{13}C NMR (176 MHz, $CDCl_3$): δ 166.50, 149.91, 148.91, 139.07, 129.32, 129.10, 127.36, 120.04, 119.42, 48.43, 33.91, 26.19. HRMS (ESI) m/z $[M + H]^+$ calcd for: $C_{16}H_{17}N$: 224.1434; found: 224.1436. IR (neat): v = 2947, 2865, 1594, 1546, 1499, 1472, 1448, 1398, 1343, 1298, 1184.

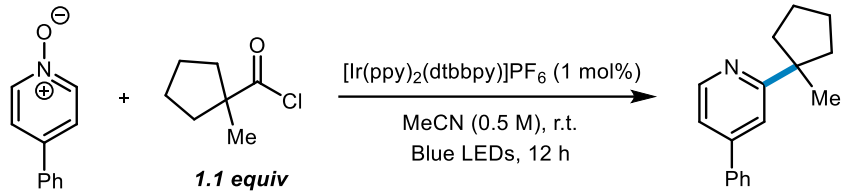

2-(1-methylcyclohexyl)-4-phenylpyridine (2.14)

The reaction was run according to General Procedure A and was purified by column chromatography (0% to 15% ethyl acetate in hexanes) to afford the title compound (81 mg, 40%) as a pale yellow oil and 4-phenylpyridine (59 mg, 47%). R_f = 0.71 (ethyl acetate/hexanes 1:4; UV). ^{1}HNMR ($CDCl_3$, 700 MHz): δ 8.64 (d, *J* = 5.0 Hz, 1H), 7.65 – 7.61 (m, 2H), 7.53 (s, 1H), 7.49 (dd, *J* = 10.5, 4.7 Hz, 2H), 7.43 (t, *J* = 7.4 Hz, 1H), 7.29 (dd, *J* = 5.1, 1.6 Hz, 1H), 2.25 (d, *J* = 9.9 Hz, 2H), 1.64 – 1.59 (m, 4H), 1.48 – 1.42 (m, 4H), 1.28 (s, 3H). ^{13}C NMR (176 MHz, $CDCl_3$): δ 169.39, 149.59, 148.89, 139.52, 129.32, 129.01, 127.44, 119.02, 118.57, 41.24, 37.62, 37.54, 26.65, 23.15. HRMS (ESI) m/z $[M + H]^+$ calcd for: $C_{17}H_{19}N$: 252.1751; found: 252.1752. IR (neat): v = 2922, 2853, 1592, 1547, 1496, 1469, 1445, 1390, 1350.

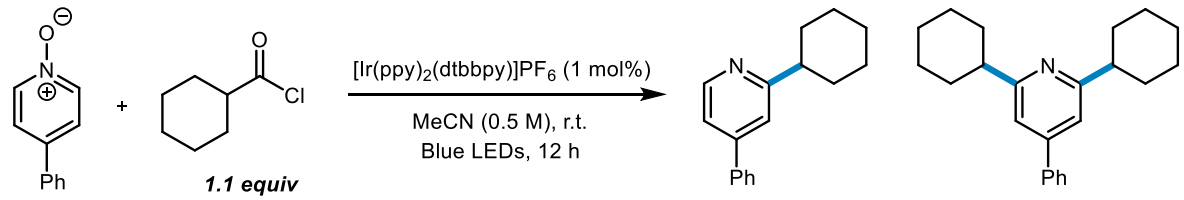

2-cyclohexyl-4-phenylpyridine and 2,6-dicyclohexyl-4-phenylpyridine (2.15)

The reaction was run according to General Procedure A and was purified by column chromatography (0% to 15% ethyl acetate in hexanes) to afford 2-cyclohexyl-4-phenylpyridine (94 mg, 50%) and 2,6-dicyclohexyl-4-phenylpyridine (10 mg, 5%) as colorless oils. In addition, 4-phenylpyridine (13 mg, 10%) was recovered. The acquired ^{1}H and ^{13} CNMR spectra were identical to those reported in the literature.[140]

2-cyclohexyl-4-phenylpyridine: R_f = 0.38 (ethyl acetate/hexanes 1:4; UV). ^{1}H NMR (700 MHz, $CDCl_3$): δ 8.57 (d, *J* = 5.1 Hz, 1H), 7.63 (dd, *J* = 5.2, 3.3 Hz, 2H), 7.48 (dd, *J* = 10.3, 4.7 Hz, 2H), 7.45 – 7.40 (m, 1H), 7.36 (s, 1H), 7.31 (dd, *J* = 5.1, 1.7 Hz, 1H), 2.77 (tt, *J* = 12.0, 3.4 Hz, 1H), 2.00 (dd, *J* = 13.5, 1.6 Hz, 2H), 1.91 – 1.84 (m, 2H), 1.80 – 1.73 (m, 1H), 1.59 (qd, *J* = 12.7, 3.3 Hz, 2H), 1.44 (qt, *J* = 13.0, 3.4 Hz, 2H), 1.36 – 1.27 (m, 1H). ^{13}C NMR (176 MHz, $CDCl_3$): δ 167.31, 149.77, 149.07, 139.07, 129.28, 129.08, 127.33, 119.47, 119.35, 47.01, 33.30, 26.93, 26.40. HRMS (ESI) m/z $[M + H]^+$ calcd for: $C_{17}H_{19}N$: 238.1590; found: 238.1592.

2,6-dicyclohexyl-4-phenylpyridine: R_f = 0.75 (ethyl acetate/hexanes 1:4; UV). ^{1}HNMR ($CDCl_3$, 700 MHz): δ 7.64 – 7.59 (m, 2H), 7.46 (t, *J* = 7.6 Hz, 2H), 7.40 (t, *J* = 7.4 Hz, 1H), 7.16 (s, 2H), 2.75 (tt, *J* = 11.9, 3.4 Hz, 2H), 2.02 – 2.01 (m, 4H), 1.88 – 1.83 (m, 4H), 1.78 – 1.74 (m, 2H), 1.54 (ddd, *J* = 24.8, 12.7, 3.1 Hz, 4H), 1.48 – 1.41 (m, 4H), 1.33 – 1.27 (m, 2H). ^{13}C NMR (176 MHz, $CDCl_3$): δ 166.60, 149.34, 139.98, 129.22, 128.81, 127.48, 116.33, 47.12, 33.56, 27.00, 26.56. HRMS (ESI) m/z $[M + H]^+$ calcd for: $C_{23}H_{29}N$: 320.2373; found: 320.2377. IR (neat): v = 3059, 2921, 2849, 1726, 1595, 1551, 1498, 1448, 1407, 1172.

4-phenyl-2-(2-phenylcyclopropyl)pyridine (2.16)

The reaction was run according to General Procedure A and was purified by column chromatography (0% to 15% ethyl acetate in hexanes) to afford the title compound (67 mg, 31%) as a yellow oil and 4-phenylpyridine (51 mg, 41%). R_f = 0.50 (ethyl acetate/hexanes 1:4; UV). ^{1}HNMR ($CDCl_3$, 700 MHz): δ 8.54 (d, *J* = 5.1 Hz, 1H), 7.65 – 7.60 (m, 2H), 7.47 (t, *J* = 7.5 Hz, 2H), 7.45 – 7.39 (m, 2H), 7.32 – 7.27 (m, 3H), 7.21 – 7.17 (m, 3H), 2.62 – 2.55 (m, 1H), 2.38 – 2.33 (m, 1H), 1.86 – 1.81 (m, 1H), 1.51 (ddd, *J* = 8.6, 6.0, 4.8 Hz, 1H). ^{13}C NMR (176 MHz, $CDCl_3$): δ 161.95, 150.17, 148.69, 142.62, 138.80, 129.37, 129.22, 128.73, 127.35, 126.23, 126.17, 120.40, 119.20, 29.99, 28.52, 19.27. HRMS (ESI) m/z $[M + H]^+$ calcd for: $C_{20}H_{17}N$: 272.1438; found: 272.1437. IR (neat): v = 3025, 1949, 1594, 1545, 1496, 1473, 1457, 1415, 1371, 1191, 1076.

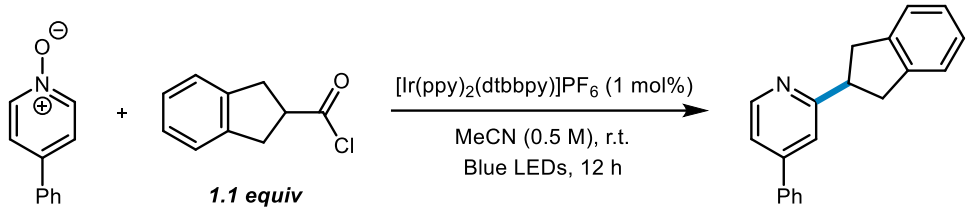

2-(2,3-dihydro-1H-inden-2-yl)-4-phenylpyridine (2.17)

The reaction was run according to General Procedure A and was purified by column chromatography (0% to 15% ethyl acetate in hexanes) to afford the title compound (93 mg, 43%) as a pale yellow solid and 4-phenylpyridine (44 mg, 35%). R_f = 0.50 (ethyl acetate/hexanes 1:4; UV). ^{1}HNMR ($CDCl_3$, 500 MHz): δ 8.62 (d, *J* = 5.1 Hz, 1H), 7.62 (d, *J* = 8.0 Hz, 2H), 7.50 – 7.45 (m, 3H), 7.43 (t, *J* = 7.3 Hz, 1H), 7.36 (dd, *J* = 5.1, 1.5 Hz, 1H), 7.28 – 7.26 (m, 2H), 7.21 – 7.17 (m, 2H), 3.95 (p, *J* = 8.8 Hz, 1H), 3.43 (dd, *J* = 15.7, 8.5 Hz, 2H), 3.35 (dd, *J* = 15.7, 9.1 Hz, 2H). ^{13}C NMR (176 MHz, $CDCl_3$): δ 165.14, 149.96, 149.16, 143.03, 138.84, 129.36, 129.23, 127.35, 126.78, 124.66, 119.96, 119.83, 47.85, 40.06. HRMS (ESI) m/z $[M + H]^+$ calcd for: $C_{20}H_{17}N$: 272.1437; found: 272.1434. IR (neat): v = 3036, 3019, 1596, 1543, 1471, 1401.

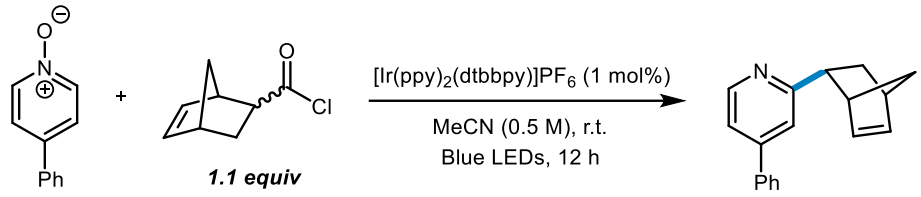

2-(bicyclo[2.2.1]hept-5-en-2-yl)-4-phenylpyridine (2.18)

The reaction was run according to General Procedure A and was purified by column chromatography (0% to 15% ethyl acetate in hexanes) to afford the title compound (55 mg, 28%) as a colorless oil and 4-phenylpyridine (59 mg, 48%). R_f = 0.53 (ethyl acetate/hexanes 1:4; UV). ^{1}HNMR ($CDCl_3$, 700 MHz): δ 8.58 (d, *J* = 5.1 Hz, 1H), 7.63 (d, *J* = 7.8 Hz, 2H), 7.48 (t, *J* = 7.5 Hz, 2H), 7.45 – 7.42 (m, 2H), 7.32 – 7.29 (m, 1H), 6.28 (dd, *J* = 5.4, 3.0 Hz, 1H), 6.22 (dd, *J* = 5.3, 2.8 Hz, 1H), 3.03 (d, *J* = 10.9 Hz, 2H), 2.90 (dd, *J* = 8.7, 4.5 Hz, 1H), 2.14 (dt, *J* = 11.7, 4.0 Hz, 1H), 1.81 (d, *J* = 8.3 Hz, 1H), 1.65 – 1.61 (m, 1H), 1.42 (d, *J* = 8.2 Hz, 1H). ^{13}C NMR (176 MHz, $CDCl_3$): δ 165.98, 149.71, 148.88, 139.11, 138.38, 137.33, 129.37, 129.16, 127.41, 120.92, 119.36, 49.03, 46.70, 46.00, 42.66, 32.59. HRMS (ESI) m/z $[M + H]^+$ calcd for: $C_{18}H_{17}N$: 248.1437; found: 248.1436. IR (neat): v = 3057, 2937, 2864, 1787, 1594, 1544, 1497, 1470, 1397, 1342, 1303, 1254, 1173.

2D NMR Data

- COSY, HSQC, HMBC, and NOESY experiments were employed to assign various resonances and confirm the structure of the resultant *endo*-product.

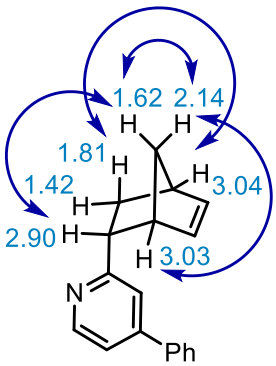

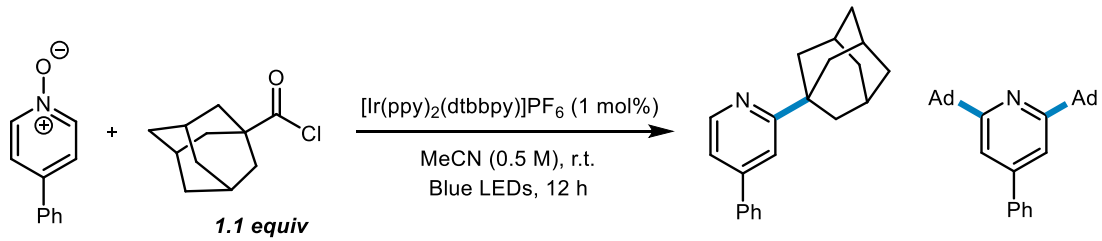

2-adamantyl-4-phenylpyridine and 2,6-diadamantyl-4-phenylpyridine (2.19)

The reaction was run according to General Procedure A and was purified by column chromatography (0% to 15% ethyl acetate in hexanes) to afford 2-adamantyl-4-phenylpyridine (97 mg, 42%) and 2,6-diadamantyl-4-phenylpyridine (41 mg, 12%) as white solids. In addition, 4-phenylpyridine (43 mg, 10%) was recovered.

2-adamantyl-4-phenylpyridine: R_f = 0.50 (ethyl acetate/hexanes 1:4; UV). ^{1}HNMR ($CDCl_3$, 700 MHz): δ 8.63 (d, *J* = 5.0 Hz, 1H), 7.63 (d, *J* = 7.3 Hz, 2H), 7.48 (dd, *J* = 9.2, 5.8 Hz, 3H), 7.42 (t, *J* = 7.3 Hz, 1H), 7.30 (dd, *J* = 5.0, 1.5 Hz, 1H), 2.14 (s, 3H), 2.07 (d, *J* = 2.2 Hz, 6H), 1.82 (d, *J* = 12.8 Hz, 6H). ^{13}C NMR (176 MHz, $CDCl_3$): δ 169.91, 149.50, 148.98, 139.50, 129.30, 129.01, 127.42, 119.25, 117.38, 42.32, 39.40, 37.15, 29.15. HRMS (ESI) m/z $[M + H]^+$ calcd for: $C_{21}H_{23}N$: 290.1903; found: 290.1905. IR (neat): v = 3056, 2899, 2846, 1591, 1547, 1467, 1450, 1392, 1320, 1101.

2,6-diadamantyl-4-phenylpyridine: R_f = 0.78 (ethyl acetate/hexanes 1:4; UV). ^{1}HNMR ($CDCl_3$, 700 MHz): δ 7.61 (d, *J* = 7.9 Hz, 2H), 7.45 (t, *J* = 7.6 Hz, 2H), 7.39 (t, *J* = 7.3 Hz, 1H), 7.21 (s, 2H), 2.13 (d, *J* = 19.2 Hz, 6H), 2.06 (d, *J* = 1.8 Hz, 12H), 1.79 (d, *J* = 12.1 Hz, 12H). ^{13}C NMR (176 MHz, $CDCl_3$): δ 168.29, 148.94, 140.84, 129.14, 128.51, 127.59, 114.09, 42.41, 39.70, 37.39, 29.31. HRMS (ESI) m/z $[M + H]^+$ calcd for: $C_{31}H_{37}N$: 424.2999; found: 424.2999. IR (neat): v = 3057, 2899, 2847, 1592, 1549, 1495, 1449, 1402, 1342, 1314, 1100.

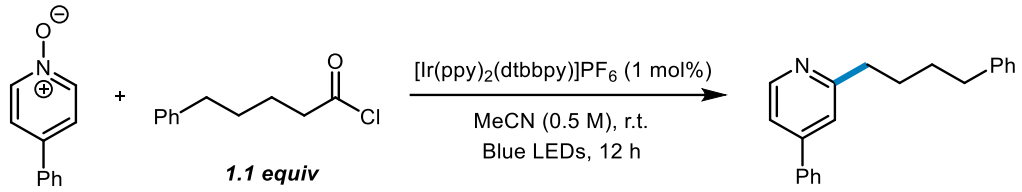

4-phenyl-2-(4-phenylbutyl)pyridine (2.20)

The reaction was run according to General Procedure A and was purified by column chromatography (0% to 15% ethyl acetate in hexanes) to afford the title compound (64 mg, 28%) as a pale yellow oil and 4-phenylpyridine (51 mg, 41%). R_f = 0.39 (ethyl acetate/hexanes 1:4; UV). ^{1}HNMR ($CDCl_3$, 500 MHz): δ 8.57 (d, *J* = 5.1 Hz, 1H), 7.62 (d, *J* = 7.3 Hz, 2H), 7.51 – 7.39 (m, 3H), 7.36 – 7.29 (m, 2H), 7.34 – 7.26 (m, 2H), 7.20 – 7.14 (m, 3H), 2.88 (t, *J* = 7.7 Hz, 2H), 2.67 (t, *J* = 7.6 Hz, 2H), 1.88 – 1.78 (m, 2H), 1.76 – 1.70 (m, 2H). ^{13}C NMR (126 MHz, $CDCl_3$): δ 162.94, 149.89, 149.12, 142.81, 138.80, 129.35, 129.22, 128.74, 128.59, 127.36, 125.98, 121.02, 119.46, 38.63, 36.14, 31.54, 29.91. HRMS (ESI) m/z $[M + H]^+$ calcd for: $C_{21}H_{21}N$: 288.1747; found: 288.1746. IR (neat): v = 3024, 2926, 2855, 1596, 1546, 1495, 1473, 1452, 1399.

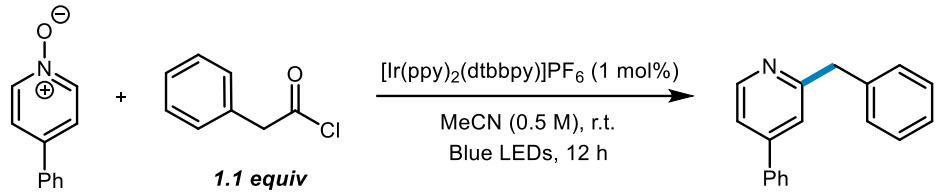

2-benzyl-4-phenylpyridine (2.21)

The reaction was run according to General Procedure A and was purified by column chromatography (0% to 15% ethyl acetate in hexanes) to afford the title compound (29 mg, 15%) as a pale yellow oil and 4-phenylpyridine (91 mg, 73%). R_f = 0.42 (ethyl acetate/hexanes 1:4; UV). ^{1}HNMR ($CDCl_3$, 500 MHz): δ 8.60 (d, *J* = 5.5 Hz, 1H), 7.57 (d, *J* = 7.1 Hz, 2H), 7.44 (dt, *J* = 14.0, 7.0 Hz, 3H), 7.34 - 7.31 (m, 6H), 7.23 (dd, *J* = 8.5, 4.3 Hz, 1H), 4.22 (s, 2H). ^{13}C NMR (126 MHz, $CDCl_3$): δ 161.80, 150.11, 149.37, 139.81, 138.72, 129.45, 129.36, 129.27, 128.96, 127.37, 126.76, 121.44, 119.76, 45.14. HRMS (ESI) m/z $[M + H]^+$ calcd for: $C_{18}H_{15}N$: 246.1277; found: 246.1279. The acquired ^{1}H and ^{13} CNMR spectra were identical to those reported in the literature.[54]

4-phenyl-2-(tetrahydro-2H-pyran-4-yl)pyridine (2.22)

The reaction was run according to General Procedure A and was purified by column chromatography (0% to 15% ethyl acetate in hexanes) to afford the title compound (71 mg, 37%) as a colorless oil and 4-phenylpyridine (55 mg, 44%). R_f = 0.64 (ethyl acetate/hexanes 1:4; UV). ^{1}H NMR (500 MHz, Chloroform-*d*) δ 8.59 (d, *J* = 5.1 Hz, 1H), 7.63 (dd, *J* = 7.4, 1.7 Hz, 2H), 7.52 – 7.41 (m, 3H), 7.38 (s, 1H), 7.35 (dd, *J* = 5.1, 1.7 Hz, 1H), 4.12 (dt, *J* = 11.3, 3.0 Hz, 2H), 3.58 (td, *J* = 11.4, 3.0 Hz, 2H), 3.02 (td, *J* = 11.1, 5.5 Hz, 1H), 2.02 – 1.92 (m, 4H). ^{13}C NMR (126 MHz, $CDCl_3$) δ 164.89, 149.65, 149.04, 138.55, 129.05, 128.93, 127.02, 119.61, 118.83, 68.14, 43.57, 32.53. HRMS (ESI) m/z $[M + H]^+$ calcd for: $C_{16}H_{17}NO$: 240.1383; found: 240.1384. IR (neat): v = 2947, 2839, 1937, 1594, 1546, 1472, 1443, 1384, 1357, 1237, 1124, 1084.

2-(1-fluorocyclopropyl)-4-phenylpyridine (2.23)

The reaction was run according to General Procedure A and was purified by column chromatography (0% to 15% ethyl acetate in hexanes) to afford the title compound (56 mg, 33%) as a colorless oil and 4-phenylpyridine (66 mg, 52%). R_f = 0.63 (ethyl acetate/hexanes 1:4; UV). ^{1}H NMR (500 MHz, $CDCl_3$) δ 8.51 (d, *J* = 5.1 Hz, 1H), 7.85 (s, 1H), 7.71 – 7.66 (m, 2H), 7.52 – 7.42 (m, 3H), 7.35 (dd, *J* = 5.2, 1.7 Hz, 1H), 1.54 – 1.47 (m, 4H). ^{13}C NMR (126 MHz, $CDCl_3$) δ 160.03, 159.83, 149.56, 148.77, 138.33, 129.05, 127.09, 119.56, 116.76, 80.29 (d, *J* = 214.1 Hz), 15.50, 15.41. ^{19}F NMR (470 MHz, $CDCl_3$) δ -193.55 (s). HRMS (ESI) m/z $[M + H]^+$ calcd for: $C_{14}H_{12}FN$: 214.1027; found: 214.1025. IR (neat): v = 3086, 3011, 2925, 1594, 1552, 1501, 1473, 1436, 1339, 1302, 1248, 1142, 1105.

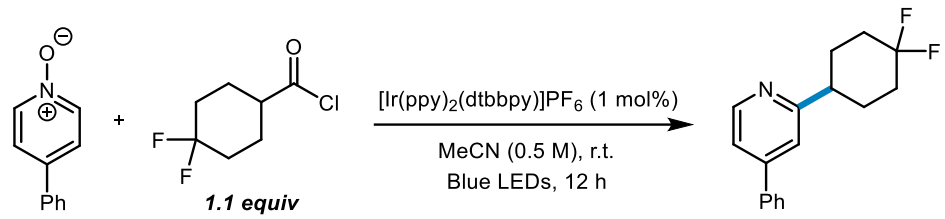

2-(4,4-difluorocyclohexyl)-4-phenylpyridine (2.24)

The reaction was run according to General Procedure A and was purified by column chromatography (0% to 15% ethyl acetate in hexanes) to afford the title compound (105 mg, 48%) as a colorless oil and 4-phenylpyridine (38 mg, 31%). R_f = 0.69 (ethyl acetate/hexanes 1:4; UV). ^{1}H NMR (500 MHz, Chloroform-*d*) δ 8.58 (d, *J* = 5.1 Hz, 1H), 7.62 (d, *J* = 7.5 Hz, 2H), 7.46 (dt, *J* = 24.1, 7.3 Hz, 3H), 7.40 – 7.32 (m, 2H), 2.90 – 2.85 (m, 1H), 2.31 – 2.18 (m, 2H), 2.14 – 2.04 (m, 2H), 2.04 – 1.92 (m, 3H), 1.90 – 1.84 (m, 1H). ^{13}C NMR (126 MHz, $CDCl_3$) δ 164.40, 149.60, 149.12, 138.42, 129.70, 128.99, 127.02, 123.13 (dd, *J* = 242.3, 239.7 Hz), 119.75, 118.88, 44.35, 33.77 (dd, *J* = 25.6, 22.8 Hz), 28.86 (d, *J* = 9.8 Hz). ^{19}F NMR (470 MHz, $CDCl_3$) δ -91.79 (d, *J* = 235.9 Hz), -101.70 (d, *J* = 236.5 Hz). HRMS (ESI) m/z $[M + H]^+$ calcd for: $C_{17}H_{17}F_2N$: 274.1402; found: 274.1400. IR (neat): v = 2936, 1723, 1595, 1547, 1472, 1447, 1372, 1269, 1097.

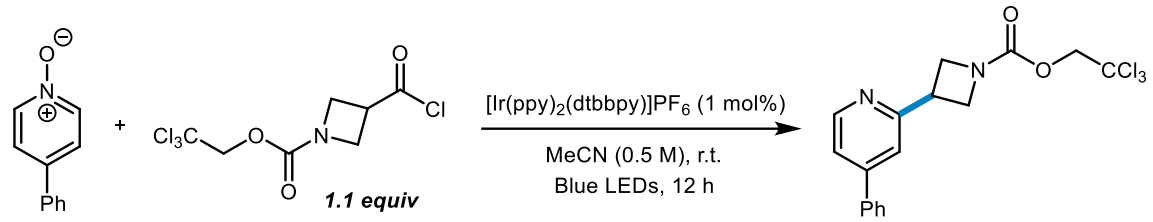

2,2,2-trichloroethyl 3-(4-phenylpyridin-2-yl)azetidine-1-carboxylate (2.25)

The reaction was run according to General Procedure A and was purified by column chromatography (20% to 50% ethyl acetate in hexanes) to afford the title compound (83 mg, 27%) as a colorless oil and 4-phenylpyridine (60 mg, 48%). R_f = 0.53 (ethyl acetate/hexanes 1:1; UV). ^{1}H NMR (500 MHz, Chloroform-*d*) δ 8.67 (d, *J* = 5.0 Hz, 1H), 7.62 (d, *J* = 7.0 Hz, 2H), 7.52 – 7.43 (m, 3H), 7.43 – 7.39 (m, 2H), 4.84 – 4.63 (m, 2H), 4.56 – 4.34 (m, 4H), 4.05 (tt, *J* = 8.8, 6.3 Hz, 1H). ^{13}C NMR (126 MHz, $CDCl_3$) δ 160.52, 154.35, 150.31, 149.23, 138.00, 129.19, 129.14, 127.00, 120.31, 119.89, 95.67, 74.55, 55.56, 54.91, 35.66. HRMS (ESI) m/z $[M + H]^+$ calcd for: $C_{17}H_{15}Cl_3N_2O_2$: 385.0272; found: 385.0274. IR (neat): v = 2951, 2884, 1718, 1596, 1547, 1401, 1349, 1126, 1059.

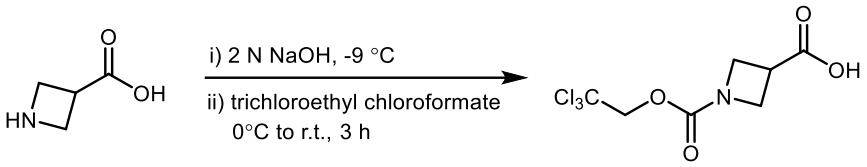

1-((2,2,2-trichloroethoxy)carbonyl)azetidine-3-carboxylic acid

Azetidine-3-carboxylic acid (1 g, 10 mmol) was placed in a round bottom flask equipped with a magnetic stir bar, dissolved in 15 mL of 2.0 N aqueous NaOH solution, and cooled to -10 ºC. 2,2,2-Trichloroethyl chloroformate (1.4 mL, 11 mmol) was then added dropwise to the stirred solution at 0 ºC. The mixture was stirred for 1 h at 0 ºC and an additional 2 h at r.t. After the reaction, the mixture was extracted with diethyl ether (3 x 10 mL) and the aqueous phase was acidified to pH 2 with 2 N HCl. The aqueous phase was extracted with ethyl acetate (4 x 20 mL), and the combined ethyl acetate extracts were washed with brine, dried with Na_2SO_4, and concentrated to yield the desired product (2.4 g, 87%) as a white solid. ^{1}H NMR (700 MHz, Chloroform-*d*) δ 10.63 (s, 1H), 4.71 (d, *J* = 11.4 Hz, 2H), 4.31 (d, *J* = 34.4 Hz, 4H), 3.51 (p, *J* = 7.5 Hz, 1H). ^{13}C NMR (176 MHz, $CDCl_3$) δ 176.67, 153.46, 94.73, 73.96, 51.15 (d, *J* = 111.6 Hz), 31.79. HRMS (ESI) m/z $[M + H]^+$ calcd for: $C_7H_8Cl_3NO_4$: 275.9592; found: 275.9597. IR (neat): v = 2967, 2901, 2632, 1724, 1699, 1425, 1413, 1338, 1279, 1235, 1126.

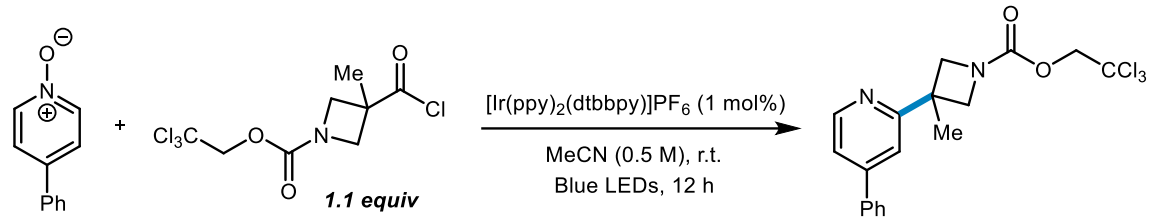

2,2,2-trichloroethyl 3-methyl-3-(4-phenylpyridin-2-yl)azetidine-1-carboxylate (2.26)

The reaction was run according to General Procedure A and was purified by column chromatography (20% to 50% ethyl acetate in hexanes) to afford the title compound (138 mg, 43%) as a colorless oil and 4-phenylpyridine (50 mg, 40%). R_f = 0.57 (ethyl acetate/hexanes 1:1; UV). ^{1}H NMR (500 MHz, Chloroform-*d*) δ 8.63 (d, *J* = 4.9, 1.1 Hz, 1H), 7.64 – 7.59 (m, 2H), 7.52 – 7.43 (m, 3H), 7.41 – 7.37 (m, 2H), 4.79 – 4.66 (m, 2H), 4.64 – 4.53 (m, 2H), 4.17 – 4.04 (m, 2H), 1.76 (s, 3H). ^{13}C NMR (126 MHz, $CDCl_3$) δ 164.68, 154.58, 149.73, 149.76, 149.34, 138.23, 129.17, 127.05, 119.87, 117.63, 95.71, 74.59 – 74.46 (m), 61.25, 60.50, 40.57, 27.31. HRMS (ESI) m/z $[M + H]^+$ calcd for: $C_{18}H_{17}Cl_3N_2O_2$: 399.0428; found: 399.0436. IR (neat): v = 2965, 2876, 1727, 1595, 1541, 1447, 1418, 1362, 1194, 1152, 1109.

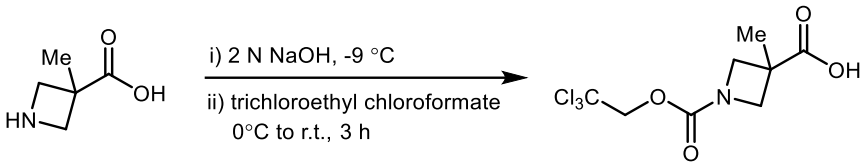

3-methyl-1-((2,2,2-trichloroethoxy)carbonyl)azetidine-3-carboxylic acid

3-Methylazetidine-3-carboxylic acid (0.5 g, 4.34 mmol) was placed in a round bottom flask equipped with a magnetic stir bar, dissolved in 6.5 mL of 2.0 N aqueous NaOH solution, and cooled to -9 ºC. 2,2,2-Trichloroethyl chloroformate (0.6 mL, 4.77 mmol) was then added dropwise to the stirred solution at 0 ºC. The mixture was stirred for 1 h at 0 ºC and an additional 2 h at r.t. After the reaction, the mixture was extracted with diethyl ether (3 x 10 mL) and the aqueous phase was acidified to pH 2 with 2 N HCl. The aqueous phase was extracted with ethyl acetate (4 x 20 mL), and the combined ethyl acetate extracts were washed with brine, dried with Na_2SO_4, and concentrated to yield the desired product (1.1 g, 84%) as a white solid. ^{1}H NMR (700 MHz, Chloroform-*d*) δ 10.31 (s, 1H), 4.71 (d, *J* = 13.7 Hz, 2H), 4.43 (d, *J* = 42.7 Hz, 2H), 3.88 (d, *J* = 33.7 Hz, 2H), 1.62 (s, 3H). ^{13}C NMR (176 MHz, $CDCl_3$) δ 178.96, 153.68, 94.80, 73.95, 57.76 (d, *J* = 119.2 Hz), 38.61, 21.62. HRMS (ESI) m/z $[M + H]^+$ calcd for: $C_8H_{10}Cl_3NO_4$: 289.9752; found: 289.9748. IR (neat): v = 2968, 2895, 2582, 1723, 1964, 1466, 1434, 1414, 1358, 1317, 1302, 1227, 1187, 1139.

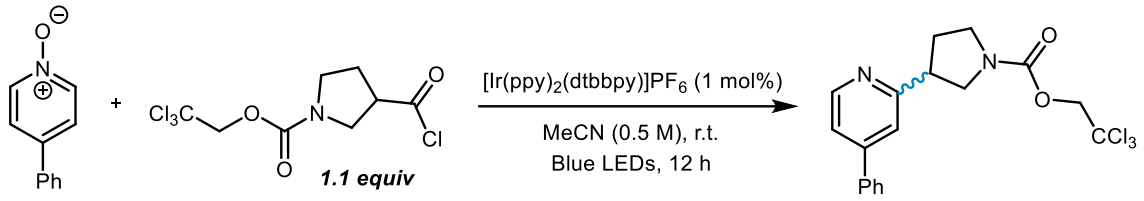

2,2,2-trichloroethyl 1-(4-phenylpyridin-2-yl)pyrrolidine-3-carboxylate (2.27)

The reaction was run according to General Procedure A and was purified by column chromatography (10% acetone in dichloromethane) to afford the title compound (42 mg, 13%) as a colorless oil and 4-phenylpyridine (77 mg, 62%). R_f = 0.65 (10% acetone/dichloromethane; UV). ^{1}H NMR (500 MHz, Chloroform-*d*) (50:50 mixture of rotamers) δ 8.63 – 8.58 (m, 1H), 7.62 (d, *J* = 7.5 Hz, 2H), 7.57 – 7.42 (m, 3H), 7.42 – 7.36 (m, 2H), 4.85 – 4.70 (m, 2H), 4.00 (ddd, *J* = 18.3, 10.9, 7.8 Hz, 1H), 3.86 – 3.70 (m, 2H), 3.70 – 3.52 (m, 2H), 2.43 – 2.27 (m, 2H). ^{13}C NMR (126 MHz, $CDCl_3$) (50:50 mixture of rotamers) δ 160.79, 160.61, 152.89, 152.86, 150.00, 149.97, 149.94, 149.22, 149.17, 138.13, 129.13, 127.02, 120.22, 120.16, 120.10, 120.01, 119.95, 95.86, 95.78, 74.86, 74.83, 51.62, 51.23, 46.48, 46.19, 45.99, 45.35, 32.14, 31.48. HRMS (ESI) m/z [M + H]$^+$ calcd for: $C_{18}H_{17}Cl_3N_2O_2$: 289.9748; found: 289.9748. IR (neat): v = 2949, 2881, 1713, 1595, 1547, 1473, 1410, 1352, 1333, 1174, 1122, 1057.

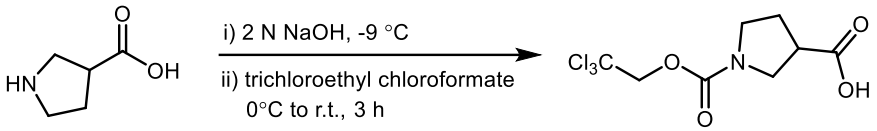

1-((2,2,2-trichloroethoxy)carbonyl)pyrrolidine-3-carboxylic acid

Pyrrolidine-3-carboxylic acid (1 g, 8.7 mmol) was placed in a round bottom flask equipped with a magnetic stir bar, dissolved in 13 mL of 2.0 N aqueous NaOH solution, and cooled to -9 ºC. 2,2,2-Trichloroethyl chloroformate (1.2 mL, 9.57 mmol) was then added dropwise to the stirred solution at 0 ºC. The mixture was stirred for 1 h at 0 ºC and an additional 2 h at r.t. After the reaction, the mixture was extracted with diethyl ether (3 x 10 mL) and the aqueous phase was acidified to pH 2 with 2 N HCl. The aqueous phase was extracted with ethyl acetate (4 x 20 mL), and the combined ethyl acetate extracts were washed with brine, dried with Na_2SO_4, and concentrated to yield the desired product (2.3 g, 90%) as a white solid. ^{1}H NMR (700 MHz, Chloroform-*d*) δ 10.37 (s, 1H), 4.80 – 4.69 (m, 2H), 3.76 (dd, *J* = 21.7, 6.9 Hz, 2H), 3.69 – 3.48 (m, 2H), 3.17 (dp, *J* = 22.1, 7.5 Hz, 1H), 2.25 (tt, *J* = 14.2, 7.2 Hz, 2H). ^{13}C NMR (176 MHz, $CDCl_3$) δ 177.58, 177.48, 152.15, 152.09, 94.95, 94.92, 74.31, 47.73, 47.16, 45.10, 44.62, 42.26, 41.46, 28.08, 27.40. HRMS (ESI) m/z $[M + H]^+$ calcd for: $C_8H_{10}Cl_3NO_4$: 275.9592; found: 275.9597. IR (neat): v = 3184, 2899, 1721, 1696, 1450, 1426, 1367, 1345, 1295, 1282, 1245, 1198, 1131.

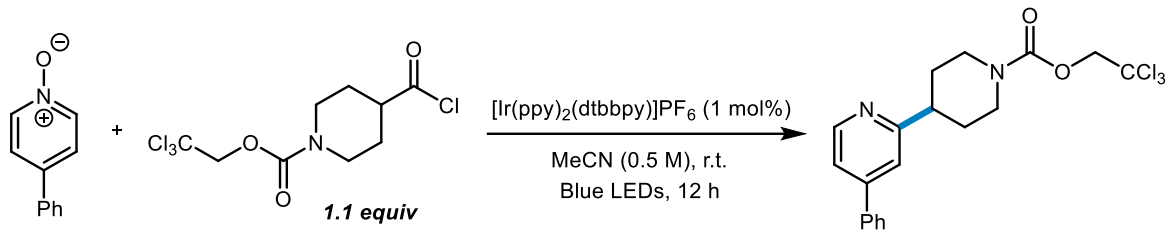

2,2,2-trichloroethyl 4-(4-phenylpyridin-2-yl)piperidine-1-carboxylate (2.28)

The reaction was run according to General Procedure A and was purified by column chromatography (20% to 50% ethyl acetate in hexanes) to afford the title compound (331 mg, 36%) as a colorless oil and 4-phenylpyridine (52 mg, 42%). R_f = 0.55 (ethyl acetate/hexanes 1:1; UV). ^{1}H NMR (500 MHz, Chloroform-*d*) δ 8.58 (d, *J* = 5.3 Hz, 1H), 7.64 – 7.59 (m, 2H), 7.46 (dt, *J* = 23.5, 7.4 Hz, 4H), 7.36 (d, *J* = 3.8 Hz, 2H), 4.77 (s, 2H), 4.45 – 4.35 (m, 3H), 3.07 (t, *J* = 13.2 Hz, 1H), 2.99 (td, *J* = 12.0, 6.1 Hz, 2H), 2.08 – 2.01 (m, 3H), 1.87 (qd, *J* = 12.7, 4.3 Hz, 3H). ^{13}C NMR (126 MHz, $CDCl_3$) δ 164.33, 153.39, 149.72 (d, *J* = 6.0 Hz), 149.16, 138.39, 129.09, 129.03, 127.01, 119.79 (d, *J* = 10.4 Hz), 119.01 (d, *J* = 10.3 Hz), 95.75, 75.21 – 75.01 (m), 44.62 (d, *J* = 15.6 Hz), 44.36, 31.59 (d, *J* = 26.1 Hz). HRMS (ESI) m/z $[M + H]^+$ calcd for: $C_{19}H_{19}Cl_3N_2O_2$: 413.0585; found: 413.0589. IR (neat): v = 2747, 1706, 1594, 1548, 1468 1428, 1273, 1213, 1125.

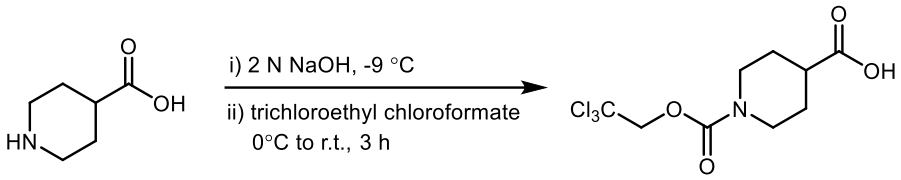

1-((2,2,2-trichloroethoxy)carbonyl)piperidine-4-carboxylic acid

Piperidine-4-carboxylic acid (1 g, 7.0 mmol) was placed in a round bottom flask equipped with a magnetic stir bar, dissolved in 10 mL of 2.0 N aqueous NaOH solution, and cooled to -9 ºC. 2,2,2-Trichloroethyl chloroformate (1 mL, 7.7 mmol) was then added dropwise to the stirred solution at 0 ºC. The mixture was stirred for 1 h at 0 ºC and an additional 2 h at r.t. After the reaction, the mixture was extracted with diethyl ether (3 x 10 mL) and the aqueous phase was acidified to pH 2 with 2 N HCl. The aqueous phase was extracted with ethyl acetate (4 x 20 mL), and the combined ethyl acetate extracts were washed with brine, dried with Na_2SO_4, and concentrated to yield the desired product (2.0 g, 93%) as a white solid. ^{1}H NMR (700 MHz, Chloroform-*d*) δ 10.61 (s, 1H), 4.75 (d, *J* = 12.2 Hz, 2H), 4.21 – 4.05 (m, 2H), 3.18 – 2.92 (m, 2H), 2.58 (tt, *J* = 10.6, 4.0 Hz, 1H), 1.97 (d, *J* = 10.3 Hz, 2H), 1.73 (qd, *J* = 11.1, 4.2 Hz, 2H). ^{13}C NMR (176 MHz, $CDCl_3$) δ 180.43, 153.72, 95.98, 75.46, 43.79 (d, *J* = 18.9 Hz), 40.80, 27.91 (d, *J* = 41.1 Hz). HRMS (ESI) m/z $[M + H]^+$ calcd for: $C_9H_{12}Cl_3NO_4$: 303.9905; found: 303.9909. IR (neat): v = 3209, 2861, 1725, 1686, 1445, 1428, 1365, 1389, 1242, 1171, 1129.

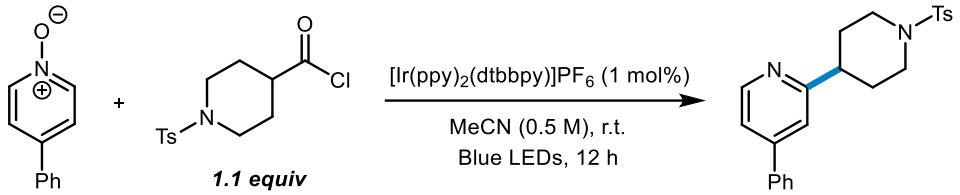

4-phenyl-2-(1-tosylpiperidin-4-yl)pyridine (2.29)

The reaction was run according to General Procedure A and was purified by column chromatography (20% to 50% ethyl acetate in hexanes) to afford the title compound (314 mg, 31%) as a colorless oil and 4-phenylpyridine (60 mg, 48%). R_f = 0.51 (ethyl acetate/hexanes 1:1; UV). ^{1}H NMR (500 MHz, Chloroform-*d*) δ 8.55 (d, *J* = 5.1 Hz, 1H), 7.69 (d, *J* = 7.9 Hz, 2H), 7.61 – 7.58 (m, 2H), 7.51 – 7.41 (m, 3H), 7.37 – 7.33 (m, 3H), 7.31 (s, 1H), 4.00 – 3.90 (m, 2H), 2.69 (tt, *J* = 12.0, 3.9 Hz, 1H), 2.48 – 2.37 (m, 5H), 2.11 – 1.91 (m, 4H). ^{13}C NMR (126 MHz, $CDCl_3$) δ 164.07, 149.65 (d, *J* = 4.9 Hz), 149.13, 143.45, 138.34, 133.34, 129.63 (d, *J* = 8.3 Hz), 129.08, 127.73 (d, *J* = 7.2 Hz), 126.99, 119.83 (d, *J* = 9.3 Hz), 118.76 (d, *J* = 9.3 Hz), 46.52, 46.49, 43.65, 31.17, 21.53 (d, *J* = 7.2 Hz). HRMS (ESI) m/z $[M + H]^+$ calcd for: $C_{23}H_{24}N_2O_2S$: 393.1631; found: 393.1634. IR (neat): v = 2918, 2855, 1702, 1592, 1468, 1443, 1274, 1216, 1158, 1130, 1092.

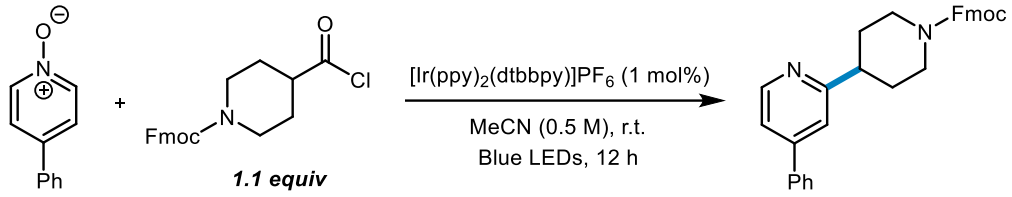

(9H-fluoren-9-yl)methyl 4-(4-phenylpyridin-2-yl)piperidine-1-carboxylate (2.30)

The reaction was run according to General Procedure A and was purified by column chromatography (20% to 50% ethyl acetate in hexanes) to afford the title compound (85 mg, 23%) as a colorless oil and 4-phenylpyridine (73 mg, 59%). R_f = 0.54 (ethyl acetate/hexanes 1:1; UV). ^{1}H NMR (500 MHz, Chloroform-*d*) δ 8.59 (d, *J* = 5.1 Hz, 1H), 7.76 (d, *J* = 7.5 Hz, 2H), 7.67 – 7.54 (m, 4H), 7.55 – 7.42 (m, 3H), 7.42 – 7.35 (m, 4H), 7.32 (t, *J* = 7.4 Hz, 2H), 4.44 (t, *J* = 4.5 Hz, 3H), 4.27 (t, *J* = 6.9 Hz, 2H), 2.96 (ddt, *J* = 12.2, 7.5, 3.7 Hz, 3H), 2.00 (d, *J* = 13.1 Hz, 2H), 1.79 (s, 2H). ^{13}C NMR (126 MHz, $CDCl_3$) δ 164.61, 155.21, 149.71, 149.69, 149.13, 144.13, 141.33, 138.46, 129.09, 129.01, 127.63, 127.03, 125.03, 119.95, 119.76, 119.01, 67.27, 47.42, 44.54, 44.37, 31.66. HRMS (ESI) m/z $[M + H]^+$ calcd for: $C_{31}H_{28}N_2O_2$: 461.2331; found: 461.2332. IR (neat): v = 3037, 2919, 2796, 2751, 1702, 1595, 1546, 1491, 1475, 1444, 1366, 1335, 1267, 1131.

Ethyl 2-(*tert*-butyl)isonicotinate (2.31)

The reaction was run according to General Procedure A and the *N*-oxide substrate was prepared according to a reported procedure.[141] The crude product was purified by column chromatography (0% to 15% ethyl acetate in hexanes) to afford the title compound (124 mg, 75%) as a colorless oil. R_f = 0.71 (ethyl acetate/hexanes 1:4; UV). ^{1}H NMR (500 MHz, $CDCl_3$) δ 8.70 (d, *J* = 5.0 Hz, 1H), 7.89 (d, *J* = 1.5 Hz, 1H), 7.63 (dd, *J* = 4.9, 1.5 Hz, 1H), 4.41 (q, *J* = 7.2 Hz, 2H), 1.44 – 1.38 (m, 12H). ^{13}C NMR (126 MHz, $CDCl_3$) δ 170.52, 165.70, 149.29, 137.83, 119.80, 118.38, 61.61, 37.65, 30.09, 14.22. HRMS (ESI) m/z $[M + H]^+$ calcd for: $C_{12}H_{17}NO_2$: 208.1332; found: 208.1332. The acquired ^{1}H and ^{13}CNMR spectra were identical to those reported in the literature.[142]

2-*tert*-butyl-4-acetylpyridine (2.32)

The reaction was run according to General Procedure A and the *N*-oxide substrate was prepared according to a reported procedure.[143] The crude product was purified by column chromatography (0% to 15% ethyl acetate in hexanes) to afford the title compound (74 mg, 52%) as a colorless oil. R_f = 0.5 (ethyl acetate/hexanes 1:4; UV). ^{1}H NMR (500 MHz, $CDCl_3$) δ 8.74 (d, *J* = 5.0 Hz, 1H), 7.77 (s, 1H), 7.55 – 7.48 (m, 1H), 2.62 (s, 3H), 1.39 (s, 9H). ^{13}C NMR (126 MHz, $CDCl_3$) δ 198.35, 171.30, 150.06, 143.55, 118.81, 116.79, 38.07, 30.45, 27.09. HRMS (ESI) m/z $[M + H]^+$ calcd for: $C_{11}H_{15}NO$: 178.1226; found: 178.1225. IR (neat): v = 2959, 2867, 1694, 1594, 1557, 1480, 1398, 1357, 1287, 1232, 1140, 1092.

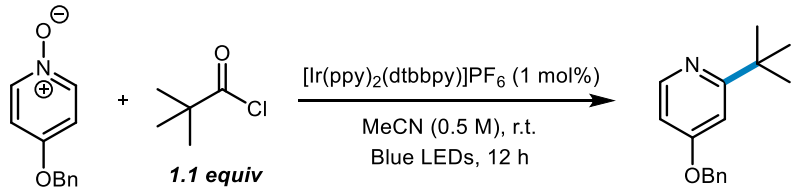

2-*tert*-butyl-4-benzyloxypyridine (2.33)

The reaction was run according to General Procedure A and the *N*-oxide substrate was prepared according to a reported procedure.[144] The crude product was purified by column chromatography (0% to 15% ethyl acetate in hexanes) to afford the title compound (147 mg, 76%) as a colorless oil. R_f = 0.45 (ethyl acetate/hexanes 1:4; UV). ^{1}H NMR (700 MHz, $CDCl_3$) δ 8.41 (d, *J* = 5.6 Hz, 1H), 7.47 – 7.31 (m, 5H), 6.93 (s, 1H), 6.72 – 6.67 (m, 1H), 5.09 (s, 2H), 1.34 (s, 9H). ^{13}C NMR (176 MHz, $CDCl_3$) δ 171.44, 165.44, 150.32, 136.22, 129.03, 128.65, 127.93, 107.20, 106.89, 70.01, 37.66, 30.41. HRMS (ESI) m/z $[M + H]^+$ calcd for: $C_{16}H_{19}NO$: 242.1539; found: 242.1541. IR (neat): v = 2954, 1701, 1592, 1560, 1495, 1478, 1453, 1416, 1378, 1361, 1290, 1227, 1205, 1129.

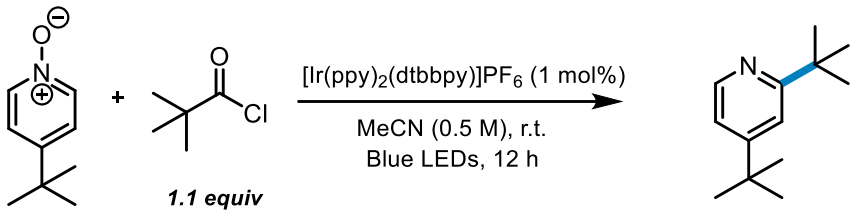

2,4-di-*tert*-butylpyridine (2.34)

The reaction was run according to General Procedure A on a 0.5 mmol scale and the *N*-oxide substrate was prepared according to a reported procedure.[55] The crude product was purified by column chromatography (0% to 30% ethyl acetate in hexanes) to afford the title compound (53 mg, 55%) as a colorless oil. R_f = 0.56 (ethyl acetate/hexanes 1:4; UV). ^{1}H NMR (700 MHz, $CDCl_3$) δ 8.47 (d, *J* = 5.6 Hz, 1H), 7.32 (d, *J* = 1.4 Hz, 1H), 7.08 (dd, *J* = 5.6, 1,4 Hz, 1H), 1.37 (s, 9H) 1.31 (s, 9H). ^{13}C NMR (176 MHz, $CDCl_3$) δ 168.98, 159.86, 148.32, 117.75, 115.68, 37.39, 34.74, 30.61, 30.28. HRMS (ESI) m/z $[M + H]^+$ calcd for: $C_{13}H_{21}N$: 192.1747; found: 192.1747. IR (neat): v = 2960, 2869, 1810, 1767, 1743, 1597, 1551, 1481, 1461, 1396, 1364, 1296, 1255, 1192, 1153, 1094, 1042, 1006, 940.

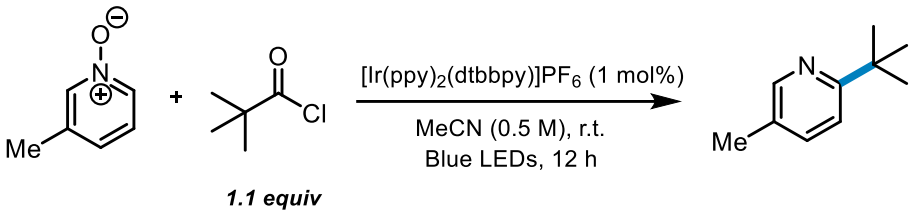

2-(*tert*-butyl)-5-methylpyridine- (2.35)

The reaction was run according to General Procedure A on a 0.5 mmol scale and the *N*-oxide substrate was purchased from ArkPharm and distilled under vacuum prior to use. Following the reaction, triethylamine (69 uL, 50.6 mg, 0.5 mmol) was added to the crude reaction mixture, and the crude reaction mixture was filtered through Celite. The mixture was then purified by column chromatography (0% to 60% ethyl acetate in hexanes) to afford the title compound (40 mg, 54%) as a colorless oil. R_f = 0.61 (ethyl acetate/hexanes 1:4; UV). ^{1}H NMR (700 MHz, $CDCl_3$) δ 8.40 (d, *J* = 2.3 Hz, 1H), 7.41 (dd, *J* = 8.2, 2.2 Hz, 1H), 7.23 (d, *J* = 8.1 Hz, 1H), 2.29 (s, 3H), 1.35 (s, 9H). ^{13}C NMR (176 MHz, $CDCl_3$) δ166.68, 149.25, 137.13, 130.10, 118.90, 30.59, 27.53, 18.30. HRMS (ESI) m/z $[M + H]^+$ calcd for: $C_{10}H_{16}N$: 150.1277; found: 150.1278. IR (neat): v = 2956, 2924, 2853, 1729, 1510, 1462, 1366, 1259, 1121, 1087, 1018, 909.

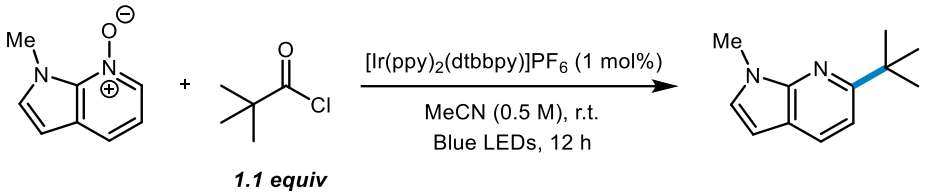

6-(*tert*-butyl)-1-methyl-1H-pyrrolo[2,3-*b*]pyridine (2.36)

The reaction was run according to General Procedure A and the *N*-oxide substrate was prepared according to a reported procedure.[145] The crude product was purified by column chromatography (0% to 15% ethyl acetate in hexanes) to afford the title compound (41 mg, 27%) as a colorless oil. R_f = 0.56 (ethyl acetate/hexanes 1:4; UV). ^{1}H NMR (500 MHz, $CDCl_3$) δ 8.27 (d, *J* = 5.0 Hz, 1H), 7.15 (d, *J* = 3.5 Hz, 1H), 6.97 (d, *J* = 5.1 Hz, 1H), 6.64 (d, *J* = 3.5 Hz, 1H), 3.89 (s, 3H), 1.49 (s, 9H). ^{13}C NMR (126 MHz, $CDCl_3$) δ 152.65, 148.31, 143.04, 127.25, 118.15, 112.03, 100.37, 35.81, 31.45, 30.28. HRMS (ESI) m/z $[M + H]^+$ calcd for: $C_{12}H_{16}N_2$: 189.1386; found: 189.1382. IR (neat): v = 2961, 1782, 1742, 1682, 1552, 1455, 1363, 1317, 1253.

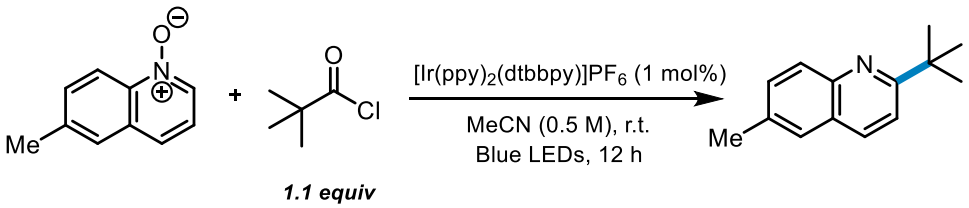

2-(*tert*-butyl)-6-methylquinoline- (2.37)

The reaction was run according to General Procedure A on a 0.5 mmol scale and the *N*-oxide substrate was prepared according to a reported procedure.[55] The crude product was purified by column chromatography (0% to 20% ethyl acetate in hexanes) to afford the title compound (49 mg, 49%) as a colorless oil. R_f = 0.64 (ethyl acetate/hexanes 1:4; UV). ^{1}H NMR (700 MHz, $CDCl_3$) δ 8.03 (d, *J* = 8.61 Hz, 1H), 7.60 (d, *J* = 9.2 Hz, 1H), 7.53- 7.49 (m, 2H), 7.36 (dd, *J* = 8.0 Hz, 1H), 2.81 (s, 3H), 1.47 (s, 9H). ^{13}C NMR (176 MHz, $CDCl_3$) δ167.76, 146.11, 137.37, 135.93, 128.96, 126.16, 125.28, 125.07, 117.71, 38.40, 30.20, 17.71.HRMS (ESI) m/z $[M + H]^+$ calcd for: $C_{14}H_{17}N$: 200.1434; found: 200.1435. IR (neat): v = 2954, 2923, 2864, 1616, 1599, 1568, 1501, 1460, 1427, 1362, 1310, 1276, 1147.

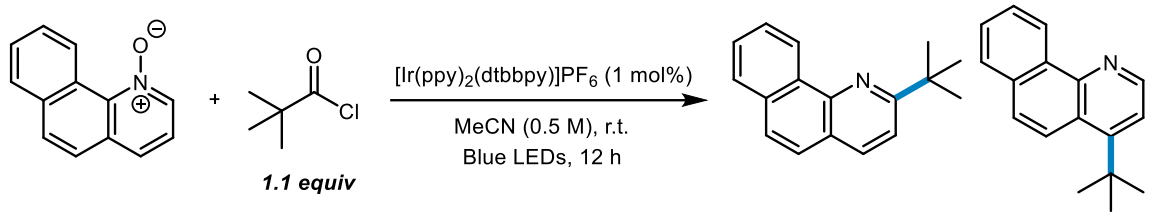

2-*tert*-butylbenzoquinoline (2.38a) and 4-*tert*-butylbenzoquinoline (2.38b)

The reaction was run according to General Procedure A and the *N*-oxide substrate was prepared according to a reported procedure.[55] The crude product was purified by column chromatography (0% to 15% ethyl acetate in hexanes) to afford 2-*tert*-butylbenzoquinoline (68 mg, 36%) and 4-*tert*-butylbenzoquinoline (19 mg, 10%) as colorless oils.

2-*tert*-butylbenzoquinoline (2.38a): R_f = 0.88 (ethyl acetate/hexanes 1:4; UV). ^{1}H NMR (700 MHz, $CDCl_3$) δ 9.40 (d, *J* = 8.1 Hz, 1H), 8.10 (d, *J* = 8.3 Hz, 1H), 7.88 (d, *J* = 7.8 Hz, 1H), 7.75 (d, *J* = 8.7 Hz, 1H), 7.73 – 7.68 (m, 1H), 7.69 – 7.64 (m, *J* = 10.5, 5.0 Hz, 2H), 7.62 (d, *J* = 8.3 Hz, 1H), 1.55 (s, 9H). ^{13}C NMR (176 MHz, $CDCl_3$) δ 168.35, 145.42, 136.07, 134.00, 132.25, 128.07, 127.95, 126.97, 126.97, 125.43, 124.94, 124.32, 118.56, 38.72, 30.77. HRMS (ESI) m/z $[M + H]^+$ calcd for: $C_{17}H_{17}N$: 236.1434; found: 236.1435. IR (neat): v = 2960, 1594, 1561, 1496, 1476, 1389, 1359, 1144, 1129.

4-*tert*-butylbenzoquinoline (2.38b): R_f = 0.67 (ethyl acetate/hexanes 1:4; UV). ^{1}H NMR (500 MHz, $CDCl_3$) δ 9.35 (d, *J* = 8.1 Hz, 1H), 8.90 (d, *J* = 4.8 Hz, 1H), 8.34 (d, *J* = 9.4 Hz, 1H), 7.89 (d, *J* = 7.5 Hz, 1H), 7.80 (d, *J* = 9.4 Hz, 1H), 7.74 – 7.65 (m, 2H), 7.51 (d, *J* = 4.8 Hz, 1H), 1.66 (s, 9H). ^{13}C NMR (126 MHz, $CDCl_3$) δ 155.97, 148.81, 147.87, 132.86, 132.79, 128.31, 127.58, 127.14, 126.23, 125.47, 125.37, 124.27, 119.24, 36.42, 31.76. HRMS (ESI) m/z $[M + H]^+$ calcd for: $C_{17}H_{17}N$: 236.1434; found: 236.1435. IR (neat): v = 2956, 2873, 1755, 1621, 1564, 1514, 1443, 1397, 1368, 1266, 1154, 1108.

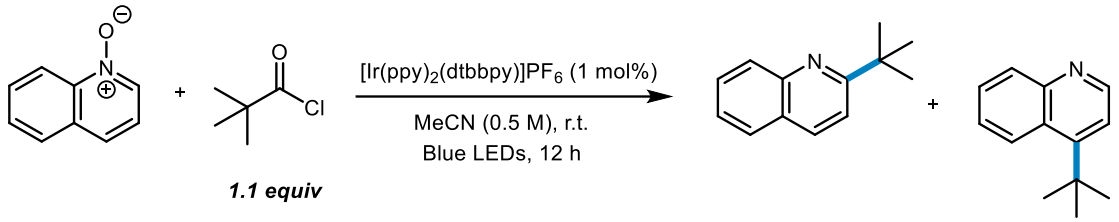

2-(tert-butyl)quinoline (2.39a) and 4-(tert-butyl)quinoline (2.39b)

The reaction was run according to General Procedure A and was purified by column chromatography (0% to 15% ethyl acetate in hexanes) to afford 2-(*tert*-butyl)quinoline (64 mg, 43%) and 4-(*tert*-butyl)quinoline (49 mg, 33%) as colorless oils. The acquired ^{1}H and ^{13} CNMR spectra were identical to those reported in the literature.[146]

2-(tert-butyl)quinoline (2.39a): R_f = 0.71 (ethyl acetate/hexanes 1:4; UV). ^{1}H NMR (700 MHz, $CDCl_3$): δ 8.09 – 8.04 (m, 2H), 7.76 (dd, *J* = 8.1, 1.4 Hz, 1H), 7.66 (ddd, *J* = 8.4, 6.9, 1.4 Hz, 1H), 7.52 (d, *J* = 8.7 Hz, 1H), 7.47 (ddd, *J* = 8.0, 6.9, 1.2 Hz, 1H), 1.47 (s, 9H). ^{13}C NMR (176 MHz, $CDCl_3$): δ 169.22, 147.42, 135.80, 129.41, 128.93, 127.18, 126.42, 125.58, 118.19, 38.11, 30.17, 30.13. HRMS (ESI) m/z $[M + H]^+$ calcd for: $C_{13}H_{15}N$: 186.1277; found: 186.1274.

4-(tert-butyl)quinoline (2.39b): R_f = 0.56 (ethyl acetate/hexanes 1:4; UV). ^{1}HNMR ($CDCl_3$, 700 MHz): δ 8.81 (d, *J* = 4.7 Hz, 1H), 8.41 (dd, *J* = 8.7, 1.3 Hz, 1H), 8.14 (dd, *J* = 8.4, 1.4 Hz, 1H), 7.67 (ddd, *J* = 8.2, 6.8, 1.3 Hz, 1H), 7.56 – 7.50 (m, 1H), 7.35 (d, *J* = 4.7 Hz, 1H), 1.62 (s, 9H). ^{13}C NMR (176 MHz, $CDCl_3$): δ 155.68, 150.21, 149.44, 131.14, 128.06, 127.08, 126.45, 125.10, 118.10, 36.10, 31.23. HRMS (ESI) m/z $[M + H]^+$ calcd for: $C_{13}H_{15}N$: 186.1277; found: 186.1274.

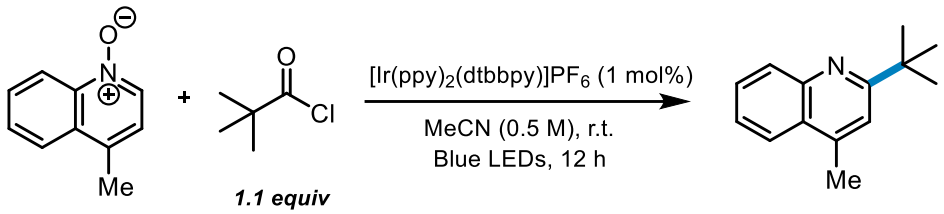

2-(*tert*-butyl)lepidine (2.40)

The reaction was run according to General Procedure A on a 0.5 mmol scale and the *N*-oxide substrate was prepared according to a reported procedure.[55] The crude product was purified by column chromatography (0% to 20% ethyl acetate in hexanes) to afford the title compound (21 mg, 21%) as a colorless oil. The reaction of lepidine N-oxide immediately discolors to a dark purple upon the addition of acyl chloride, this is believed to be due to a competing decomposition pathway. R_f = 0.68 (ethyl acetate/hexanes 1:4; UV). ^{1}H NMR (700 MHz, $CDCl_3$) δ 8.06 (d, *J* = 7.8 Hz, *1H*), 7.94 (d, *J* = 8.2 Hz, 1H), 7.66 (t, *J* = 6.9 Hz, 1H), 7.49 (t, *J* = 6.9 Hz, 1H), 7.35 (s, 1H), 2.69 (s, 3H), 1.46 (s, 9H). ^{13}C NMR (176 MHz, $CDCl_3$) δ 169.07, 147.43, 143.72, 130.09, 128.81, 126.67, 125.51, 123.52, 119.04, 38.06, 30.27, 19.12. HRMS (ESI) m/z $[M + H]^+$ calcd for: $C_{14}H_{17}N$: 200.1434; found: 200.1436. IR (neat): v = 3061, 2955, 2863, 1601, 1558, 1506, 1480, 1411, 1392, 1363, 1334, 1270, 1246, 1228, 1153, 1107, 1023, 932, 862, 810, 755, 709.

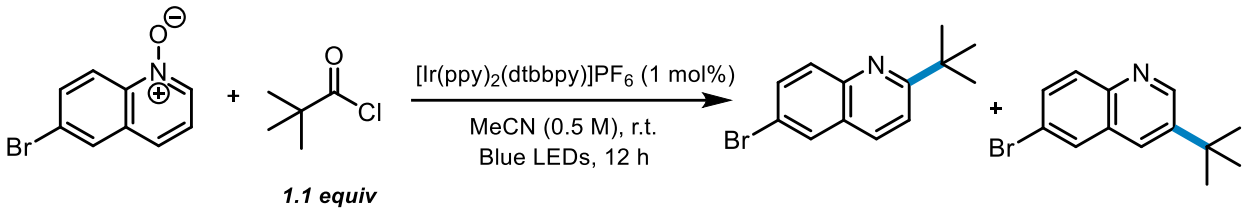

2-(*tert*-butyl)-6-bromoquinoline (2.41a) and 3-(*tert*-butyl)-6-bromoquinoline (2.41b)

The reaction was run according to General Procedure A on a 0.5 mmol scale and the *N*-oxide substrate was prepared according to a reported procedure.[55] The crude product was purified by column chromatography (0% to 30% ethyl acetate in hexanes) to afford 2-(*tert*-butyl)-6-bromoquinoline (43 mg, 33%) as a yellow oil and 3-(*tert*-butyl)-6-bromoquinoline (14 mg, 11%) as a colorless oil.

2-(*tert*-butyl)-6-bromoquinoline (2.41a)

R_f = 0.64 (ethyl acetate/hexanes 1:4; UV). ^{1}H NMR (700 MHz, $CDCl_3$) 7.98 (d, *J* = 8.8 Hz, 1H), 7.92 (d, *J* = 8.9 Hz, 1H), 7.92 (d, *J* = 2.1 Hz, 1H) 7.72 (dd, *J* = 9.0, 2.0 Hz, 1H), 7.54 (d, *J* = 8.7 Hz, 1H), 1.45 (s, 9H). ^{13}C NMR (126 MHz, $CDCl_3$) δ 170.11, 146.36, 135.19, 132.68, 131.56, 129.58, 127.92, 119.61, 119.43, 38.58, 30.38. HRMS (ESI) m/z $[M + H]^+$ calcd for: $C_{13}H_{14}BrN$: 264.0382; found: 264.0385. IR (neat): v = 2958, 2865, 1594, 1550, 1487, 1458, 1363, 1301, 11889, 1104, 1059.

3-(*tert*-butyl)-6-bromoquinoline (2.41b)

R_f = 0.24 (ethyl acetate/hexanes 1:4; UV). ^{1}H NMR (700 MHz, $CDCl_3$) δ 8.81 (d, *J* = 4.7 Hz, 1H), 8.56 (s, 1H), 8.00 (d, *J* = 8.9 Hz, 1H), 7.74 (d, *J* = 9.0 Hz, 1H), 7.37 (d, J = 4.8 Hz, 1H), 1.61 (s, 9H) ppm. ^{13}C NMR (176 MHz, $CDCl_3$) δ 155.15, 150.72, 148.21, 132.94, 131.74, 128.97, 128.40, 119.49, 119.02, 36.26, 31.40 ppm. HRMS (ESI) m/z $[M + H]^+$ calcd for: $C_{13}H_{14}BrN$: 264.0382; found: 264.0384. IR (neat): v = 2965, 2215, 1600, 1581, 1492, 1365, 1333, 1259, 1179, 1068, 997.

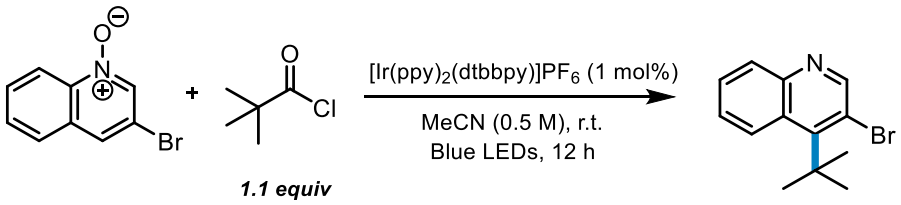

4-(*tert*-butyl)-3-bromoquinoline (2.42)

The reaction was run according to General Procedure A on a 0.5 mmol scale and the *N*-oxide substrate was prepared according to a reported procedure.[55] The crude product was purified by column chromatography (0% to 30% ethyl acetate in hexanes) to afford the title compound (27 mg, 20%) as a colorless oil. R_f = 0.75 (ethyl acetate/hexanes 1:4; UV). ^{1}H NMR (700 MHz, $CDCl_3$) δ 8.35 (s,1H), 8.02 (d, *J* = 8.4 Hz, 1H), 7.70 - 7.65 (m, 2H), 7.50 (t, *J* = 7.0 Hz, 1H) 1.64 (s, 9H). ^{13}C NMR (176 MHz, $CDCl_3$) δ 163.96, 145.29, 141.54, 129.59, 129.53, 127.80, 126.96, 126.13, 116.57, 40.38, 29.16. HRMS (ESI) m/z $[M + H]^+$ calcd for: $C_{13}H_{14}BrN$: 264.0382; found: 264.0370. IR (neat): v = 2954, 2927, 2868, 1587, 1480, 1459, 1397, 1363, 1321, 1300, 1200, 1152, 1133, 1110, 961.

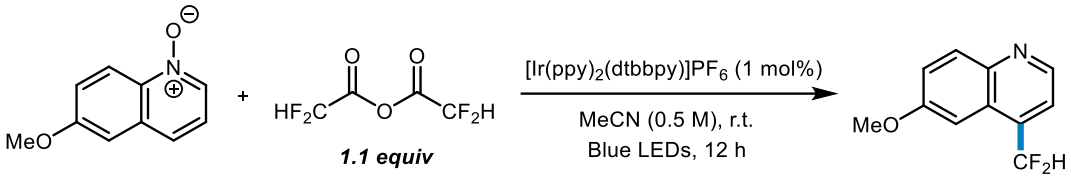

4-(difluoromethyl)-6-methoxyquinoline (2.43)

The reaction was run according to General Procedure A and the *N*-oxide substrate was prepared according to a reported procedure.[55] The crude product was purified by column chromatography (0% to 15% ethyl acetate in hexanes) to afford the title compound (54 mg, 32%) as a colorless oil. R_f = 0.63 (ethyl acetate/hexanes 1:4; UV). ^{1}H NMR (500 MHz, $CDCl_3$) δ 8.86 (d, *J* = 4.4 Hz, 1H), 8.09 (d, *J* = 9.2 Hz, 1H), 7.54 (d, *J* = 4.4 Hz, 1H), 7.44 (dd, *J* = 9.3, 2.7 Hz, 1H), 7.31 (dt, *J* = 2.6, 1.4 Hz, 1H), 7.09 (t, *J* = 54.6 Hz, 1H), 3.97 (s, 3H). ^{13}C NMR (126 MHz, $CDCl_3$) δ 158.54, 147.23, 144.88, 136.22 (t, *J* = 3.2 Hz), 131.77, 125.29 (t, *J* = 3.0 Hz), 122.64, 118.38 (t, *J* = 7.8 Hz), 113.74 (t, *J* = 240.1 Hz), 101.21, 55.61. ^{19}F NMR (471 MHz, $CDCl_3$) δ -115.32 (d, *J* = 54.7 Hz). HRMS (ESI) m/z $[M + H]^+$ calcd for: $C_{11}H_9F_2NO$: 210.0725; found: 210.0725. IR (neat): v = 2937, 1921, 1678, 1622, 1508, 1479, 1358, 1308, 1245, 1229, 1108, 1081, 1026.

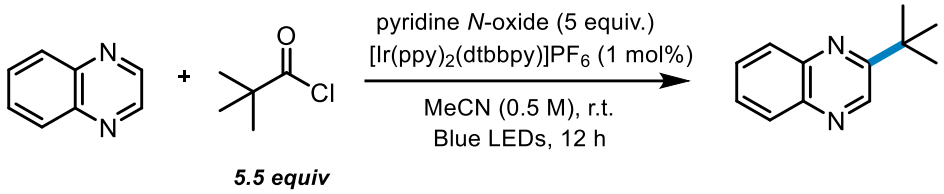

2-(*tert*-butyl)-quinoxaline (2.44)

The reaction was run according to General Procedure B on a 0.5 mmol scale and was purified by column chromatography (5% to 80% ethyl acetate in hexanes) to afford the title compound (68 mg, 73%) as a light yellow oil. Rf = 0.56 (ethyl acetate/hexanes 1:4; UV). ^{1}H NMR (700 MHz, $CDCl_3$) δ 8.99 (s, 1H), 8.06 (d, *J* = 5.7 Hz, 1H), 8.05 (d, J = 5.6 Hz, 1H), 7.73 (t, *J* = 7.0 Hz, 1H), 7.70 (t, J = 7.0 Hz, 1H) 1.52 (s, 9H). ^{13}C NMR (176 MHz, $CDCl_3$) δ 163.65, 143.40, 141.56, 140.72, 129.60, 129.24, 128.86, 128.84, 37.21, 29.71 ppm. HRMS (ESI) m/z $[M]^+$ calcd for: $C_{12}H_{15}N_2$: 186.1157; found: 186.1162. IR (neat): v = 3025, 2963, 2669, 1596, 1546, 1495, 1464, 1409, 1366, 1273, 1226, 1203, 1128, 1074, 1023, 995.

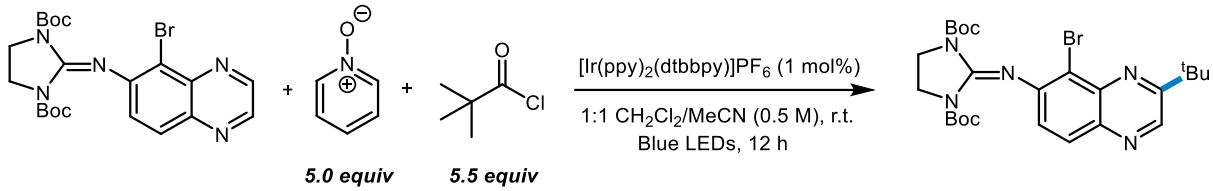

2-*tert*-butyl-4-acetylpyridine (2.45)

The reaction was run according to General Procedure B using 1:1 dichloromethane/MeCN (0.5 M) as the reaction solvent. The crude material was purified by column chromatography (10% to 30% ethyl acetate in hexanes) to afford the title compound (48 mg, 11%) as a yellow solid. R_f = 0.58 (ethyl acetate/hexanes 1:4; UV). ^{1}H NMR (500 MHz, $CDCl_3$) δ 8.97 (s, 1H), 7.87 – 7.79 (m, 1H), 7.49 – 7.41 (m, 1H), 3.90 – 3.85 (m, 4H), 1.48 (s, 9H), 1.30 (s, 18H). ^{13}C NMR (126 MHz, $CDCl_3$) δ 161.46, 149.92, 143.04, 139.61, 138.93, 127.97, 127.21, 126.60, 126.32, 83.10, 42.71, 29.75, 27.88, 27.85. HRMS (ESI) m/z $[M + H]^+$ calcd for: $C_{25}H_{34}BrN_5O_4$: 548.1867; found: 548.1874. IR (neat): v = 2978, 1805, 1737, 1710, 1666, 1603, 1471, 1368, 1310, 1252, 1235, 1149, 1107.

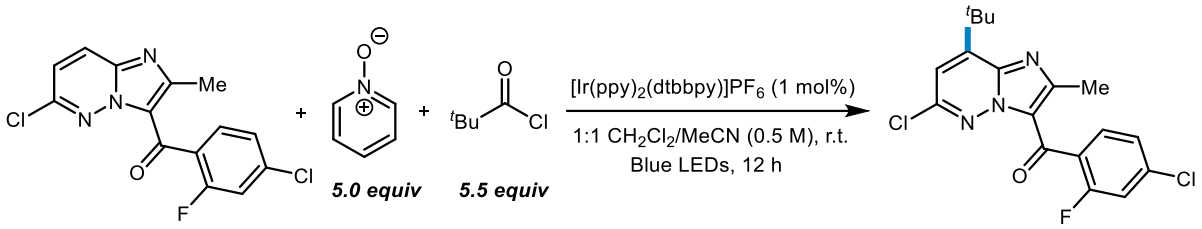

(8-(tert-butyl)-6-chloro-2-methylimidazo[1,2-b]pyridazin-3-yl)(4-chloro-2-fluorophenyl)methanone (2.46)

The reaction was run according to General Procedure B on a 0.5 mmol scale using 1:1 dichloromethane/MeCN (0.5 M) as the reaction solvent. The crude material was purified by column chromatography (0% to 30% ethyl acetate in hexanes) to afford the title compound (84 mg, 44%) as a white solid. R_f = 0.59 (ethyl acetate/hexanes 1:4; UV). ^{1}H NMR (700 MHz, $CDCl_3$) δ 7.60 (t, *J* = 7.8 Hz, 1H), 7.29 (d, *J* = 6.5 Hz, 1H), 7.12 (d, *J* = 10.1 Hz, 1H), 6.98 (s, 1H), 2.66 (s, 3H), 1.58 (s, 9H). ^{13}C NMR (176 MHz, $CDCl_3$) δ 180.57, 161.37, 159.92, 151.55, 150.69, 147.13, 139.08, 139.02, 138.79, 131.54, 131.51, 127.25, 127.17, 125.40, 125.38, 125.09, 117.43, 116.73, 116.58, 36.44, 29.13, 16.81. ^{19}F NMR (377 MHz, $CDCl_3$) δ -112.42 (dd, *J* = 10.1, 7.5 Hz). HRMS (ESI) m/z [M + H]+ calcd for: $C_{18}H_{17}Cl_2FN_3O$: 380.0727; found: 380.0731. IR (neat): v = 3091, 2959, 1636, 1604, 1573, 1539, 1506, 1480, 1410, 1376, 1345, 1316, 1290, 1257, 1242, 1210, 1161, 1118, 1077, 1052, 995.

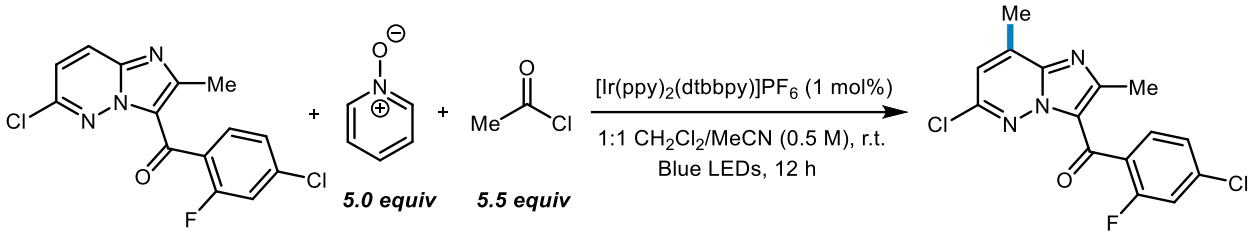

(6-chloro-2,8-dimethylimidazo[1,2-*b*]pyridazin-3-yl)(4-chloro-2-fluorophenyl)methanone (2.47)

The reaction was run according to General Procedure B using 1:1 dichloromethane/MeCN (0.5 M) as the reaction solvent. The crude material was purified by column chromatography (0% to 30% ethyl acetate in hexanes) to afford the title compound (43 mg, 16%) as a white solid. R_f = 0.56 (ethyl acetate/hexanes 1:4; UV). ^{1}H NMR (500 MHz, $CDCl_3$) δ 7.62 (t, *J* = 7.9 Hz, 1H), 7.30 (dd, *J* = 8.4, 1.8 Hz, 1H), 7.12 (dd, *J* = 10.0, 1.9 Hz, 1H), 7.02 (d, *J* = 1.5 Hz, 1H), 2.69 (s, 3H), 2.67 (s, 3H). ^{13}C NMR (126 MHz, $CDCl_3$) δ 180.15, 160.37 (d, *J* = 255.1 Hz), 152.00, 146.58, 139.55, 138.99 (d, *J* = 10.6 Hz), 138.47, 131.26 (d, *J* = 3.7 Hz), 126.59 (d, *J* = 13.9 Hz), 125.66, 125.13 (d, *J* = 3.4 Hz), 120.75, 116.35 (d, *J* = 25.7 Hz), 16.65, 16.25. ^{19}F NMR (377 MHz, $CDCl_3$) δ -112.41 (dd, *J* = 10.2, 7.5 Hz). HRMS (ESI) m/z $[M + H]^+$ calcd for: $C_{15}H_{10}Cl_2FN_3O$: 338.0258; found: 338.0263. IR (neat): v = 2051, 2922, 1636, 1606, 1553, 1503, 1480, 1400, 1379, 1347, 1290, 1224, 1136, 1078.

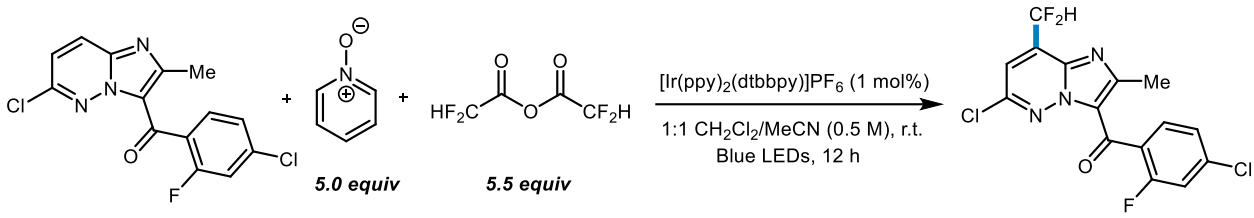

(4-chloro-2-fluorophenyl)(6-chloro-8-(difluoromethyl)-2-methylimidazo[1,2-*b*]pyridazin-3-yl)methanone (2.48)

The reaction was run according to General Procedure B using 1:1 dichloromethane/MeCN (0.5 M) as the reaction solvent. The crude material was purified by column chromatography (0% to 30% ethyl acetate in hexanes) to afford the title compound (39 mg, 13%) as a white solid. R_f = 0.61 (ethyl acetate/hexanes 1:4; UV). ^{1}H NMR (500 MHz, $CDCl_3$) δ 8.21 (s, 1H), 7.69 – 7.62 (m, 1H), 7.32 (d, *J* = 8.3 Hz, 1H), 7.14 (d, *J* = 10.0 Hz, 1H), 6.84 (t, *J* = 54.1 Hz, 1H), 2.73 (s, 3H). ^{19}F NMR (471 MHz, $CDCl_3$) δ -112.50 (t, *J* = 8.7 Hz), -117.65 (d, *J* = 54.3 Hz). ^{13}C NMR (126 MHz, $CDCl_3$) δ 179.82, 161.18, 159.73, 153.40, 146.64, 139.62 (d, *J* = 10.6 Hz), 135.33, 131.95 – 130.86 (m, 2C), 126.38 – 125.53 (m), 125.35 (d, *J* = 3.4 Hz), 117.58 (t, *J* = 6.2 Hz), 116.47 (d, *J* = 25.5 Hz), 109.15 (t, *J* = 242.0 Hz). 16.23. HRMS (ESI) m/z $[M + H]^+$ calcd for: $C_{11}H_{15}NO$: 374.0069; found: 374.0071. IR (neat): v = 3432, 3100, 2921, 1634, 1609, 1572, 1503, 1480, 1417, 1316, 1146, 1087, 1048.

[1]H and [13]C NMR Spectra

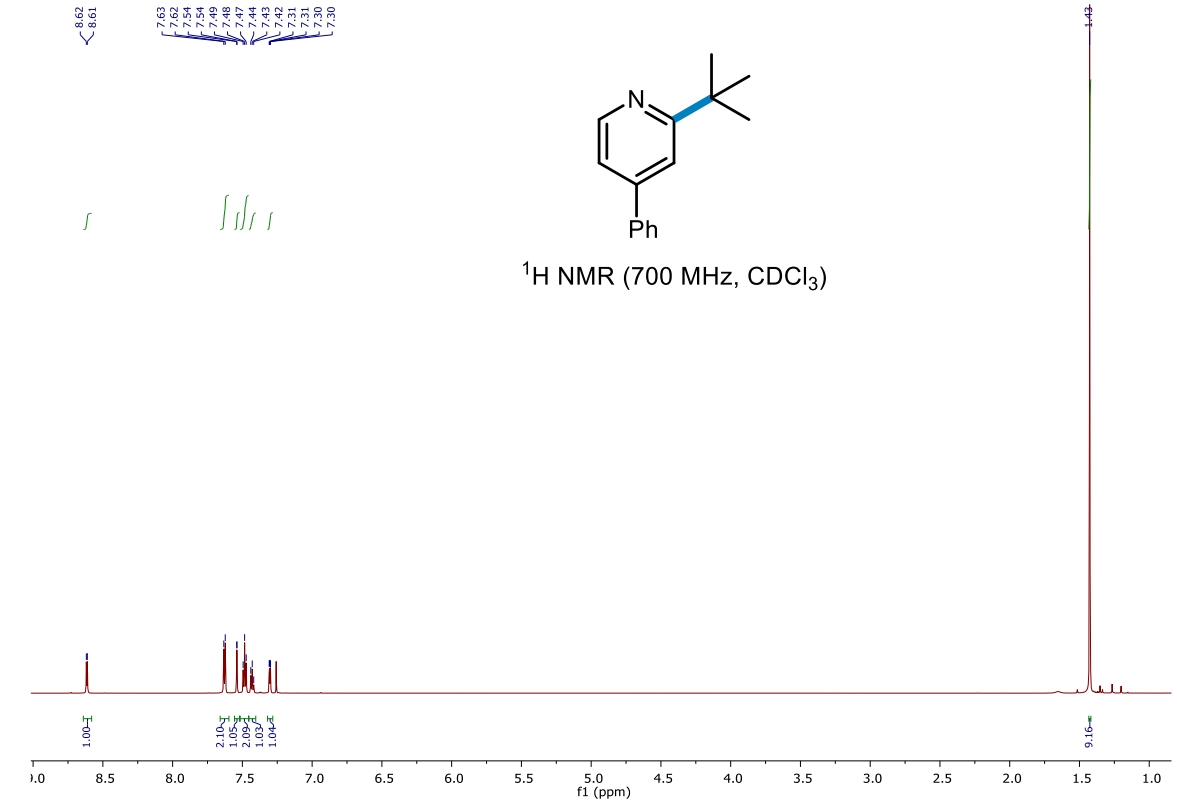

^{1}H NMR (700 MHz, $CDCl_3$)

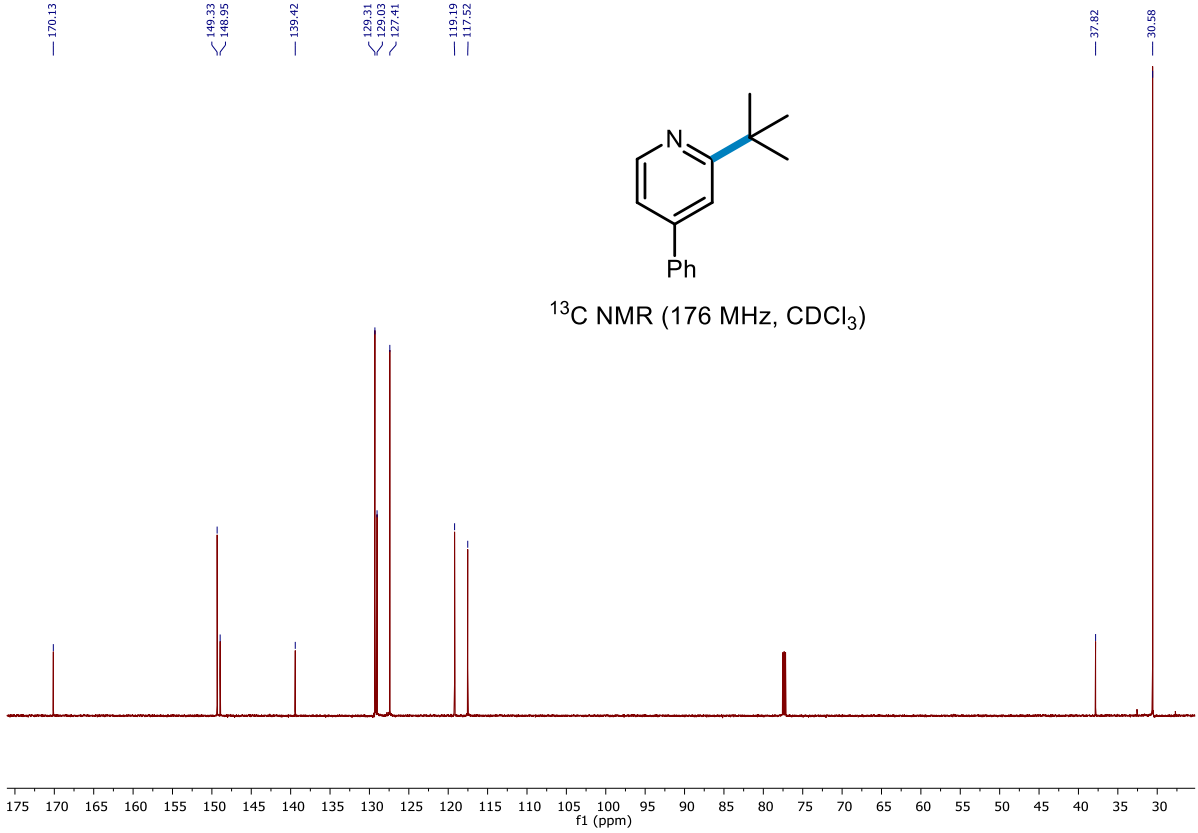

^{13}C NMR (176 MHz, $CDCl_3$)

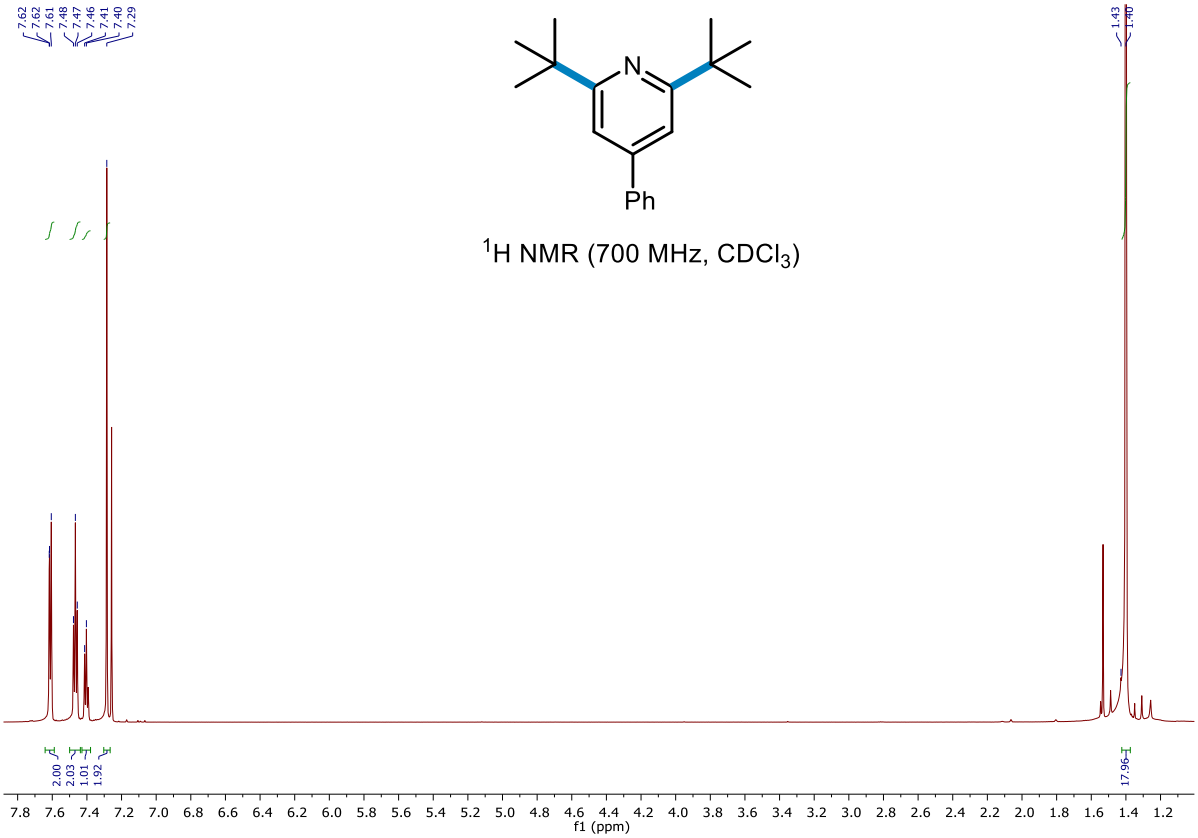

^{1}H NMR (700 MHz, $CDCl_3$)

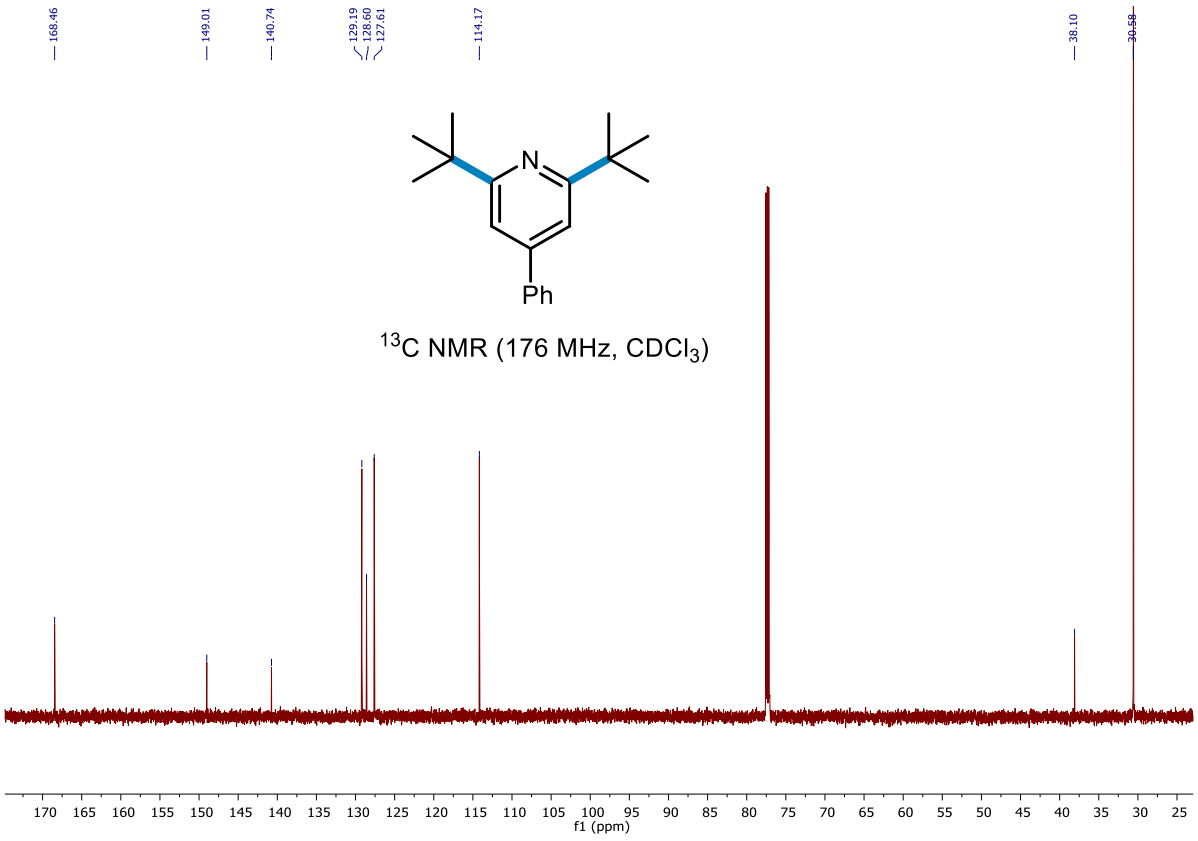

^{13}C NMR (176 MHz, $CDCl_3$)

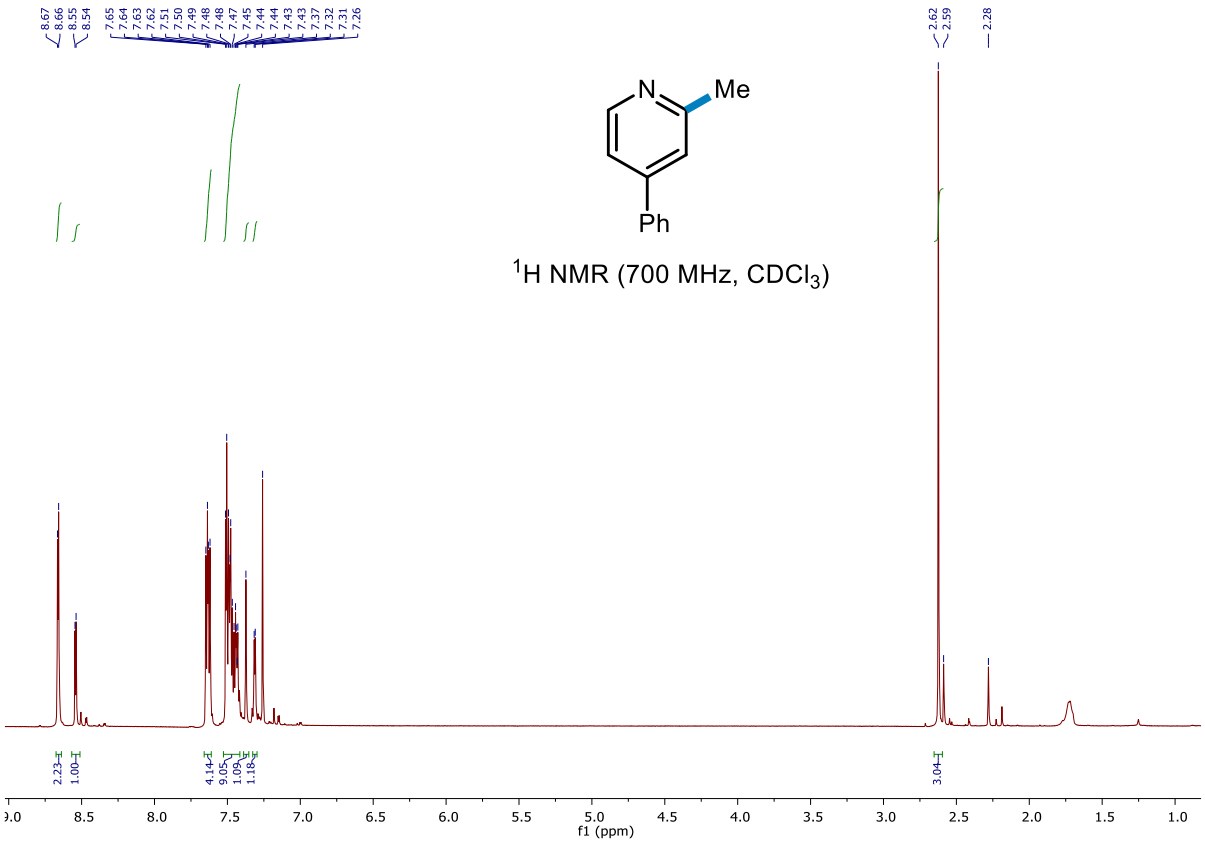

^{1}H NMR (700 MHz, $CDCl_3$)

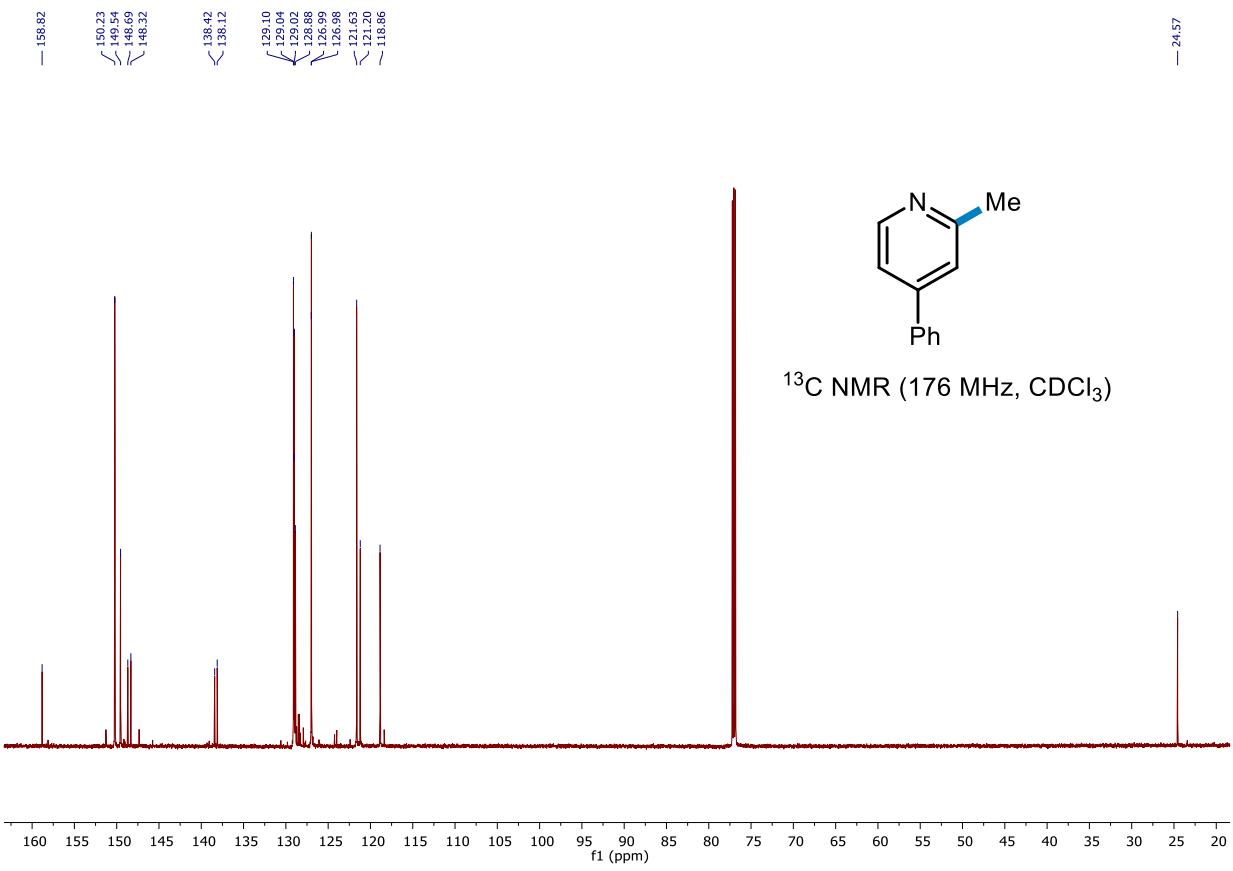

^{13}C NMR (176 MHz, $CDCl_3$)

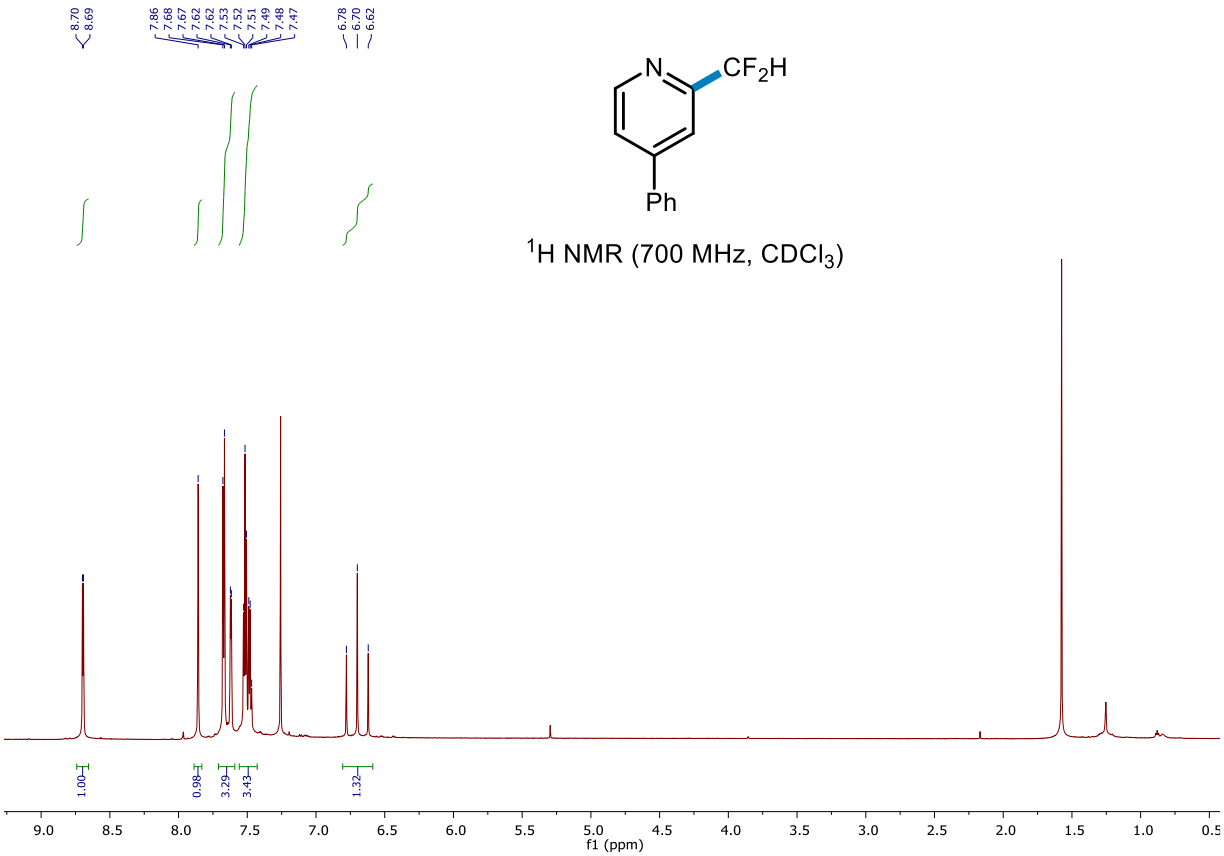
8.70
8.69
7.86
7.68
7.67
7.62
7.62
7.53
7.52
7.51
7.49
7.48
7.47
6.78
6.70
6.62
N
CF2H
Ph
1H NMR (700 MHz, CDCl3)
1.00
0.98
3.29
3.43
1.32
9.0
8.5
8.0
7.5
7.0
6.5
6.0
5.5
5.0
4.5
4.0
3.5
3.0
2.5
2.0
1.5
1.0
0.5
f1 (ppm)

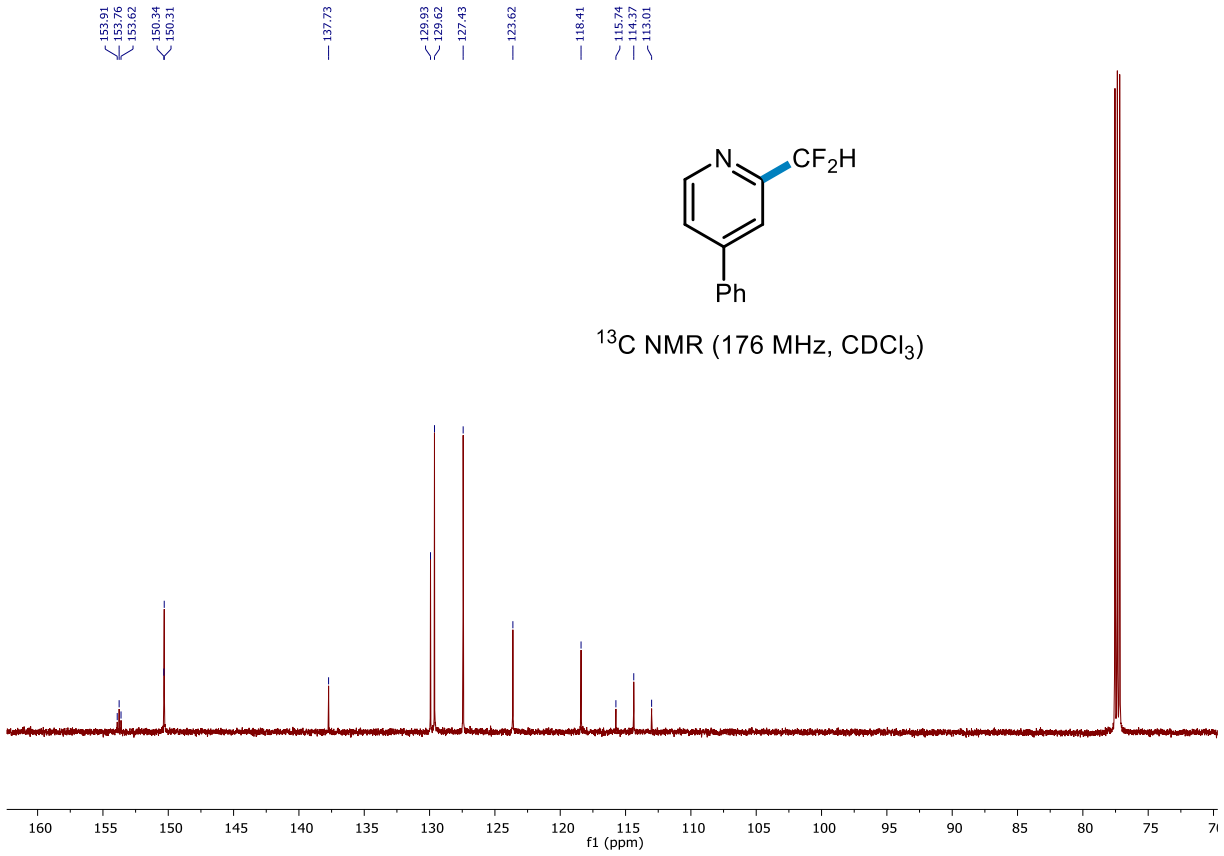
153.91
153.76
153.62
150.34
150.31
137.73
129.93
129.62
127.43
123.62
118.41
115.74
114.37
113.01
N
CF2H
Ph
13C NMR (176 MHz, CDCl3)
160
155
150
145
140
135
130
125
120
115
110
105
100
95
90
85
80
75
f1 (ppm)

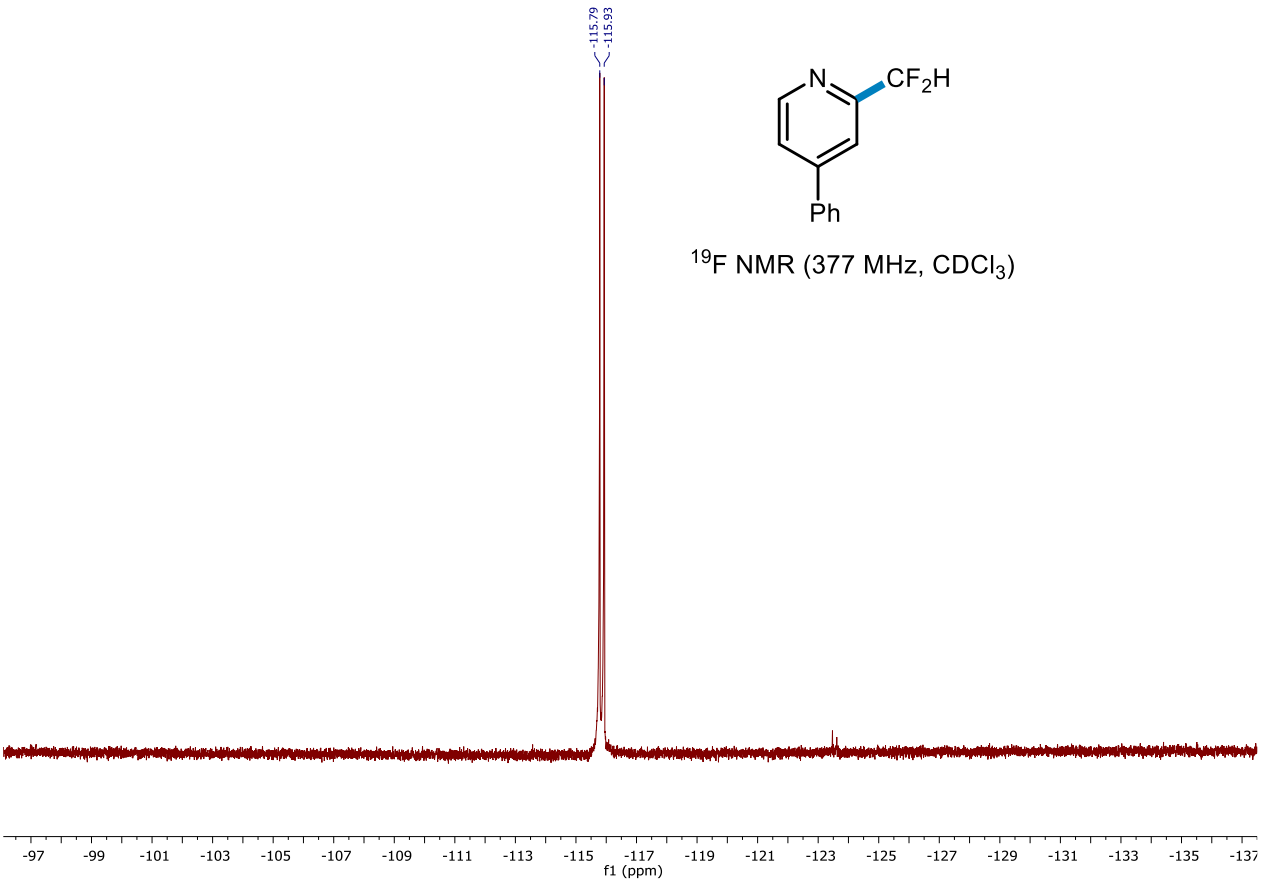

^{19}F NMR (377 MHz, $CDCl_3$)

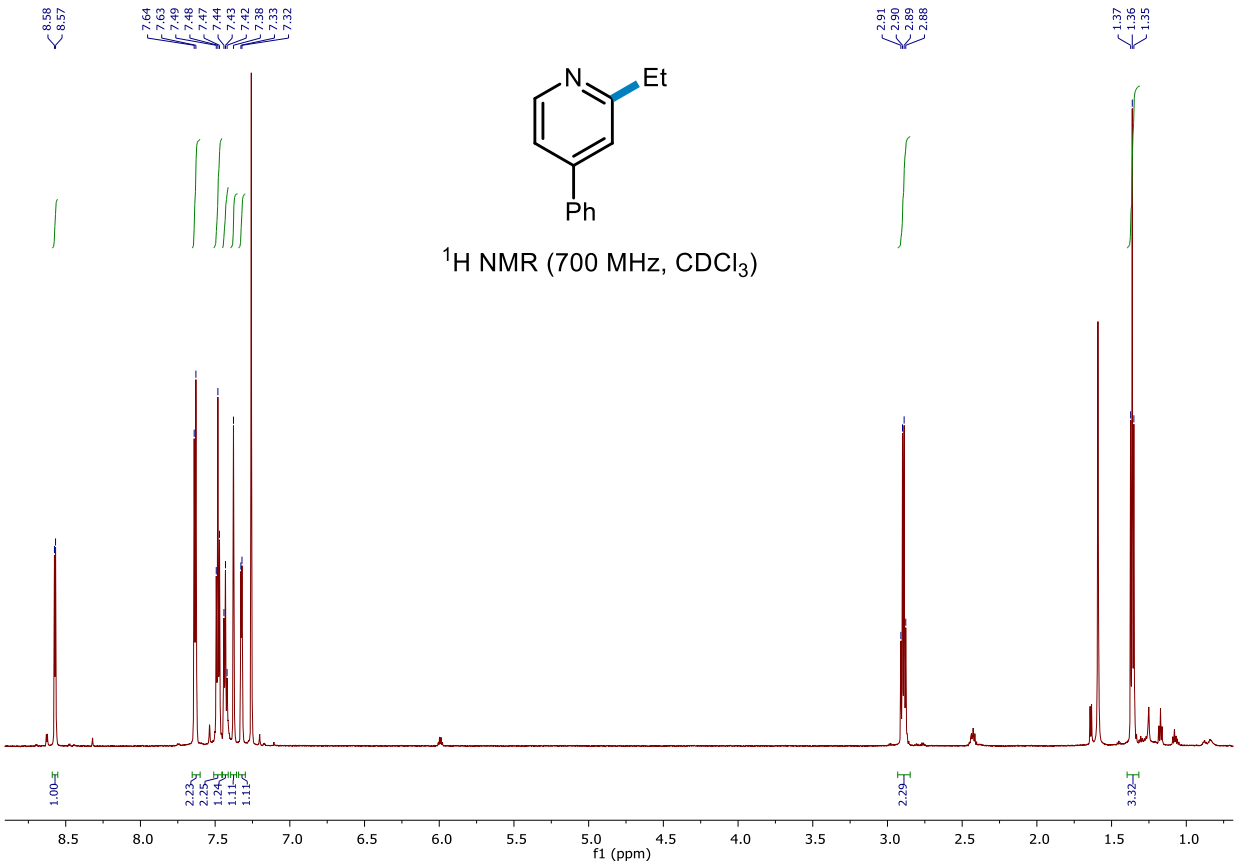

^{1}H NMR (700 MHz, $CDCl_3$)

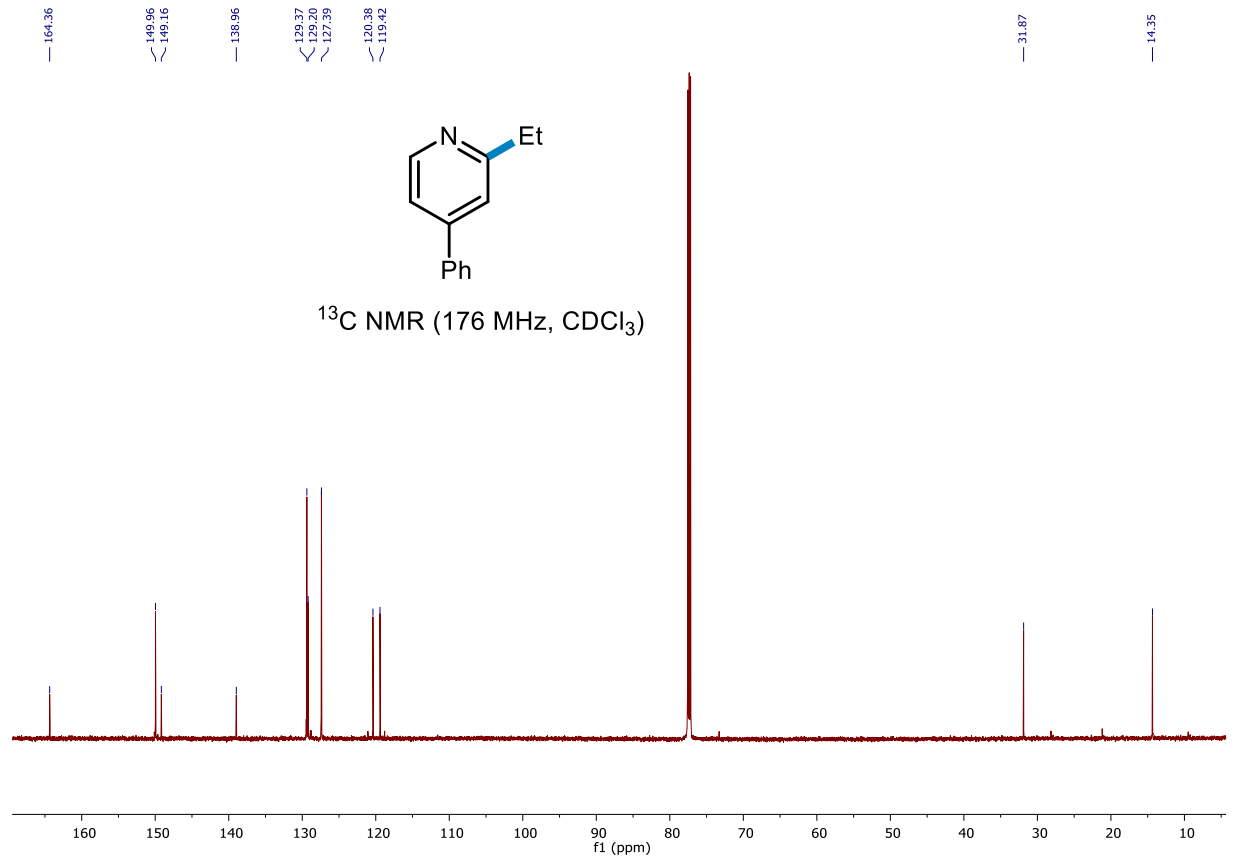

^{13}C NMR (176 MHz, $CDCl_3$)

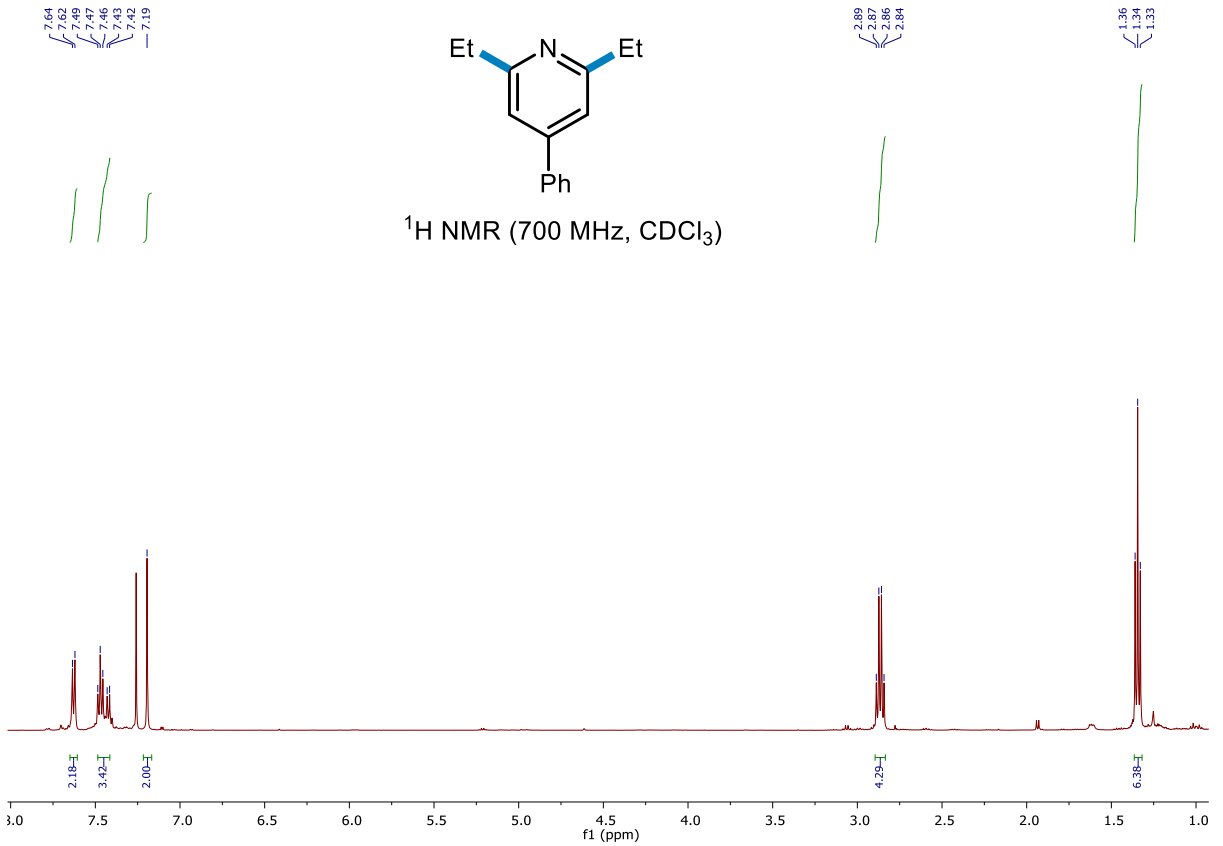

^{1}H NMR (700 MHz, $CDCl_3$)

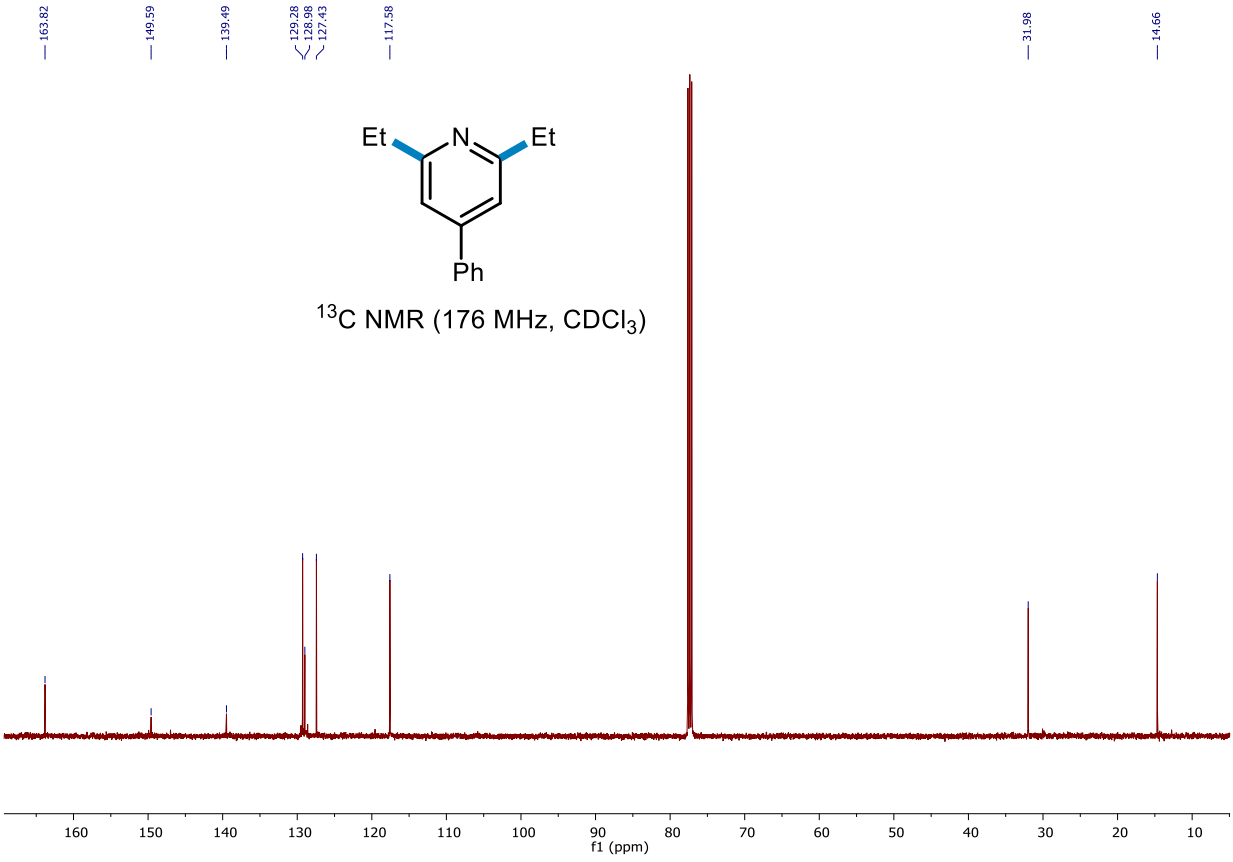

^{13}C NMR (176 MHz, $CDCl_3$)

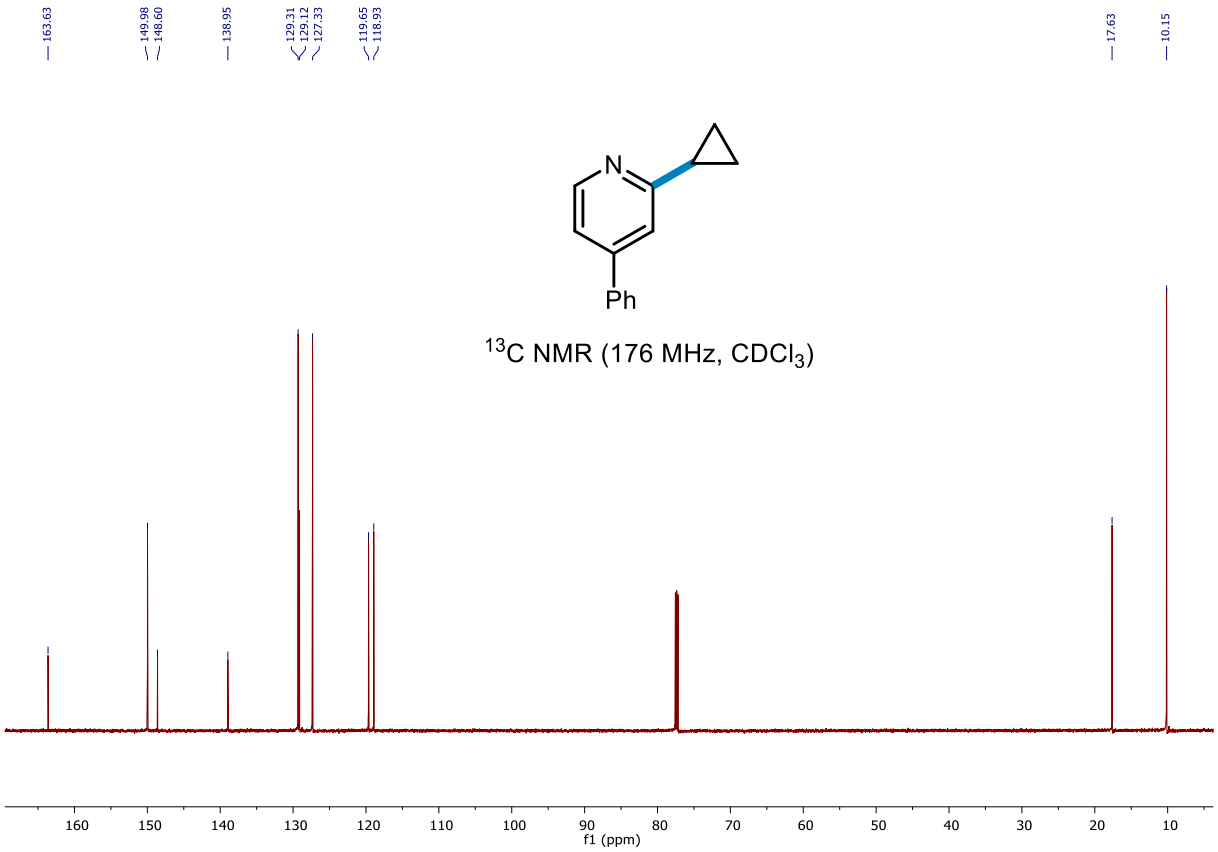

^{13}C NMR (176 MHz, $CDCl_3$)

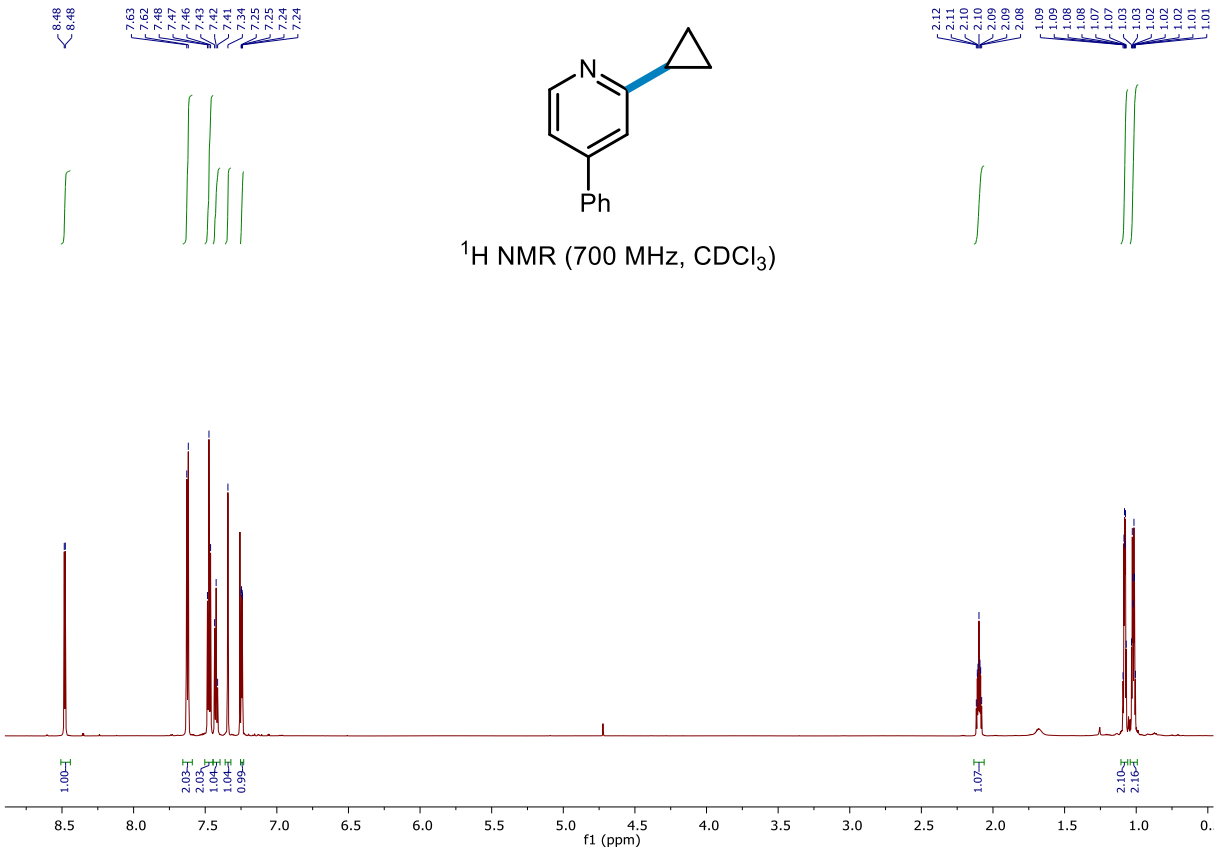

^{1}H NMR (700 MHz, $CDCl_3$)

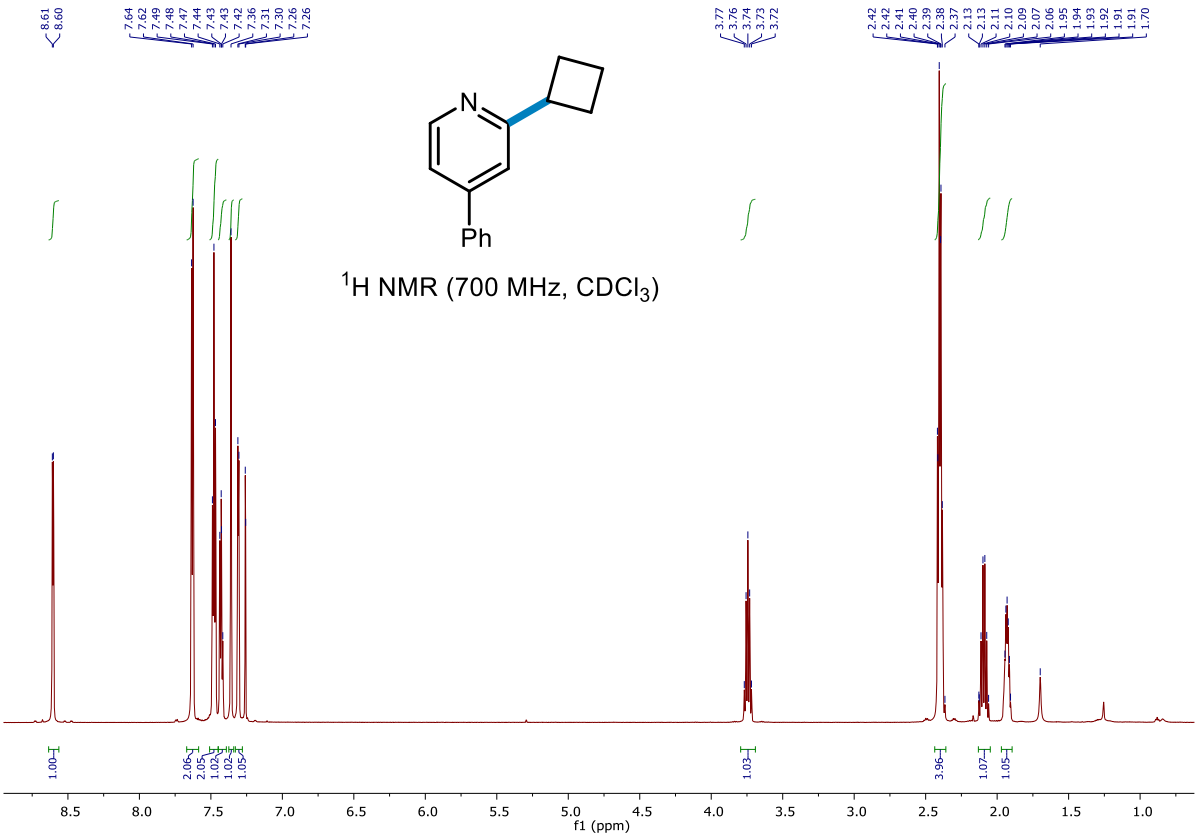

^{1}H NMR (700 MHz, $CDCl_3$)

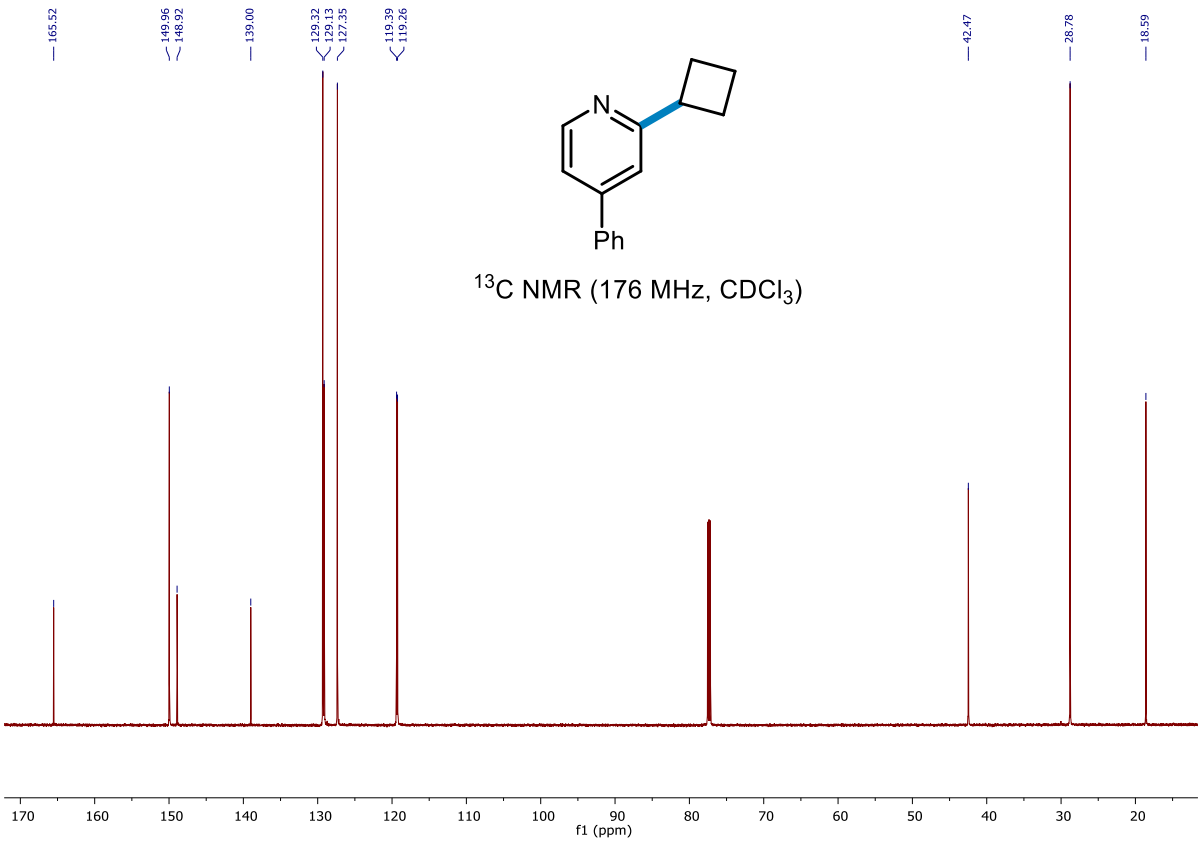

^{13}C NMR (176 MHz, $CDCl_3$)

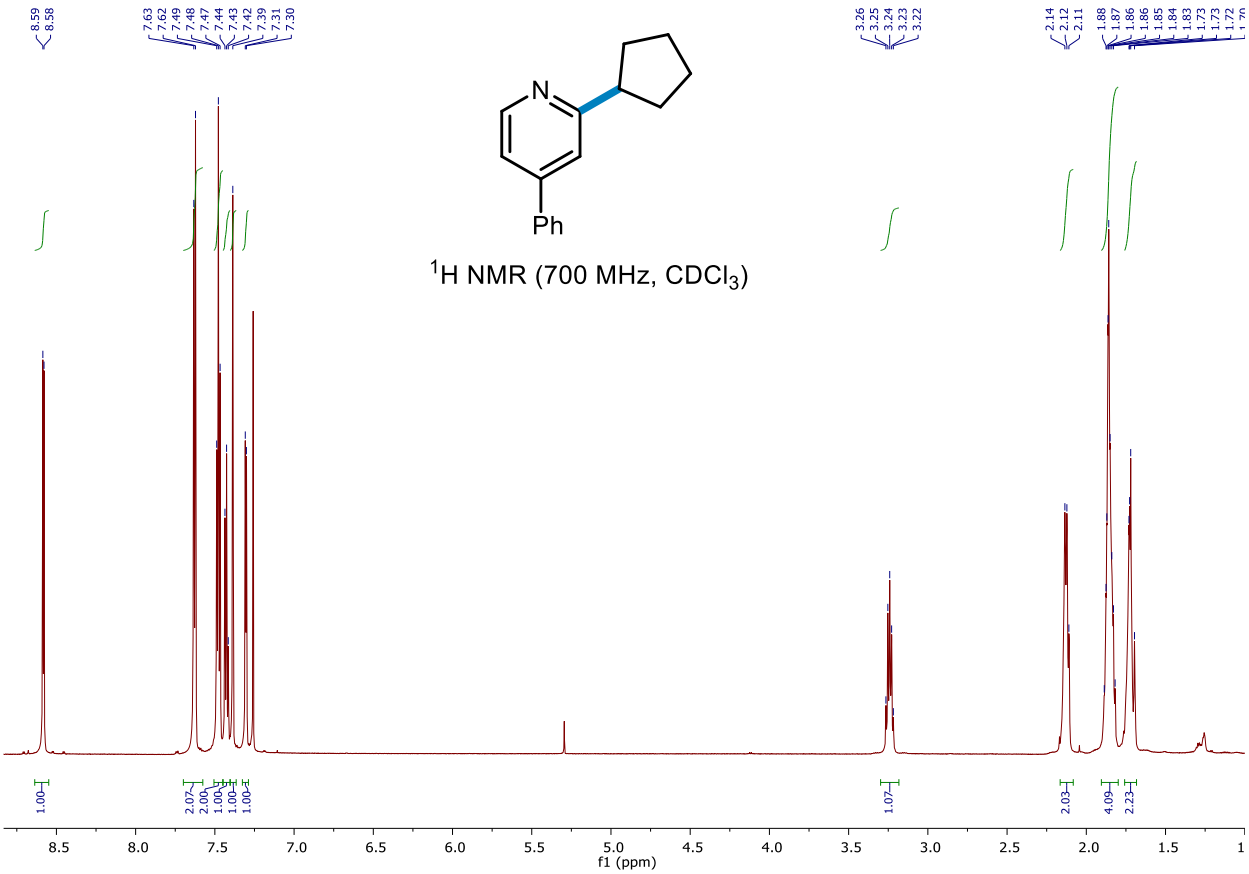

^{1}H NMR (700 MHz, $CDCl_3$)

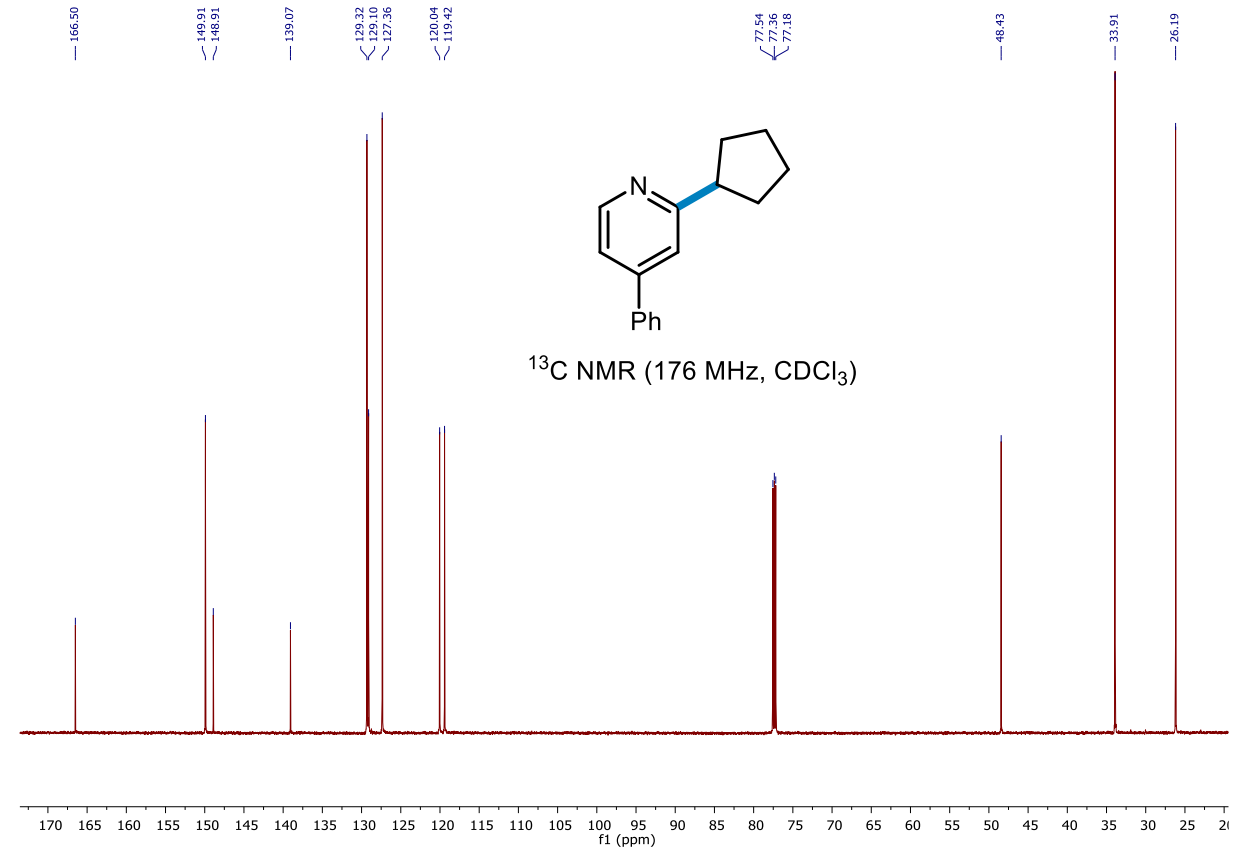

^{13}C NMR (176 MHz, $CDCl_3$)

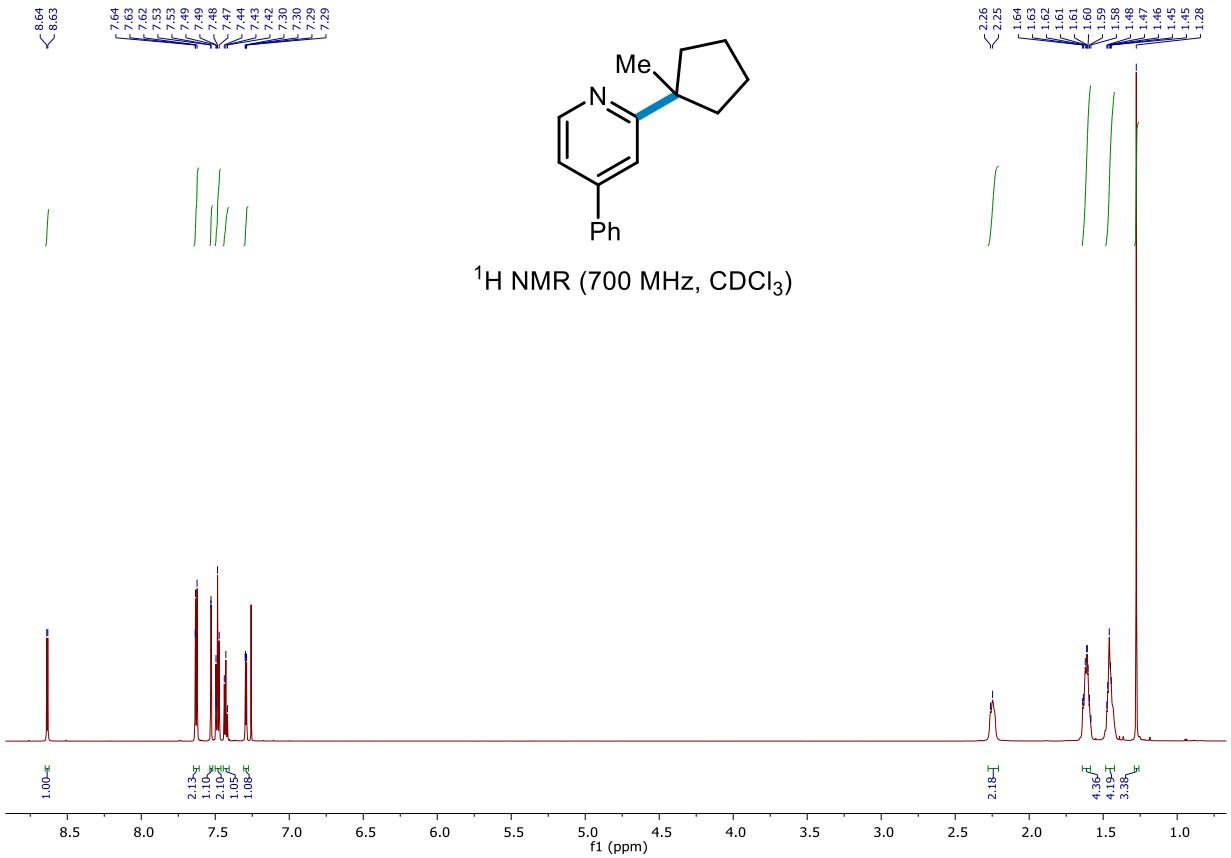

^{1}H NMR (700 MHz, $CDCl_3$)

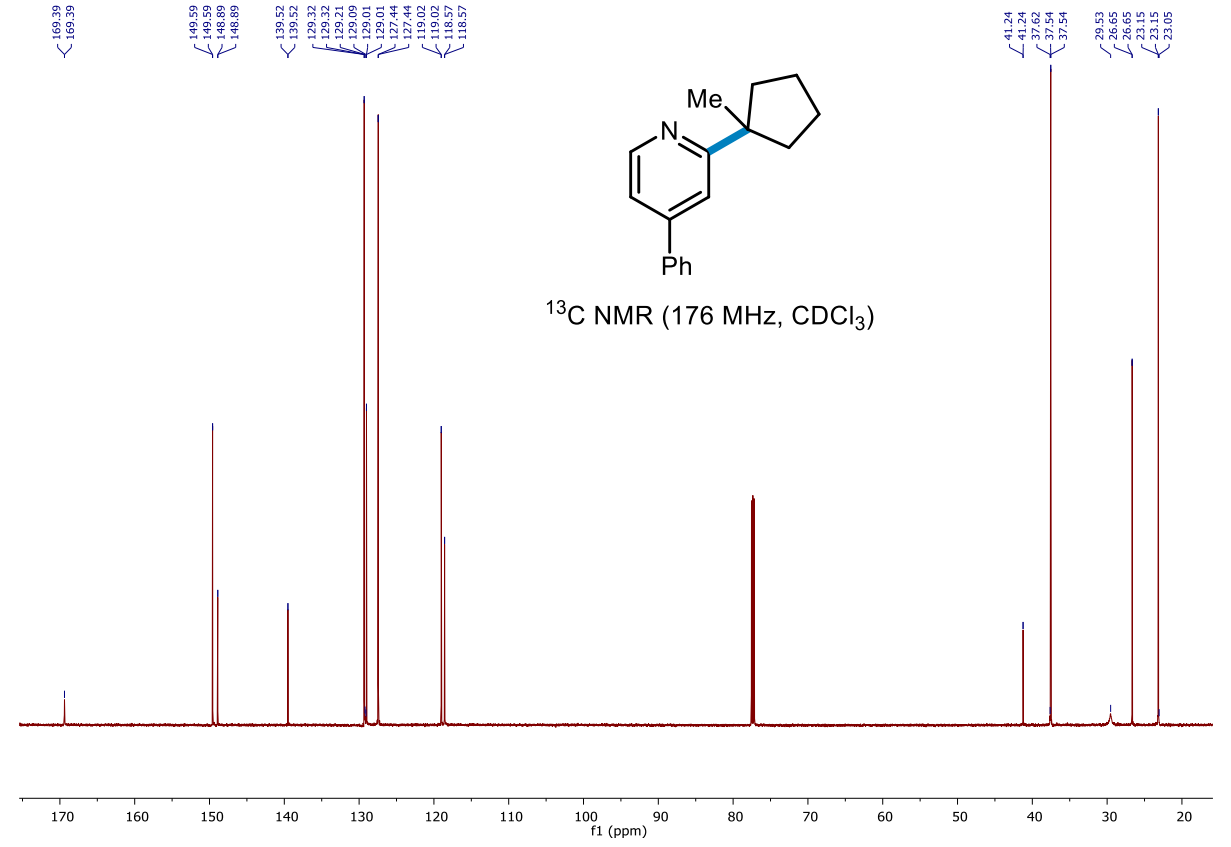

^{13}C NMR (176 MHz, $CDCl_3$)

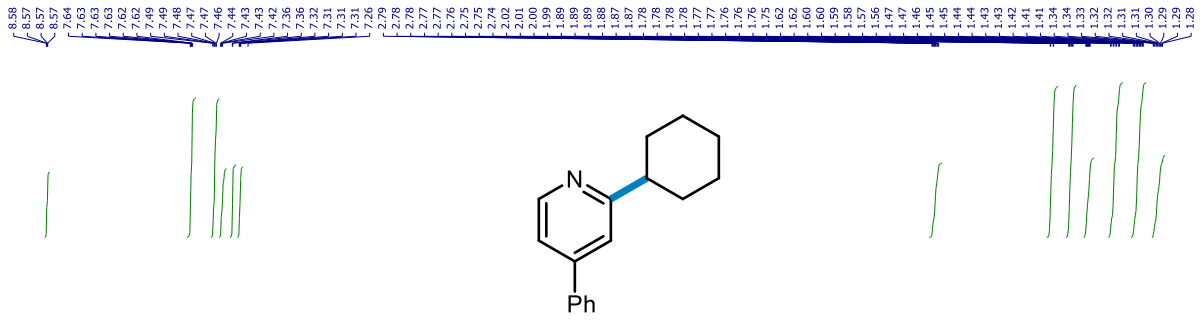

^{1}H NMR (700 MHz, $CDCl_3$)

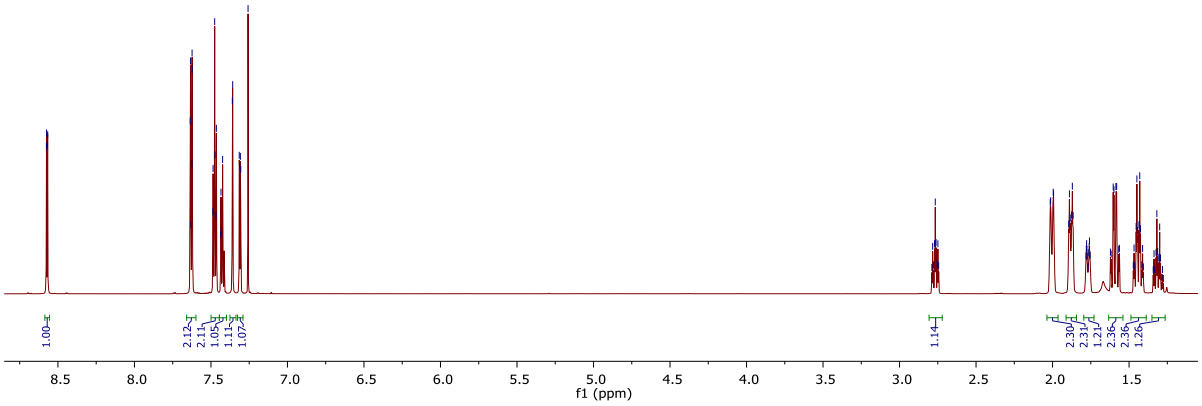

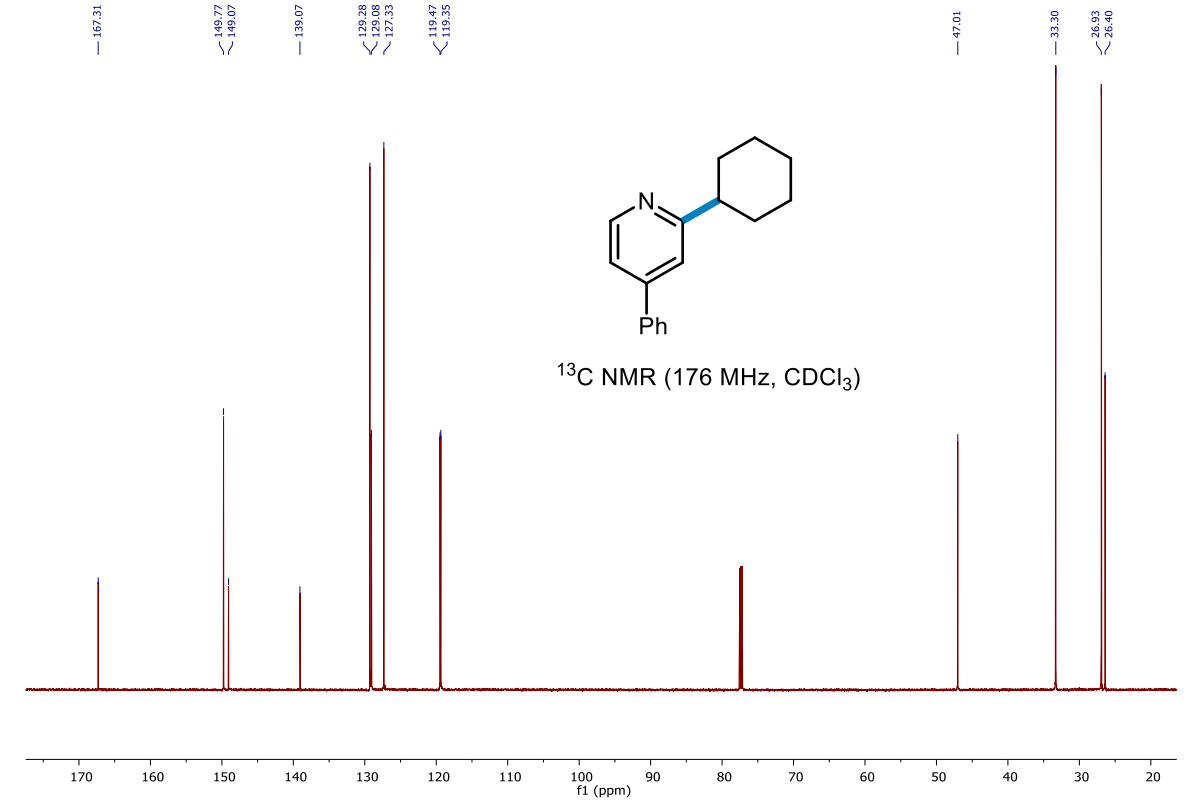

^{13}C NMR (176 MHz, $CDCl_3$)

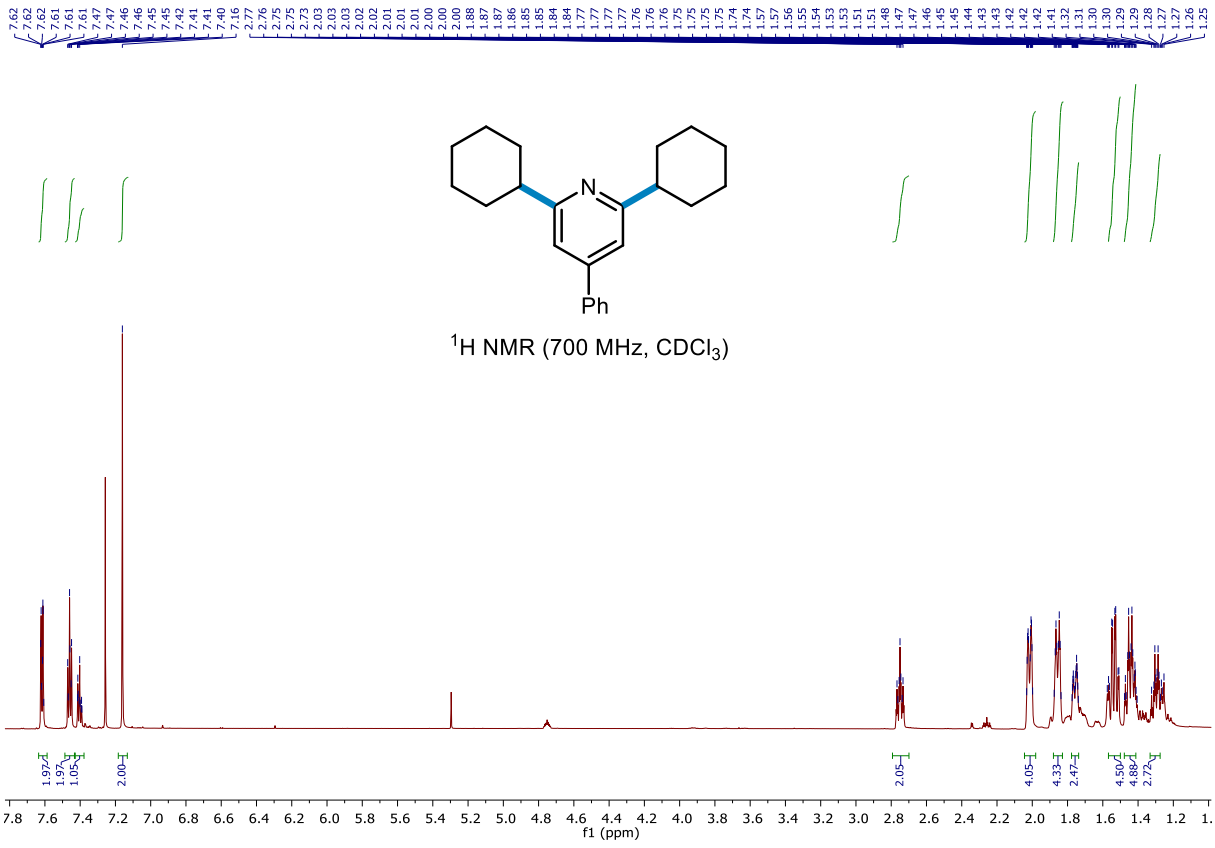

^{1}H NMR (700 MHz, $CDCl_3$)

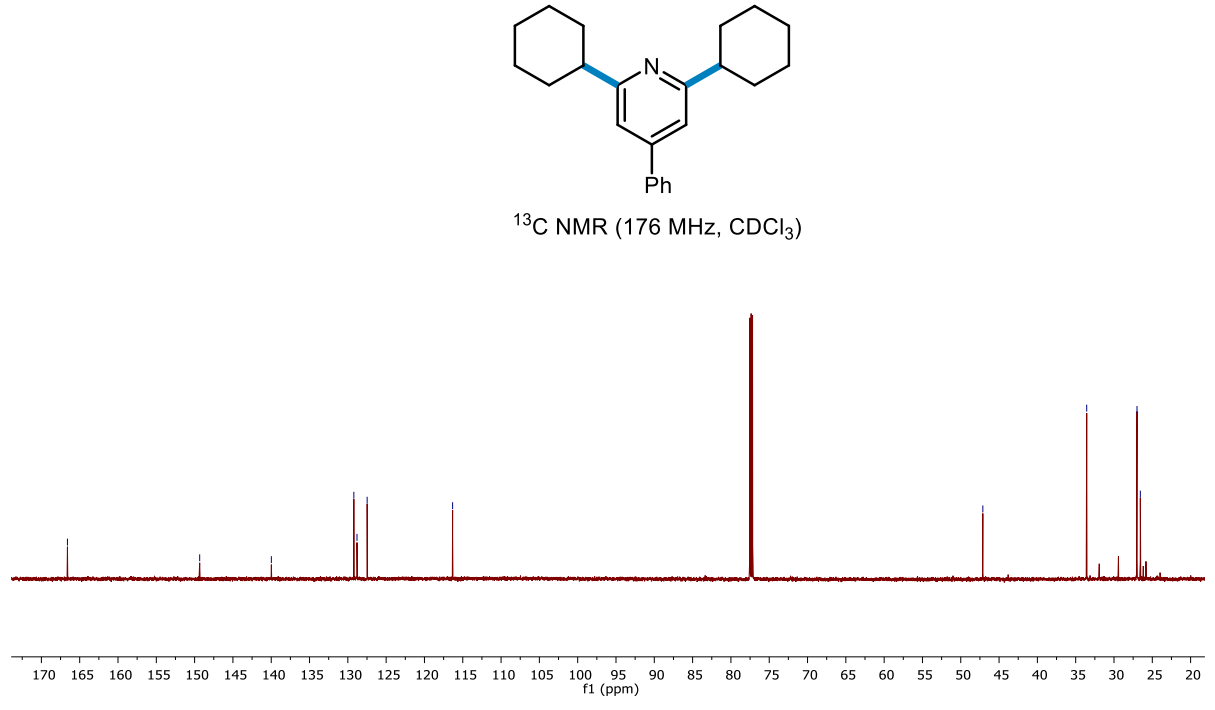

^{13}C NMR (176 MHz, $CDCl_3$)

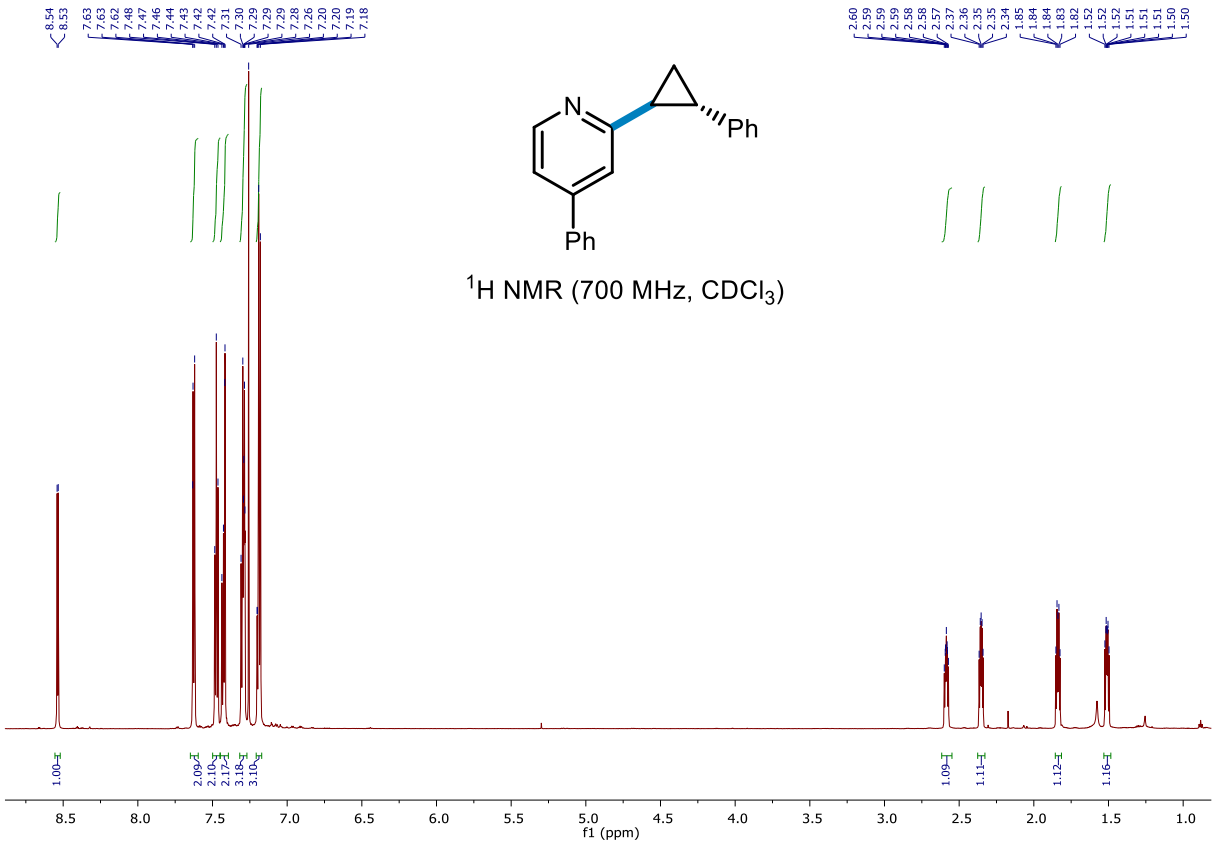

^{1}H NMR (700 MHz, $CDCl_3$)

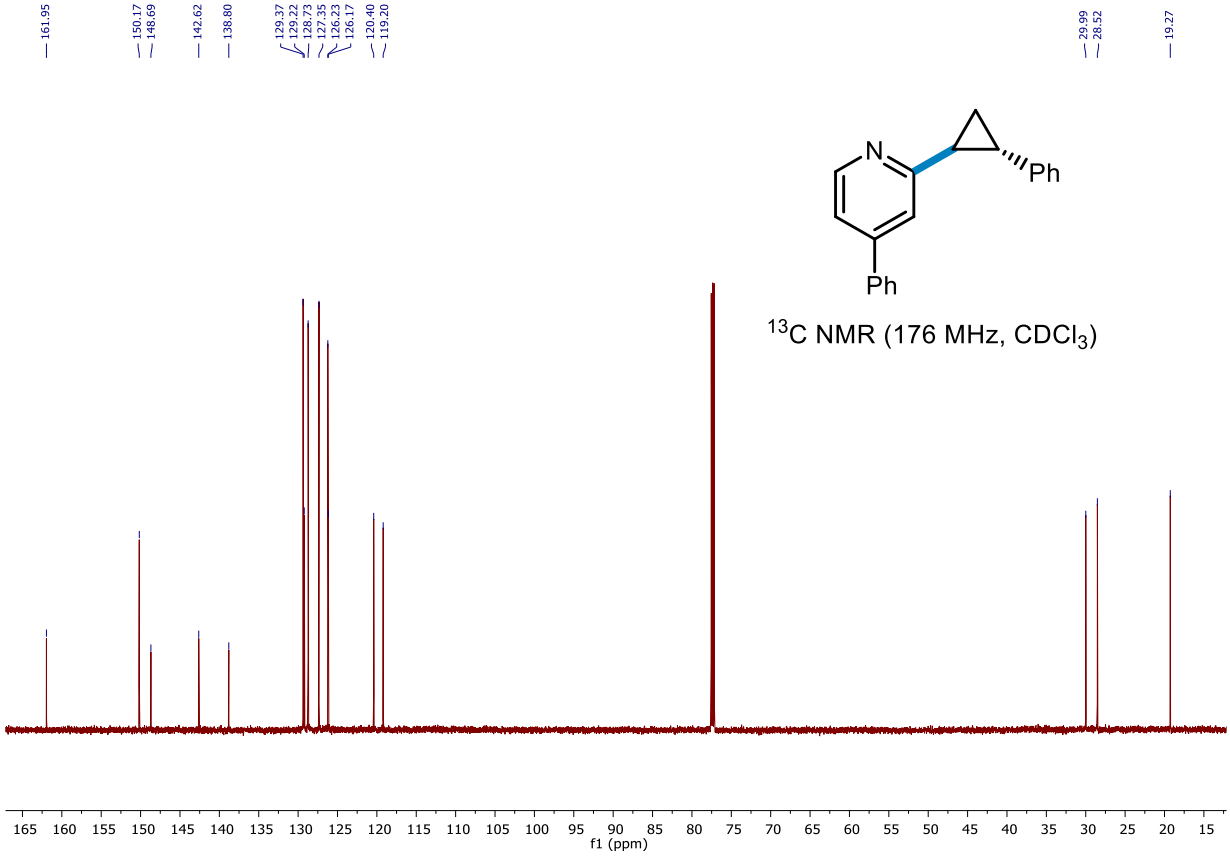

^{13}C NMR (176 MHz, $CDCl_3$)

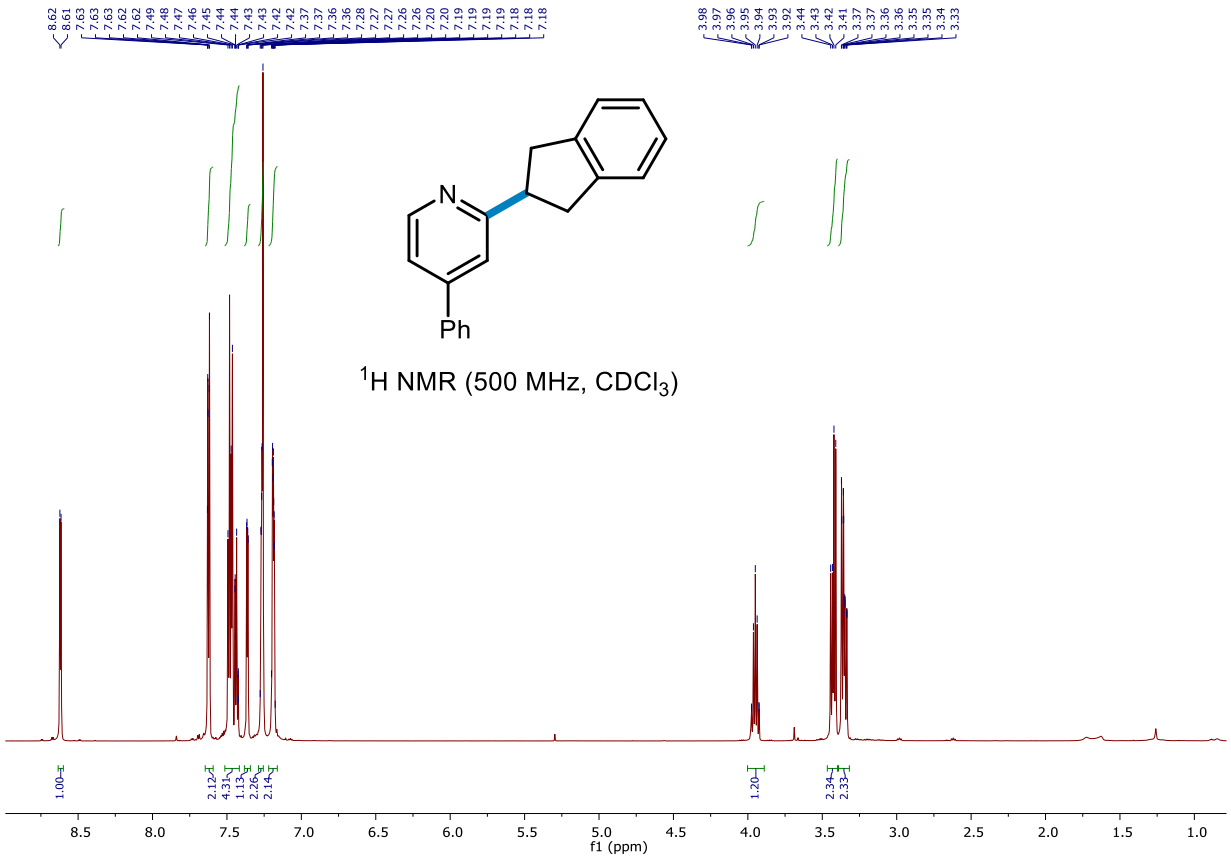
N
Ph
1H NMR (500 MHz, CDCl3)
f1 (ppm)

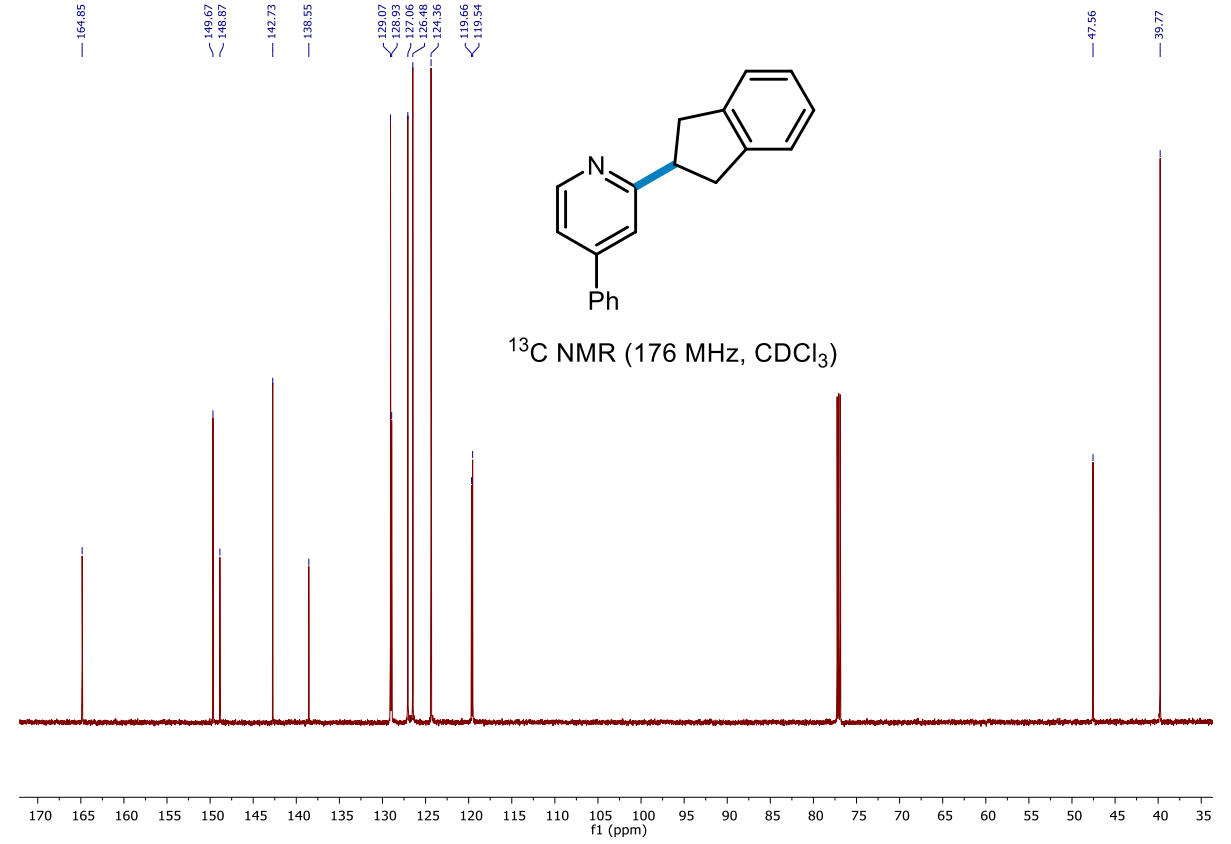
N
Ph
13C NMR (176 MHz, CDCl3)
f1 (ppm)

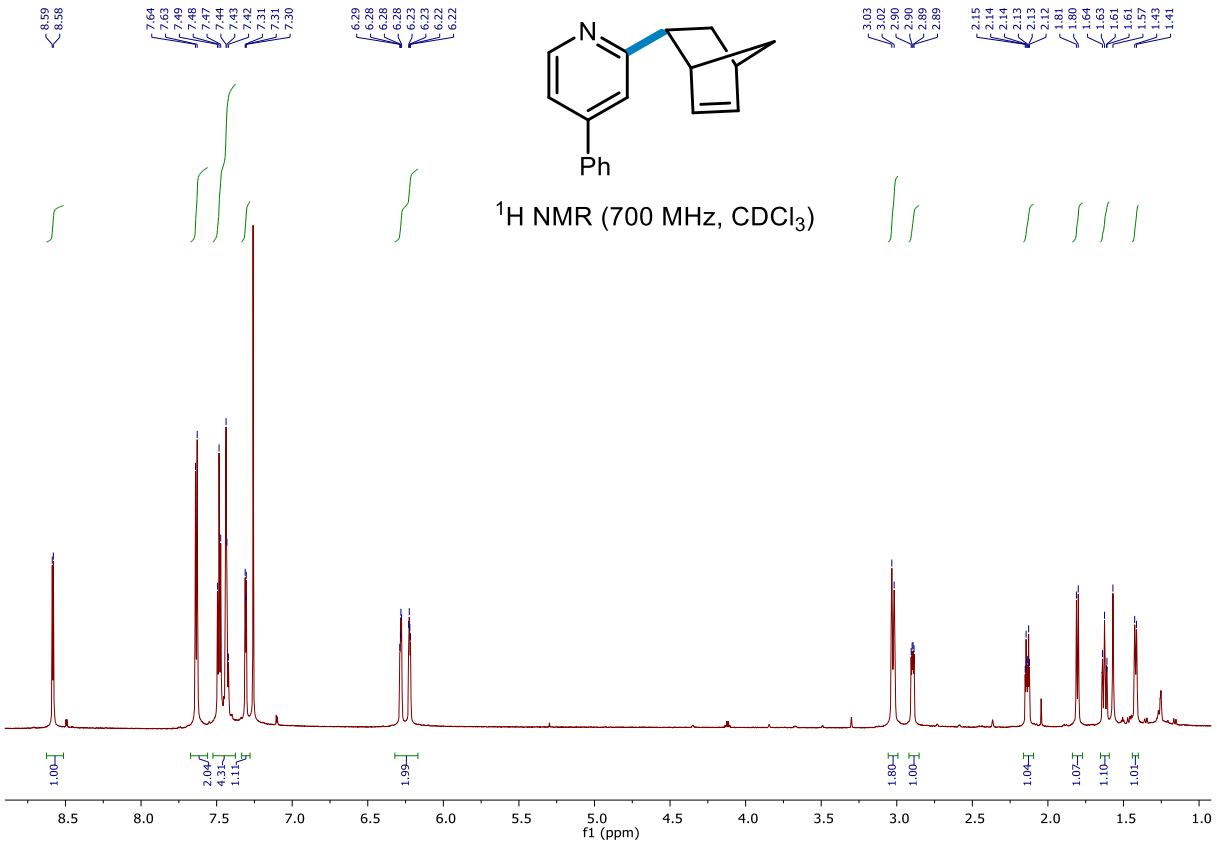
N
Ph
1H NMR (700 MHz, CDCl3)
f1 (ppm)

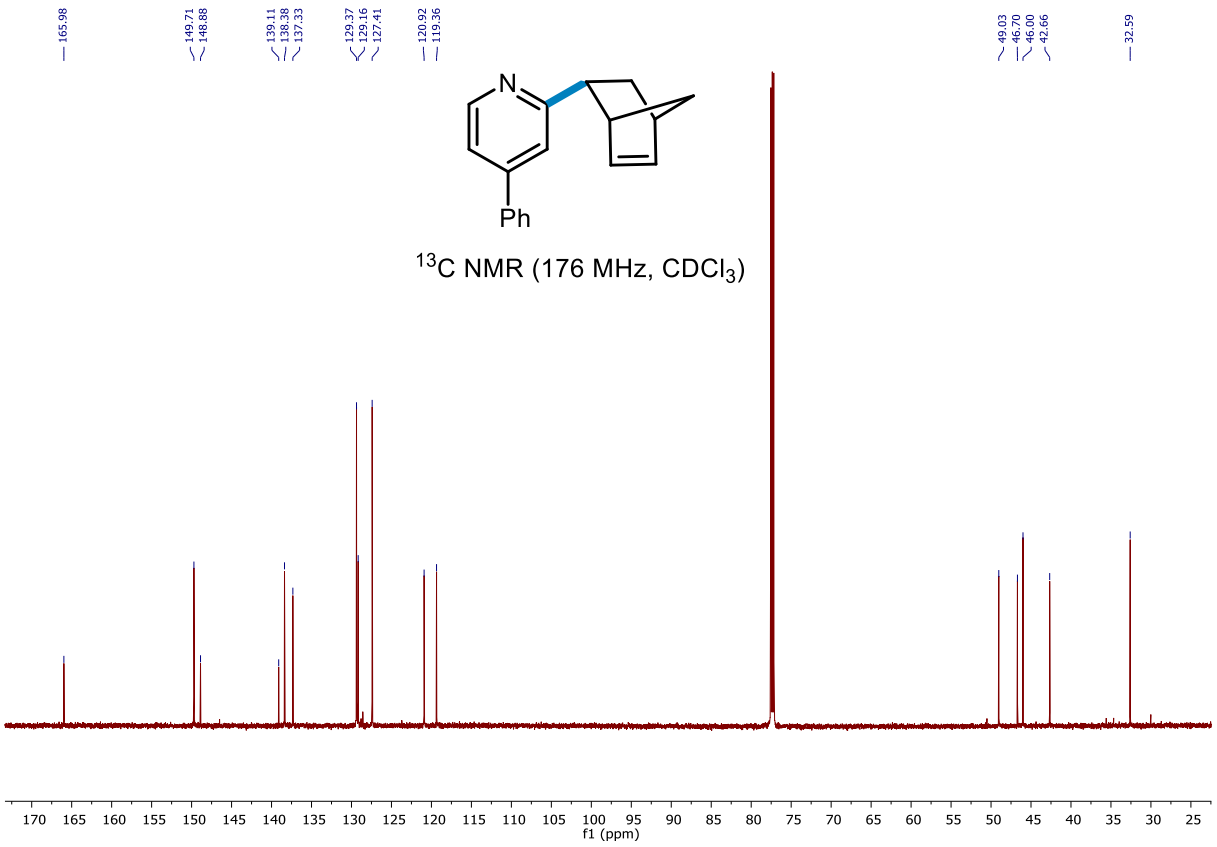
N
Ph
13C NMR (176 MHz, CDCl3)
f1 (ppm)

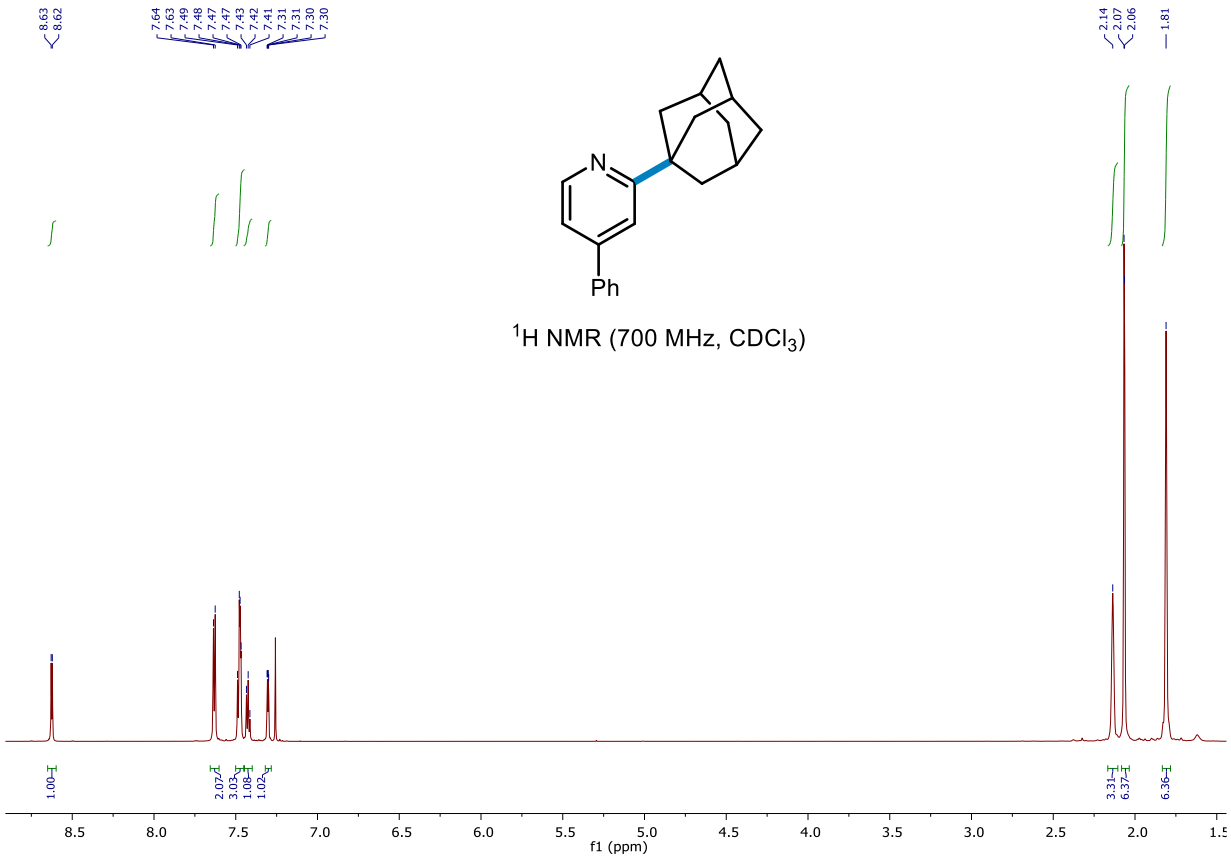

^{1}H NMR (700 MHz, $CDCl_3$)

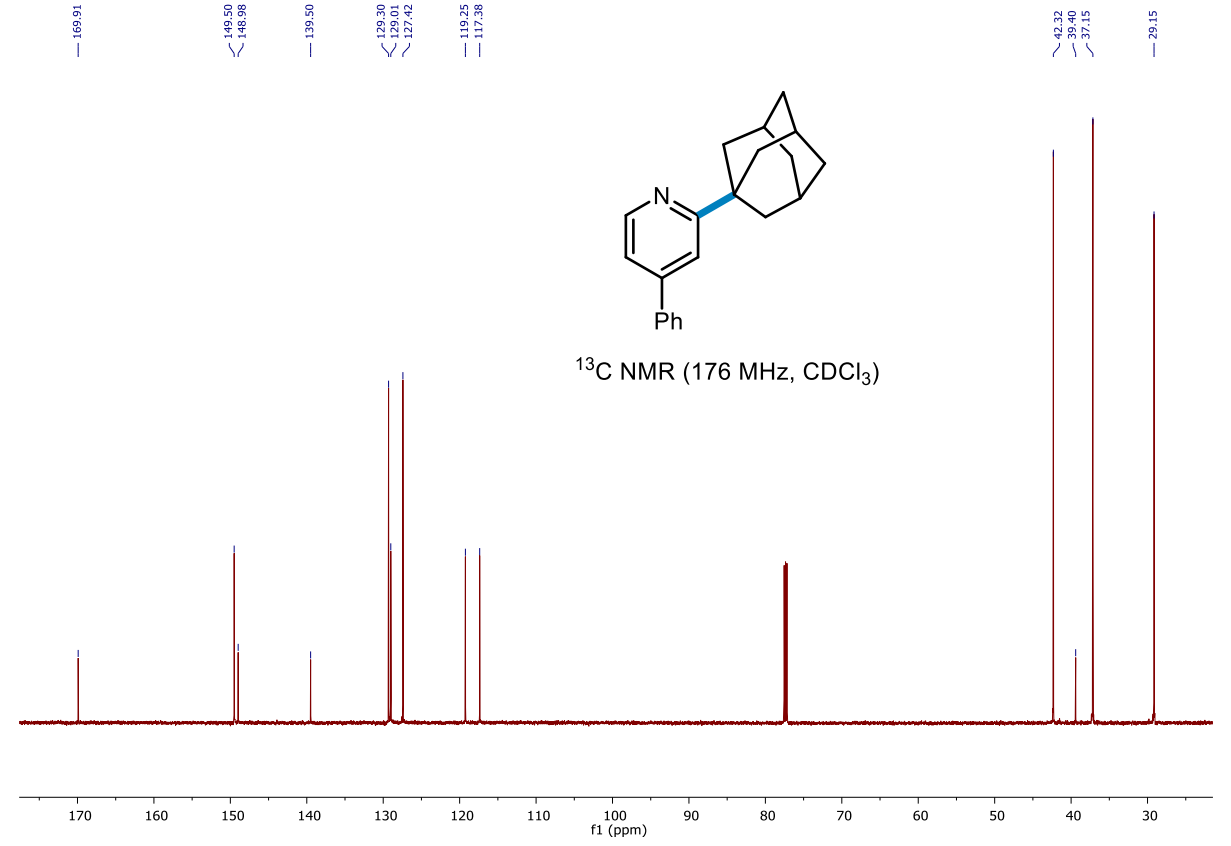

^{13}C NMR (176 MHz, $CDCl_3$)

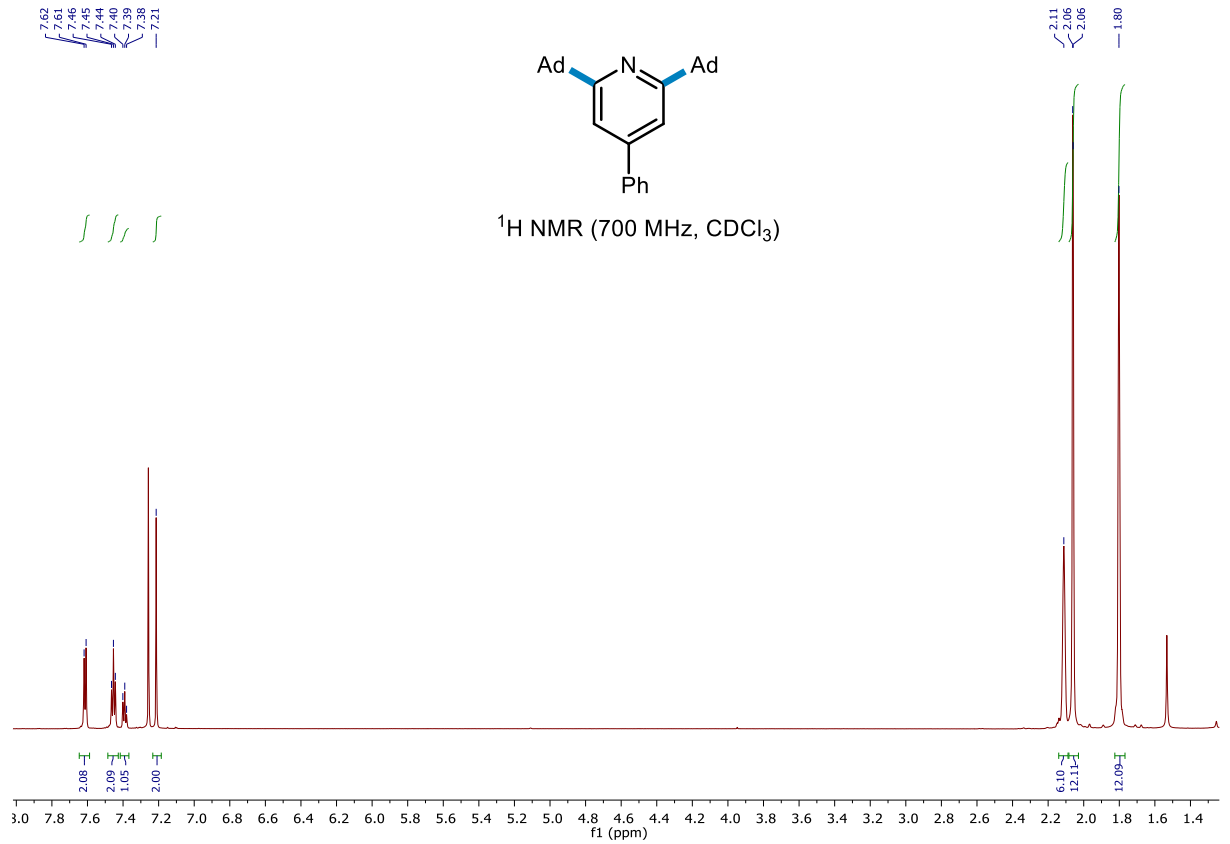

^{1}H NMR (700 MHz, $CDCl_3$)

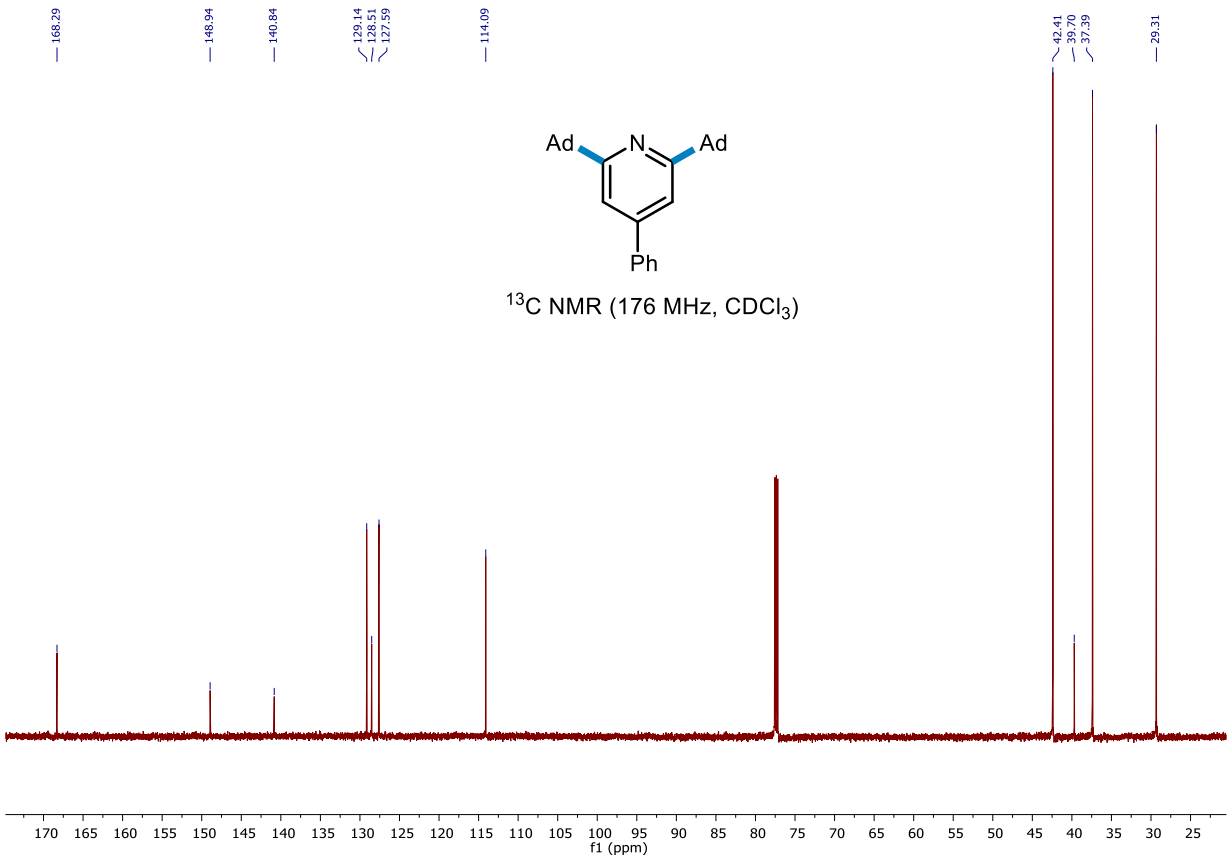

^{13}C NMR (176 MHz, $CDCl_3$)

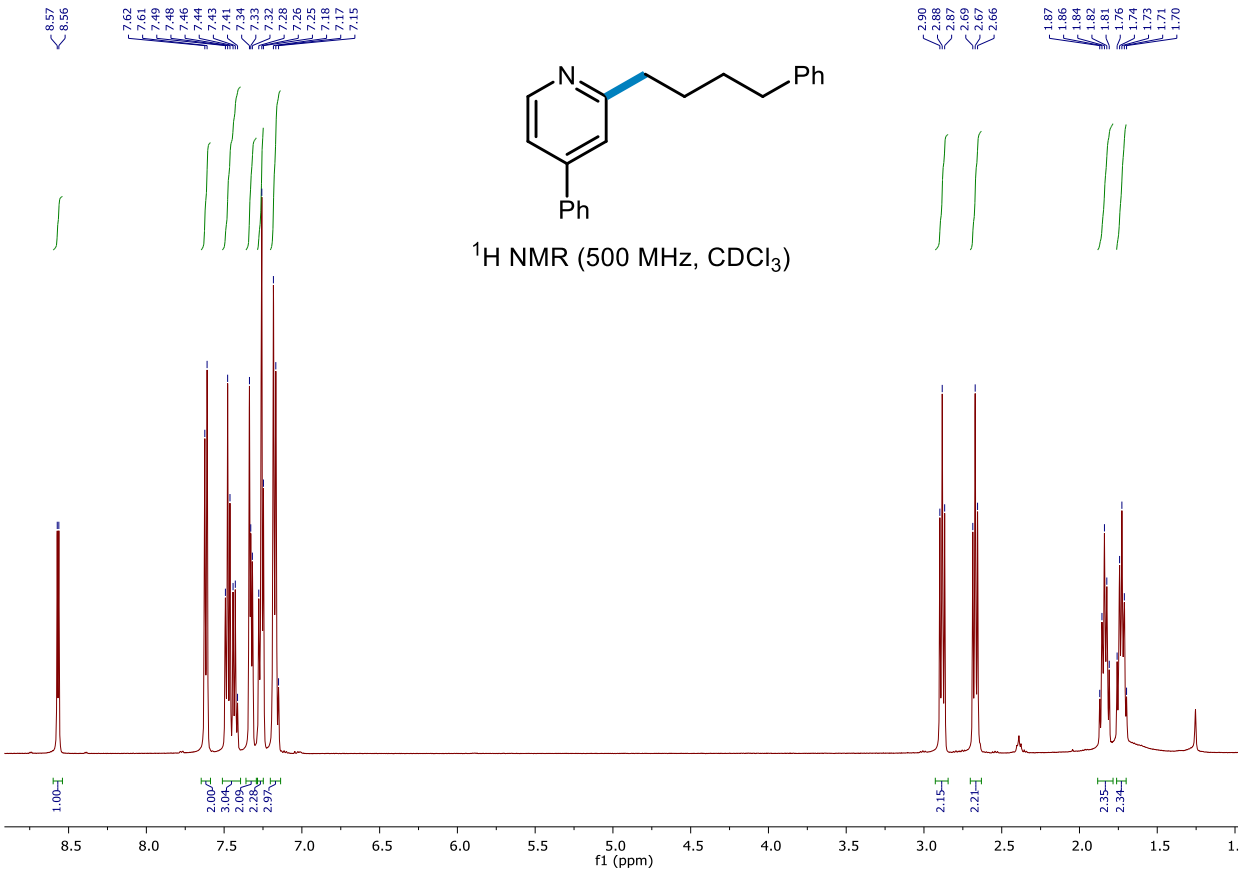

^{1}H NMR (500 MHz, $CDCl_3$)

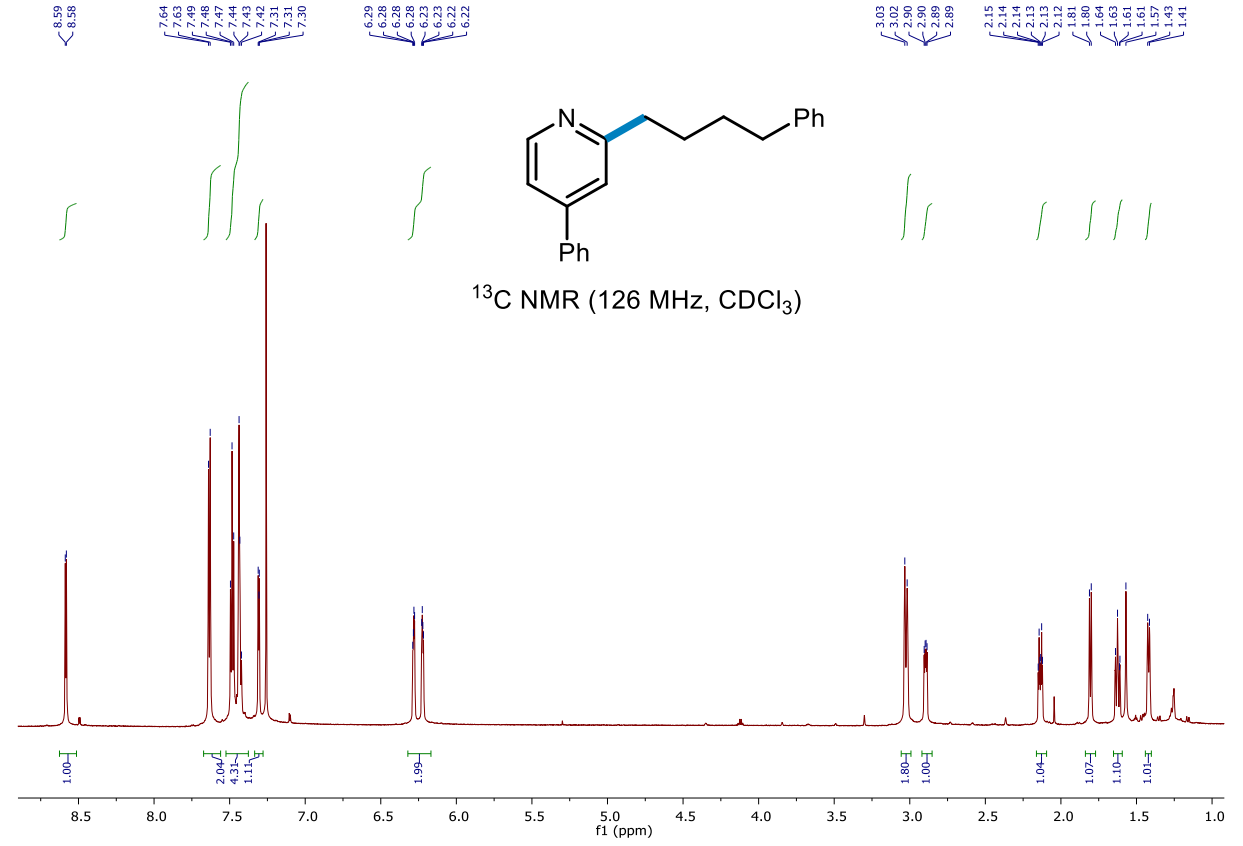

^{13}C NMR (126 MHz, $CDCl_3$)

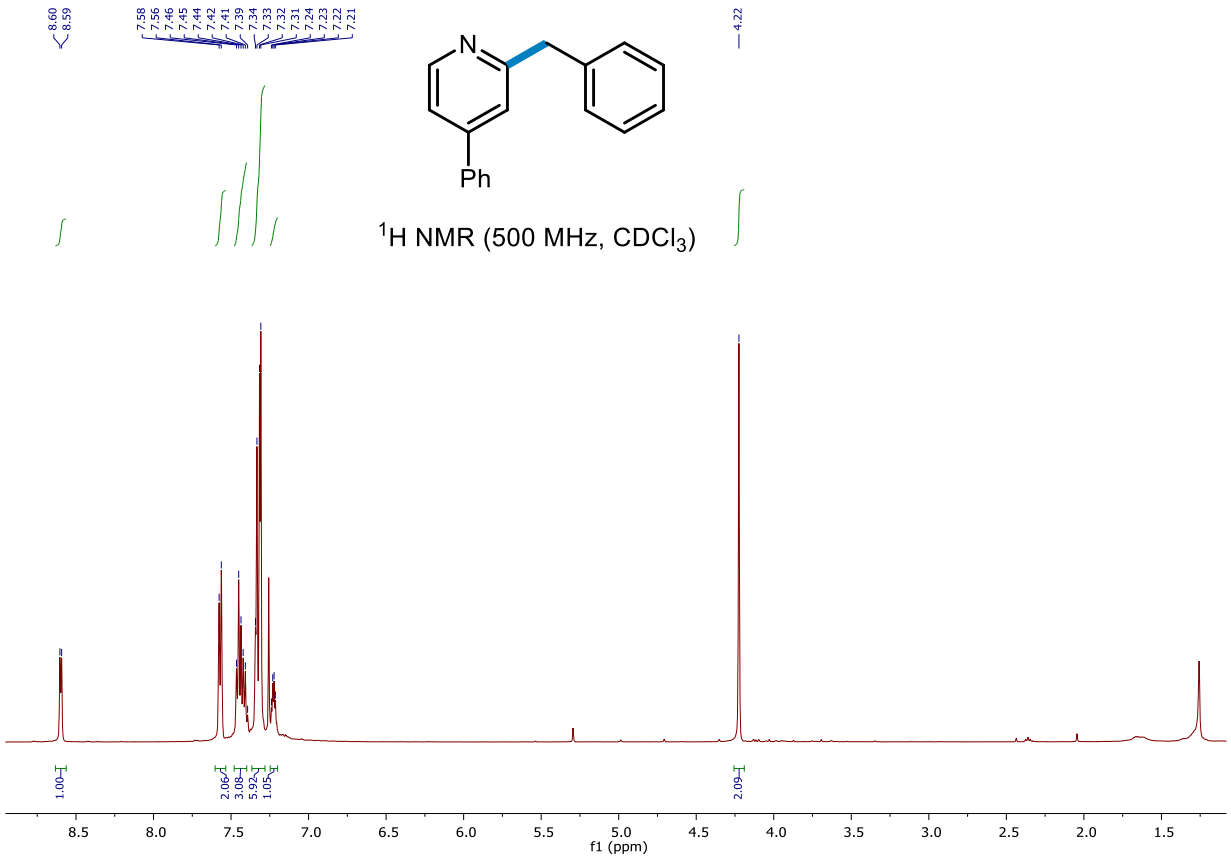

^{1}H NMR (500 MHz, $CDCl_3$)

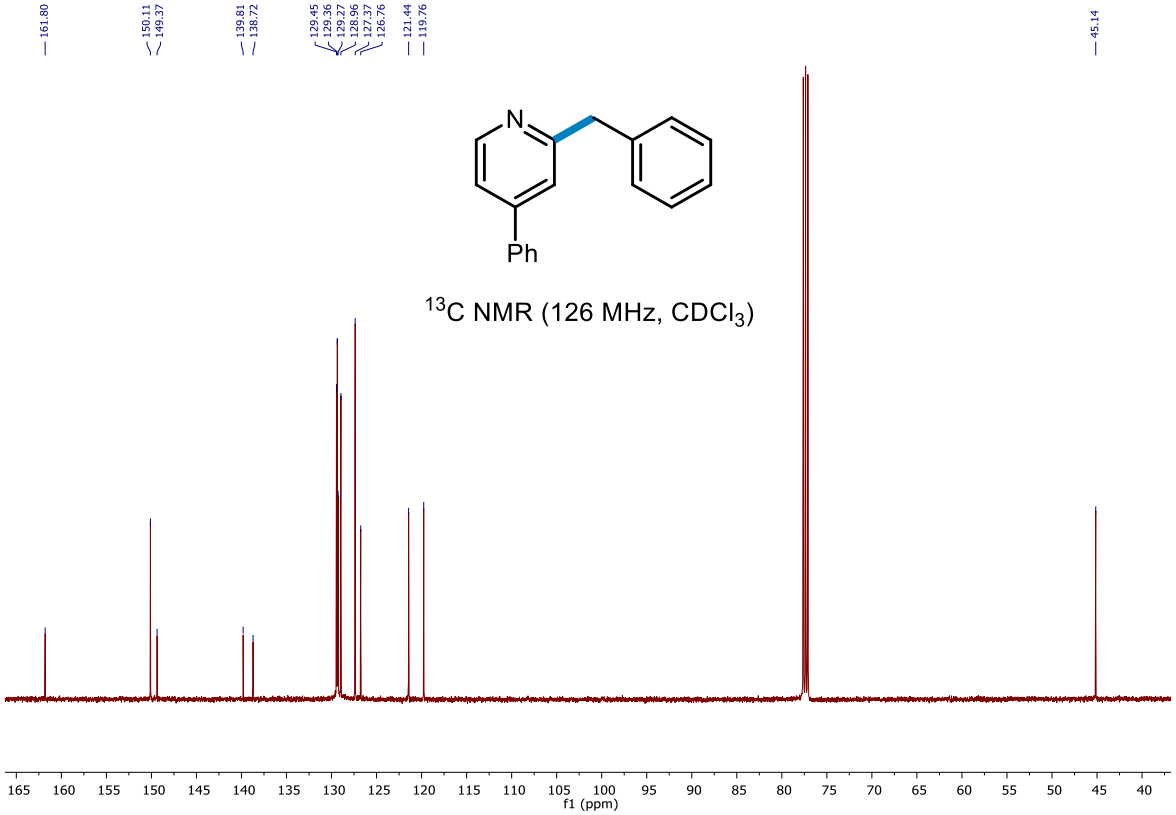

^{13}C NMR (126 MHz, $CDCl_3$)

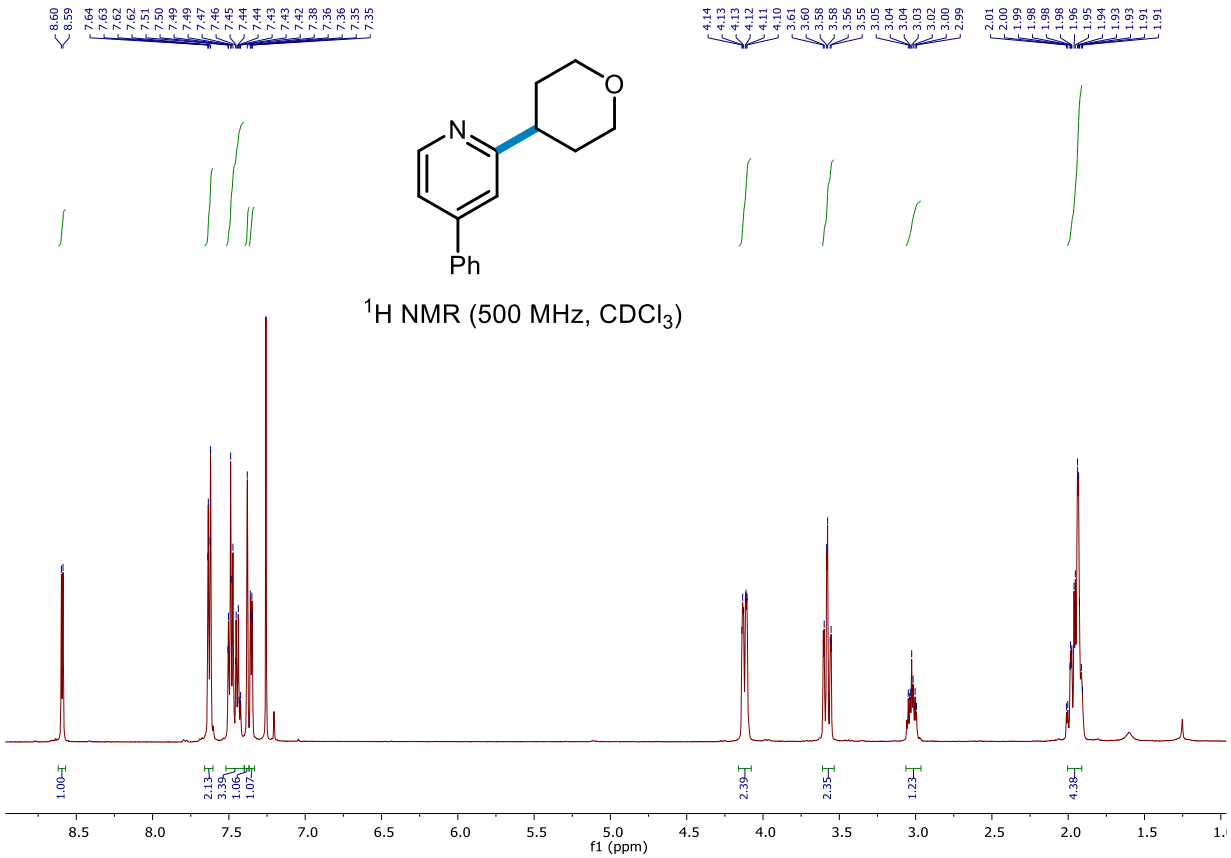

^{1}H NMR (500 MHz, $CDCl_3$)

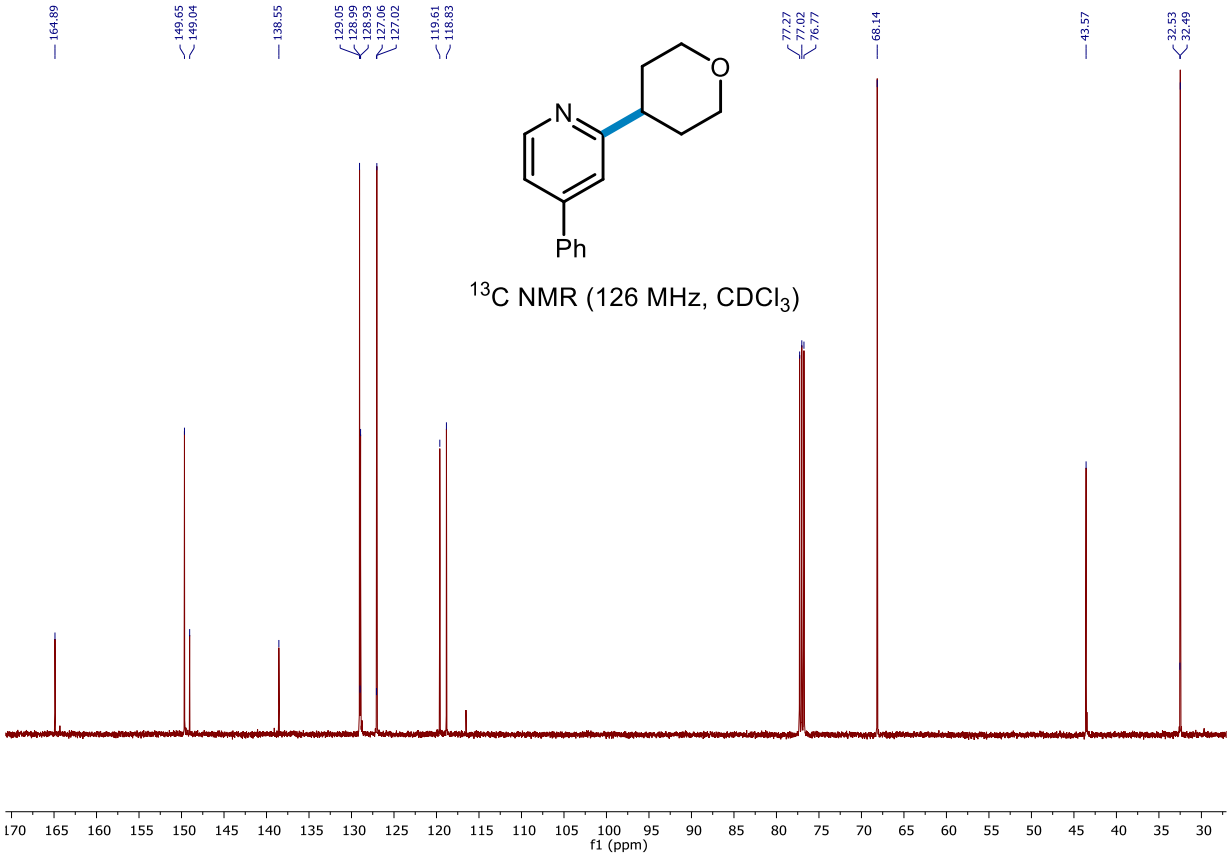

^{13}C NMR (126 MHz, $CDCl_3$)

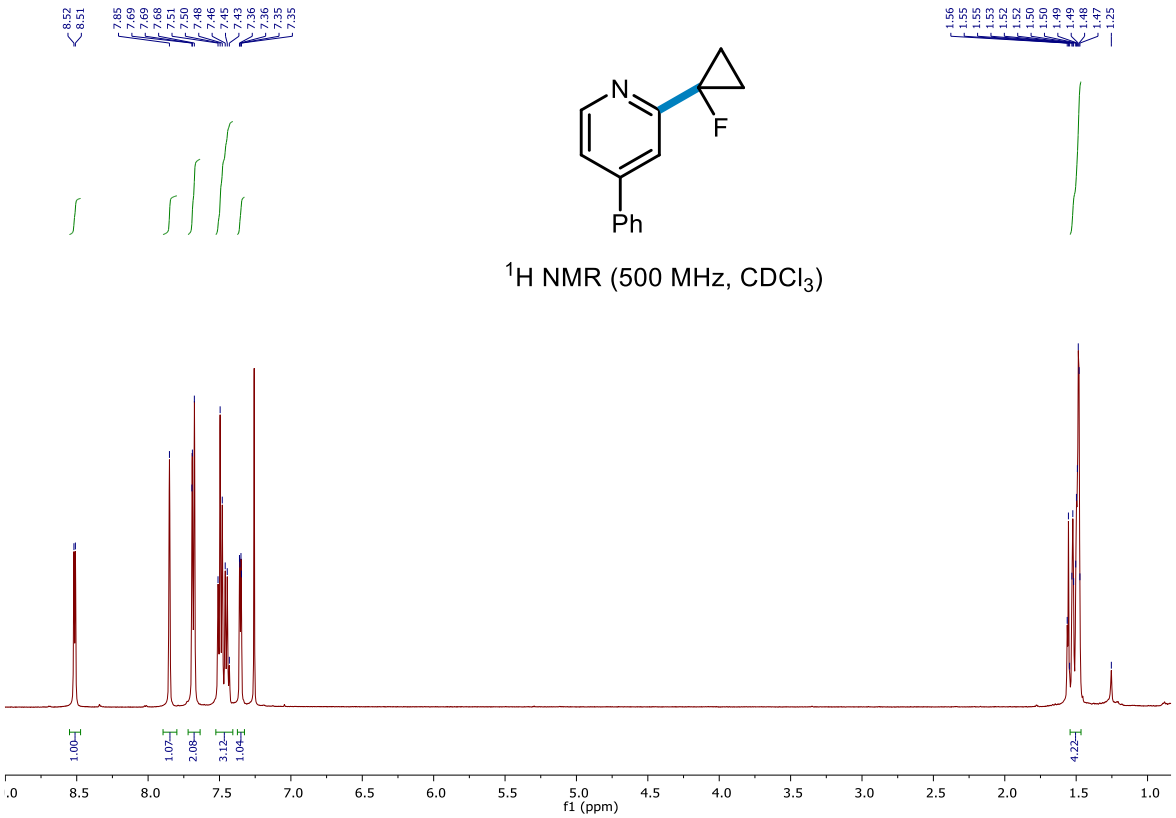

^{1}H NMR (500 MHz, $CDCl_3$)

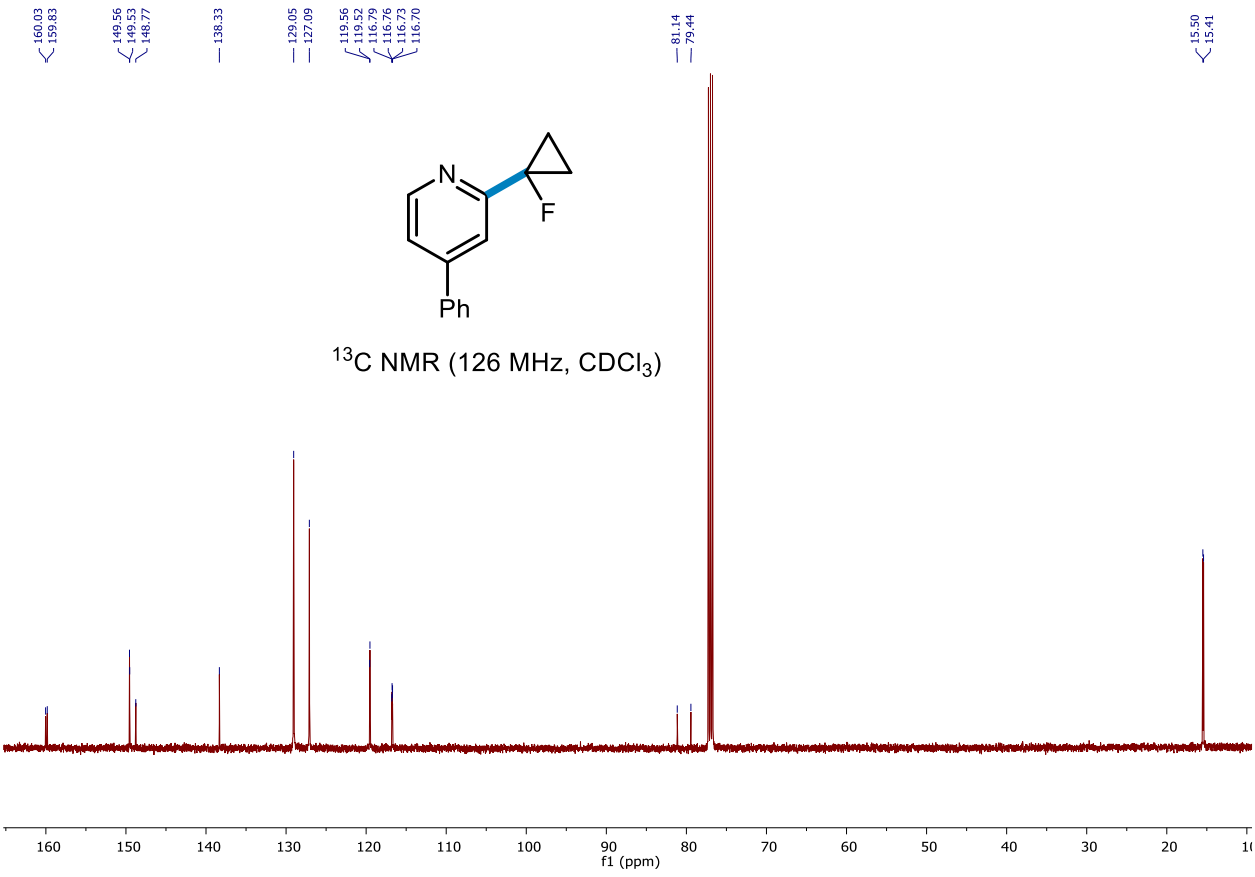

^{13}C NMR (126 MHz, $CDCl_3$)

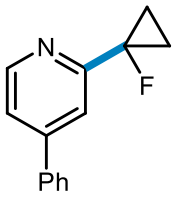

^{19}F NMR (470 MHz, $CDCl_3$)

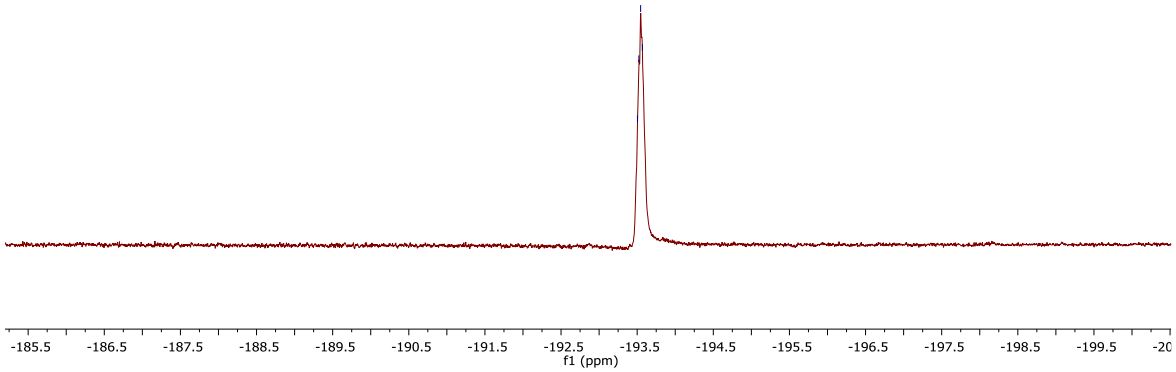

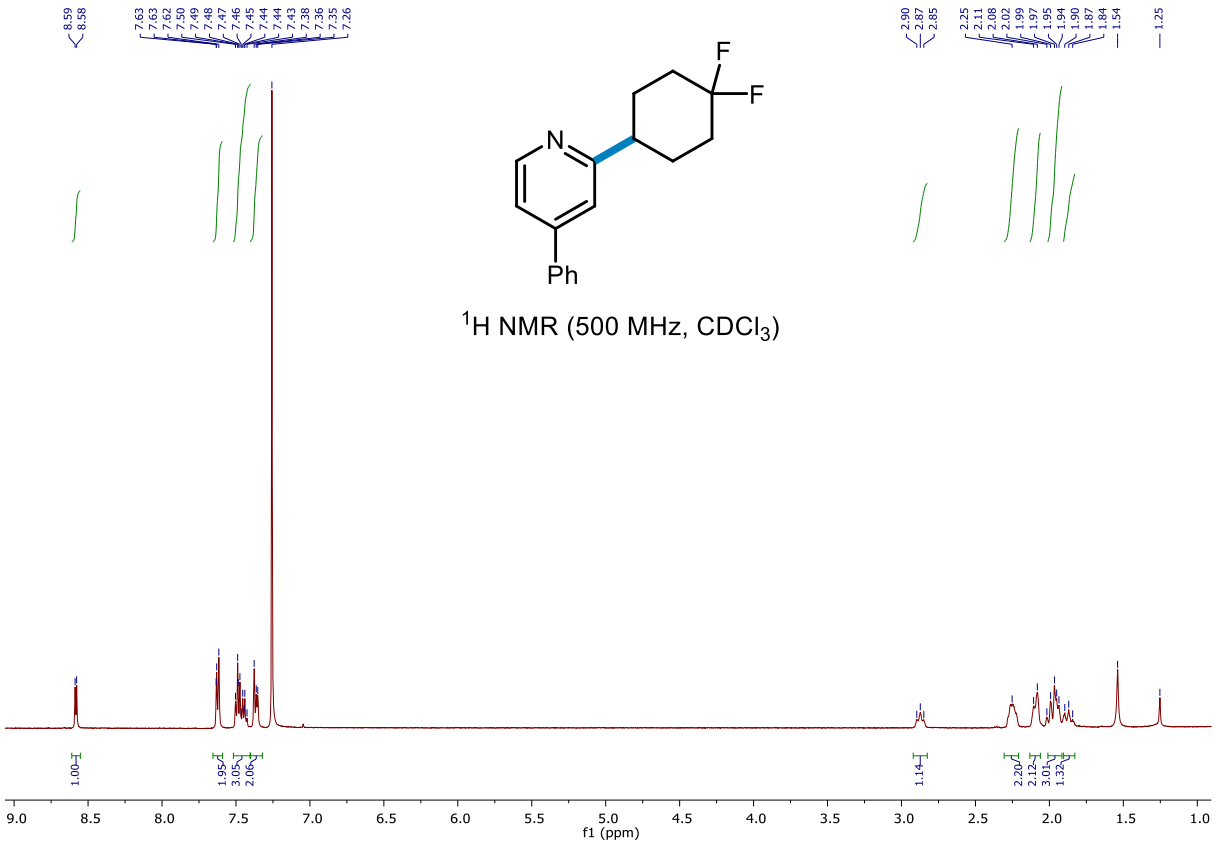

^{1}H NMR (500 MHz, $CDCl_3$)

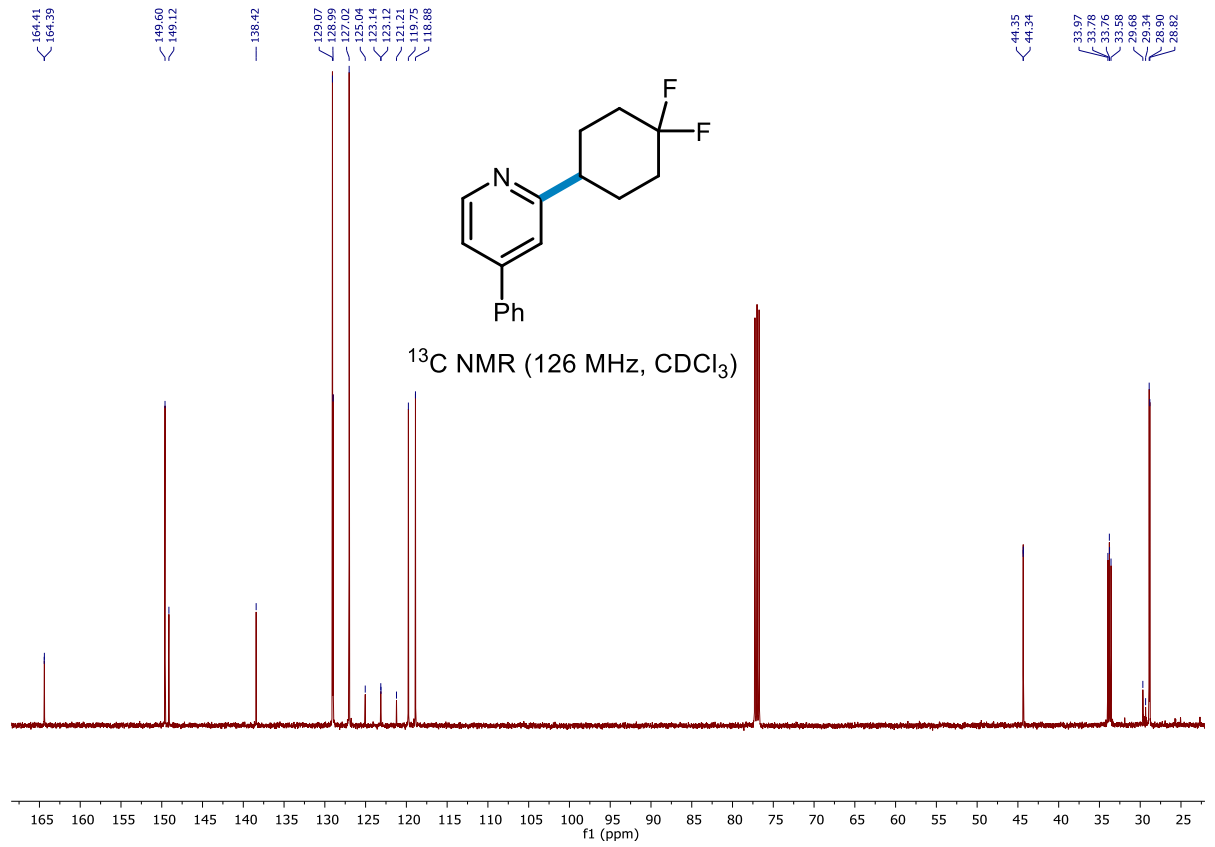

^{13}C NMR (126 MHz, $CDCl_3$)

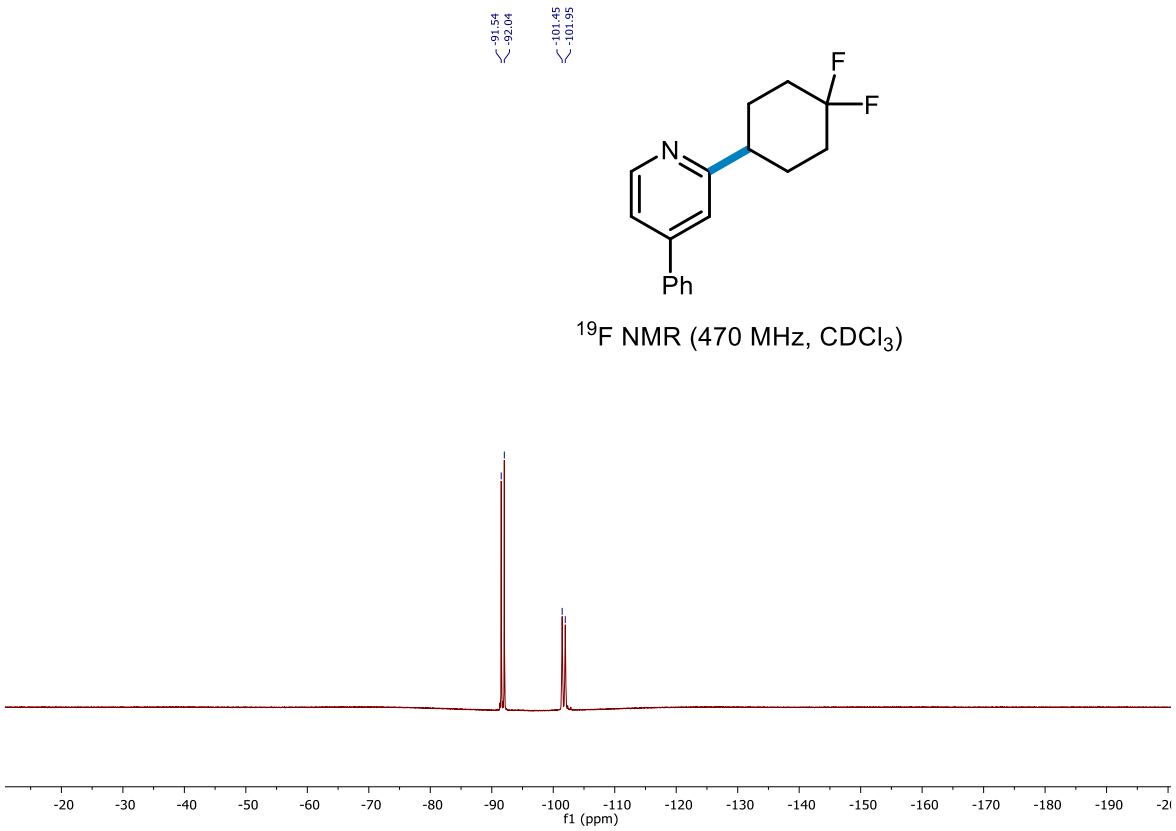

^{19}F NMR (470 MHz, $CDCl_3$)

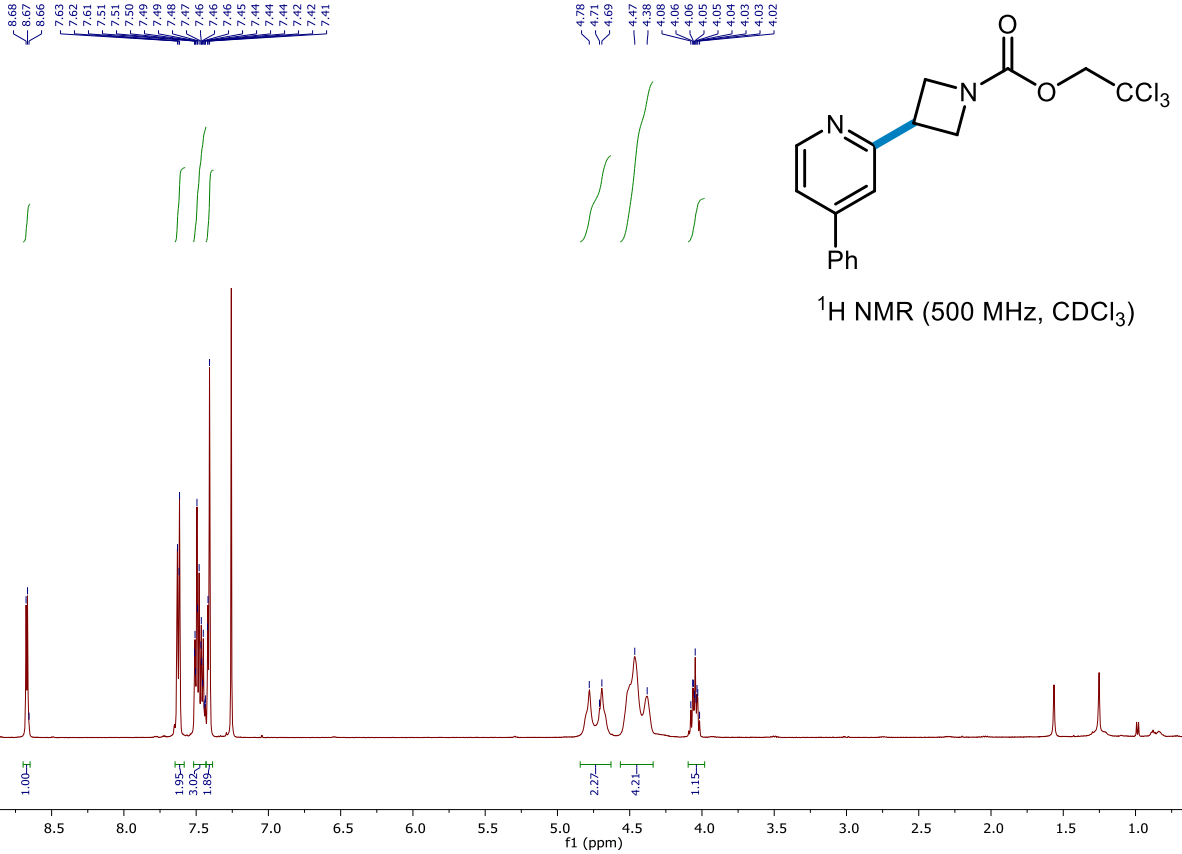

^{1}H NMR (500 MHz, $CDCl_3$)

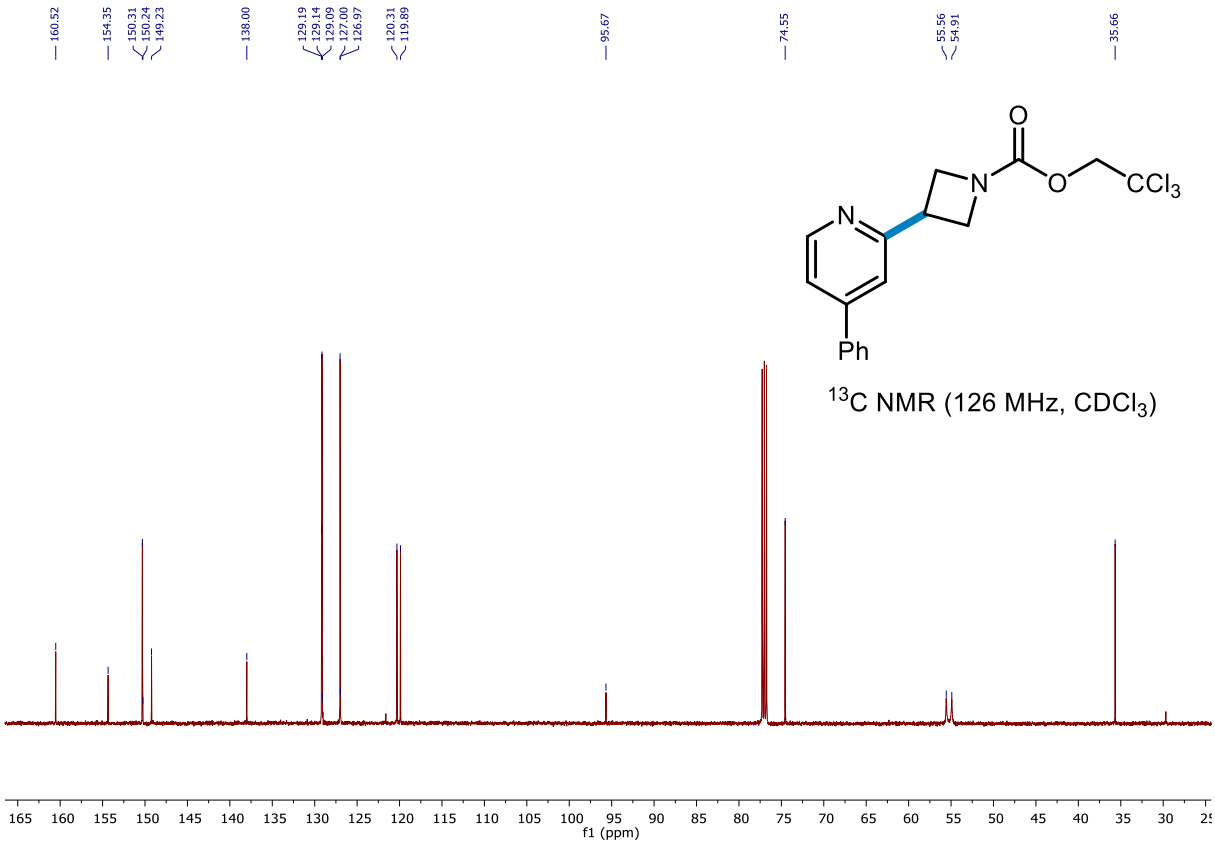
160.52
154.35
150.31
150.24
149.23
138.00
129.19
129.14
129.09
127.00
126.97
120.31
119.89
95.67
74.55
55.56
54.91
35.66
O
N
O
CCl3
N
Ph
13C NMR (126 MHz, CDCl3)
165 160 155 150 145 140 135 130 125 120 115 110 105 100 95 90 85 80 75 70 65 60 55 50 45 40 35 30 25
f1 (ppm)

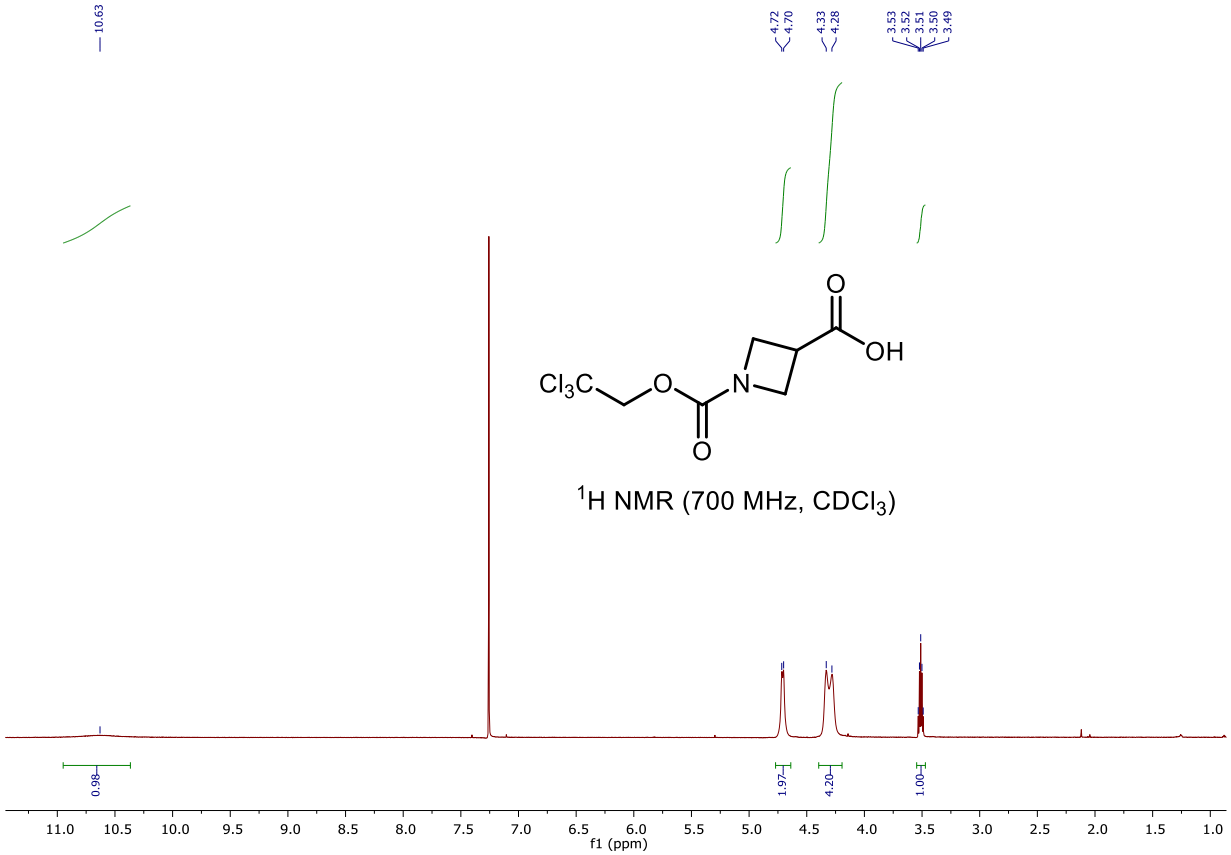

^{1}H NMR (700 MHz, $CDCl_3$)

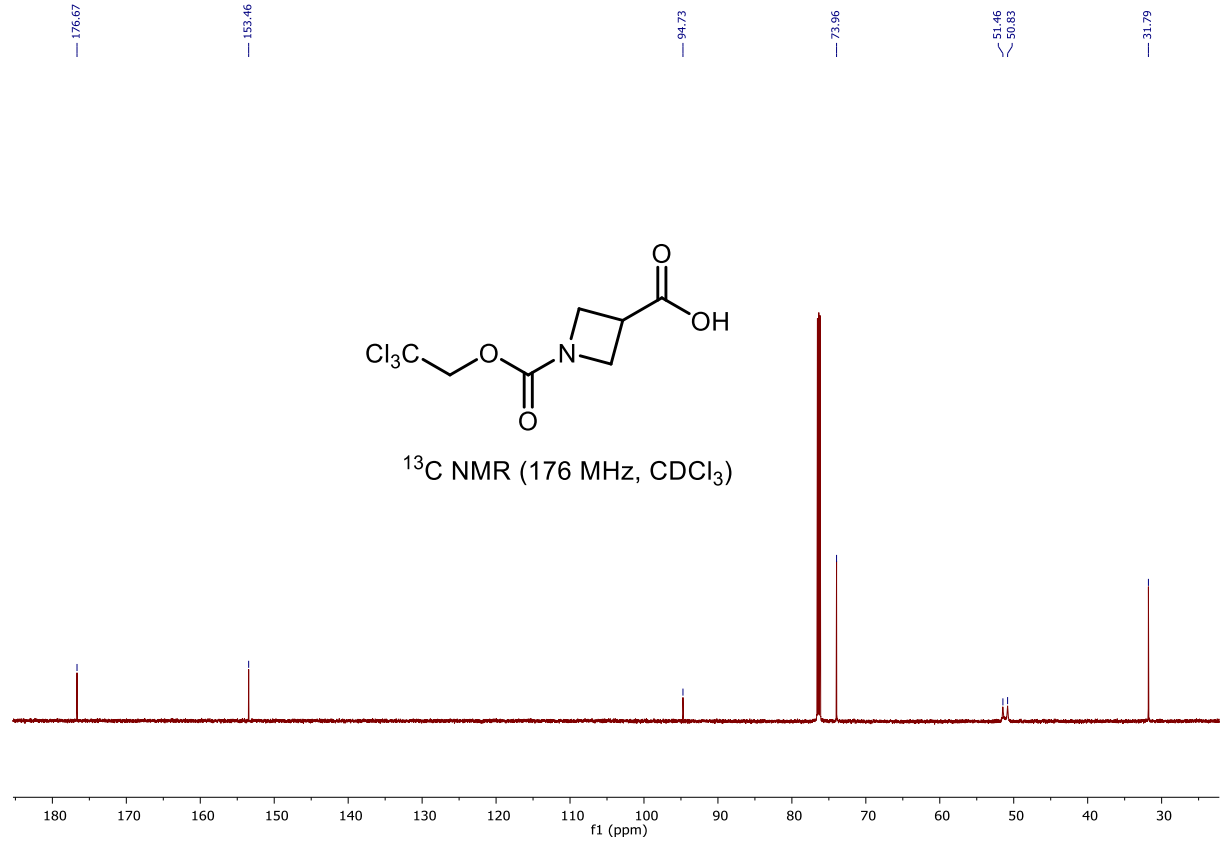

^{13}C NMR (176 MHz, $CDCl_3$)

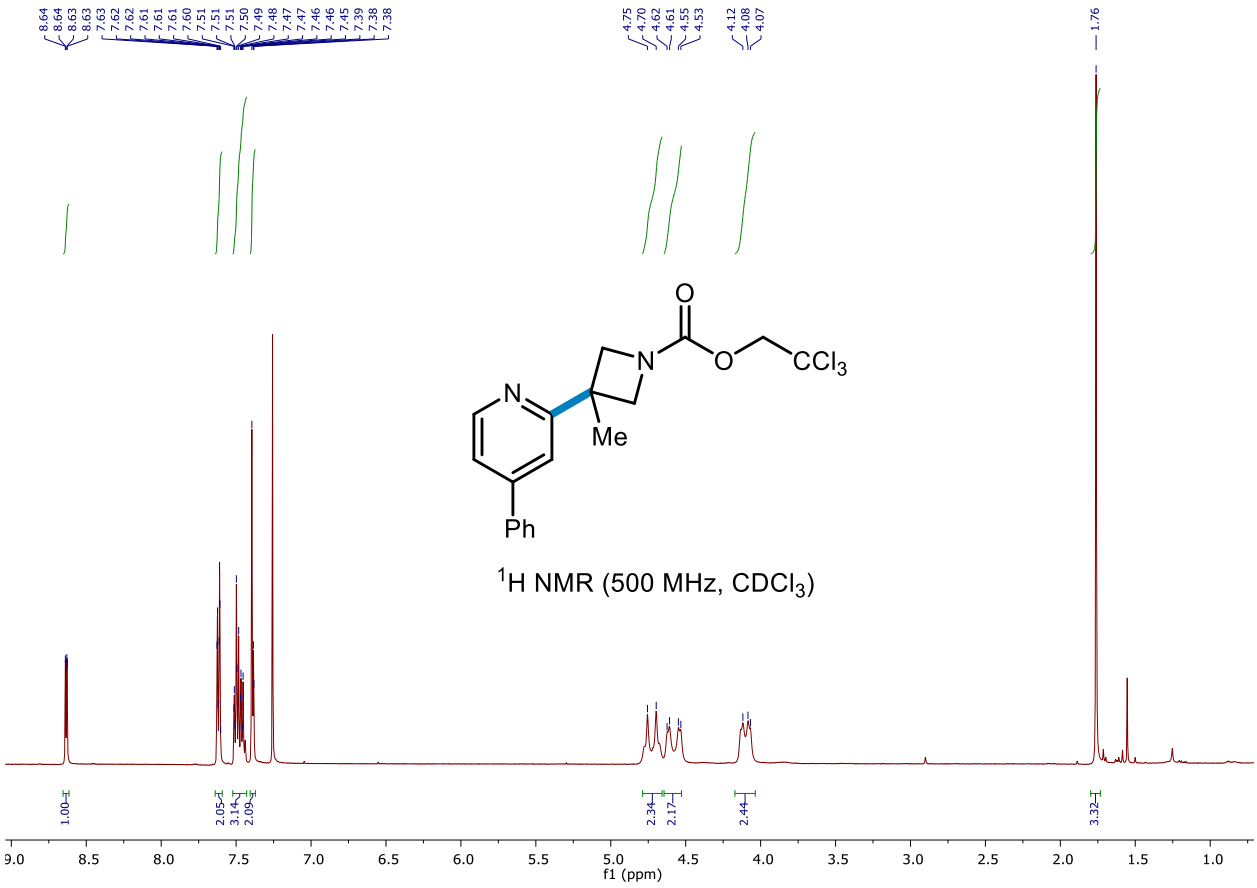

^{1}H NMR (500 MHz, $CDCl_3$)

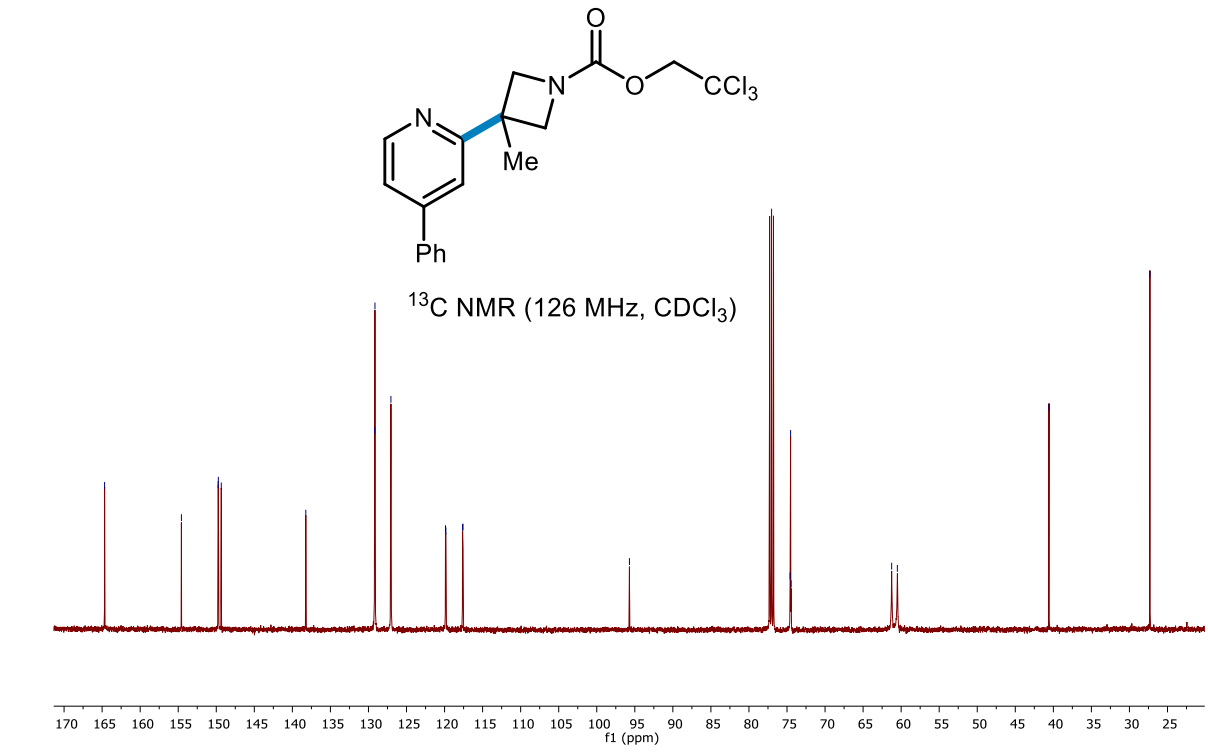

^{13}C NMR (126 MHz, $CDCl_3$)

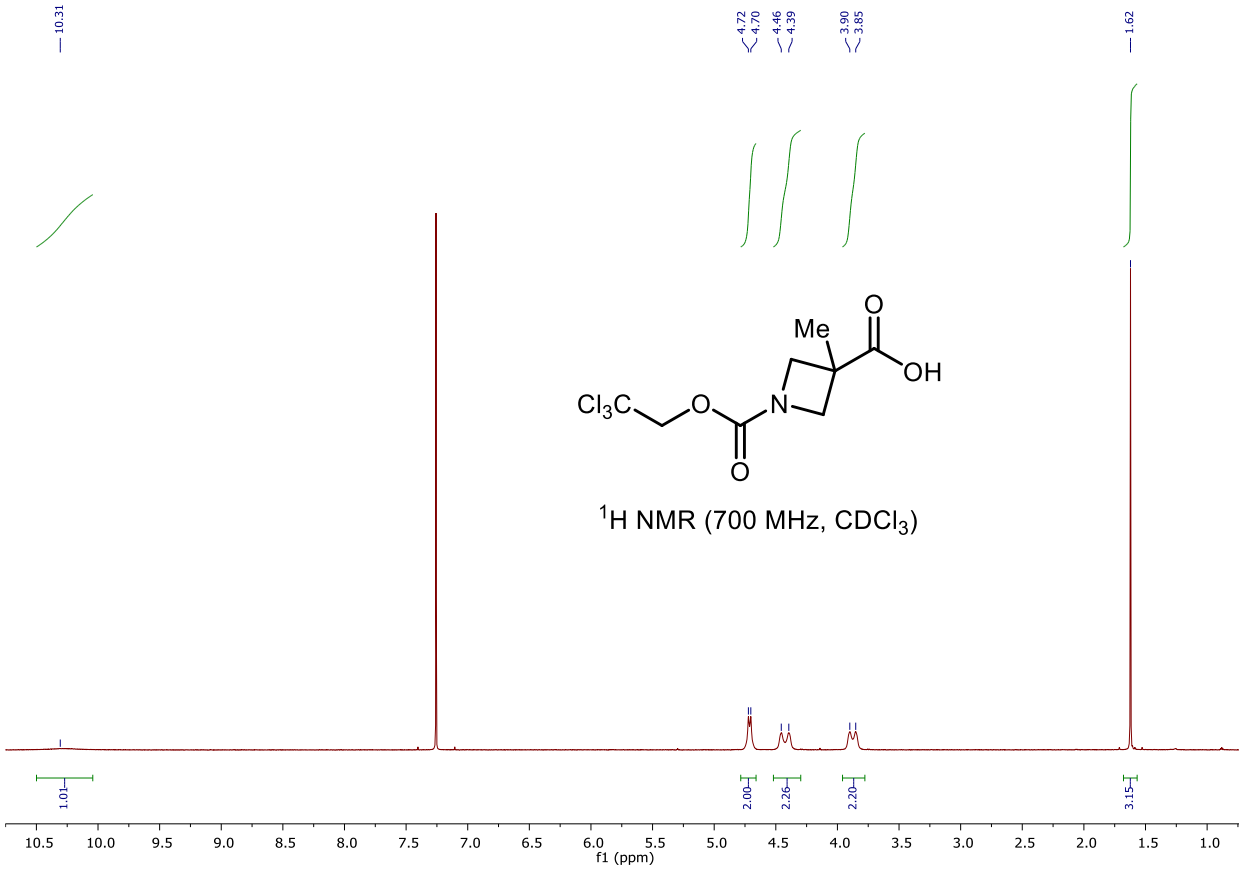

^{1}H NMR (700 MHz, $CDCl_3$)

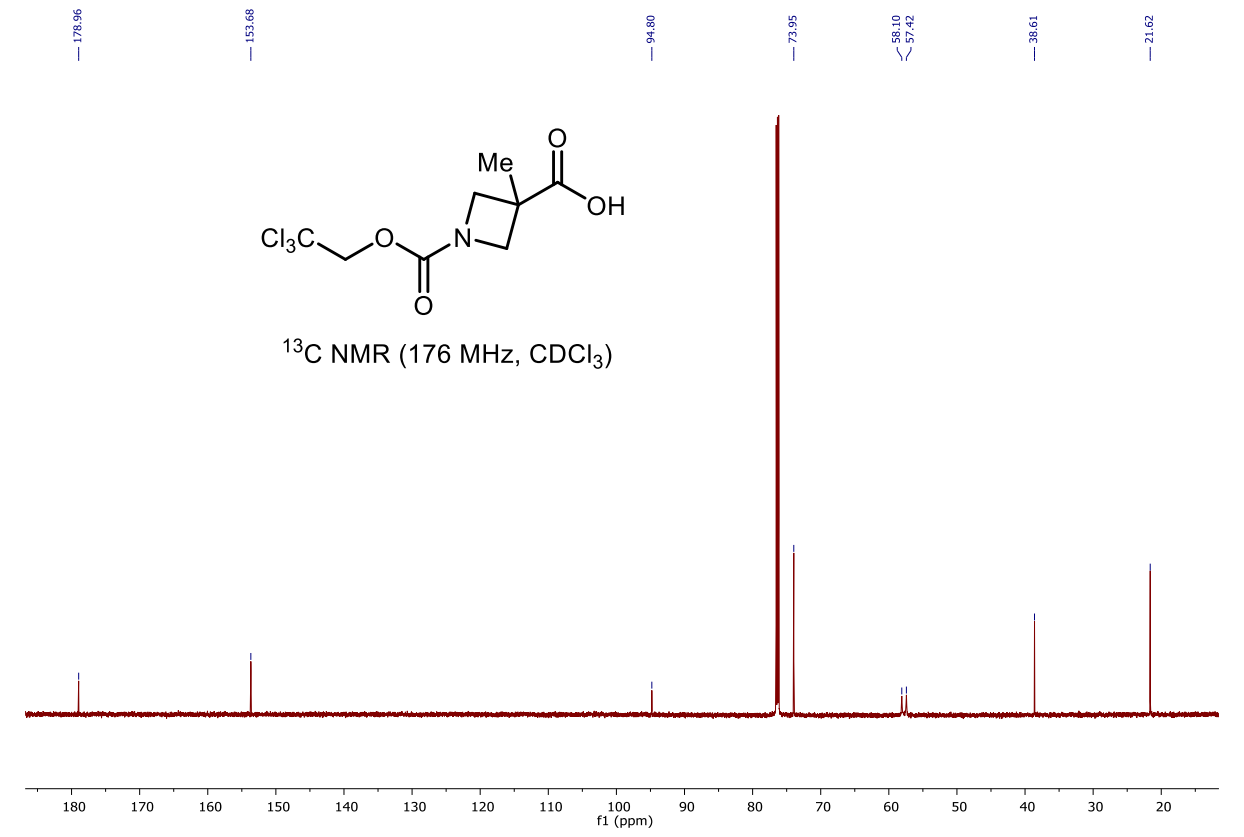

^{13}C NMR (176 MHz, $CDCl_3$)

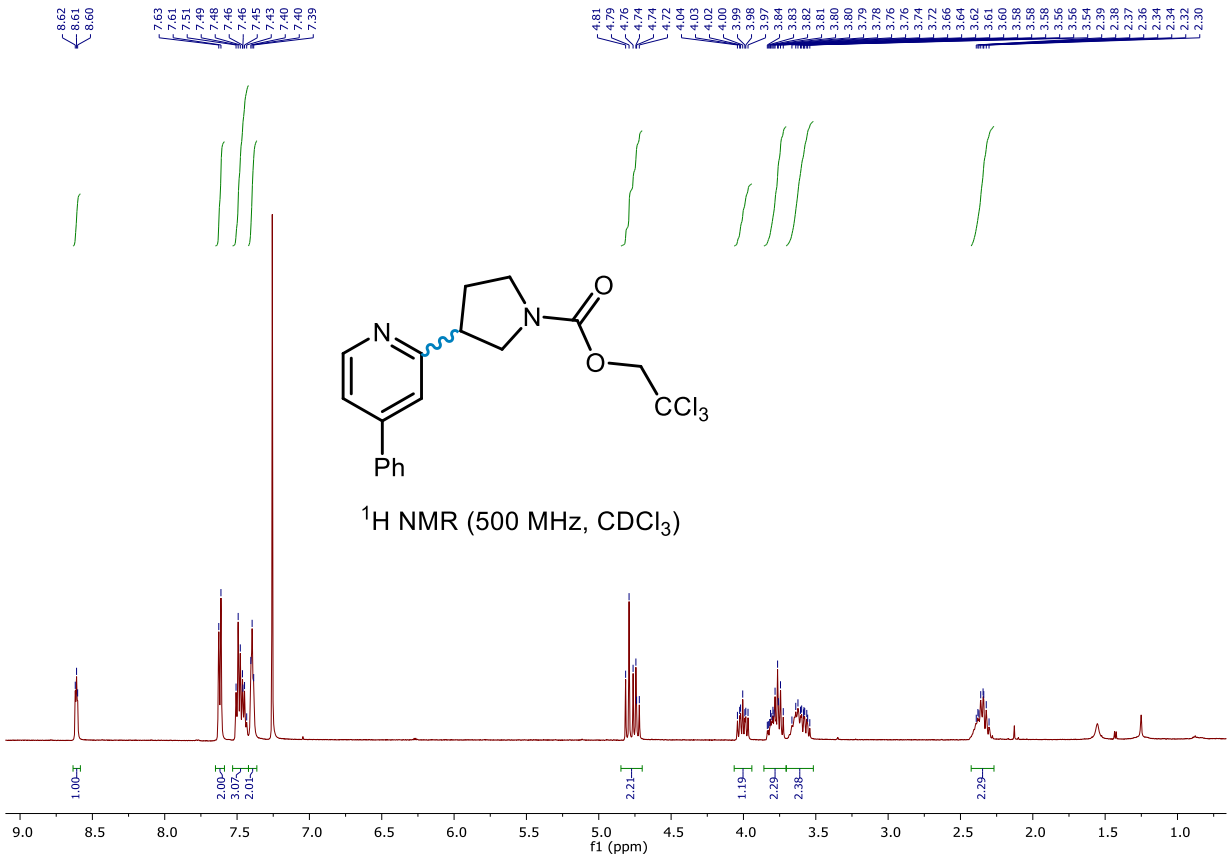
8.62
8.61
8.60
7.63
7.61
7.51
7.49
7.48
7.46
7.46
7.45
7.43
7.40
7.40
7.39
4.81
4.79
4.76
4.74
4.74
4.72
4.04
4.03
4.02
4.00
3.99
3.98
3.97
3.84
3.83
3.82
3.81
3.80
3.80
3.79
3.78
3.76
3.76
3.74
3.72
3.66
3.64
3.62
3.61
3.60
3.58
3.58
3.58
3.56
3.56
3.54
2.39
2.38
2.37
2.36
2.34
2.34
2.32
2.30
N
O
N
O
CCl3
Ph
1H NMR (500 MHz, CDCl3)
1.00
2.00
3.07
2.01
2.21
1.19
2.29
2.38
2.29
9.0
8.5
8.0
7.5
7.0
6.5
6.0
5.5
5.0
4.5
4.0
3.5
3.0
2.5
2.0
1.5
1.0
f1 (ppm)

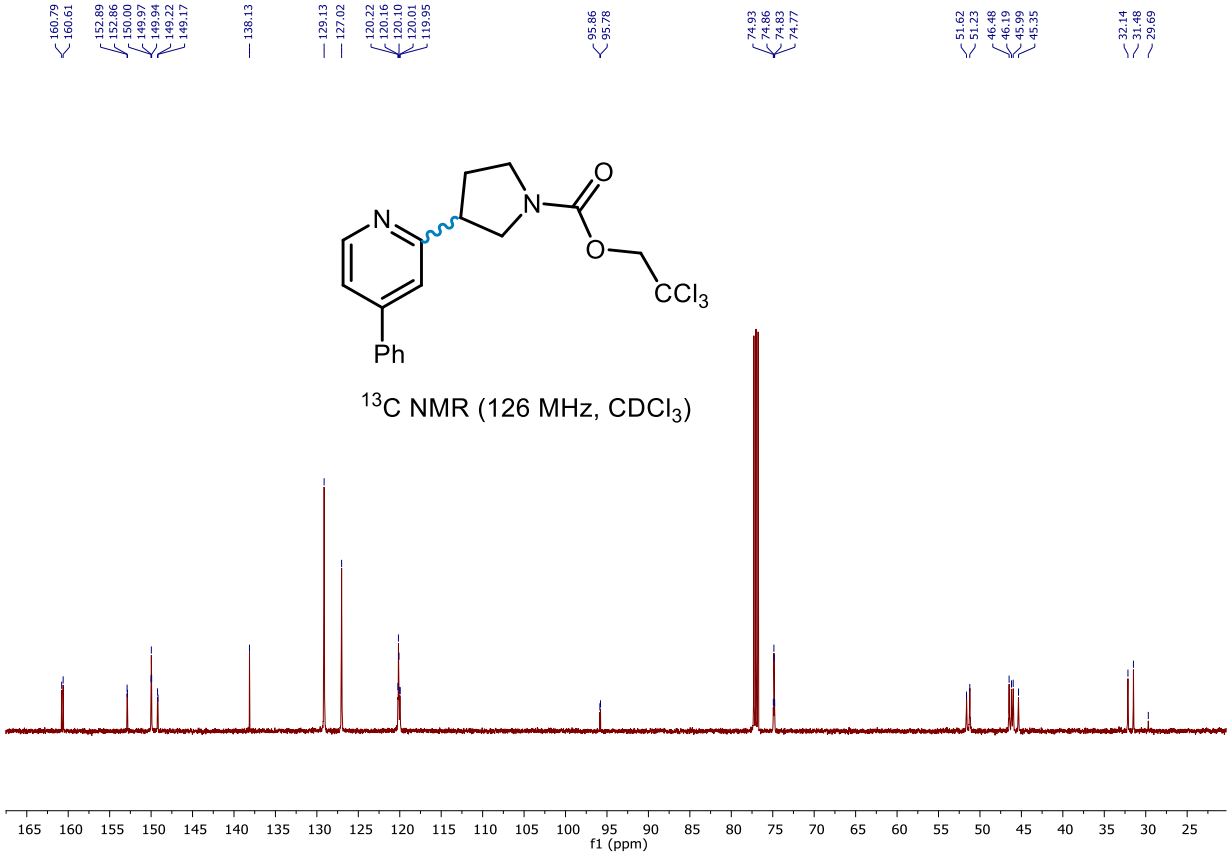
160.79
160.61
152.89
152.86
150.00
149.97
149.94
149.22
149.17
138.13
129.13
127.02
120.22
120.16
120.10
120.01
119.95
95.86
95.78
74.93
74.86
74.83
74.77
51.62
51.23
46.48
46.19
45.99
45.35
32.14
31.48
29.69
N
O
N
O
CCl3
Ph
13C NMR (126 MHz, CDCl3)
165
160
155
150
145
140
135
130
125
120
115
110
105
100
95
90
85
80
75
70
65
60
55
50
45
40
35
30
25
f1 (ppm)

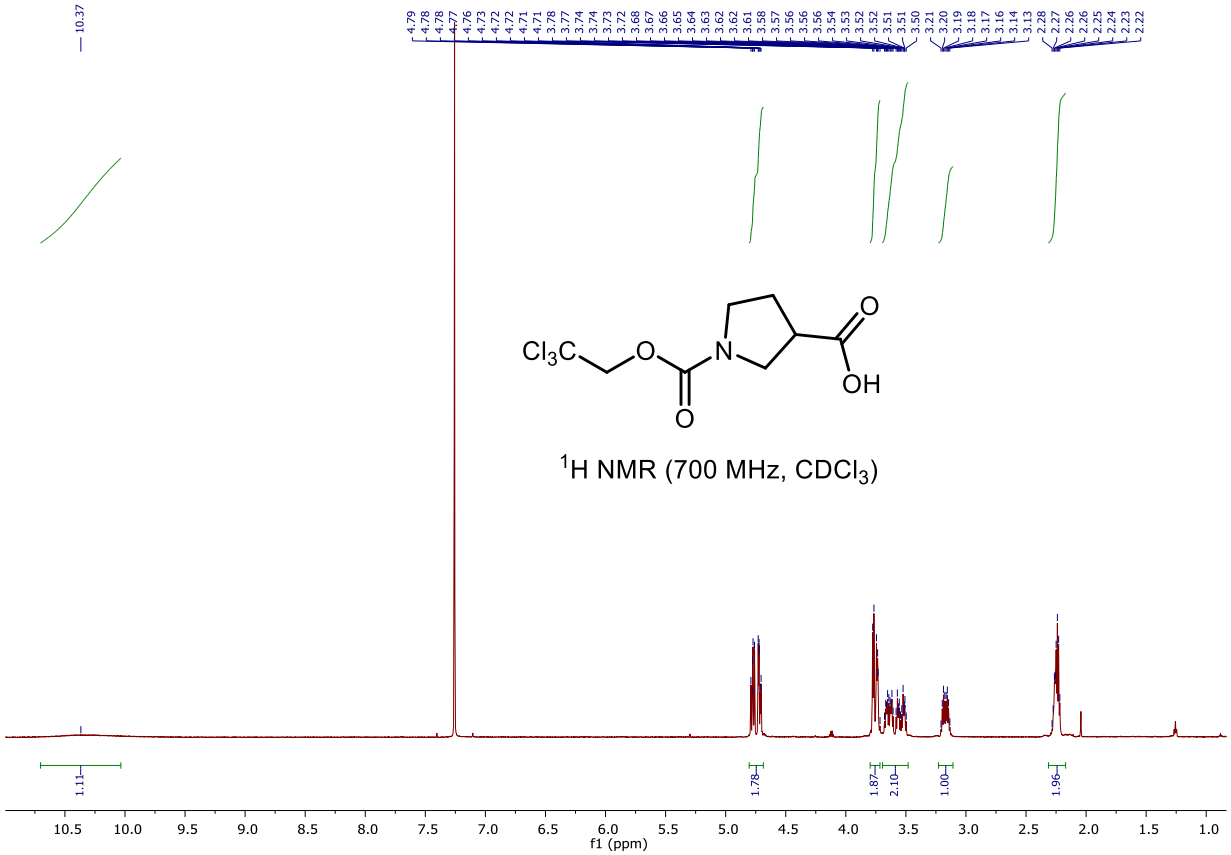
Cl3C
O
N
O
OH
O
1H NMR (700 MHz, CDCl3)
f1 (ppm)

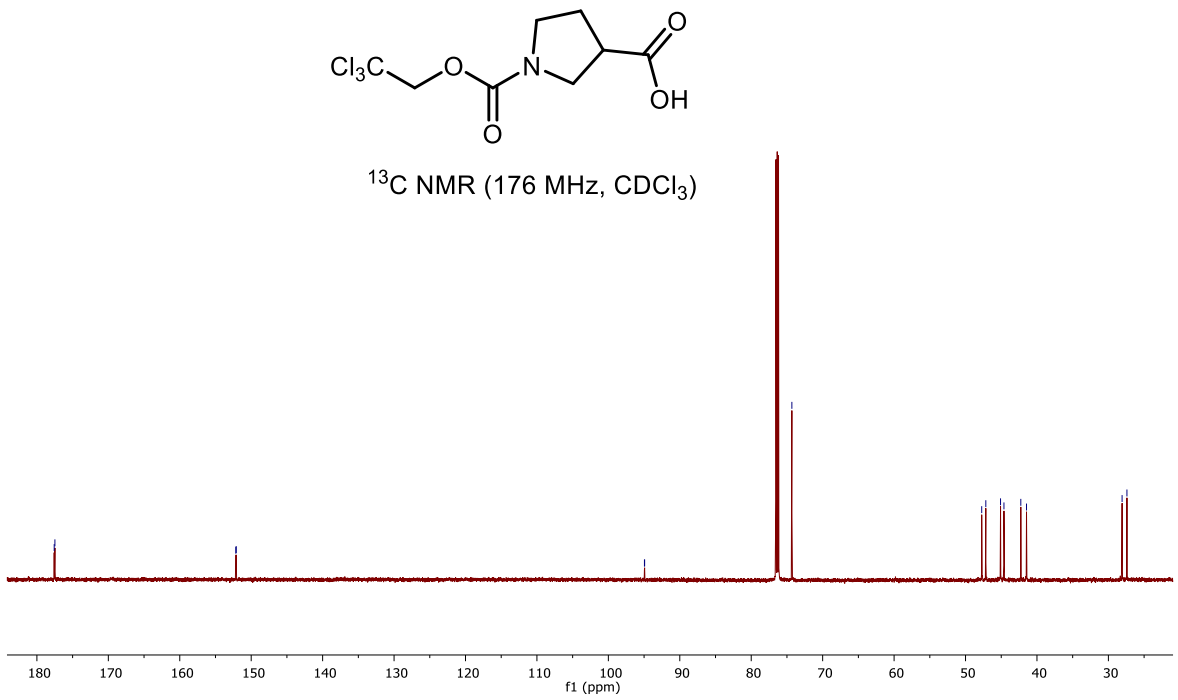
Cl3C
O
N
O
OH
O
13C NMR (176 MHz, CDCl3)
f1 (ppm)

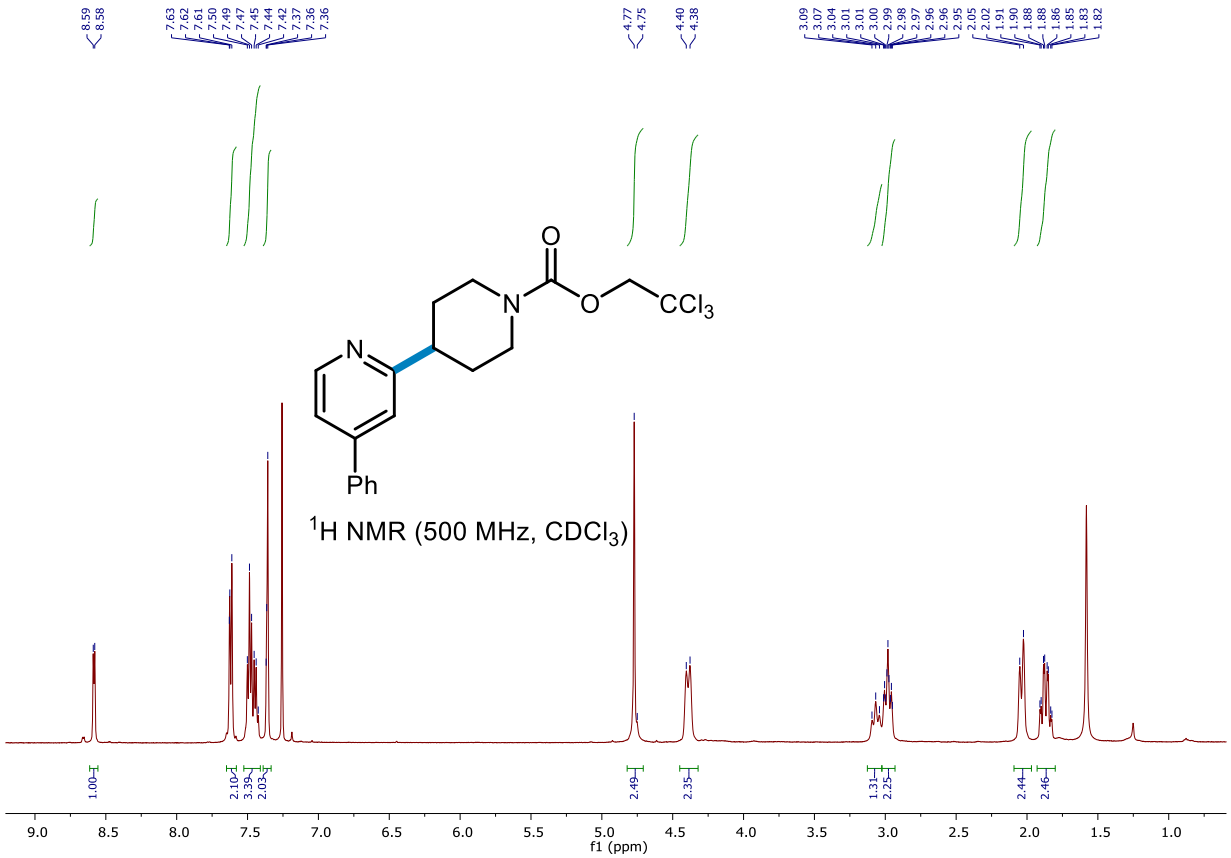
8.59
8.58
7.63
7.62
7.61
7.50
7.49
7.47
7.45
7.44
7.42
7.37
7.36
7.36
4.77
4.75
4.40
4.38
3.09
3.07
3.04
3.01
3.01
3.00
2.99
2.98
2.97
2.96
2.96
2.95
2.05
2.02
1.91
1.90
1.88
1.88
1.86
1.85
1.83
1.82
O
N
O
CCl3
N
Ph
1H NMR (500 MHz, CDCl3)
1.00
2.10
3.39
2.03
2.49
2.35
1.31
2.25
2.44
2.46
9.0
8.5
8.0
7.5
7.0
6.5
6.0
5.5
5.0
4.5
4.0
3.5
3.0
2.5
2.0
1.5
1.0
f1 (ppm)

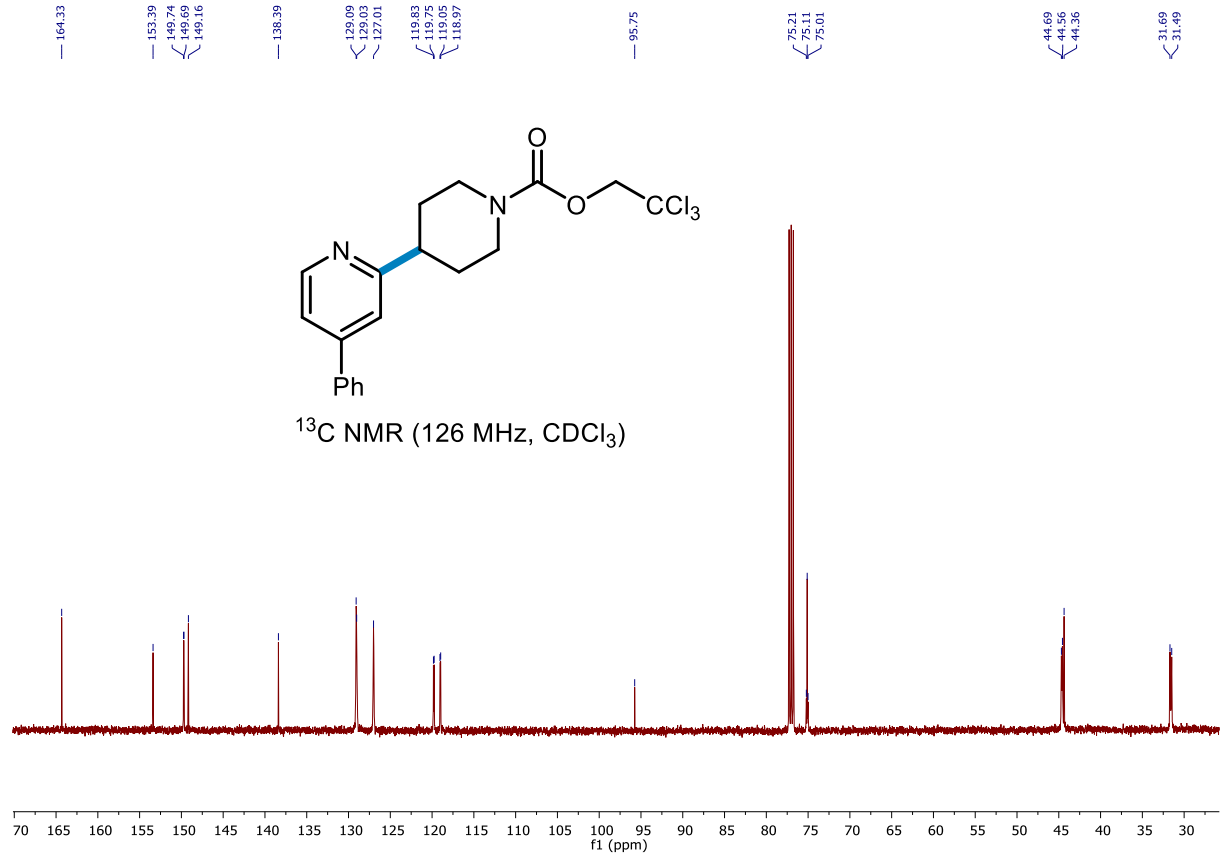
164.33
153.39
149.74
149.69
149.16
138.39
129.09
129.03
127.01
119.83
119.75
119.05
118.97
95.75
75.21
75.11
75.01
44.69
44.36
44.36
31.69
31.49
O
N
O
CCl3
N
Ph
13C NMR (126 MHz, CDCl3)
70
165
160
155
150
145
140
135
130
125
120
115
110
105
100
95
90
85
80
75
70
65
60
55
50
45
40
35
30
f1 (ppm)

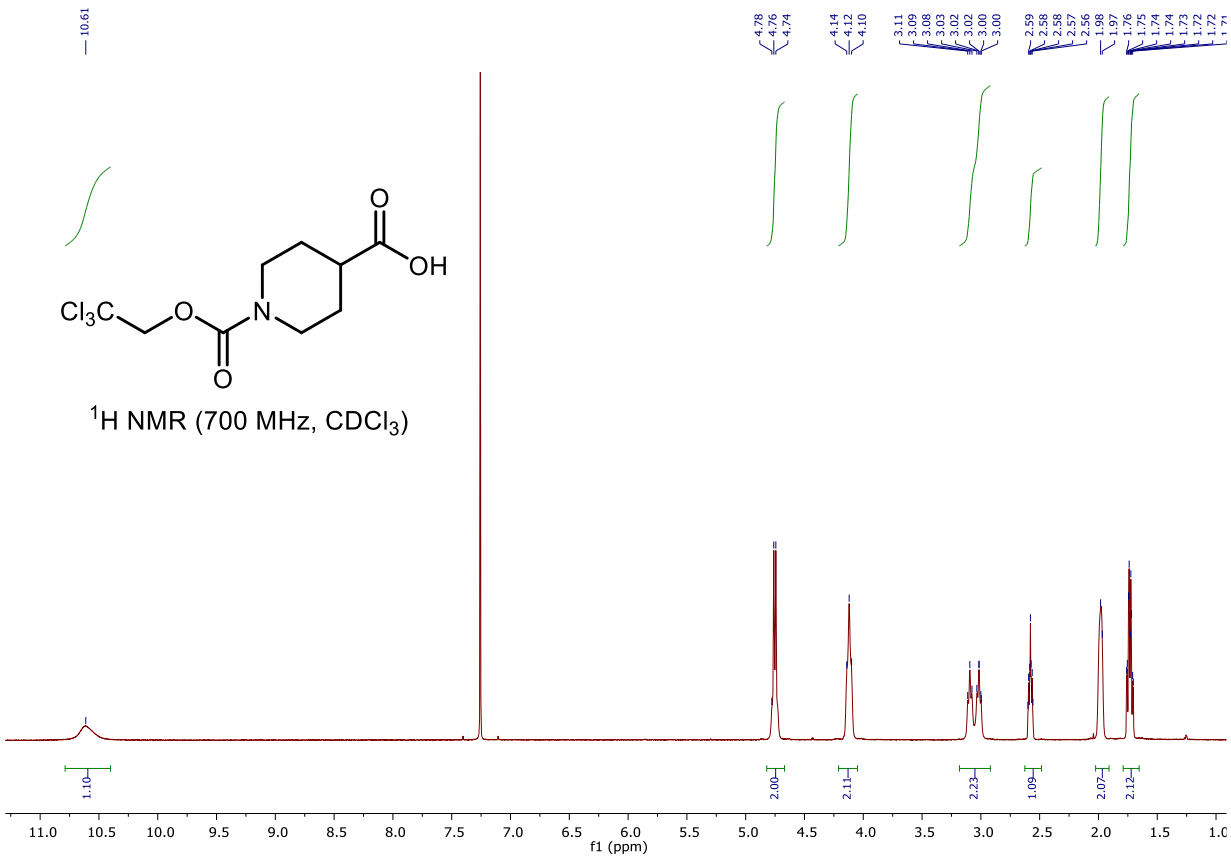

^{1}H NMR (700 MHz, $CDCl_3$)

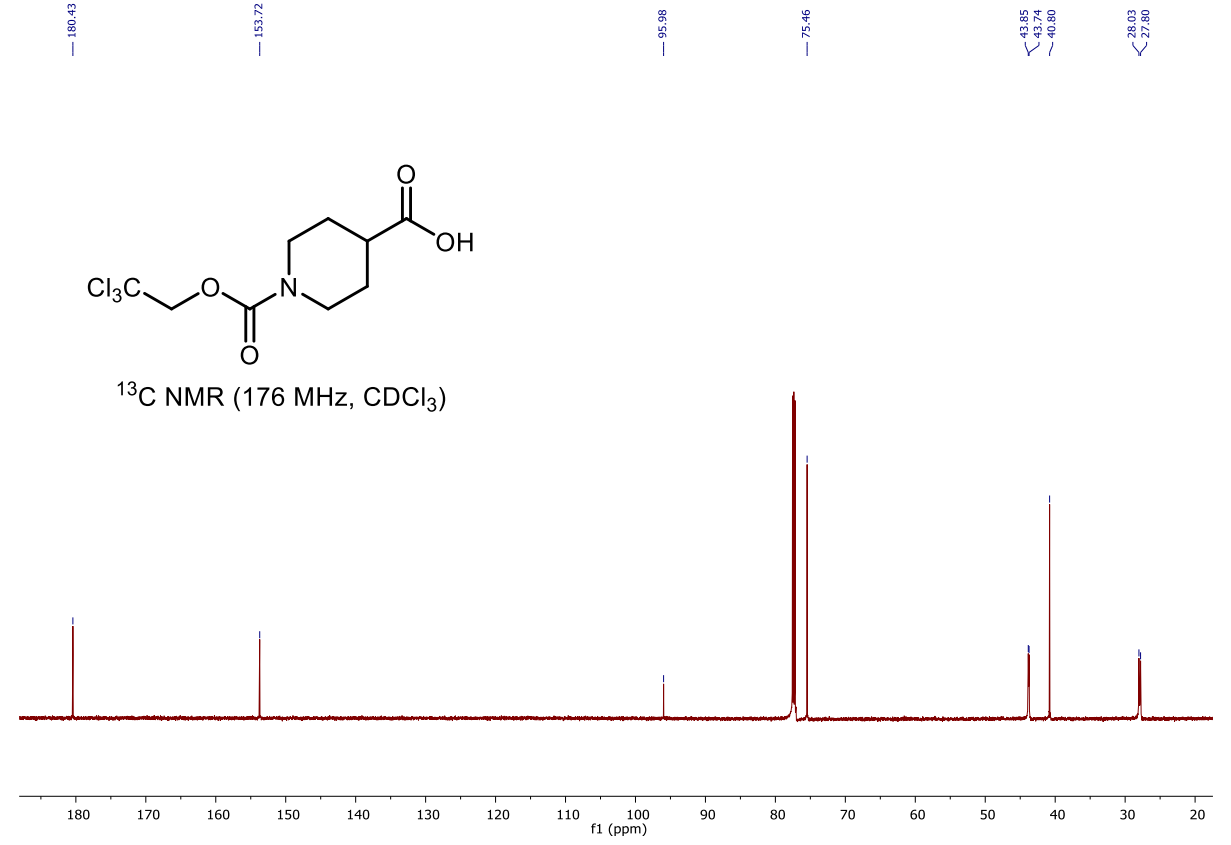

^{13}C NMR (176 MHz, $CDCl_3$)

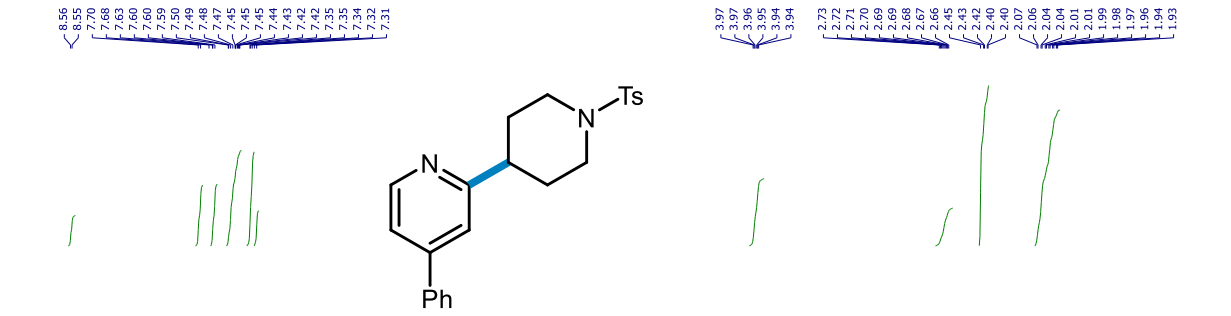

^{1}H NMR (500 MHz, $CDCl_3$)

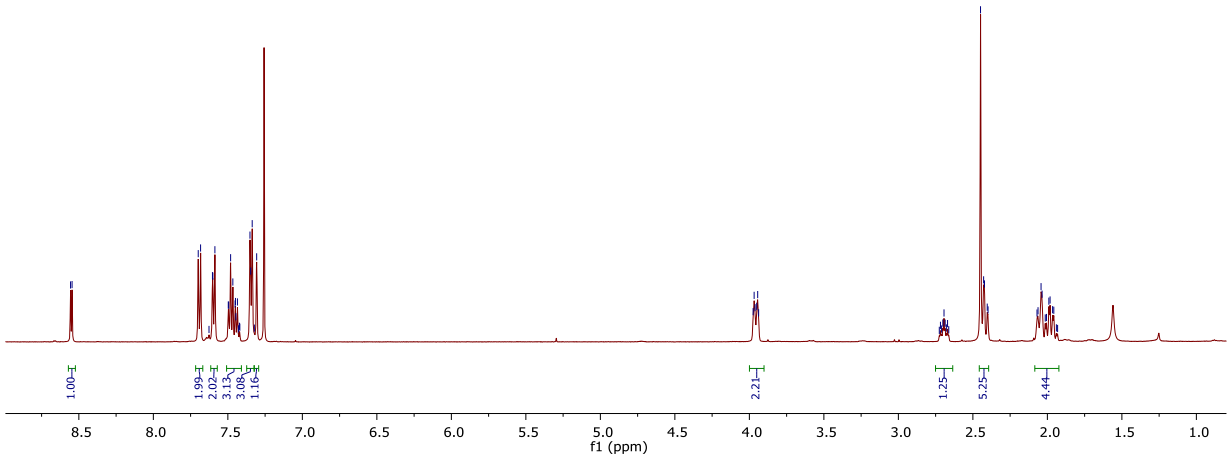

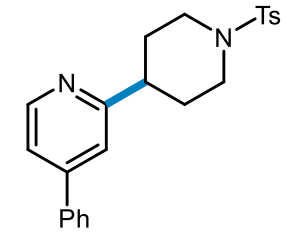

^{13}C NMR (126 MHz, $CDCl_3$)

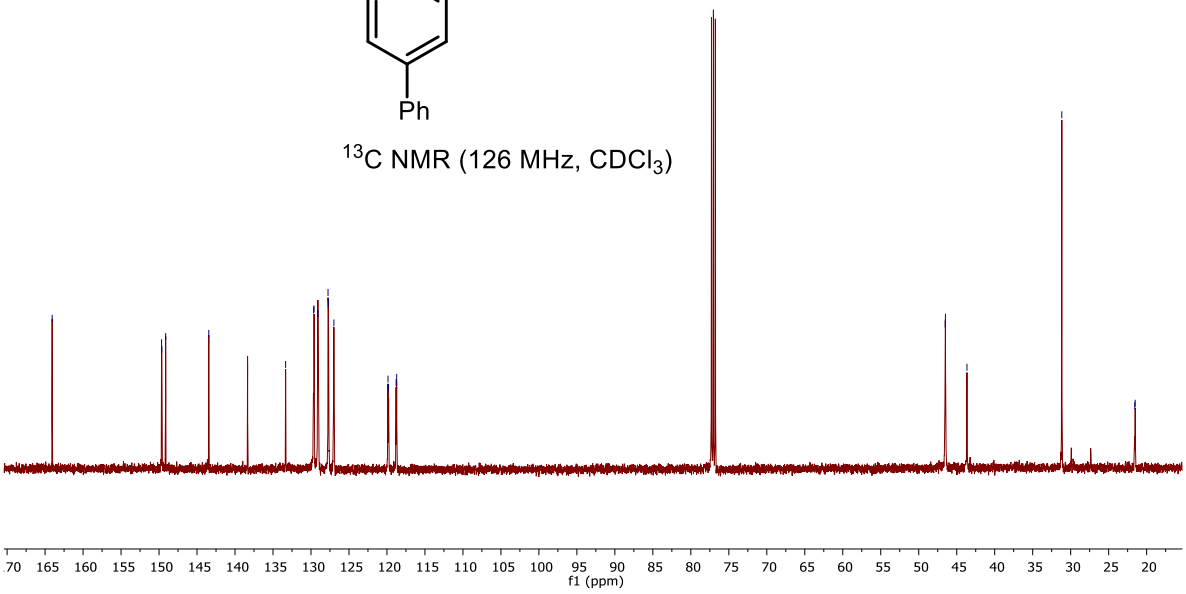

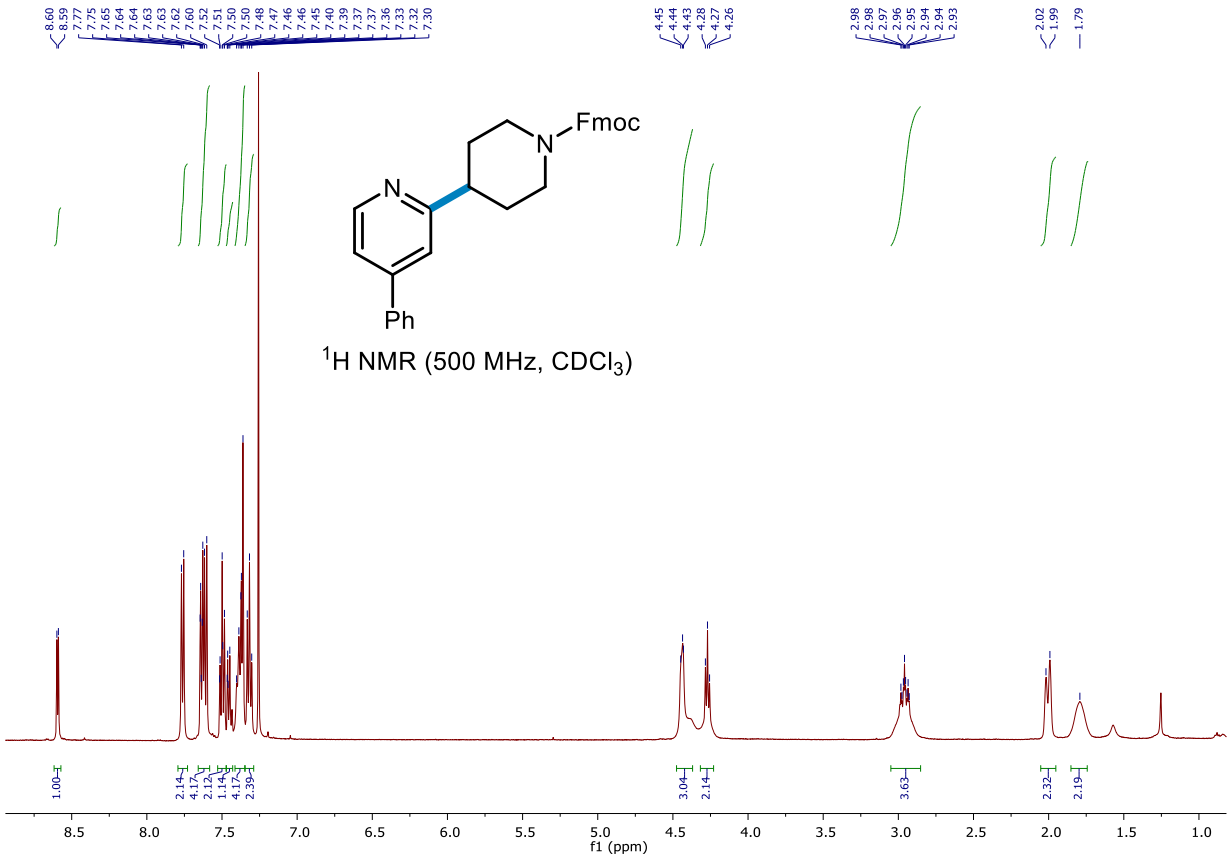

^{1}H NMR (500 MHz, $CDCl_3$)

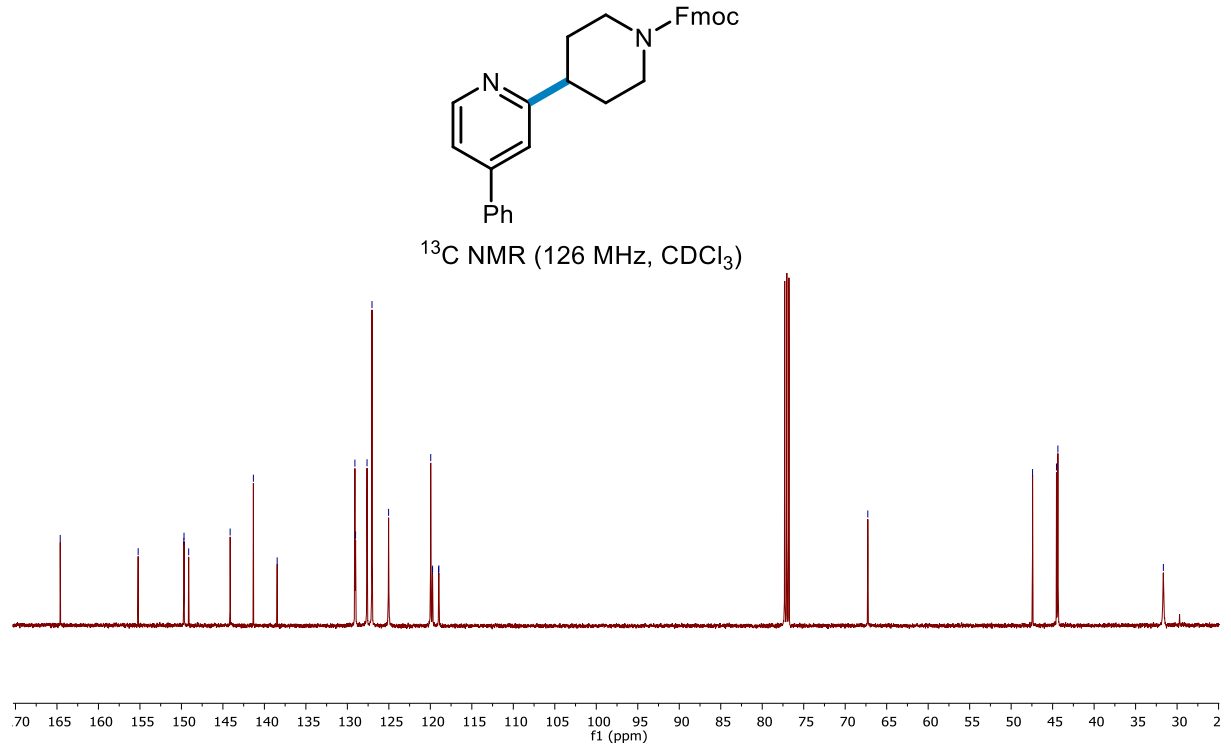

^{13}C NMR (126 MHz, $CDCl_3$)

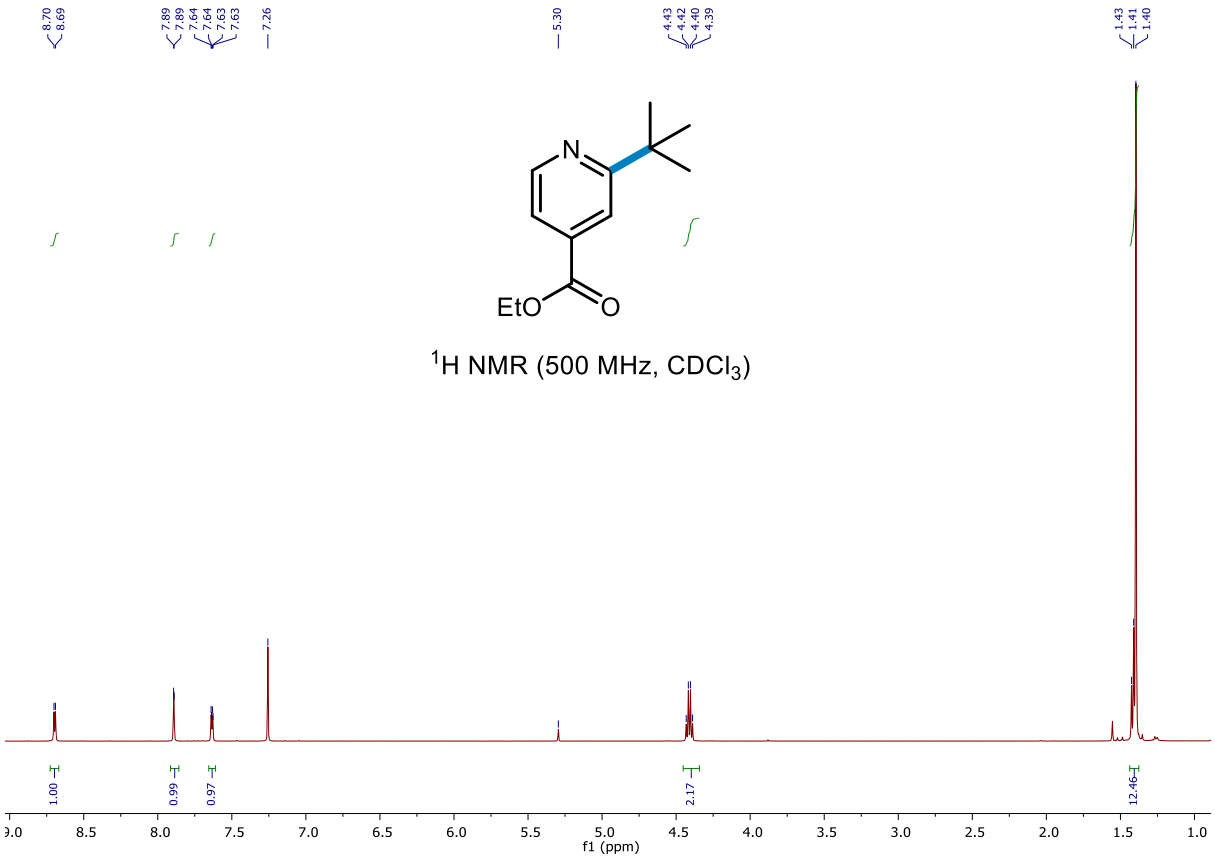

^{1}H NMR (500 MHz, $CDCl_3$)

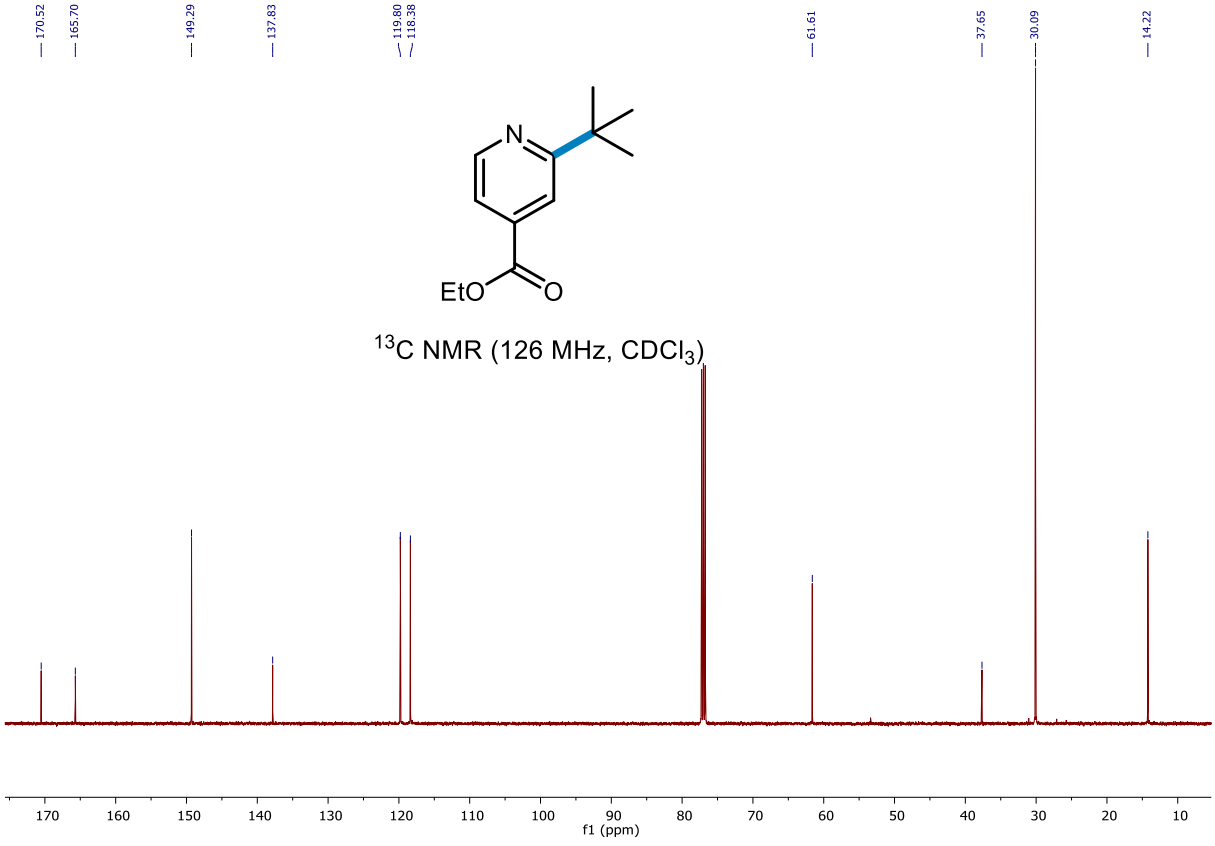

^{13}C NMR (126 MHz, $CDCl_3$)

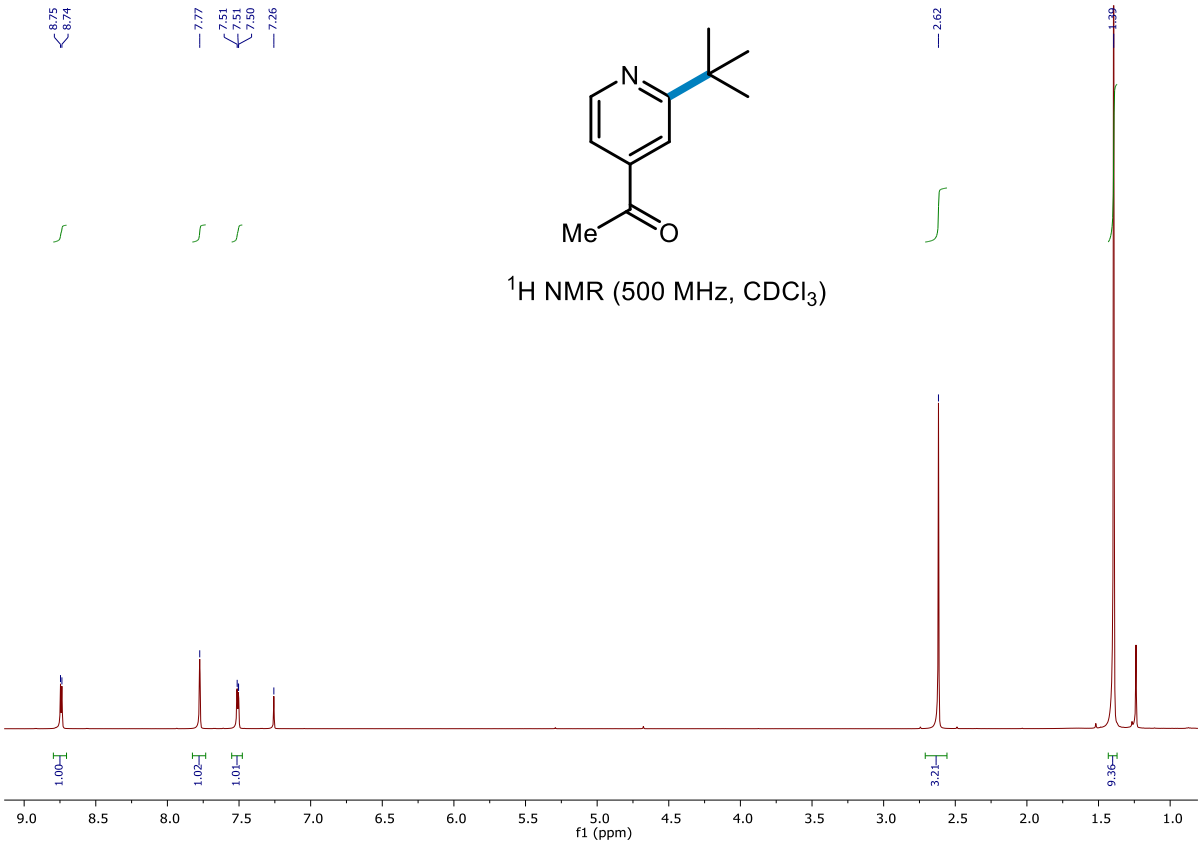

^{1}H NMR (500 MHz, $CDCl_3$)

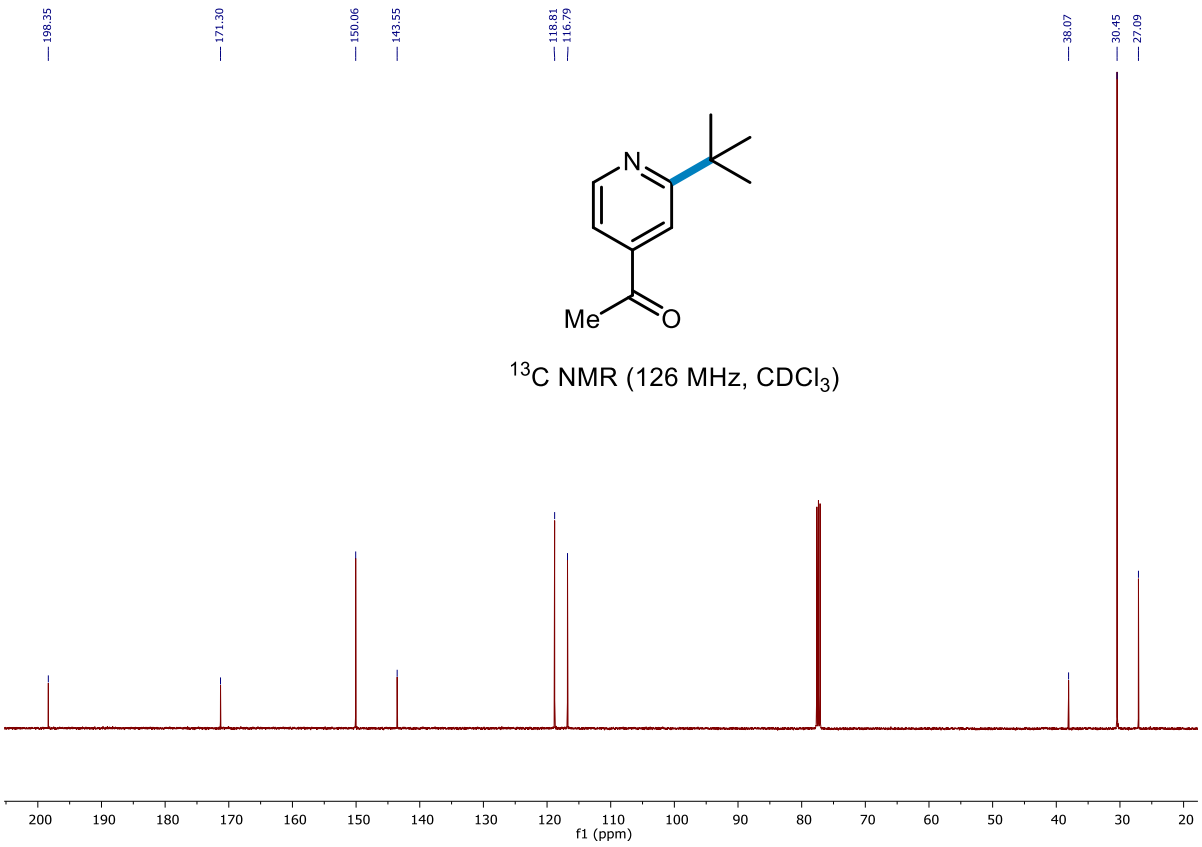

^{13}C NMR (126 MHz, $CDCl_3$)

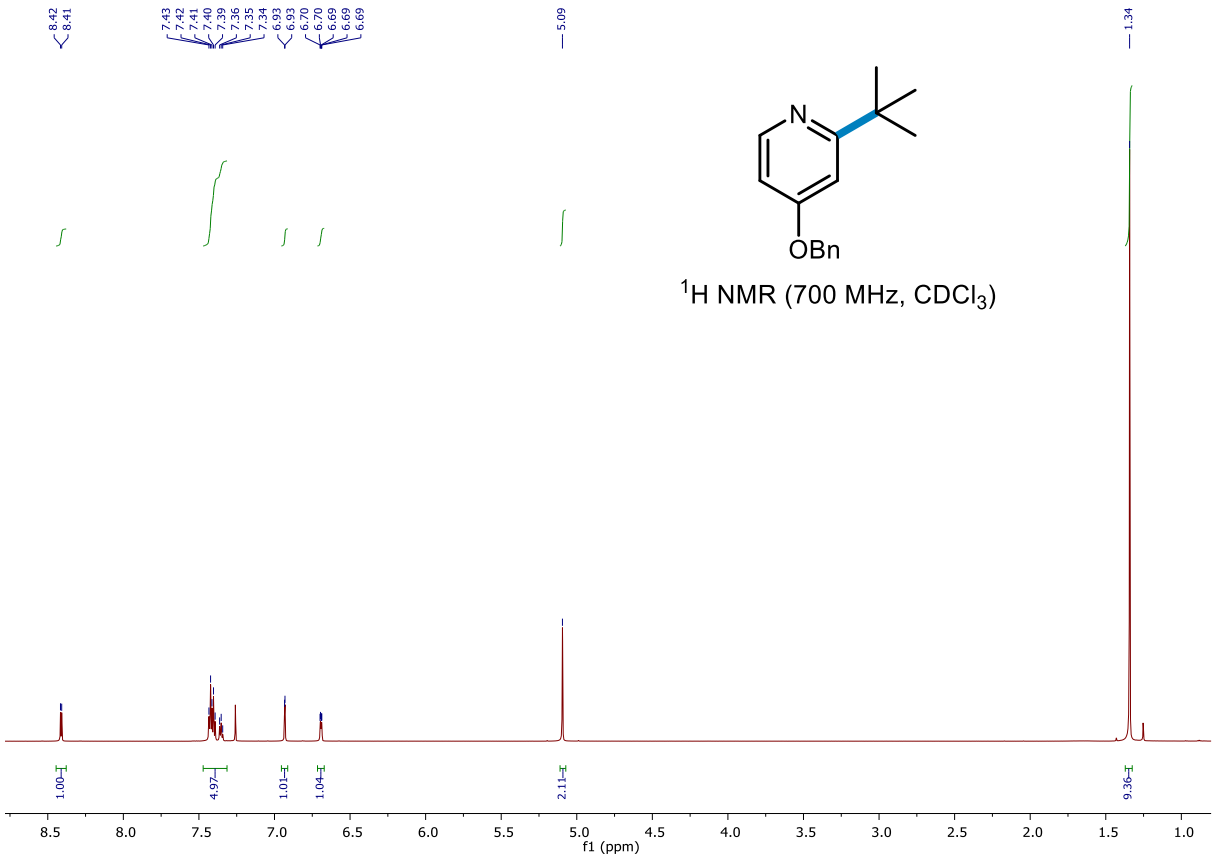

^{1}H NMR (700 MHz, $CDCl_3$)

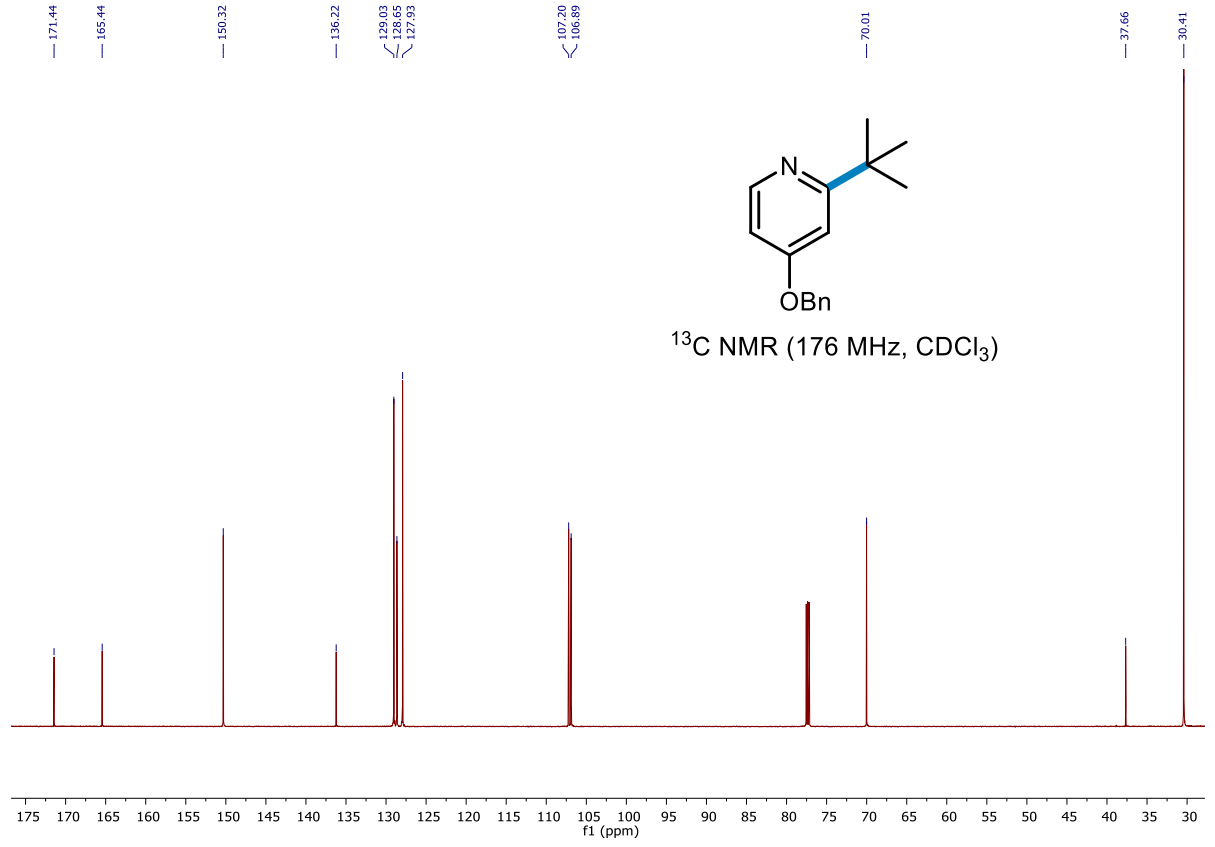

^{13}C NMR (176 MHz, $CDCl_3$)

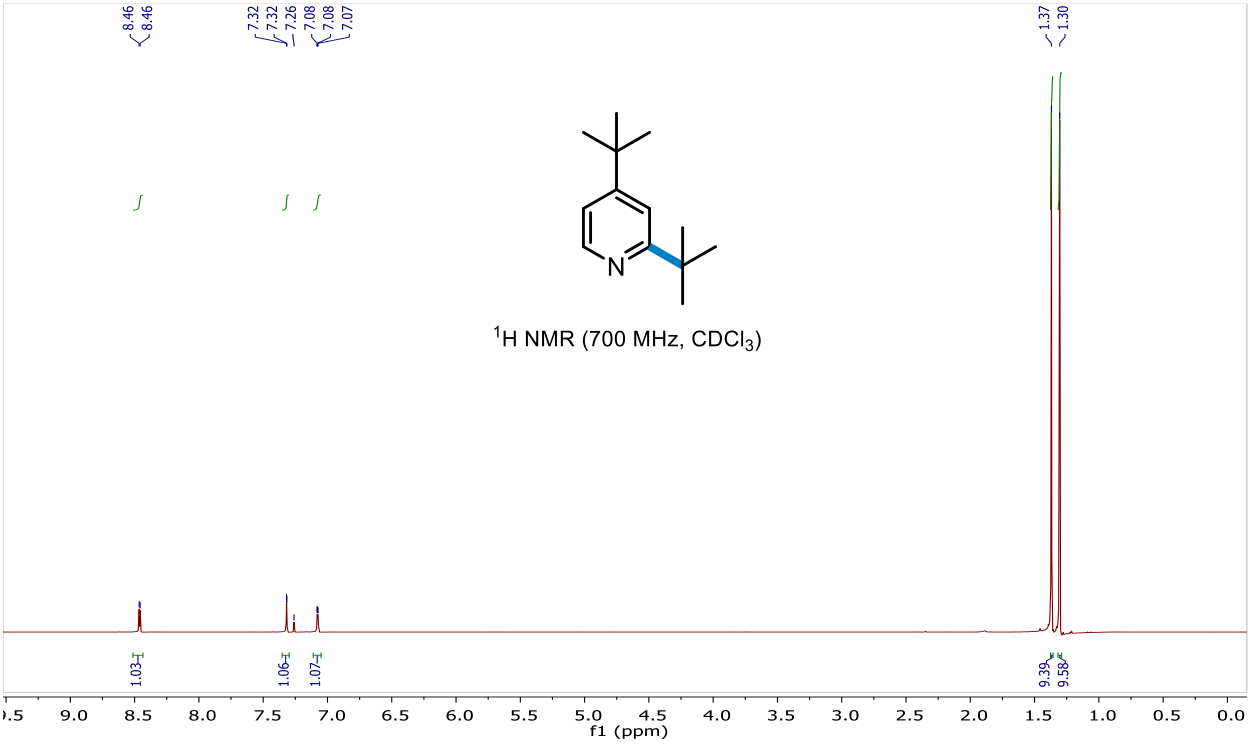

^{1}H NMR (700 MHz, $CDCl_3$)

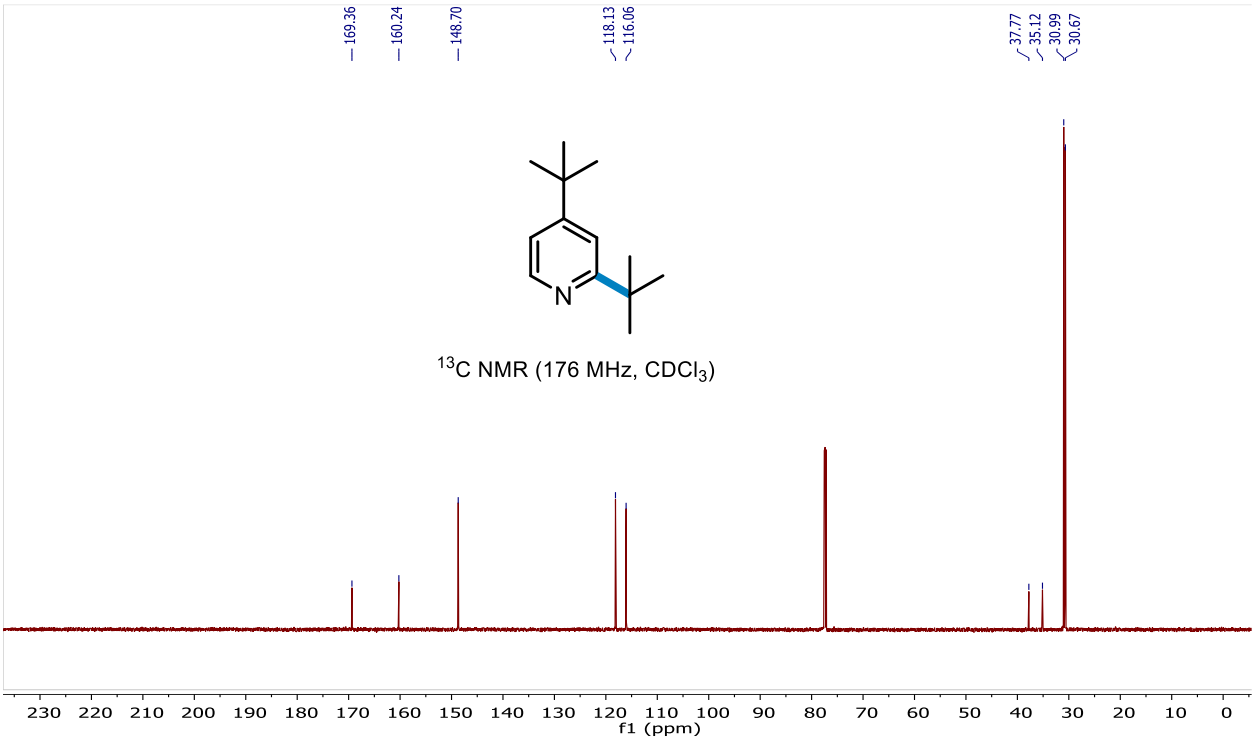

^{13}C NMR (176 MHz, $CDCl_3$)

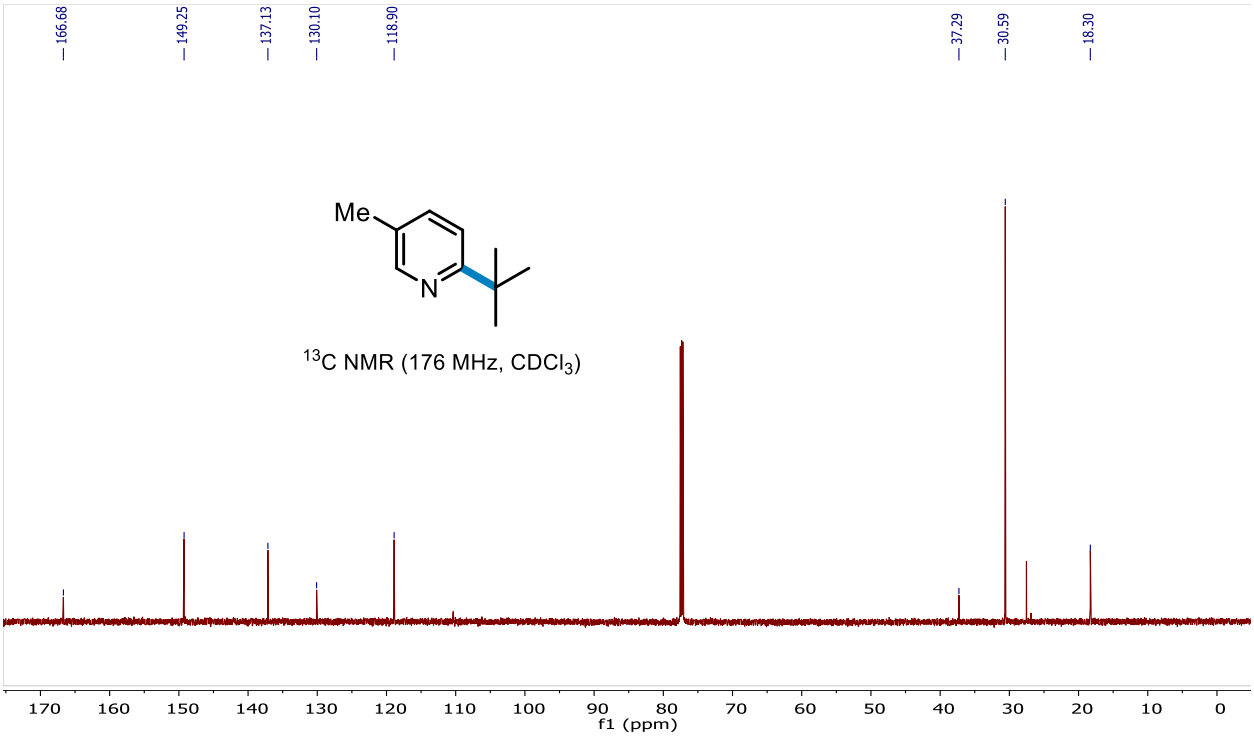

^{13}C NMR (176 MHz, $CDCl_3$)

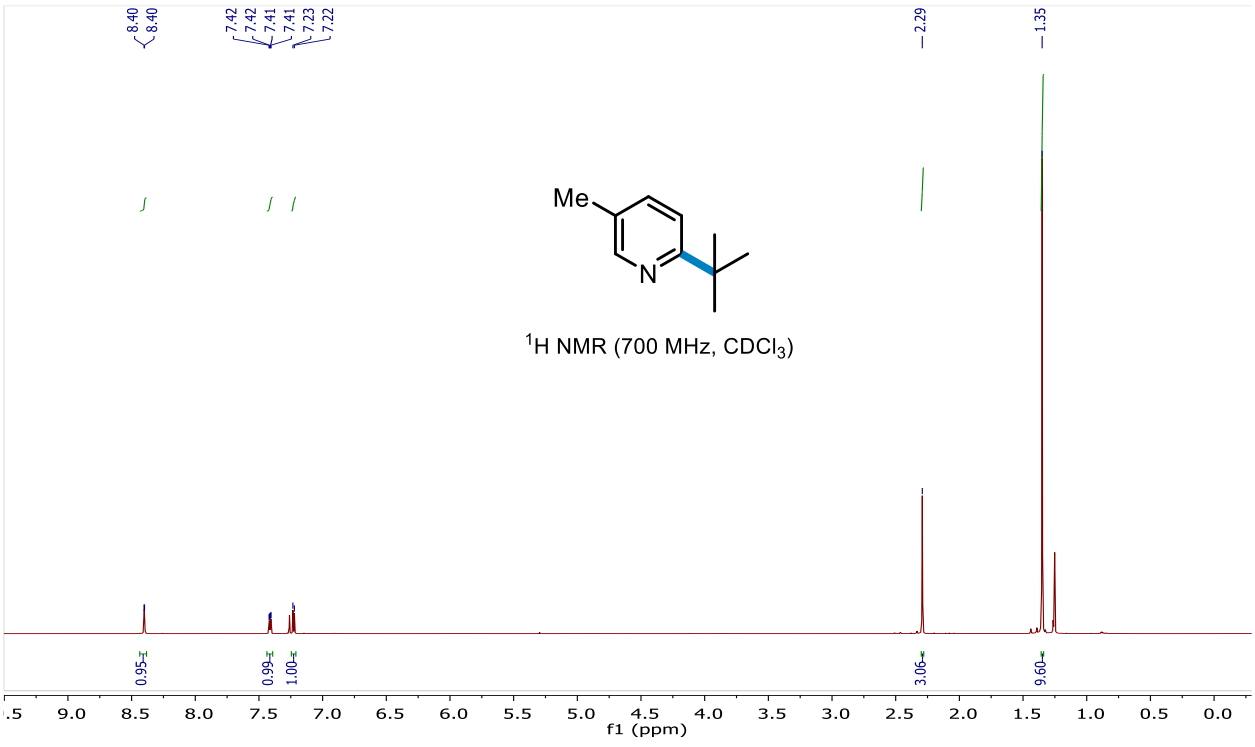

^{1}H NMR (700 MHz, $CDCl_3$)

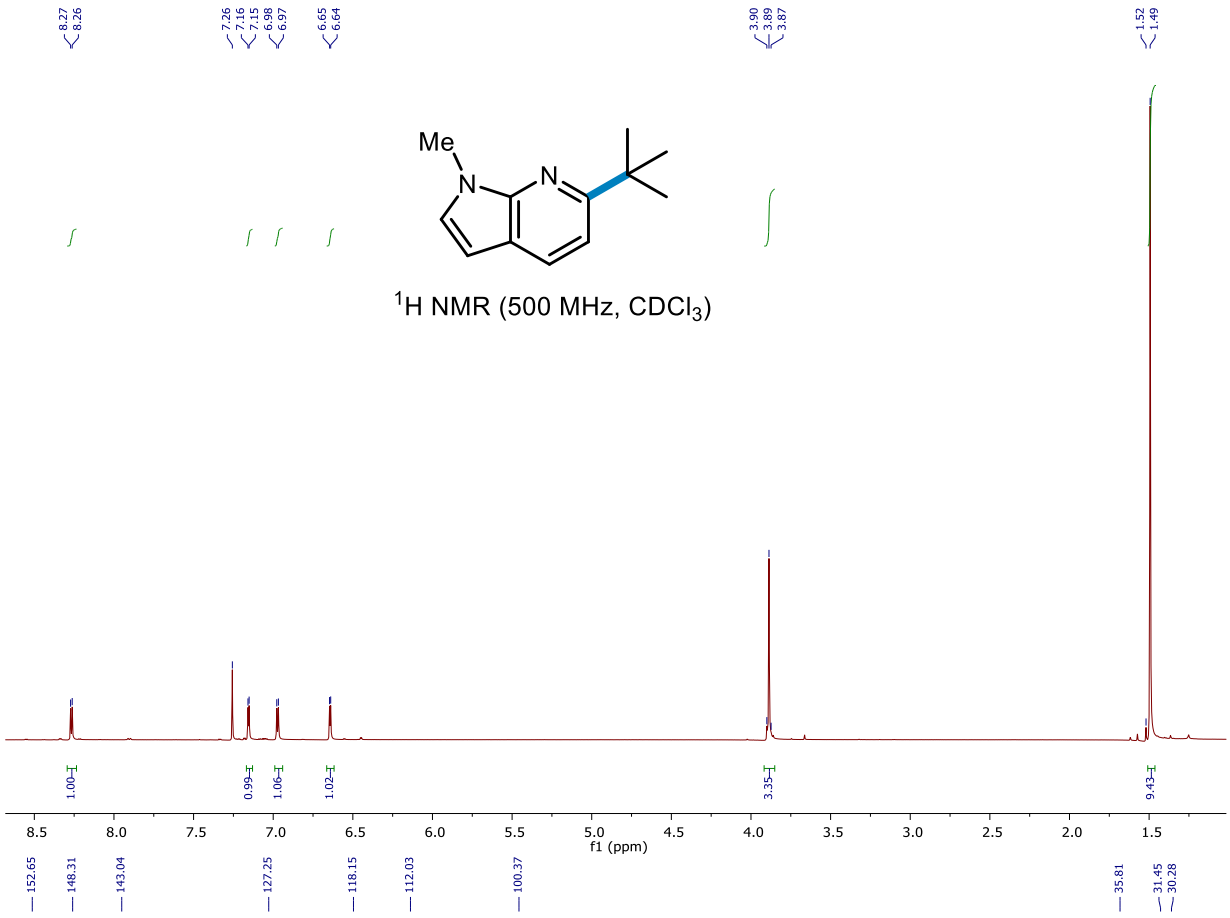

^{1}H NMR (500 MHz, $CDCl_3$)

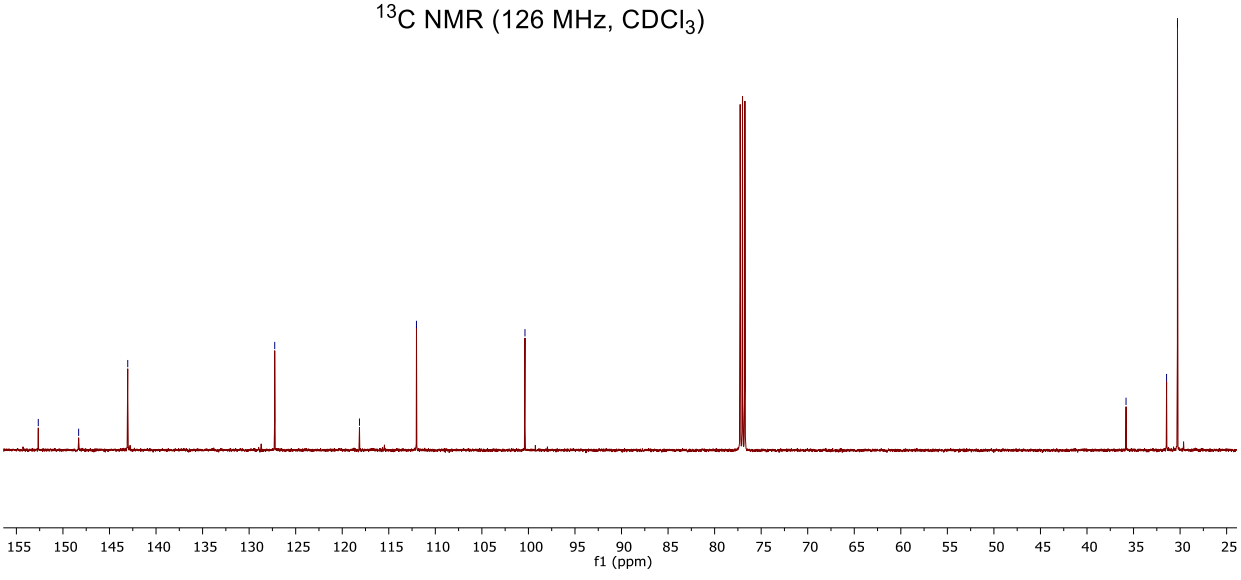

^{13}C NMR (126 MHz, $CDCl_3$)

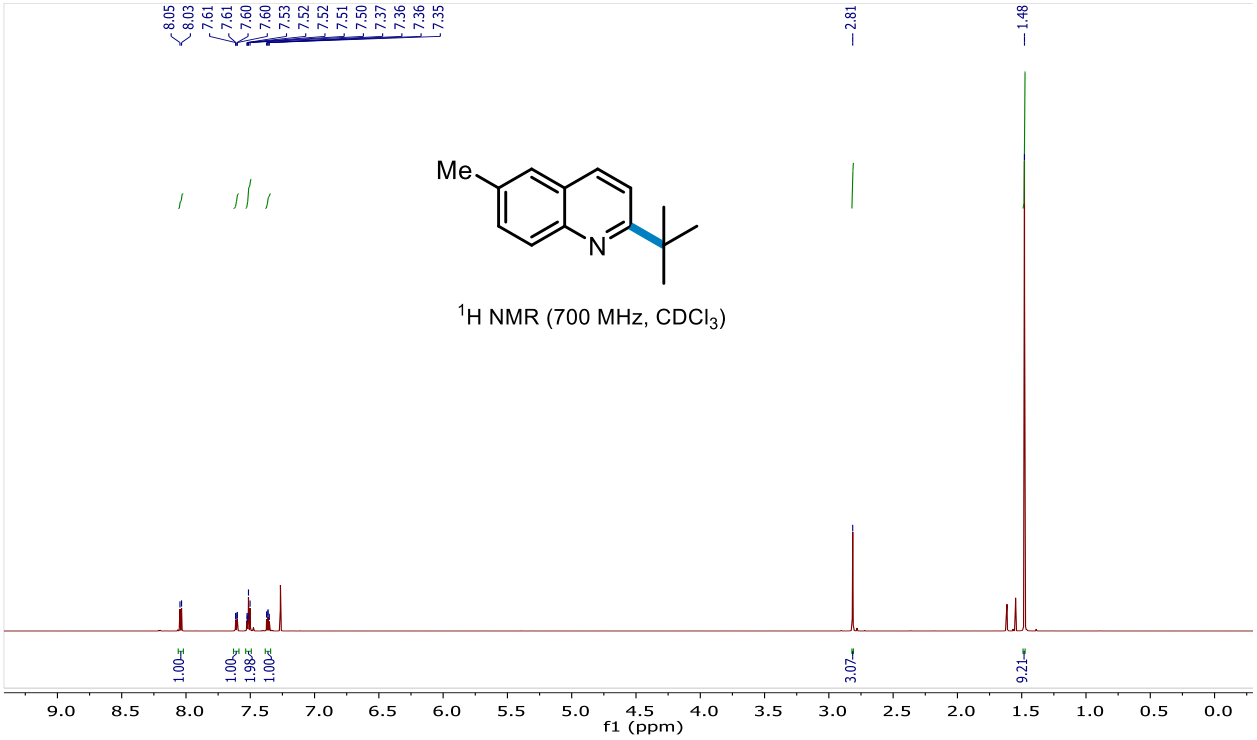

^{1}H NMR (700 MHz, $CDCl_3$)

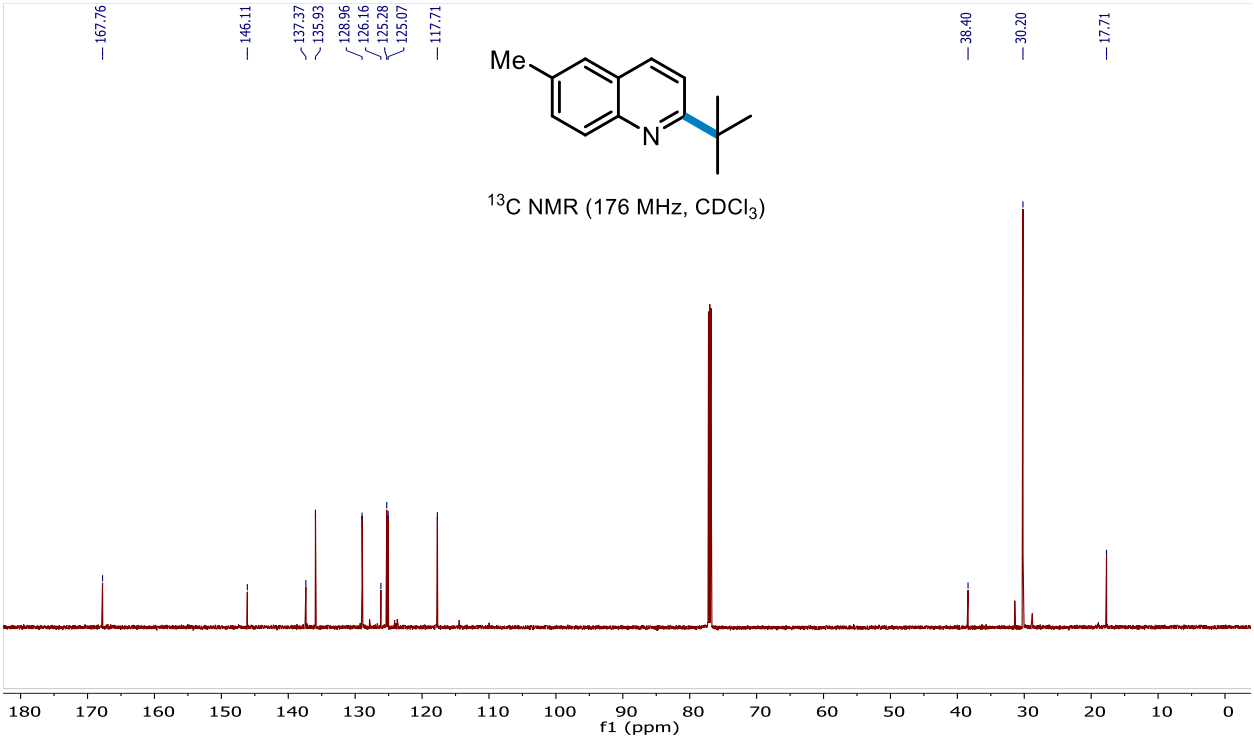

^{13}C NMR (176 MHz, $CDCl_3$)

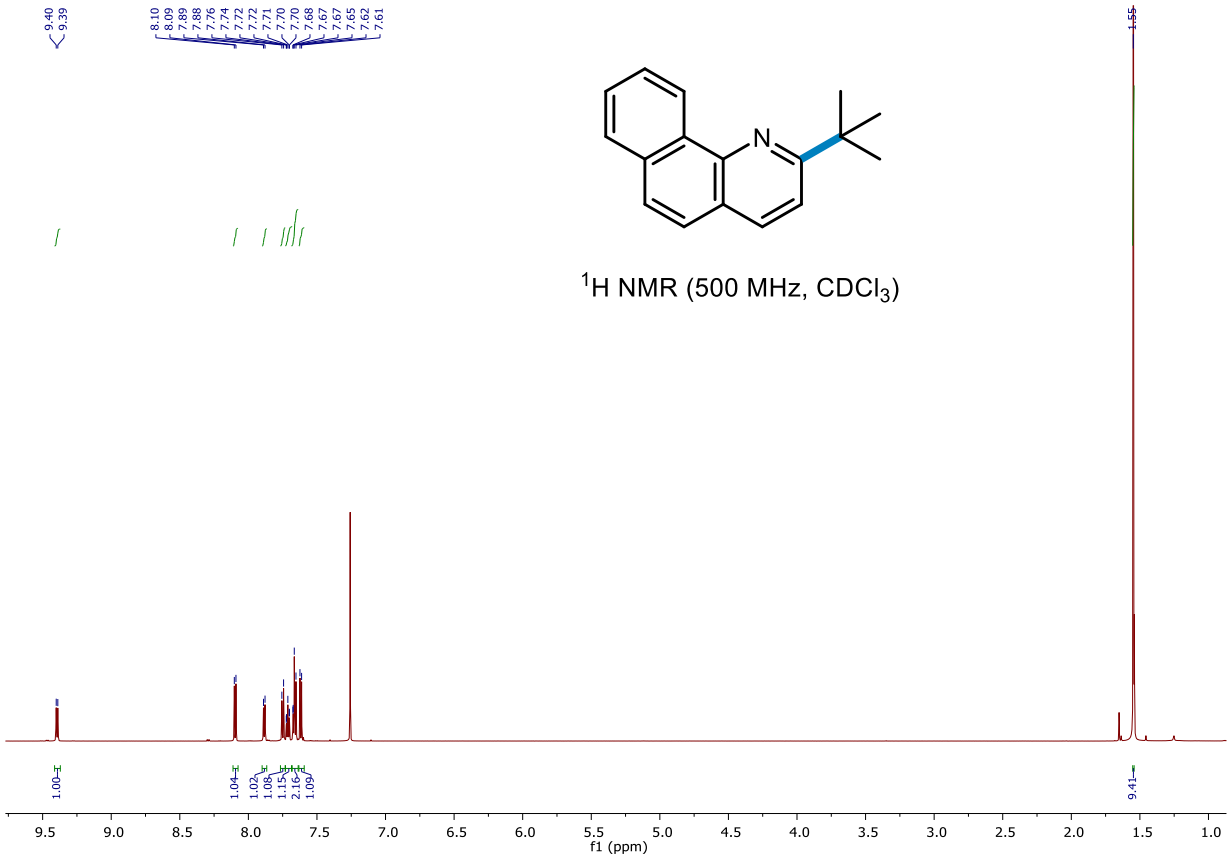

^{1}H NMR (500 MHz, $CDCl_3$)

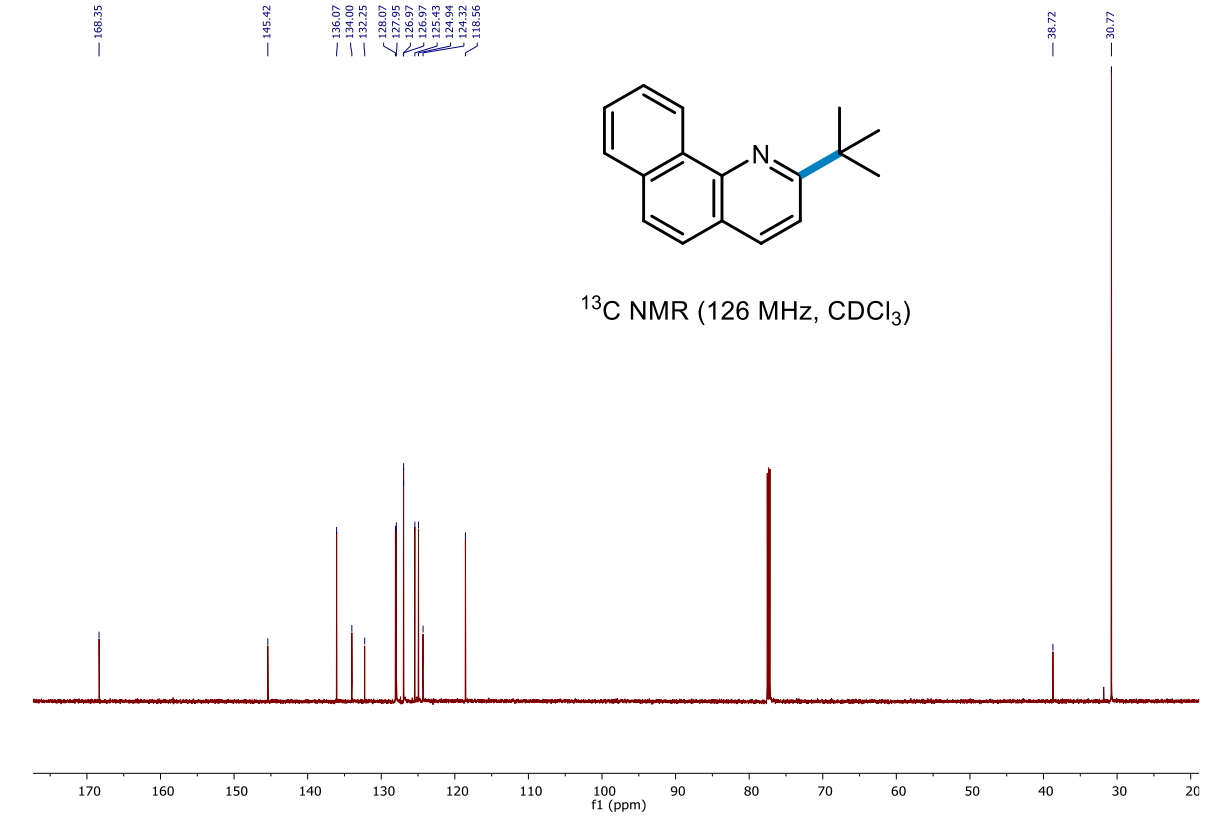

^{13}C NMR (126 MHz, $CDCl_3$)

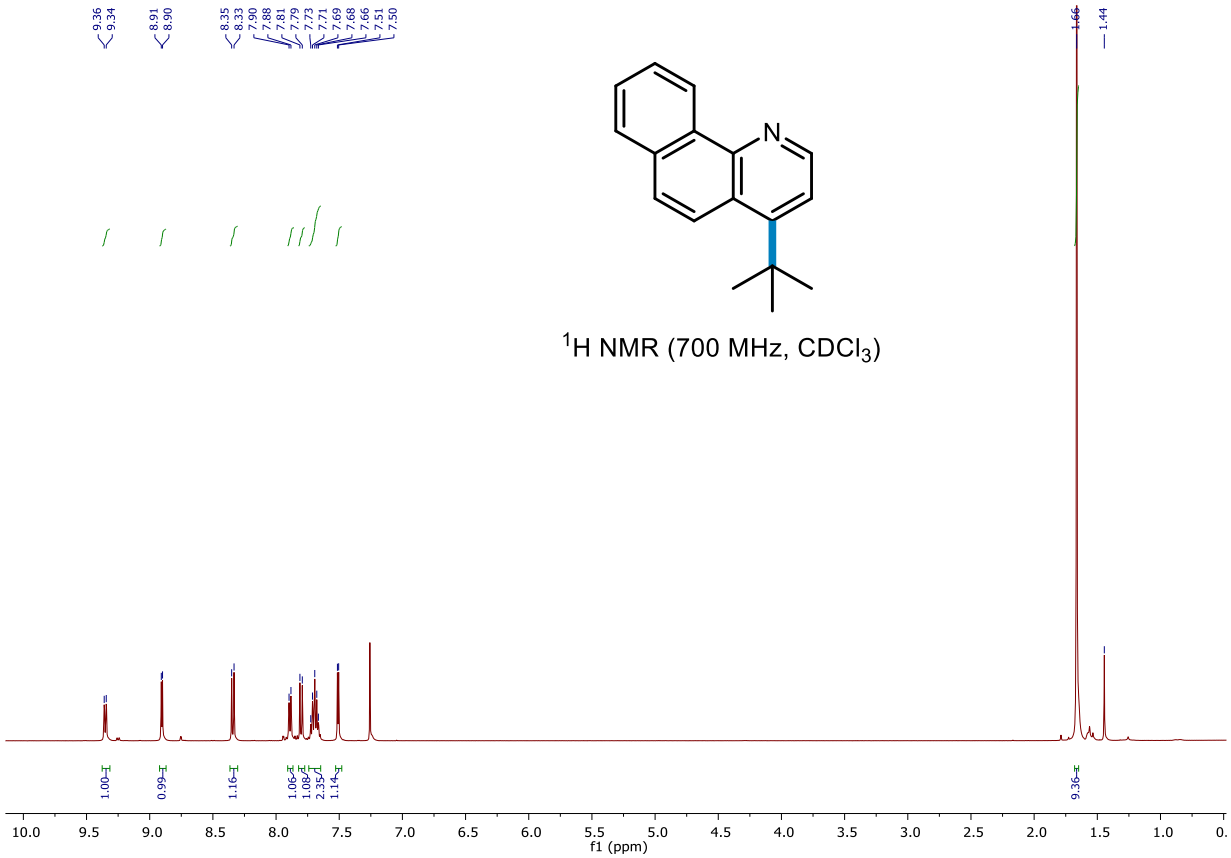

^{1}H NMR (700 MHz, $CDCl_3$)

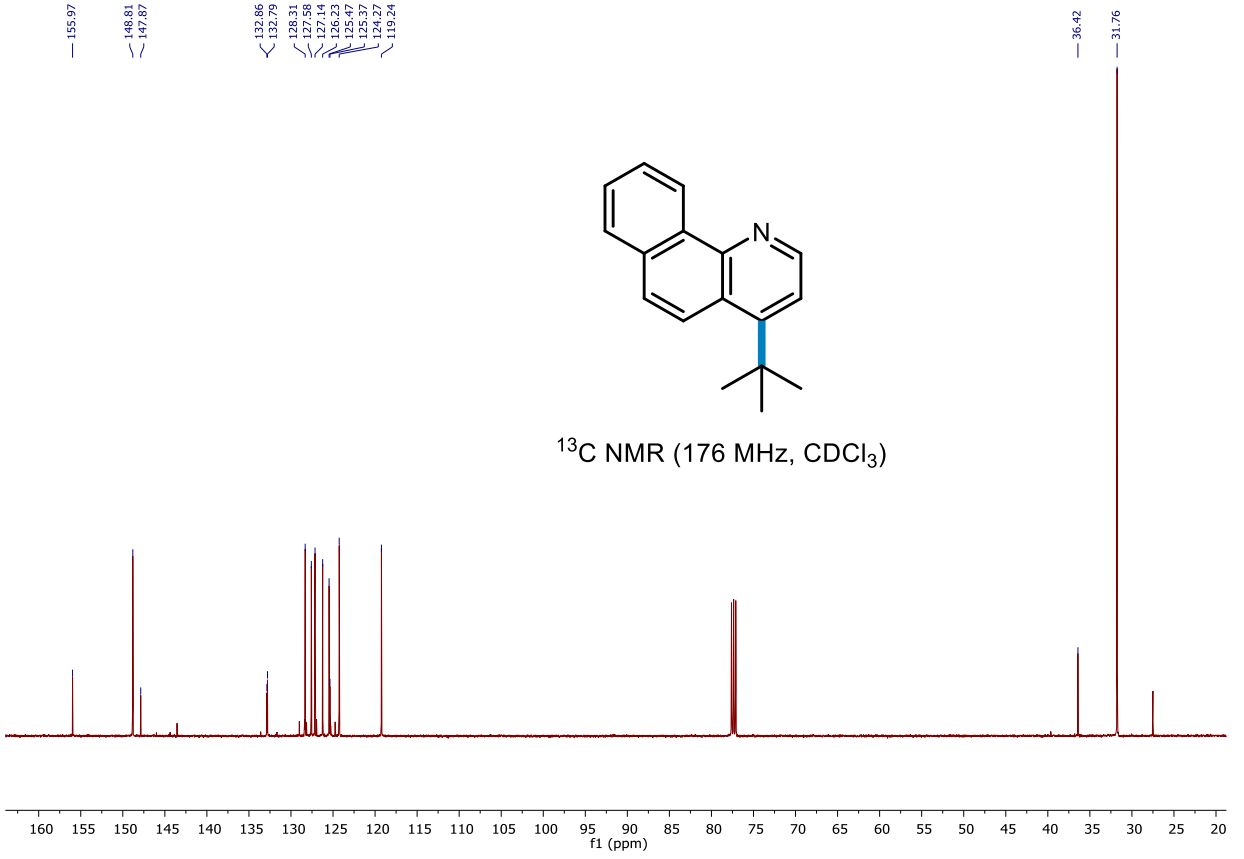

^{13}C NMR (176 MHz, $CDCl_3$)

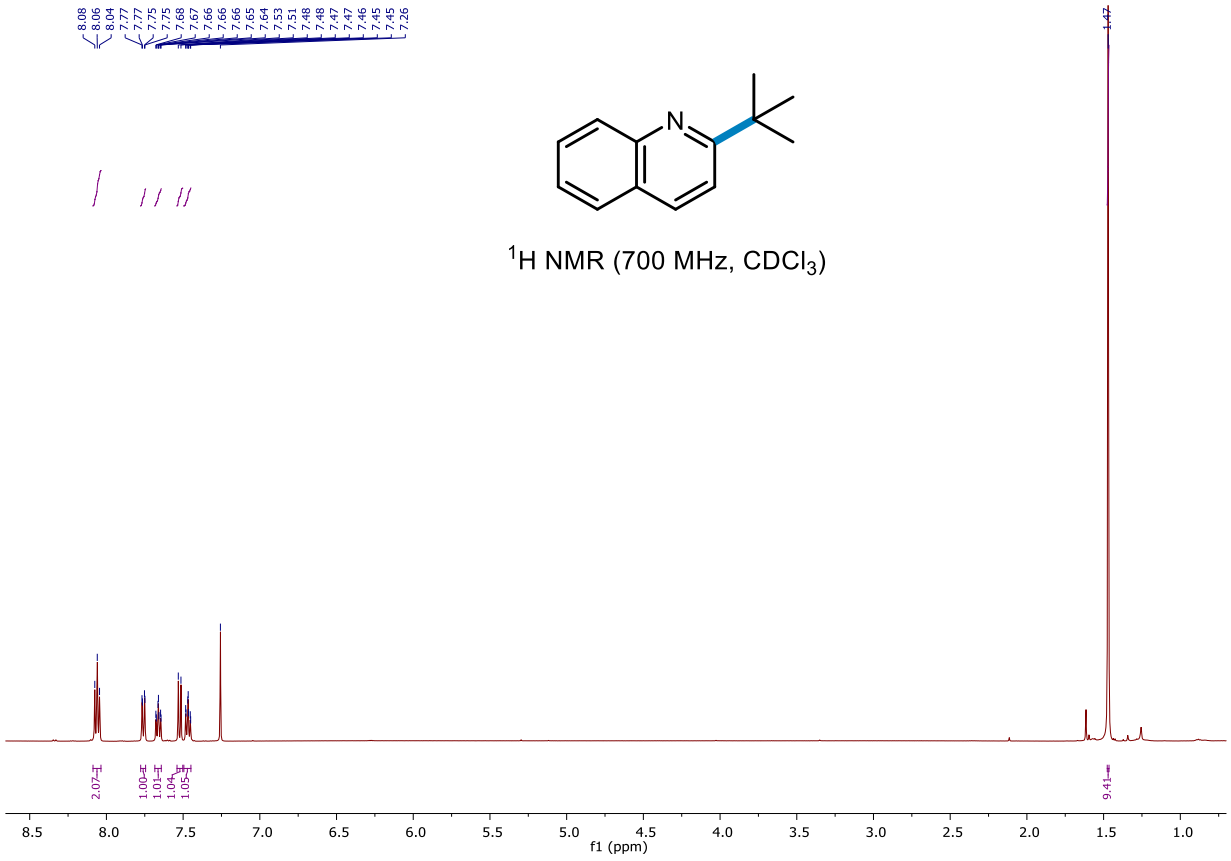

^{1}H NMR (700 MHz, $CDCl_3$)

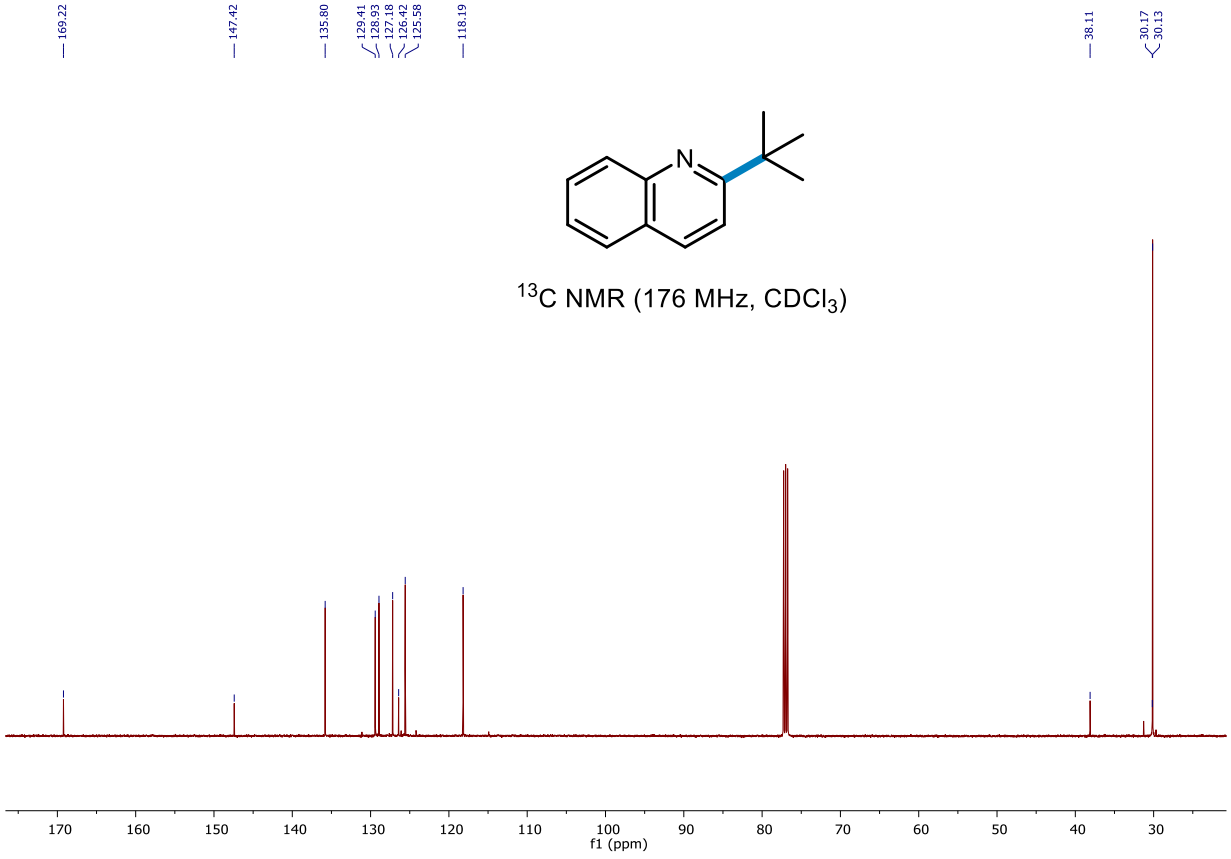

^{13}C NMR (176 MHz, $CDCl_3$)

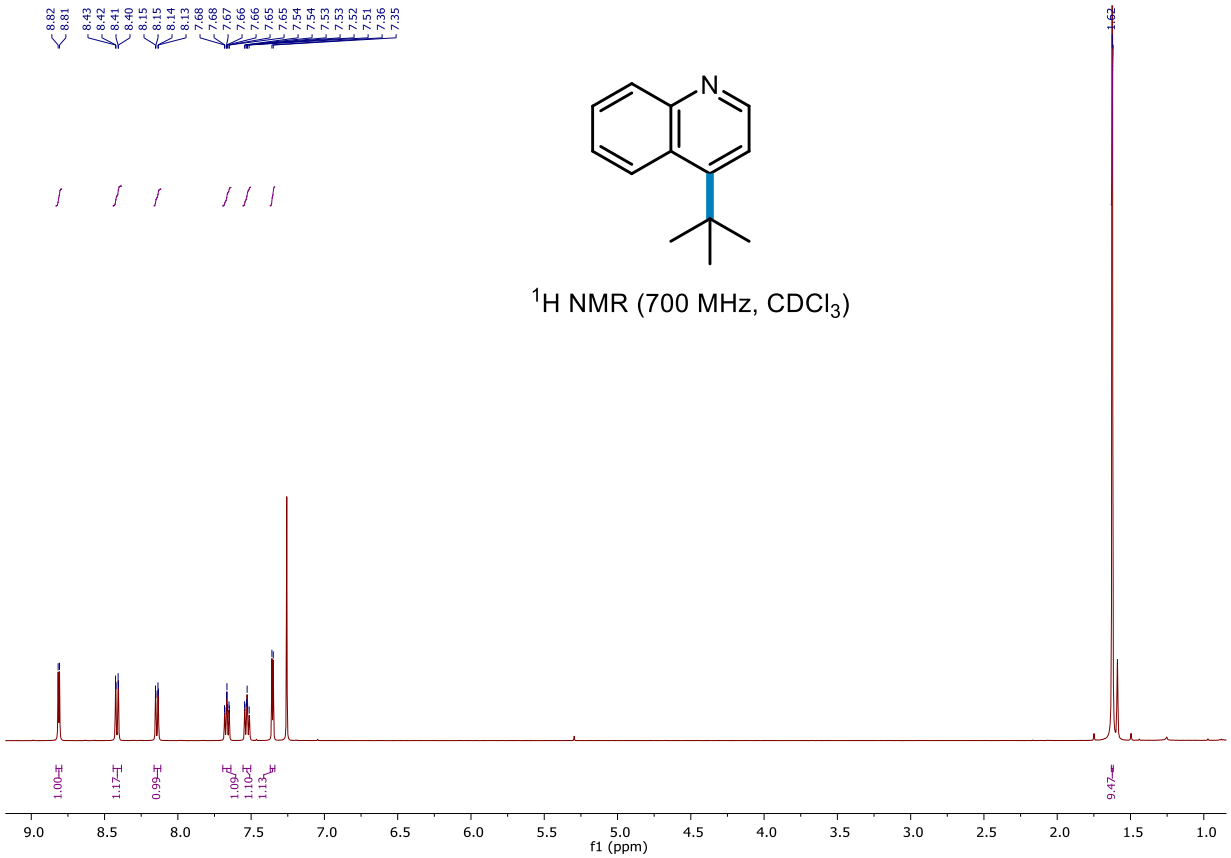

^{1}H NMR (700 MHz, $CDCl_3$)

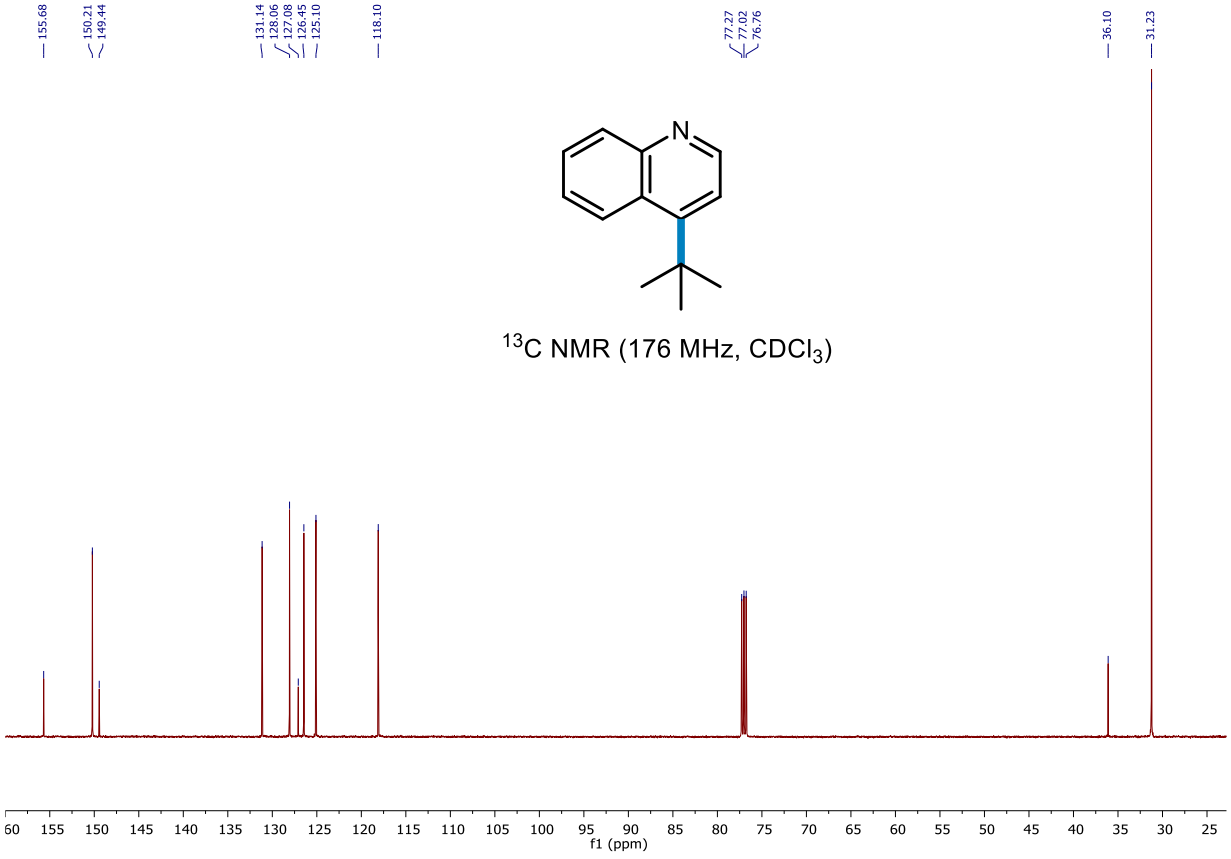

^{13}C NMR (176 MHz, $CDCl_3$)

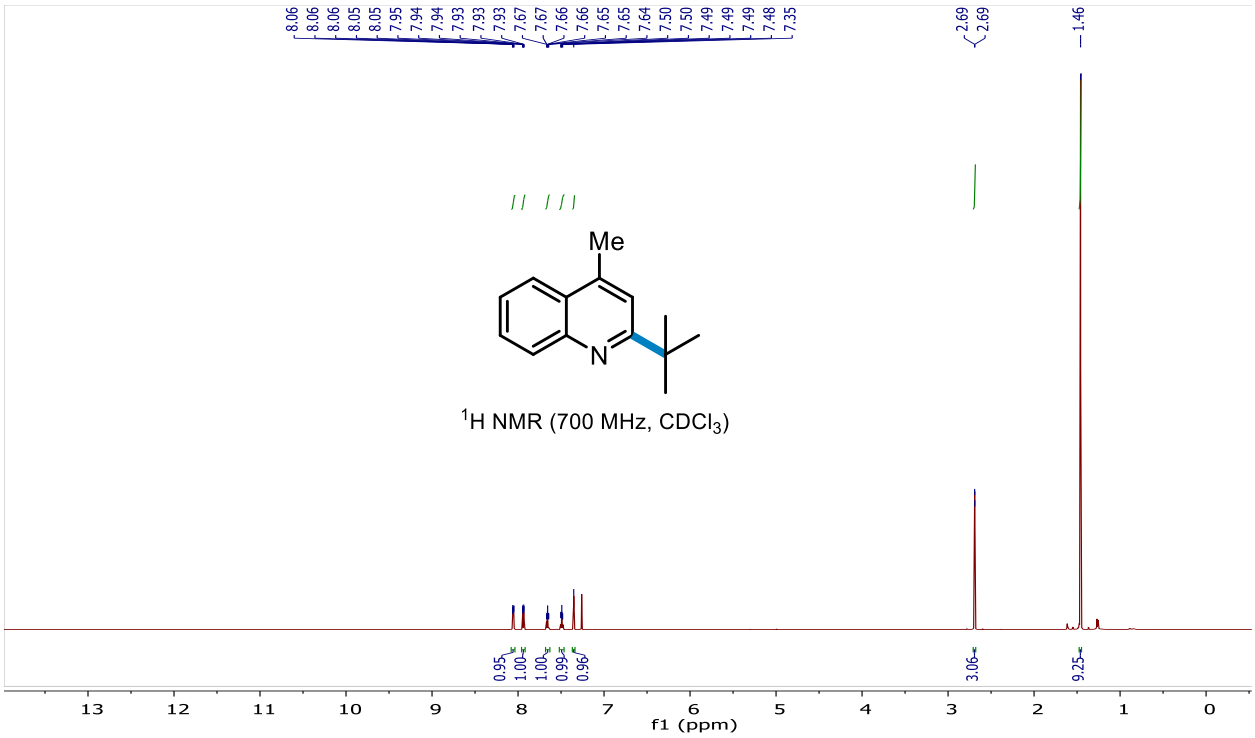
Me
N
1H NMR (700 MHz, CDCl3)
f1 (ppm)

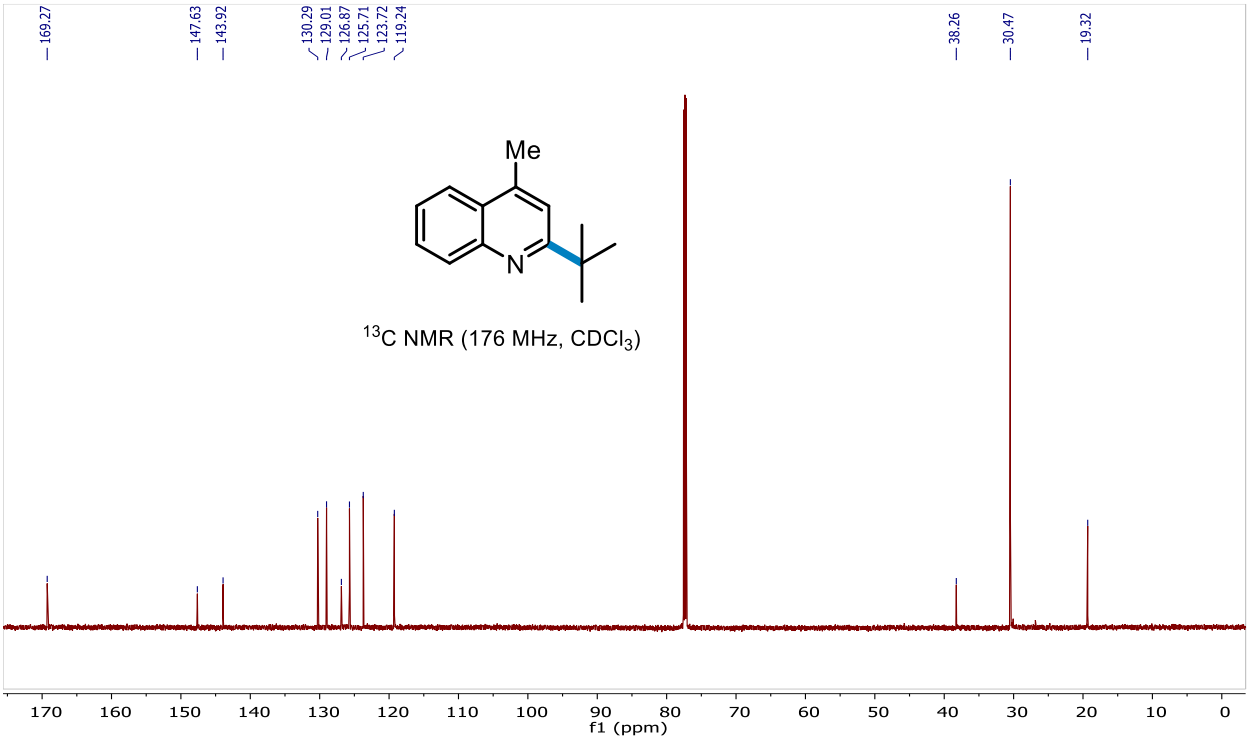
Me
N
13C NMR (176 MHz, CDCl3)
f1 (ppm)

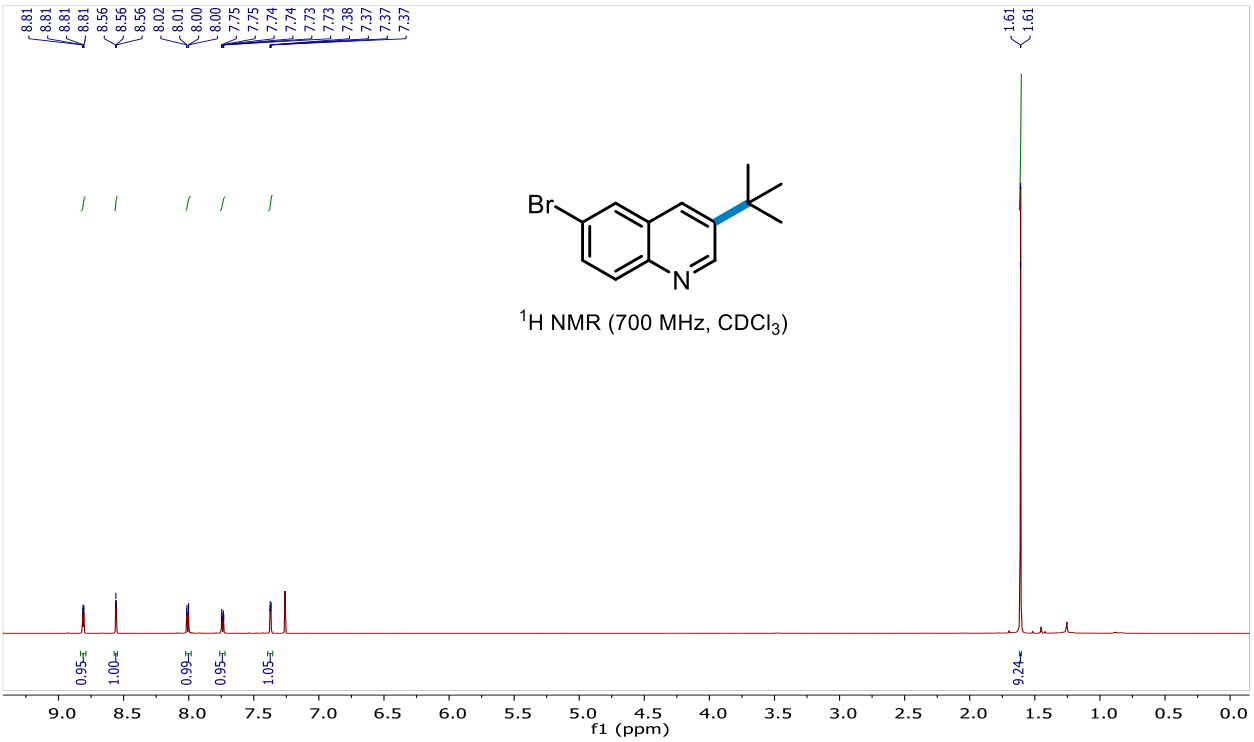

^{1}H NMR (700 MHz, $CDCl_3$)

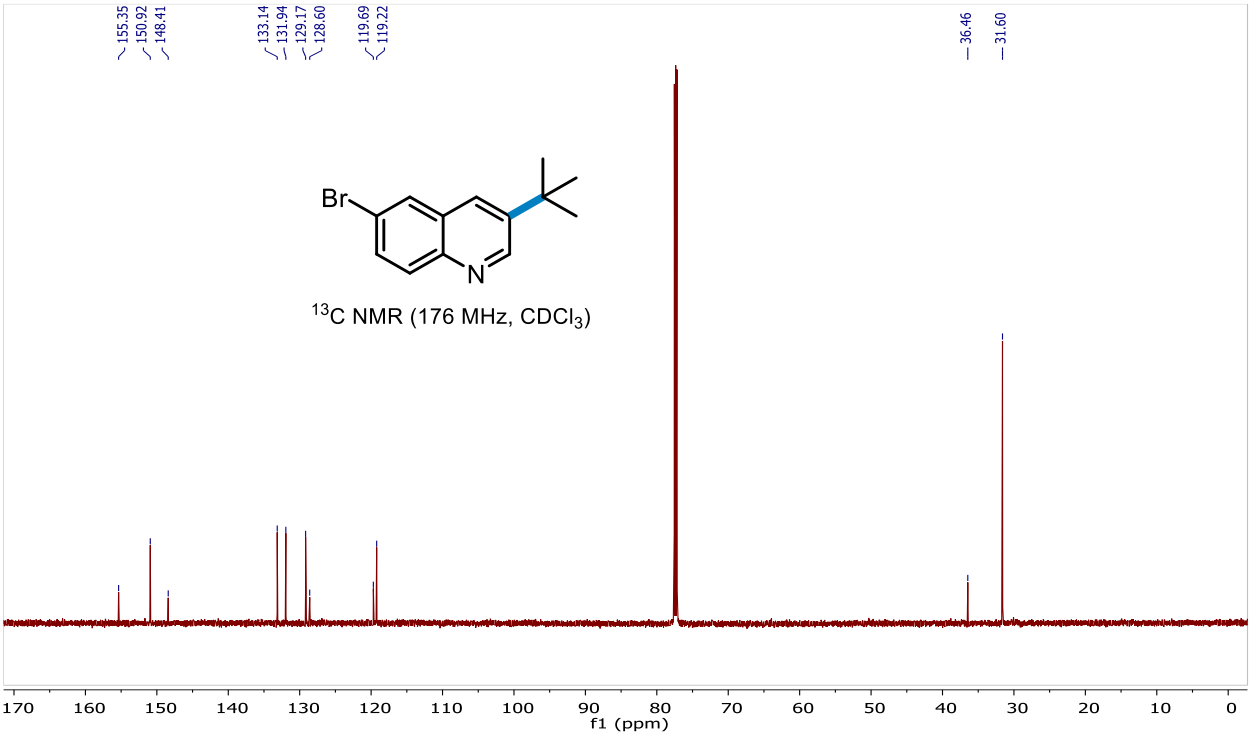

^{13}C NMR (176 MHz, $CDCl_3$)

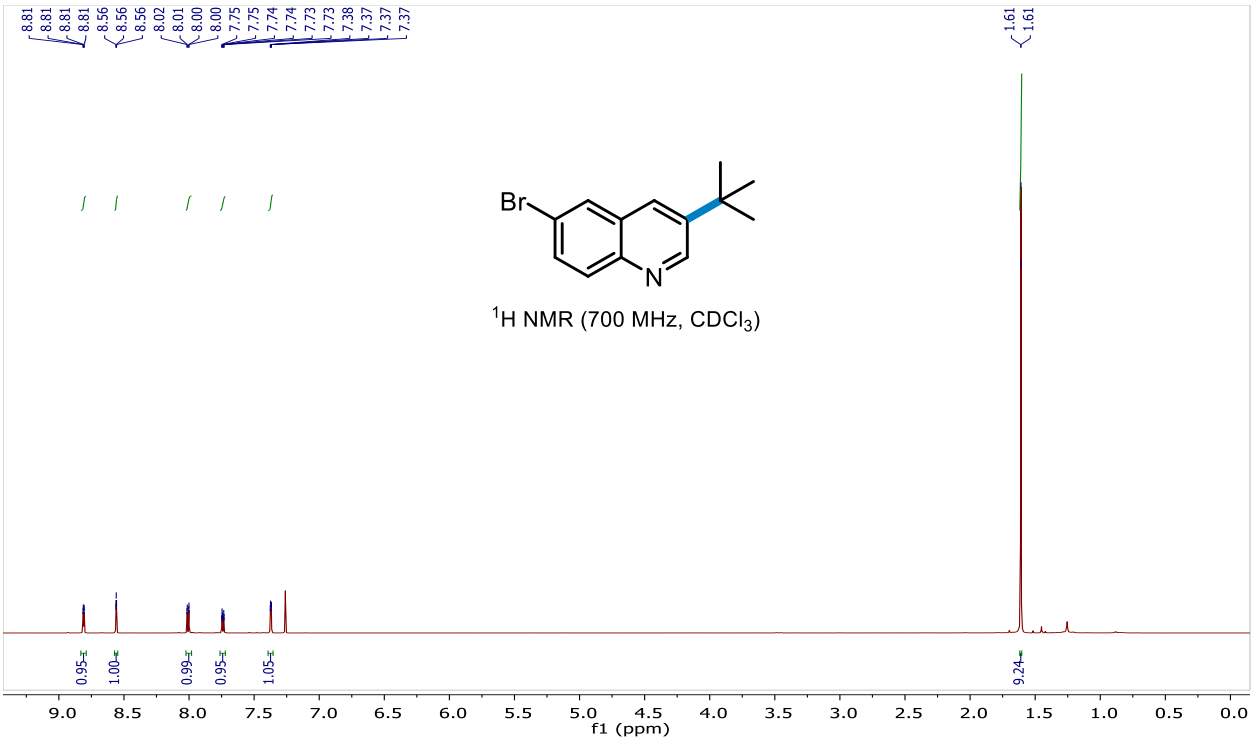

^{1}H NMR (700 MHz, $CDCl_3$)

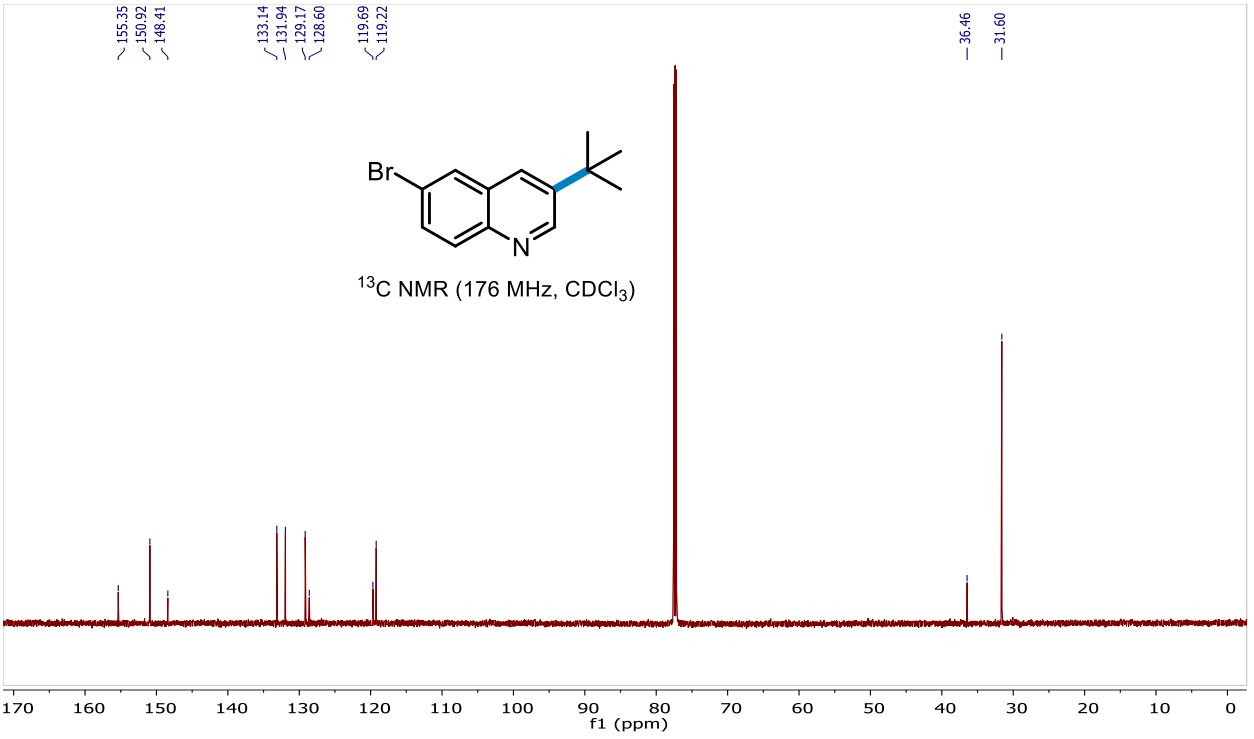

^{13}C NMR (176 MHz, $CDCl_3$)

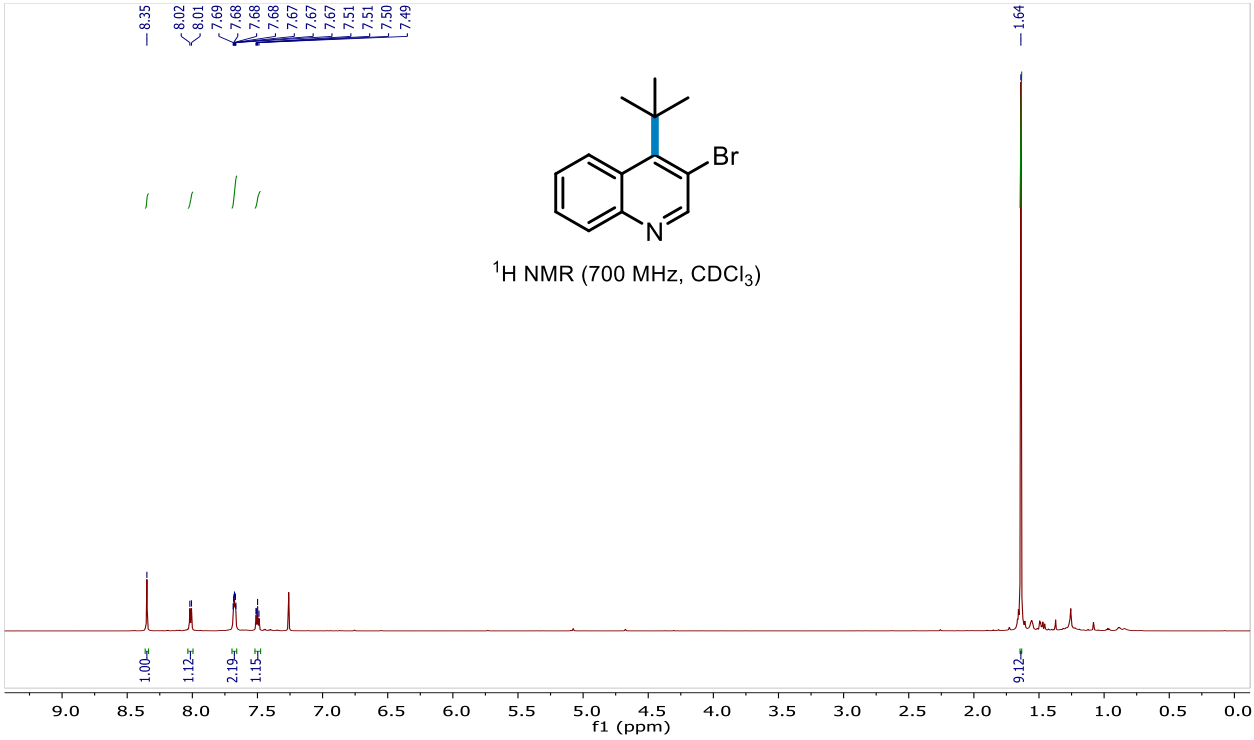
8.35
8.02
8.01
7.69
7.68
7.68
7.68
7.67
7.67
7.67
7.51
7.51
7.50
7.49
1.64
Br
N
1H NMR (700 MHz, CDCl3)
1.00
1.12
2.19
1.15
9.12
9.0 8.5 8.0 7.5 7.0 6.5 6.0 5.5 5.0 4.5 4.0 3.5 3.0 2.5 2.0 1.5 1.0 0.5 0.0
f1 (ppm)

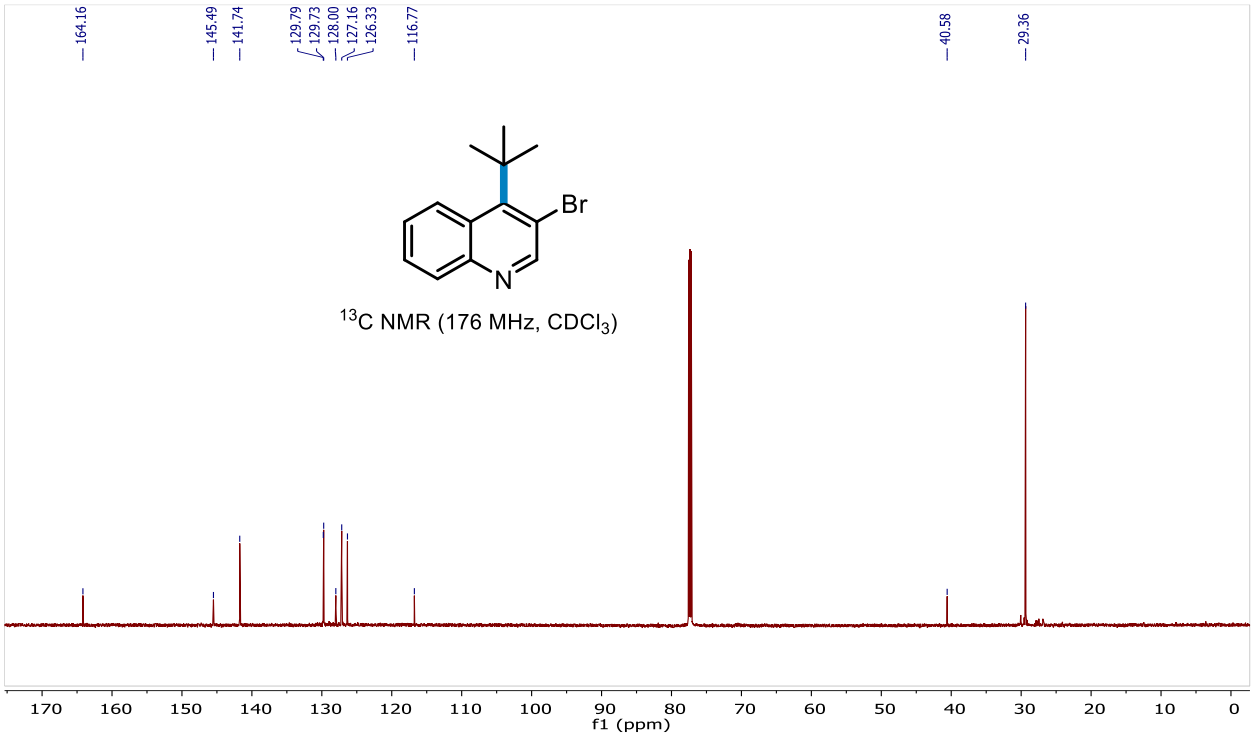
164.16
145.49
141.74
129.79
129.73
128.00
127.16
126.33
116.77
40.58
29.36
Br
N
13C NMR (176 MHz, CDCl3)
170 160 150 140 130 120 110 100 90 80 70 60 50 40 30 20 10 0
f1 (ppm)

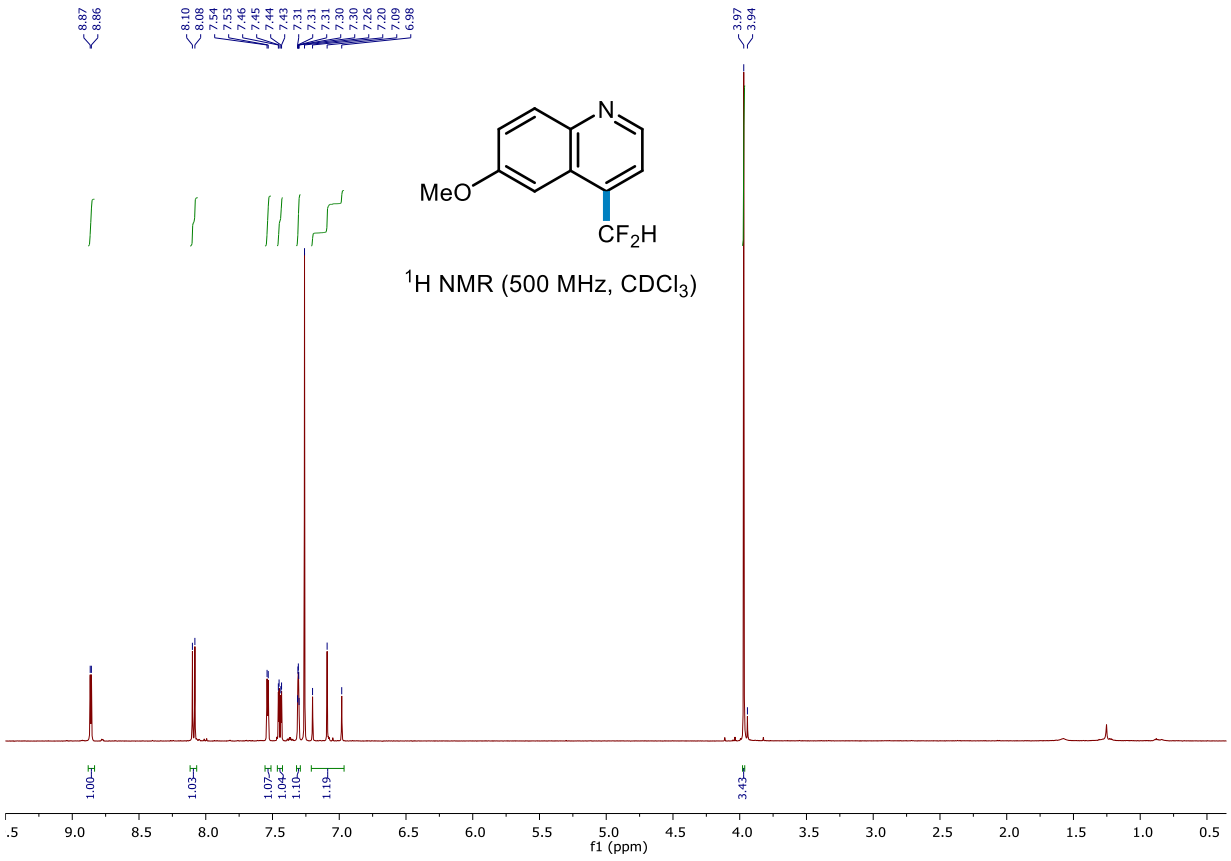
8.87
8.86
8.10
8.08
7.54
7.53
7.46
7.45
7.44
7.43
7.31
7.31
7.31
7.30
7.30
7.26
7.20
7.09
6.98
3.97
3.94
N
MeO
CF2H
1H NMR (500 MHz, CDCl3)
1.00
1.03
1.07
1.04
1.10
1.19
3.43
f1 (ppm)

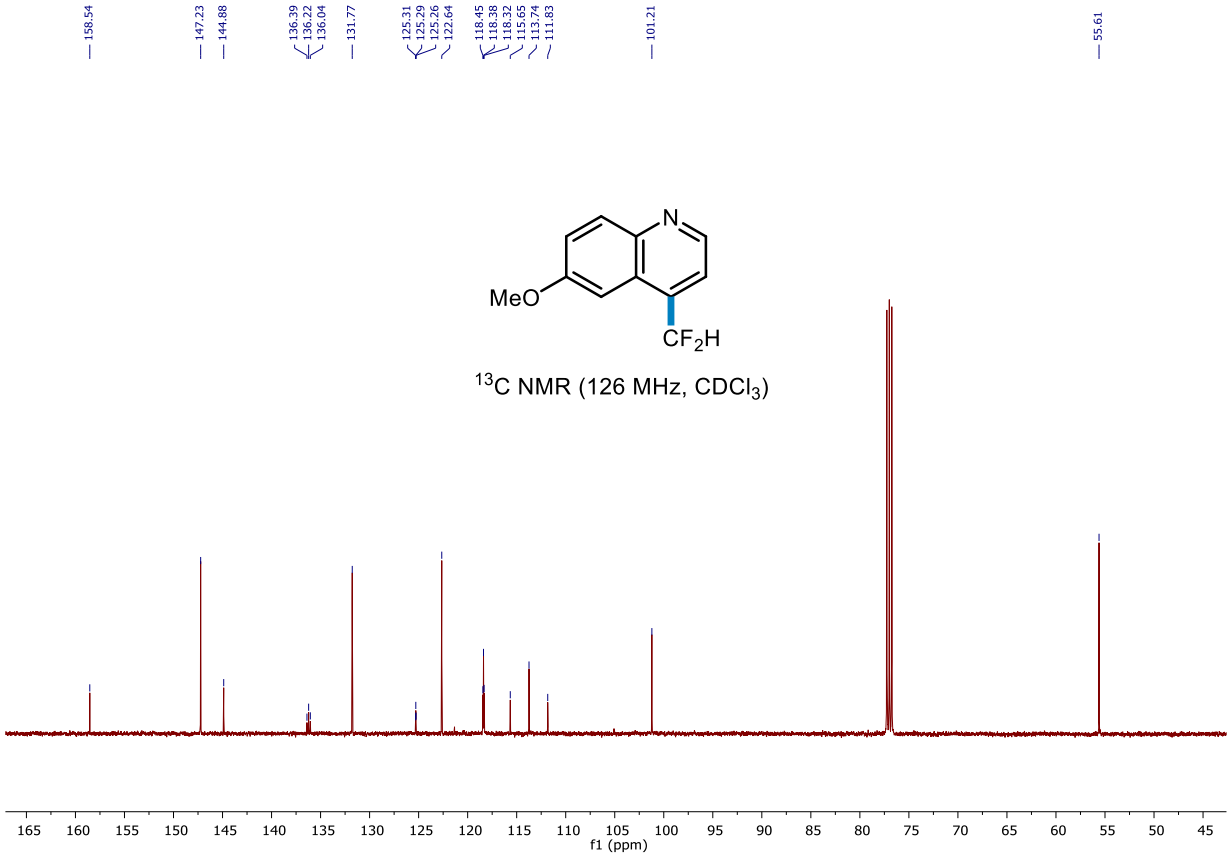
158.54
147.23
144.88
136.39
136.22
136.04
131.77
125.31
125.29
125.26
122.64
118.45
118.38
118.32
115.65
113.74
111.83
101.21
55.61
N
MeO
CF2H
13C NMR (126 MHz, CDCl3)
f1 (ppm)

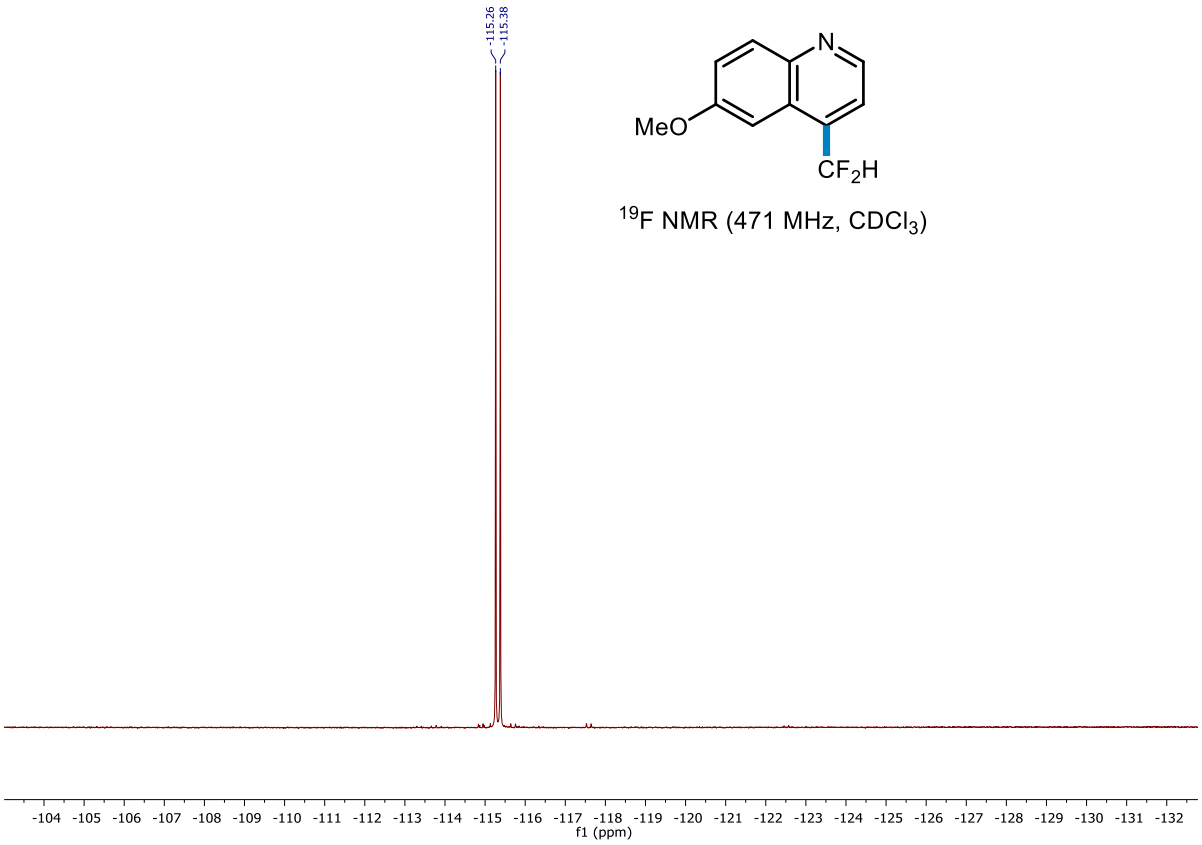
-115.26
-115.38
N
MeO
CF2H
19F NMR (471 MHz, CDCl3)
-104 -105 -106 -107 -108 -109 -110 -111 -112 -113 -114 -115 -116 -117 -118 -119 -120 -121 -122 -123 -124 -125 -126 -127 -128 -129 -130 -131 -132
f1 (ppm)

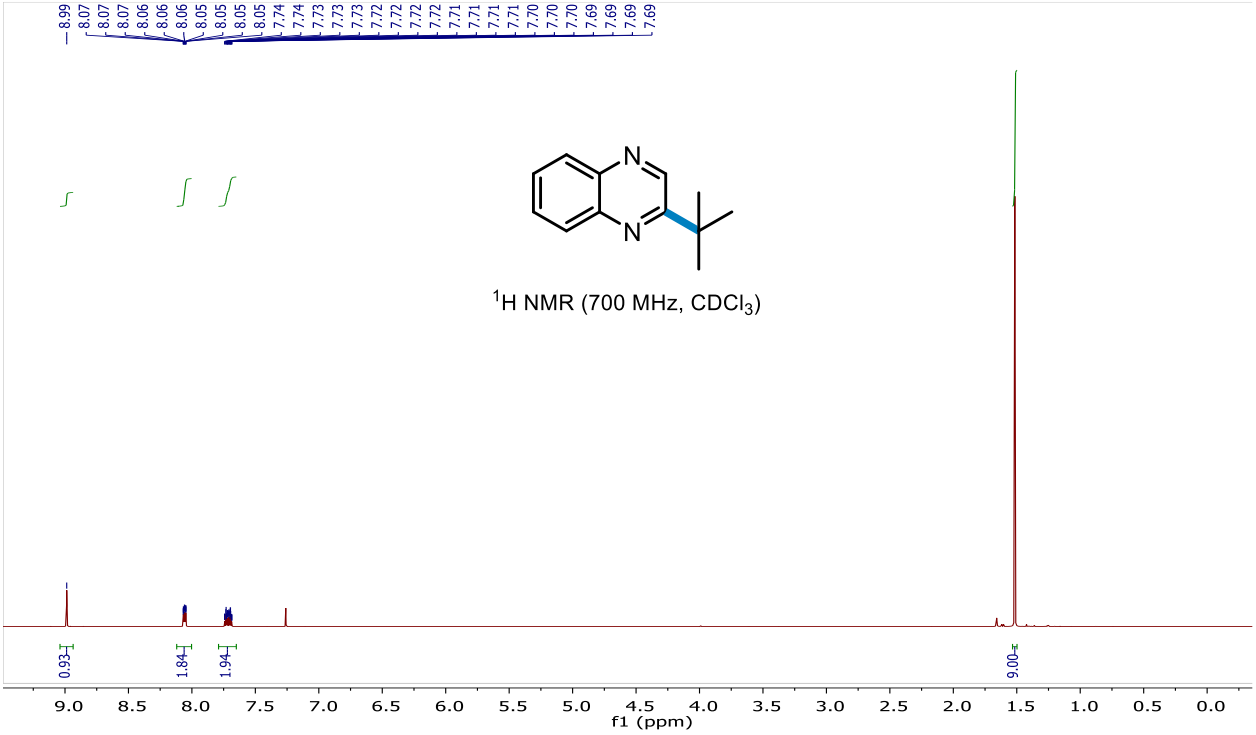

^{1}H NMR (700 MHz, $CDCl_3$)

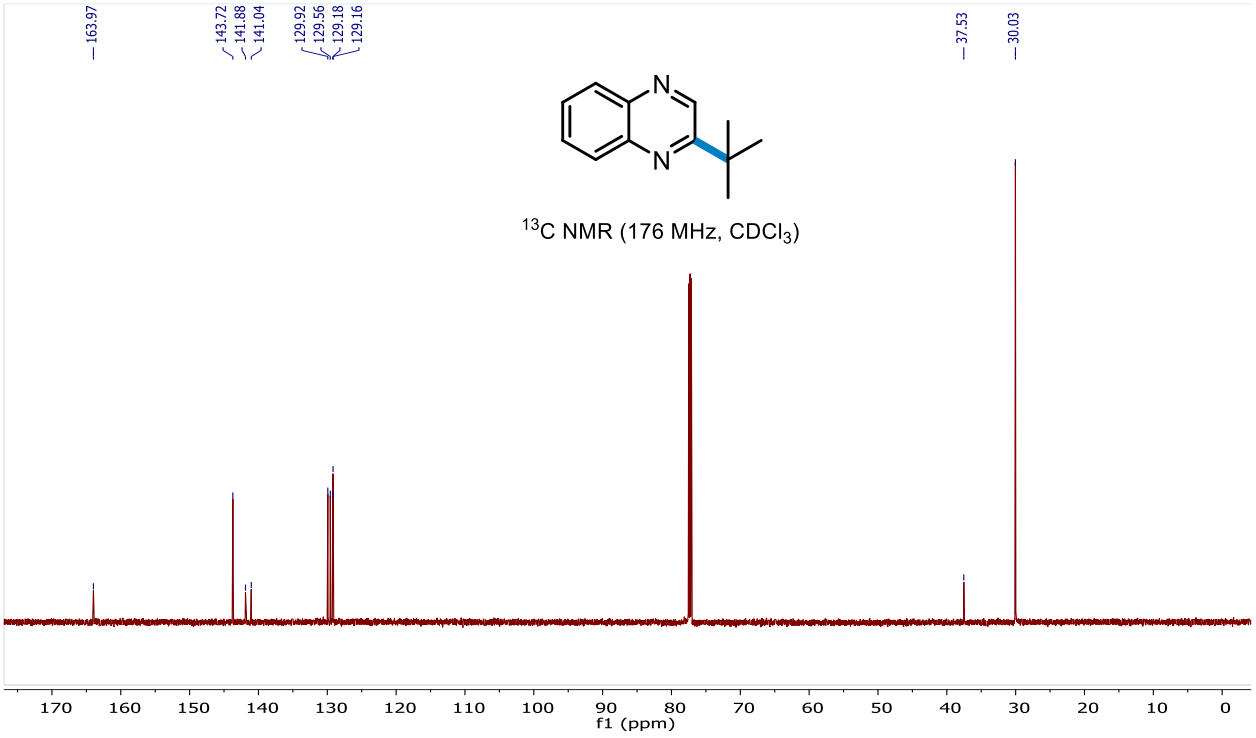

^{13}C NMR (176 MHz, $CDCl_3$)

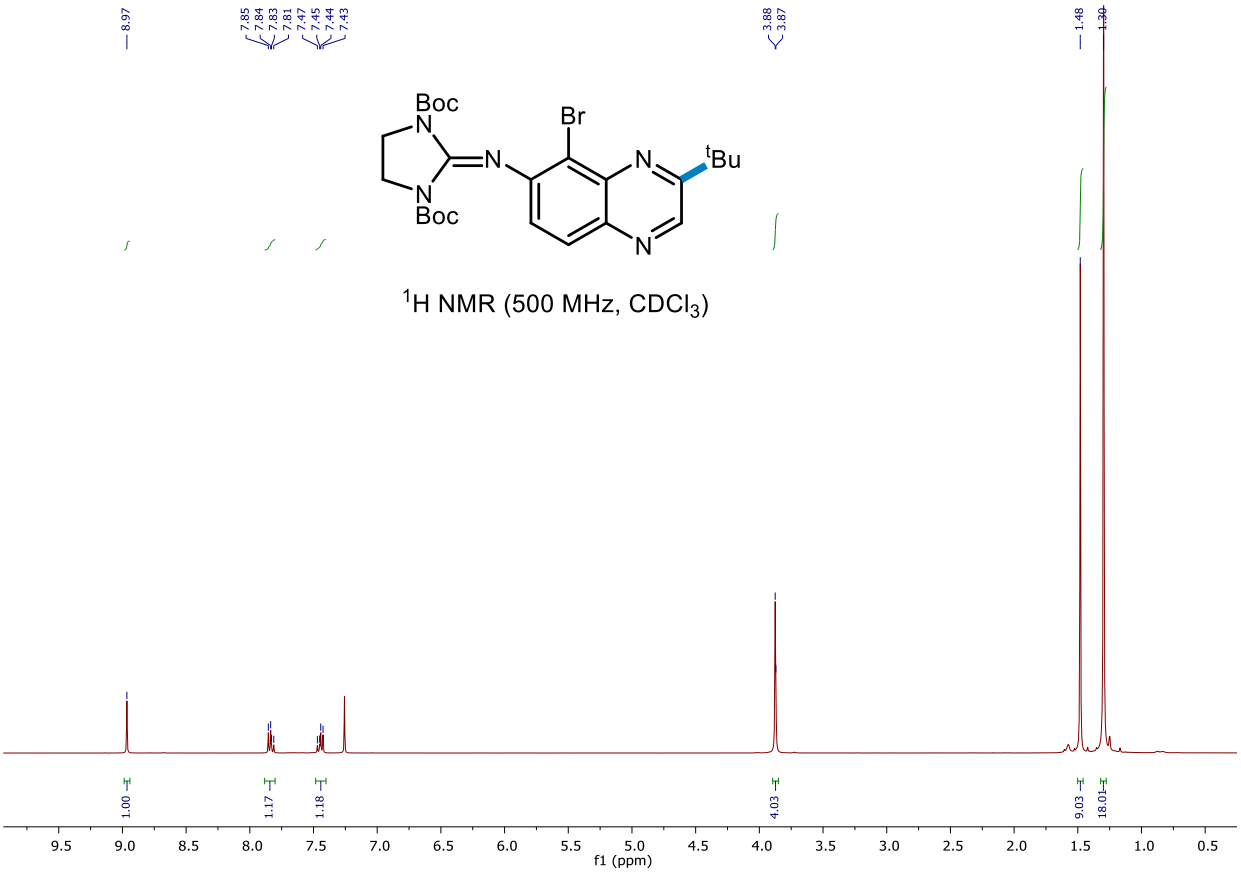

^{1}H NMR (500 MHz, $CDCl_3$)

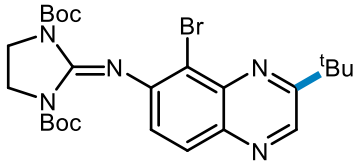

^{13}C NMR (126 MHz, $CDCl_3$)

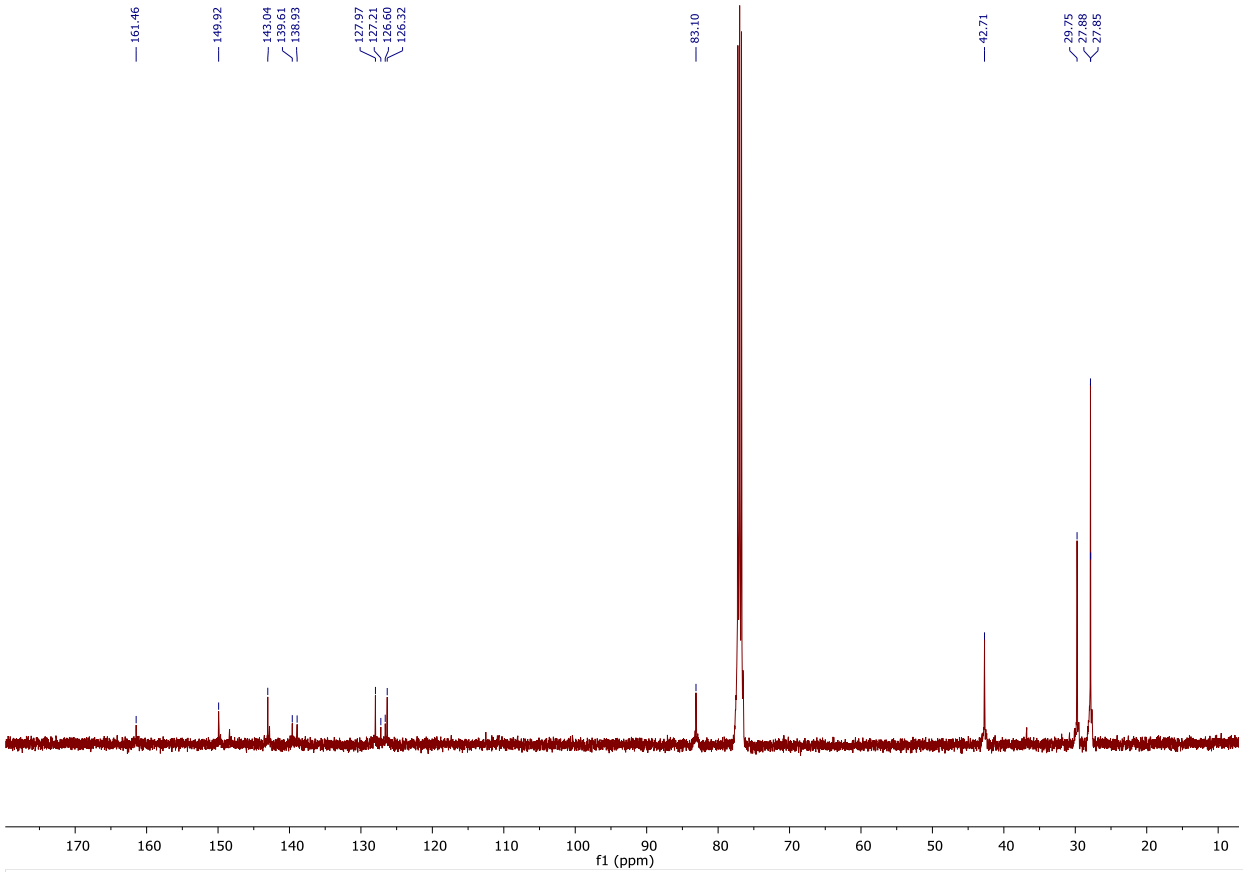

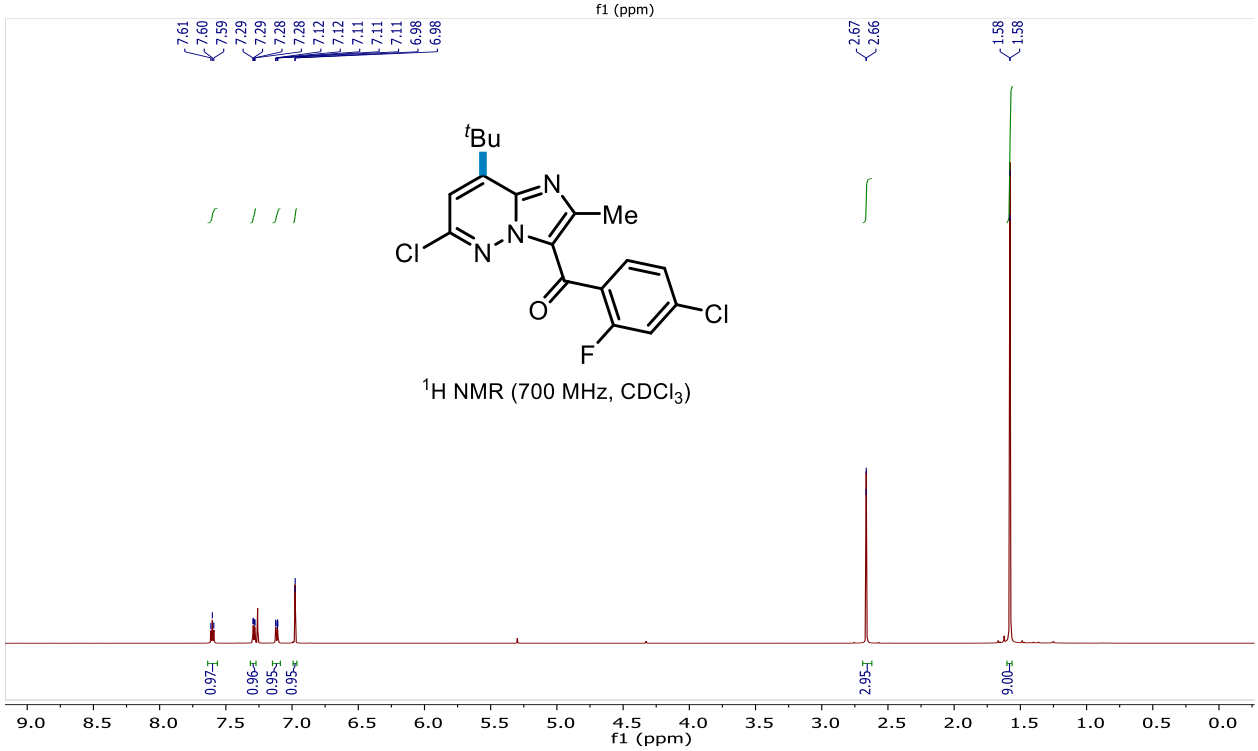

^{1}H NMR (700 MHz, $CDCl_3$)

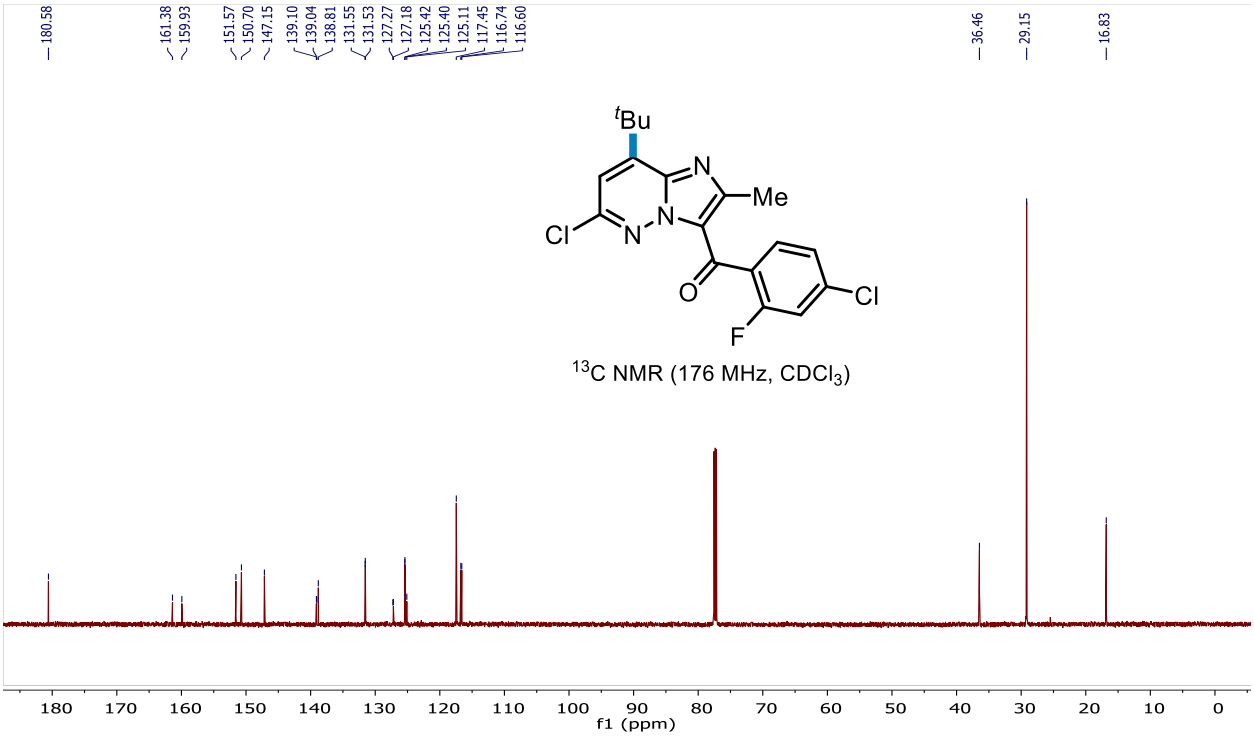
180.58
161.38
159.93
151.57
150.70
147.15
139.10
139.04
138.81
131.55
131.53
127.27
127.18
125.42
125.40
125.11
117.45
116.74
116.60
36.46
29.15
16.83
tBu
N
Me
Cl
N
N
O
Cl
F
13C NMR (176 MHz, CDCl3)
180
170
160
150
140
130
120
110
100
90
80
70
60
50
40
30
20
10
0
f1 (ppm)

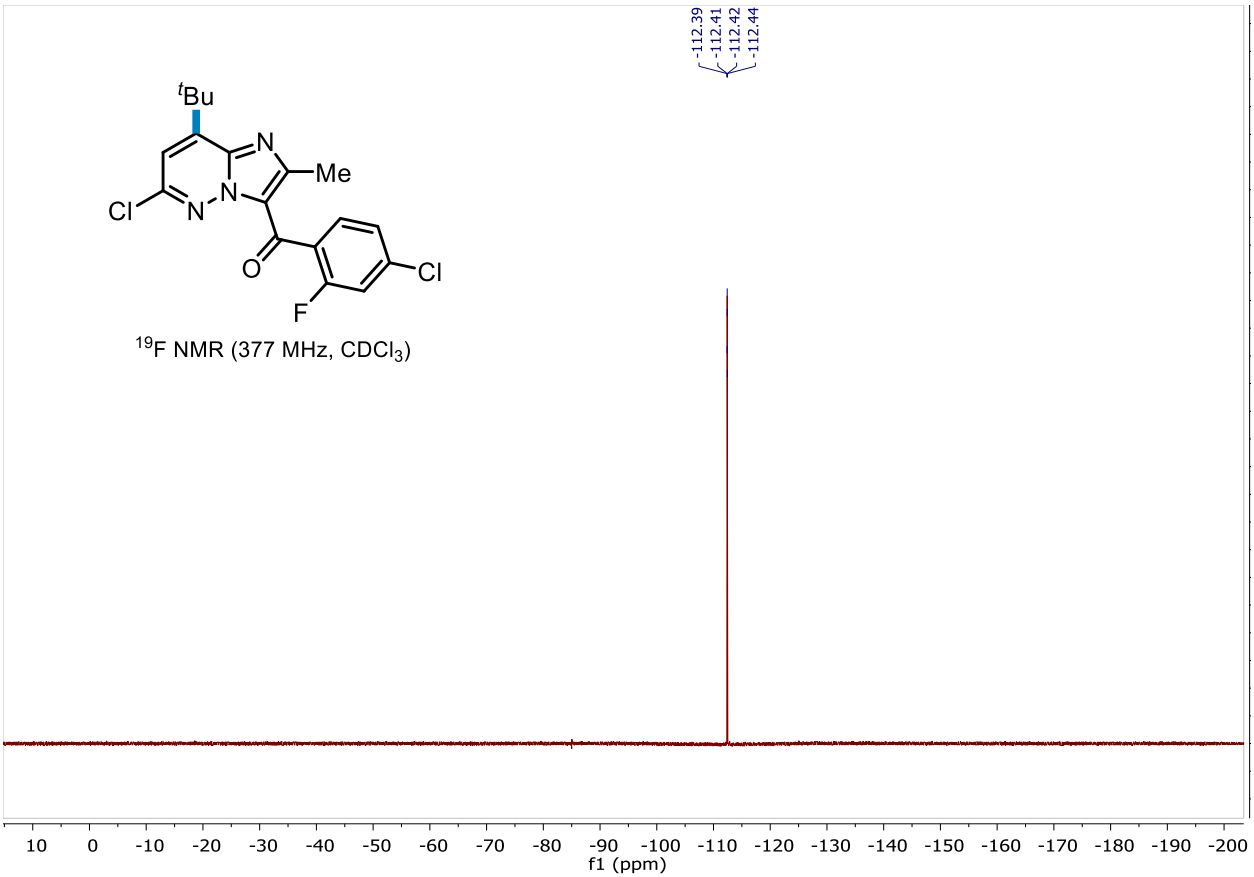
-112.39
-112.41
-112.42
-112.44
tBu
N
Me
Cl
N
N
O
Cl
F
19F NMR (377 MHz, CDCl3)
10 0 -10 -20 -30 -40 -50 -60 -70 -80 -90 -100 -110 -120 -130 -140 -150 -160 -170 -180 -190 -200
f1 (ppm)

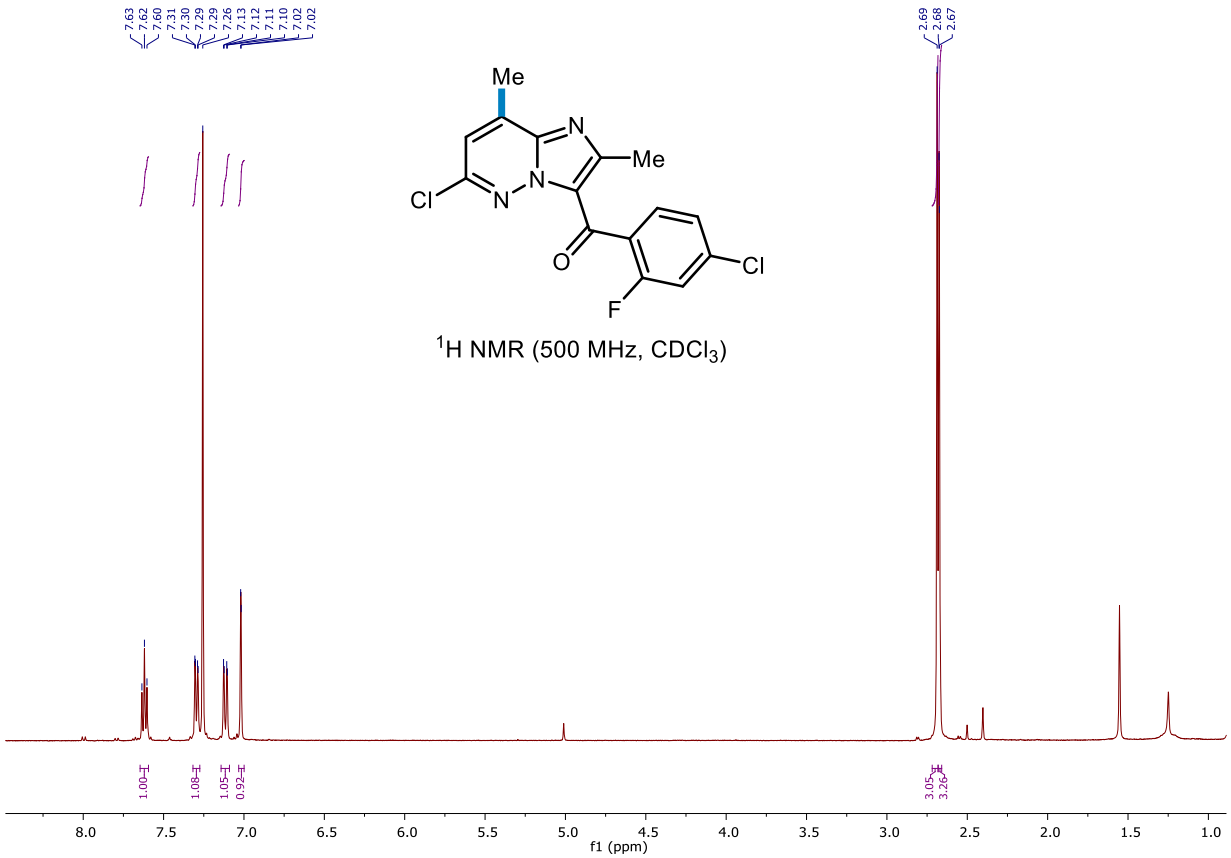

^{1}H NMR (500 MHz, $CDCl_3$)

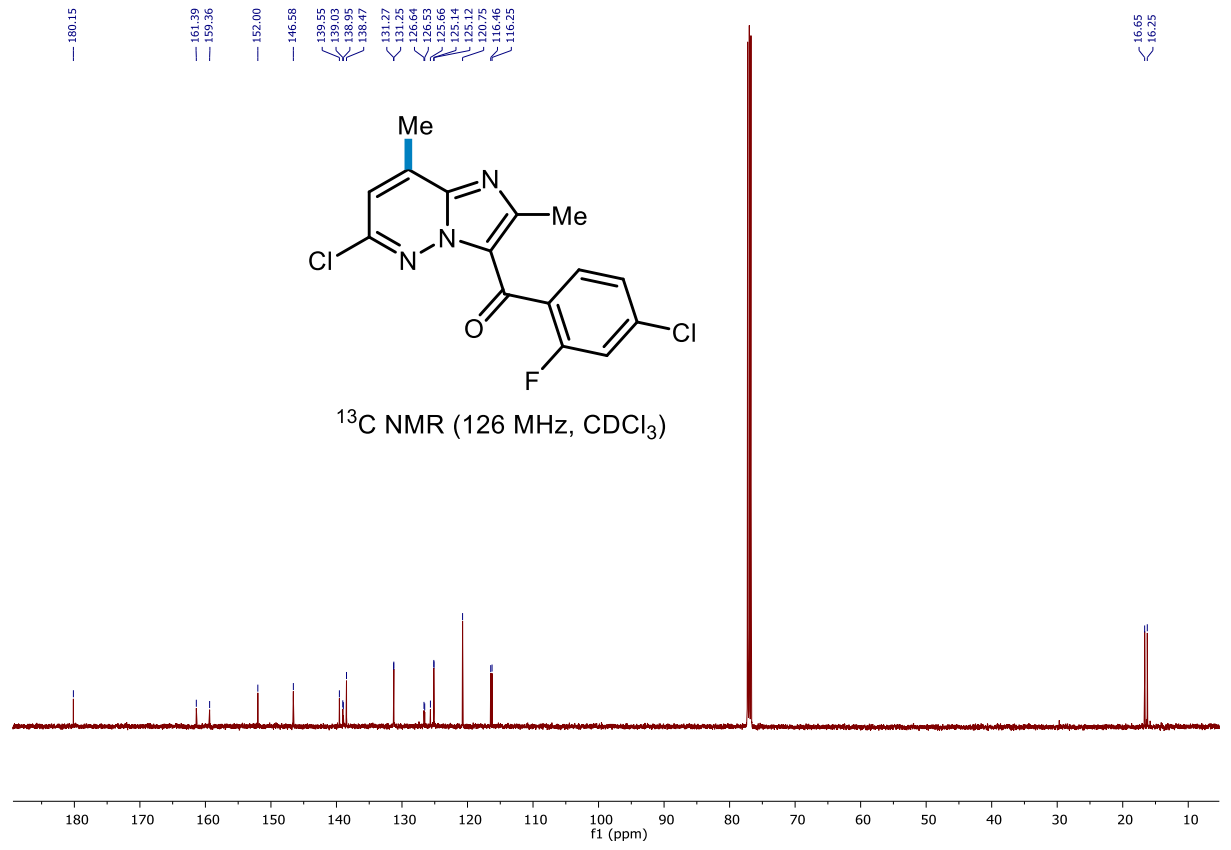

^{13}C NMR (126 MHz, $CDCl_3$)

^{19}F NMR (377 MHz, $CDCl_3$)

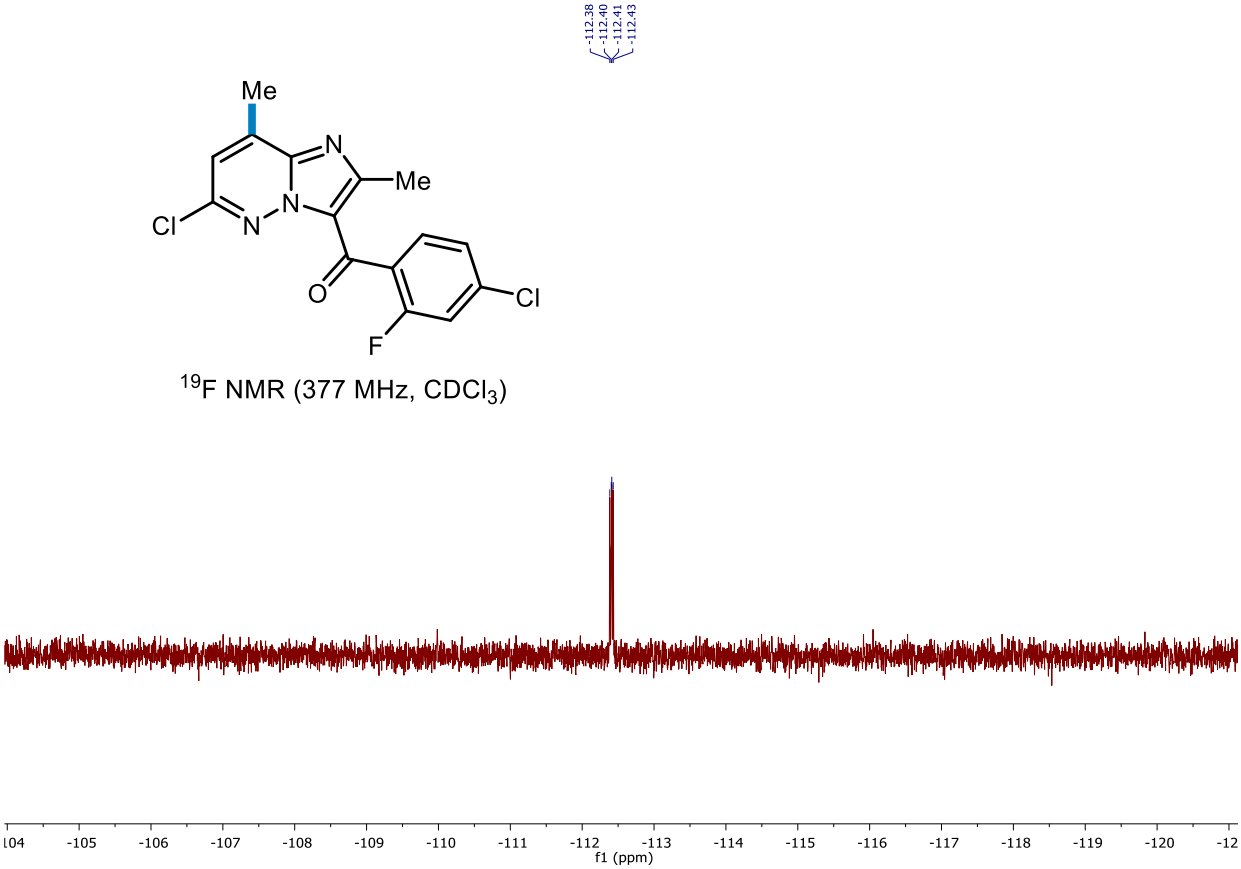

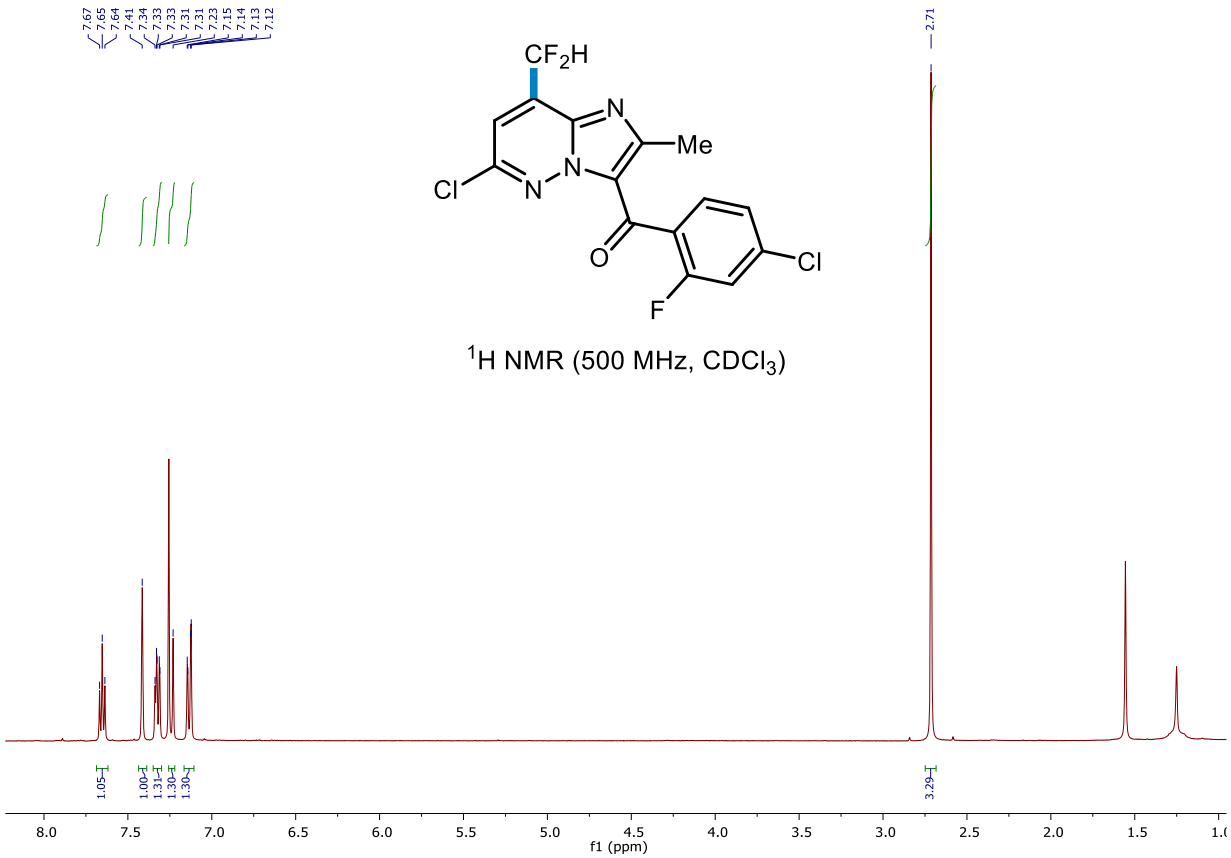

^{1}H NMR (500 MHz, $CDCl_3$)

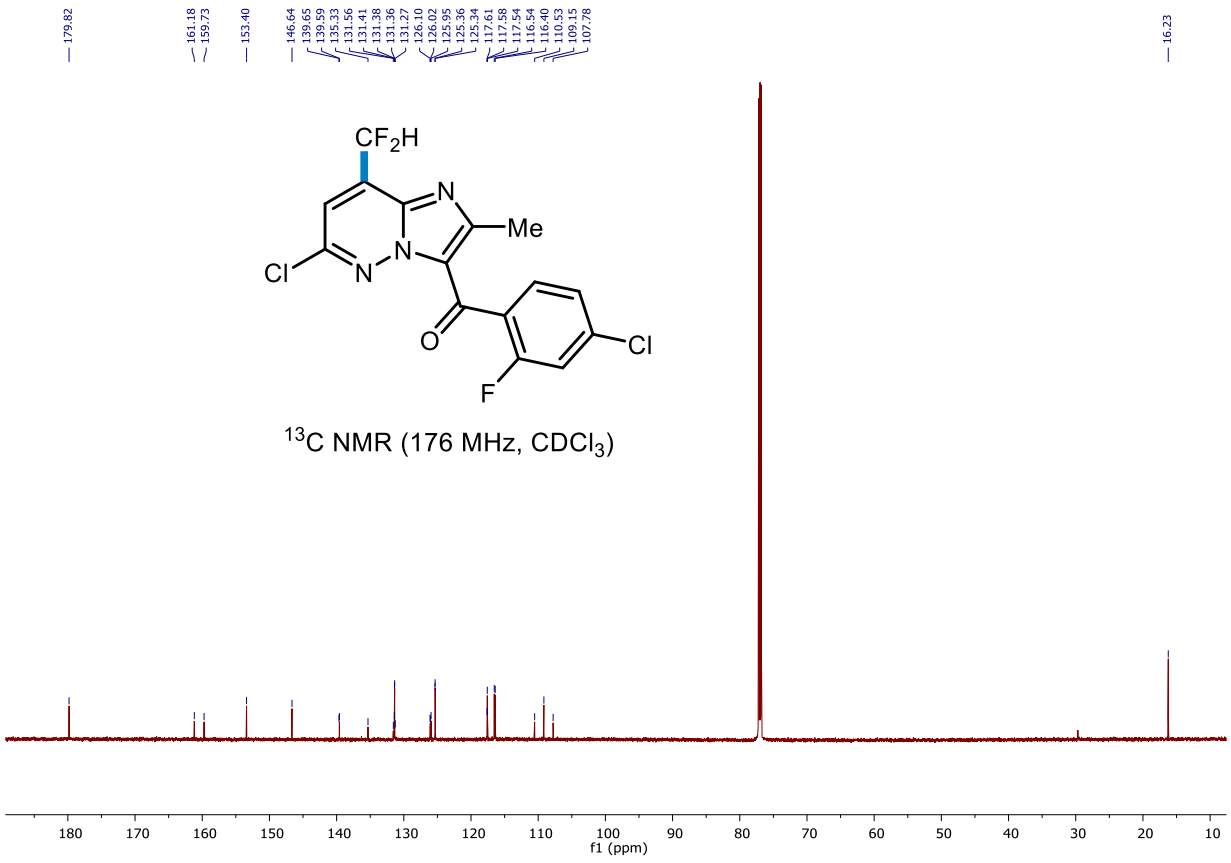

^{13}C NMR (176 MHz, $CDCl_3$)

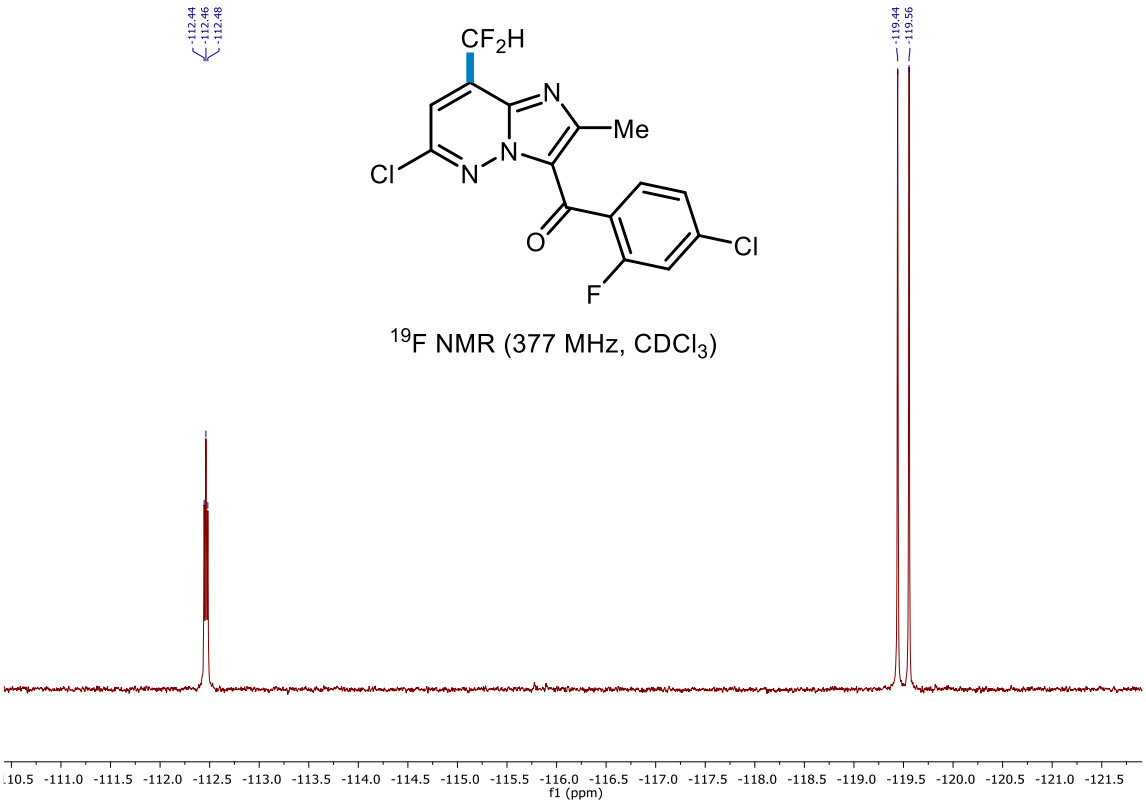

^{19}F NMR (377 MHz, $CDCl_3$)

Chapter 3: High-Throughput Optimization of Photoredox Catalysis Reactions Using Segmented Flow Nanoelectrospray Ionization-Mass Spectrometry

This work was performed with equal contribution from Daniel Steyer. Contributions of A. Sun include the development of an HTE photoreactor setup, preparation of reaction screens, as well as characterization and isolation of products. Contributions of D. Steyer to this work include the development and implementation of droplet generation methods, MS assays, and statistical analyses.

3.1 Introduction

3.1.1 High-Throughput Experimentation in Organic Synthesis

In the search for breakthrough medicines, materials, and agrichemicals, the accelerated preparation of complex small molecules in a miniaturized fashion can have a profound impact on reducing chemical footprint while expanding upon reaction space.[147 - 150] High-throughput experimentation (HTE) technology offers avenues for rapid data collection and process automation, and its implementation in organic synthesis has enabled the expedited discovery and optimization of various reaction manifolds. From a pharmaceutical standpoint, the rapid development and application of novel synthetic methodology plays a central role in accelerating access to highly functionalized drug leads.[151-155] Given the short supply of substrate libraries at the start of a drug discovery program, it is often necessary to decrease the scale of experimentation to access broader chemical space. The use of HTE techniques represents a streamlined approach for enabling the exploration of a myriad of catalysts and reaction conditions in a time and resource-efficient manner. Recent advances in miniaturized HTE have supported the diversification of expansive pharmaceutical libraries *via* palladium-catalyzed C–C, C–O, and C–N bond forming reactions at nanomole scale, using both continuous flow and plate-based approaches.[156] Most

notably, seminal work reported by Dreher, Cernak, and co-workers at Merck in 2015 provided an elegant solution to enable chemistry an nanomole scale using equipment and technology from biological assay screening.[7] Iterative screening in 1000 nL volumes allowed for the successful optimization of a Pd-catalyzed Buchwald-Hartwig cross coupling to yield an extensive library of drug compound fragements. Impressively, 1536 reactions were evaluated in 2.5 hours with little as 0.02 mg per reaction. These innovative HTE methods promise to empower chemists to run orders of magnitude more experiments while utilizing "big data" informatic approaches for reaction design and troubleshooting. Furthermore, platforms that integrate high throughput reaction optimization with subsequent biological evaluation provide additional opportunities for streamlining bioactive molecular discovery.[1,8]

3.1.2 Mass Spectrometry-Based Methods for High-Throughput Experimentation

The combined objectives of rapid reaction screening and product analysis are contingent upon integration of high throughput analytical instrumentation to provide near real-time data collection. Conventional screening methodologies rely on optical detection techniques to rapidly assess reaction progress. While these methods provide high throughput levels, reactions can be difficult to directly monitor if they lack a change in optical response upon product formation or there are high optical backgrounds associated with reaction matrices. This often necessitates the application of time intensive chemical separations, optical labelling of substrates, or the addition of a secondary reaction. Mass spectrometry (MS) detection has been demonstrated as an enabling technology in HTE, due to the high degree of chemical information and specificity imparted in these measurements.[7,9] The application of rapid liquid chromatography and solid phase extraction techniques have led to the MS-based analysis of reactions at upwards of 5 s/sample.[7,9,157] Alternatively, direct analysis of samples by MS has enabled even higher throughput levels.

Commercially available flow injection electrospray ionization (ESI)-MS systems provide a throughput as high as 2.5 s/sample.[11,158] Ionization methods based on plating samples, such as matrix-assisted laser desorption (MALDI) and desorption electrospray ionization (DESI) have both been utilized for the analysis of organic synthesis reactions at throughput levels exceeding 1 sample/s.[159-161] Acoustic mist systems can also be used for the generation of nL volume droplets, and they have found applications in pre-MS analysis sample transfer, as well as in the direct formation of gaseous ions for MS analysis at a rate of 3 samples/s.[162-165]

While the aforementioned approaches present impressive capabilities in MS-based HTE, interfacing MS with droplet microfluidics can unlock further avenues in HTE. Droplet microfluidics is a powerful approach for sample handling, as discrete fL-μL volume "droplet" samples can be isolated by an immiscible carrier phase and manipulated in a high throughput manner. Since multiple microsample units can be formed rapidly, parallel processing and analysis can be easily achieved, enabling the efficient acquisition of large data sets. As a result, droplet microfluidics has found utility across a variety of chemical and biological applications.[166-168] Pairing droplet microfluidics with MS, typically through ESI or MALDI, has produced powerful systems for HTE work.[169-175] NanoESI (nESI) is a nL/min flow variant on conventional ESI and presents significant advantages in sensitivity and matrix tolerance, compatibility with low volume samples, as well as observation of structurally unstable molecules through gentle ionization. Application of nESI-MS has led to the development of systems for monitoring the molecular content of pL-nL volume droplets with high analytical stability at throughputs as high as 10 droplets/s.[176-179]

3.1.3 Development of a Droplet Microfluidics/nESI-MS Platform for Screening Photochemical Reactions

As it stands, analytical platforms that combine droplet microfluidics and MS for organic synthesis applications have been very limited in scope.[29] The development of novel droplet microfluidic MS approaches and application to chemical transformations of rising interest is therefore necessary to drive further innovations in HTE. Over the past decade, photoredox catalysis has risen to the forefront of organic synthesis by enabling rapid access to nontraditional bond constructions and aiding in sustainability efforts through the use of visible light.[180-183] In particular, photoredox catalysis has gained meaningful traction in medicinal chemistry applications by providing versatile access to scaffolds and building blocks that previously required a significant number of operations.[184-186] Nonetheless, one key challenge faced in achieving widespread implementation of photoredox catalysis within medicinal chemistry stems from the scalability and generality of existing reactor platforms. In order to use these visible light-driven methods to their full potential, development of a user-friendly benchtop photoreactor featuring reaction screening and facile scale-up capabilities is needed. With the goal of facilitating the rapid exploration and optimization of photoredox reactions, we have implemented a combined droplet microfluidics/MS-based high throughput screening platform to expand upon the robust capabilities and impact of photoredox catalysis in drug discovery and development. By interfacing droplet microfluidics with nanoESI-MS, we report the design of a system that allows for the rapid manipulation of nanoliter volume samples to enable the efficient screening of pharmaceutical libraries for visible light-mediated late-stage C–H functionalization reactions (**Figure 3.1**).

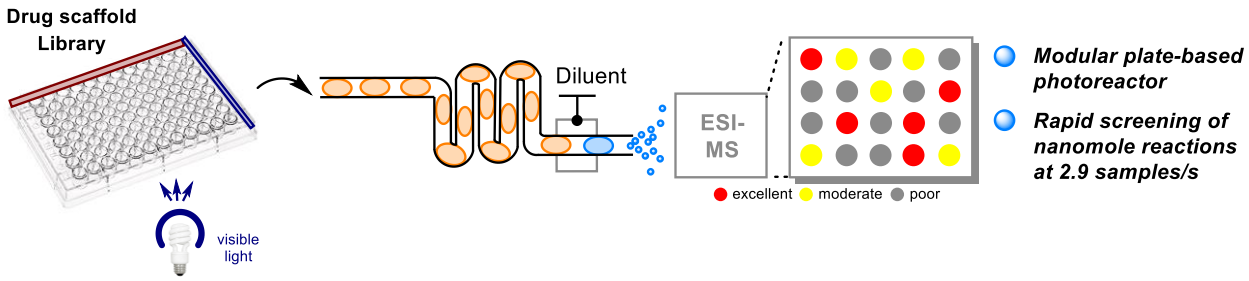

Figure 3.1. Development of a droplet microfluidics nESI-MS screening platform

Screening of photoredox catalysis fluoroalkylation reactions was performed with the concerted objectives of enabling reaction discovery and high throughput optimization of 'hit' reaction conditions. ESI-MS analysis throughput as high as 3 samples/s and methods for accounting for ionization in variable sample matrices were demonstrated, providing a robust system for the high-throughput MS analysis of photoredox droplet reaction samples. Successful translation of nanomole-scale conditions to millimole-scale reactions was further demonstrated, highlighting the ability to concertedly perform rapid reaction discovery as well as subsequent scale-up.

With the goal of enabling high throughput photochemical reaction discovery and optimization for the synthesis of novel therapeutics, we aimed to leverage droplet microfluidics in the development of a nESI-MS-based screening platform. To achieve this objective, our preliminary studies have centered on the design of a system that allows for the rapid manipulation of nanoliter volume samples to enable the efficient screening of pharmaceutical libraries for visible light-mediated late-stage C–H functionalization reactions. Upon establishing a segmented flow nESI-MS method to screen photochemical reactions in multiwell plates, we have also demonstrated the rapid screening of reaction parameters for the radical perfluoroalkylation of pharmaceutical compound libraries. Through a collaboration with Pfizer, we have gained access to an extensive library of complex drug scaffolds to validate the application and immediate benefit of our technology towards accelerating drug discovery. Specifically, we intend to utilize the wealth of

HTE data collected by our system to facilitate downstream structure-activity relationship (SAR) studies and biological assays in a medicinal chemistry setting. Translation of nanomole-scale conditions to millimole-scale reactions have also been investigated, in order to highlight the ability to concertedly perform rapid reaction discovery as well as subsequent scale-up. Ultimately, our objective is to develop a fully continuous platform that enables the integration of automated droplet generation from a standard multiwell plate with in-line nESI-MS analysis of droplet reaction samples.

3.2 Results and Discussion

3.2.1 Multiwell Plate Photoreactor and Droplet nESI-MS Platform Development

Our studies into leveraging droplet microfluidics technology for reaction discovery have been centered on the development of a nESI-MS platform, which can be utilized for characterizing visible light-driven late-stage functionalization reactions. We chose to employ a radical perfluoroalkylation strategy developed by the Stephenson group[187-190] as a model reactive system for the diversification of pharmaceutical compound libraries. As such, we have developed a droplet microfluidics-based HTE platform that interfaces nESI-MS analysis with a custom plate-based photoreactor to accommodate the rapid screening of complex drug molecule libraries. We envisioned that this setup would be amenable to applications including the late-stage functionalization of drug scaffolds and rapid optimization of substrate-specific reaction conditions.

Notably, our system includes an upstream setup for the high-throughput handling of pharmaceutical libraries and reagent stock solutions in 96, 384, or 1536 multiwell plates. With the objective of maximizing photon flux while enhancing reproducibility, we aimed to design a modular bench-top photoreactor for the irradiation of multiwell plate reactions using high-powered

Cree Royal Blue XTE LEDs (2 W per LED). We constructed a 25 LED array (approx. 50 W total output) to accommodate the dimensions of a standard 96, 384, or 1536 well plate (**Figure 3.2A**).

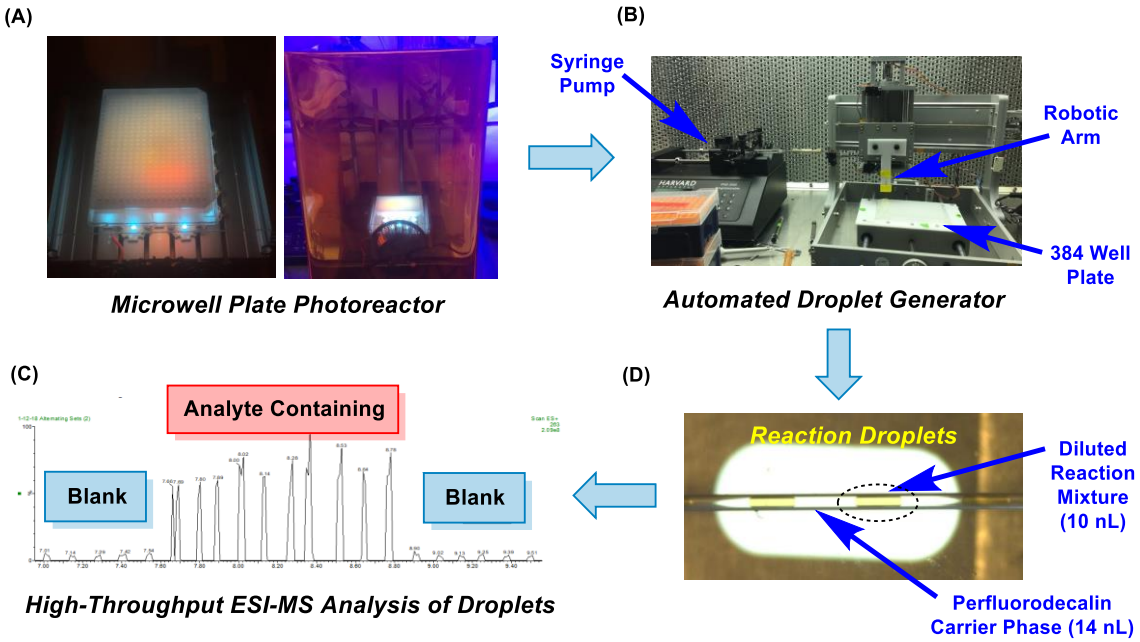

Figure 3.2. Optimized workflow for droplet nESI-MS analysis

The LEDs were mounted onto a heat sink, with two fans placed below and adjacent to the heat sink, in order to provide sufficient cooling to maintain reactions at ambient temperatures. An acrylic shield positioned 5 cm above the LED array provided a mounting stage for the well plate, as well as an additional layer of protection for the LEDs. A custom-built plastic amber light shield was placed around the setup for user eye protection. Following irradiation and subsequent dilution, our platform enables the automated generation of nanoliter-volume reaction droplets. Furthermore, downstream nESI-MS analysis of individual droplets provides real time data analysis on product formation and reaction kinetics.

The optimized workflow (**Figure 3.2**) for droplet generation involved loading a pre-mixed stock solution onto a microwell plate, followed by blue light irradiation. A small fraction of each reaction was then withdrawn and diluted. The dilution served to both quench the reaction and

facilitate MS analysis, as the analysis of high concentration (> 1 mM) analytes can lead to saturation of MS signal and contamination of the MS source. 8 µL of each diluted reaction mixture was deposited into a separate well plate and covered with perfluorodecalin (PFD) for subsequent droplet formation in perfluoroalkoxy (PFA) tubing (150 x 360 µm internal diameter x outer diameter). Droplet samples (5-10 nL) were generated from microwell plates using equipment and methods previously reported by the Kennedy group.[25,26]

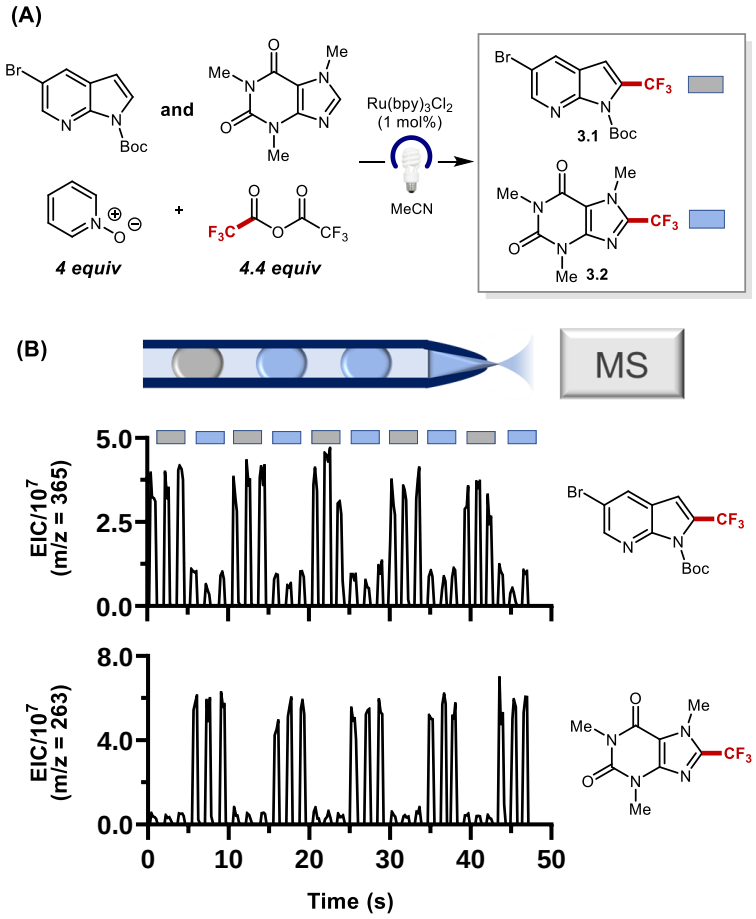

Figure 3.3. Validation of droplet microfluidics nESI-MS method. (A) Photoredox trifluoromethylation of caffeine and 5-Br-7-(*N*-Boc)azaindole substrates (B) Droplet nESI-MS analysis of photoredox trifluoromethylation reactions. Droplet trains of repeating 3x3 format were flowed at to nESI-MS analysis at a rate of 0.67 droplets/s. The two traces represent the extracted m/z for **3.1** (m/z=367, top) and **3.2** (m/z=263, bottom) products. Bars above traces represent droplets formed from **3.1** (blue) and **3.2** (grey) reactions.

To demonstrate the general capabilities of our system, samples were prepared from the photoredox trifluoromethylation of *N*-Boc-5-bromo-7-azaindole and caffeine substrates (**Figure 3.3**). Sample droplets (8 nL) were formed in a repeating 3x3 fashion. Droplet analysis was performed at a rate of 0.67 droplets/s, allowing for triplicate analysis to be performed in under 5 s. Analysis throughput was limited only by the rate at which our mass spectrometer could scan the desired region, which required 170 ms to scan the range of 75-750 m/z. By extracting out the m/z values associated with expected products (m/z for **3.1**, m/z 263 for **3.2**), we were able to successfully monitor product formation for both reactions. As shown in **Figure 3.3**, two separate droplet populations can be observed in the anticipated 3x3 fashion. Droplets that show high response for product formation in one trace show low response in the other, yielding an offset product signal pattern across the two traces. These results not only validate the capability of our system to detect product formation, but also demonstrate the ability to perform rapid analysis while maintaining the identity of the individual samples, with minimal material carryover between droplets. In this manner, we were able to establish proof-of-concept for the rapid analysis of photoredox reaction droplets to yield hit/no-hit responses by means of nESI-MS detection.

3.2.2 Accelerated Late-Stage Functionalization of Drug Compound Libraries

With the developed system, we aimed to achieve two goals: (1) accomplish late-stage functionalization using diverse radical coupling partners and (2) perform the high throughput optimization of reaction conditions for individual drug scaffolds. To achieve our first objective of performing the late-stage functionalization of complex drug molecules, we carried out the fluoroalkylation (CF_3, CF_2H, CF_2Cl) of 17 drug and drug-like compounds provided to us through Pfizer's Sigma Aldrich compound library (**Figure 3.4**). Reactions were irradiated with blue light for 1 hour in a 384 polypropylene well plate prior to dilution and subsequent droplet generation

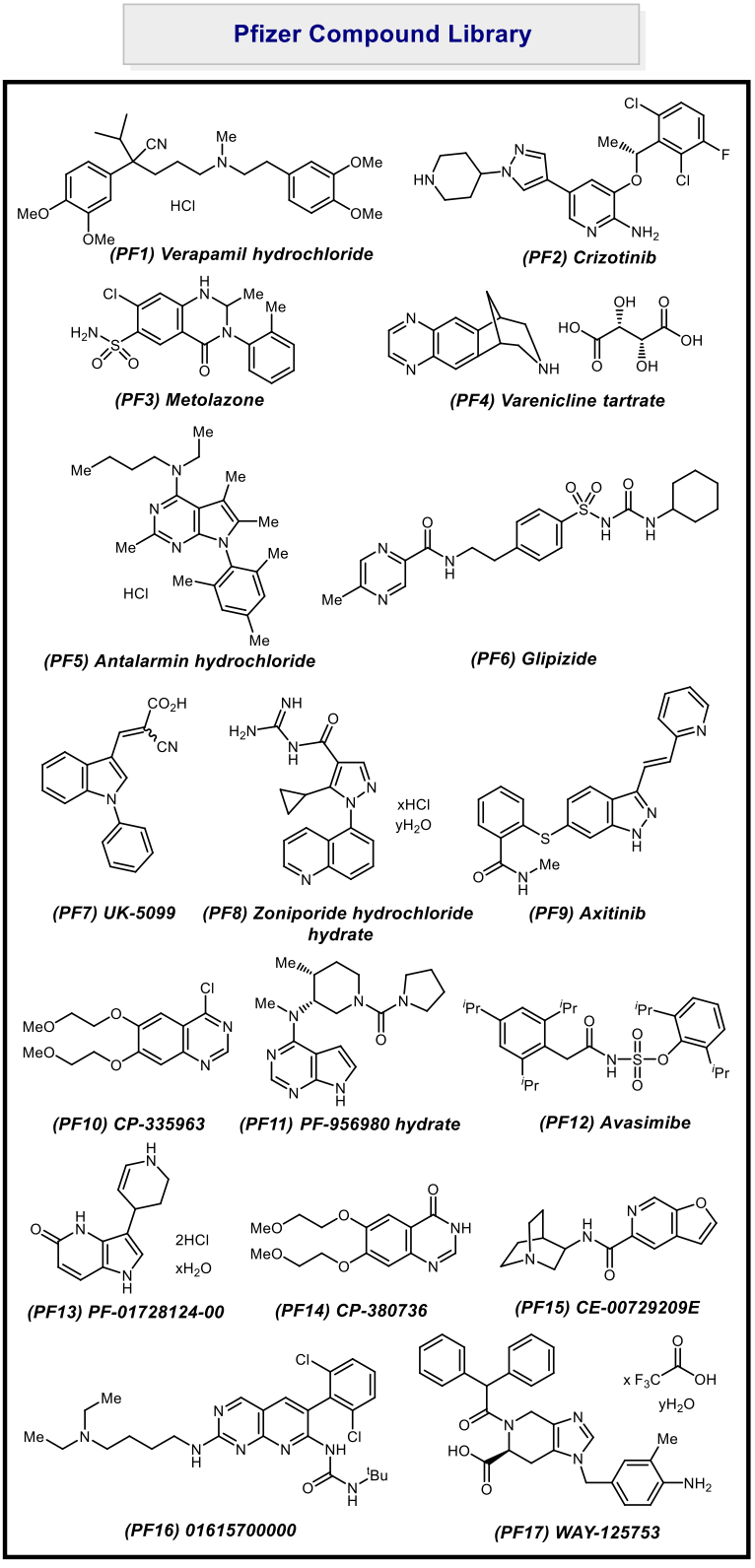

Figure 3.4. Library of Pfizer compounds investigated in screen

for nESI-MS analysis. In order to enhance substrate solubility and maintain homogeneity of reactions, substrate stock solutions were prepared using a 10% DMF/MeCN solvent system. Excess amounts of trifluoroacetic anhydride (16 equiv) were added to accommodate acylation by nucleophilic functionalities (e.g. free amines and alcohols) on substrates within our targeted library.

Upon generating reaction droplets in triplicate to ensure reproducibility, nESI-MS analysis was performed at a throughput of under 5s/sample. As a control experiment, "control background" samples containing no added substrate were run for each type of fluoroalkylation reaction. This enabled us to differentiate between MS signals that derived from the reaction of interest and signals that were simply artifacts of our sample matrices. Shown in **Figure 3.5A** is the extracted mass trace (523 m/z) for the trifluoromethylated product of compound PF1, Verapamil HCl. Upon analysis of the droplets containing compound PF1, a significant spike in signal is observed in comparison to the control background samples, suggesting successful product formation. This same approach was applied to each of the tested substrates in our library.

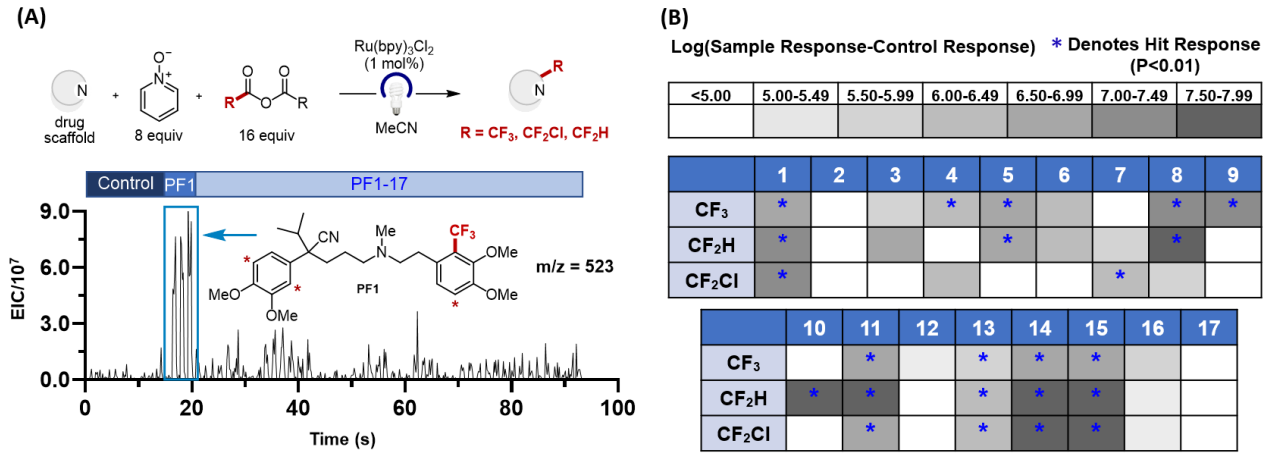

Figure 3.5. Screen for late-stage fluoroalkylation of pharmaceutical compounds by droplet nESI-MS. (A) General scheme for fluoroalkylation of 17-compound library. (B) Mass trace for predicted verapamil HCl (compound 1) product. Displayed is the m/z = 523, which is the predicted MH^+ ion of mono-trifluoromethylated verapamil HCl. (C) Coloration on heat map describes increased response for desired product MH^+ ion over control, while blue asterisks denote statistical significance in response increase.

We were able to identify several "hit" reactions for each perfluoroalkylation condition (indicated by blue asterisks), in which desired product m/z signals were observed. Product m/z signals were further confirmed using isotopic modeling and tandem MS analysis. In order to qualitatively assign "hit"/"no hit" responses to each reaction, we conducted statistical analyses to assess the statistical relevance of our product m/z signals over background noise. A two-sample t-test was performed, in which each reaction of interest was compared against the control background samples to confirm the presence of newly generated product m/z signals (**Figure 3.5B**). Reactions were deemed a hit if they achieved a $P<0.01$. Across 5 distinct substrates that yielded "hit" responses, significant product m/z signal increases were observed for all three fluoroalkylation conditions, demonstrating the capability of our method to successfully detect product formation across a diversity of complex small molecules. MS counts were also utilized to show the strength of "hit" responses. A $\log_{10}$(product response-control response) test was used to gauge the magnitude of the signal increase and in turn, highlight promising reaction conditions.

Three "hit" reactions were scaled up on 0.1 mmol scale for subsequent purification and product isolation to further validate our nESI-MS results. Successful isolation of monotrifluoromethylated (40% yield) and bis-trifluoromethylated (45% yield) varenicline tartrate was achieved, validating our corresponding nESI-MS screen data. Isolation of trifluoromethylated Verapamil HCl and PF15 products was attempted to elucidate regioisomer formation; however, desired products could not be successfully isolated as a result of low yields and product decomposition upon column chromatography. The HTE data obtained from our screen provided insight into several reactivity trends that arose from varying substrates and perfluoroalkyl radical reagents. Our screen revealed "hit" responses across 11 substrates (65% of 17 compound library), as well as successful product formation across all three perfluoroalkylation conditions for 5 substrates (compounds PF 1, 11, 13,

14, and 15). Among our "hit" compounds, a variety of heteroarene scaffolds, including quinoxalines, furo[2,3]pyridines, quinazolinones, pyrrolopyrimidines, and pyrrolopyridinones could be accessed. We were gratified to see that several of these "hit" response scaffolds expanded upon the scope of structures formerly reported by the Stephenson group. These results highlight the successful application of this methodology for substrates of increased complexity and diverse functionality. Upon isolation of trifluoromethylated and difluoromethylated varenicline tartrate products, we were intrigued to find that the regiochemical outcome varied across these two conditions, most likely due to differences in substrate and radical electronics. While trifluoromethylation occurred exclusively at the electron-rich 6-position of the quinoxaline scaffold, the more nucleophilic difluoromethyl radical gave rise to functionalization at the electron-deficient 2-position. These results suggest a preference for the formation of electronically matched radical functionalization products. Among substrates that did not yield any product formation (PF 2, 3, 6, 12, 16, 17), we noted that the presence of electron rich alkyl amine motifs (PF 2, 12, 16) could be problematic, as these functionalities can be prone to single electron oxidation and subsequent decomposition. Additionally, the presence of sterically hindered aromatic groups (PF 12) could further hinder radical functionalization.

3.2.3 High-Throughput Reaction Optimization

In addition to enabling the accelerated late-stage functionalization of diverse pharmaceuticals, our droplet microfluidics platform can also be utilized for the high throughput optimization of photoredox reaction conditions. To demonstrate this feature, we set out to optimize reaction parameters for three of our "hit" compounds and one "potential hit" compound from our original compound library screen. Reaction variables including photocatalyst (8 photocatalysts screened) and pyridine *N*-oxide reagent (3 *N*-oxides screened) were evaluated across the four selected

substrates, yielding a total of 96 individual reactions (**Figure 3.6**). Upon irradiating reaction mixtures (60 nanomole scale) with blue light for 1 hour and performing subsequent droplet generation and MS analysis, we were able to identify distinct optimal conditions for each drug molecule. Most importantly, the high throughput capabilities of our system were effectively captured by the expedient generation and ESI-MS analysis of 228 droplet reactions within 20 minutes. Our results suggest that subtle changes in photocatalyst and *N*-oxide identity give rise to significant variations in product conversion, as exemplified by a 60% increase in MS product signal intensity upon substituting the $Ru(bpy)_3Cl_2$ photocatalyst for $Ir(ppy)_2(dtbbpy)PF_6$ in the trifluoromethylation of Verapamil HCl (**Figure 3.7**).

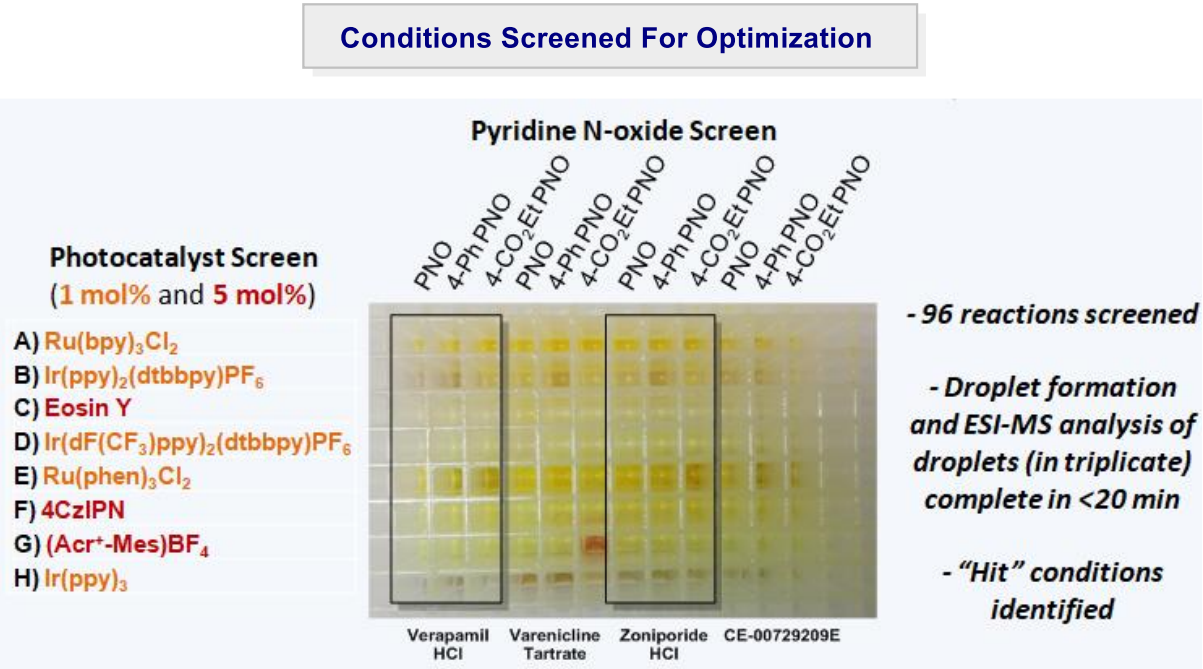

Figure 3.6. Parameters screened for optimization of photoredox trifluoromethylation reaction

With the broader aim of obtaining quantitative insight into product conversion and reaction kinetics, as well as expanding upon screen parameters to include various solvent systems, we have developed both quantitative and semi-quantitative ESI-MS methods for measuring product formation. To expand upon our platform's high-throughput reaction optimization capabilities, we

aimed to test a broad set of parameters for the radical trifluoromethylation of caffeine, including solvents, photocatalysts, and heterocyclic *N*-oxide reagents. Specifically, we set out to establish a robust analytical method to enable quantitative measurement of product conversion while accommodating sample-to-sample variability in product response due to matrix effects. Our efforts focused on minimizing background signals and accounting for variations in ionization efficiency.

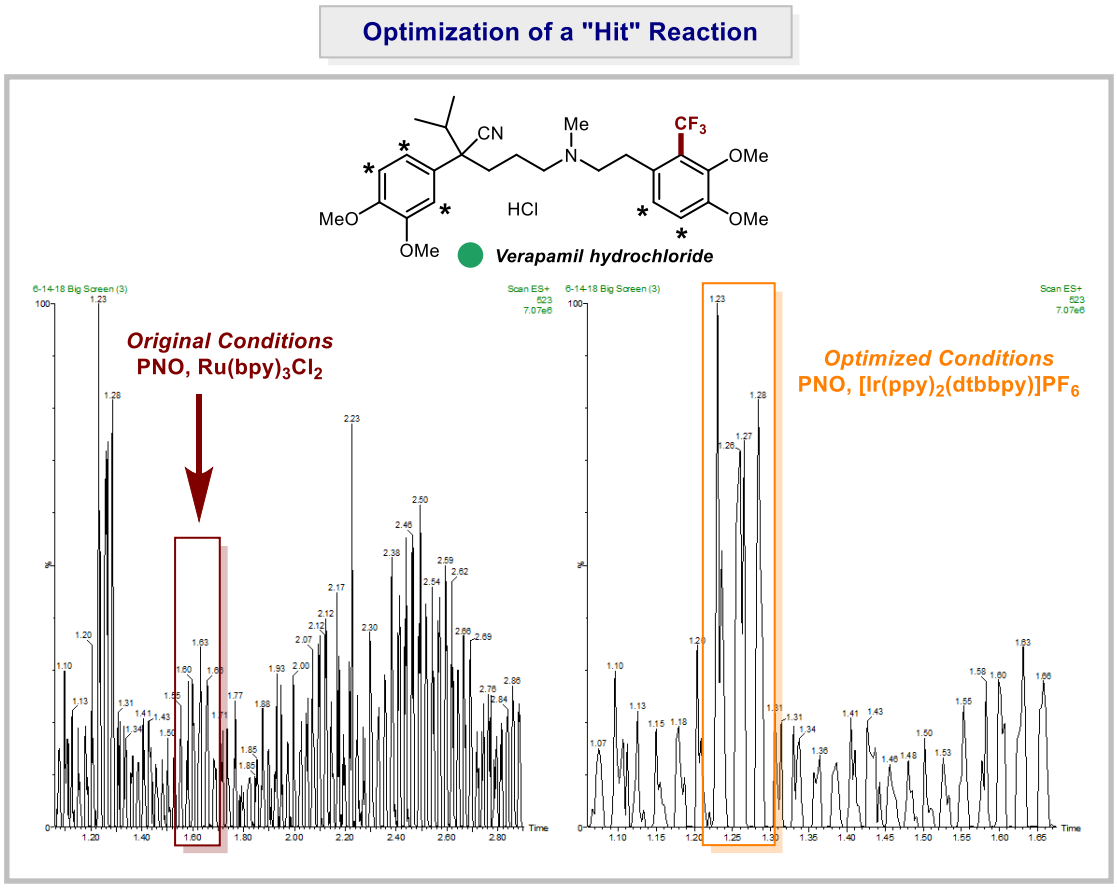

Figure 3.7. Optimization of Verapamil HCl trifluoromethylation reaction

To lower background signals, MS-MS analysis was performed to target a specific fragmentation pattern arising from the trifluoromethylated caffeine analyte (m/z = 263→206). Development of an MS-MS assay can help to reduce, and possibly remove, background noise by increasing assay specificity towards the product of interest. In order to accommodate different solvent systems, we also needed to address challenges associated with ion suppression, as changes

(e.g. solvent environment) in the sample matrix can drastically affect analyte ionization and observed MS response. While this effect is typically resolved through sample cleanup methods (e.g. liquid chromatography and chemical extractions), we aimed to implement a methodology that would allow for the direct analysis of droplet samples to maximize throughput.

By using the radical trifluoromethylation of caffeine as our model reaction system, we have demonstrated successful screening of co-solvent systems including 10% co-solvent/MeCN (co-solvents: DMF, DMA, CH_2Cl_2, $MeNO_2$, DMSO). In the presence of these co-solvents, analyte response was found to observe nearly a 4-fold drop, despite constant analyte concentrations, which would have major ramifications in a condition screen.

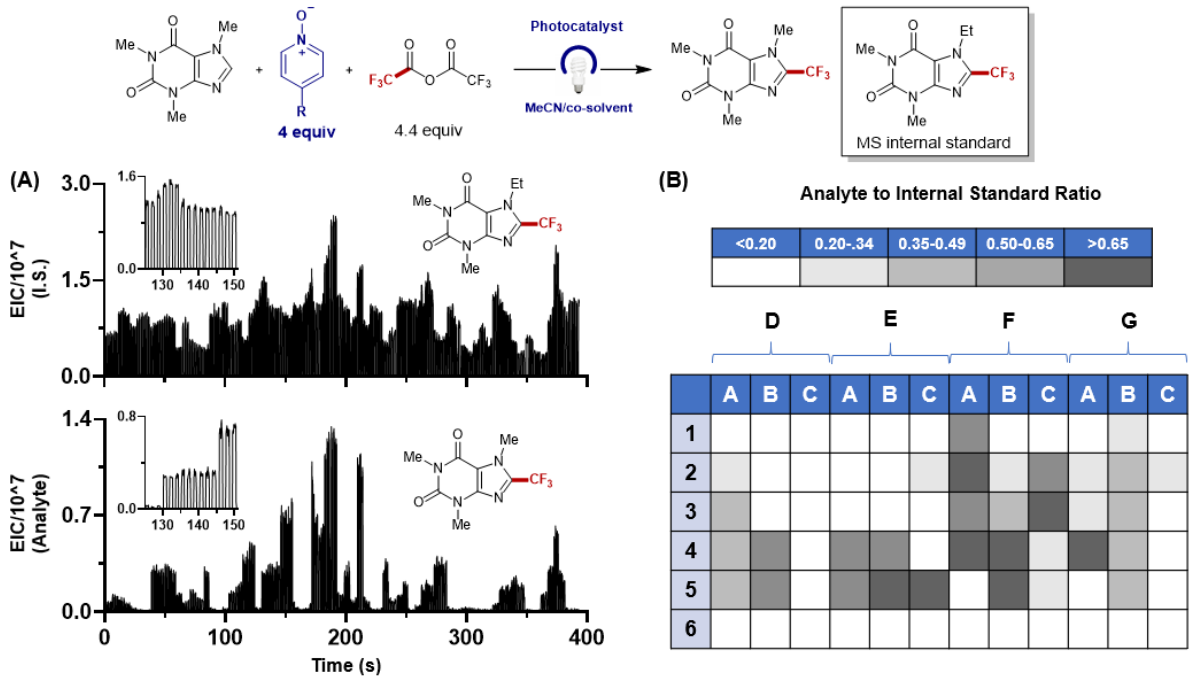

Figure 3.8. Condition screen for photoredox caffeine trifluoromethylation reaction. (A) Internal standard trace (m/z = 277→192, top) and product MS-MS trace (m/z = 263→206, bottom) across 72-reaction screen. Insets are enlarged regions for 125-150s (left) and molecular structures (right). (B) Heat map results based on the analyte to internal standard ratios. Each cell represents the average of 3 droplets. Darker shading represents a higher observed ratio, indicating greater observed product turnover.

To overcome matrix effects, we explored three methods: the use of standard addition, internal standard, and higher dilution factor. Moving forward, we chose to use ethyltheophylline as an

internal standard, as it provided excellent results with regards to signal normalization and minimizing variability in measurement.

Additionally, the generation of an ESI-MS calibration curve enabled us to extract quantitative yield data from our reaction optimization screens, in order to benchmark and compare results obtained from different conditions. A 72-reaction screen was then performed to optimize the caffeine trifluoromethylation reaction by screening parameters including photocatalyst, *N*-oxide reagent, and co-solvent (**Figure 3.8**). The triplicate analysis of all 72 reactions was performed in 380 s (1.7 s/droplet). Successful product formation was observed over a wide range of conditions. Solvent choice was found to have the largest influence on product formation. The use of 10% DMSO (6) yielded very poor turnover, while 10% DMF and DMA (4 and 5 respectively) gave the highest turnover across multiple conditions. These results highlight the importance of addressing matrix effects. DMF and DMA were both observed to suppress product signal, and as such, would not likely have been viable co-solvents prior to adjusting for variable ionization efficiencies.

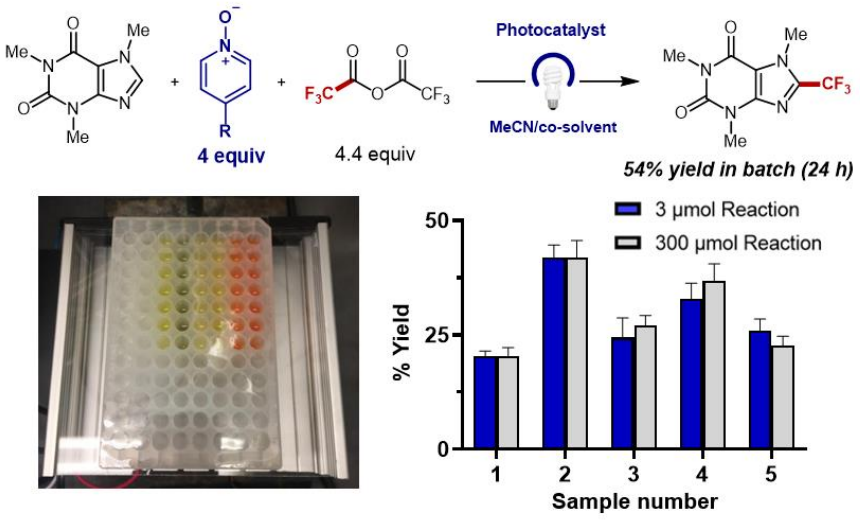

Figure 3.9. Demonstration of reliability in scaling up reactions. Droplet nESI-MS comparison (n=10 droplets) of samples run at screen scale (3 µmol) and 100x scale (300 µmol) showed similar response for all 5 different reaction conditions. Normalization of results was performed within each pairing. The top 5 reaction conditions are listed in order as conditions 1-5.

Five of our top performing reactions were selected for subsequent scale-up on 300 umol scale and irradiated in a 96 well plate (**Figure 3.9**). Gratifyingly, ESI-MS results suggested that the yields obtained from the scale-up reaction show strong correlation with that of our small-scale screens, which further validates the scalability of our screening method and the opportunity to quantitatively benchmark reaction performance in a high-throughput manner.

3.2.4 Increasing Analysis Throughput and Analysis of Reaction Droplets

With the aim of enhancing the throughput of our nESI-MS screening platform beyond a duty cycle of 40 ms, we focused on the optimization of two system components: the internal diameter (i.d.) of the fused silica nESI emitter and the size of the droplets (**Figure 3.10**). Our original caffeine trifluoromethylation nESI-MS analysis conditions involved the use of a 75 µm i.d. emitter

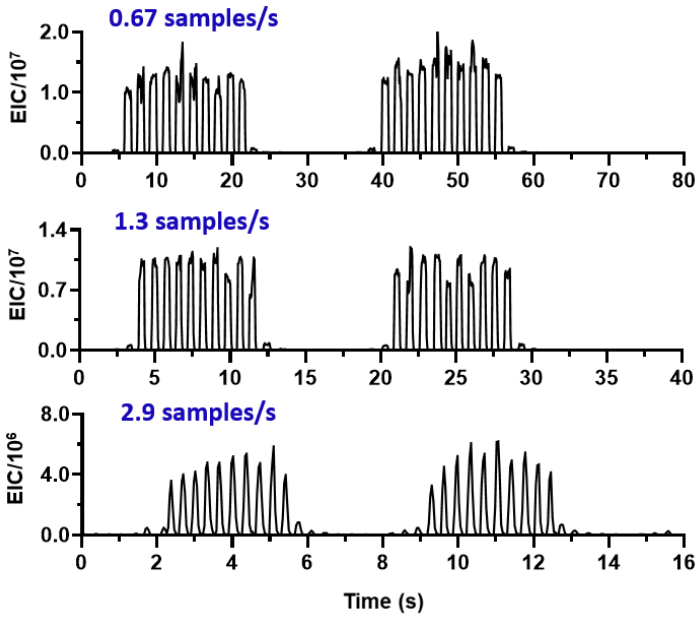

Figure 3.10. Efforts toward increasing analytical throughput. Traces are for the MS-MS detection of trifluormethylated caffeine (m/z = 263→191). Samples were formatted into repeat 10x10 units of samples (50 µm product) and blanks (Top) The use of 75 µm i.d. capillary emitter, 8 nL droplets, and 12 nL PFD spacing was capable of stable analysis at 800 nL/min flow and 0.67 droplet/s throughput (Middle). The use of 100 µm i.d. capillary emitter, 8 nL droplets, and 12 nL PFD spacing was capable of stable analysis at 1500 nL/min flow and 1.3 droplet/s throughput (Bottom). The use of 100 µm i.d. capillary emitter, 4 nL droplets, and 3 nL PFD spacing was capable of stable analysis at 1500 nL/min flow and 2.9 droplet/s throughput.

capillary to form 8 nL droplets with 12 nL PFD segmentation, flowed at 800 nL/min to give a throughput of 0.67 droplets/s. While increasing analysis flow rate caused breakage of droplets inside of the emitter, we discovered that increasing the capillary i.d. to 100 μm allowed for stable flow of droplets at higher flow rates. Stable droplet transfer through the capillary at 1500 nL/min flow was now possible, yielding an analysis throughput of 1.3 droplets/s. To further increase throughput, the volumes of the droplets and PFD spacing were decreased to 3 nL and 4 nL, respectively. By combining reduced sample volumes with higher flow rates, analysis throughput was successfully increased to 2.9 droplets/s.

3.3 Conclusion

In summary, an HTE platform for the screening of visible light-driven reactions was developed and successfully applied to photoredox catalysis reactions. Simultaneous irradiation of samples in micro well plates, followed by translation into segmented droplets post-reaction facilitated rapid reaction screening and delivery to downstream analysis. The use of nESI-MS provided detection of a diverse population of reaction products with minimal assay development, as well as highly gentle ionization for the observation of labile species. The implementation of methods to address variable ionization efficiency in droplet nESI-MS analysis enabled the screening across a variety of photoredox reaction conditions. The systems and methodologies presented show great promise for future work in visible light-driven reaction design and rapid diversification of pharmaceutical libraries to provide enhanced material and time efficiency in drug discovery.

3.4 Experimental Methods

3.4.1 General Information

Chemical Reagents and Analytical Instrumentation

All chemicals were used as received. Perfluorodecalin (PFD) was purchased from Oakwood Products (Estill, SC). All other reagents were purchased from Fisher Scientific or Millipore Sigma. Compounds PF1-17 were generously provided by Pfizer. Reactions were monitored by TLC and visualized with a dual short wave/long wave UV lamp. Column flash chromatography was performed using 230-400 mesh silica gel or via automated column chromatography. NMR spectra were recorded on Varian MR400, Varian Inova 500, Varian Vnmrs 500, or Varian Vnmrs 700 spectrometers. Chemical shifts for ^{1}HNMR were reported as δ, parts per million, relative to the signal of CHCl3 at 7.27 ppm. Chemical shifts for ^{13}CNMR were reported as δ, parts per million, relative to the center line signal of the CDCl3 triplet at 77.16 ppm. Chemical shifts for ^{19}FNMR were reported as δ, parts per million, relative to the signal of a trifluorotoluene internal standard at –63.72 ppm. The abbreviations s, br. s, d, dd, br. d, ddd, t, q, br. q, qi, m, and br. m stand for the resonance multiplicity singlet, broad singlet, doublet, doublet of doublets, broad doublet, doublet of doublet of doublets, triplet, quartet, broad quartet, quintet, multiplet and broad multiplet, respectively. IR spectra were recorded on a Perkin-Elmer Spectrum BX FT-IR spectrometer fitted with an ATR accessory. Mass Spectra were recorded at the Mass Spectrometry Facility at the Department of Chemistry of the University of Michigan in Ann Arbor, MI on an Agilent Q-TOF HPCL-MS with ESI high resolution mass spectrometer. LED lights and the requisite heat sink, fan, and power supplies were purchased from LED Supply (https://ledsupply.com) with the following item codes: CREEXTE-ROY-X (XLamp XT-E Royal Blue LEDs), MAKERSLED (MakersLED Heat Sink), PDA060B-XXXB (60W Phihong IP67 Constant Current AC Drivers).

A Westpointe Electrical Co Wp 4'' Hi Velocity Fan 1002 Personal Fan was purchased from http://amazon.com.

Irradiation Chamber Setup

A 25 LED array of Cree Royal Blue XTE LEDs (2 W per LED, 50 W total output) was assembled to accommodate the dimensions of a standard 96, 384, or 1536 microwell plates (**Figure 3.11**). The LEDs were mounted onto a heat sink, with two fans placed below and adjacent to the heat sink, in order to provide sufficient cooling to maintain reactions at ambient temperatures. An acrylic shield positioned 5 cm above the LED array provided a mounting stage for the well plate, as well as an additional layer of protection for the LEDs. A custom-built plastic amber light shield was placed around the setup for user eye protection.

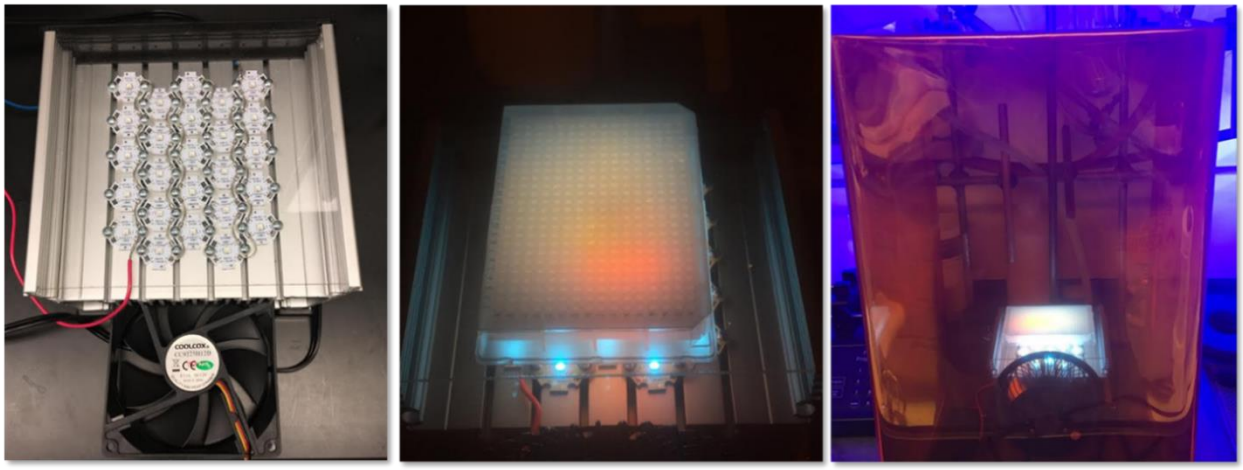

Figure 3.11. (Left) Setup for irradiation of multiwell plate with blue LED lights (Middle) Close-up view of irradiation device in operation (Right) Entire setup for irradiation of multiwell plates.

Reagent Preparation for Fluoroalkylation Reactions

1 mol% photocatalyst and 4 equivalents of *N*-oxide reagent were dissolved in acetonitrile. The reagent solutions were sparged with a stream of nitrogen gas for 5 min. 4.4 equivalents of acetic anhydride reagent were subsequently added, and the mixtures were stirred for 10 min to facilitate complete conversion to the acylated species. Separate solutions of substrate in acetonitrile (0.1 M),

with co-solvent when applicable, were also prepared. 10 µL of each solution were mixed together in a 384 multiwell plate to form the final reaction solution.

Droplet Generation

Before generation, all samples were diluted down 500:1 by a 50:50 methanol:water solution w/0.5% formic acid, with the exception of the trifluoromethylation condition screen, in which samples were diluted down to an additional 4:1 with acetonitrile. Droplet plugs were generated from microwell plates using equipment and methods described in our previous work.[25] Briefly, samples were drawn into either 100 or 150 µm inner diameter (i.d) x 360 µm outer diameter (o.d) perfluoroalkoxyalkane (PFA) tubing (IDEX Health and Science, Oak Harbor, WA) by a PHD 2000 Programmable syringe pump (Harvard Apparatus, Holliston, TX). Samples of 8 µL in volume were deposited into 384-microwell PCR plates (Corning, Corning, NY) with PFD placed on top. To form the droplet samples, an XYZ-position manipulator moved the tubing between sample wells and fluorous phase while the syringe was continuously withdrawing. When diluted only with methanol:water diluent, 8 nL droplets with 12 nL perfluorodecalin spacing were generated at 800 nL/min, except when otherwise stated. When additional acetonitrile dilution was performed, droplets were found to be less stable, so 6 nL droplets with 10 nL spacing were generated at a flow rate of 600 nL/min .

nESI-MS and ESI-MS Analysis

Connections from PFA tubing to nanoelectrospray emitters were formed using zero dead-volume Picoclear^{TM} unions (New Objective, Woburn, MA). nESI emitters were pulled from 75 or 100 µm i.d. x 360 µm o.d. fused silica capillary to an i.d. of 30 µm (FS360-50-30-CE, New Objective, Woburn, MA). Electrospray potential of 1.75 kV was applied to the exterior of the platinum coated emitters, with 35 V applied to the sample cone. Mass spectrometry analysis was

performed on a Micromass Quattro Ultima triple-quadrupole mass spectrometer (Waters, Milford, MA). Nitrogen cone gas emerging from sampling inlet was set to 125 L/h to help stabilize the electrospray. For data analysis in MS-only scanning, droplet response was reported as the average of three data points in the center of each droplet. For MS-MS analysis, 5 data points were used. Flow rates to nESI-MS analysis matched droplet generation flow rates, except in experiments testing higher throughputs, which were flowed at 1500 nL/min. For work using a standard electrospray source, ESI voltage was 3.0 kV, the source was heated to 100 ºC, the cone gas was set at 225 L/h, the desolvation gas was 300 L/h and 200 ºC. The nebulizing gas flow was not measured, but it was adjusted to one half turn of the dial.

3.4.2 ESI vs. nESI-MS Signal Detection Studies

We found that nESI could promote the formation of molecular ions even when ESI could not (**Figure 3.12**), further highlighting the potential utility of a nESI-MS in screening applications. Samples composed of 50 mM trifluoromethyl azaindole before dilution were examined by both nESI-MS and ESI-MS analysis. nESI-MS analysis of sample containing analyte at a flow rate of 800 nL/min yielded spectra that showed the intact MH^+ molecular ion at m/z=365 and 367, along with prominent fragments at 309 and 311. MS-MS analysis of the 365 m/z ion showed the formation of the m/z=309 ion with very little energy applied, validating it as a fragment of the original molecular ion. When using the standard ESI source with sample flow at 100 µL/min, the molecular ion was not visible as nearly complete fragmentation was observed. While some fragmentations can be easily predicted (e.g. Boc protection), predicting fragmentation patterns and performing more in-depth structural assignments would not be amenable to HT work, making an ionization method that maximizes the chance of observing molecular ions more favored.

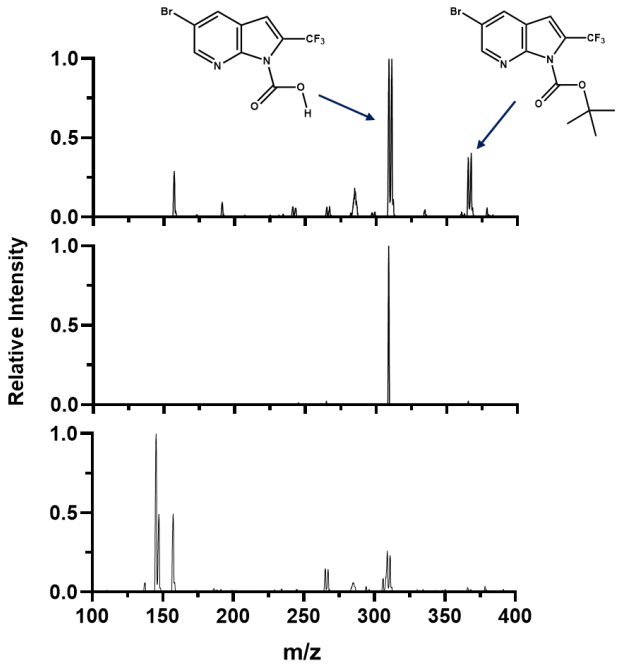

Figure 3.12. Comparison of ESI and nESI analysis. Predicted structures for intact molecule (Right) and loss of t-butyl group (Left) are shown. Arrows point to m/z peaks associated with each structure. (Top) nESI-MS analysis affording observation of the labile MH^+ molecular ion. While the 309/311 m/z fragments are the most prominent, the 365/367 m/z molecular ions were readily apparent. (Middle) nESI-MS-MS analysis of 365 m/z ion at 10 eV collision energy. Fragmentation of the 365 m/z ion showed almost complete conversion to 309 m/z ion, validating that molecular ions can fragment to form the 309/311 m/z ions observed in MS spectra. (Bottom) ESI-MS analysis of same sample. In this spectrum, molecular ions are no longer observed.

3.4.3 MS Strategies for Overcoming Matrix Effects

In addition to enabling the accelerated late-stage functionalization of diverse pharmaceuticals, our screening platform can also be utilized for the high throughput optimization of photoredox reaction conditions. To explore capability in such applications, we aimed to test a broad set of conditions for the trifluoromethylation of caffeine and discover new conditions for enhancingproduct formation. To make this type of work possible, an analytical method needed to be established to measure product conversion while tolerating sample-to-sample variability in product response due to matrix effects. Our efforts focused on minimizing background signals and accounting for variations in ionization efficiency. To lower backgrounds, MS-MS analysis was performed to target a specific fragmentation pattern demonstrated by the trifluoromethylated

caffeine analyte (m/z = 263→206). The development of an MS-MS assay will reduce or even remove backgrounds by increasing the assay specificity towards the product of interest. The second point is a general concern in the direct analysis of samples by MS. Changes in the sample matrix can drastically affect analyte ionization and observed MS response. This effect is typically resolved through sample cleanup methods such as liquid chromatography and chemical extractions. Because the use of such methods is time-intensive, we aimed to implement methodologies that would allow for the direct analysis of droplet samples.

Shown in **Figure 3.13** are the MS traces associated with the detection of trifluoromethylated caffeine in the presence of suppressing solvents.

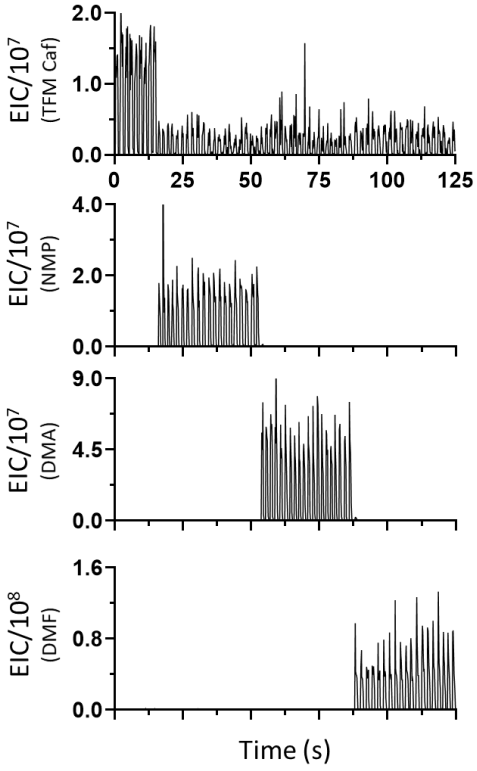

Figure 3.13. **Analysis of trifluoromethylated caffeine in the presence of suppressing cosolvents.** (Top) MS trace for TFM caffeine (m/z = 263). Droplet samples over the first 13 seconds of analysis were dissolved in 100% acetonitrile. The following droplets had one of the cosolvents present and saw massively decreased response for the trifluoromethylated caffeine. (2nd, 3rd and 4th traces) In descending order, the MS traces for NMP (m/ z= 100), DMA (m/z = 88) and DMF (m/z = 74).

Trifluoromethylated caffeine analyte was dissolved in either acetonitrile (50 mM), or in acetonitrile with 4% of either N-methyl-2-pyrollidone (NMP), dimethylformamide (DMF), or dimethylacetamide (DMA) present. These represent commonly used cosolvents in photoredox reactions, and even after diluting samples 500:1, were found to have a major effect on analyte ionization. In the presence of cosolvent, analyte response was found to observe nearly a 4-fold drop, even though analyte concentration remained constant, which would have major ramifications in a condition screen.

To overcome matrix effects, we explored three methods: the use of standard addition, internal standard, and higher dilution factor. (**Figures 3.14, 3.15, 3.16**).

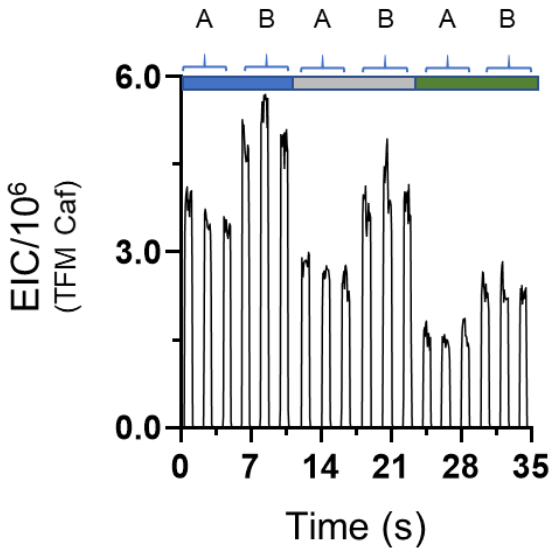

Figure 3.14. Trifluoromethylated caffeine MS-MS trace (m/z = 263→206) for standard addition method. Droplets with "A" designation were diluted normally, while "B" designation denotes droplets that were diluted with additional solution. 0% DMF (blue bar), 4% DMF (grey bar), and 10% DMF (green bar) showed variable ionization, but these changes could be accounted for upon normalization of Samples A against Samples B (A/B).

For these experiments, sample solutions consisted of 30 mM trifluoromethylated caffeine in reaction mixture, which was then diluted 1:1 with 0%, 8% or 20% DMF, respectively, in acetonitrile. The first method involved the use of standard addition, a commonly employed tactic

for addressing samples that have unknown matrix effects (**Figure 3.14**). For this approach, each sample of interest was further split into two samples to analyze. The first was made by the previously described 500:1 dilution. The second used the same dilution solvent with 15 µM trifluoromethylated caffeine standard present. Because both samples contain the same matrices and therefore similar analyte ionization efficiencies, taking the ratio of the two responses gives a measure of analyte concentration that accounts for matrix effects.

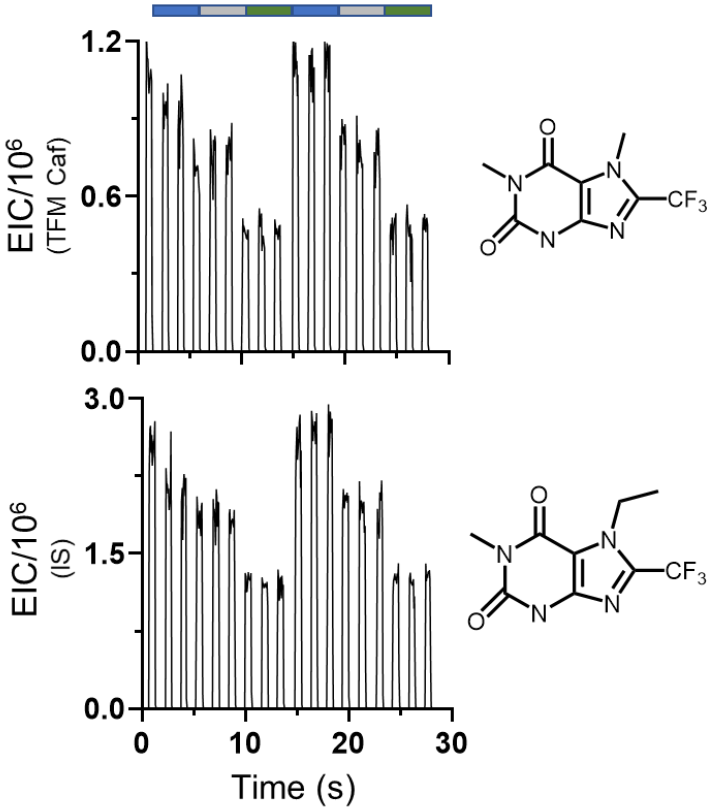

Figure 3.15. Internal standard method. Trifluoromethylated caffeine MS-MS trace (m/z = 263→206, top) and trifluoromethylated ethyl theophylline (m/z = 277→192, bottom) for internal standard method. 0% DMF (blue bar), 4% DMF (grey bar), and 10% DMF (green bar) showed variable ionization, but upon normalizing each droplet's analyte response against its internal standard response (A/IS), these effects can be accounted for.

The second method entailed the addition of an internal standard (**Figure 3.15**). For our caffeine trifluoromethylation reaction, we chose to use trifluoromethylated ethyltheophylline as the internal standard, as it only varies in structure by a single methylene group. This change is easily

discernable by MS but should not significantly affect ionization. Trifluoromethyl ethyl theophylline was present in the dilution phase at a concentration of 30 µM. For each droplet sample, the response for analyte could be normalized against internal standard, which should show similar changes in ionization from variable matrices. Finally, the use of a higher dilution factor (10,000x vs. 500x) was examined (**Figure 3.16**). By increasing the dilution and therefore further reducing the concentration of matrix components, we sought to reduce matrix effects to a negligible level.

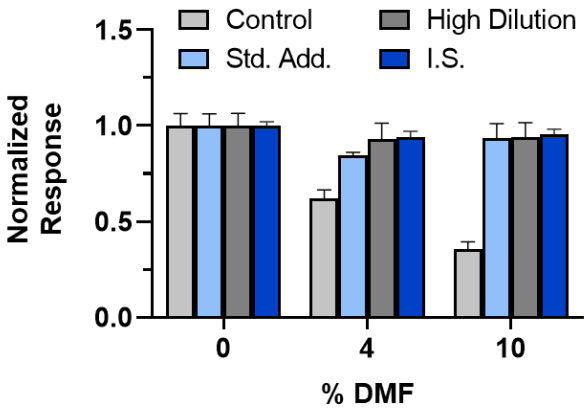

Figure 3.16. Comparison of performance across high dilution, standard addition (Std. Add.) and internal standard (I.S.) methods. Each bar represents the results from 15 separate samples analyzed in triplicate. Control samples were prepared from trifluoromethylated caffeine responses from base conditions with no extra measures employed. Responses are normalized within each method.

Each of the examined methods have associated strengths and weaknesses. The standard addition method directly accounts for matrix effects but halves throughput by doubling the number of samples. Use of internal standard performed gave the best performance both in precision of measurements (RSDs for all samples were less than 4%) and ability to normalize for matrix effects (normalized responses ranged from 0.94-1.00). The major drawback is that internal standards function best for structurally similar molecules, potentially requiring a need for new molecular standards when switching between substrates. The increased dilution method would be desirable for its simplicity in implementation but would not account for any remaining variability in matrix

effects. This method also gave the worst performance with regards to measured precision (RSDs ranged from 6-9%), possibly due to the lower analyte concentration associated with a higher dilution factor.

In our droplet microfluidics reaction optimization screen, we opted to use an internal standard, as it provided excellent results in terms of enabling signal normalization and minimizing variability in measurement. Namely, a 72-reaction screen was then performed to optimize the caffeine trifluoromethylation reaction by screening parameters including photocatalyst, *N*-oxide reagent, and co-solvent (**Table 3.1**).

	Solvent
1	100% MeCN
2	10% $MeNO_2$/90% MeCN
3	10% DCM/90% MeCN
4	10% DMF/90% MeCN
5	10% DMA/90% MeCN
6	10% DMSO/90% MeCN

	N-Oxide Reagent
A	Pyridine N-oxide
B	4-phenylpyridine N-oxide
C	4-CO_2Et pyridine N-oxide

	Photocatalyst
D	$Ru(bpy)_3Cl_2$
E	$Ir(ppy)_3$
F	$[Ir(ppy)_2(dtbbpy)]PF_6$
G	$[Ir(dF(CF_3)ppy)_2(dtbbpy)]PF_6$

Table 3.1. Parameters examined for optimization of caffeine trifluoromethylation reaction

The triplicate analysis of all 72 reactions was performed in 380 s (1.7 s/droplet) by ESI-MS (**see section 3.2 for results**). ^{19}F-NMR was applied as an orthogonal detection technique to validate our MS results (**Figure 3.17**). Analysis of our 5 scaled-up reactions showed yields ranging from 22-57%. The relative rankings of the reactions did not match between the original screen and scale-up, i.e. the best response from the screen did not give the highest product formation by ^{19}F-NMR. This can be accounted for by day-to-day or sample-to-sample variability in the reaction performance, as formation of the acylated N-oxide species required for trifluoromethyl radical formation is moisture sensitive. Heterogeneity in the screen samples also presents a potential source of error.

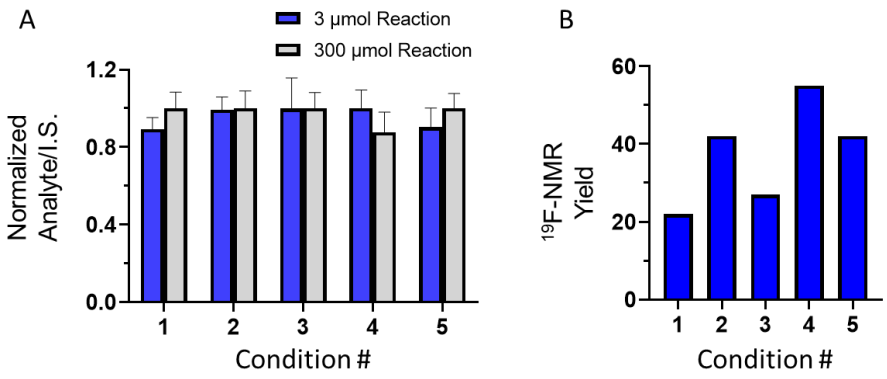

Figure 3.17. Validation of optimization screen MS results. The top 5 reaction conditions are listed in order as conditions 1-5 (A) Demonstration of reliability in scaling up reactions. Droplet nESI-MS comparison (n=10 droplets) of samples run at screen scale (3 µmol) and 100x scale (300 µmol) showed similar response for all 5 different reaction conditions. Normalization of results was performed within each pairing. (B) ^{19}F-NMR analysis of 300 µmol reactions.

Chapter 4: Development of a Droplet Microfluidic Platform for the High-Throughput Screening of Photoredox Catalysis Reactions

This work was performed with equal contribution from Daniel Steyer. Contributions of A. Sun include performance of in-droplet reaction screens and continuous flow reaction scale-up, as well as characterization and isolation of products. Contributions of D. Steyer to this work include the development and implementation of droplet incubation and reagent addition methods, as well as performance of MS assays and statistical analyses.

*Portions of this chapter have been published in Telmesani, R. Sun, A. C., Beeler, A. B.; Stephenson, C. R. J., Flow Photochemistry in Organic Synthesis. *Science of Synthesis: Flow Chemistry in Organic Synthesis*, **2018**, *103*, Stuttgart, Germany: Thieme.

4.1 Introduction

4.1.1 Continuous Flow Photochemistry

Over the past decade, visible light-mediated photoredox catalysis has emerged as a robust strategy to activate small molecules, forge challenging chemical bonds, and construct complex molecular scaffolds.[191-194] In particular, visible light (400-700 nm) irradiation offers a more chemoselective means of initiating radical-based transformations, as the lack of visible light absorbance by most organic molecules eliminates side reactions that may be triggered by UV light. With the burgeoning development and application of photoredox catalysis methodology across the synthetic community, efforts to address the scalability of these highly pathlength-dependent processes have spurred the adaptation of photoredox catalysis reactions in continuous flow systems.[195-198]

$$\text{Absorbance} = \log_{10}(T) = \varepsilon \cdot c \cdot l$$

Equation 1. The Beer-Lambert-Bouger Law

The efficiency of photochemical reactions is necessarily dependent on the availability of photons in a reaction mixture. The challenges associated with this availability are readily illustrated by the Beer-Lambert-Bouger law (**Equation 1**), which relates absorbance to the molar absorption coefficient (ε) of light absorbing molecules, their concentrations (*c*), and the path length of light propagation (*l*). As it relates to photoredox catalysis, the high molar absorptivity (**Table 4.1**) of traditional photocatalysts (e.g. tris(bipyridine)ruthenium(II)chloride) puts severe limitations on the scalability of batch processing, as the intensity of incident radiation decreases rapidly beyond the reactor surface, with minimal productive radiation at the center of the reactor (**Figure 4.1**).[199,200]

Photocatalyst	Molar Absorption Coefficient ($M^{-1}cm^{-1}$)	Measured Wavelength (nm)	Ref
$Ru(bpy)_3^{2+}$	13000	452	11
fac-$Ir(ppy)_3$	1100	462	12
$Ir(ppy)_2(dtbbpy)^+$	900	465	13
$Ir(dF(CF_3)ppy)_2(dtbbpy)^+$	180	452	14

Table 4.1. Molar absorption coefficients of commonly utilized photocatalysts[201-204]

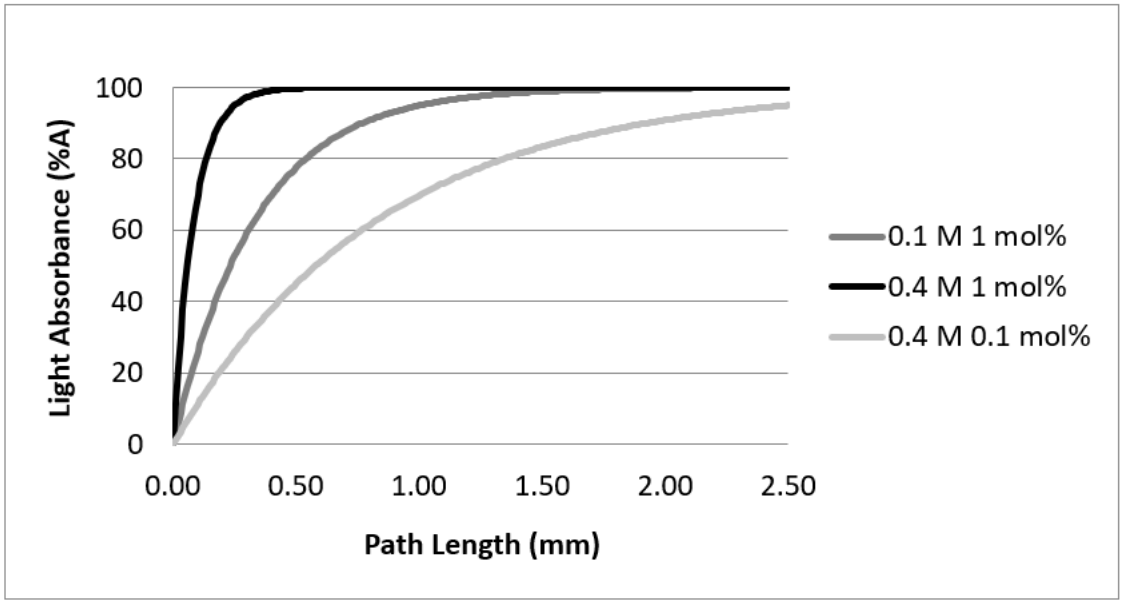

Figure 4.1. Light absorbance as a function of path length for different concentrations of $Ru(bpy)_3Cl_2$

In particular, the extent of photocatalyst light absorbance may have a significant impact on reactions that do not exhibit high levels of radical chain propagation and are characterized by quantum yield values ≤ 1. Quantum yield (ϕ) measurements can be used to determine the efficiency of product formation relative to the total number of photons absorbed by the reaction medium (**Equation 2**). Quantum yield values above 1 indicate the presence of radical chain pathways, in which absorption of a photon leads to the propagative generation of radical intermediates.[205,206] On the other hand, values between 0 and 1 may be suggestive of non-chain reactions that show a greater dependence on photon flux density.[207]

$$\Phi = \frac{\text{amount of product generated}}{\text{amount of photons absorbed}} = \frac{\text{mol product}}{\text{(photon flux) (time) (absorbance)}}$$

Equation 2. Quantum Yield Measurement

The use of continuous flow reactors for photoredox catalysis is especially appealing, as the greater surface area-to-volume ratio results in increased photon flux density, which can lead to reaction acceleration.[7,9] Using actinometry measurements, Loubière and co-workers observed a 150-fold increase in photon flux absorbance when transitioning from a batch to microreactor setup.[208] In addition to providing more productive irradiation and enabling the scale-up of photochemical reactions, continuous flow reactor technology also imparts other advantages, including better mass and heat transfer, increased operational safety, and opportunities for performing automated multi-step syntheses[7,18-211] The continued development and implementation of photochemical flow processes is critical for the efficient production of high-value chemical compounds across a multitude of synthetic applications and industrial sectors. It is anticipated that future advancements in this field will support the design of systems that offer enhanced operational

flexibility, place an emphasis on sustainability, and provide additional platforms for reaction discovery and optimization.

4.1.2 Continuous Flow-Based Screening Platforms in Organic Synthesis

High-throughput experimentation (HTE) techniques hold the potential to revolutionize modern catalysis and reaction discovery by enabling the exploration of myriad reaction conditions in a time and resource-efficient manner.[212-217] In recent years, efforts have been directed towards the development of mass spectrometry-based (MS) HTE systems for the automated processing of Pd-based cross coupling reactions on nanomole scale, in both batch and continuous flow settings.[218219220221] In order to overcome challenges associated with solvent evaporation and heating in nanomole plate-based screening, there has been a significant drive to develop next-generation continuous flow-based HTE platforms for organic synthesis. These innovative HTE methods promise to empower chemists to run orders of magnitude more experiments while utilizing "big data" informatic approaches for reaction design and troubleshooting.

In 2017, the Jensen group reported the elegant design of an automated flow chemistry platform that allows for the optimization of single, microliter-sized droplet reactions.[222] More recently, researchers at Pfizer have developed a modular, automated system to enable nanomole scale screening and micromole scale synthesis in continuous flow. This platform was successfully employed to expedite reaction discovery in flow while providing an analysis throughput of over 1500 samples/day (1 sample/45 s).[30] While the above screening technology have been successfully applied to non-photochemical reactions, we are interested in developing a novel HTE platform for screening visible light-driven photochemical reactions in continuous flow by leveraging droplet microfluidics.

4.1.3 Leveraging Droplet Microfluidics Technology for Photoredox Catalysis

Among the repertoire of modern catalysis methods, photoredox catalysis has exerted a significant influence on industrial chemistry by enabling otherwise infeasible bond disconnections and aiding sustainability efforts.[223] The widespread implementation of photoredox catalysis renders the development and dissemination of flow technology for reaction scale-up to be broadly impactful.[7,224] The use of continuous flow reactors for photochemical reactions is especially appealing, as the greater surface area-to-volume ratio accessible results in increased photon flux, which can lead to reaction acceleration.[7]

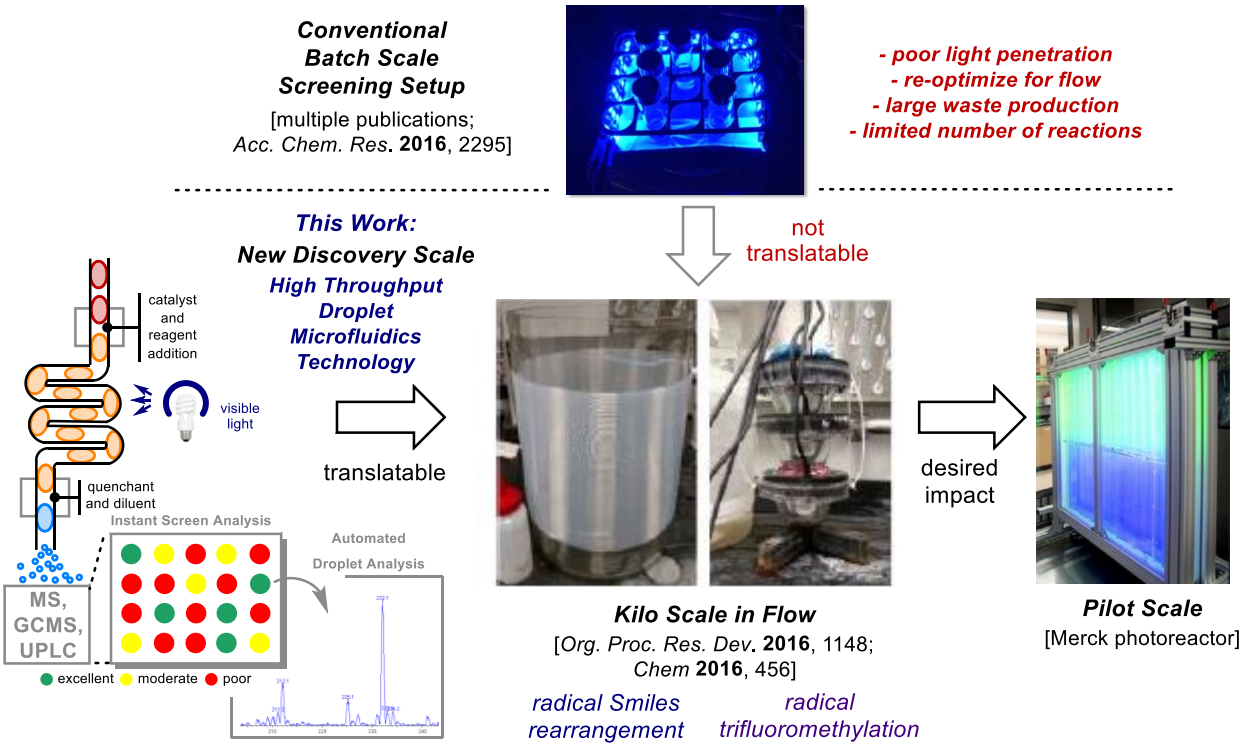

Figure 4.2. Development of a droplet microfluidics screening platform for photoredox reactions

However, conditions developed for an efficient discovery-scale (i.e. milligram-scale) batch process often do not translate effectively to a pilot-scale (i.e. kilogram-scale) flow system, and significant resources can be wasted during re-optimization. For example, 0.5 kg of starting material was wasted on optimizing the residence time for a trifluoromethylation reaction in a large scale

photoflow reactor built by our group in collaboration with Eli Lilly.[225] Given the time and resource constraints of translating discovery scale (i.e. microgram scale) batch reactions to large scale (i.e. kilogram scale) continuous flow conditions, we envision employing droplet microfluidics as a unique platform for continuous flow-based reaction discovery and optimization (**Figure 4.2**). To increase throughput in conventional flow reaction screening, multiple reaction plugs, spaced by reaction solvent, need to be present in the reactor simultaneously. Taylor diffusion of these plugs into surrounding carrier solvent makes the determination of exact reaction conditions impossible and leads to cross contamination over longer incubation times. It is in this context that we aim to develop novel droplet microfluidics HTE technology, with the goal of expanding upon the robust capabilities and impact of photoredox catalysis in drug discovery and development.

We have identified droplet microfluidics as an excellent platform for continuous flow-based reaction discovery. Over the past decade, droplet microfluidics has been used to enable further miniaturization and higher throughput in biological and chemical experiments. Segmentation of samples with an immiscible phase can enable the simultaneous handling of numerous samples over extended periods of time.[32] From a material consumption standpoint, droplet microfluidics screens are typically performed at nanoliter to femtoliter scale, which can translate to a reduction in starting material usage by six to eight orders of magnitude relative to a traditional multiwell plate-based screen. Droplet microfluidics is also well suited for photocatalytic reactions, as the micrometer dimension of the reaction vessel allows for high photon flux through the reaction channel in an analogous manner to the narrow tubing employed in flow reactors.[9,226-229] Manipulating droplet samples in closed systems also provides the benefit of avoiding solvent evaporation, allowing for the use of volatile solvents over extended incubation times. In addition to providing reduced reagent consumption, droplet microfluidics systems can improve screening efficiency through

process automation and online analysis. The disruptive impact and utility of droplet microfluidics has been demonstrated across several biological applications, including single-cell analysis, droplet-based polymerase chain reactions, and directed enzyme evolution.[36,230,231,232-238] The ability to manipulate discrete droplets through immiscible multi-phase fluids in microchannels shows potential for chemical synthesis by allowing for cost reduction through small reagent volumes, rapid reactions on the order of milliseconds, and greater control over local conditions to enhance product selectivity. In recent years, droplet microfluidic reactors have been developed to rapidly merge two libraries of reagents in creating a combinatorial product library.[239]

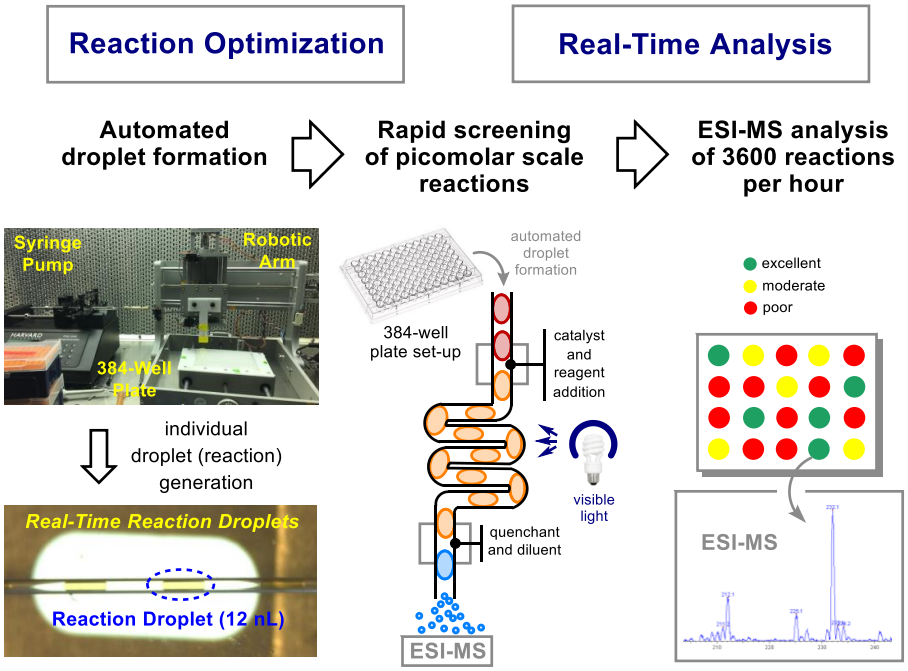

Figure 4.3. Highlights of droplet microfluidcs screening platform

As such, we envisioned employing droplet microfluidics as a new platform for high-throughput reaction discovery and optimization, to further reduce material consumption while increasing chemical space coverage in early-stage pharmaceutical discovery (**Figure 4.3**). We aimed to develop a droplet microfluidic reactor that would enable prepare nanoliter-sized reaction droplets,

perform photochemical reactions on picomole scale, as well as conduct subsequent ESI-MS analysis, all in a continuous and automated manner (**Figure 4.4**). We have designed a microfluidic reactor that features the integration of a reagent addition chip, oscillatory photoreactor, as well as in-line dilution and nESI-MS analysis capabilities in one continuous flow system. Namely, the use of a reagent addition microfluidic chip would provide the benefit of performing direct, in-droplet reagent addition to streamline and expedite droplet preparation. This helps increase material efficiency, as stock solutions can be conserved for further use, without the need for pre-mixed solutions.

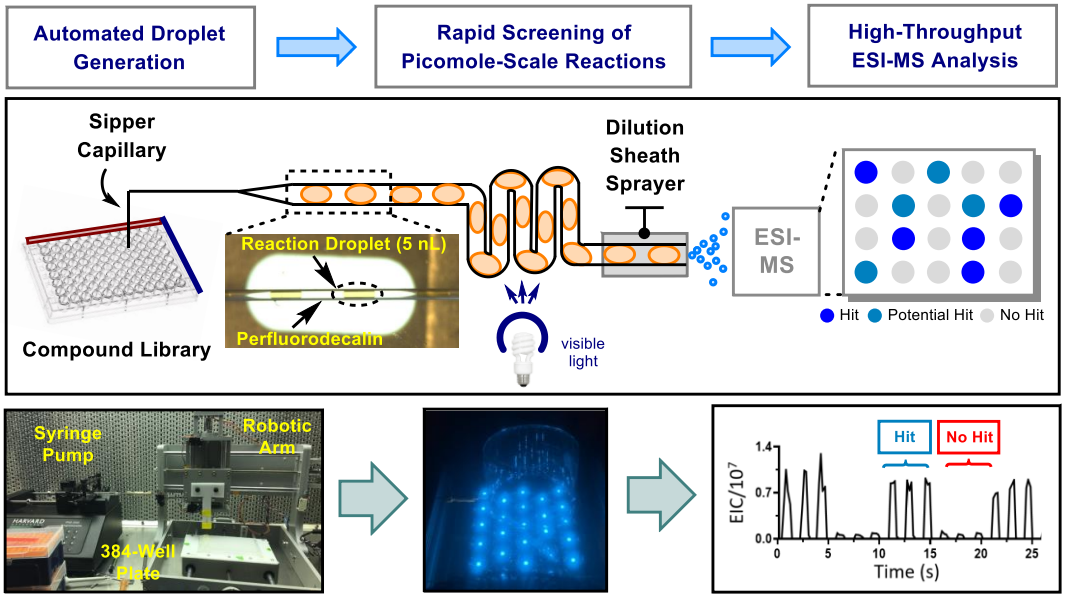

Figure 4.4. Photoredox droplet microfluidic reactor design features

Additionally, we aimed to design an oscillatory flow setup, which would give us the opportunity to optimize reaction residence time at a constant volume and flow rate. We anticipate that the use of droplet microfluidics will propel forward in-flow screening efforts to where throughputs can approach or even match the throughput of batch-scale screens, while more accurately reflecting optimal continuous flow conditions to facilitate subsequent photochemical reaction scale-up (i.e. gram to kilogram scale). Here, we report the advances towards a droplet microfluidic/MS platform

to enable picomole-scale discovery of visible light-driven reactions and provide robust translatability to millimole flow scale-up processes. We foresee the synergistic combination of droplet microfluidics, MS, and photoredox catalysis as an enabling platform for accelerating pharmaceutical discovery and development, with a concerted emphasis on time and material efficiency.

4.2 Results and Discussion

Our studies into leveraging droplet microfluidics technology for reaction discovery have been centered on the development of an ESI-MS platform, which can be utilized for characterizing product formation in visible light-driven reactions. Previous applications of ESI-MS have led to the development of systems for monitoring the molecular content of pL-nL volume droplets with high analytical stability at throughput levels as high as 10 droplets/s.[240-247] In this work, we aimed to develop a droplet microfluidic reactor that would enable us to perform on-chip reagent addition, droplet reaction irradiation, in-line dilution, and subsequent ESI-MS analysis in one continuous system (**Figure 4.4**)**.** Additionally, we aimed to design an oscillatory flow setup, which would give us the opportunity to optimize reaction residence times at a constant volume and flow rate.

Our optimized workflow for droplet generation begins with the upstream formation of reaction droplets (5-10 nL) from a standard 384 or 1536 microwell plate using equipment and methods previously reported by the Kennedy group.[50-53] In our preliminary studies, we constructed an easily assembled, low-footprint photoreactor that could enable us to flow irradiated reaction droplets directly into our triple quadrupole mass spectrometer for analysis. We assembled our photoreactor by wrapping a single strip of 4.4 W blue LEDs around the inner diameter of an aluminum foil-lined petri dish, at the center of which was fitted with a coil of perfluoroalkoxy (PFA) tubing (100 µm inner diameter; 360 µm outer diameter). Upon flowing reaction droplets

through our photoreactor chamber, simultaneous dilution and ESI-MS analysis were performed using a sheath sprayer.[50] In-line dilution of droplets served to both quench the reaction and facilitate MS analysis, as the analysis of high concentration (> 1 mM) analytes can lead to saturation of MS signal and contamination of the MS source.

In our preliminary studies, we chose to employ a radical perfluoroalkylation strategy developed by the Stephenson group[248,249] as a model reactive system for the late-stage functionalization of complex pharmaceutical intermediates. To demonstrate the general operation of our system, we performed the in-droplet trifluoromethylation of four distinct substrates, three of which were either approved therapeutics or drug candidates provided from Pfizer's Millipore Sigma Library. Reaction droplets (4 nL), segmented by a perfluorodecalin (PFD) carrier phase (8 nL), were formed in a 100 µm internal diameter (i.d.) PFA tubing. Droplet reactions containing different substrates were generated in a consecutive manner (**Figure 4.5**).

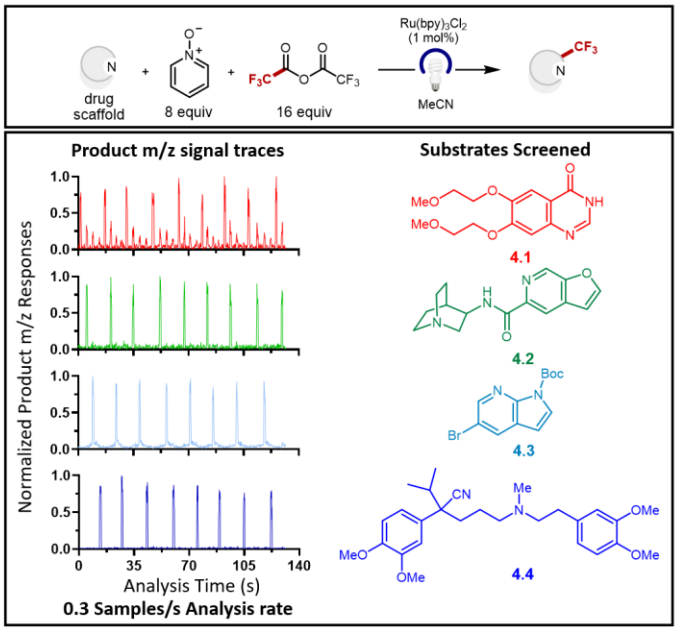

Figure 4.5. ESI-MS analysis of in-droplet trifluoromethylation reactions. Extracted m/z ratios for trifluoromethylated products. MH^+ molecular ions were monitored for all trifluoromethylated products except for **4.3**, which was prominently observed as a m/z=309 fragment.

After a 10 min irradiation, droplets were flowed at 500 nL/min into the sheath sprayer and merged with a dilution stream of 50:50 methanol:water w/ 0.5% formic acid (1:500 dilution, 100 µL/min flow rate). ESI-MS analysis of droplet samples was performed at 17 droplets/min (0.3 samples/s). Product formation was monitored by extracting out the expected m/z values for each trifluoromethylated product. As anticipated, prominent product m/z signals were observed iteratively throughout the four traces in the expected ABCD pattern. These results not only validate the capability of our system to detect product formation, but also demonstrate the ability to perform rapid in-line analysis while maintaining the identity of individual samples, with minimal material carryover between droplets. Notably, the analytes were not subject to Taylor diffusion as in a conventional plug flow reactor. In this manner, we established proof-of-concept for the successful performance and ESI-MS analysis of in-droplet organic synthesis reactions.

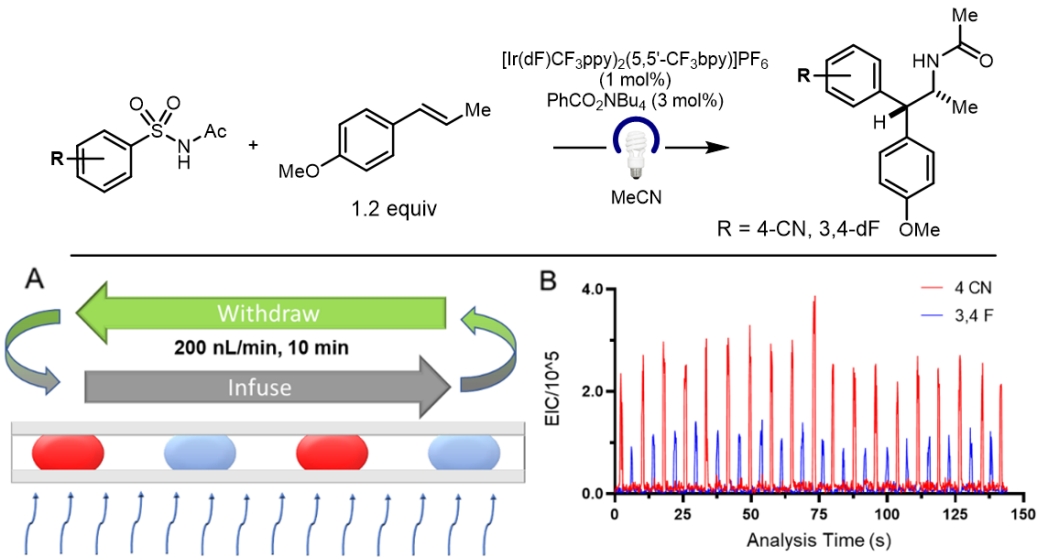

Figure 4.6. Design of an oscillatory flow reactor for in-droplet alkene aminoarylation reactions. (A) Scheme for oscillatory flow reactor. While being irradiated, droplet flow was cycled between moving towards (withdraw) or away from (infuse) the syringe to allow for continuous flow in a linear, volume limited reactor. (B) Extracted traces for 4 CN (m/z = 309) and 3,4 F (m/z = 320) substrate reaction products, showing the formation of the two products in alternating droplets.

Upon demonstrating the success of our in-droplet reactions, we set out to explore droplet-based flow reactions. In order to perform residence time optimization at a constant flow rate (between 0.2 - 0.5 μL/min) and reactor volume, we designed an oscillatory flow system for the irradiation of continuous flow droplet reactions (**Figure 4.6**). We implemented the Stephenson group's visible light-driven alkene aminoarylation reaction[250] as our reactive system of choice (**Figure 4.6**) to provide us with a manifold for performing high-throughput reaction discovery in continuous flow. Initial validation of our oscillatory system was conducted using 3,4-F and 4-CN-substituted sulfonamides, with reaction droplets formed in an alternating fashion between the two substrates. Upon irradiation, the droplet reactions were run at a flow rate of 200 nL/min in an oscillatory manner by programming a syringe pump to alternate between refill and infusion modes at 10 min intervals, yielding a total residence time of 1 h. Successful product formation for both reactions was observed upon ESI-MS analysis. Notably, while current state-of-the-art oscillatory flow systems have been limited to a single reaction plug during each incubation period, this setup can accommodate a throughput of >100x more samples per incubation period.[251-253]

With our optimized system on hand, our next goal was to perform HTE reaction discovery of the alkene aminoarylation methodology. Given the demonstrated throughput and material efficiency of our droplet microfluidic HTE platform, we aimed to screen an extensive library of sulfonamides on picomole scale to furnish a wealth of reactivity data generated from each substrate combination. Following our in-droplet reaction screen, incremental scale-up of select droplet flow reactions (0.01 mmol and 0.1 mmol, respectively) would serve to both validate product formation and demonstrate the translatability of droplet reaction parameters to millimole scale flow conditions. 10 sulfonamides and 10 alkenes were selected for our screen (500 pmol scale), resulting in the potential generation of 100 distinct product combinations (**Figure 4.7**). For these

studies, droplet reactions were irradiated using a custom-built Cree LED array photoreactor, in order to maximize photon flux. Our optimized oscillatory flow setup was employed to maintain a residence time of 30 min at a flow rate of 200 nL/min during reaction irradiation. ESI-MS analysis was performed at a throughput of 0.3 samples/sec (435 total samples over 24 min). ESI-MS results suggested the identification of 37 hit conditions, for which significant product m/z signals were observed.

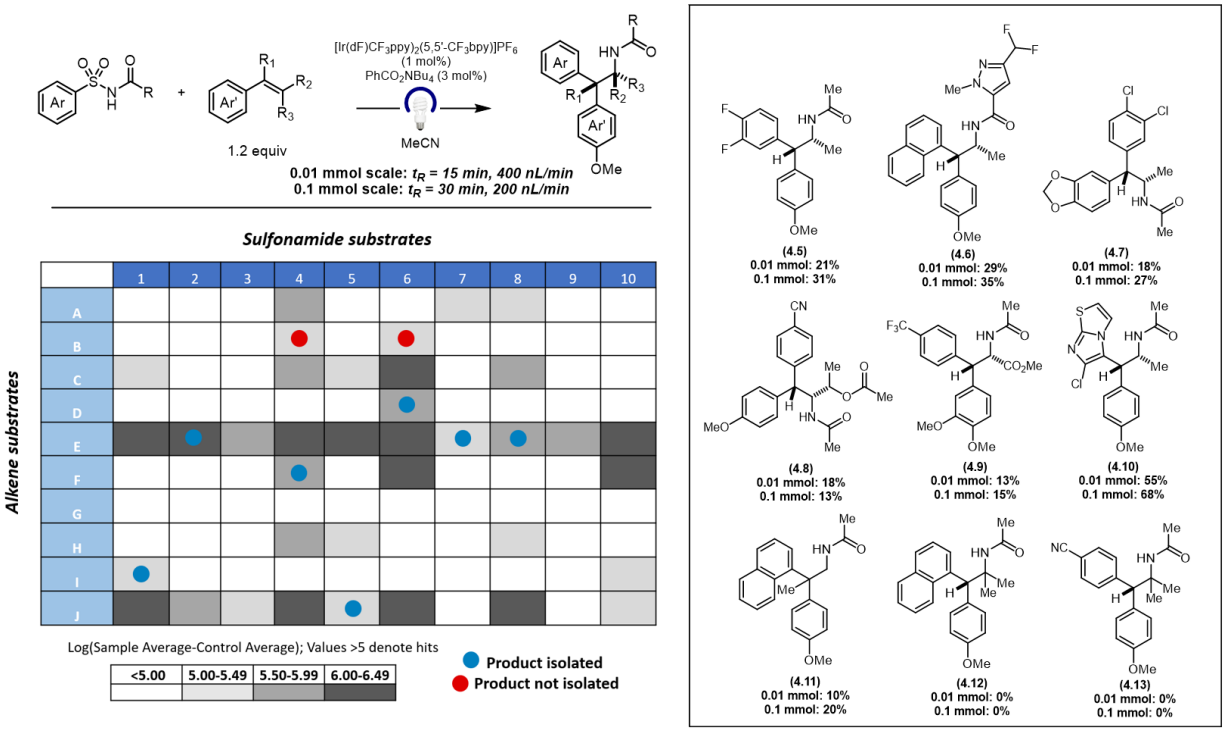

Figure 4.7. Droplet microfluidics-enabled HTE reaction discovery on picomole scale. (A) Heatmap of coupling 10 sulfonamides with a matrix of 10 alkene substrates. Gray boxes denote potential hit/hit responses. Boxes containing red and blue circles indicate reactions that were performed on 0.01 mmol and 0.1 mol scale. (B) Product yields for millimole scale-up flow reactions.

In line with previously reported batch reaction results, the employment of trans-anethole yielded product formation across the entire scope of sulfonamide substrates. Furthermore, this data suggests that electron deficient sulfonamides generally gave rise to enhanced reactivity and broader alkene compatibility. Notably, pharmaceutically relevant sulfonamides containing

heteroarenes (**4.6, 4.10**) also yielded several hit responses in our droplet screen. Our in-droplet reaction discovery screen has significantly expanded upon the scope of our reported alkene aminoarylation methodology to incorporate substrates of increased structural complexity, as well as enabled the elucidation of reactivity trends to inform ongoing mechanistic studies.

In order to validate our ESI-MS screen results, we selected 9 of our droplet reactions to perform 0.01 mmol scale-up in flow to provide sufficient material for product isolation (**Figure 4.7**). These reactions were carried out in the same PFA tubing (100 um i.d., 360 o.d.) and run in a continuous stream (non-droplet format) at a flow rate of 400 nL/min, providing a residence time of 15 min. Upon irradiation, purification was performed using mass-directed HPLC methods. Of the 9 reactions selected, 7 of the hit reactions were successfully validated through product isolation. In the case of the reactions **4.12** and **4.13**, product isolation was unsuccessful despite ESI-MS detection of product m/z signals in both the 500 pmol and 0.01 mmol scale reactions. Control experiments suggest the formation of an unidentified byproduct that gives the same m/z signal as the desired product. Finally, we set out to demonstrate the translatability of our droplet screen results to a microscale flow reaction, in order to generate milligram scale quantities of material for discovery chemistry applications. As such, a 100 µL plug flow reactor was constructed using 0.03'' ID PFA tubing. Our 0.1 mmol scale reactions were irradiated in the reactor with a residence time of 30 min at a flow rate of 3 µL/min. The same 8 reactions were scaled up to yield isolation results that showed strong correlation with that of the 0.01 mmol scale flow reactions. These experiments highlight the utility of our droplet microfluidics platform for enabling reaction discovery in a high throughput, material efficient, and data-rich manner. At the same time, this platform shows significant promise in its applicability and translatability to larger flow conditions.

Our final goal was to investigate the incorporation of on-chip reagent addition capabilities into our system. Namely, the use of a reagent addition microfluidic chip would provide the benefit of performing direct, in-droplet reagent addition to streamline and expedite droplet preparation. Most importantly, in-line reagent addition would alleviate the need to prepare individual reaction mixture stock solutions in a multiwell plate prior to droplet generation, which leads to increased substrate and reagent consumption (0.02 mmol of reagent per 384 reaction screen, per 60 nmol scale reaction stock solution). By adding valuable reagents directly into substrate-containing droplets, increased material efficiency can be achieved, as the consumption of valuable reagents (e.g. photocatalysts) is at or approaching the amount found in the droplets, thereby alleviating the need for excess amounts of stock solutions.

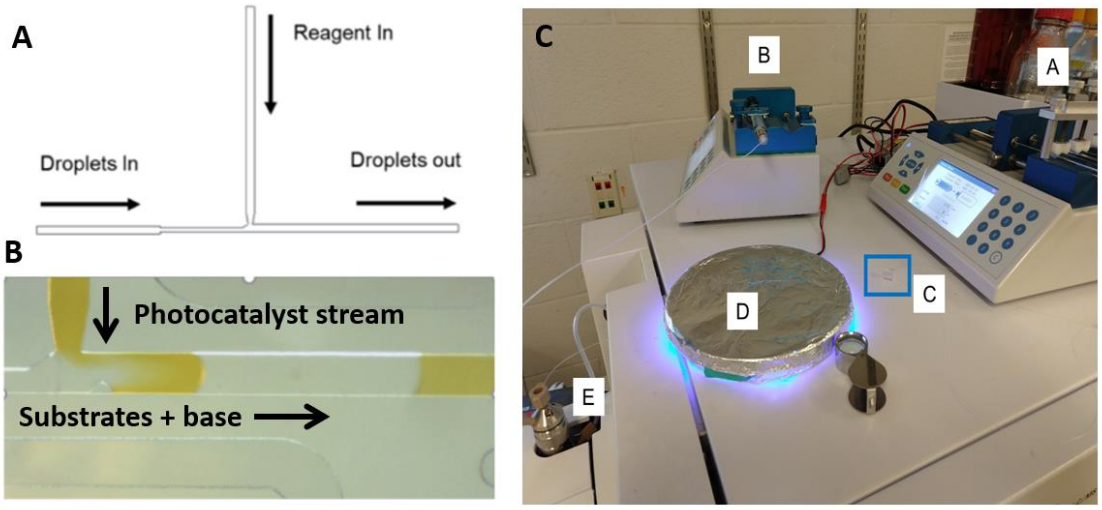

Figure 4.8. Incorporation of a microfluidic chip for reagent addition. (A) Reagent addition device design. (B) Device in operation. Each incoming droplet from the left received solution from the upper channel and moved right to export. (C) Full setup for in-droplet flow reaction screening. (a) Syringe pump driving both droplet flow and reagent flow into reagent addition chip. (b) Syringe pump driving sheath flow. (c, in blue box) Reagent addition device. (d) Photoreactor chamber (e) Sheath sprayer for ESI-MS analysis.

Polydimethylsiloxane (PDMS) chips were fabricated to enable individual droplets to be imported from 100 µm i.d. PFA tubing, flowed through an addition region to receive reagents (photocatalyst

solution), and subsequently exported to a 150 μm i.d. PFA tubing for irradiation and ESI-MS analysis. Upon achieving consistent addition of reagent amounts to each droplet by optimizing flow rate and channel geometry, the reagent addition device was implemented as part of a fully continuous flow reactor system (**Figure 4.8**). Aminoarylation reactions were performed in the final system, at a residence time of 7 min. Analysis of droplets post-irradiation at 20 droplets/min (0.3 samples/s) not only showed that product had formed, but that the formation was highly consistent across all of the droplet samples (**Figure 4.8**). The device demonstrated low carryover between droplets. These experiments have provided initial proof-of-concept for performing successful reagent addition using our current droplet and carrier fluid combination.

4.3 Conclusion

The droplet microfluidics platform described in this study provides a notable advancement in the ability to screen photochemical reactions in a miniaturized (i.e. picomole scale) fashion in continuous flow. The use of droplet microfluidics presents several significant advantages for performing in-flow reaction discovery. By designing an oscillatory flow reactor, our reported setup allows for the simultaneous irradiation of up to 100 picomole-scale reaction droplets, representing a marked improvement from current state-of-the-art systems that typically accommodate one droplet/incubation period. Furthermore, this system enables in-droplet reaction discovery to rapidly generate high-volume compound libraries and provide access to greater magnitudes of chemical space. Upon translating our picomole scale droplet reactions to millimole scale flow conditions, we have also validated the successful flow scale-up of our droplet reactions to enable product isolation. Notably, the application of in-line ESI-MS provides a highly versatile analytical approach for monitoring reaction turnover at an analysis throughput of 0.5 samples/s. Future studies will be targeted towards establishing a system to enable continuous droplet

generation, as well as further developing reagent addition capabilities to accommodate larger screening campaigns. From an early discovery standpoint, this droplet microfluidics HTE platform has the potential to facilitate rapid photochemical reaction discovery in flow for the expedited generation of compound libraries to enable subsequent biological and pharmacokinetic evaluation. We anticipate that this automated HTE platform for droplet generation will continue to expand upon and enhance the utility of visible light-mediated transformations from the bench to the drug pipeline.

4.4 Experimental Methods

4.4.1 General Information

Chemical Reagents and Analytical Instrumentation

Chemicals were either used as received or purified according to the procedures outlined in *Purification of Common Laboratory Chemicals*. Perfluorodecalin and trichloro(1*H*,1*H*,2*H*,2*H*-perfluorooctyl)silane were purchased from Oakwood Products (Estill, SC). All other reagents were purchased from Fisher Scientific or Sigma Aldrich. Hygroscopic *N*-oxide substrates were dried on a high vaccuum line for 6 h at ambient temperature prior to use. Pyridine *N*-oxide was dried on a high vacuum line at 60 °C for 12 hours. Thin-layer chromatography (TLC) analysis of reaction mixtures was performed using Merck silica gel 60 F254 TLC plates and visualized by a dual short wave/long wave UV lamp. Column flash chromatography was performed using 230–400 mesh silica gel or via automated column chromatography.

Nuclear magnetic resonance (NMR) spectra were recorded using an internal deuterium lock on Varian MR400, Varian Inova 500 and Varian Vnmrs 700 spectrometers. Chemical shifts for ^{1}HNMR were reported as δ, parts per million, relative to the signal of $CHCl_3$ at 7.26 ppm. Chemical shifts for ^{13}CNMR were reported as δ, parts per million, relative to the center line signal of the

$CDCl_3$ triplet at 77.36 ppm. Multiplicities are reported using the following abbreviations: s = singlet, d = doublet, t = triplet, q = quartet, quint = quintet, m = multiplet, br = broad resonance, dd = doublet of doublet, dt = doublet of triplet, etc. High-resolution mass spectra (ESI) were recorded at the Mass Spectrometry Facility at the Department of Chemistry of the University of Michigan in Ann Arbor, MI, on a Micromass AutoSpec Ultima Magnetic Sector mass spectrometer using electrospray ionization (ESI), positive ion mode. IR spectra were recorded on a Perkin-Elmer Spectrum BX FT-IR spectrometer fitted with an ATR accessory.

LED lights and the requisite power box and cables were purchased from Creative Lighting Solutions (http://www.creativelightings.com) with the following item codes: CL-FRS5050-12WP-12V (4.4 W blue LED light strip), CL-FRS5050WPDD-5M- 12V-BL (72 W LED strip), CL-PS94670-25W (25 W power supply), CL-PS16020-150W (150 W power supply), CL-PC6FT-PCW (power cord), CL-TERMBL-5P (terminal block).

Droplet Generation

Droplet generation from microwell plates was performed using equipment and methods described in our previous work. Briefly, samples were drawn into either 100 µm inner diameter (i.d) x 360 µm outer diameter (o.d) perfluoroalkoxyalkane tubing (IDEX Health and Science, Oak Harbor, WA) by a PHD 2000 Programmable syringe pump (Harvard Apparatus, Holliston, TX). 6 µL samples were deposited into 384 PCR MWPs (Corning, Corning, NY) with PFD placed on top. While solution was being withdrawn through the tubing, an XYZ-position manipulator moved the tubing between sample wells and fluorous phase to form alternating droplet/carrier phase trains.

Photoreactor Chamber Assembly

All reactions were run in a photoreaction chamber constructed in-house (**Figure 4.9**). A 150 mm wide x 15 mm deep polystyrene petri dish was lined with aluminum foil to promote internal

reflection of light. A 4.4 W blue LED strip (Creative Lighting Solutions, Columbia Station, OH) was placed around the edge of the interior of the dish. A small slit was cut from the petri dish wall to run wires and tubing through. During the reaction, tubing was coiled in the middle of the dish, only approaching the edge by the inlet.

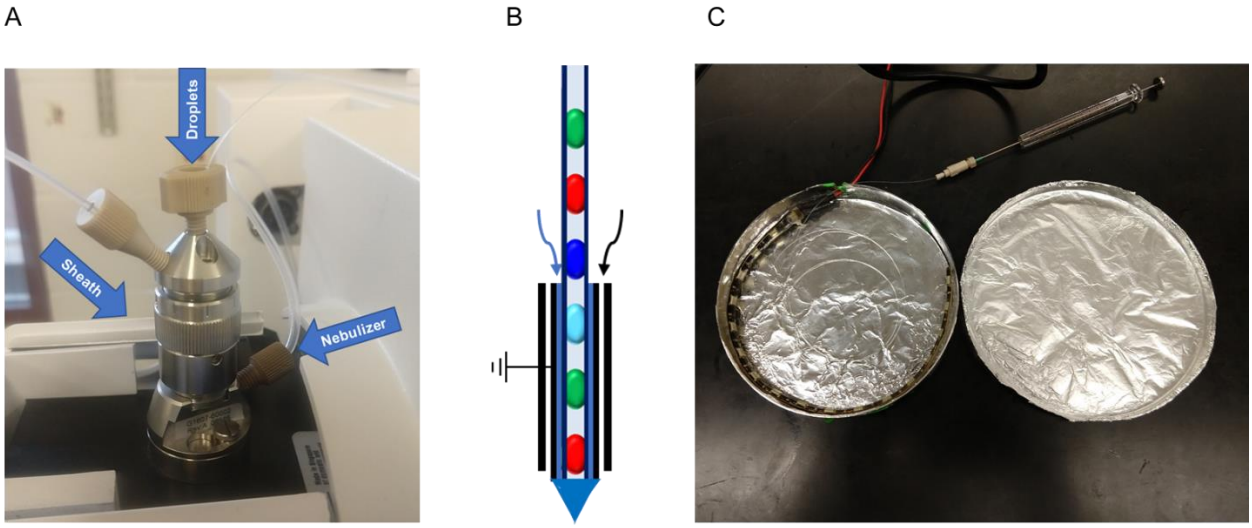

Figure 4.9. Setup for irradiation and ESI-MS analysis of droplet samples. (A) Setup of sheath sprayer. (B) Schematic of sheath sprayer for droplet work. PFA tubing with droplets runs through the middle of the sprayer. Sheath liquid flows directly around tubing (Blue arrow). Electrospray is aided by use of nebulizer gas (Black arrow) (C) Photoreactor setup. To irradiate droplets in tubing, a petri dish was coated with aluminum foil, with an LED array lining the rim.

Sheath Spray and MS Setup

Tubing containing droplets was threaded through a sheath sprayer (Agilent Technologies, Santa Clara, CA) until approximately 0.5 mm was protruding (**Figure 4.9**). Sheath and droplet flows were driven by Fusion 400 syringe pumps (Chemyx, Stafford, TX). After a 10 min irradiation, droplets were flowed at 500 nL/min into the sheath sprayer and merged with a dilution stream of 50:50 methanol:water w/ 0.5% formic acid (1:500 dilution, 100 µL/min flow rate). ESI-MS analysis was performed on an Agilent 6410 triple quadrupole mass spectrometer (Agilent Technologies, Santa Clara, CA). ESI potential was set to 2500 V, nebulizer gas to 15 psi, and drying gas from MS source was 10 L/min at 325 ºC. Mass spectrometer was set to scan from 75

to 750 m/z at 73 ms per scan. Experiment using nESI-MS followed procedures from Chapter 3. Briefly droplets were flowed from PFA tubing to a nESI emitter by use of a Picoclear™ union (New Objective, Woburn, MA). Applied nESI potential was 1.75 kV. Mass spectrometry analysis was performed on a Micromass Quattro Ultima triple-quadrupole mass spectrometer (Waters, Milford, MA). Droplet responses for any given m/z value were taken as the average of 3 consecutive data points from inside of each droplet's observed peak.

Chip Fabrication

Microfluidic chips were fabricated using standard soft lithography procedures.[254] SU-8 2050 photoresist was spun to 100 µm depth on silicon wafers (University Wafer, Boston, MA) then developed using photolithography to form negative masters. Uncured PDMS (Curbell Plastics, Livonia, MI) was poured on top of clean masters or blank wafers and allowed to cure for 1 h at 65 °C. Patterned PDMS and blank PDMS were baked for 1 h at 150 °C, followed by 1 min of exposure to atmospheric plasma and baking for 2 h at 150 °C to create an irreversible bond. Chip channel surfaces were treated with 2% trichloro(1H,1H,2H,2H-perfluorooctyl)silane in PFD by flowing 10 internal volumes through over 10 minutes, followed by 2 hours baking at 65 ºC. Chips were soaked in acetonitrile overnight to prevent solvent loss from droplets.

Reagent Addition Chip Setup

PDMS devices were 100 µm depth. Droplets flowed in from a 100 µm wide channel that expanded to 200 µm wide at the point of intersection with reagent addition channel, which was 100 µm wide at this point. The final device was 200 µm wide at all openings to accommodate direct insertion of 360 µm o.d. tubing. Channels were wetted with PFD to help ease insertion of tubing.

4.4.2 Preliminary Droplet Experiments

nESI-MS vs. ESI-MS Analysis of Reaction Droplets

To analyze the contents of droplets post-irradiation, three separate approaches were explored. Since organic synthesis reactions are typically highly concentrated with reagents often present at > 10mM, our approaches for ESI-MS analysis aimed to lower this concentration down before analysis avoid saturation of MS signal. First, the nESI-MS method from Chapter 3 was used for the analysis of a 25 mM trifluoromethylated *N*-Boc-5-bromo-7-azaindole solution in MeCN. Stable detection of analyte from these samples was easily achieved without saturating the observed MS signal (**Figure 10**). This result suggested that droplet formation and nESI-MS analysis can be performed without the need for the dilution solvent from Chapter 4 (50:50 methanol:water w/0.5% formic acid); however, this approach would only be compatible with reactions that can be run at lower (< 1 mM) concentrations.

The second method investigated was the in-line dilution of droplet samples into a continuous stream. Droplet samples composed of undiluted 25 mM trifluoromethylated azaindole were flowed at 200 nL/min into a stainless-steel tee containing 100 µm i.d. channels. A separate dilution stream, composed of 50:50 methanol:water w/0.5% formic acid, was flowed at 100 µL/min, giving a nominal 500x dilution before ESI-MS analysis. Lines leading in and out of the tee were comprised of 100 µm i.d. PFA tubing. Each individual droplet was observable in the azaindole MS trace at 7 droplets/min, though restrictions on greater throughputs were seen based on widening of sample bands in the continuous stream.

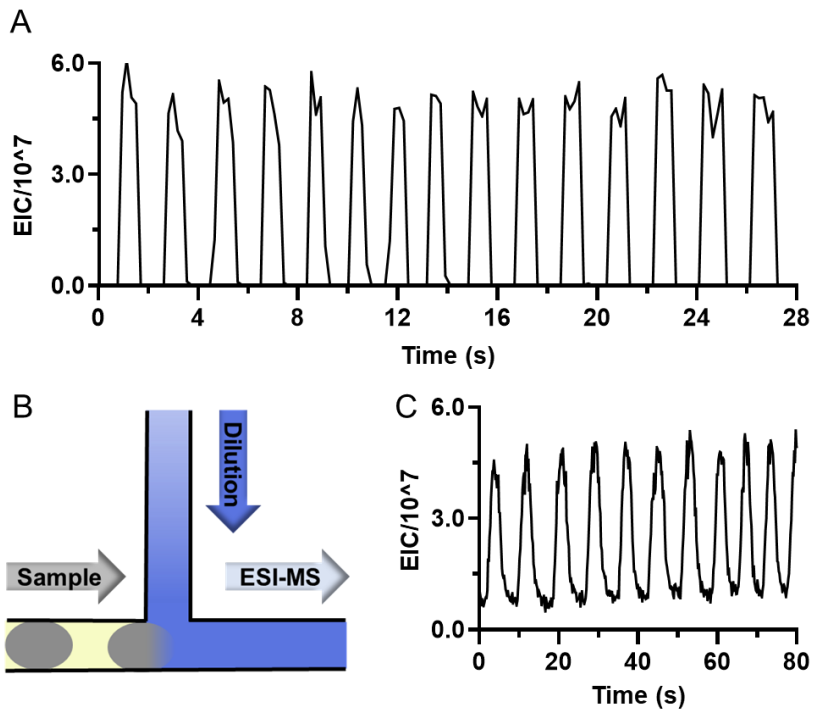

Figure 4.10. nESI-MS and Tee-dilution ESI-MS systems for in-droplet photoredox reaction analysis. (A) Trace for trifluoromethyl azaindole (m/z = 365) using nESI-MS system and acetonitrile-only dilution (B) Schematic of in-line dilution of droplets into continuous stream. (C) Trace for trifluoromethyl azaindole fragment (m/z = 309) using in-line dilution.

To remove the restrictions in throughput caused by widening of sample bands after dilution while keeping reaction concentrations high, a sheath sprayer was employed (**Figure 9**). Droplets samples emerging from PFA tubing merge into a continuously spraying sheath flow and immediately to ESI-MS analysis. Operation of this system has been shown for analyzing enzymatic reactions at throughputs exceeding 1 droplet/s.[52] For the analysis of droplet photoredox reactions, the sheath flow rate was kept high (100 µL/min) and droplet flow low (0.5-1.0 µL/min) to dilute the droplets (nominally 100-200x) during the electrospray process.

Comparison of In-Droplet vs. Small Scale Batch Reactions

Experiments were conducted to compare reactivity in 4 nL droplets with batch reactions run on a standard multiwell plate screen scale of 20 µL (**Figure 4.11**). 4 nL droplet reactions were prepared and run according to the aforementioned procedures and irradiated for 10 min inside of

our photoreactor. 20 µL reactions were performed in PCR tubes, with the PCR tubes placed directly in the middle of the photoreactor for 10 minutes of irradiation. Following irradiation, the solutions were then formed into 4 nL droplets for direct comparison to the two volume scales. The quotient of the product signal over the summed product and substrate signals ($\frac{P}{P+S}$) was used to appraise reaction progress. For the two substrates that performed the best in the 20 µL reactions (**4.3** and **4.4**), only slight increases in product formation were observed when run in droplet format; however, the increase was drastic for the lower performing substrates (**4.1** and **4.2**) (**Figure 4.11**).

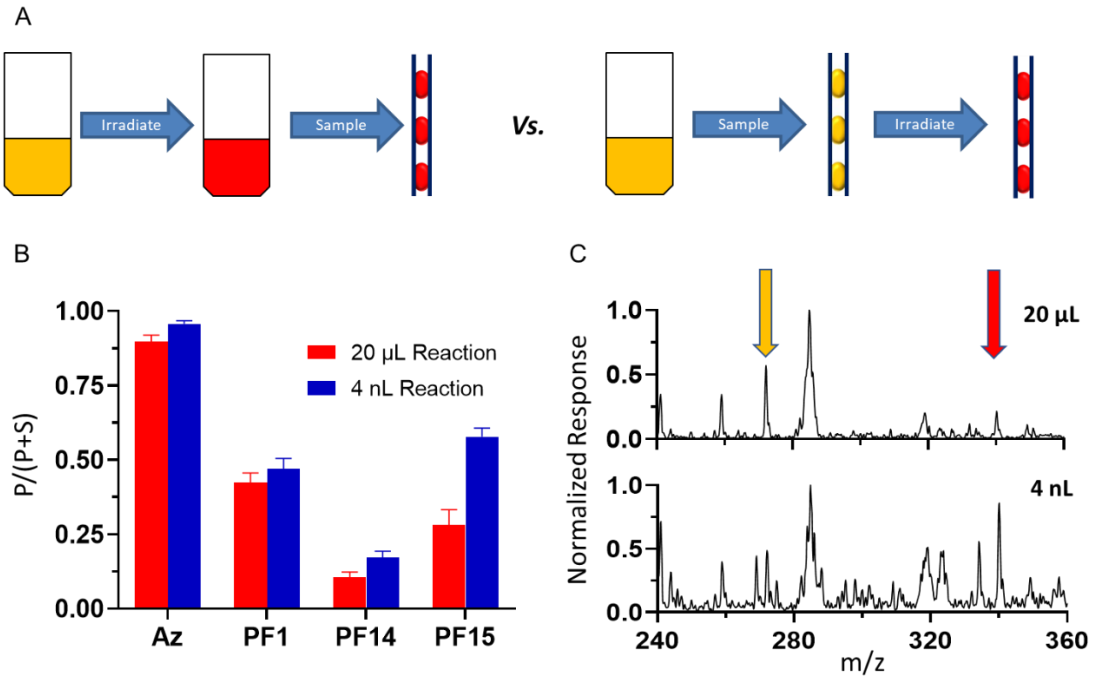

Figure 4.11. Comparison of in-droplet reactions vs. non-droplet batch reactions. (A) General schemes for running reactions at different scales (Left) Reactions run at 20 µL were irradiated immediately after mixing in PCR tubes and then reformatted into 4 nL droplets for analysis (Right) For in-droplet reactions, premixed solution was reformatted into 4 nL droplets, which were then irradiated. (B) Evaluation of performance across 4 substrates in either 20 µL or 4 nL volume. In every case, P/(P+S) response was found to be similar or significantly higher in droplet format. N=20 droplets for each reaction. (C) Example spectra from both 20 µL (Top) or 4 nL (Bottom) volume PF15 reactions. The yellow arrow indicates substrate m/z value, while the red arrow indicates product m/z value. In the 20 µL reaction, the substrate response was over double that of the product; however, the product response was even greater than that of the substrate in the 4 nL reaction.

The observed changes in reaction performance can be attributed to the narrower sample geometry. The 100 µm i.d. tubing presents a drastically narrower pathlength, decreasing the pathlength of irradiation and increasing photon flux across the entire sample. Such an effect may be helpful in promoting the observation of product in poorly performing reactions, or in reducing reaction time requirements for in-droplet reaction screens.

Oscillatory Flow Reactor

To allow for extended flow reactions inside of our PFA tubing, an oscillatory flow scheme was employed (**Figure 6**). We implemented the Stephenson group's visible light-driven alkene aminoarylation reaction[60] as our reactive system of choice to provide us with a manifold for performing high throughput reaction discovery in continuous flow. Droplets were formed from substrate and reaction mixture into a 100 µm i.d. PFA tube, with droplet contents alternating between containing the N-((3,4-difluorophenyl)sulfonyl)acetamide substrate and the N-((4-cyanophenyl)sulfonyl)acetamide substrate, denoted as 3,4 F and 4 CN substrates respectively. A PCR tube had a 400 µm hole drilled into the cap and was filled with PFD. The outlet of the tubing was threaded through the hole and submerged in PFD to avoid evaporation of samples inside of the tubing. Upon irradiation, the droplets were flowed at 200 nL/min, first withdrawing towards the syringe pump for 10 min, followed by 10 min of infusing away from syringe. This process was performed 3 times, allowing for 1 hour of continuous flow reaction. Upon analysis under the same conditions as the previous experiments, both reactions were observable in alternating fashion by monitoring the product m/z traces. Measured turnover for both reactions was found to be significant by $\frac{P}{P+S}$, with values of 0.919 ± 0.022 for the 4 CN substrate and 0.499 ± 0.044 for the 3,4 F substrate in the droplet samples shown in **Figure 4.6** (substrate traces not shown). There was observed variability in the product response for droplets of the same content (RSD in product

response was 16% for both populations), which may indicate variable performance of the sheath sprayer. Further improvement to setup procedures and ESI parameters could help to lower this variability. The current setup allowed for 40 droplets for flow reaction and could conceivably increase to >100 droplets with longer tubing lengths and shorter oscillation periods.

Reagent Addition and Online Screening System

Reagent addition PDMS chips were fabricated to enable individual droplets to be imported from 100 µm i.d. PFA tubing, flowed through an addition region to receive reagents, and then be exported to 150 µm i.d. PFA tubing for irradiation and ESI-MS analysis. Larger 150 µm i.d. tubing was used for the droplets post-addition as the larger volume droplets were sometimes unstable in the 100 µm i.d. tubing. Consistent addition of reagent to 4 nL acetonitrile droplets was achieved with the employed geometry (**Figure 4.12A-C**). By keeping droplet flow consistent (800 nL/min), the amount of reagent added to each droplet was controllable by the flow of the reagent stream. The reagent solution for the trifluoromethylation reaction was utilized in the demonstration of the reagent addition device, as it showed a deep yellow color. At 100 nL/min reagent flow, the final droplets were composed of 33 ± 2% added reagent, while a 200 nL/min reagent flow created droplets with 45 ± 4% added reagent, showing consistent addition to droplets at both flow rates. Also tested was for this geometry was the carry-over between droplets. To test for this, droplets were formed in 10x10 units, alternating between blank acetonitrile samples and trifluoromethylation reagent solution, with blank acetonitrile used as the addition stream. As the reagent addition stream is now colorless, any material carry-over from trifluoromethylation reagent droplets into the addition stream would lead to a yellow hue in the proceeding droplets. From this approach, pure acetonitrile droplets following trifluoromethylation reagent droplets had

no observable yellow coloration, showing that this geometry can be performed with minimal carry-over between droplets (**Figure 4.12D and E**).

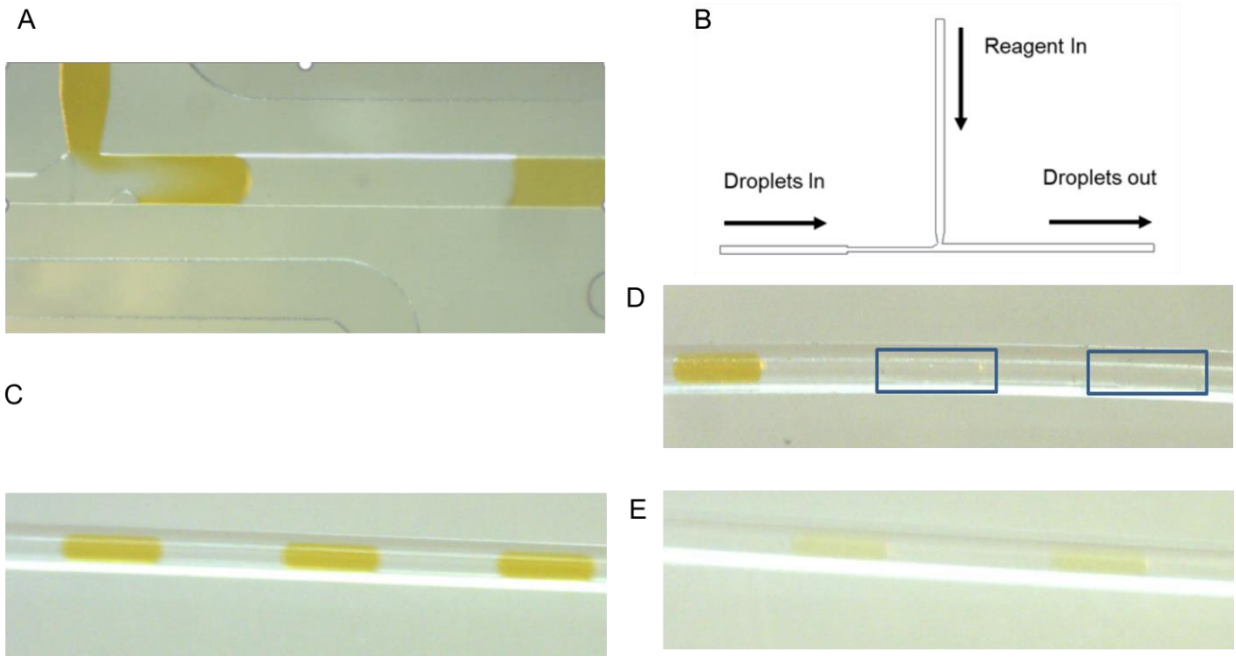

Figure 4.12. Reagent addition device operation. Samples used were either pure acetonitrile (clear, colorless) or trifluoromethylation reagent solution (dark yellow). Droplets were 4 nL initially, with 12 nL PFD spacing. (A) Device in operation. Each incoming droplet from the left received solution from the upper channel and moved right to export. Additional channels on top and bottom of channel were placed for optional saltwater electrodes. This feature was not necessary, as droplets coalesced with reagent stream without application of electric field. (B) Final design of reagent addition device, with electrodes removed. (C) Droplets post addition in PFA tubing. Droplet flow in was 800 nL/min, while reagent addition flow was 200 nL/min. Output droplets were found to contain 45 ± 4% added reagent. (D) Carry-over evaluation. Droplets were generated from either pure acetonitrile or reagent mixture. Blank acetonitrile was added to each droplet. Acetonitrile droplets (highlighted by blue boxes) flowed through addition device after reagent droplets show no coloration, indicating that very low carry-over occurs during the operation of the reagent addition device. (E) Droplets at 6% reagent, showing significantly more yellow coloration than the blank droplets in (D).

The above system was applied to the Smiles-Truce rearrangement described in Section 4.2. 4 nL acetonitrile droplets containing the 4-CN sulfonylacetamide substrate and trans-anethole with 12 nL PFD segmentation were flowed through the reagent addition device at 800 nL/min, with 200 nL/min reagent flow, forming 7 nL reaction droplets for irradiation and analysis. Irradiation time was approximately 7 min, calculated from the volume of tubing contained within the reactor and the 1000 nL/min volumetric flow rate. Analysis of droplets post-irradiation at 20 droplets/min not

only showed that product had formed, but that formation was highly consistent across all the droplet samples (**Figure 4.13**). To confirm that signal was a result of in-droplet chemistry, premixed reaction mixture was made into droplets and analyzed in the same manner. Very little signal was observed, with the droplet samples barely distinguishable from background noise. These results indicate the successful application of our system for performing and analyzing in-droplet photoredox reactions.

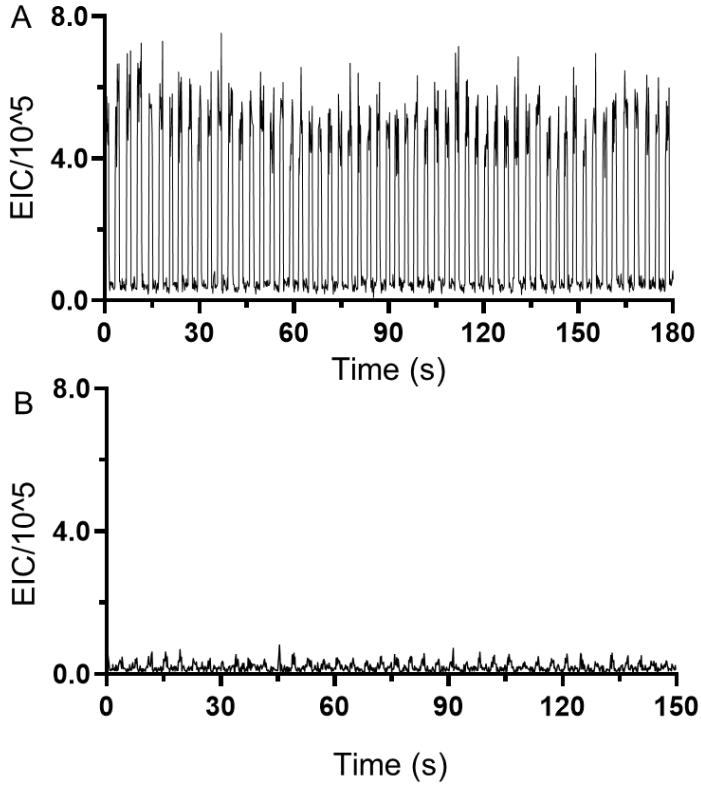

Figure 4.13. Results from online flow reactor and control experiments. Traces represent the m/z values of the Smiles-Truce rearrangement product for the 4-CN sulfonamide and trans-anethole (m/z = 309). (A) Droplet samples processed with online flow reactor. (B) Control samples for (A), where no irradiation was applied. Very little signal was observed, indicating that results from (A) are the result of in-droplet chemistry.

4.4.3 General Experimental Procedures

General Procedure A: Preparation of Trifluoromethylation Reaction Solutions

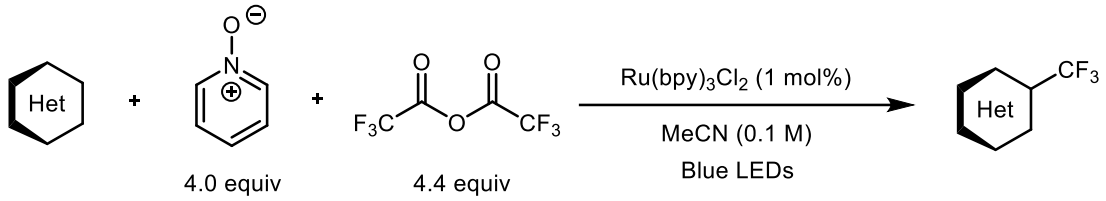

Photocatalyst (1 mol%), pyridine N-oxide (4 equiv), and acetonitrile (0.2 M) were added to a vial charged with a stir bar. The solution was sparged with a stream of nitrogen gas for 5 min. Acetic anhydride (4 equiv) was subsequently added, and the solution was stirred for 10 min to facilitate formation of the acylated species. Separate solutions of substrate in acetonitrile (0.2 M) were also prepared. 10 µL of each solution were combined in a PCR tube to yield the final reaction mixture.

General Procedure B: Preparation of Smiles-Truce Rearrangement Reaction Solutions

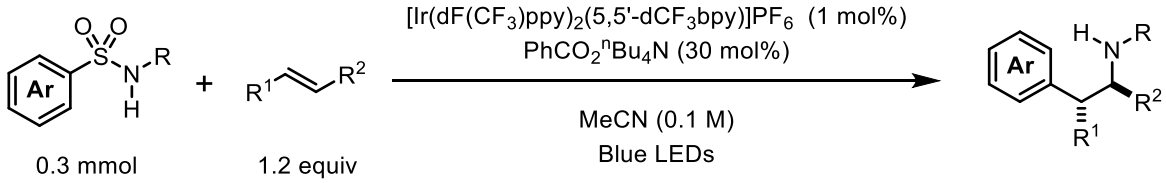

To a flame dried 1-dram vial was added tetrabutylammonium benzoate (30 mol%), and $[Ir(dF(CF_3)ppy)_2(5,5'd(CF_3)bpy)]PF_6$ photocatalyst (1 mol%). The vial contents were then dissolved in anhydrous acetonitrile (0.2 M). Finally, the alkene was added (1.2 equiv). This solution was sparged under argon for 15 min. Separate solutions of substrate in acetonitrile (0.2 M) were also prepared. For reactions formed directly from well-plates, 10 µL of each solution were deposited into a well to form the final reaction mixture. For reagent addition experiments, droplets were formed from substrate solution, and reagents were added on-chip (see Section 4.3.1 for droplet generation procedures).

General Procedure C: In-Droplet Reaction Screen Setup

Following droplet generation, reactor tubing (100 µm i.d., 360 µm o.d.) containing droplets was wrapped around a 100 x 50 mm glass recrystallization dish and placed on top of our 25 LED array light setup (see Figure 3.11 for photoreactor details) for irradiation. Droplet reactions were run at a flow rate of 200 nL/min in an oscillatory manner by programming a syringe pump to alternate between refill and infusion modes at 10 min intervals, yielding a total residence time of 1 h (**Figure 4.14**). Following irradiation, droplet samples were characterized by ESI-MS analysis.

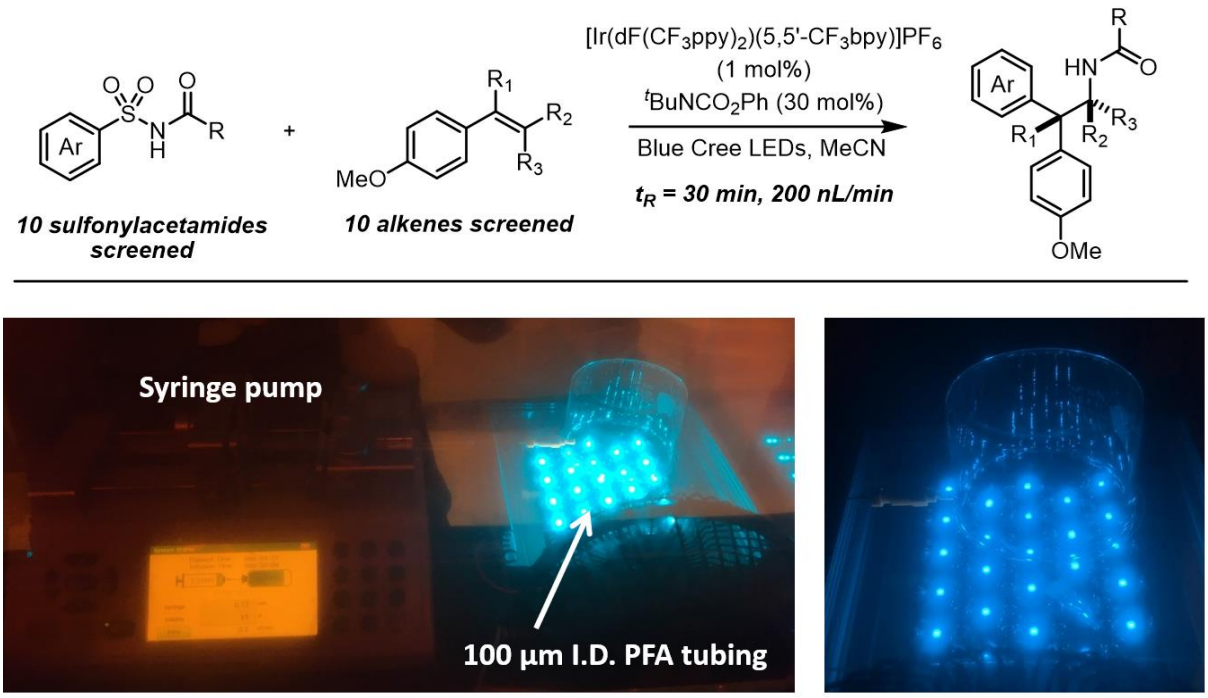

Figure 4.14. Continuous flow setup for in-droplet reaction screens.

General Procedure D: Flow Scale-up (0.01 mmol) Setup

We selected 9 of our droplet reactions to perform 0.01 mmol scale-up in flow to provide sufficient material for product isolation. Reactions were set up according to General Procedure B. These reactions were carried out in the same PFA tubing (100 um i.d., 360 o.d.) and run in a continuous stream (non-droplet format) at a flow rate of 400 nL/min, providing a residence time of 15 min.

Irradiation was performed using the 25 LED array setup described in Chapter 3. Purification was performed using an HPLC-MS (Agilent) with an eluent of 50% MeCN/ H_2O (50% to 100% MeCN/ H_2O across 30 min).

General Procedure E: Flow Scale-up (0.1 mmol) Setup

We selected 9 of our droplet reactions to perform 0.1 mmol scale-up in flow (**Figure 4.15**). Reactions were set up according to General Procedure B. These reactions were carried out in PFA tubing (0.03'' i.d., 1/16'' o.d., 100 μL internal volume) and run in a continuous stream (non-droplet format) at a flow rate of 300 nL/min, providing a residence time of 30 min. Irradiation was performed using the 25 LED array setup described in Chapter 3. Purification was performed using flash chromatography on SiO_2 with an eluent of 70% ethyl acetate (spiked with 1% acetic acid)/hexanes (20% to 70% ethyl acetate/hexanes gradient across 20 min).

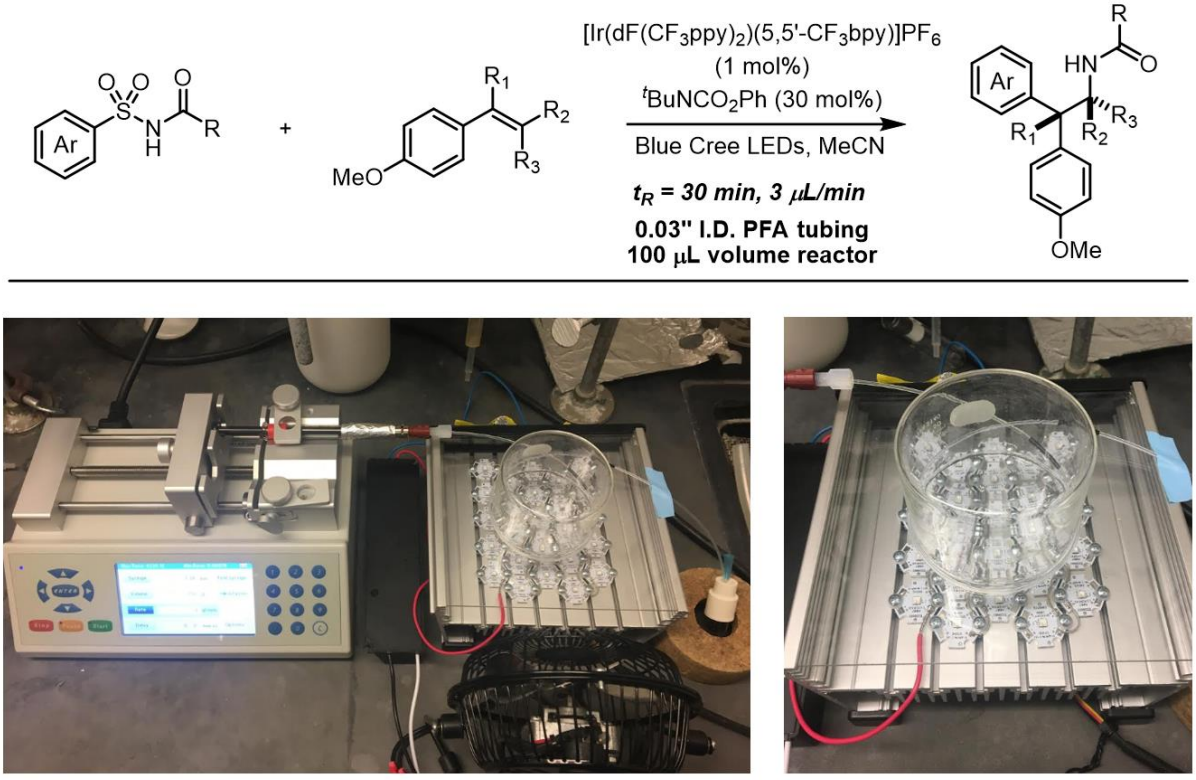

Figure 4.15. Continuous flow setup for 0.1 mmol scale-up reactions.

4.4.4 Compound Characterization

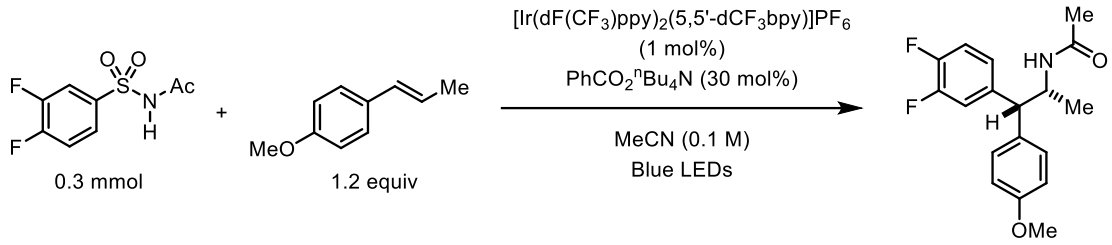

***N*-(1-(3,4-difluorophenyl)-1-(4-methoxyphenyl)propan-2-yl)acetamide (4.5)**

The reaction was run according to General Procedures B and E on 0.1 mmol scale. The crude reaction was purified by column chromatography (20% to 70% ethyl acetate in hexanes; 1% spiked acetic acid in ethyl acetate) to afford the title compound (10 mg, 31%) as a light yellow foam. Rf = 0.20 (ethyl acetate/hexanes 7:3 with 1% acetic acid in ethyl acetate; UV). ^{1}H NMR (700 MHz, $CDCl_3$) δ 7.16 – 7.10 (m, 2H), 7.06 (qd, *J* = 9.4, 3.5 Hz, 2H), 7.02 (s, 1H), 6.87 – 6.78 (m, 2H), 5.19 (s, 1H), 4.82 – 4.74 (m, 1H), 3.77 (d, *J* = 3.1 Hz, 3H), 3.75 (d, *J* = 9.3 Hz, 1H), 1.86 – 1.81 (m, 3H), 1.13 – 1.06 (m, 3H). ^{13}C NMR (176 MHz, $CDCl_3$) δ 169.3, 158.5, 150.8 (d, *J* = 12.7 Hz), 149.7 (d, *J* = 12.3 Hz), 149.4 (d, *J* = 13.2 Hz), 148.3 (d, *J* = 12.6 Hz), 139.4, 133.3, 129.1, 123.6, 117.3 (d, *J* = 17.0 Hz), 116.9 (d, *J* = 17.4 Hz), 114.2, 56.5, 55.2, 47.7, 23.3, 20.1. The acquired ^{1}H and ^{13}C NMR spectral data corresponding to the product were identical to those reported in the literature.[60]

^{1}H NMR (700 MHz, $CDCl_3$) for **4.5**

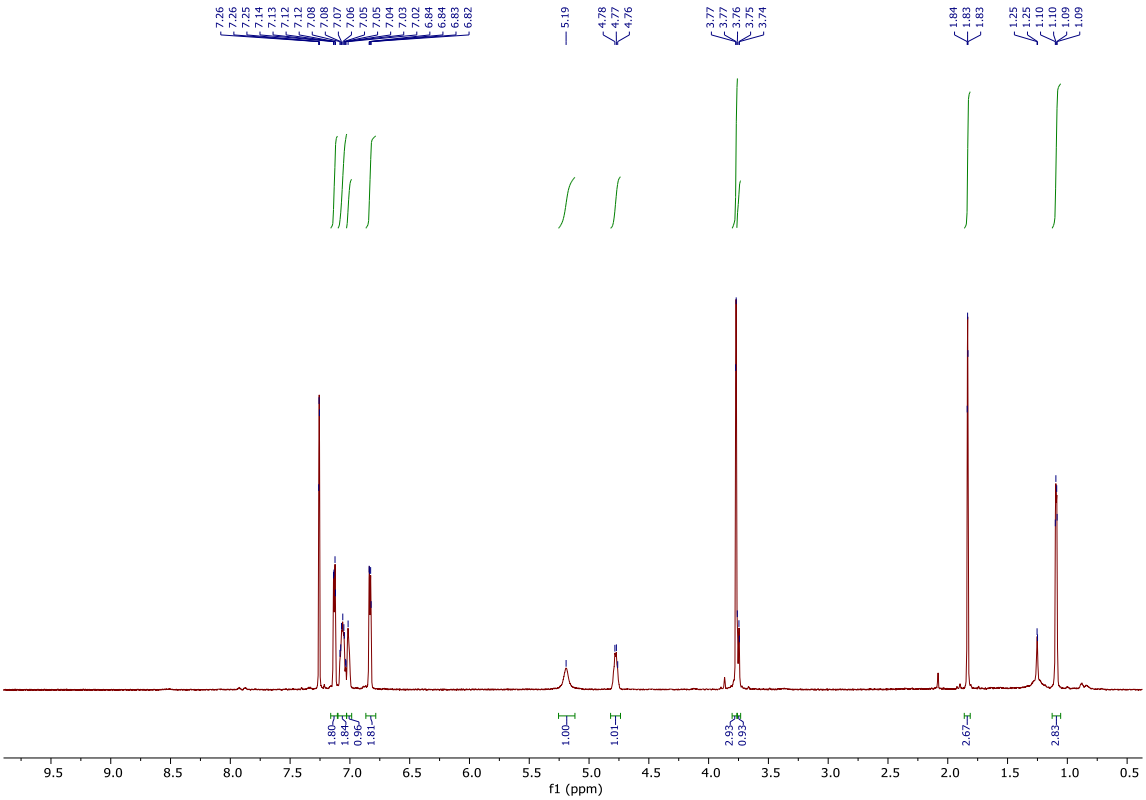

^{13}C NMR (176 MHz, $CDCl_3$) for **4.5**

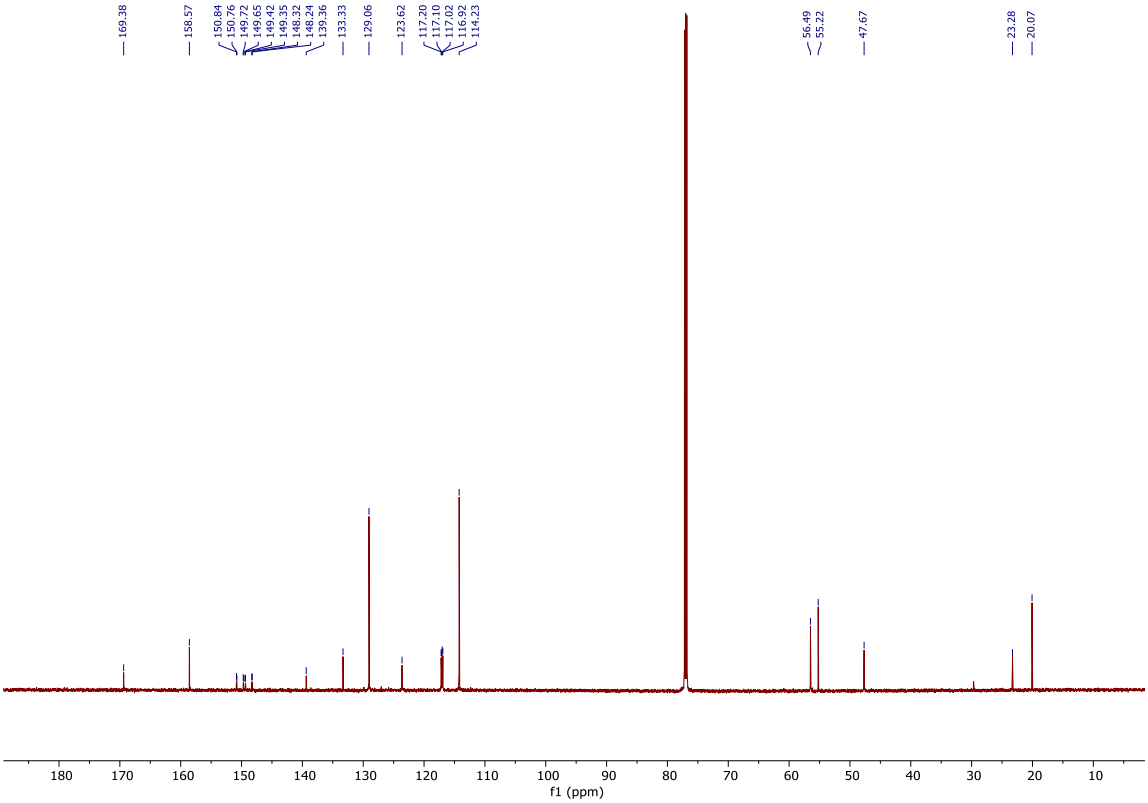

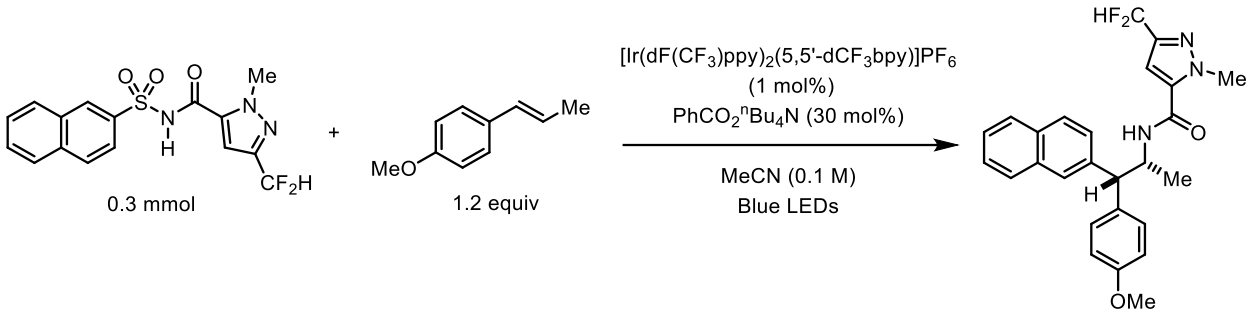

3-(difluoromethyl)-*N*-1-(4-methoxyphenyl)-1-(naphthalen-2-yl)propan-2-yl)-1-methyl-1H-pyrazole-5-carboxamide (4.6)

The reaction was run according to General Procedures B and E on 0.1 mmol scale. The crude reaction was purified by column chromatography (20% to 70% ethyl acetate in hexanes; 1% spiked acetic acid in ethyl acetate) to afford the title compound (16 mg, 35%) as a light yellow foam. Rf = 0.24 (ethyl acetate/hexanes 7:3 with 1% acetic acid in ethyl acetate; UV). ^{1}H NMR (500 MHz, $CDCl_3$) δ 8.17 (d, *J* = 8.6 Hz, 1H), 7.80 (d, *J* = 8.1 Hz, 1H), 7.73 – 7.66 (m, 2H), 7.59 (s, 1H), 7.51 – 7.39 (m, 3H), 7.30 (d, *J* = 8.3 Hz, 2H), 6.80 (dd, *J* = 6.3, 3.9 Hz, 2H), 6.51 (t, *J* = 54.2 Hz, 2H), 6.03 (s, 1H), 5.12 – 5.02 (m, 1H), 4.72 (d, *J* = 10.2 Hz, 1H), 3.81 (s, 3H), 3.73 (d, *J* = 1.2 Hz, 3H), 1.27 (d, *J* = 6.5 Hz, 3H). ^{13}C NMR (176 MHz, $CDCl_3$) δ 160.5, 158.3, 142.8 (t, *J* = 27.6 Hz), 137.4, 134.1, 134.1, 133.7, 132.0, 129.5, 128.9, 127.2, 126.0, 125.5, 125.2, 124.3, 123.2, 116.9, 114.0, 111.0 (t, *J* = 233.9 Hz), 55.2, 51.7, 48.5, 39.3, 20.5. ^{19}F NMR (471 MHz, $CDCl_3$) δ -110.14 (dd, *J* = 1476.3, 54.1 Hz), -110.14 (dd, *J* = 862.4, 54.5 Hz).

^{1}H NMR (500 MHz, $CDCl_3$) for **4.6**

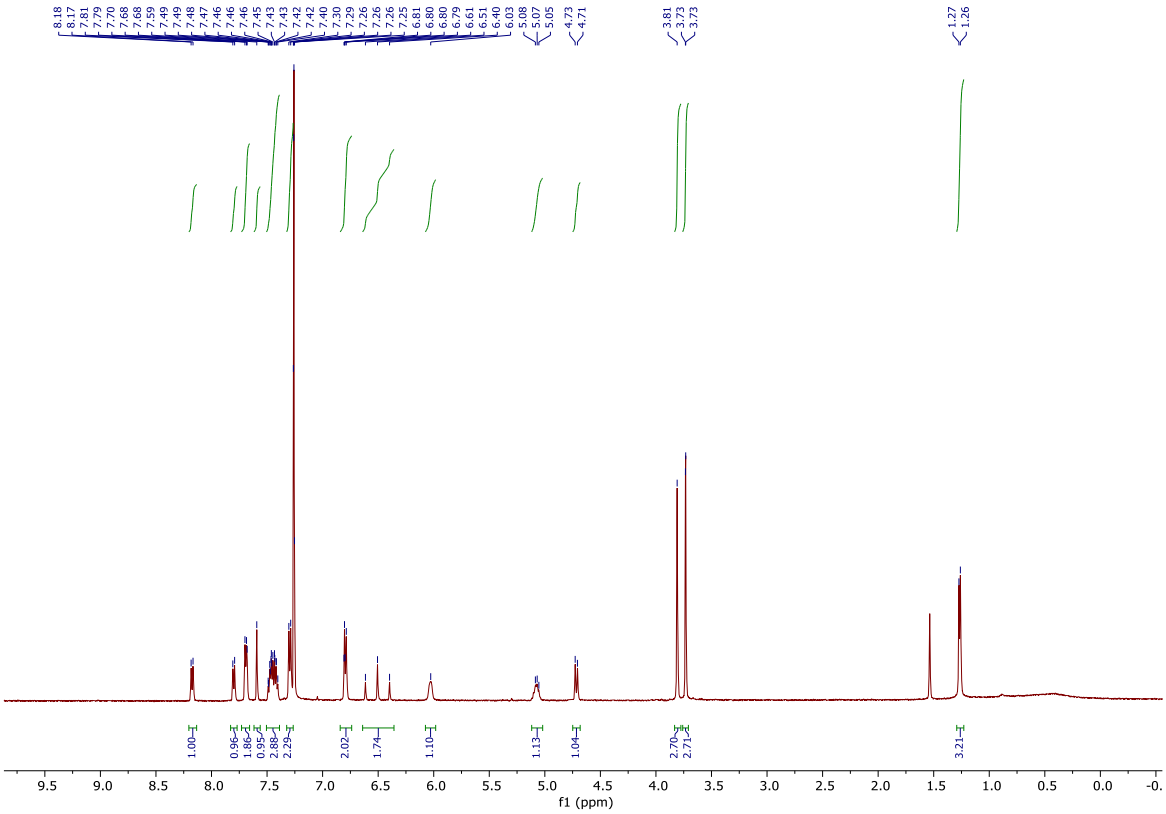

^{13}C NMR (176 MHz, $CDCl_3$) for **4.6**

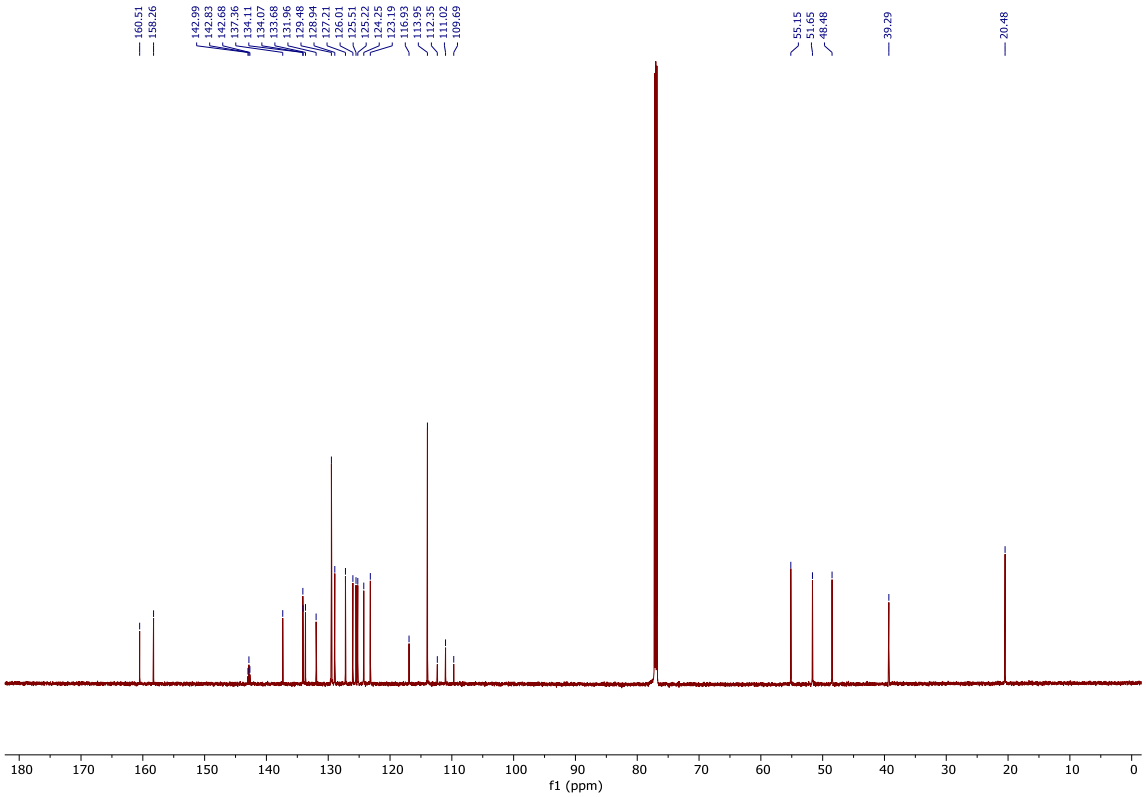

^{19}F NMR (471 MHz, $CDCl_3$) for **4.6**

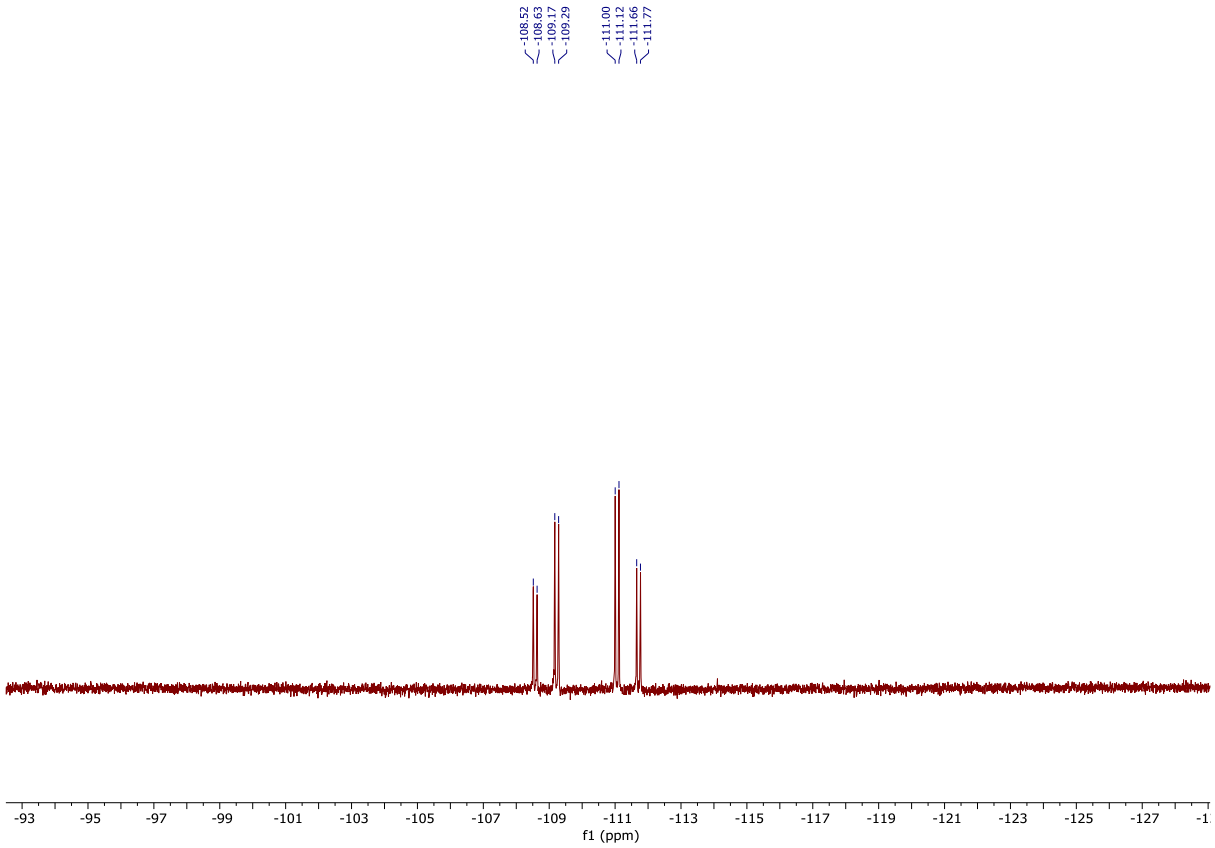

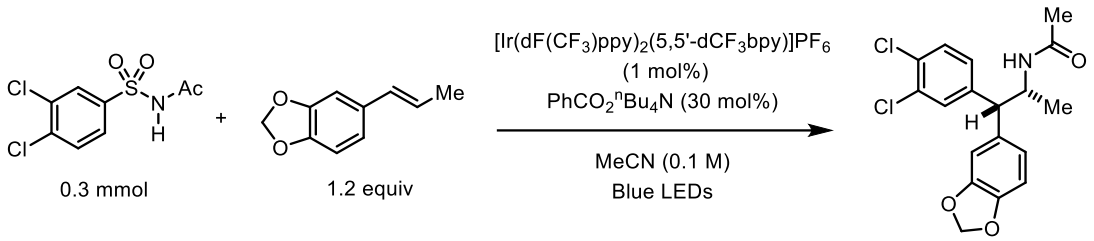

***N*-1-(benzo[d][1,3]dioxol-5-yl)-1-(3,4-dichlorophenyl)propan-2-yl)acetamide (4.7)**

The reaction was run according to General Procedures B and E on 0.1 mmol scale. The crude reaction was purified by column chromatography (20% to 70% ethyl acetate in hexanes; 1% spiked acetic acid in ethyl acetate) to afford the title compound (10 mg, 27%) as a light yellow foam. Rf = 0.25 (ethyl acetate/hexanes 7:3 with 1% acetic acid in ethyl acetate; UV). ^{1}H NMR (500 MHz, $CDCl_3$) δ 7.37 – 7.31 (m, 2H), 7.16 (dd, *J* = 8.3, 2.2 Hz, 1H), 6.73 (d, *J* = 7.8 Hz, 1H), 6.71 – 6.66 (m, 2H), 5.95 – 5.89 (m, 2H), 5.13 (d, *J* = 9.2 Hz, 1H), 4.76 (d, *J* = 6.4 Hz, 1H), 3.70 (d, *J* = 10.3 Hz, 1H), 1.83 (s, 3H), 1.11 (d, *J* = 6.6 Hz, 3H). ^{13}C NMR (176 MHz, $CDCl_3$) δ 169.2, 148.1, 146.7, 142.3, 134.9, 132.4, 130.6, 130.5, 130.2, 126.9, 121.3, 108.5, 108.2, 101.1, 57.1, 47.3, 23.4, 20.2.

^{1}H NMR (500 MHz, $CDCl_3$) for **4.7**

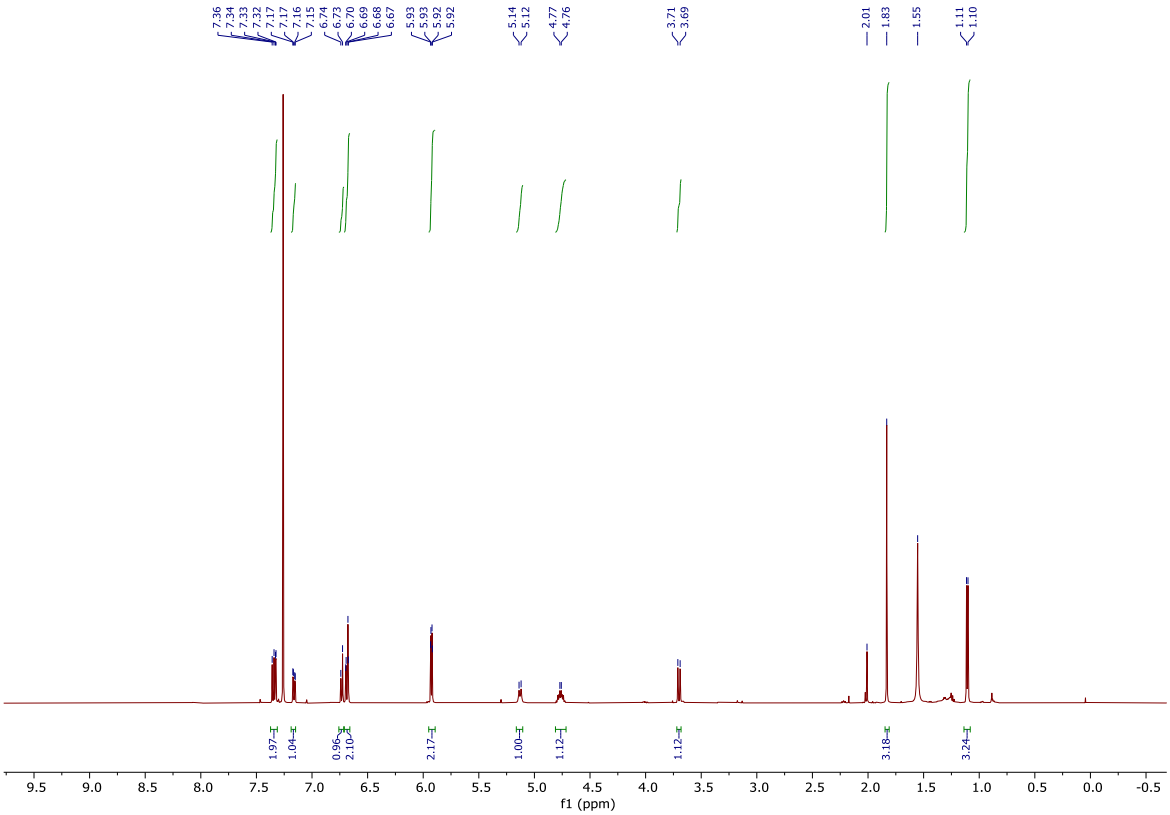

^{13}C NMR (176 MHz, $CDCl_3$) for **4.7**

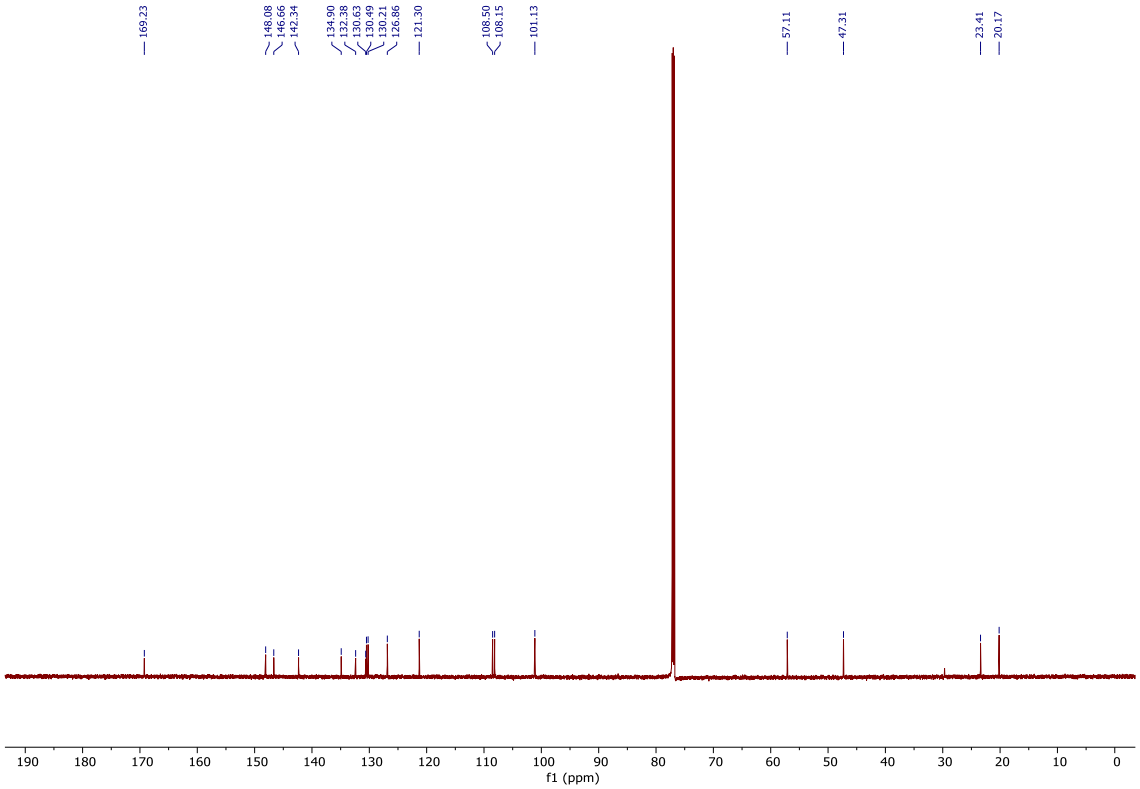

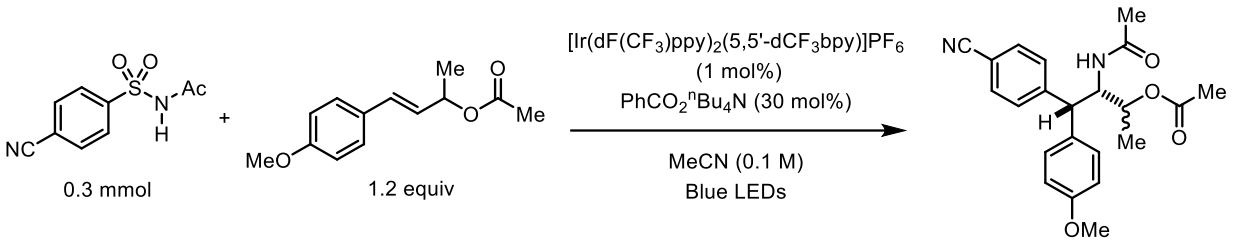

3-acetamido-4-(4-cyanophenyl)-4-(4-methoxyphenyl)butan-2-yl acetate (4.8)

The reaction was run according to General Procedures B and E on 0.1 mmol scale. The crude reaction was purified by column chromatography (20% to 70% ethyl acetate in hexanes; 1% spiked acetic acid in ethyl acetate) to afford the title compound (5 mg, 13%) as a light yellow foam. Rf = 0.22 (ethyl acetate/hexanes 7:3 with 1% acetic acid in ethyl acetate; UV). A 1:1.5 ratio of diastereomers (minor diastereomer **4.8A** and major diastereomer **4.8B**) was observed by ^{1}H and ^{13}C NMR. ^{1}H NMR (700 MHz, $CDCl_3$) δ 7.57 – 7.54 (m, 2H, 8A), 7.55 – 7.52 (m, 2H, 8B), 7.43 (d, *J* = 7.8 Hz, 2H, 8A), 7.40 – 7.35 (m, 2H, 8B), 7.25 – 7.22 (m, 2H, 8B), 7.07 (d, *J* = 8.1 Hz, 2H, 8A), 6.87 – 6.83 (m, 2H, 8B), 6.83 – 6.80 (m, 2H, 8A), 5.43 (d, *J* = 10.3 Hz, 1H, 8A), 5.29 (d, *J* = 5.0 Hz, 1H, 8B), 5.27 (s, 1H, 8A), 5.14 (d, *J* = 10.3 Hz, 1H, 8B), 4.90 (t, *J* = 11.0 Hz, 1H, 8A), 4.83 (d, *J* = 5.3 Hz, 1H, 8B), 4.74 (d, *J* = 6.6 Hz, 1H, 8A), 3.94 (d, *J* = 11.8 Hz, 1H, 8A), 3.85 (d, *J* = 11.2 Hz, 1H, 8B), 3.76 (d, *J* = 1.7 Hz, 3H, 8B), 3.75 (d, *J* = 1.8 Hz, 3H, 8A), 2.14 (d, *J* = 1.8 Hz, 3H, 8A), 1.96 (d, *J* = 1.8 Hz, 3H, 8B), 1.85 (d, *J* = 1.8 Hz, 3H, 8A), 1.81 (d, *J* = 1.8 Hz, 3H, 8B), 1.18 – 1.16 (m, 3H, 8A), 1.16 – 1.13 (m, 3H, 8B). ^{13}C NMR (176 MHz, $CDCl_3$) δ 170.6, 170.0, 169.8, 169.4, 158.9, 158.9, 147.5, 147.4, 132.4, 132.3, 131.9, 131.6, 128.8, 128.7, 128.7, 128.5, 118.8, 118.7, 114.7, 114.6, 110.5, 110.4, 70.2, 70.1, 55.2, 55.2, 54.3, 53.9, 53.3, 52.1, 23.2, 23.1, 21.2, 21.1, 17.4, 13.8.

^{1}H NMR (700 MHz, $CDCl_3$) for **4.8A** and **4.8B**

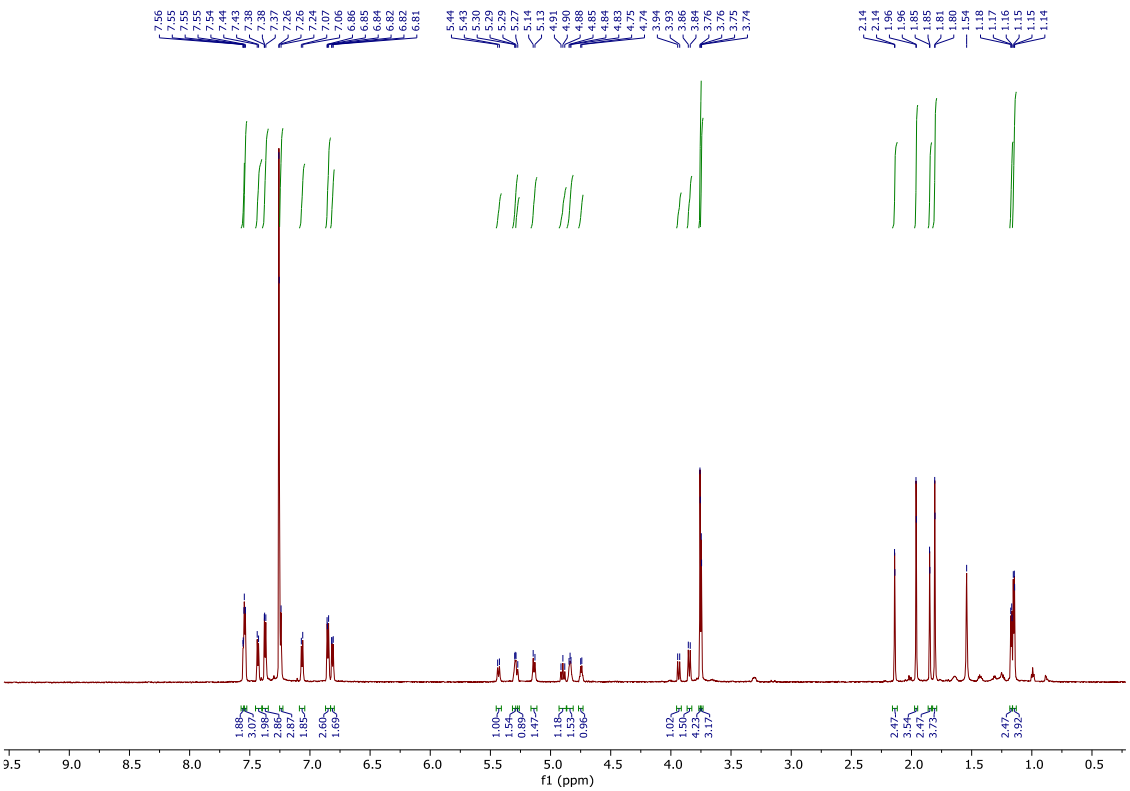

^{13}C NMR (176 MHz, $CDCl_3$) for **4.8A** and **4.8B**

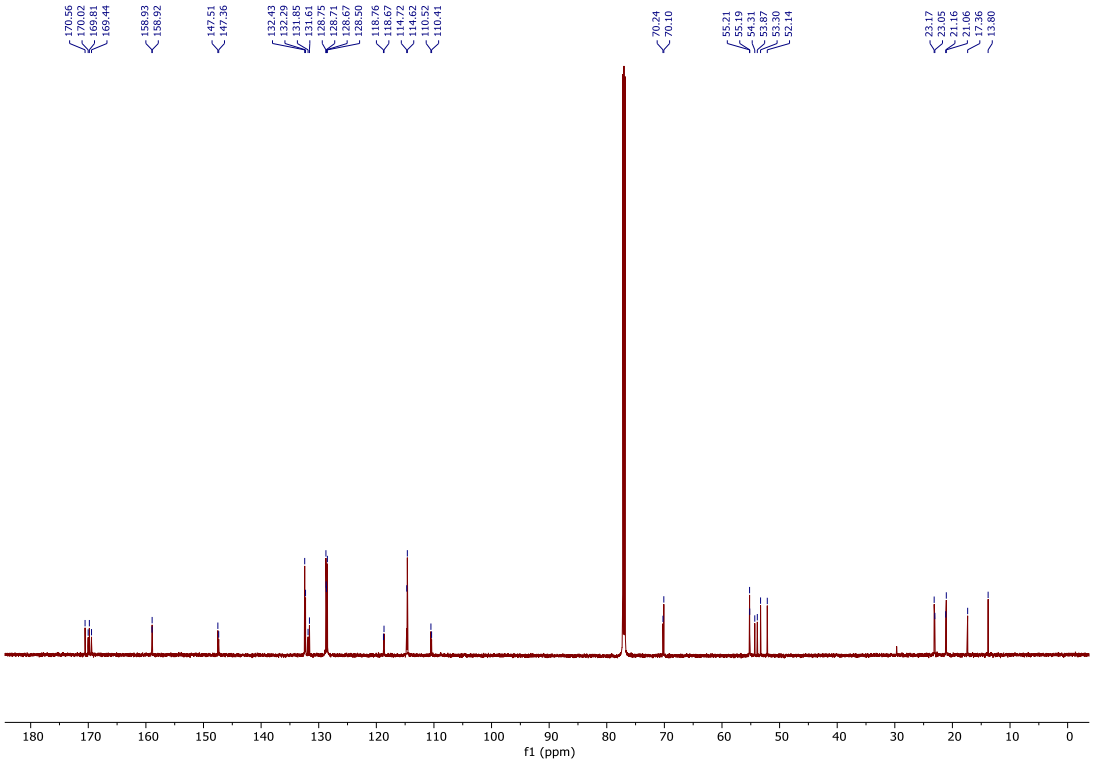

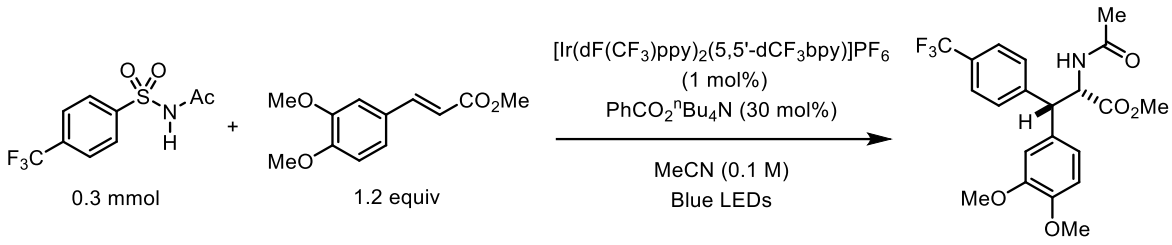

Methyl-(2-acetamido-3-(3,4-dimethoxyphenyl)-3-(4-(trifluoromethyl)phenyl)propanoate (4.9)

The reaction was run according to General Procedures B and E on 0.1 mmol scale. The crude reaction was purified by column chromatography (20% to 70% ethyl acetate in hexanes; 1% spiked acetic acid in ethyl acetate) to afford the title compound (7 mg, 15%) as a light yellow foam. Rf = 0.23 (ethyl acetate/hexanes 7:3 with 1% acetic acid in ethyl acetate; UV). ^{1}H NMR (700 MHz, $CDCl_3$) δ 7.57 (d, *J* = 8.0 Hz, 2H), 7.38 (d, *J* = 7.9 Hz, 2H), 6.80 – 6.74 (m, 2H), 6.72 (s, 1H), 5.67 (d, *J* = 9.2 Hz, 1H), 5.45 (t, *J* = 9.2 Hz, 1H), 4.40 (d, *J* = 9.1 Hz, 1H), 3.84 (s, 3H), 3.82 (s, 3H), 3.53 (d, *J* = 1.8 Hz, 3H), 1.90 (d, *J* = 1.9 Hz, 3H). ^{13}C NMR (176 MHz, $CDCl_3$) δ 172.2, 169.8, 149.0, 148.4, 143.9, 131.4, 129.5 (q, *J* = 32.6 Hz), 128.6, 125.7 (q, *J* = 3.7 Hz), 124.0 (q, *J* = 272.0 Hz), 120.5, 111.3, 111.2, 55.9, 55.8, 55.0, 53.2, 52.3, 23.1. ^{19}F NMR (471 MHz, $CDCl_3$) δ -62.59.

^{1}H NMR (700 MHz, $CDCl_3$) for **4.9**

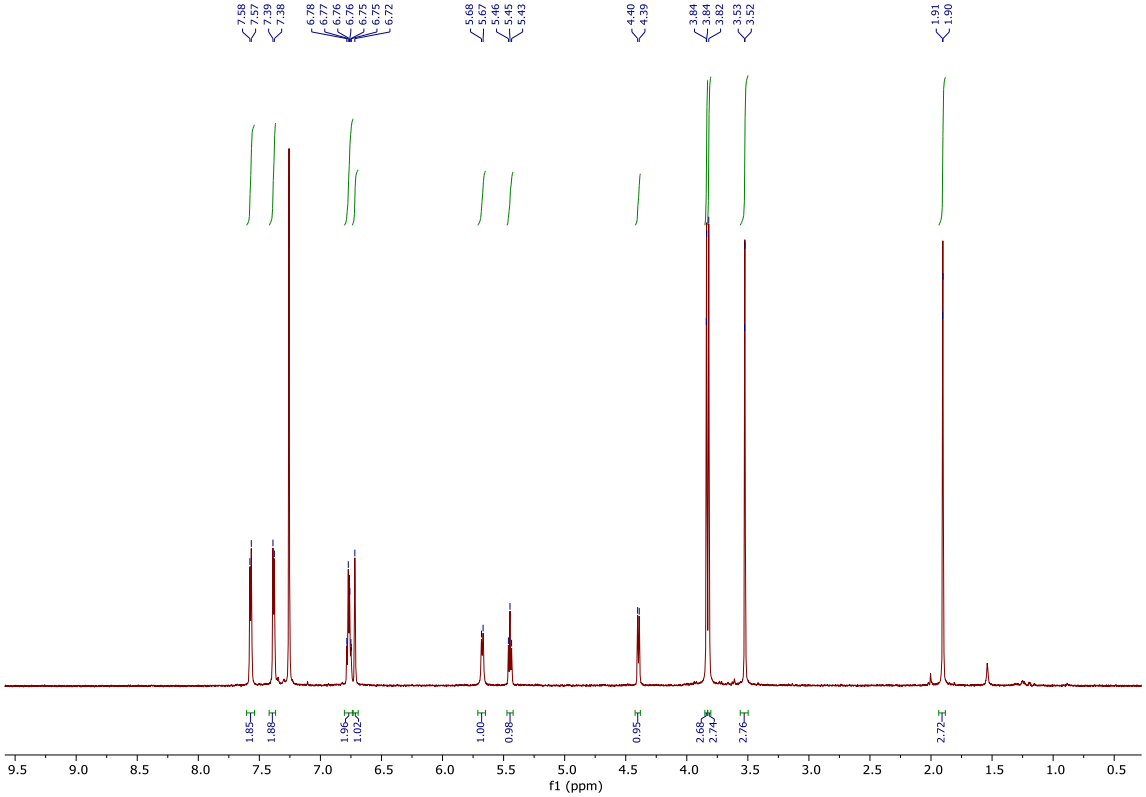

^{13}C NMR (176 MHz, $CDCl_3$) for **4.9**

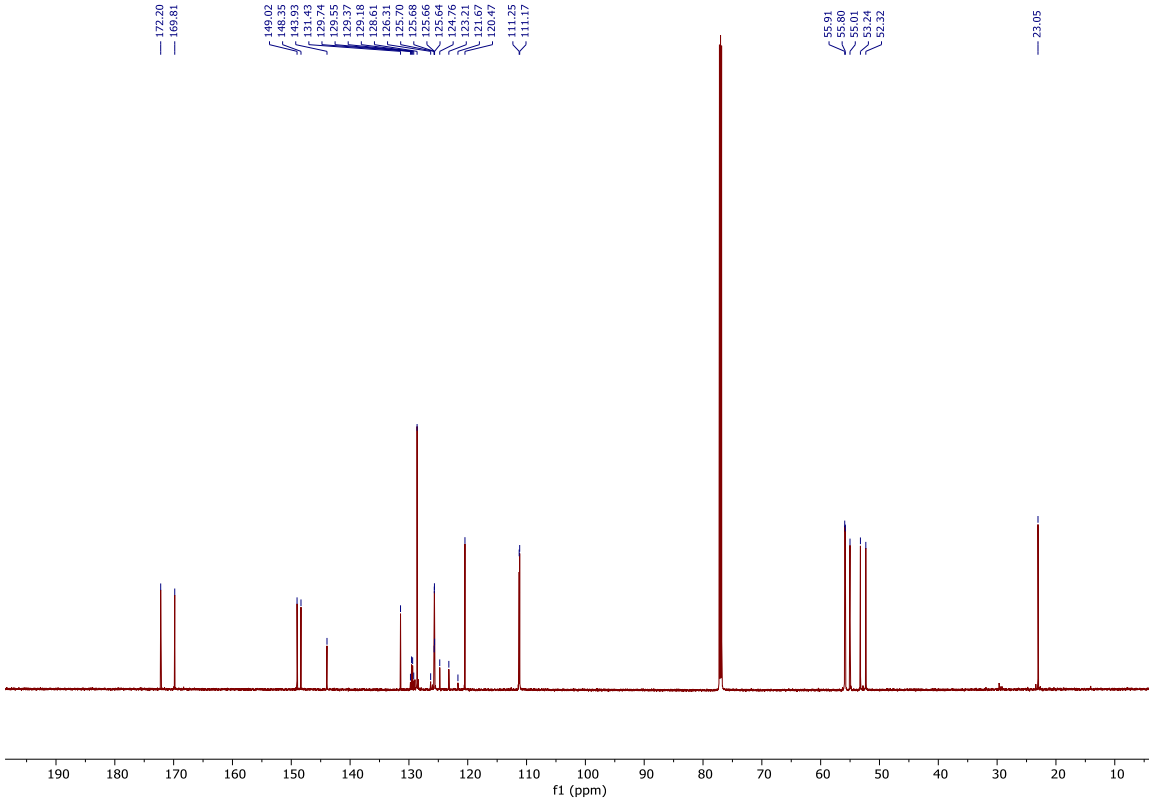

^{19}F NMR (471 MHz, $CDCl_3$) for **4.9**

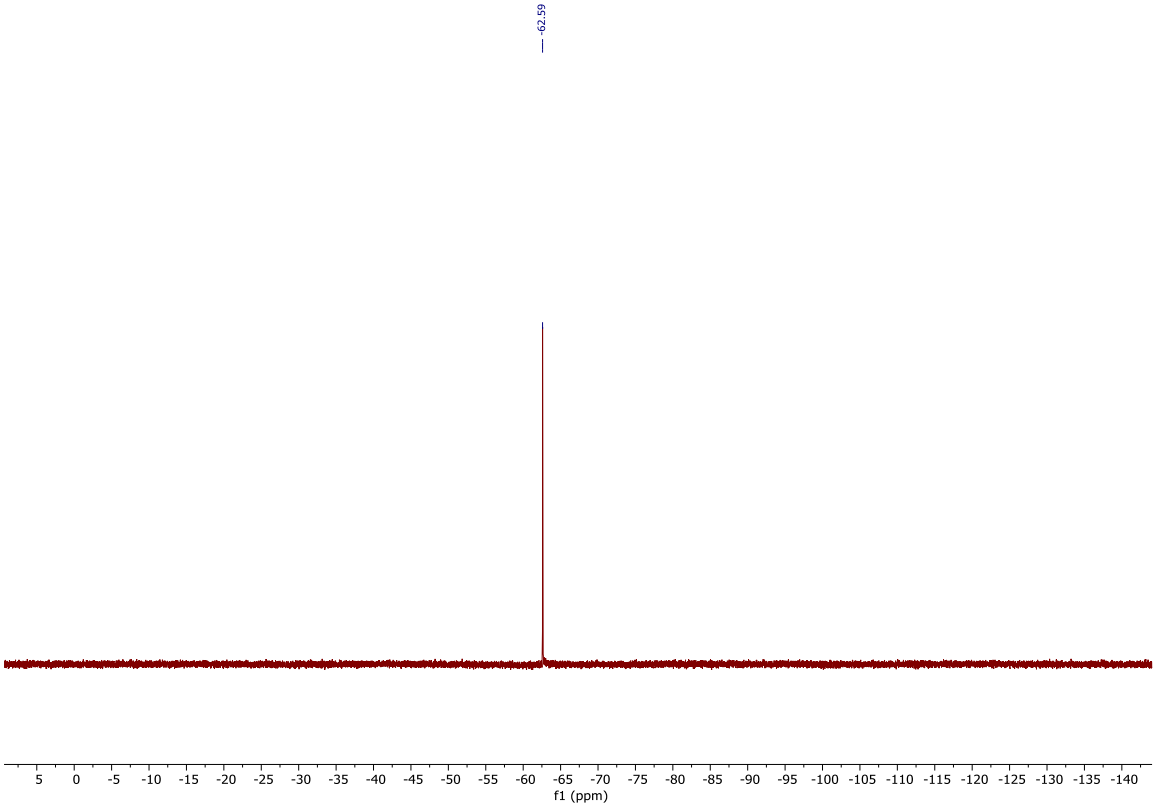

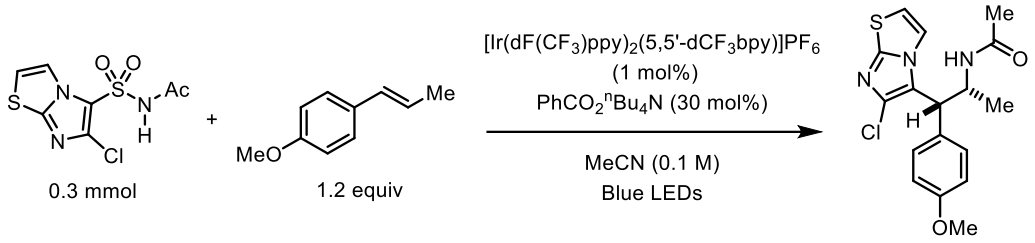

***N*-1-(6-chloroimidazo[2,1-b]thiazol-5-yl)-1-(4-methoxyphenyl)propan-2-yl)acetamide (4.10)**

The reaction was run according to General Procedures B and E on 0.1 mmol scale. The crude reaction was purified by column chromatography (20% to 70% ethyl acetate in hexanes; 1% spiked acetic acid in ethyl acetate) to afford the title compound (25 mg, 68%) as a light yellow foam. Rf = 0.19 (ethyl acetate/hexanes 7:3 with 1% acetic acid in ethyl acetate; UV). ^{1}H NMR (700 MHz, $CDCl_3$) δ 7.24 (d, *J* = 6.6 Hz, 2H), 7.17 (d, *J* = 4.4 Hz, 1H), 6.86 (d, *J* = 8.3 Hz, 2H), 6.74 (d, *J* = 4.5 Hz, 1H), 5.33 (d, *J* = 9.2 Hz, 1H), 5.00 (q, *J* = 8.4 Hz, 1H), 4.34 (d, *J* = 9.4 Hz, 1H), 3.78 (d, *J* = 2.6 Hz, 3H), 1.80 (d, *J* = 2.7 Hz, 3H), 1.29 (d, *J* = 6.5 Hz, 3H). ^{13}C NMR (176 MHz, $CDCl_3$) δ 169.5, 158.8, 147.0, 131.9, 129.8, 129.0, 121.8, 118.5, 114.4, 112.1, 55.2, 46.8, 46.2, 23.4, 20.6.

^{1}H NMR (700 MHz, $CDCl_3$) for **4.10**

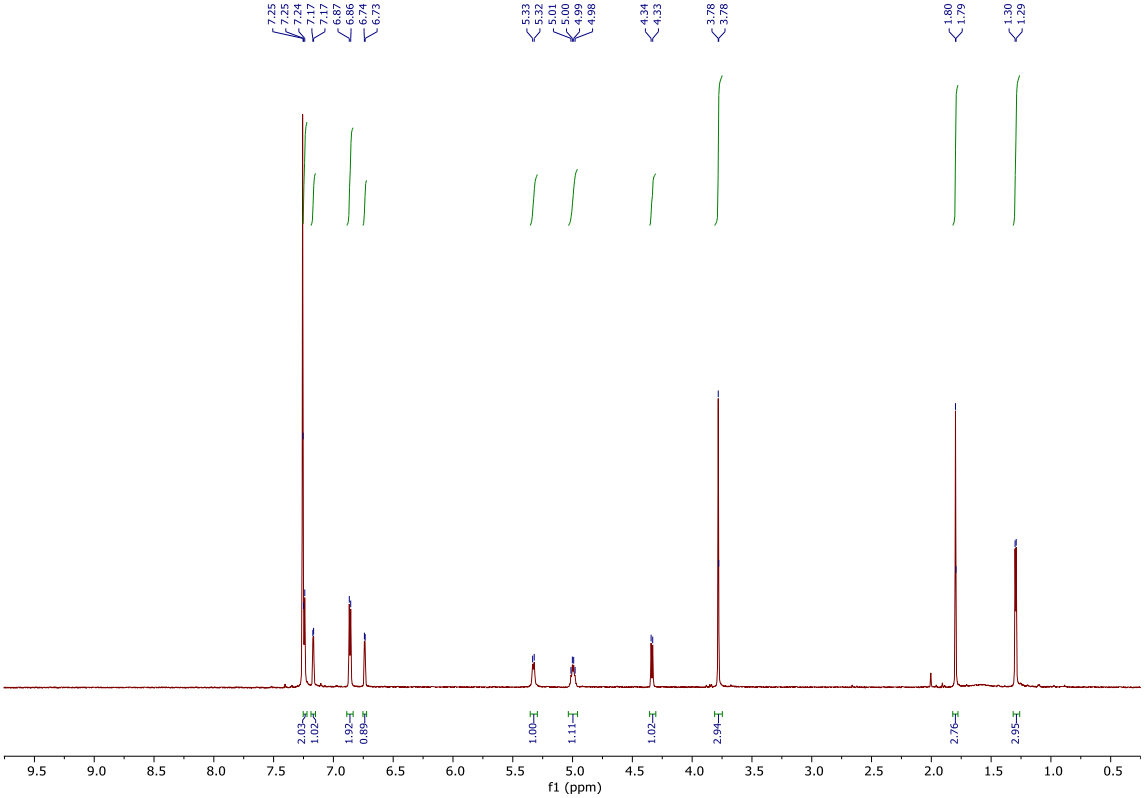

^{13}C NMR (176 MHz, $CDCl_3$) for **4.10**

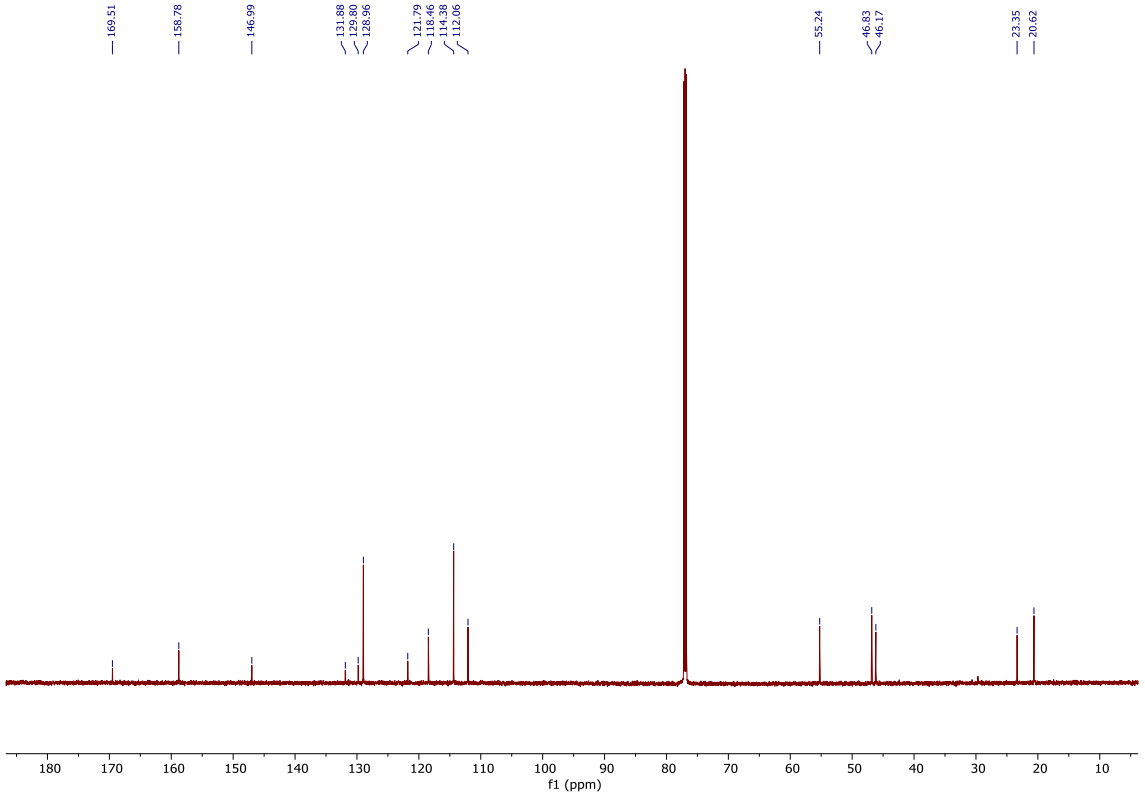

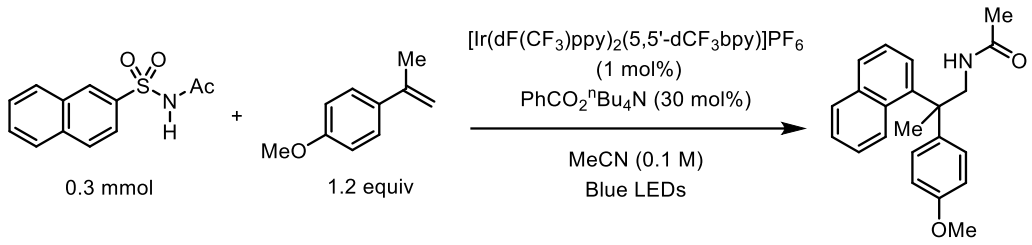

***N*-(2-(4-methoxyphenyl)-2-(naphthalen-1-yl)propyl)acetamide (4.11)**

The reaction was run according to General Procedures B and E on 0.1 mmol scale. The crude reaction was purified by column chromatography (20% to 70% ethyl acetate in hexanes; 1% spiked acetic acid in ethyl acetate) to afford the title compound (7 mg, 20%) as a light yellow foam. Rf = 0.26 (ethyl acetate/hexanes 7:3 with 1% acetic acid in ethyl acetate; UV). ^{1}H NMR (700 MHz, $CDCl_3$) δ 7.82 (t, *J* = 9.6 Hz, 2H), 7.64 (d, *J* = 7.5 Hz, 1H), 7.50 (t, *J* = 7.8 Hz, 1H), 7.47 (d, *J* = 8.8 Hz, 1H), 7.34 (t, *J* = 7.3 Hz, 1H), 7.14 (t, *J* = 7.9 Hz, 1H), 7.10 (d, *J* = 8.4 Hz, 2H), 6.84 – 6.78 (m, 2H), 4.90 (s, 1H), 4.28 – 4.21 (m, 1H), 4.01 (dd, *J* = 13.3, 4.1 Hz, 1H), 3.78 (d, *J* = 2.5 Hz, 3H), 1.85 (d, *J* = 2.5 Hz, 3H), 1.78 (s, 3H). ^{13}C NMR (176 MHz, $CDCl_3$) δ 170.1, 157.9, 141.0, 139.5, 135.1, 130.9, 129.2, 128.5, 127.3, 127.0, 125.0, 125.0, 125.0, 124.9, 114.1, 55.2, 49.0, 47.0, 27.7, 23.4.

^{1}H NMR (700 MHz, $CDCl_3$) for **4.11**

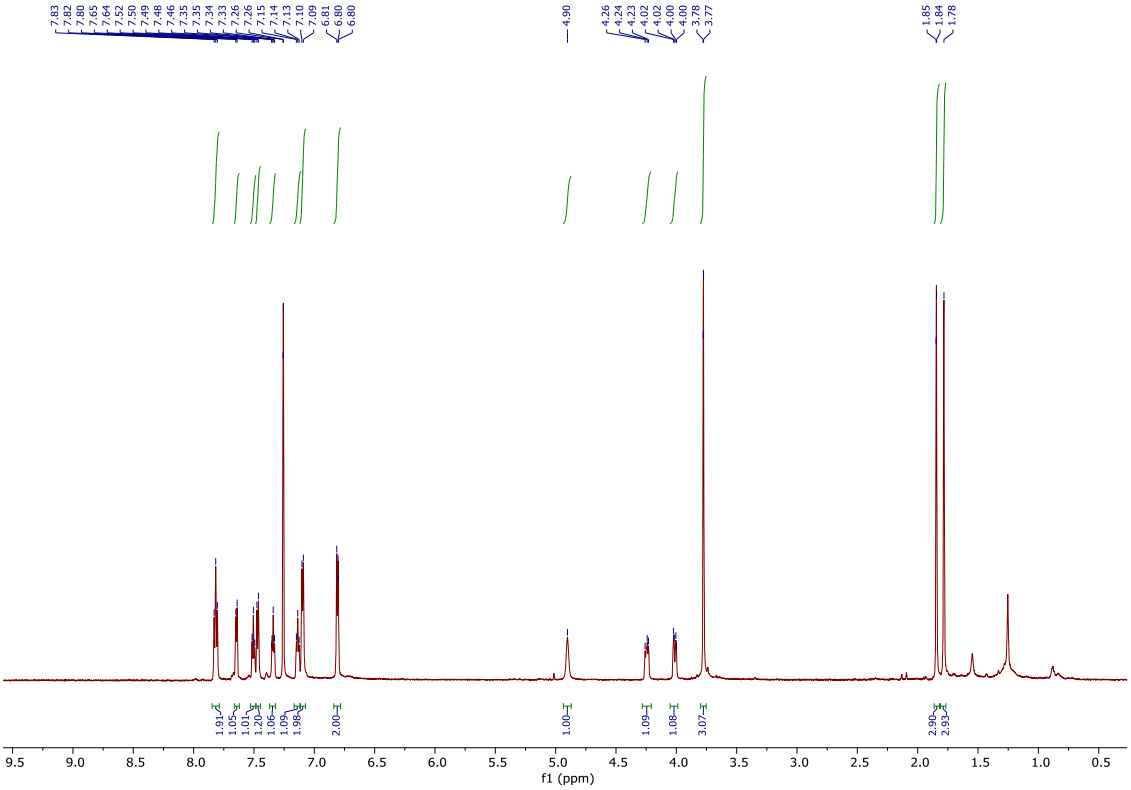

^{13}C NMR (176 MHz, $CDCl_3$) for **4.11**

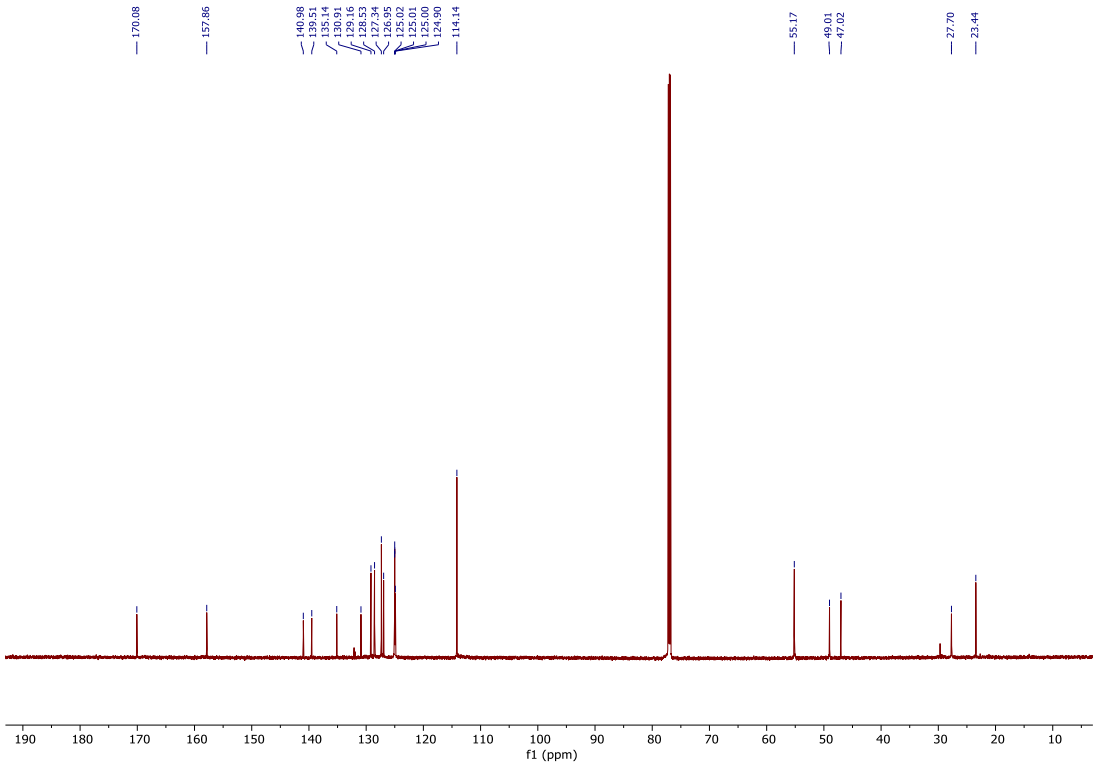

Chapter 5: Synthesis and Derivatization of $Ir(III)^+$ Polypyridyl Complexes using Microwave Heating

Portions of this chapter have been published in Timothy M. Monos, Alexandra C. Sun, Rory C. McAtee, James J. Devery III, Corey R. J. Stephenson, *J. Org. Chem*. **2016**, *81*, 6988-6994.

5.1 Introduction

5.1.1 Preparation and Applications of Heteroleptic $Ir(III)^+$ Polypyridyl Complexes

The development of visible light-mediated redox catalysis is an energy conscious response to the multifaceted challenges of chemical sustainability.[255] In this context, photoabsorbing Ru(II) and Ir(III) polyimine complexes have been widely applied in organic light emmiting diodes (OLEDs)[256], organic synthesis[257,258], polymer synthesis[259,260], oxygen sensors[261] and bio-analytical devices[262]. The field of photoredox catalysis has adopted Ru(II) and Ir(III) complexes in preference to other metals[263,264] due to the fact that these complexes are bench stable solids with highly efficient photophysical properties and tunable reactivity. Such characteristics have enabled these complexes to be used in the exploration of small molecule synthesis[257,258], natural product synthesis[265,266,267] and multi-catalytic technologies[268,269,270,271] in an effort to develop safe and sustainable synthetic methods.

Among the variety of known polypyridyl Ir(III) complexes[272], the cationic, heteroleptic Ir(III) complexes represent a relatively new class of photosensitizers. The ligand scaffold (**Figure 5.1A**) is a combination of two cyclometalating ligands [(C^N) = arylpyridine] and one dative ligand [(N^N) = bipyridine] that give rise to a substitutionally inert, photoexcitable species.[273] Such heteroleptic complexes were originally developed by Bernhard, Malliaras, and coworkers, to improve upon Ru(II) and neutral Ir(III)-based electroluminescent materials.[274,275] $Ir(III)^+$

chromophores exhibit superior chemical stability, as well as a higher quantum yield, than the corresponding Ru(II) materials. This boost in performance has been attributed to the improved photophysical characteristics of ligand field stabilization energy (LFSE) and decreased non-radiative quenching tendencies.[276]

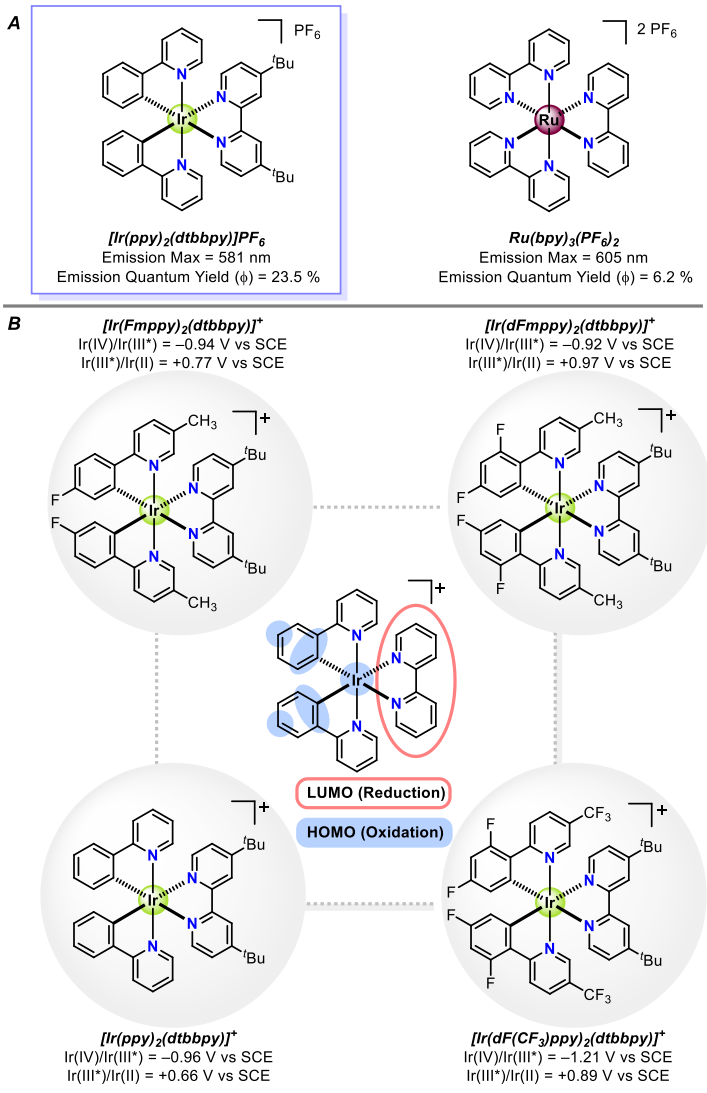

Figure 5.1. (A) Comparison of the archetypical Ru and Ir polyimine complexes and (B) orthogonal tuning of Ir(III)$^+$ redox behavior based on ligand choice.

A significantly notable characteristic of the Ir(III)$^+$ heteroleptic complexes is the spatial separation of redox events that allow for individual, redox tuning. Specifically, the HOMOs are understood to exist between the Ir metal center and the C^N ligand, and the LUMOs are separately

located on the N^N ligand (**Figure 5.1B**). Bernhard and Malliaras experimentally demonstrated this phenomenon by comparing the redox events of various fluorinated $Ir(III)^+$ complexes. In this manner, incorporation of fluorine substituents on the C^N ligand increased the oxidation potential by 100 mV while the reduction potential was minimally affected.[275] This phenomenon was observed previously by King and Watts, who detected two separate metal-to-ligand charge transfer (MLCT) emission peaks from the excitation of $Ir(ppy)_2(bpy)^+$ – one emission peak corresponding to the MLCT–N^N transition (major process) and the second corresponding to the MLCT–C^N transition (minor process).[277] These results support the notion that the HOMOs and LUMOs are spatially separated and that orthogonal electrochemical modulation is possible through the independent variation of the C^N and N^N ligand electronics.[278]

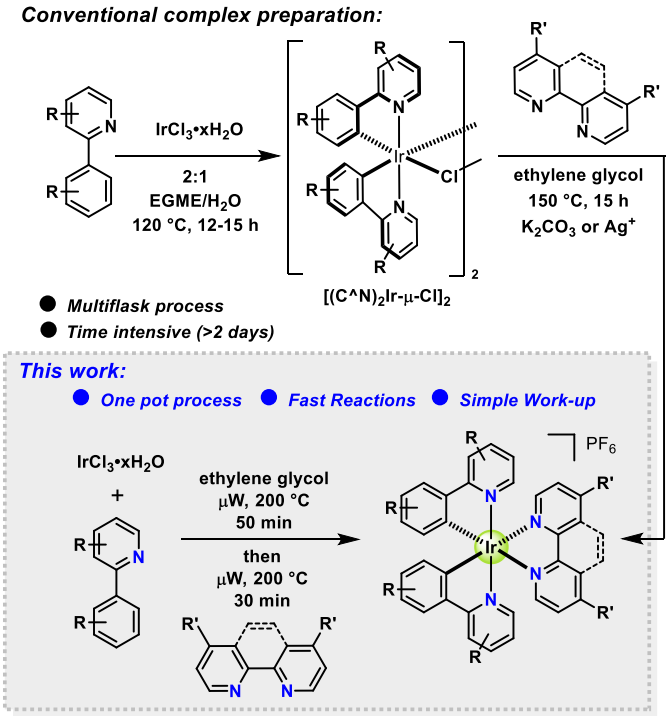

Figure 5.2. Synthesis of $Ir(III)^+$ complexes

Despite the great utility of these compounds, synthetic methods for their production are time and energy intensive. These requirements can limit the screening diversity of catalysts during

project development, thus minimizing the actual benefits of this design aspect. By convention, there are two methods for producing $Ir(III)^+$ polypyridyl complexes (**Figure 5.2**). Both of these methods rely on the initial synthesis of an $[(C\text{^}N)_2Ir\text{-}\mu\text{-}Cl]_2$ dimer. From this intermediate, a dative bipyridyl ligand can be introduced by either cracking the dimer through silver salt metathesis[279], or by an additional reflux step with the dative ligand.[280] In both cases, these multi-step processes require between 12 and 24 hours, totaling more than 48 hours for the synthesis of a single complex.

We have alleviated the time and energy requirements necessary for the synthesis of heteroleptic $Ir(III)^+$ complexes through microwave heating. Microwave heating utilizes polar solvents for highly efficient internal temperature regulation[281,282,283,284,285], allowing for rapid temperature equilibration and in many cases, enhanced reaction kinetics.[286,287] Microwave heating has proven beneficial in a number of contexts including transition metal catalysis[284], continuous flow processing[288], and combinatorial chemistry.[281] These reports bolster this technique as a *bona fide* method for reliably heating, scaling, and conducting synthetic operations in a reasonable time frame.[289] In this report, we detail the application of microwave heating towards the synthesis of heteroleptic $Ir(III)^+$ complexes in a high yielding, operationally simple protocol, which can be completed in 3 hours.

We identified the benefits of microwave heating in the application of organometallic $Ir(III)^+$ complex synthesis because of the canonically chosen reaction solvent, ethylene glycol. Ethylene glycol is one of the best solvents for microwave heating, boasting a "heating" factor quotient ($\tan\delta$) of 1.350. This quotient is calculated by the ratio of the dielectric loss factor (ε'') – which indicates heating efficiency – over the dielectric constant (ε') – which describes the polarization of the molecule – and indicates the possibility of microwave excitation (**Equation 1**). For example, these

values range from ethylene glycol to non-polar solvents such as toluene (1.350 and 0.040, respectively) (**Figure 5.3**).[290]

$$\tan\delta = \frac{\varepsilon''}{\varepsilon'}$$

Equation 1. Heating Factor Quotient

Additionally, we sought microwave heating as an optimal tool for catalyst synthesis because the reaction course from $IrCl_3 \bullet xH_2O$ to $Ir(C\hat{}N)_2(N\hat{}N)^+$ displayed diagnostic color and solubility changes. The organometallic Ir complexes were differentially colored and soluble in ethylene glycol, whereas the $IrCl_3 \bullet xH_2O$ was an insoluble black powder.[291] We later followed this with a formal optimization of the two ligation processes.

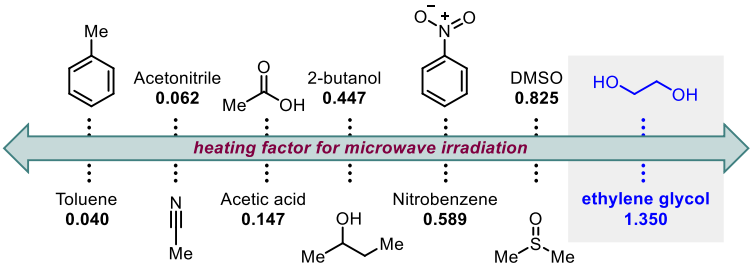

Figure 3. *tan*δ Values (heating factor) for common solvents in organic synthesis

5.1.2 Synthesis of Transition Metal-Based Nanohoop Complexes

Cycloparaphenylenes (CPPs), also referred to as carbon nanohoops, represent a unique class of compounds that possess strikingly distorted phenylene moieties and radially oriented π-systems. The [*n*]CPPs are composed of *n* benzene rings linked end-to-end at the para positions, which results in a rigid, three dimensional, fully sp^2 hybridized cylindrical molecular structure. Initially designed as building blocks for the size-selective growth of carbon nanotubes, [*n*]CPPs have garnered significant synthetic interest since their seminal preparation in 2008 by Jasti, Bertozzi, and co-workers.[292,293,294] The bent cyclic geometries of [*n*]CPPs have given rise to a wealth of novel, unexpected electronic and photophysical properties, which show significant promise for

future materials science applications.[295,296] [*n*]CPPs possess unique electronic properties, including a HOMO–LUMO energy gap that decreases as the number of phenylenes in the hoop are reduced, as well as a red-shifting fluorescence associated with decreasing size.[297,298] This trend is opposite to that observed for the linear paraphenylene species, in which the HOMO–LUMO energy gap decreases with increased chain length, due to extended conjugation. In fact, [*n*]CPPs have narrower HOMO–LUMO gaps than even the longest linear paraphenylene species, thereby highlighting their potential in the design of novel organic semiconductors. Additionally, the presence of a radially oriented π-system provides a hydrophobic, electron-rich cavity that enables effective host-guest interactions with electron poor guest substrates such as C_{60}.[299] Given the combination of these unique chemical properties, [*n*]CPPs have been investigated as biocompatible fluorophores for targeted live cell imaging, as well as electronic materials that are tunable by functionalization or guest uptake.[300,301,302]

The development of novel redox active ligands is critical in the design of highly efficient and selective transition metal complexes for applications including small molecule activation, photocatalysis, and photovoltaics. Since many redox active ligands utilized in chemical catalysis are derived from flat, linear aromatic scaffolds, the incorporation of three dimensional, cyclic aromatic ligands into metal-ligand frameworks would offer new avenues for catalyst design and reactivity. In 2017, Jasti and co-workers reported the first synthetic method for accessing 2,2'-bipyridyl (bipy)-embedded nanohoops in a size selective and scalable manner (**Figure 3.4**).[303] They were able to demonstrate the successful synthesis of both a homoleptic Pd(II) nanohoop dimer and a Ru(II) nanohoop complex. These bipyridyl-containing CPP nanohoops show promise as a new class of ligands for the construction of cylindrical coordination cages, as well as transition metal photosensitizers with supramolecular capabilities.

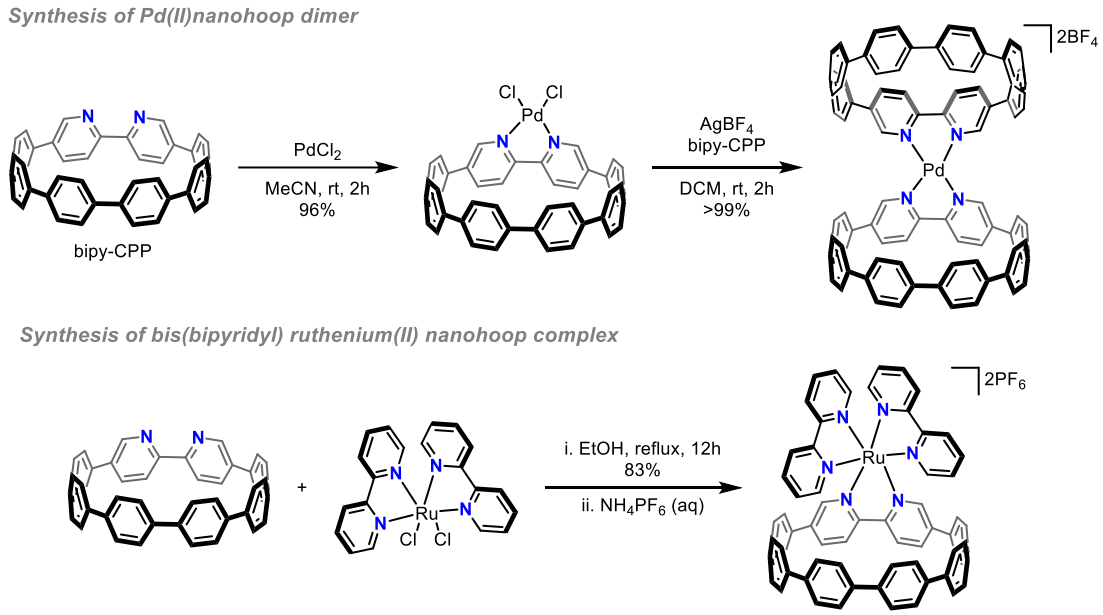

Figure 5.4. Current examples of 2,2'-bipy-embedded nanohoop transition metal complexes

Given the prevalence of heteroleptic $Ir(III)^+$ polypyridyl complexes in photocatalysis and photovoltaics, we aimed to explore the synthesis of iridium-based transition metal complexes containing the 2,2'-bipy-embedded CPP ligand. We envision that the introduction of CPP nanohoops into common iridium photosensitizers could unlock new opportunities for tuning the electronic and photophysical properties of these transition metal complexes to facilitate catalysis. At the same time, the incorporation of a nanohoop ligand framework could potentially generate a chiral environment for supramolecular host-guest interactions to enable asymmetric catalysis. We have been able to utilize our reported microwave synthetic procedure[304] to synthesize a library of heteroleptic $Ir(III)^+$ polypyridyl nanohoop complexes. Additionally, we have carried out initial studies on the electronic and photophysical properties of these complexes using cyclic voltammetry and UV-vis spectroscopy.

5.2 Results and Discussion

5.2.1 Microwave-Assisted Synthesis of Common Ir(III)$^+$ Photocatalysts and Analogs

In our initial studies, we investigated the generation of the $[Ir(dF(CF_3)ppy)_2Ir\text{-}\mu\text{-}Cl]_2$ dimeric species *en route* to $[Ir(dF(CF_3)ppy)_2(dtbbpy)]PF_6$. We highlight the synthetic process with this C^N ligand because we sought a robust cyclometallation protocol capable of utilizing either electron deficient or electron rich C^N ligands, while notably the cyclometallation of electron poor arylpyridines was expected to be more difficult. Heating a mixture of $IrCl_3 \bullet xH_2O$ and 2 equivalents of 2-(2,4-difluorophenyl)-5-(trifluoromethyl)pyridine (***L1***) in ethylene glycol with microwave irradiation provided $[(dF(CF_3)ppy)_2Ir\text{-}\mu\text{-}Cl]_2$ in 40% yield, after 1 hour (**Figure 5.5**, **Entry 1**). This reaction was visibly heterogeneous, consisting of amorphous green solids which were attributed to unreacted $IrCl_3$.[291] Increasing the equivalents of ***L1*** provided a slight increase in yield to 52% (**Entry 2**). The highest yield of the $[(dF(CF_3)ppy)_2Ir\text{-}\mu\text{-}Cl]_2$ dimer (59%) was obtained with 8 equivalents of the cyclometalling ***L1*** ligand after 1 hour of reaction time (**Entry 3**). Extending the reaction time or changing the reaction temperature (250 °C, in triethylene glycol monoethyl ether) failed to increase dimer yield and only resulted in dimer decomposition (**Entry 4** and **Entry 5**). Under identical reaction conditions, the $[(ppy)_2Ir\text{-}\mu\text{-}Cl]_2$ dimer was isolated in 84% yield (**Entry 6**), thus supporting our original hypothesis on the difference in reactivity among 2-arylpyridine derivatives. While the use of 8 equivalents of ***L1*** or ***L2*** is seemingly excessive, the high ligand concentration is thought to neutralize the stoichiometric HCl generated during cyclometallation. Additionally, the mass balance of 2-phenylpyridine ligands could be recovered by an organic extraction following the reaction.

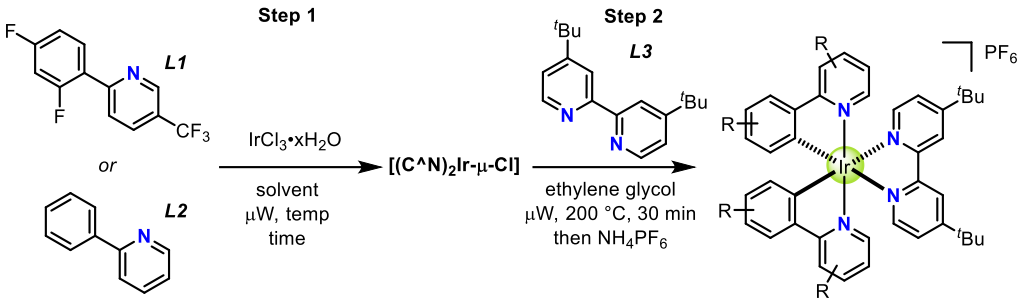

Entry	Ligand	Temperature/Solvent	equiv	Step 1 Time (% Yield)	Step 2 % Yield*
1	L1	200 °C/ethylene glycol	2	1 h (40)	-
2	L1	200 °C/ethylene glycol	4	1 h (52)	-
3	**L1**	**200 °C/ethylene glycol**	**8**	**1 h (59)**	**96**
4	L1	200 °C/ethylene glycol	8	4 h (0)	-
5	L1	250 °C/triethylene glycol monoethyl ether	8	1 h (0)	-
6	**L2**	**200 °C/ethylene glycol**	**8**	**1 h (84)**	**98**

Figure 5.5. Optimization of reaction conditions

The second step of the one-pot sequence was performed by simply opening the microwave reaction vial, adding 4,4'-di-*tert*-butyl-2,2'-bipyridine (***L3***) and recapping for another irradiation cycle. Notably, this avoided the addition of silver salts[279] or exogenous base (K_2CO_3)[280] in order to facilitate the second ligation event. Conversion of the dimeric $[(dF(CF_3)ppy)_2Ir\text{-}\mu\text{-}Cl]_2$ complex to $[Ir(dF(CF_3)ppy)_2(dtbbpy)]PF_6$ was successfully accomplished using 1.5 equivalents of the N^N ligand ***L3*** and microwave heating for 30 minutes, followed by anion metathesis with ammonia hexafluorophosphate to give a 96% isolated yield (**Entry 3**, Step 2). Conversion of the $[(ppy)_2Ir\text{-}\mu\text{-}Cl]_2$ dimer gave the $[Ir(ppy)_2(dtbbpy)]PF_6$ complex in high yield (**Entry 6**, Step 2).

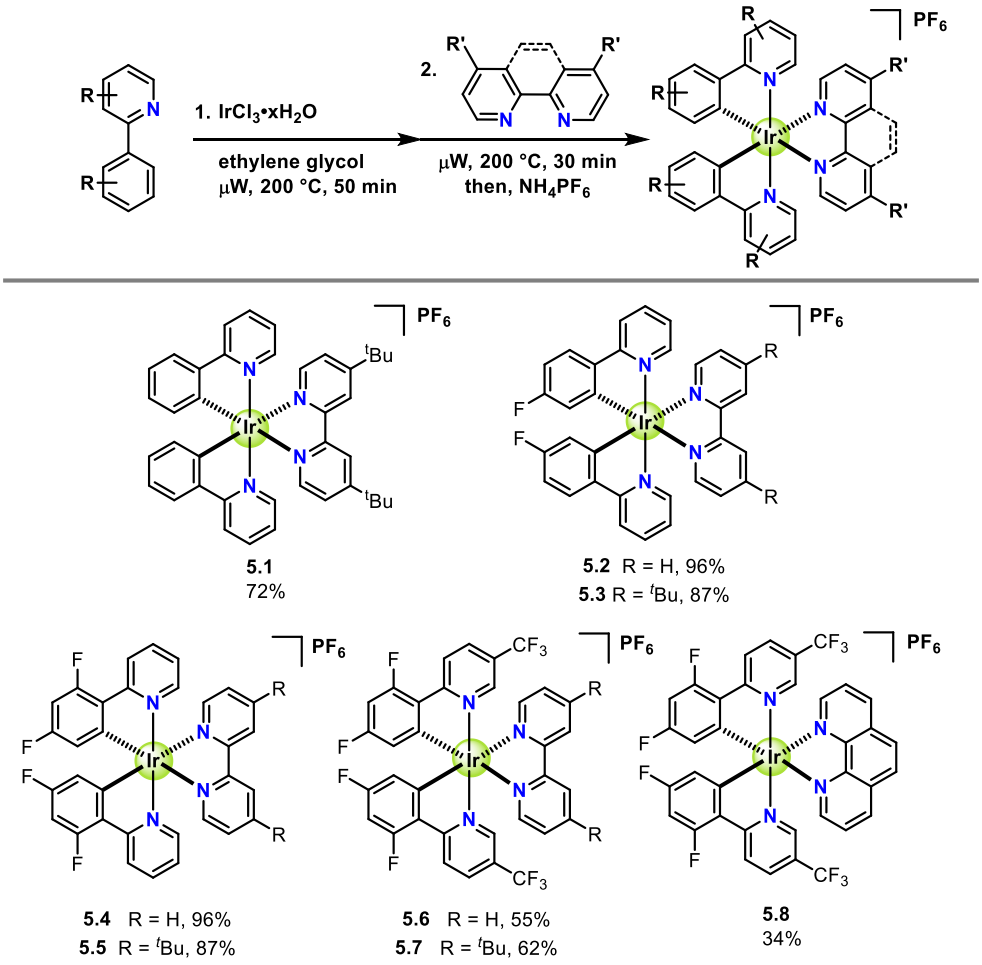

Figure 5.6. Scope of Ir(III)$^+$ complexes synthesized. Reaction conditions: (1) 1.0 equiv $IrCl_3$•xH_2O (50 mg or 100 mg), 8.0 equiv cyclometalating ligand, in ethylene glycol (5 mL) and microwave irradiation (200 °C) for 50 min. (2) 1.5 equiv dative ligand was added to the reaction solution followed by microwave irradiation (200 °C) for 30 min.

With optimized conditions in hand, we explored the scope of our method for the preparation of synthetically useful and known heteroleptic Ir(III)$^+$ complexes (**Figure 5.6**).[273] The conditions proved efficient for generating the Ir(III)$^+$ complex **5.1** with 2-phenylpyridine (***L2***) as the C^N ligand and 4,4'-di-*tert*-butyl-2,2'-bipyridine (***L3***) as the N^N ligand. Alternative difluoro and monofluoro 2-phenylpyridines gave the corresponding iridium complexes in 60-95% yield when partnered with the dative 4,4'-di-*tert*-butyl-2,2'-bipyridine and 2,2'-bipyridine ligands (**5.2**, **5.3**, **5.4**, **5.5**). Ligand solubility in ethylene glycol influenced the overall efficiency of the reaction. A moderate decrease in reaction yield was observed when the partially soluble ***L1*** as well as

phenanthroline ligands were used as cyclometallating and dative ligands, respectively (**5.6**, **5.7**, **5.8**).

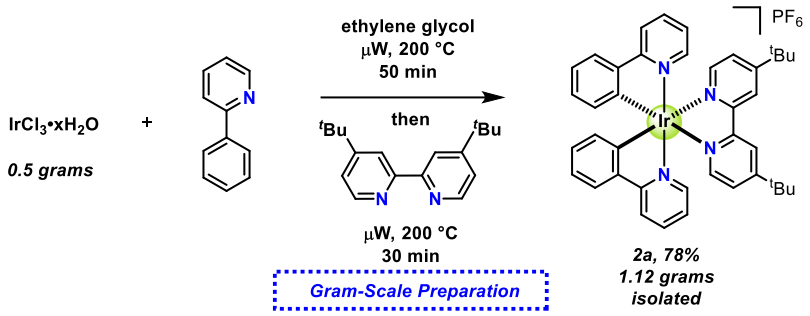

Figure 5.7. Gram-scale preparation of [Ir(ppy)$_2$(dtbbpy)]PF$_6$

To demonstrate the utility of this process, a gram scale preparation of [Ir(ppy)$_2$(dtbbpy)]PF$_6$ was performed (**Figure 5.7**). Satisfyingly, a 78% (1.12 grams) isolated yield of complex **5.1** was obtained without derivation from the optimized conditions. Notably, this reaction could be performed start to finish in less than 5 hours, demonstrating a substantial advance over currently existing methods. This reaction showcases the practicality of the method towards catalyst derivatization efforts.

In conclusion, we have reported an operationally simple, time efficient, and scalable microwave heating method for the preparation of heteroleptic Ir(III)$^+$ complexes, an important class of photosensitizers for organic synthesis and light emitting materials. We envision that microwave heating can provide a direct replacement for conventional heating methods in the synthesis of metal-imine complexes. Importantly, this method is ideal for metal complex diversification, wherein uniquely functionalized complexes can be synthesized from a common [(C^N)$_2$Ir-μ-Cl]$_2$ intermediate, in a synthetic process that is directly streamlined and capable of completion with minimal time at the bench.

5.2.2 Synthesis of Ir(III)$^+$ Polypyridyl Nanohoop Complexes

In our initial studies, we have prepared a library of Ir(III)$^+$ polypyridyl complexes containing both bipy-8-CPP and bipy-9-CPP nanohoop ligands. Both bipy-CPP ligands were synthesized according to procedures reported by Jasti *et al.*[49] To investigate the feasibility of appending the nanohoop ligand onto an Ir(III)$^+$ polypyridyl framework, we began by synthesizing three $[(C\text{^}N)_2Ir\text{-}\mu\text{-}Cl]_2$ dimers derived from common Ir photocatalysts (**Figure 5.8**) using our reported microwave method. Addition of the bipy-8-CPP nanohoop ligand (1.5 equiv), followed by 30 min of microwave irradiation at 200°C, resulted in the successful formation of Ir(III)$^+$ bipy-CPP complexes **5.9**, **5.10**, and **5.11** (66-78% isolated yields).

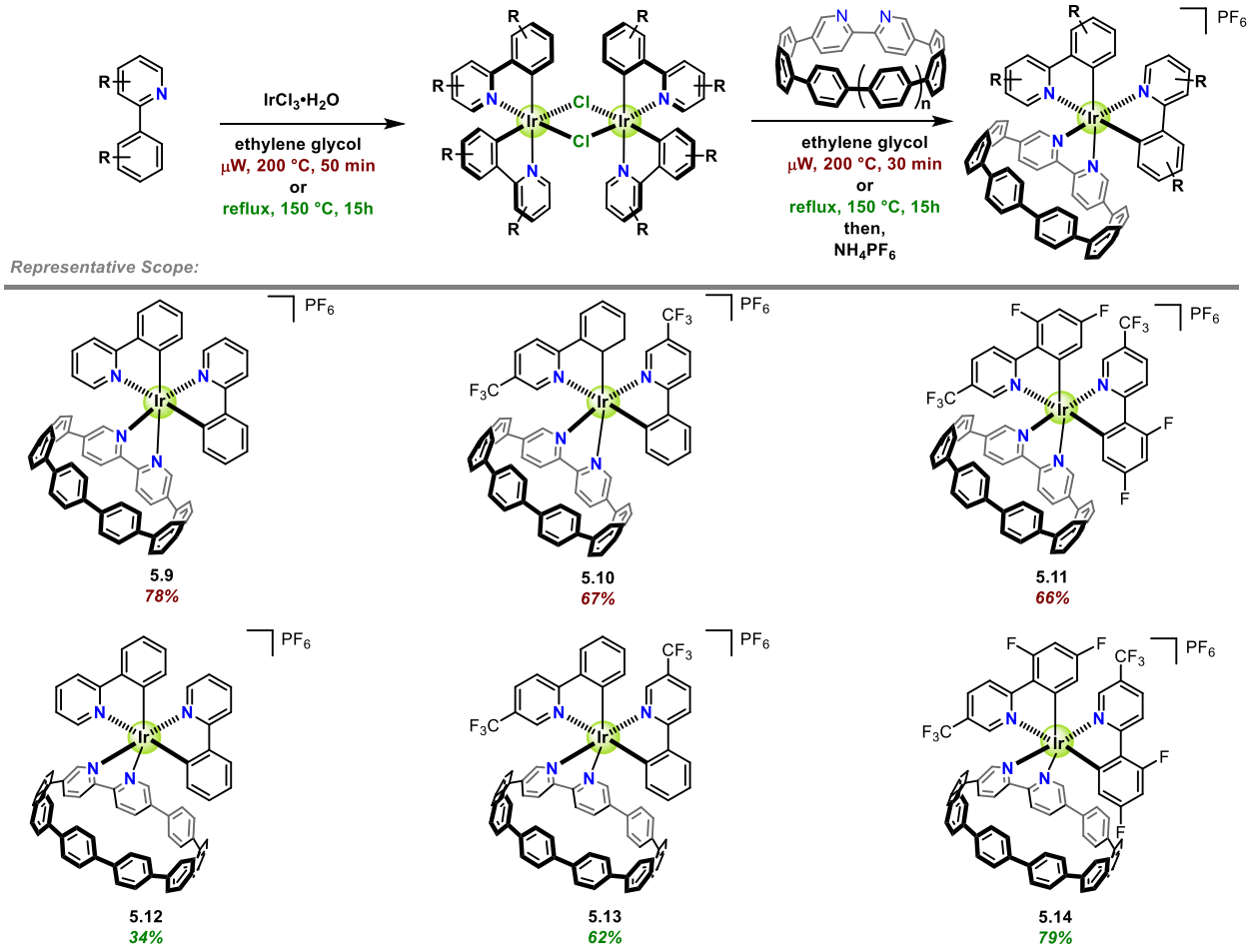

Figure 5.8. Synthesis of Ir(III)$^+$ bipy-8-CPP and bipy-9-CPP complexes

We were able to validate generation of the desired heteroleptic Ir(III)$^+$ nanohoop complexes using NMR spectroscopy and HRMS. X-ray crystallographic structures were also obtained for complexes **5.19** and **5.10**, showcasing successful incorporation of the nanohoop ligand (**Figure 5.9**). At the same time, we expanded upon our library to include heteroleptic Ir complexes(III)$^+$ containing the bipy-9-CPP ligand, yielding the synthesis of complexes **5.11**, **5.12**, and **5.13**. X-ray crystallographic data was acquired for compound **5.12**.

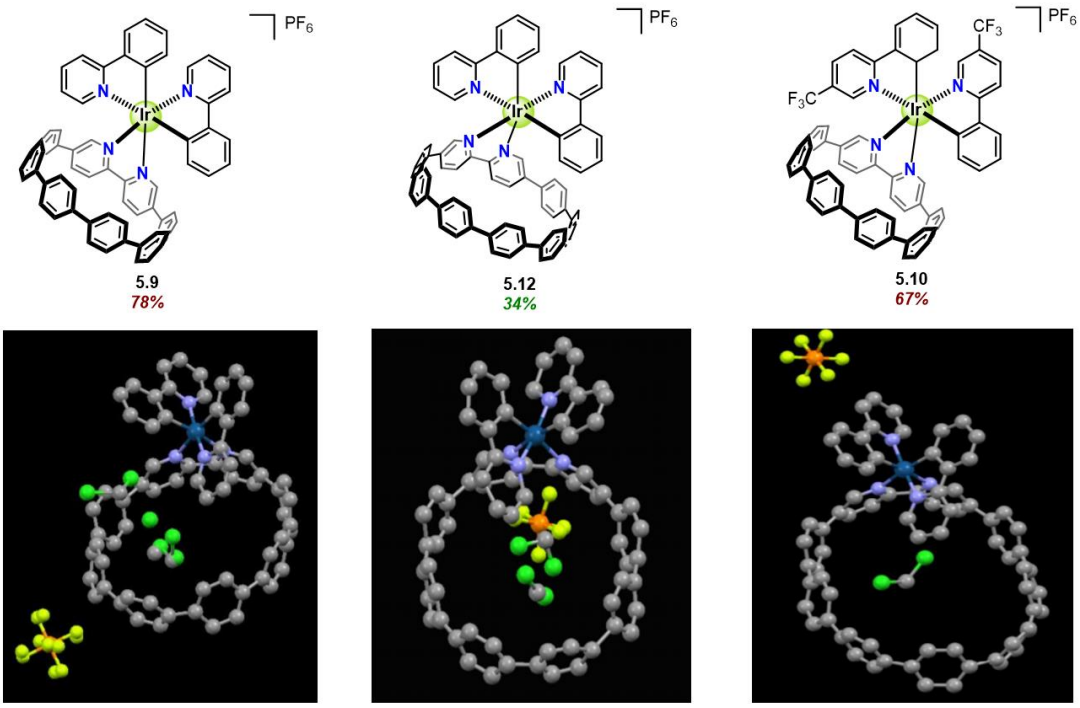

Figure 5.9. X-ray crystallographic data for select Ir(III)$^+$ nanohoop complexes

Based on our x-ray crystallographic data, we observed that in complexes **5.9**, **5.10**, and **5.12**, the pyridyl group of one of the cyclometallating 2-phenylpyridine (ppy) ligands was positioned at an orientation that pointed inwards toward the nanohoop. Additionally, all three structures contained dichloromethane solvent molecules that had co-crystallized within the nanohoop. This led us to propose that the appendage of functionality (e.g. hydrogen bond donors/acceptors) at the 2-position of the cyclometallating ligand could potentially lead to interactions between the complex and small molecule substrates, docked within the nanohoop, in a supramolecular host-

guest fashion. To test this hypothesis, we have synthesized several Ir(III)$^+$ nanohoop derivatives (**Figure 5.10**) that contain both hydrogen bond donor and acceptor functionalities, including carboxylic acid, amide, and ketone moieties (**5.17**, **5.18**, **5.19**). Ongoing efforts have been targeted towards the isolation and characterization of our expanded scope of nanohoop complexes.

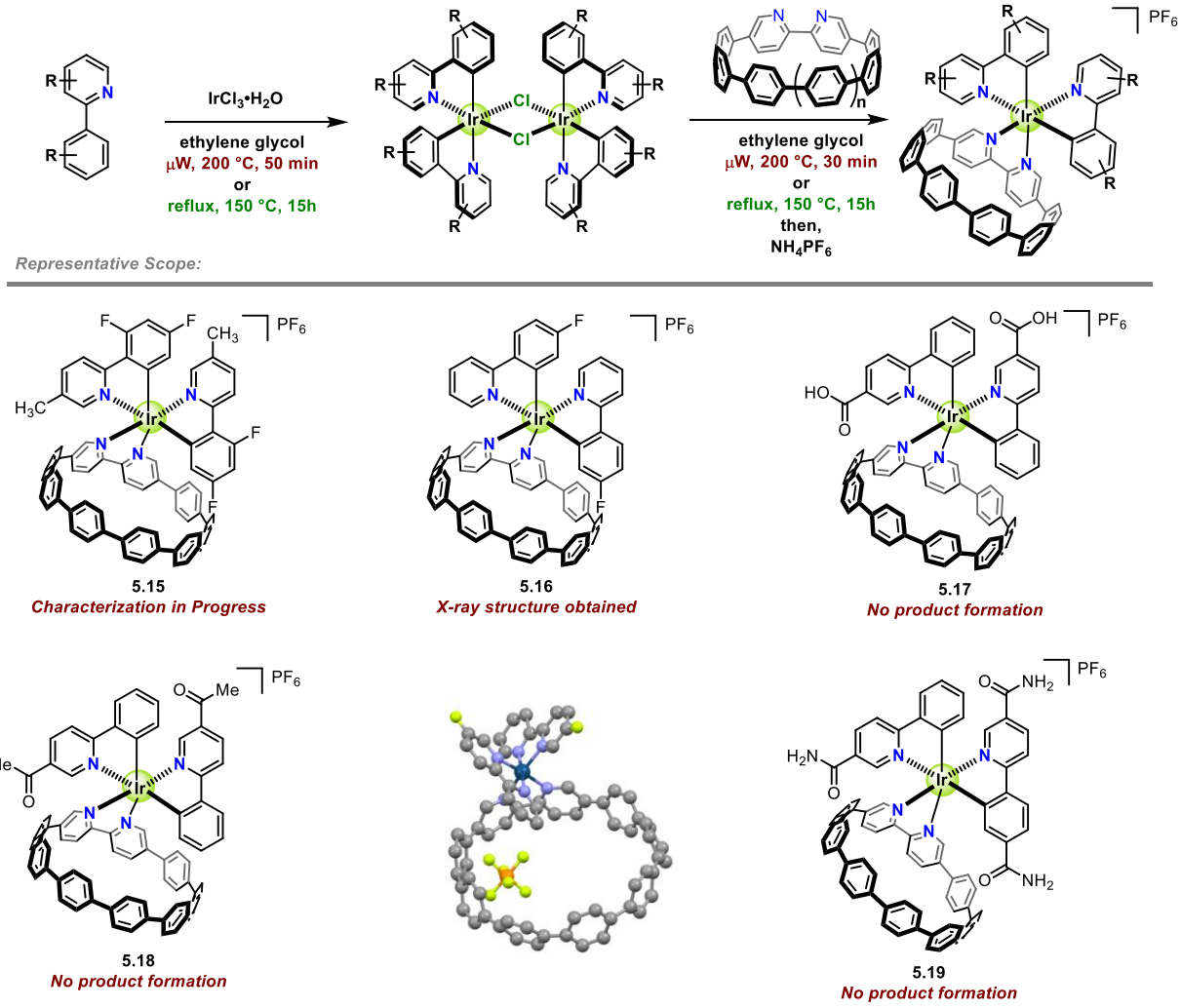

Figure 5.10. Synthesis of Ir(III)$^+$ bipy-9-CPP complexes

In order to investigate the photophysical properties of our Ir(III)$^+$ nanohoop complexes, UV-vis experiments were performed to measure the absorbances of complexes **5.9**–**5.14** (**Figure 5.11**). Absorbance of these complexes were measured in acetonitrile (10 μM). The measured maximum absorbances for complexes **5.9**–**5.14** were observed to be between 318 – 344 nm, with complexes

bearing more electron deficient ligand substituents being more blue-shifted. This phenomenon can be rationalized by the presence of electron withdrawing groups (e.g. fluorine and trifluoromethyl groups) that lower HOMO energies, resulting in larger HOMO–LUMO gaps and greater absorbance energies (more blue-shifted). In comparison with the photocatalyst $[Ir(dF(CF_3)ppy)_2(dtbbpy)]PF_6$, which exhibits a higher maximum absorbance value of 476 nm,[38] these Ir nanohoop complexes are observed to be more blue-shifted, with maximum absorbances prevalent in the near UV region.

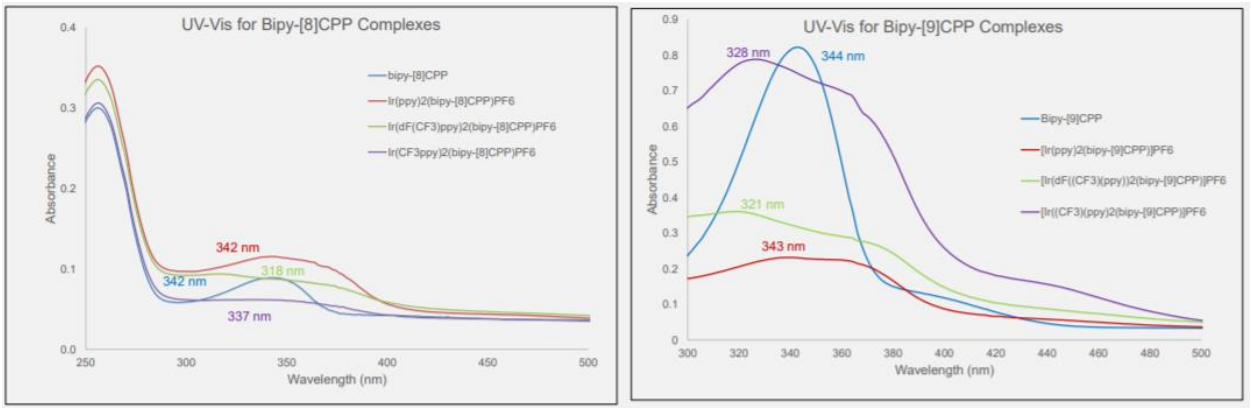

Figure 5.11. UV-vis Spectroscopy Data for Select Ir(III)$^+$ Nanohoop Complexes

Having investigated the photophysical properties of these complexes, we next turned to study their electrochemical properties *via* cyclic voltammetry (CV). Our CV data (**Figure 5.12**) were reported relative to the ferrocenium/ferrocene redox couple. The cyclic voltammograms of complexes were collected at scan rates of 100 mV/s in acetonitrile. CV experiments revealed that complexes **5.12**, **5.13**, **5.14** underwent reduction at -0.92 V, -0.90 V, and -0.80 V, respectively, with reduction potentials decreasing for more electron deficient complexes. Varying levels of reversibility were observed in the reduction waves of these complexes, with complex **5.12** exhibiting the highest level of reversibility. On the other hand, all three complexes, including the bipy-9-CPP nanohoop ligand demonstrated irreversible oxidation potentials of over 1.8 V, which suggests potential decomposition of the nanohoop ligand upon oxidation. Ongoing experiments

have been focused on optimizing CV experimental parameters to more effectively measure redox potentials while preventing decomposition of the analyte.

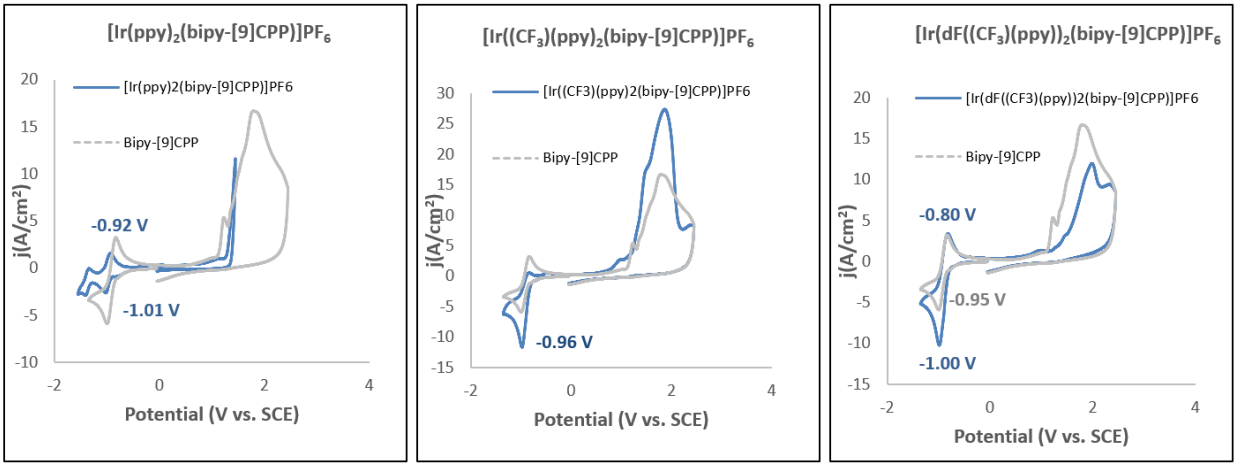

Figure 5.12. Cyclic voltammetry data for select Ir(III)$^{+}$ nanohoop complexes

5.3 Experimental Methods

5.3.1 General Information and Experimental Procedures

All reagents were obtained from commercial suppliers and used without further purification unless otherwise noted. $IrCl_3 \bullet xH_2O$ was purchased from Pressure Chemical, NH_4PF_6 was purchased from Oakwood Products, Inc. and all ligands were obtained from Sigma-Aldrich unless otherwise specified. Microwave heated reactions were carried out in sealed microwave flasks (2-5 mL [CG-4920-01] or 10-20mL [CG-4920-02], Chemglass) and heated by a Biotage Initiator+ microwave synthesizer with a Robot Eight automated sampler. Temperature and pressure were monitored by an infrared sensor on the surface exterior of the vial. Pressure was monitored by a pressure transducer situated at the top of the vial. NMR spectra were obtained on a 700 MHz Varian VNMRS spectrometer and a 500 MHz Varian VNMRS spectrometer. ^{1}H and ^{13}C NMR chemical shifts are reported in ppm relative to the residual acetone (δ 2.09) solvent peak.[37] Reactions were monitored by thin layer chromatography (TLC) using silica TLC plates obtained

from EMD Millipore; silica gel 60 F_{254}, glass-backed, 250 μm, and were visualized with ultraviolet light.

General Procedure for C^N ligand synthesis[38]

2-(2,4-difluorophenyl)-5-(trifluoromethyl)pyridine.

To a three-necked, 100 mL round bottom flask charged with a magnetic stir bar were added 2-chloro-5-(trifluoromethyl)pyridine (3.1 g, 17.0 mmol, 0.9 equiv), 2,4-difluorophenylboronic acid (3.0 g, 19.0 mmol, 1.0 equiv), 2 M aqueous sodium carbonate (4.03 g, 38.0 mmol, 2.0 equiv), benzene (23 mL), and toluene (17 mL). The mixture was degassed by sparging with N_2 for 15 min. Then $Pd(PPh_3)_4$ (0.505 g, 0.437 mmol) was added to the reaction mixture and degassing was continued for another 15 min. The reaction mixture was heated to reflux for 48 h to generate a yellow solution with yellow precipitate. The progress of the reaction was monitored by TLC (85% ethyl acetate in hexanes). Upon completion of the reaction, the mixture was cooled to room temperature and then extracted with dichloromethane (4 x 20 mL), washed with brine (3 x 20 mL), and dried over Na_2SO_4. Solvent was removed under reduced pressure to give a dark brown oil which solidified at room temperature. The crude product was purified by flash chromatography using 100% dichloromethane to afford a yellow oil, which crystallized at room temperature. The yellow oil was further dried *in vacuo* to afford the pure ligand in 77% yield (3.81 g, 14.7 mmol) as white crystals. ^{1}H NMR chemical shifts match literature values.[38]

2-(4-fluorophenyl)pyridine.

To a three-necked, 100 mL round bottom flask charged with a magnetic stir bar were added 2-chloropyridine (2.00 g, 17.61 mmol, 1.0 equiv), 4-fluorophenylboronic acid (2.96 g, 21.14 mmol, 1.2 equiv), triphenylphosphine (0.46 g, 1.76 mmol, 0.1 equiv), 2 M aqueous potassium carbonate (6.55 g, 47.39 mmol), and dimethoxyethane (20 mL). The mixture was degassed with N_2 for 15

min. Then 2.5 mol% $Pd(OAc)_2$ (0.1 g, 0.441 mmol) was added to the reaction mixture and degassing was continued for another 15 min. The reaction mixture was heated to reflux for 18 h to generate an orange solution with orange precipitate. The progress of the reaction was monitored by TLC (10% ethyl acetate/hexanes). Upon completion of the reaction, the mixture was cooled to room temperature and then extracted with dichloromethane (4 x 20 mL), washed with brine (3 x 20 mL), and dried over Na_2SO_4. Solvent was removed under reduced pressure, and the crude product was purified by flash chromatography (0-5% ethyl acetate in hexanes) on a 30 g silica column. The pure ligand was obtained in 55% yield (1.68 g, 9.7 mmol) as a white solid. ^{1}H NMR chemical shifts match literature values.[38]

General Procedure A for the Synthesis of Heteroleptic Ir(C^N)(N^N)$_2$ Complexes

(100 mg scale)

To a Chemglass microwave vial (size 2-5 mL) equipped with a magnetic stir bar were added $IrCl_3$•xH_2O (50 or 100 mg, 1.0 equiv), cyclometalating ligand (8.0 equiv), and ethylene glycol (5 mL, 32 or 64 μM). The vial was sealed and pre-stirred for 1 min prior to heating under microwave irradiation (200 ^{o}C, 50 min) at atmospheric pressure.* Upon allowing the mixture to cool to room temperature, the dative ligand was added (1.5 equiv), and the vial was heated under microwave irradiation (200 ^{o}C, 30 min) at atmospheric pressure. After cooling to room temperature, the reaction mixture was diluted with DI H_2O (25 mL) and extracted with hexanes (3 x 20 mL). The aqueous portion was collected and heated to 75 ^{o}C for 15 min to remove remaining organic solvent. Aqueous ammonium hexafluorophosphate (2.0 g in 20 mL DI H_2O) was added to the mixture, and the mixture was cooled in an ice bath. The resulting precipitate was collected and washed with cold DI H_2O (10 mL) and cold diethyl ether (10 mL). Finally, the precipitate was taken up in acetone and dried *in vacuo* to afford the desired product.

Procedure for the 500 mg scale synthesis of [Ir(ppy)$_2$(dtbbpy)]PF$_6$

The general procedure A was followed, using $IrCl_3 \cdot H_2O$ (500 mg, 1.6 mmol, 1.0 equiv), 2-phenylpyridine (1.8 μL, 12.6 mmol, 8.0 equiv), and ethylene glycol (15 mL) to obtain a bright yellow solution with yellow solids. **2a** was synthesized using 4,4'-di-*t*-butyl-2,2'-bipyridine (636 mg, 2.36 mmol, 1.5 equiv) to afford a homogeneous orange solution. **2a** was obtained in 78% yield (1.12 g, 1.22 mmol) as a yellow solid after recrystallization with acetone and diethyl ether at low temperatures.

Procedure for the 500 mg scale synthesis of [Ir(dF(CF)$_3$ppy)$_2$(dtbbpy)]PF$_6$

The general procedure A was followed, using $IrCl_3 \cdot H_2O$ (500 mg, 1.6 mmol), 2-(2,4-difluorophenyl)-5-(trifluoromethyl)pyridine (3.28 g, 12.6 mmol), and ethylene glycol (15 mL). The reaction mixture was sonicated before microwave irradiation to increase homogeneity of the solution. A bright orange solution with green amorphous solids was obtained. **2g** was synthesized using 4,4'-di-*t*-butyl-2,2'-bipyridine (636 mg, 2.36 mmol) to afford an orange solution with green solids. The reaction mixture was diluted with DI H_2O (100 mL) and extracted with hexanes (3 x 75 mL) and ethyl acetate (4 x 75 mL). The ethyl acetate extract was collected, filtered to remove unreacted $IrCl_3$ solids, dried over Na_2SO_4, and concentrated in vacuo to afford an orange oil with yellow solids. DI H_2O (75 mL) was combined with the mixture to generate a yellow solution with free-flowing yellow solids. Aqueous ammonium hexafluorophosphate (10.0 g in 100 mL DI H_2O) was then added to the mixture, and the whole was cooled in an ice bath. The resulting yellow precipitate was collected and washed sequentially with cold DI H_2O (4 x 25 mL) and hexanes (4 x 25 mL). Finally, the precipitate was taken up in acetone and dried in vacuo to afford a mixture of yellow solids and an orange oil. **2g** was obtained in 50% yield (883 mg, 0.79 mmol) as a light yellow solid after recrystallization with acetone and diethyl ether at low temperatures.

5.3.2 Compound Characterization

Characterization of Heteroleptic Ir(III)$^+$ Complexes

[Ir(ppy)$_2$(dtbbpy)]PF$_6$ (**5.1**): **^{1}H-NMR** (Acetone-d_6, 700 MHz): δ 8.88 (s, 2H), 8.23 (d, J = 8.2 Hz, 2H), 8.03 - 7.92 (m, 3H), 7.88 (d, J = 7.6 Hz, 2H), 7.78 (d, J = 5.7 Hz, 2H), 7.70 (d, J = 5.7 Hz, 2H), 7.12 (t, J = 6.5 Hz, 2H), 7.02 (t, J = 7.4 Hz, 2H), 6.90 (t, J = 7.3 Hz, 2H), 6.33 (d, J = 7.5 Hz, 2H), 1.40 (s, 13H).**^{13}C-NMR** (Acetone-d_6, 176 MHz): δ 167.88 (s), 163.97 (s), 155.89 (s), 151.00 (s), 150.18 (s), 149.02 (s), 144.03 (s), 138.55 (s), 131.53 (s), 130.31 (s), 125.48 (s), 124.89 (s), 123.47 (s), 122.32 (s), 121.98 (s), 119.87 (s), 35.51 (s), 29.51 (s).

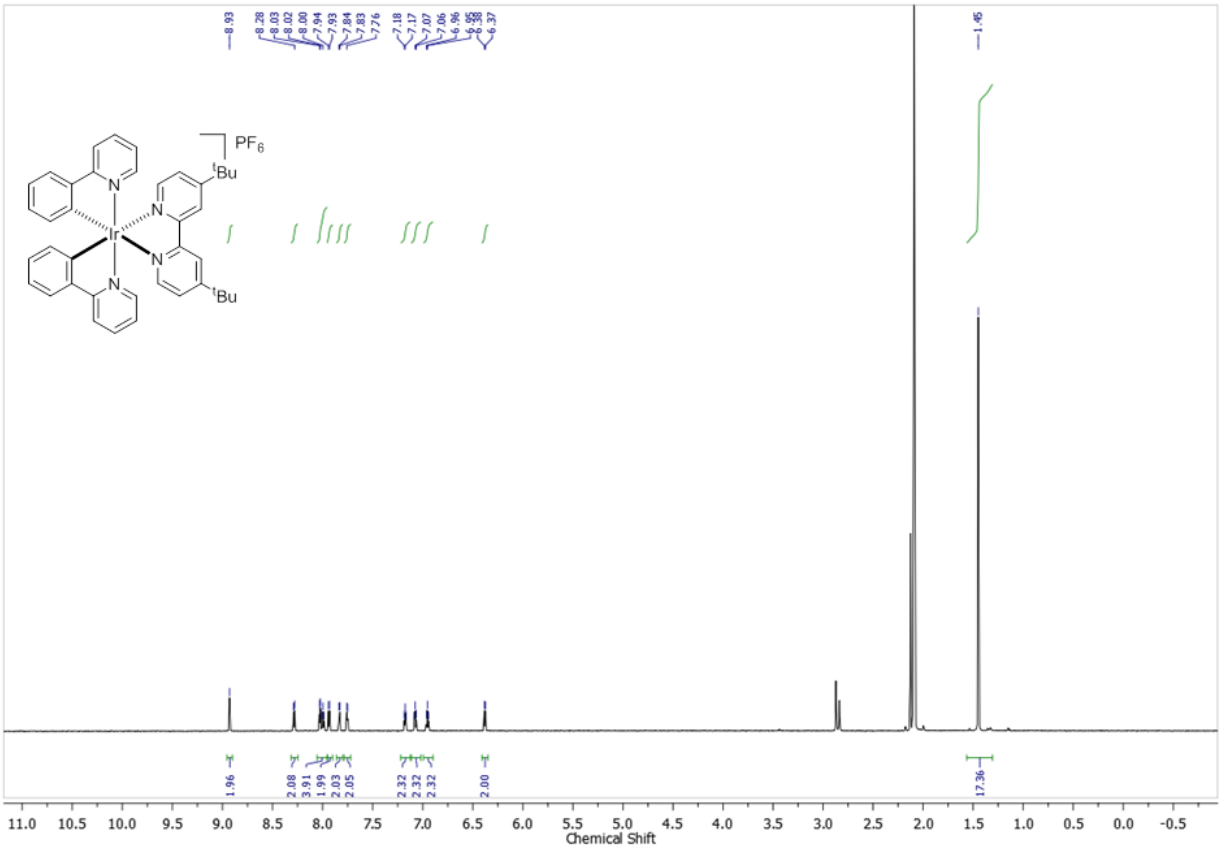

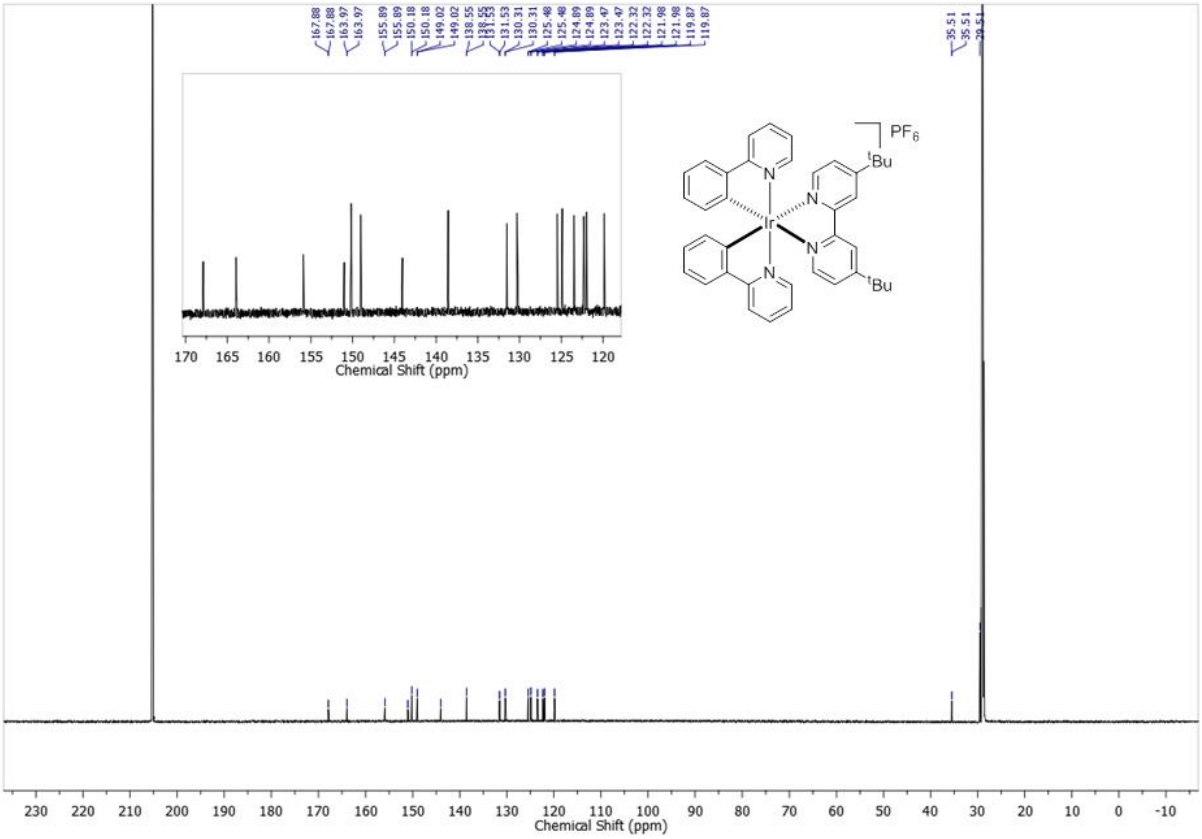
Chemical Shift (ppm)
PF6
tBu
tBu
Ir
N

[Ir(Fppy)$_2$(bpy)]PF$_6$ (**5.2**): **^{1}H-NMR** (Acetone-d_6, 500 MHz): δ 8.91 (d, *J* = 8.2 Hz, 2H), 8.37 (td, *J* = 8.0, 1.4 Hz, 2H), 8.28 (d, *J* = 8.2 Hz, 2H), 8.21 (d, *J* = 5.3 Hz, 2H), 8.11 - 7.97 (m, 4H), 7.87 (d, *J* = 5.8 Hz, 2H), 7.81 - 7.73 (m, 2H), 7.22 (t, *J* = 6.6 Hz, 2H), 6.87 (td, *J* = 8.8, 2.5 Hz, 2H), 5.98 (dd, *J* = 9.5, 2.5 Hz, 2H). **^{13}C-NMR** (Acetone-d_6, 176 MHz): δ 166.48 (s), 164.40 (s), 162.96 (s), 155.92 (s), 153.51 (d, *J* = 5.8 Hz), 150.78 (s), 149.28 (s), 140.51 (s), 139.91 (s), 139.06 (s), 128.74 (s), 127.22 (d, *J* = 9.3 Hz), 124.97 (s), 123.68 (s), 120.11 (s), 117.40 (d, *J* = 17.8 Hz), 109.70 (s), 109.57 (s).

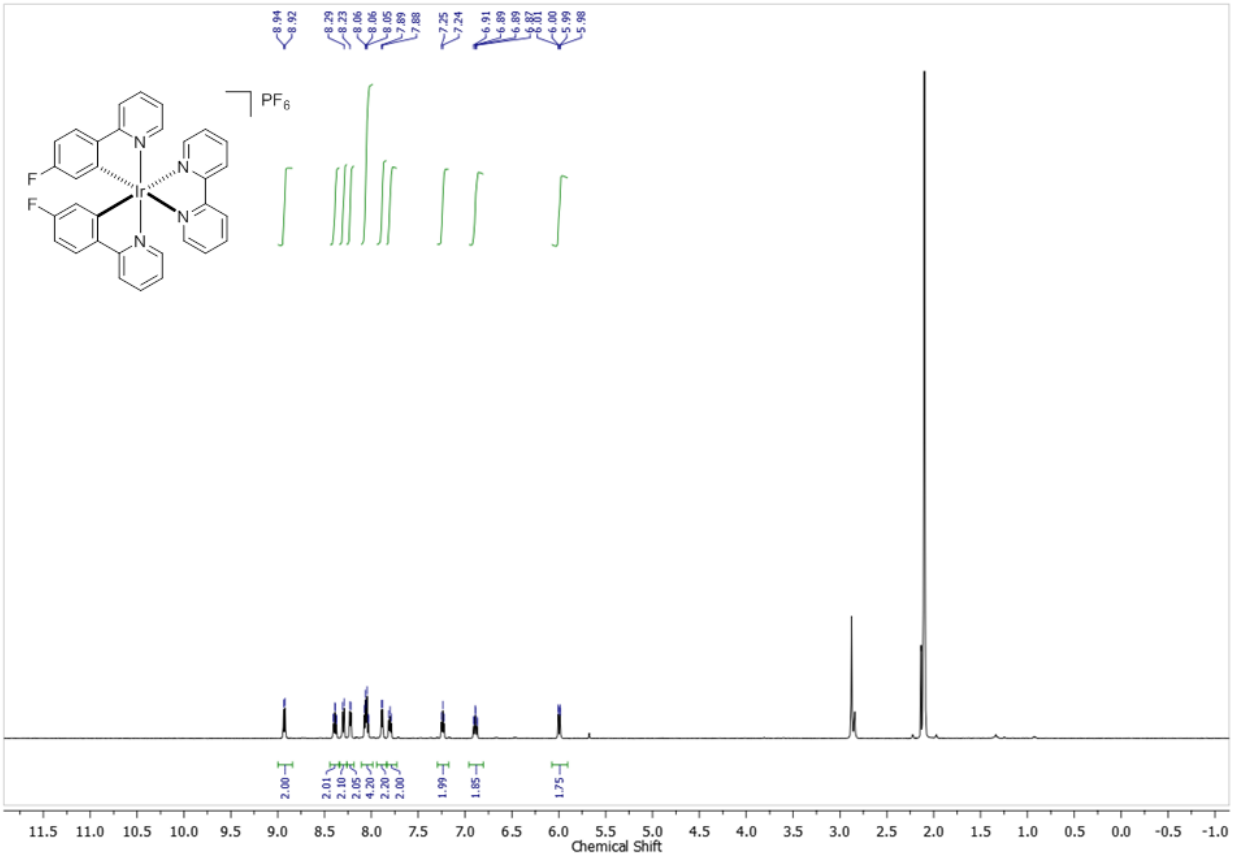

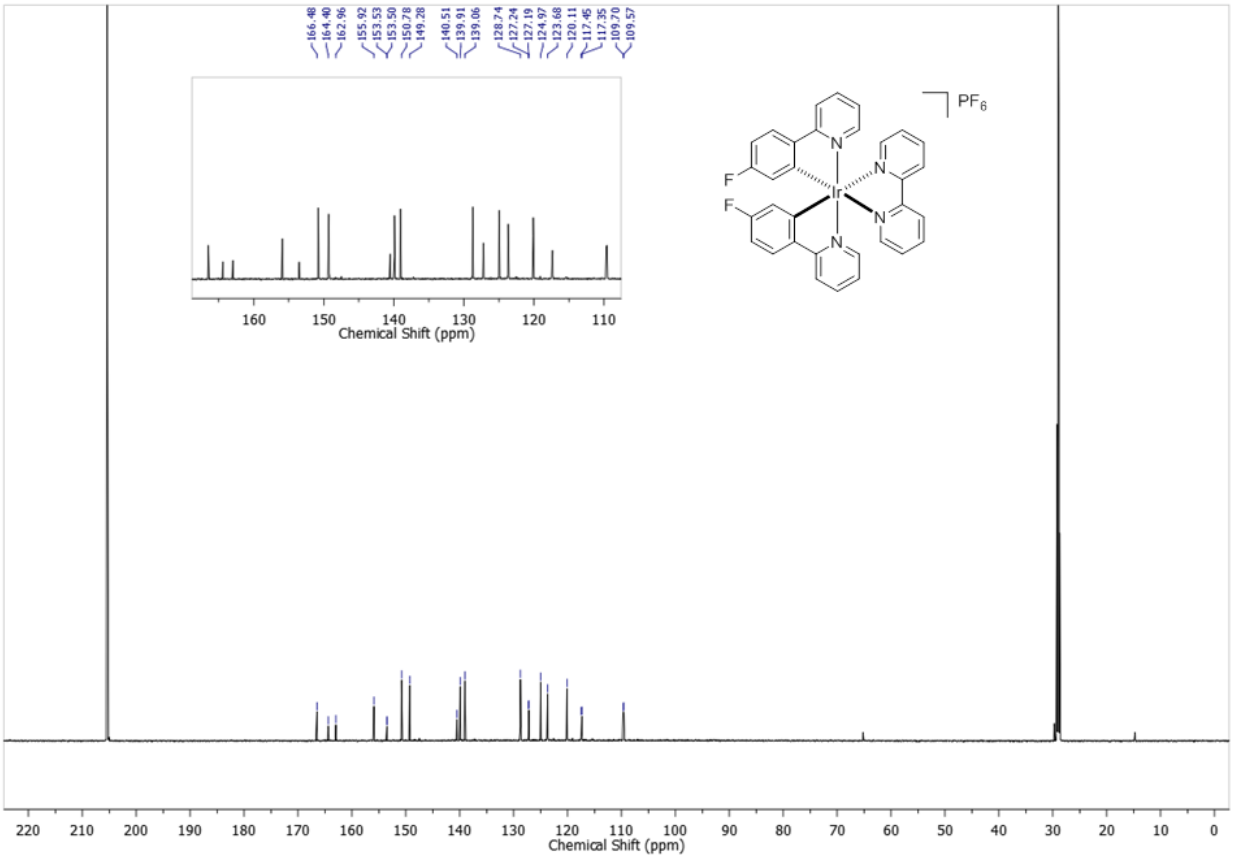
166.48
164.40
162.96
155.92
153.53
153.50
150.78
149.28
140.51
139.91
139.06
128.74
127.24
127.19
124.97
123.68
120.11
117.45
117.35
109.70
109.57
160
150
140
130
120
110
Chemical Shift (ppm)
PF6
F
F
Ir
N
N
N
N
220
210
200
190
180
170
160
150
140
130
120
110
100
90
80
70
60
50
40
30
20
10
0
Chemical Shift (ppm)

[Ir(Fppy)$_2$(dtbbpy)]PF$_6$ (**5.3**): **^{1}H-NMR** (Acetone-d_6, 700 MHz): δ 8.94 (s, 2H), 8.28 (d, *J* = 8.2 Hz, 2H), 8.13 - 7.96 (m, 4H), 7.82 (d, *J* = 5.5 Hz, 2H), 7.77 (dd, *J* = 5.8, 1.7 Hz, 2H), 7.19 (t, *J* = 6.2 Hz, 2H), 6.87 (td, *J* = 8.8, 2.5 Hz, 2H), 5.97 (dd, *J* = 9.5, 2.5 Hz, 2H), 1.45 (s, 18H). **^{13}C-NMR** (Acetone-d_6, 176 MHz): δ 166.66 (s), 164.46 (s), 164.29 (s), 163.02 (s), 155.81 (s), 154.08 (d, *J* = 5.6 Hz), 150.37 (s), 149.07 (s), 140.50 (s), 138.99 (s), 127.20 (d, *J* = 9.3 Hz), 125.66 (s), 123.56 (s), 122.17 (s), 120.11 (s), 117.30 (d, *J* = 17.7 Hz), 109.57 (s), 109.44 (s), 29.49 (s).

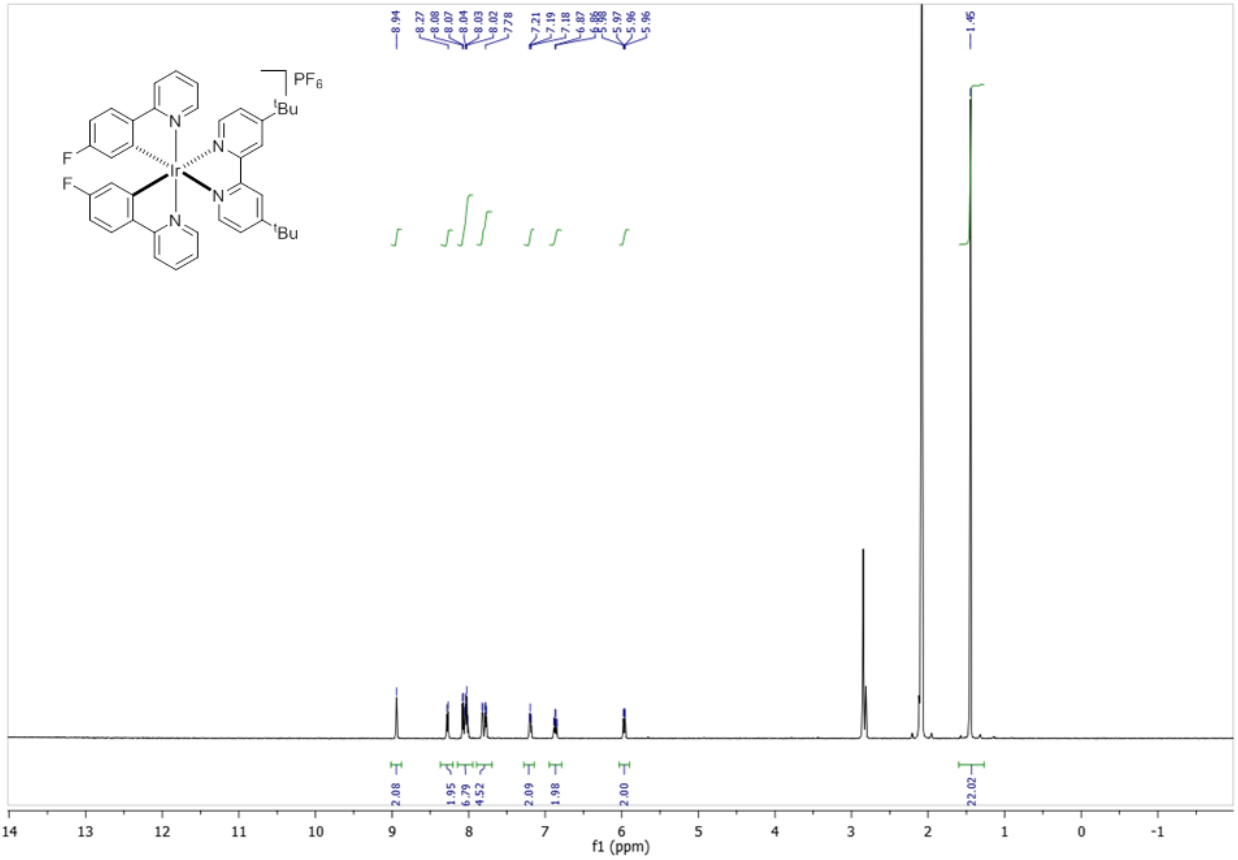

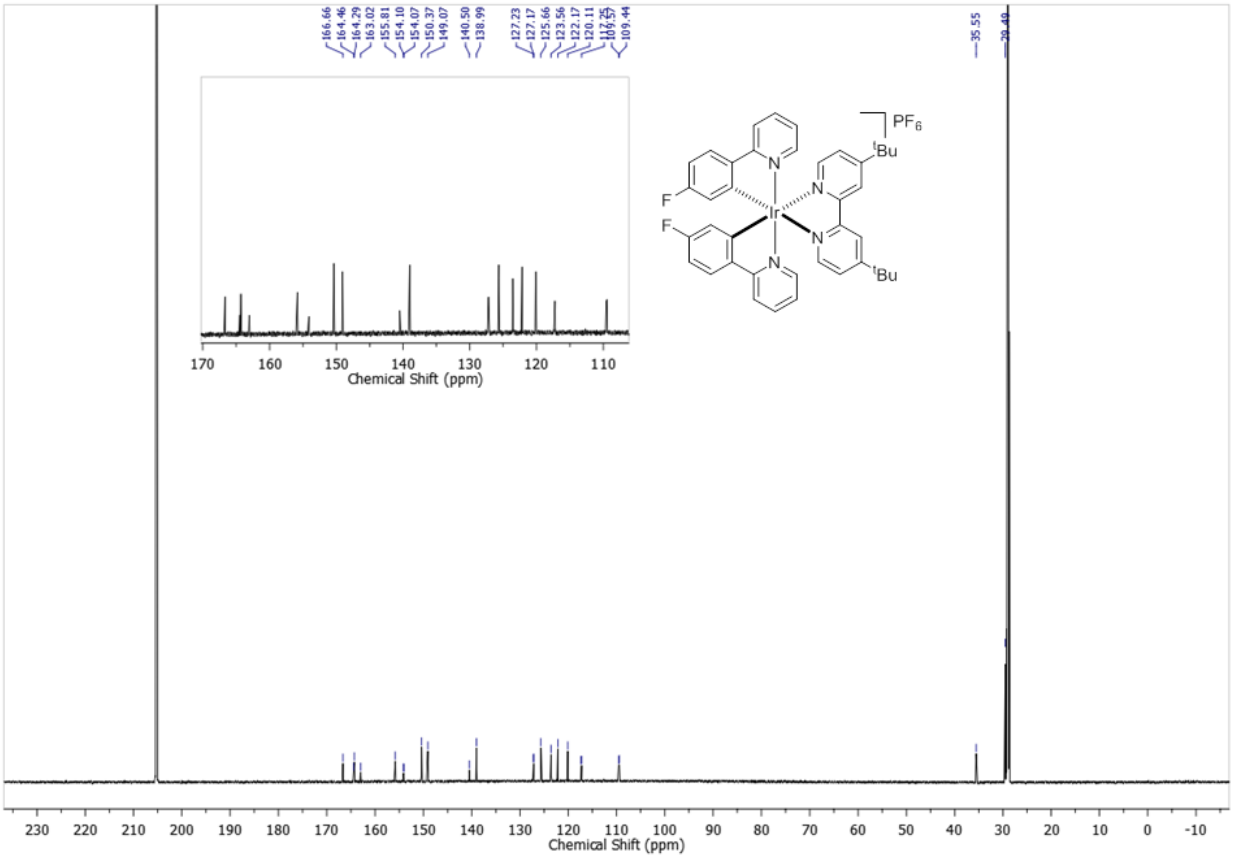
166.66
164.46
164.29
163.02
155.81
154.10
154.07
150.37
149.07
140.50
138.99
127.23
127.17
125.66
123.56
122.17
120.11
109.44
35.55
29.49
PF6
tBu
tBu
F
F
N
N
N
N
Ir
170 160 150 140 130 120 110
Chemical Shift (ppm)
230 220 210 200 190 180 170 160 150 140 130 120 110 100 90 80 70 60 50 40 30 20 10 0 -10
Chemical Shift (ppm)

[Ir(dFppy)$_2$(bpy)]PF$_6$ (**5.4**): **^{1}H-NMR** (Acetone-d_6, 700 MHz): δ 8.94 (s, 2H), 8.62 (d, *J* = 8.9 Hz, 2H), 8.41 (d, *J* = 8.7 Hz, 2H), 8.19 (d, *J* = 5.8 Hz, 2H), 7.94 - 7.70 (m, 4H), 6.87 (t, *J* = 10.3 Hz, 2H), 5.97 (d, *J* = 7.9 Hz, 2H), 1.43 (s, 18H). **^{13}C-NMR** (Acetone-d_6, 176 MHz): δ 167.83 (s), 165.33 (d, *J* = 18.6 Hz), 163.85 (d, *J* = 12.6 Hz), 163.19 (d, *J* = 12.7 Hz), 161.70 (d, *J* = 13.2 Hz), 156.00 (s), 155.77 (d, *J* = 6.9 Hz), 151.09 (s), 145.72 (d, *J* = 4.7 Hz), 137.18 (s), 126.81 (s), 126.03 (s), 125.23 (d, *J* = 34.6 Hz), 124.11 - 124.03 (m), 123.90 (d, *J* = 20.9 Hz), 122.91 (s), 122.67 (s), 121.37 (s), 114.44 (d, *J* = 17.9 Hz), 99.31 (d, *J* = 27.1 Hz), 99.09 (s), 99.08 (s), 35.70 (s), 29.45 (s).

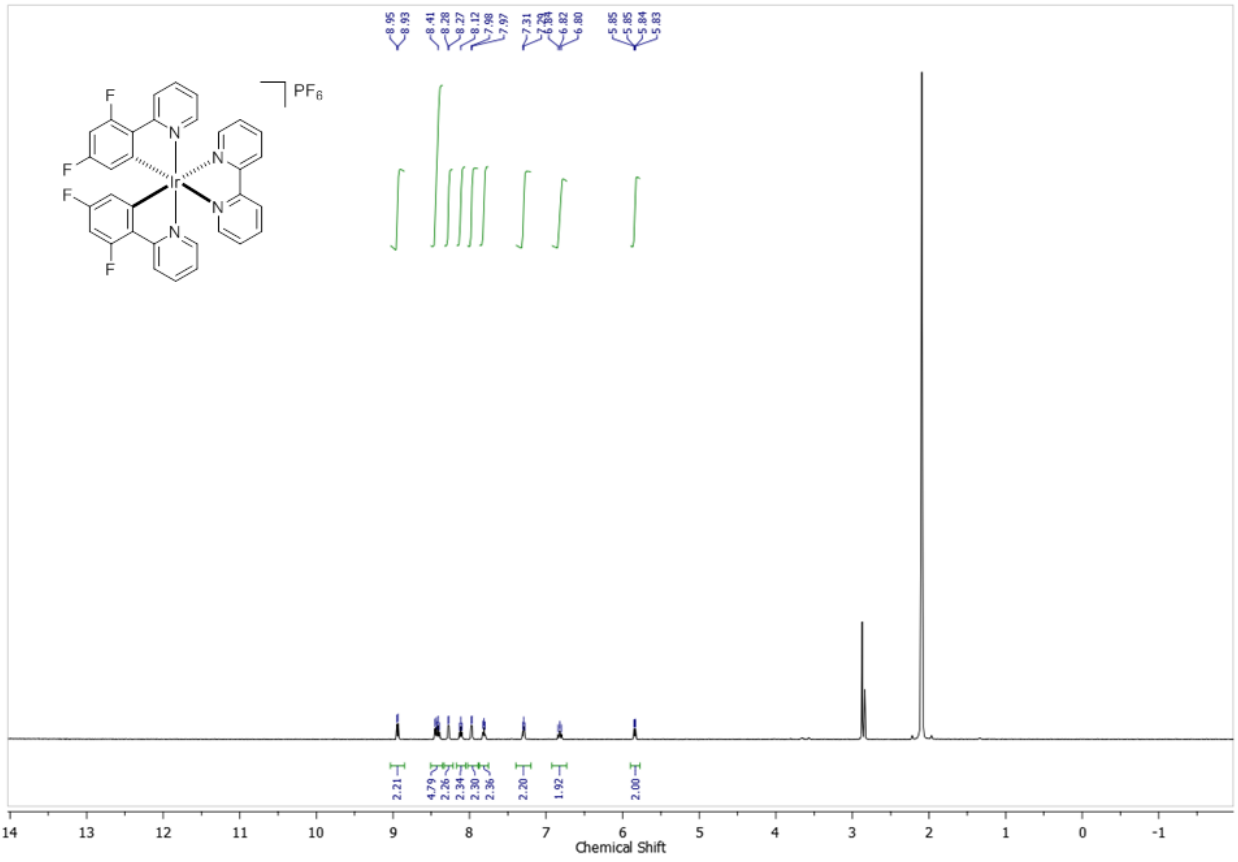

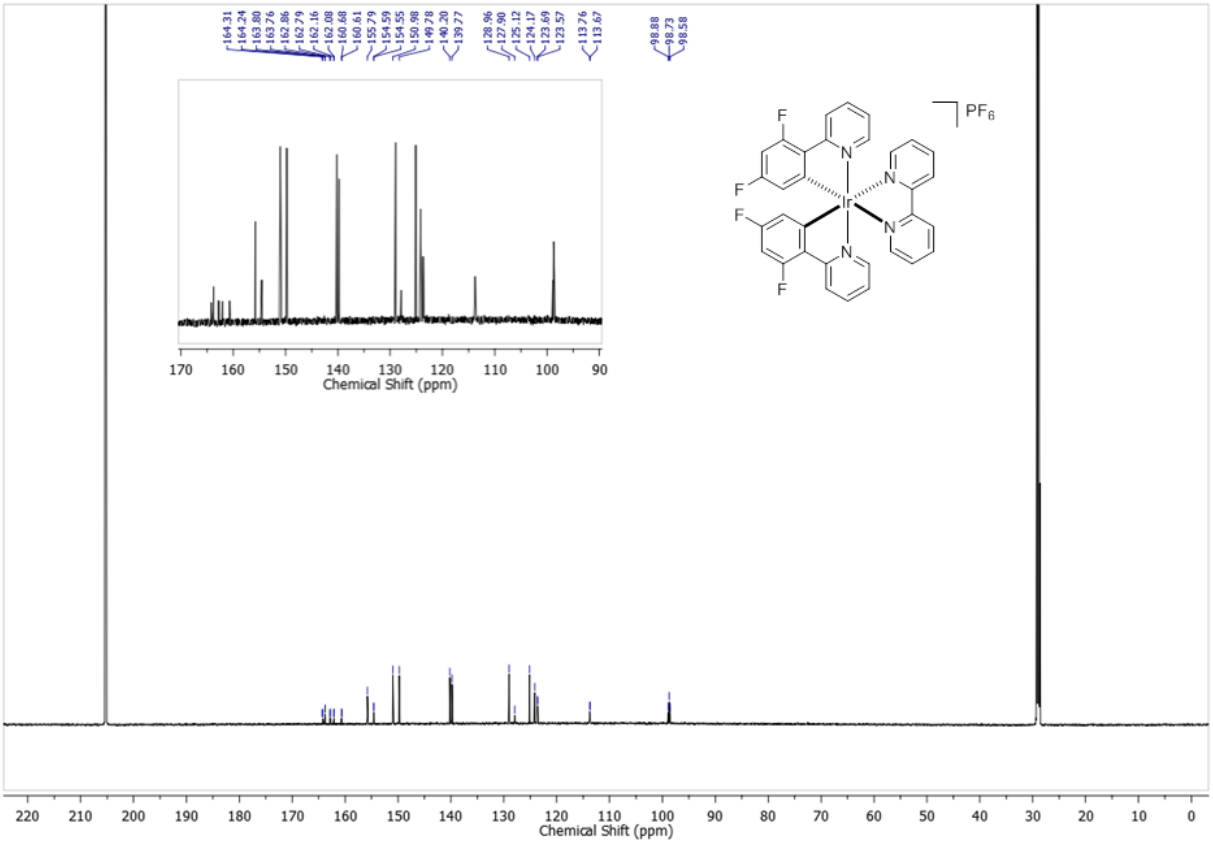
164.31
164.24
163.80
163.76
162.86
162.79
162.16
162.08
160.68
160.61
155.79
154.59
154.55
150.98
149.78
140.20
139.77
128.96
127.90
125.12
124.17
123.69
123.57
113.76
113.67
98.88
98.73
98.58
170 160 150 140 130 120 110 100 90
Chemical Shift (ppm)
F
F
F
F
N
N
N
N
Ir
PF6
220 210 200 190 180 170 160 150 140 130 120 110 100 90 80 70 60 50 40 30 20 10 0
Chemical Shift (ppm)

[Ir(dFppy)$_2$(dtbbpy)]PF$_6$ (**5.5**): **^{1}H-NMR** (Acetone-d_6, 500 MHz): δ 8.96 (s, 2H), 8.41 (d, *J* = 8.4 Hz, 2H), 8.09 (dd, *J* = 14.1, 6.8 Hz, 4H), 7.90 (d, *J* = 5.6 Hz, 2H), 7.77 (dd, *J* = 5.8, 1.7 Hz, 2H), 7.24 (t, *J* = 6.7 Hz, 2H), 6.86 – 6.70 (m, 2H), 5.80 (dd, *J* = 8.5, 2.2 Hz, 2H), 1.43 (s, 18H). **^{13}C-NMR** (Acetone-d_6, 176 MHz): δ 164.62 (s), 164.33 (d, *J* = 12.4 Hz), 163.91 (d, *J* = 7.0 Hz), 162.87 (d, *J* = 12.6 Hz), 162.14 (d, *J* = 13.1 Hz), 160.67 (d, *J* = 12.9 Hz), 155.68 (s), 155.25 (d, *J* = 6.4 Hz), 150.44 (s), 149.59 (s), 139.71 (s), 127.89 (s), 125.80 (s), 124.10 (s), 123.61 (d, *J* = 19.9 Hz), 122.44 (s), 113.63 (d, *J* = 15.2 Hz), 98.66 (d, *J* = 27.2 Hz), 98.57 - 98.50 (m), 98.43 (s), 35.59 (s), 29.48 (s).

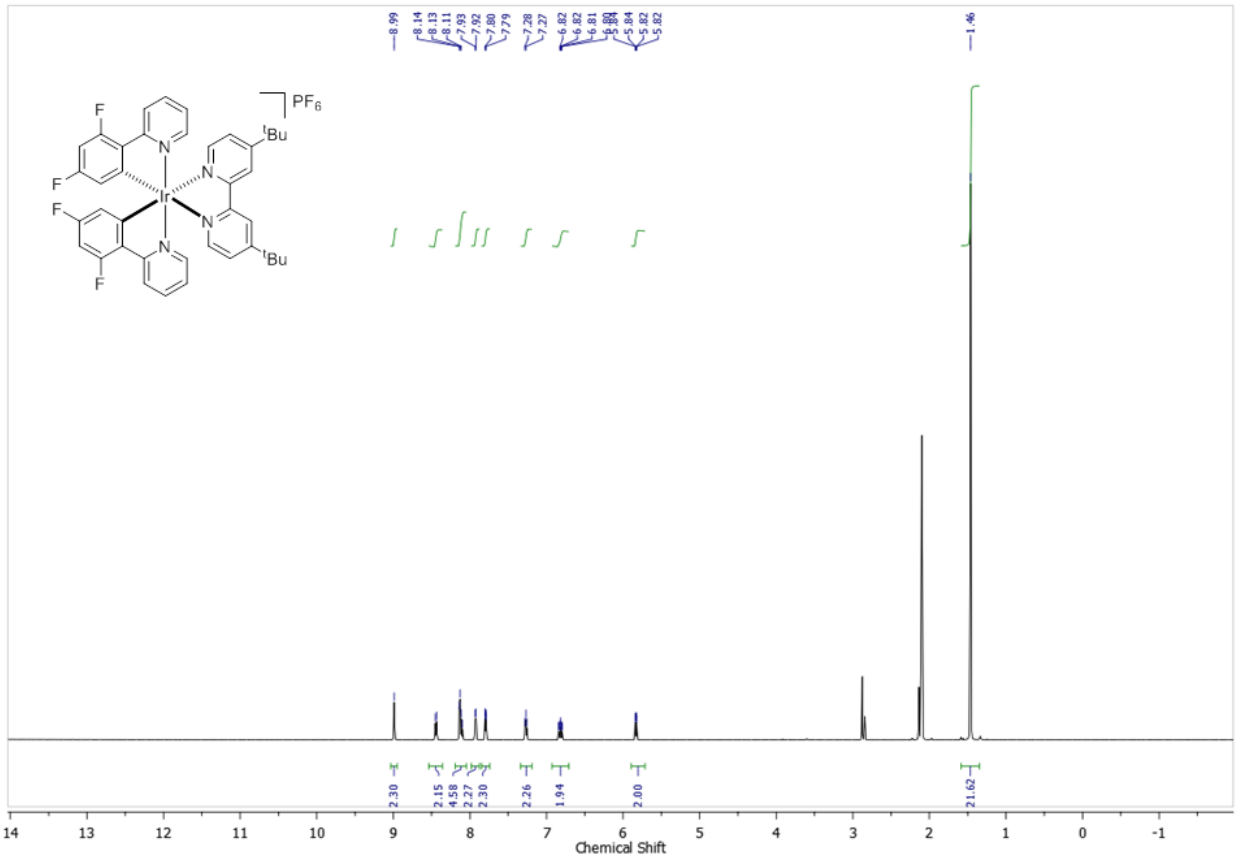

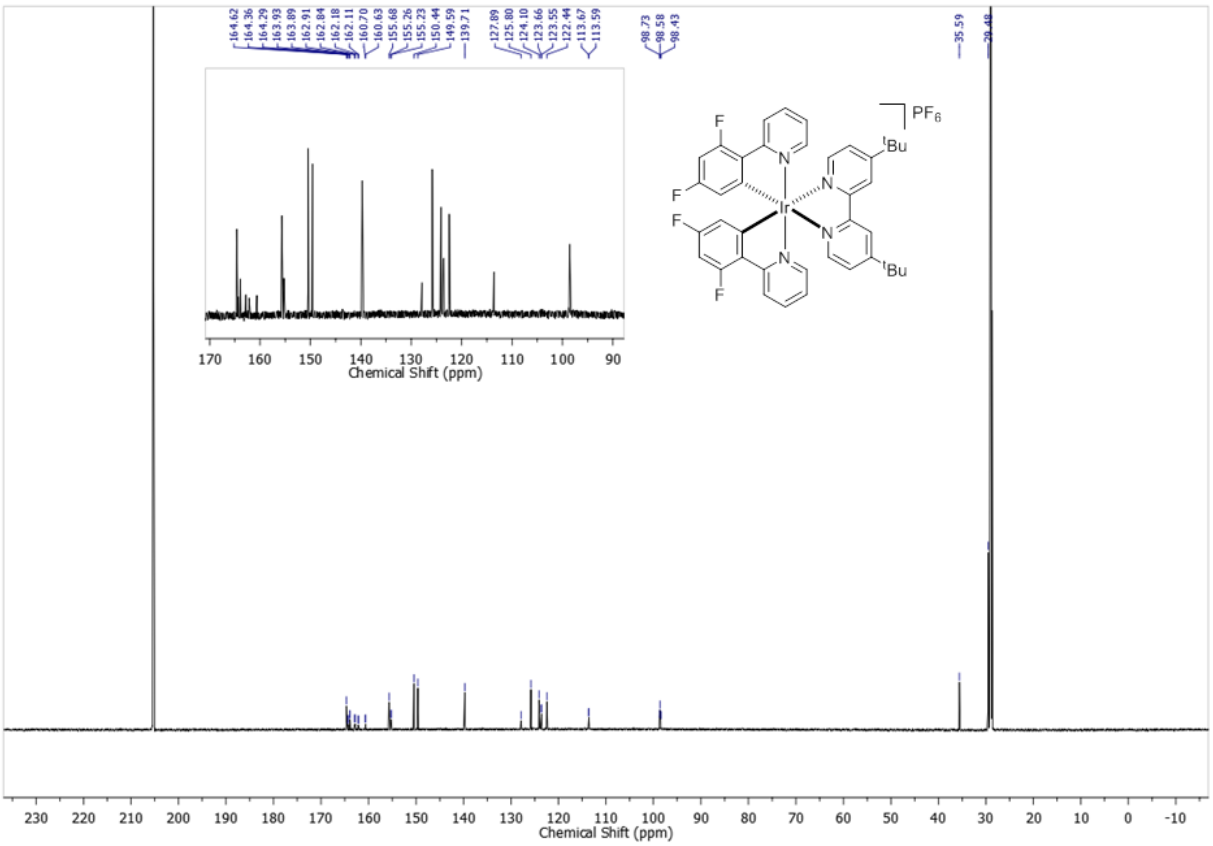
164.62
164.36
164.29
163.93
163.89
162.91
162.84
162.18
162.11
160.70
160.63
155.68
155.26
155.23
150.44
149.59
139.71
127.89
125.80
124.10
123.66
123.55
122.44
113.67
113.59
98.73
98.58
98.43
35.59
29.48
PF6
tBu
tBu
F
F
F
F
N
N
N
N
Ir
170 160 150 140 130 120 110 100 90
Chemical Shift (ppm)
230 220 210 200 190 180 170 160 150 140 130 120 110 100 90 80 70 60 50 40 30 20 10 0 -10
Chemical Shift (ppm)

[Ir(dF(CF)$_3$ppy)$_2$(bpy)]PF$_6$ (**5.6**): **^{1}H-NMR** (Acetone-*d*$_6$, 700 MHz): δ 8.90 (d, *J* = 8.2 Hz, 2H), 8.62 (d, *J* = 8.9 Hz, 2H), 8.41 (d, *J* = 7.4 Hz, 4H), 8.31 (d, *J* = 5.3 Hz, 2H), 7.98 (s, 2H), 7.87 - 7.73 (m, 2H), 6.87 (t, *J* = 10.9 Hz, 2H), 5.97 (d, *J* = 8.3 Hz, 2H). **^{13}C-NMR** (Acetone-*d*$_6$, 176 MHz): δ 167.66 (d, *J* = 6.2 Hz), 165.26 (d, *J* = 12.6 Hz), 163.80 (d, *J* = 12.3 Hz), 163.18 (d, *J* = 12.7 Hz), 161.69 (d, *J* = 13.1 Hz), 155.98 (s), 155.21 (d, *J* = 6.8 Hz), 151.48 (s), 146.20 (d, *J* = 4.4 Hz), 140.71 (s), 137.29 (s), 129.17 (s), 126.87 (s), 125.72 (s), 125.63 - 125.31 (m), 125.31 - 125.22 (m), 125.14 (s), 123.98 (s), 123.90 (d, *J* = 21.0 Hz), 122.90 (s), 121.35 (s), 119.81 (s), 114.46 (d, *J* = 17.9 Hz), 99.51 (s), 99.35 (s), 99.20 (s).

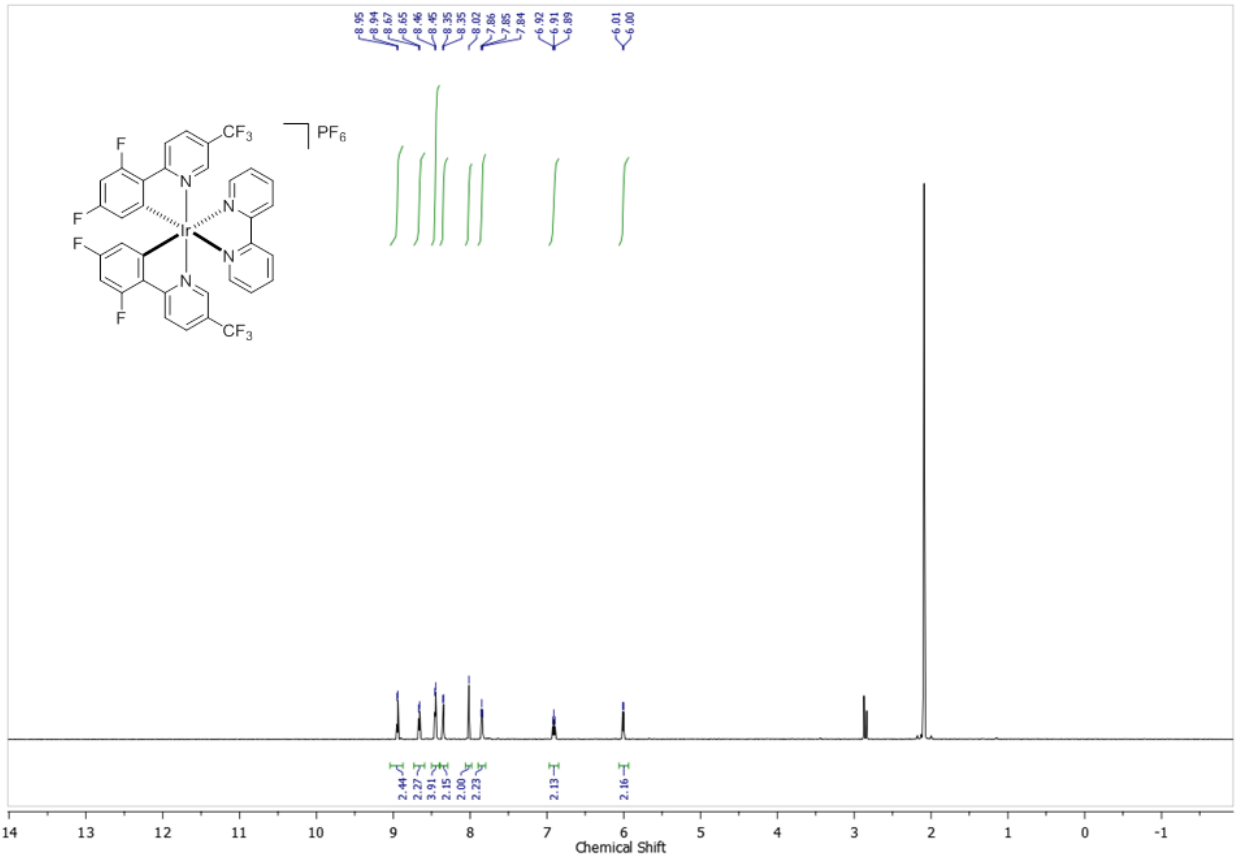

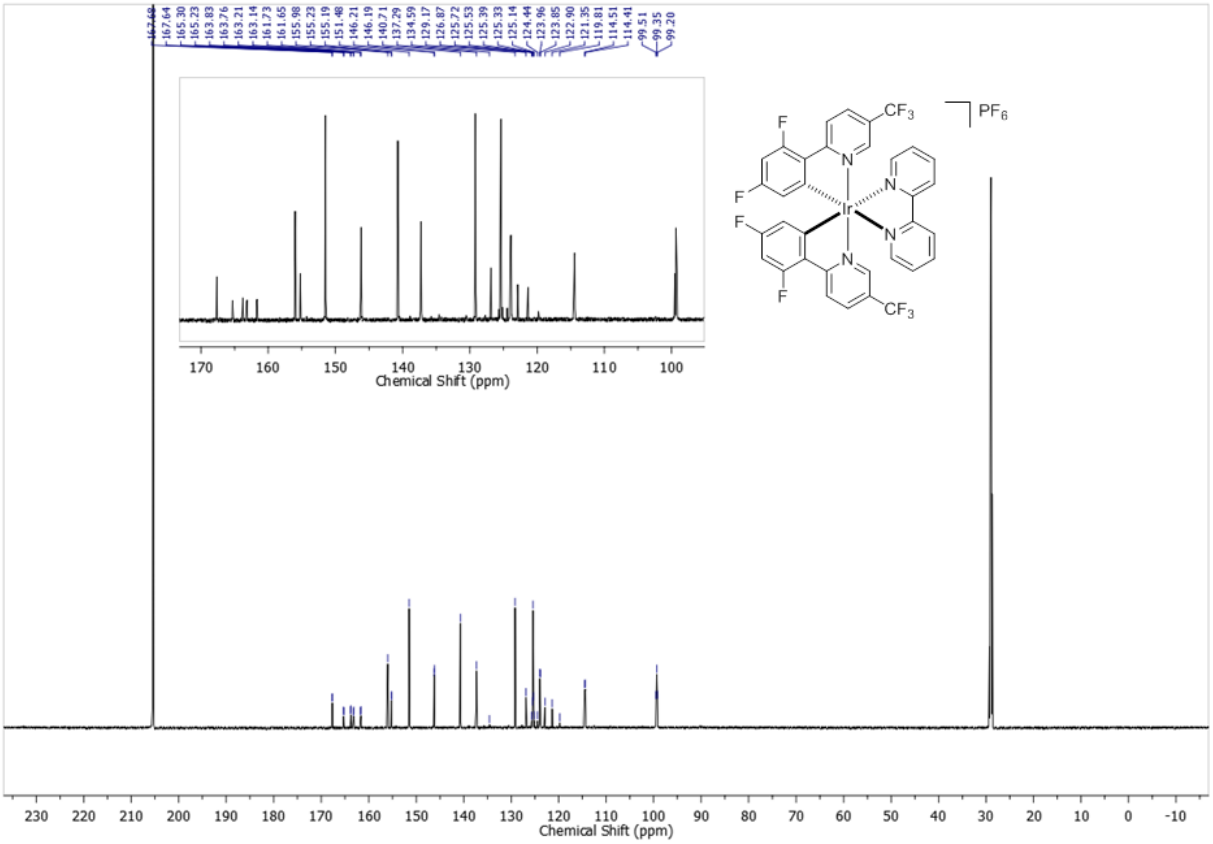
F
CF3
PF6
N
F
Ir
N
F
N
F
CF3
Chemical Shift (ppm)
Chemical Shift (ppm)

[Ir(dF(CF)$_3$ppy)$_2$(dtbbpy)]PF$_6$ (**5.7**)*:* **^{1}H-NMR** (Acetone-*d*$_6$, 700 MHz): δ 8.94 (s, 2H), 8.62 (d, *J* = 8.9 Hz, 2H), 8.41 (d, *J* = 8.7 Hz, 2H), 8.19 (d, *J* = 5.8 Hz, 2H), 7.94 - 7.70 (m, 4H), 6.87 (t, *J* = 10.3 Hz, 2H), 5.97 (d, *J* = 7.9 Hz, 2H), 1.43 (s, 18H).**^{13}C-NMR** (Acetone-*d*$_6$, 176 MHz): δ 167.83 (s), 165.33 (d, *J* = 18.6 Hz), 163.85 (d, *J* = 12.6 Hz), 163.19 (d, *J* = 12.7 Hz), 161.70 (d, *J* = 13.2 Hz), 156.00 (s), 155.77 (d, *J* = 6.9 Hz), 151.09 (s), 145.72 (d, *J* = 4.7 Hz), 137.18 (s), 126.81 (s), 126.03 (s), 125.23 (d, *J* = 34.6 Hz), 124.11 - 124.03 (m), 123.90 (d, *J* = 20.9 Hz), 122.91 (s), 122.67 (s), 121.37 (s), 114.44 (d, *J* = 17.9 Hz), 99.31 (d, *J* = 27.1 Hz), 99.09 (s), 99.08 (s), 35.70 (s), 29.45 (s).

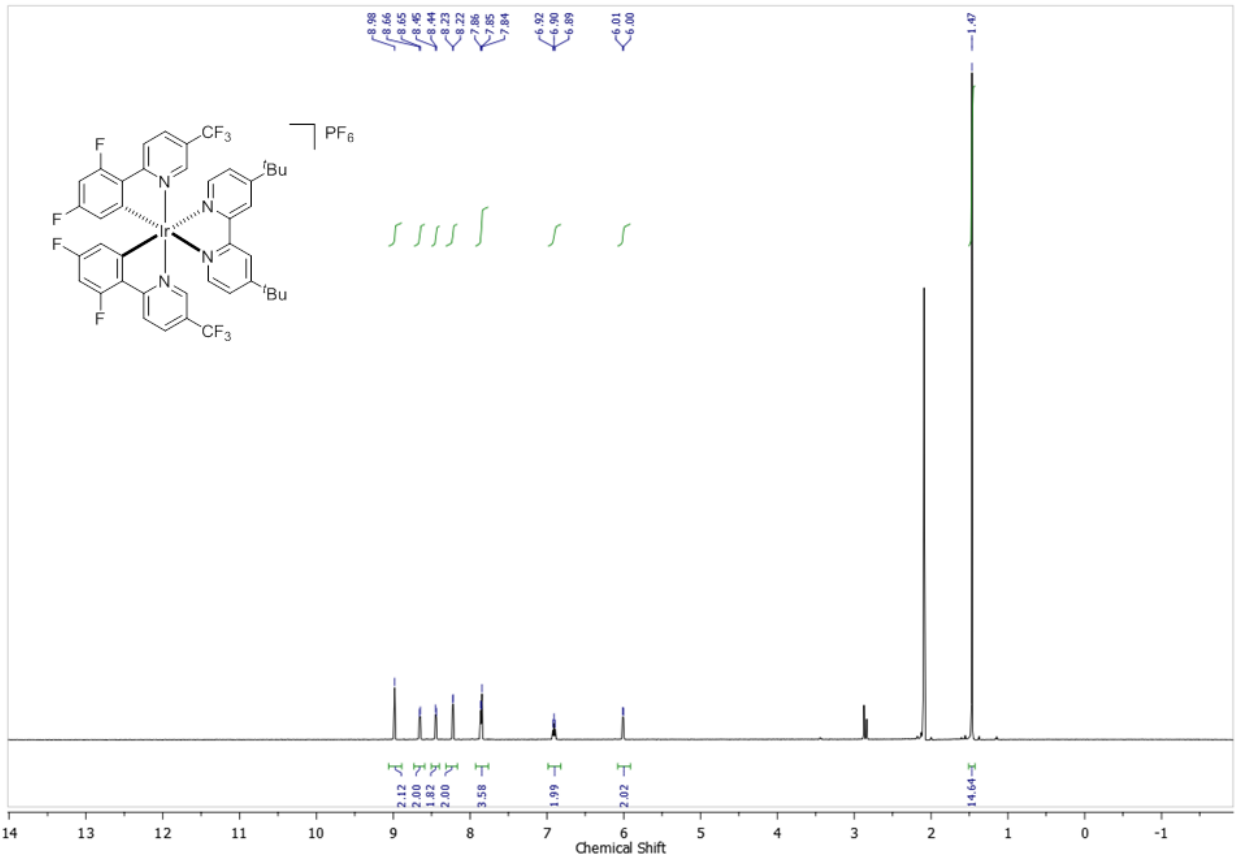

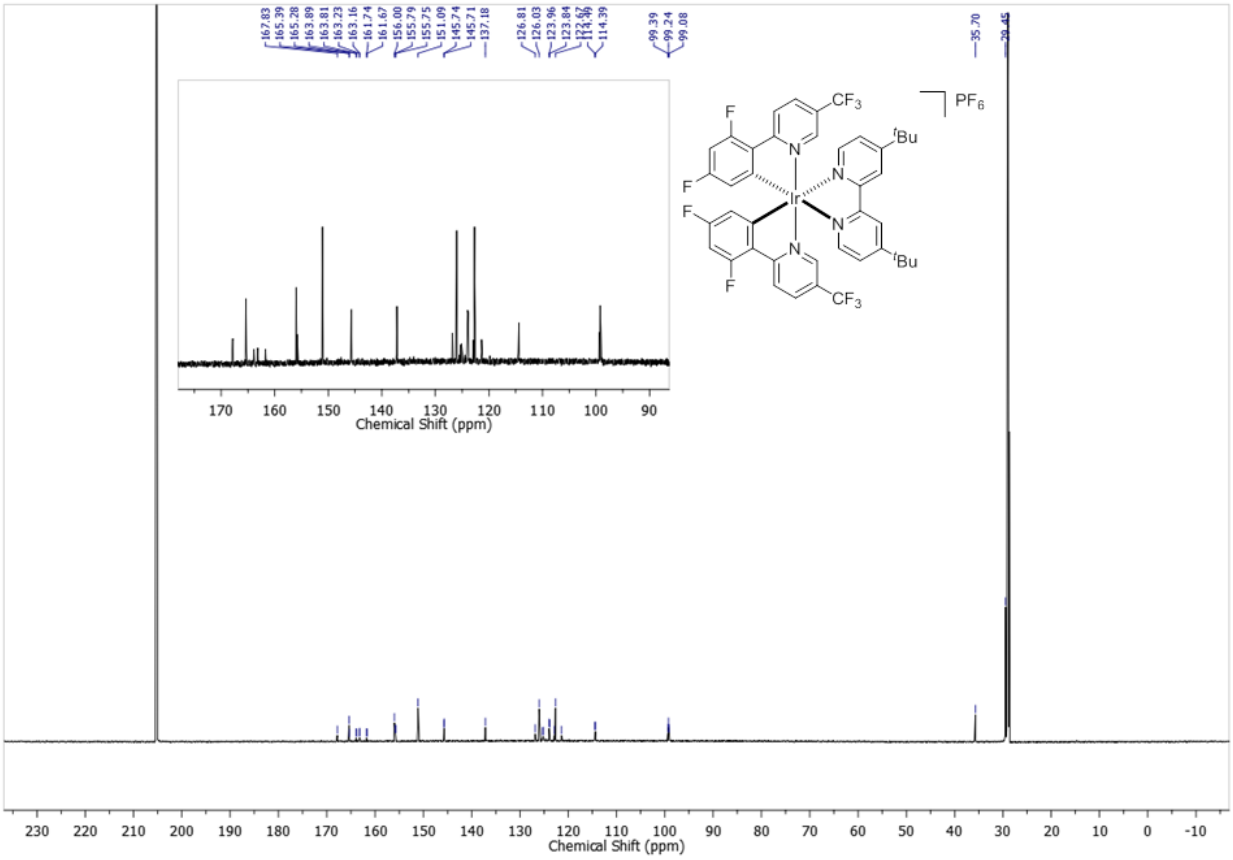
167.83
165.39
165.28
163.89
163.81
163.23
163.16
161.74
161.67
156.00
155.79
155.75
151.09
145.74
145.71
137.18
126.81
126.03
123.96
123.84
114.46
114.39
99.39
99.24
99.08
35.70
29.45
CF3
PF6
F
N
Ir
tBu
Chemical Shift (ppm)
Chemical Shift (ppm)

[Ir(dF(CF)$_3$ppy)$_2$(phen)]PF$_6$ (**5.8**): **^{1}H-NMR** (Acetone-d_6, 500 MHz): δ 9.02 (d, *J* = 8.3 Hz, 2H), 8.69 (d, *J* = 5.1 Hz, 2H), 8.62 (d, *J* = 8.6 Hz, 2H), 8.46 (s, 2H), 8.35 (d, *J* = 8.8 Hz, 2H), 8.16 (dd, *J* = 8.3, 5.1 Hz, 2H), 7.87 (s, 2H), 6.99 - 6.85 (m, 2H), 6.08 (dd, *J* = 8.4, 2.2 Hz, 2H). **^{13}C-NMR** (Acetone-d_6, 176 MHz): δ 167.69 (d, *J* = 6.9 Hz), 165.24 (d, *J* = 12.9 Hz), 163.77 (d, *J* = 12.7 Hz), 163.15 (d, *J* = 13.0 Hz), 161.66 (d, *J* = 13.1 Hz), 154.67 (d, *J* = 7.1 Hz), 152.33 (s), 146.75 (s), 146.46 (d, *J* = 4.6 Hz), 139.72 (s), 137.19 (s), 131.91 (s), 128.63 (s), 127.34 (s), 127.12 (s), 125.33 (s), 125.13 (s), 124.28 (s), 123.76 (d, *J* = 20.9 Hz), 123.69 - 123.55 (m), 122.74 (s), 121.19 (s), 114.71 (d, *J* = 18.0 Hz), 99.58 (s), 99.43 (s), 99.28 (s).

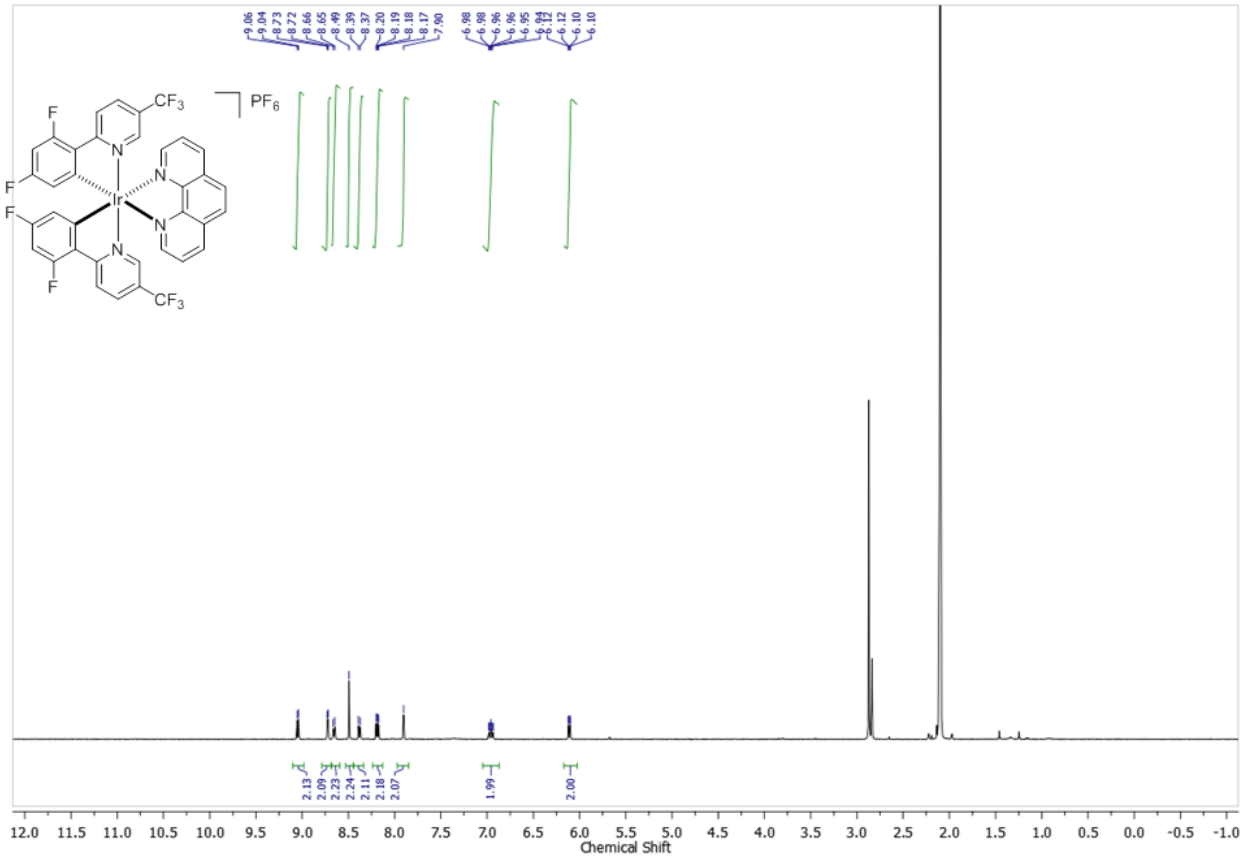

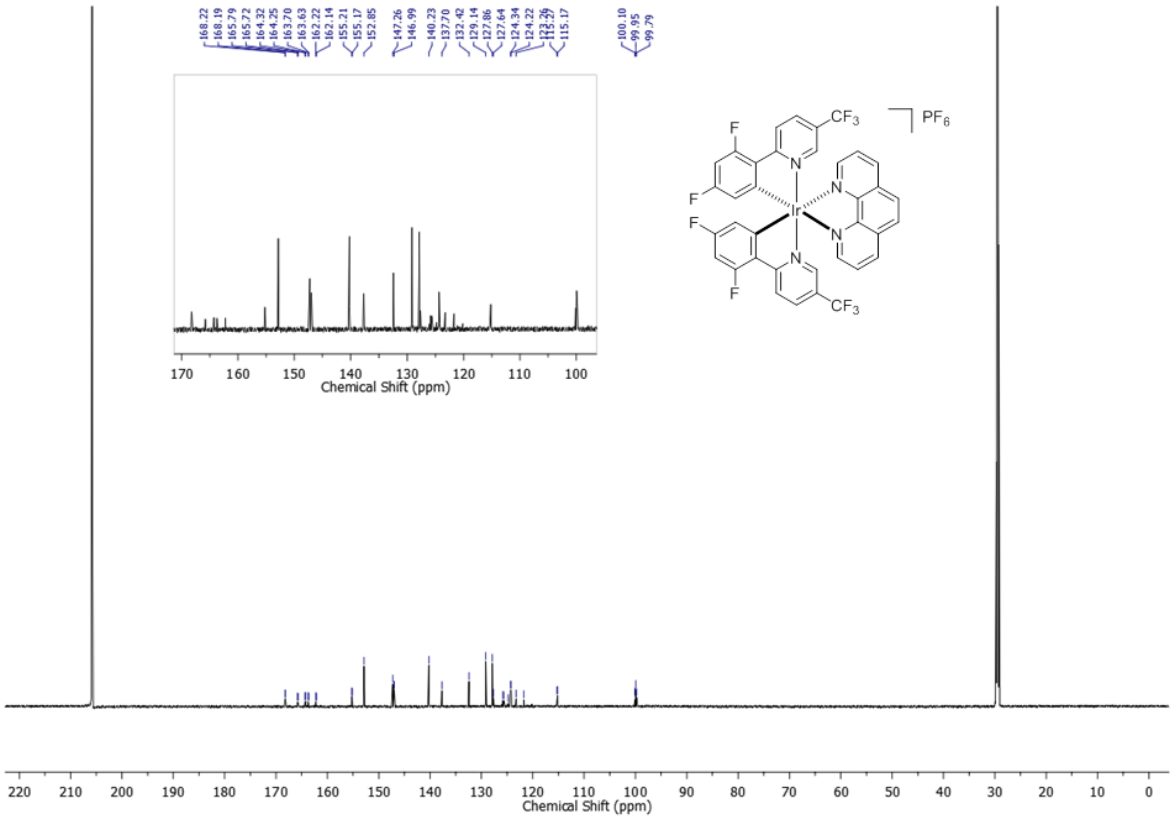
168.22
168.19
165.79
165.72
164.32
164.25
163.70
163.63
162.22
162.14
155.21
155.17
152.85
147.26
146.99
140.23
137.70
132.42
129.14
127.86
127.64
124.34
124.22
115.17
100.10
99.95
99.79
170 160 150 140 130 120 110 100
Chemical Shift (ppm)
F
CF3
PF6
N
Ir
F
F
N
N
F
CF3
220 210 200 190 180 170 160 150 140 130 120 110 100 90 80 70 60 50 40 30 20 10 0
Chemical Shift (ppm)

^{1}H NMR (700 MHz, acetone-d6)

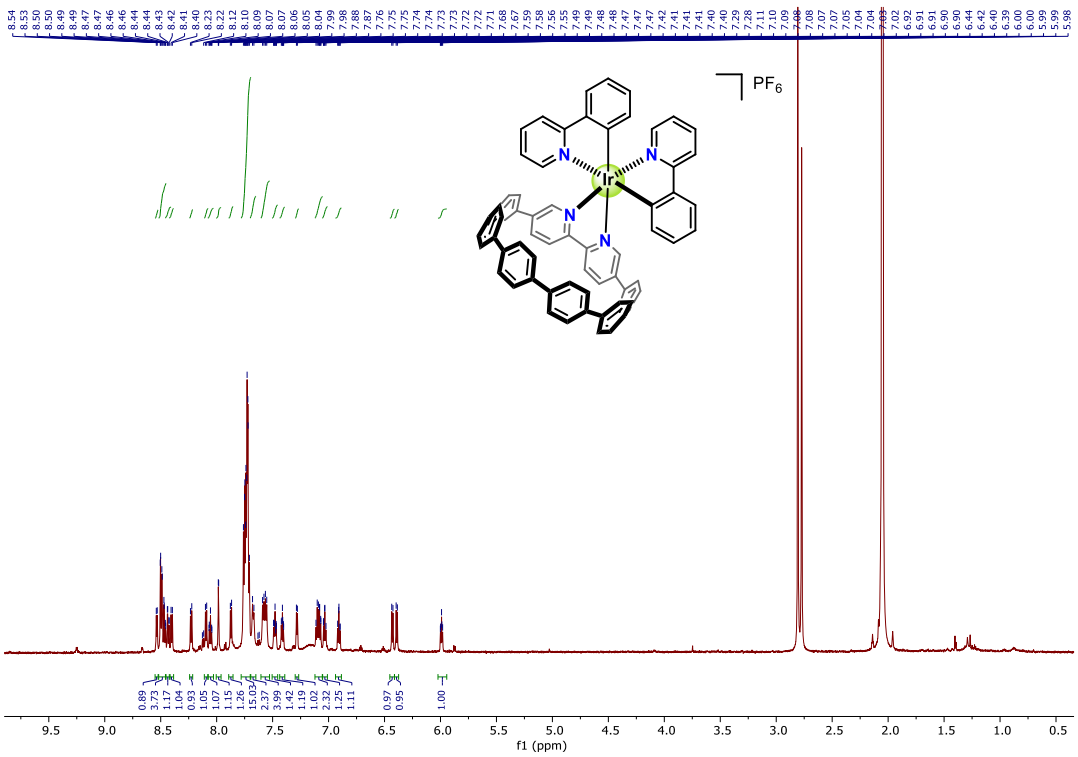

^{19}F NMR (377 MHz, acetone-d6)

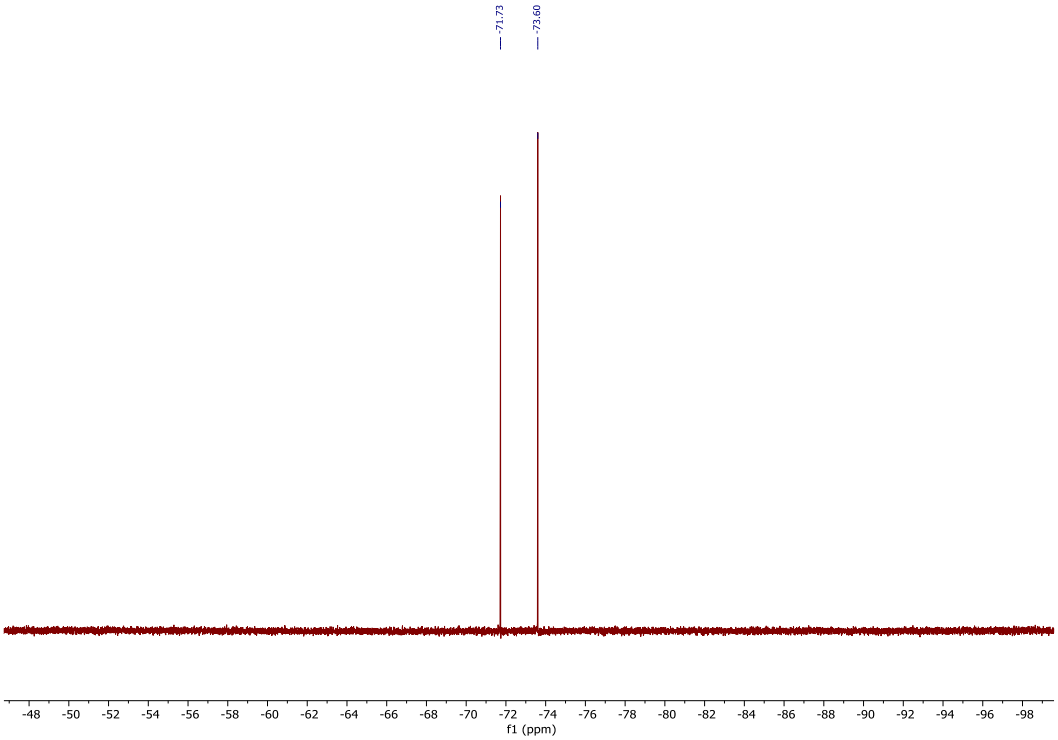

^{1}H NMR (700 MHz, acetone-d6)

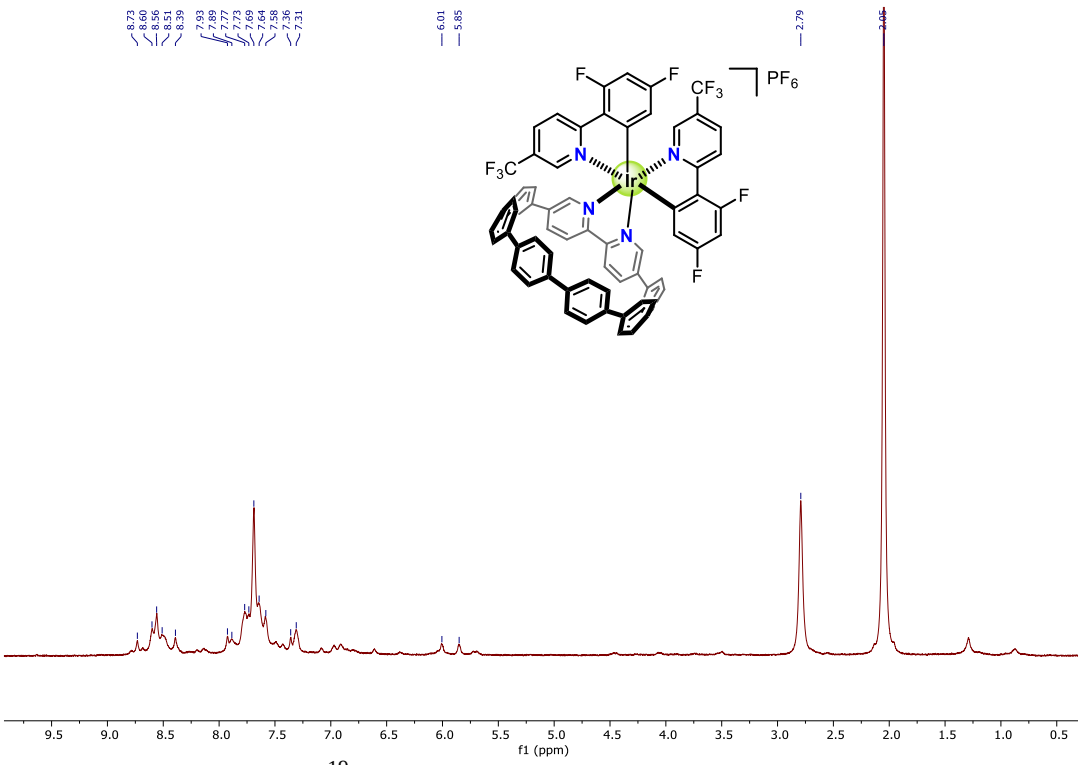

^{19}F NMR (377 MHz, acetone-d6)

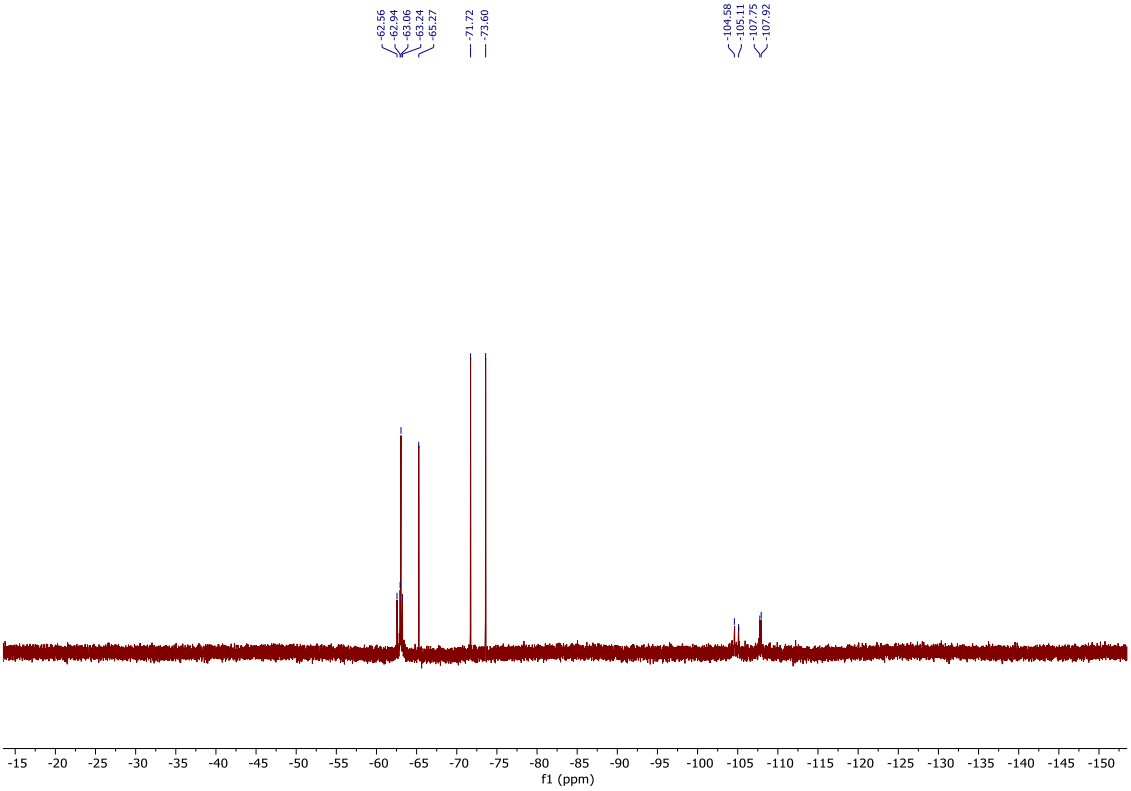

^{1}H NMR (700 MHz, acetone-d6)

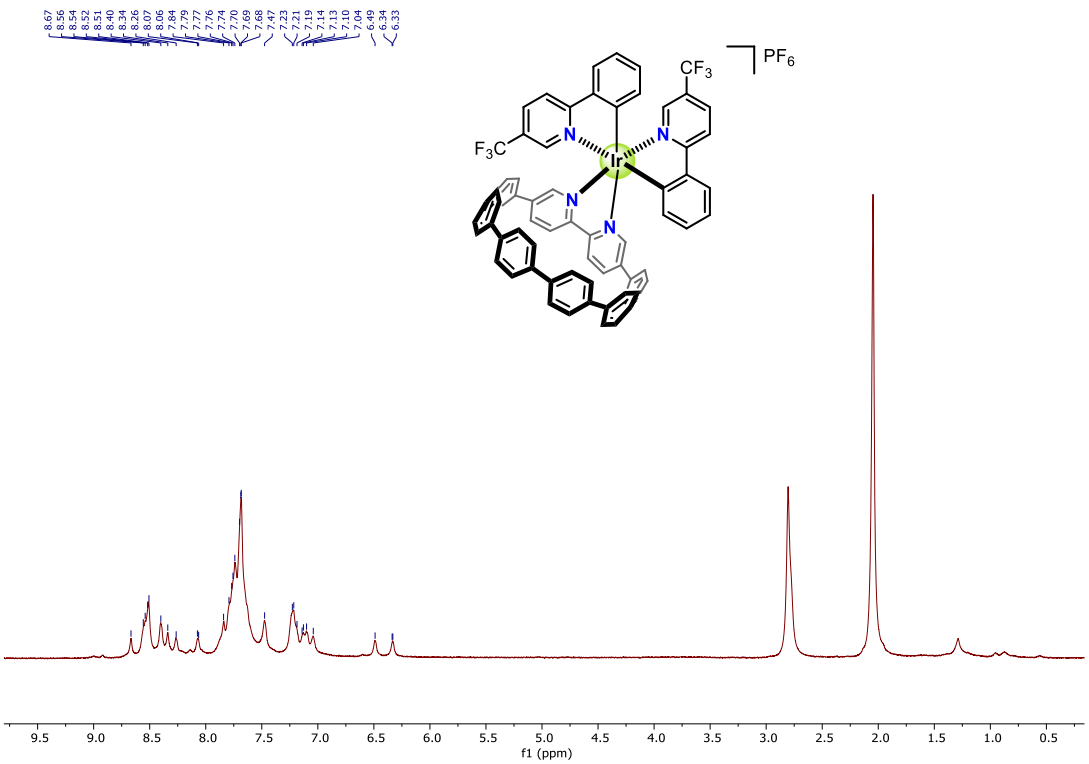

^{19}F NMR (377 MHz, acetone-d6)

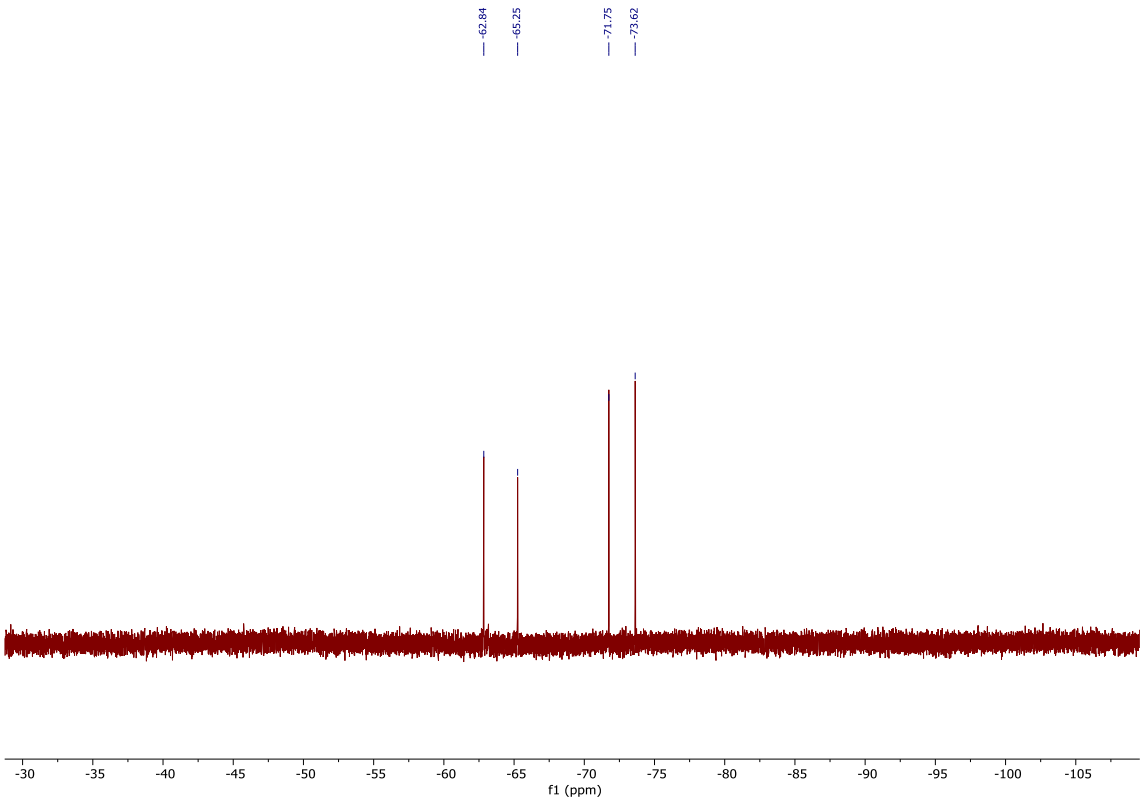

^{1}H NMR (700 MHz, acetone-d6)

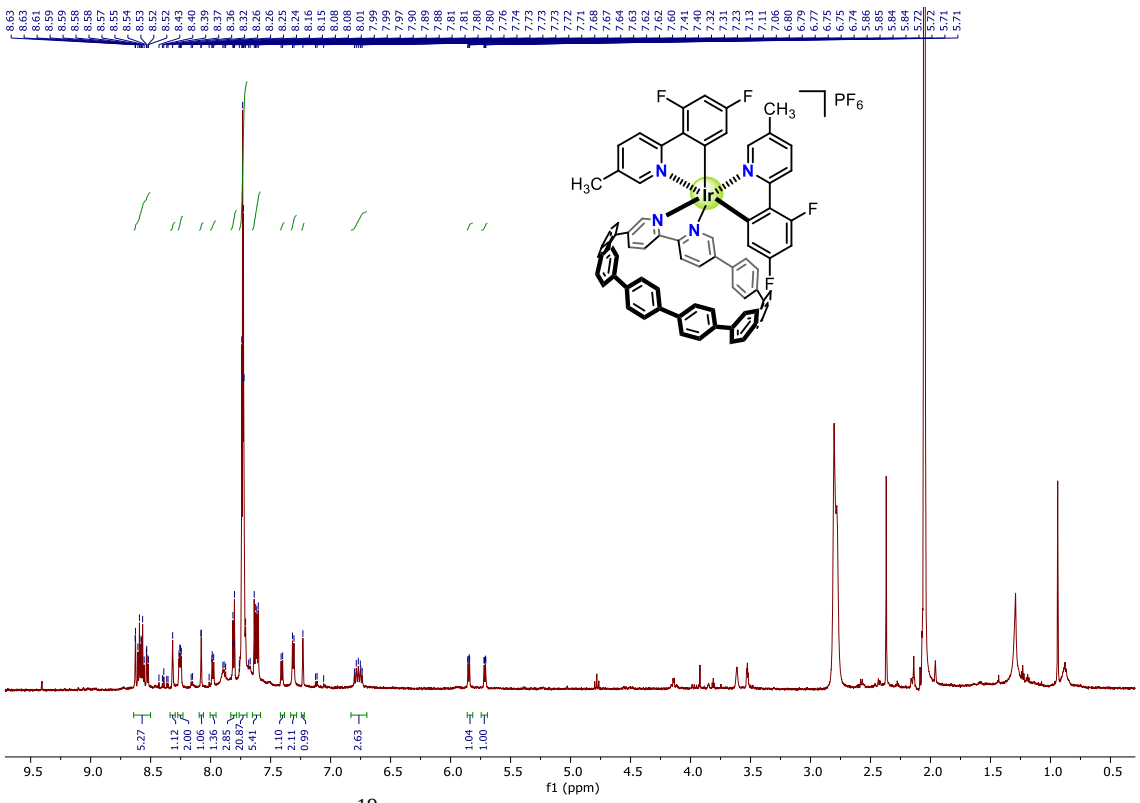

^{19}F NMR (377 MHz, acetone-d6)

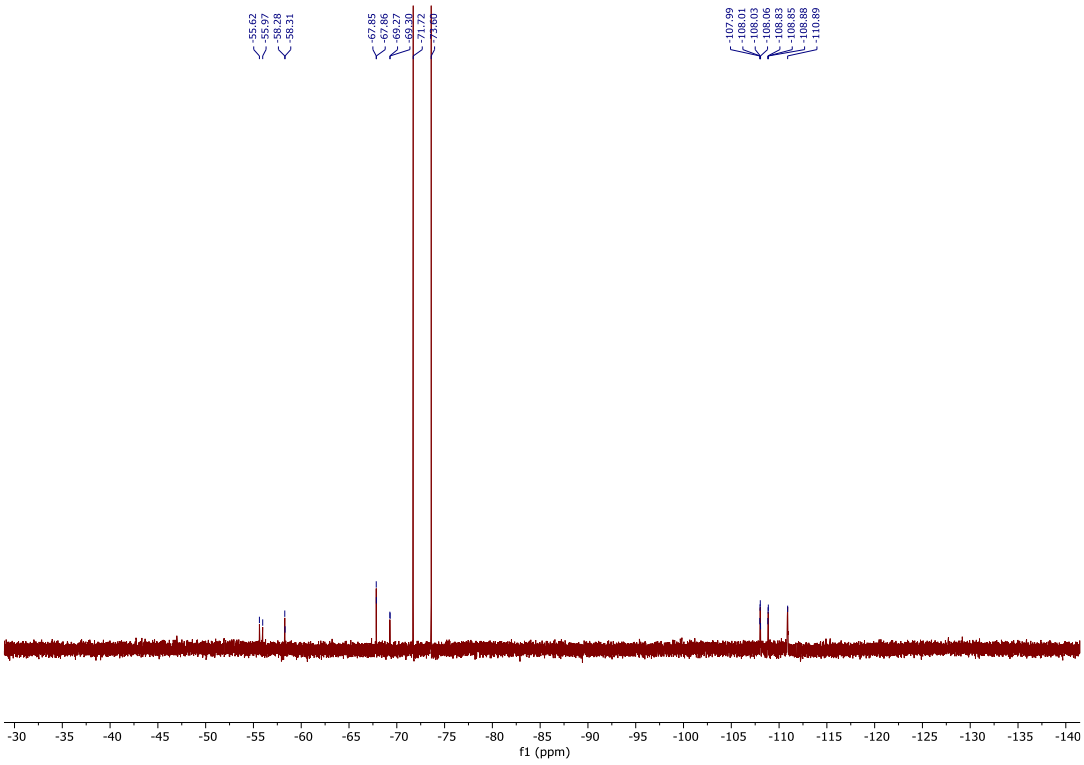

^{1}H NMR (700 MHz, acetone-d6)

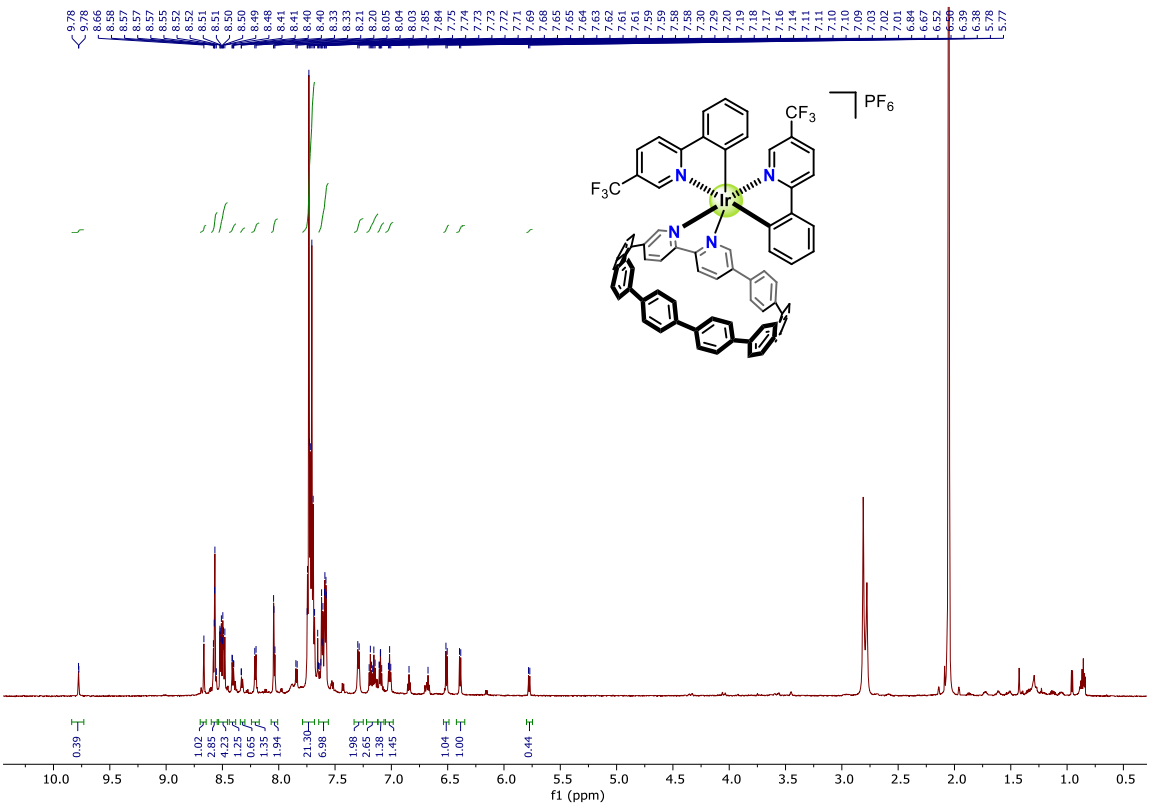

^{19}F NMR (377 MHz, acetone-d6)

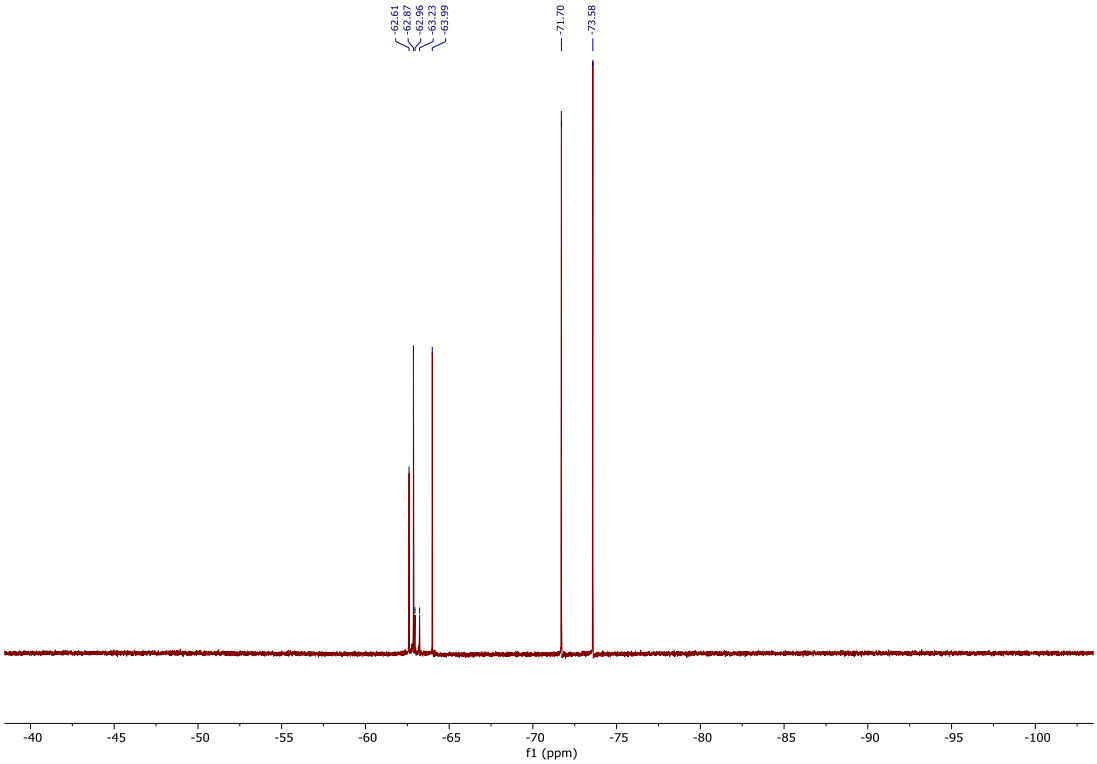

^{1}H NMR (700 MHz, acetone-d6)

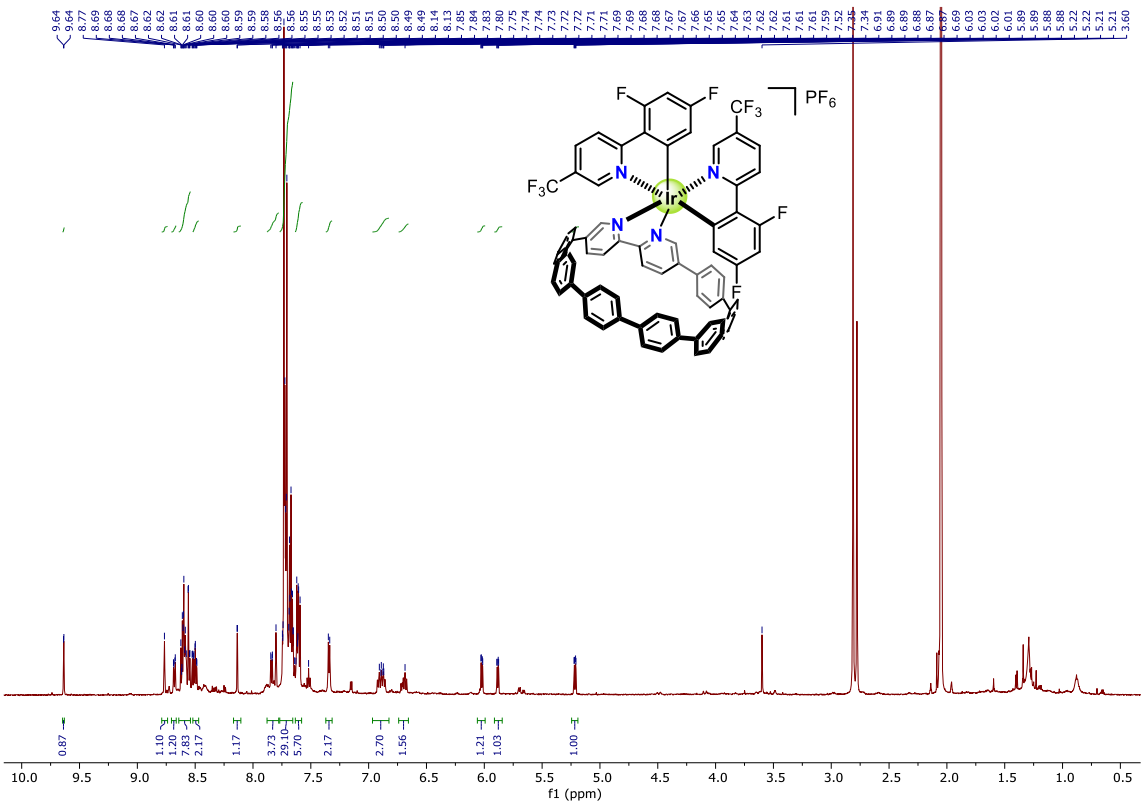

^{19}F NMR (377 MHz, acetone-d6)

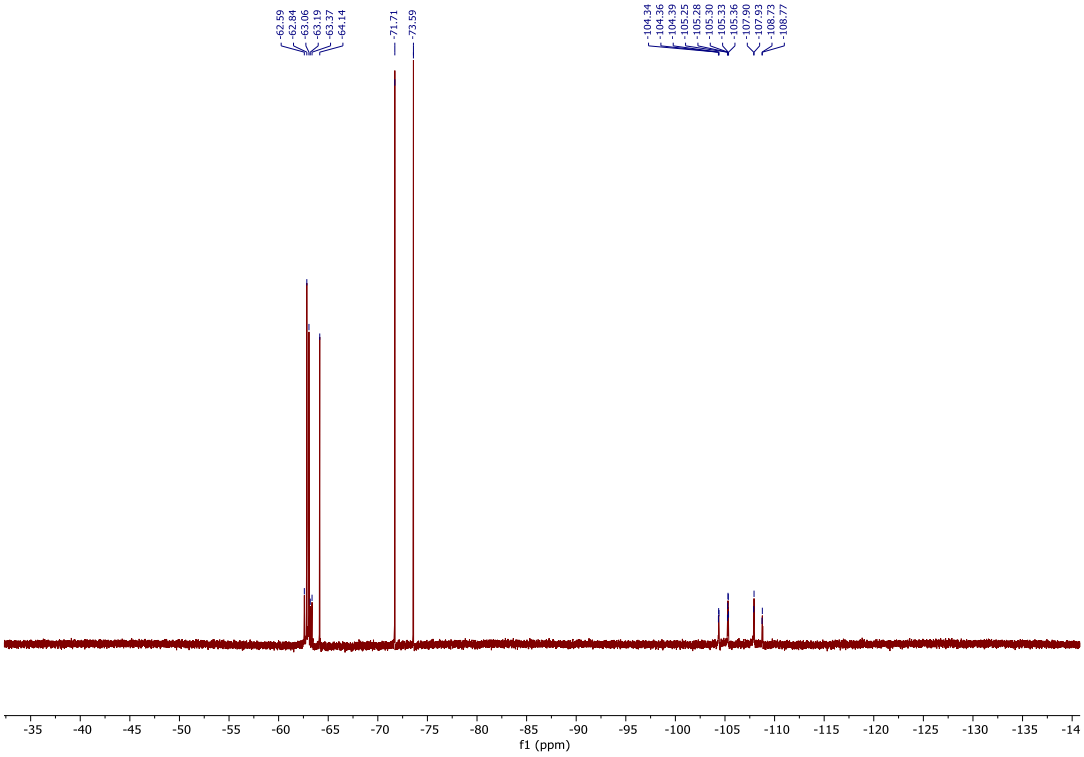

^{1}H NMR (700 MHz, acetone-d6)

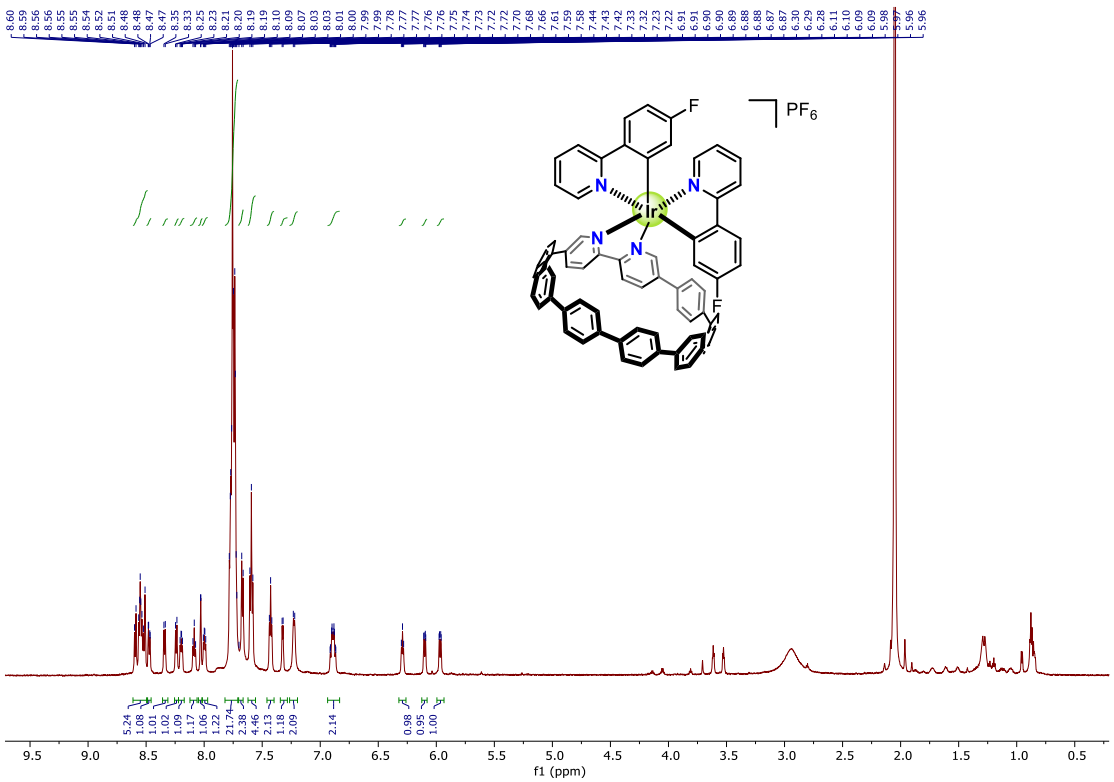

^{19}F NMR (377 MHz, acetone-d6)

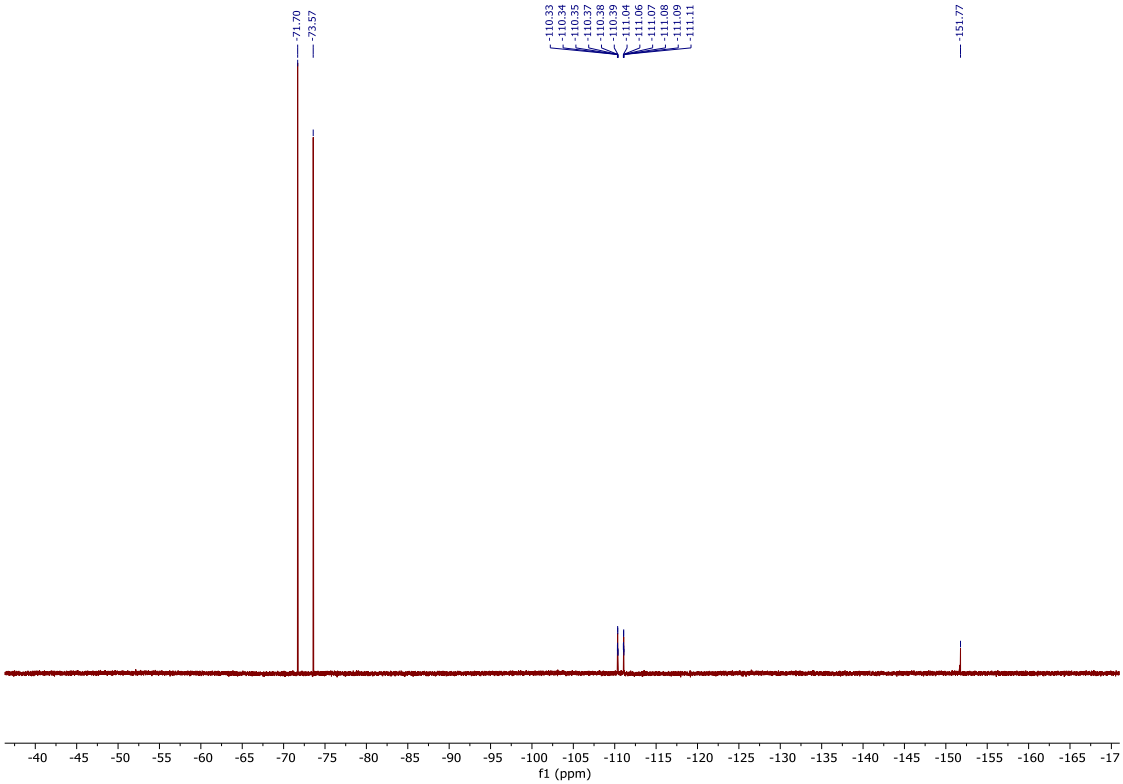

Bibliography

[1] Burstall, F.H. *J. Chem. Soc.* **1936**, 173–175.

[2] Meyer, T. J. *Acc. Chem. Res*. **1989**, 22, 163–170.

[3] O'Regan, B.; Grätzel, M. *Nature* **1991**, *353*, 737–740.

[4] Gray, H. B.; Maverick, A.W. *Science* **1981**, *214*, 1201–1205.

[5] Prier, C. K.; Rankic, D. A.; MacMillan, D. W. C. *Chem. Rev*. **2013**, *113*, 5322–5363.

[6] Tucker, J. W.; Stephenson, C. R. J. *J. Org. Chem*. **2012**, *77*, 1617–1622.

[7] Juris, A.; Balzani, V.; Belser, P.; von Zelewsky, A. *Helv. Chim. Acta.* **1981**, *64*, 2175–2182.

[8] Kalyanasundaram, K. *Coord. Chem. Rev.* **1982**, *46*, 159–244.

[9] Tucker, J.W.; Stephenson, C.R.L. *J. Org. Chem.* **2012**, *77*, 1617–1622.

[10] Adamo, A.; Beingessner, R.; Behnam, M.; Chen, J.; Jamison, T.; Jensen, K.; Monbaliu, J.; Myerson, A.; Revalor, E.; Snead, D.; Stelzer, T.; Weeranoppanant, N.; Wong, S.; Zhang, P. *Science*, **2016**, *352*, 61-67.

[11] Yayla, H.; Peng, F.; Mangion, I.; McLaughlin, M.; Campeau, L.; Davies, I.; DiRocco, D.; Knowles, R. *Chem. Sci.* **2016**, *7*, 2066-2073.

[12] Le, C.; Wismer, M.; Shi, Z.; Zhang, R.; Conway, D.; Li, G.; Vachal, P.; Davies, I.; MacMillan, D. *ACS Cent. Sci*, **2017**, *3*, 647–653.

[13] Vasudevan, A.; Villamil, C.; Trumbull, J.; Olson, J.; Sutherland, D.; Pan, J.; Djuric, S. *Tetrahedron Lett.* **2010**, *51*, 4007–4009.

[14] Douglas, J. J.; Cole, K. P.; Stephenson, C. R. J. *J. Org. Chem.* **2014**, *79*, 116311–11643.

[15] Beatty, J. W.; Douglas, J. J.; Cole, K. P.; Stephenson, C. R. J. *Nature Comm.* **2015**, *6*, 7919–7925.

[16] Beatty, J. W.; Douglas, J. J.; Miller, R.; McAtee, R. C.; Cole, K. P.; Stephenson, C. R. J. *Chem* **2016**, *1*, 456-472.

[17] Douglas, J. J.; Albright, H.; Sevrin, M. J.; Cole, K. P.; Stephenson, C. R. J. *Angew. Chem., Int. Ed.* **2015**, *54*, 14898-14902.

[18] Brown, D. G.; Bostrom, J. *J. Med. Chem.* **2016**, *59*, 4443-4458.

[19] Pozharskii, A. F.; Soldatenkov, A. T.; Katritzky, A. R. *Heterocycles in Life and Society: An Introduction to Heterocyclic Chemistry, Biochemistry, and Applications*; John Wiley & Sons: 2011.

[20] Vitaku, E.; Smith, D. T.; Njardarson, J. T. *J. Med. Chem.* **2014**, *57*, 10257-10274.

[21] Taylor, A. P.; Robinson, R. P.; Fobian, Y. M.; Blakemore, D. C.; Jones, L. H.; Fadeyi, O. *Org. Biomol. Chem.* **2016,** *14*, 6611-6637.

[22] Cernak, T.; Dykstra, K. D.; Tyagarajan, S.; Vachal, P.; Krska, S. W. *Chem. Soc. Rev.* **2016**, *45*, 546-576.

[23] Schönherr, H.; Cernak, T. *Angew. Chem., Int. Ed.* **2013**, *52*, 12256-12267.

[24] Minisci, F.; Bernardi, R.; Bertini, F.; Galli, R.; Perchinummo, M. *Tetrahedron* **1971**, *27*, 3575-3579.

[25] Langlois, B. R.; Laurent, E.; Roidot, N. *Tetrahedron Lett.* **1991**, *32*, 7525-7528.

[26] Minisci, F.; Citterio, A.; Vismara, E.; Giordano, C. *Tetrahedron* **1985**, *41*, 4157-4170.

[27] Punta, C.; Minisci, F. *Trends Heterocycl. Chem.* **2008**, *13*, 1-68.

[28] Studer, A.; Curran, D. P. *Angew. Chem., Int. Ed.* **2011**, *50*, 5018-5022.

[29] Duncton, M. A. J. *MedChemComm* **2011**, *2*, 1135-1161.

[30] Fujiwara, Y.; Dixon, J. A.; O'Hara, F.; Funder, E. D.; Dixon, D. D.; Rodriguez, R. A.; Baxter, R. D.; Herlé, B.; Sach, N.; Collins, M. R.; Ishihara, Y.; Baran, P. S. *Nature* **2012**, *492*, 95-99.

[31] Ji, Y.; Brueckl, T.; Baxter, R. D.; Fujiwara, Y.; Seiple, I. B.; Su, S.; Blackmond, D. G.; Baran, P. S. *Proc. Natl. Acad. Sci. USA* **2011**, *108*, 14411-14415.

[32] O'Hara, F.; Blackmond, D. G.; Baran, P. S. *J. Am. Chem. Soc.* **2013**, *135*, 12122-122134.

[33] Narayanam, J. M. R.; Stephenson, C. R. J. *Chem. Soc. Rev.* **2011**, *40*, 102-113.

[34] Prier, C. K.; Rankic, D. A.; MacMillan, D. W. C. *Chem. Rev.* **2013**, *113*, 5322-5363.
[35] Schultz, D. M.; Yoon, T. P. *Science* **2014**, *343*, 1239176.

[36] Blakemore, D. C.; Castro, L.; Churcher, I.; Rees, D. C.; Thomas, A. W.; Wilson, D. M.; Wood, A. *Nat. Chem.* **2018,** *10*, 383-394.

[37] Douglas, J. J.; Sevrin, M. J.; Stephenson, C. R. J. *Org. Proc. Res. Dev.* **2016**, *20*, 1134-1147.

[38] Li, Y.; Ge, L.; Muhammad, M. T.; Bao, H. *Synthesis* **2017**, *49*, 5263-5384.
[39] Liu, P.; Zhang, G.; Sun, P. *Org. Biomol. Chem.* **2016**, *14*, 10763-10777.

[40] Beatty, J. W.; Douglas, J. J.; Cole, K. P.; Stephenson, C. R. J. *Nature Comm.* **2015**, *6*, 7919-7925.

[41] Barton, D. H. R.; Crich, D.; Motherwell, W. B. *J. Chem. Soc., Chem. Commun*. **1983**, 939.

[42] Barton, D. H. R.; Lacher, B. L.; Zard, S. Z. *Tetrahedron* **1986**, *42*, 2325.

[43] Okada, K.; Okamoto, K.; Morita, N.; Okubo, K.; Oda, M. *J. Am. Chem. Soc*. **1991**, *113*, 9401-9402.

[44] Cheng, W-M.; Shang, R.; Fu, Y. *ACS Catal.* **2017**, *7*, 907-911.

[45] Cheng, W-M.; Shang, R.; Fu, M-C.; Fu, Y. *Chem. Eur. J.* **2017**, *23*, 2537-2541.

[46] Proctor, R. S. J.; Davis, H. J.; Phipps, R. J. *Science* **2018**, *360*, 419-422.

[47] Liu, X.; Liu, Y.; Chai, G.; Qiao, B.; Zhao, X.; Jiang, Z. *Org. Lett.* **2018**, *20*, 6298-6301.

[48] Sherwood, T. C.; Li, N.; Yazdani, A. N.; Dhar, T. G. M. *J. Org. Chem.* **2018**, *83*, 3000-3012.

[49] DiRocco, D. A.; Dykstra, K.; Krska, S.; Vachal, P.; Conway, D. V.; Tudge, M. *Angew. Chem. Int. Ed.* **2014**, *53*, 4802-4806.

[50] Zuo, Z.; MacMillan, D. W. C. *J. Am. Chem. Soc.* **2014**, *136*, 5257-5260.

[51] Garza-Sanchez, R. A.; Tlaheuxt-Aca, A.; Tavakoli, G.; Glorius, F. *ACS Catal.* **2017**, *7*, 4057-4061.

[52] Genovino, J.; Lian, Y.; Zhang, Y.; Hope, T. O.; Juneau, A.; Gagne, Y.; Ingle, G.; Frenette, M. *Org. Lett.* **2018**, *20*, 3229-3232.

[53] Seiple, I. B.; Su, S.; Rodriguez, R. A.; Gianatassio, R.; Fujiwara, Y.; Sobel, A. L.; Baran, P. S. *J. Am. Chem. Soc.* **2010**, *132*, 13194-13196.

[54] Ollivier, C.; Renaud, P. *Chem. Rev.* **2001**, *101*, 3415-3434.

[55] Darmency, V.; Renaud, P. In *Radicals in Synthesis I*, Springer: 2006.

[56] Vogler, T.; Studer, A. *Org. Lett.* **2008**, *10*, 129-131.

[57] Pouliot, M.; Renaud, P.; Schenk, K.; Studer, A.; Vogler, T. *Angew. Chem., Int. Ed.* **2009**, *48*, 6037-6040.

[58] Koike, T.; Akita, M. *Org. Biomol. Chem.* **2016**, *14*, 6886-6890.
[59] Yasu, Y.; Koike, T.; Akita, M. *Adv. Synth. Catal.* **2012**, *354*, 3414-3484.

[60] Tellis, J. C.; Primer, D. N.; Molander, G. A. *Science* **2014**, *345*, 433-436.

[61] Li, G.-X.; Morales-Rivera, C. A.; Wang, Y.; Gao, F.; He, G.; Liu, P.; Chen, G. *Chem. Sci.* **2016**, *7*, 6407-6412.

[62] Sorin, G.; Martinez Mallorquin, R.; Contie, Y.; Baralle, A.; Malacria, M.; Goddard, J.-P.; Fensterbank, L. *Angew. Chem., Int. Ed.* **2010**, *49*, 8721-8723.

[63] Molander, G. A.; Colombel, V.; Braz, V. A. *Org. Lett.* **2011**, *13*, 1852-1855.

[64] Presset, M.; Fleury-Brégeot, N.; Oehlrich, D.; Rombouts, F.; Molander, G. A. *J. Org. Chem.* **2013,** *78*, 4615-4619.

[65] Matsui, J. K.; Primer, D. N.; Molander, G. A. *Chem. Sci.* **2017**, *8*, 3512-3522.

[66] Kuivila, H. G. *Synthesis* **1970**, *1970*, 499.

[67] Tucker, J. W.; Narayanam, J. M. R.; Krabbe, S. W.; Stephenson, C. R. J. *Org. Lett.* **2010**, *12*, 368-371.

[68] Furst, L.; Matsuura, B. S.; Narayanam, J. M. R.; Tucker, J. W.; Stephenson, C. R. J. *Org. Lett.* **2010**, *12*, 3104.

[69] Swift, E. C.; Williams, T. M.; Stephenson, C. R. J. *Synlett* **2016**, *27*, 754-758.

[70] Bissonnette, N. B.; Boyd, M. J.; May, G. D.; Giroux, S.; Nuhant, P. *J. Org. Chem.* **2018**, *83*, 10933-10940.

[71] Dong, J.; Lyu, X.; Wang, Z.; Wang, X.; Song, H.; Liu, Y.; Wang, Q. *Chem. Sci.* **2018**, *10*, 976-982.

[72] Devery, J. J.; Nguyen, J. D.; Dai, C.; Stephenson, C. R. J. *ACS Catal.* **2016**, *6*, 5962-5967.

[73] Zhang, P.; Le, C.; MacMillan, D. W. C. *J. Am. Chem. Soc.* **2016**, *138*, 8084-8087.

[74] Nagib, D. A.; MacMillan, D. W. C. *Nature* **2011**, *480*, 224-228.

[75] Choi, W. J.; Choi, S.; Ohkubo, K.; Fukuzumi, S.; Cho, E. J.; You, Y. *Chem. Sci.* **2015**, *6*, 1454-1464.

[76] Kaldas, S. J.; Cannillo, A.; McCallum, T.; Barriault, L. *Org. Lett.* **2015**, *17*, 2864-2866.

[77] McCallum, T.; Barriault, L. *Chem. Sci.* **2016**, *7*, 4754-4758.
[78] Nuhant, P.; Oderinde, M. S.; Genovino, J.; Juneau, A.; Gagné, Y.; Allais, C.; Chinigo, G. M.; Choi, C.; Sach, N. W.; Bernier, L.; Fobian, Y. M.; Bundesmann, M. W.; Khunte, B.; Frenette, M.; Fadeyi, O. O. *Angew. Chem., Int. Ed.* **2017**, *56*, 15309-15313.

[79] Sloan, K. B.; Bodor, N. *Int. J. Pharm.* **1982**, *12*, 299-313.

[80] Jin, J.; MacMillan, D. W. C. *Nature* **2015**, *525*, 87-90.

[81] Huff, C. A.; Cohen, R. D.; Dykstra, K. D.; Streckfuss, E.; DiRocco, D. A.; Krska, S. W. *J. Org. Chem.* **2016**, *81*, 6980-6987.

[82] Liu, W.; Yang, X.; Zhou, Z.-Z.; Li, C.-J. *Chem* **2017**, *2*, 688-702.

[83] McCallum, T.; Pitre, S. P.; Morin, M.; Scaiano, J. C.; Barriault, L. *Chem. Sci.* **2017**, *8*, 7412-7418.

[84] Jin, J.; MacMillan, D. W. C. *Angew. Chem. Int. Ed.* **2014**, *54*, 1565-1569.

[85] Quattrini, M. C.; Fujii, S.; Yamada, K.; Fukuyama, T.; Ravelli, D.; Fagnoni, M.; Ryu, I. *Chem. Commun.* **2017**, *53*, 2335-2338.

[86] Bosset, C.; Beucher, H.; Bretel, G.; Pasquier, E.; Queguiner, L.; Henry, C.; Vos, A.; Edwards, J. P.; Meerpoel, L.; Berthelot, D. *Org. Lett.* **2018**, *20*, 6003-6006.

[87] Hu, A.; Guo, J.-J.; Pan, H.; Zuo, Z. *Science* **2018**, *361*, 668-672.

[88] Müller, K.; Faeh, C.; Diedrich, F. *Science* **2007**, *317*, 1881–1886.

[89] Wang, J. W.; Sánchez-Roselló, M.; Aceña, J. L.; d. Pozo, C.; Sorochinsky, A. E.; Fustero, S.; Soloshonok, V. A.; Liu, H. *Chem. Rev.* **2014**, *114*, 2432–2506.

[90] Siegemund, G.; Schwertfeger, W.; Feiring, A.; Smart, B.; Behr, F.; Vogel, H.; McKusick, B. Fluorine Compounds, Organic. In *Ullmann's Encyclopedia of Industrial Chemistry*; Wiley, 2002.

[91] DeBaillie, A. C.; Jones, C. D.; Magnus, N. A.; Mateos, C.; Torrado, A.; Wepsiec, J. P.; Tokala, R.; Raje, P. *Org. Process Res. Dev.* **2015**, *19*, 1568–1575.

[92] Mulder, J. A.; Frutos, R. P.; Patel, N. D.; Qu, B.; Sun, X.; Tampone, T. G.; Gao, J.; Sarvestani, M.; Eriksson, M. C.; Haddad, N.; Shen, S.; Song, J. J.; Senanayake, C. H. *Org. Process Res. Dev.* **2013**, *17*, 940–945.

[93] Banks, R. E. *J. Fluorine Chem.* **1994**, *67*, 193–203.

[94] McCulloch, A.; Lindley, A. A. *Atmos. Environ.* **2007**, *41*, 1560.

[95] Naumann, D.; Tyrra, W.; Kock, B. *J. Fluorine Chem.* **1994**, *67*, 91–93.

[96] Krishnamurti, R.; Bellew, D. R.; Prakash, G. K. S. *J. Org. Chem.* **1991**, *56*, 984–989.

[97] Tordeux, M.; Langlois, B.; Wakselman, C. *J. Org. Chem.* **1989**, *54*, 2452–2453.

[98] Wakselman, C.; Tordeux, M. *Bull. Soc. Chim. Fr.* **1986**, 868.

[99] Matoušek, V.; Pietrasiak, E.; Schwenk, R.; Togni, A. *J. Org. Chem.* **2013**, *78*, 6763–6768.

[100] Umemoto, T.; Ishihara, S. *J. Fluorine Chem.* **1998**, *92*, 181–187.

[101] Umemoto, T.; Ishihara, S. *Tetrahedron Lett.* **1990**, *31*, 3579–3582.

[102] Ji, Y.; Brueckl, T.; Baxter, R. D.; Fujiwara, Y.; Seiple, I. B.; Su, S.; Blackmond, D. G.; Baran, P. S. *Proc. Natl. Acad. Sci. U. S. A.* **2011**, *108*, 14411–14415.

[103] Fujiwara, Y.; Dixon, J. A.; O'Hara, F.; Funder, E. D.; Dixon, D.; Rodriguez, R. A.; Baxter, R. D.; Herlé, B.; Sach, N.; Collins, M. R.; Ishihara, Y.; Baran, P. S. *Nature*, **2012**, *492*, 95–99.

[104] (a) McReynolds, K. A.; Lewis, R. S.; Ackerman, L. K. G.; Dubinina, G. G.; Brennessel, W. W.; Vicic, D. A. *J. Fluorine Chem.* **2010**, *131*, 1108–1112. (b) Beatty, J. W.; Douglas, J. J.; Cole, K. P.; Stephenson, C. R. J. *Nat. Commun.* **2015**, *6*, 7919.

[105] Depecker, C.; Marzouk, H.; Trevin, S.; Devynck, J. *New. J. Chem.* **1999**, *23*, 739–742.

[106] Chen, M.; Buchwald, S. L. *Angew. Chem., Int. Ed.* **2013**, *52*, 11628–11631.

[107] Shi, G.; Shao, C.; Pan, S.; Yu, J.; Zhang, Y. *Org. Lett.* **2015**, *17*, 38–41.

[108] Beatty, J. W.; Douglas, J. J.; Cole, K. P.; Stephenson, C. R. J. *Nat. Commun.* **2015**, *6*, 7919.

[109] Cismesia, M. A.; Yoon, T. P. *Chem. Sci.* **2015**, *6*, 5426–5434.

[110] Some examples of perfluoroethylation and propylation: a) Morimono, M. G.; Fier, P. S.; Hartwig, J. F. *Org. Lett.* **2014**, *16*, 1744–1747. b) Litvinas, N. D.; Fier, P. S.; Hartwig, J. F. *Angew. Chem., Int. Ed.* **2012**, *124*, 551–554. c) Serizawa, H.; Aikawa, K.; Mikami, K. *Org. Lett.* **2014**, *16*, 3456–3459.

[111] Tomashenko, O. A.; Grushin, V. V. *Chem. Rev.* **2011**, *111*, 4475–4521.

[112] Fujiwara, Y.; Dixon, J. A.; Rodriguez, R. A.; Baxter, R. D.; Dixon, D. D.; Collins, M. R.; Blackmond, D. G.; Baran, P. S. *J. Am. Chem. Soc.* **2012**, *134*, 1494–1497.

[113] Cooper, T. W. J.; Campbell, I. B.; Macdonald, S. J. F. *Angew. Chem., Int. Ed.* **2010**, *49*, 8082–8091.

[114] Molander, G. A.; Trice, S. L.; Kennedy, S. M.; Dreher, S. D.; Tudge, M. T. *J. Am. Chem. Soc.* **2012**, *134*, 11667–11673.

[115] Chinchilla, R.; Nájera, C.; Yus, M. *Chem. Rev.* **2004**, *104*, 2667–2722.

[116] Sun, J.; Perfetti, M. T.; Santos, W. L. *J. Org. Chem.* **2011**, *76*, 3571–3575.

[117] Merritt, J. M.; Andiappan, M.; Pietz, M. A.; Richey, R. N.; Sullivan, K. A.; Kjell, D. P. *Org. Process Res. Dev.* **2016**, *20*, 178–188.

[118] Brown, H. C.; Rangaishenvi, M. V. *J. Organomet. Chem.* **1988**, *358*, 15–30.

[119] Lyons, T. W.; Sanford, M. S. *Chem. Rev.* **2010**, *110*, 1147–1169.

[120] (a) Minisci, F.; Bernardi, R.; Bertini, F.; Galli, R.; Perchinummo, M. *Tetrahedron* **1971**, *27*, 3575-3579. (b) Langlois, B. R.; Laurent, E.; Roidot, N. *Tetrahedron Lett.* **1991**, *32*, 7525-7528. (c) Punta, C.; Minisci, F. *Trends Heterocycl. Chem.* **2008**, *13*, 1-68.

[121] Select recent examples of Minisci alkylations: (a) Molander, G. A.; Colombel, V.; Braz, V. A. *Org. Lett.* **2011**, *13*, 1852-1855. (b) Presset, M.; Fleury-Bregeot, N.; Oehlrich, D.; Rombouts, F., Molander, G. A. *J. Org. Chem.* **2013**, *78*, 4615-4619. (c) Ji, Y.; Brueckl, T.; Baxter, R. D.; Fujiwara, Y.; Seiple, I. B.; Su, S.; Blackmond, D. G.; Baran, P. S. *Proc. Natl. Acad. Sci. USA* **2011**, *108*, 14411-14415. (d) Fujiwara, Y.; Dixon, J. A.; O'Hara, F.; Funder, E. D.; Dixon, D. D.; Rodriguez, R. A.; Baxter, R. D.; Herle, B.; Sach, N.; Collins, H. R.; Ishihara, Y.; Baran, P. S. *Nature* **2012,** *492*, 95-99.

[122] Select examples of photoredox catalysis-based alkylations: (a) Jin, J.; MacMillan, D. W. C. *Nature*, **2015**, *525*, 87-90. (b) DiRocco, D. A.; Dykstra, K.; Krska, S.; Vachal, P.; Conway, D. V.; Tudge, M. *Angew. Chem. Int. Ed.* **2014**, *53*, 4802-4806. (c) Li, G. X.; Molares-Rivera, C.; Wang, Y.; Fang, Gao.; He, G.; Liu, P.; Chen, G. *Chem. Sci.* **2016**, *7*, 6407-6412. (d) McCallum, T.; Barriault, L. *Chem. Sci.* **2016**, *7*, 4754-4758. (e) Matsui, J. K.; Primer, D. N.; Molander, G. A. *Chem. Sci.*, **2017**, *8*, 3512-3522. (f) Garza-Sanchez, R. A.; Tlahuext-Aca, A.; Tavakoli, G.;

Glorius, F. *ACS Catal.* **2017**, *7*, 4057-4061. (g) Sherwood, T. C.; Li, N.; Yazdani, A. N.; Murali Dhar, T. G. *J. Org. Chem.* **2018**, *83*, 3000-3012. (h) Proctor, R. S. J.; Davis, H. J.; Phipps, R .J. *Science* **2018**, *360*, 419-422.

[123] De Vleeschouwer, F.; Van Speybroeck, V.; Waroquier, M.; Geerlings, P.; De Proft, F. *Org. Lett.* **2007**, *9*, 2721-2724.

[124] Barreiro, E. J.; Kümmerle, A. E.; Fraga, C. A. M. *Chem. Rev.* **2011**, *111*, 5215–5246.
[125] Minisci, F. *Tetrahedron* **1971**, *27*, 3575–3579.

[126] DiRocco, D. A.; Dykstra, K.; Krsta, S.; Vachal, P.; Conway, D. V.; Tudge, M. *Angew. Chem., Int. Ed.* **2014**, *53*, 4802–4806.

[127] Gunaydin, H.; Bartberger, M. D. *ACS Med. Chem. Lett.* **2016**, *7*, 341-344.

[128] Stockdale, T. P.; Williams, C. M. *Chem. Soc. Rev.* **2015**, *44*, 7737-7763.

[129] (a) Gillis, E. P.; Eastman, K. J.; Hill, M. D.; Donelly, D. J.; Meanwell, N. A. *J. Med. Chem.* **2015**, *58*, 8315-8359. (b) Purser, S.; Moore, P. R.; Swallow, S.; Gouverneur, V. *Chem. Soc. Rev.* **2008**, *37*, 320-330. (c) Ritchie, T. J.; Macdonald, S. J. F. *Eur. J. Med. Chem.* **2016**, *124*, 1057-1068.

[130] Murphy-Benenato, K. E.; Olivier, N.; Choy, A.; Ross, P. L.; Miller, M. D.; Thresher, J.; Gao, N.; Hale, M. R. *ACS Med. Chem. Lett.* **2014**, *5*, 1213-1217.

[131] (a) Popowycz, F.; Routier, S.; Joseph, B.; Merour, J-Y. *Tetrahedron* **2007**, *63*, 1031-1064. (b) Taylor, A. P.; Robinson, R. P.; Fobian, Y. M.; Blakemore, D.C.; Jones, L. H.; Fadeyi, O. *Org. Biomol. Chem.* **2016**, *14*, 6611-6637.

[132] Baidya, M.; Brotzel, F.; Mayr, H. *Org. Biomol. Chem.* **2010**, *8*, 1929-1935.

[133] Douglas, J.J.; Cole, K.P.; Stephenson, C. R. J. *J. Org. Chem.* **2014**, *79*, 11631-11643.

[134] Ma, X.; Dang, H.; Rose, J.A.; Rablen, P.; Herzon, S.B. *J. Am. Chem. Soc.* **2017**, *139*, 5998-6007.

[135] Beatty, J.; Douglas, J.; Miller, R.; McAtee, R.; Cole, K.; Stephenson, C. *Chem* **2016**, *1*, 456-472.

[136] Brackow, J., Wanner, K.T. *Tetrahedron* **2006**, *62*, 2395-2404.

[137] Panda, S.; Coffin, A.; Nguyen, Q.N.; Tantillo, D.J.; Ready, J.M. *Angew. Chem., Int. Ed.* **2016**, *55*, 2205-2209.

[138] Jo, W.; Kim, J.; Choi, S.; Cho, S.H. *Angew. Chem., Int. Ed.* **2016**, *55*, 9842-9846.

[139] Wei, Y.; Yoshikai, N. *J. Am. Chem. Soc.* **2013**, *135*, 3756-3759.

[140] Fang, L.; Chen, L.; Yu, J.; Wang, L. *Eur. J. Org. Chem.* **2015**, *9*, 1910 - 191.

[141] Sevov, C.S.; Brooner, R.E.M.; Chenard, E.; Assary, R.S.; Moore, J.S.; Rodriguez-Lopez, J.; Sanford, M.S. *J. Am. Chem. Soc.* **2015**, *137*, 14465-14472.

[142] Galloway, J.D.; Mai, D.N.; Baxter, R.D. *Org. Lett.* **2017**, *19*, 5772-5775.

[143] Ma, X.; Dang, H.; Rose, J.A.; Rablen, P.; Herzon, S.B. *J. Am. Chem. Soc.* **2017**, *139*, 5998-6007.

[144] Ichihara, Y.; Fujimara, R.; Tsuneki, H.; Wada, T.; Okamoto, K.; Gouda, H.; Hirono, S.; Sugimoto, K.; Matsuya, Y.; Sasaoka, T.; Toyooka, N. *Eur. J. Med. Chem.* **2013**, *62*, 649-660.

[145] Huestis, M.P.; Fagnou, K. *Org. Lett.* **2009**, *11*, 1357-1360.

[146] Matsui, J.K.; Primer, D.N.; Molander, G.A. *Chem. Sci.* **2017**, *8*, 3512-3522.
[147] Chow, S.; Liver, S.; Nelson, A. *Nat. Rev. Chem.* **2018**, *2*, 174–183.

[148] Gromski, P. S.; Henson, A. B.; Granda, J. M.; Cronin, L. *Nat. Rev. Chem.* **2019**, *3*, 119–128.

[149] Allen, C. L.; Leitch, D. C.; Anson, M. S.; Zajac, M. A. *Nat. Catal.* **2019**, *2*, 2–4.

[150] Milo, A. *Science* **2019**, *363*, 122–123.

[151] Krska, S. W.; DiRocco, D. A.; Dreher, S. D.; Shevlin, M. *Acc. Chem. Res.* **2017**, *50*, 2976–2985.

[152] Schmink, J. R.; Bellomo, A.; Berritt, S. *Aldrichimica Acta* **2013**, *46*, 71–80.

[153] Santanilla, A. B.; Regalado, E. L.; Pereira, T.; Shevlin, M.; Bateman, K.; Campeau, L.; Schneeweis, J.; Berritt, S.; Shi, Z.; Nantermet, P.; Liu, Y.; Helmy, R.; Welch, C. J.; Vachal, P.; Davies, I. W.; Cernak, T.; Dreher, S. D. *Science* **2015**, *347*, 443–448.

[154] Gesmundo, N. J.; Sauvagnat, B.; Curran, P. J.; Richards, M. P.; Andrews, C. L.; Dandliker, P. J.; Cernak, T. *Nature* **2018**. *557*, 228–232.

[155] Perera, D.; Tucker, J. W.; Brahmbhatt, S.; Helal, C. J.; Chong, A.; Farrell, W.; Richardson, P.; Sach, N. W. *Science* **2018**, *359*, 429–434.

[156] Grainger, R.; Heightman, T. D.; Ley, S. V.; Lima, F.; Johnson, C. N. *Chem. Sci.* **2019**, *10*, 2264–2271.

[157] Bretschneider, T.; Ozbal, C.; Holstein, M.; Winter, M.; Buettner, F. H.; Thamm, S.; Bischoff, D.; Luippold, A. H. *SLAS Technol.* **2019**, *24*, 386-393.

[158] Jaman, Z.; Mufti, A.; Sah, S.; Avramova, L.; Thompson, D. H. *Chem. Eur. J.* **2018**, *24*, 9546–9554.

[159] Wleklinski, M.; Loren, B. P.; Ferreira, C. R.; Jaman, Z.; Avramova, L.; Sobreira, T. J. P.; Thompson, D. H.; Cooks, R. G. *Chem. Sci.* **2018**, *9*, 1647–1653.

[160] Sawicki, J. W.; Bogdan, A. R.; Searle, P. A.; Talaty, N.; Djuric, S. W. *React. Chem. Eng.* **2019**, *4*, 1589-1594.

[161] Fedick, P. W.; Iyer, K.; Wei, Z.; Avramova, L.; Capek, G. O.; Cooks, R. G. *J. Am. Soc. Mass Spectrom.* **2019**, *10*, 2144-2151.

[162] Shaabani, S.; Xu, R.; Ahmadianmoghaddam, M.; Gao, L.; Stahorsky, M.; Olechno, J.; Ellson, R.; Kossenjans, M.; Helan, V.; Dömling, A. *Green Chem.* **2019**, *21*, 225–232.

[163] Wang, Y.; Shaabani, S.; Ahmadianmoghaddam, M.; Gao, L.; Xu, R.; Kurpiewska, K.; Kalinowska-Tluscik, J.; Olechno, J.; Ellson, R.; Kossenjans, M.; Helan, V.; Groves, M.; Dömling, A. *ACS Cent. Sci.* **2019**, *5*, 451–457.

[164] Sinclair, I.; Stearns, R.; Pringle, S.; Wingfield, J.; Datwani, S.; Hall, E.; Ghislain, L.; Majlof, L.; Bachman, M. *J. Lab. Autom.* **2016**, *21*, 19–26.

[165] Sinclair, I.; Bachman, M.; Addison, D.; Rohman, M.; Murray, D. C.; Davies, G.; Mouchet, E.; Tonge, M. E.; Stearns, R. G.; Ghislain, L.; Datwani, S. S.; Majlof, L.; Hall, E.; Jones, G. R.; Hoyes, E.; Olechno, J.; Ellson, R. N.; Barran, P. E.; Pringle, S. D.; et al. *Anal. Chem.* **2019**, *91*, 3790–3794.

[166] Shang, L.; Cheng, Y.; Zhao, Y. *Chem. Rev.* **2017**, *117*, 7964–8040.

[167] Teh, S. Y.; Lin, R.; Hung, L. H.; Lee, A. P. *Lab Chip* **2008**, *8*, 198–220.

[168] Zhu, P.; Wang, L. *Lab Chip* **2017**, *17*, 34–75.

[169] Küster, S. K.; Fagerer, S. R.; Verboket, P. E.; Eyer, K.; Jefimovs, K.; Zenobi, R.; Dittrich, P. S. *Anal. Chem.* **2013**, *85*, 1285–1289.

[170] Haidas, D.; Bachler, S.; Köhler, M.; Blank, L. M.; Zenobi, R.; Dittrich, P. S. *Anal. Chem.* **2019**, *91*, 2066–2073.

[171] Sun, S.; Slaney, T. R.; Kennedy, R. T. *Anal. Chem.* **2012**, *84*, 5794–5800.

[172] Sun, S.; Kennedy, R. T. *Anal. Chem.* **2014**, *86*, 9309–9314.

[173] Diefenbach, X. W.; Farasat, I.; Guetschow, E. D.; Welch, C. J.; Kennedy, R. T.; Sun, S.; Moore, J. C. *ACS Omega* **2018**, *3*, 1498–1508.

[174] Beulig, R. J.; Warias, R.; Heiland, J. J.; Ohla, S.; Zeitler, K.; Belder, D. *Lab Chip* **2017**, *17*, 1996–2002.

[175] Holland-Moritz, D. A.; Wismer, M. K.; Mann, B. F.; Farasat, I.; Devine, P.; Guetschow, E. D.; Mangion, I.; Welch, C. J.; Moore, J. C.; Sun, S.; Kennedy, R. T. *ACS Omega* **2018**, *3*, 1498–1508.

[176] Steyer, D. J.; Kennedy, R. T. *Anal. Chem.* **2019**, 1–12.

[177] Kelly, R. T.; Page, J. S.; Marginean, I.; Tang, K.; Smith, R. D. *Angew. Chemie - Int. Ed.* **2009**, *48*, 6832–6835.

[178] Wink, K.; Mahler, L.; Beulig, J. R.; Piendl, S. K.; Roth, M.; Belder, D. *Anal. Bioanal. Chem.* **2018**, *410*, 7679–7687.

[179] Narayanam, J. M. R.; Stephenson, C. R. J. *Chem. Soc. Rev.* **2011**, *40*, 102–113.

[180] Tucker, J. W.; Stephenson, C. R. J. *J. Org. Chem.* **2012**, *77*, 1617–1622.

[181] Prier, C. K.; Rankic, D. A.; MacMillan, D. W. C. *Chem. Rev.* **2013**, *113*, 5322–5363.

[182] Romero, N. A.; Nicewicz, D. A. *Chem. Rev.* **2016**, *116*, 10075–10166.

[183] McAtee, R. C.; McClain, E. J.; Stephenson, C. R. J. *Trends Chem.* **2019**, *1*, 111–125.

[184] Douglas, J. J.; Sevrin, M. J.; Stephenson, C. R. J. *Org. Process Res. Dev.* **2016**, *20*, 1134–11147.

[185] Nagib, D. A.; MacMillan, D. W. C. *Nature* **2011**, *480*, 224–228.

[186] DiRocco, D. A.; Dykstra, K.; Krska, S.; Vachal, P. Conway, D. V.; Tudge, M. *Angew. Chem., Int. Ed.* **2014**, *53*, 4802–4806.

[187] Beatty, J. W.; Douglas, J. J.; Cole, K. P.; Stephenson, C. R. J. *Nat. Commun.* **2015**, *6*, 7919–7925.

[188] Beatty, J. W.; Douglas, J. J.; Miller, R.; McAtee, R. C.; Cole, K. P.; Stephenson, C. R. J. *Chem* **2016**, *1*, 456–472.

[189] Sun, A. C.; McClain, E. J.; Beatty, J. W.; Stephenson, C. R. J. *Org. Lett.* **2018**, *20*, 3487–3490.

[190] McAtee, R. C.; Beatty, J. W.; McAtee, C. C.; Stephenson, C. R. J. *Org. Lett.* **2018**, *20*, 3491–3495.

[191] Prier, C. K.; Rankic, D. A.; MacMillan, D. W. C. *Chem. Rev.* **2013**, *113*, 5322-5363.

[192] Schultz, D. M.; Yoon, T. P. *Science* **2014**, *343*, 1239176.

[193] Douglas, J. J.; Nguyen, J. D.; Cole, K. P.; Stephenson, C. R. J. *Aldrichimica Acta* **2014**, *47*, 15-25.

[194] Angnes, R. A.; Li, Z.; Correia, C. R. D.; Hammond, G. B. *Org. Biomol. Chem.* **2015**, *13*, 9152-9167.

[195] Garlets, Z. J.; Nguyen, J. D.; Stephenson, C. R. J. *Isr. J. Chem.* **2014**, *54*, 351-360.

[196] Plutschack, M. B.; Correia, C. A.; Seeberger, P. H.; Gilmore, K. Organic Photoredox Chemistry in Flow; Springer Verlag GmbH: Heidelberg, Germany, (2015).

[197] Cambié, D.; Bottecchia, C.; Straathof, N. J. W.; Hessel, V.; Noël, T. *Chem. Rev.* **2016**, *116*, 10276-10341.

[198] Noël, T. *Photochemical Processes in Continuous-Flow Reactors: From Engineering Principles to Chemical Applications*; World Scientific Publishing Europe Ltd: London, (2017).

[199] Tucker, J. W.; Zhang, Y.; Jamison, T. F.; Stephenson, C. R. J. *Angew., Chem. Int. Ed.* **2012**, *51*, 4144-4147.

[200] Shvydkiv, O.; Gallagher, S.; Nolan, K.; Oelgemllöer, M. *Org. Lett.* **2010**, *12*, 5170-5173.

[201] Juris, A.; Balzani, V.; Belser, P.; Von Zelewsky, A. *Helv. Chim. Acta.* **1981**, *64*, 2175-2182.

[202] Lalevée, J.; Peter, M.; Dumur, F.; Gigmes, D.; Blanchard, N.; Tehfe, M-A.; Morlet-Savary, F.; Fouassier, J. P. *Chem. Eur. J.* **2011**, *17*, 15027-15031.

[203] Goldsmith, J. I.; Hudson, W. R.; Lowry, M. S.; Anderson, T. H.; Bernhard, S. *J. Am. Chem. Soc.* **2005**, *127*, 7502-7510.

[204] Lowry, M. S.; Goldsmith, J. I.; Slinker, J. D.; Rohl, R.; Pascal, R. A.; Malliaras, G. G.; Bernhard, S. *Chem. Mater.* **2005**, *17*, 5712-5719.

[205] Studer, A.; Curran, D. P. *Angew. Chem., Int. Ed.* **2016**, *55*, 58-102.

[206] Cismesia, M. A.; Yoon, T. P. *Chem. Sci.* **2015**, *6*, 5426-5434.

[207] Kärkäs, M. D.; Matsuura, B. S.; Stephenson, C. R. J. *Science* **2015**, *349*, 1285-1286.

[208] Aillet, T.; Loubière, K.; Dechy-Cabaret, O.; Prat, L. *Int. J. Chem. React. Eng.* **2014**, *12*, 257-269.

[209] Morse, P. D.; Beingessner, R. L; Jamison, T. F. *Isr. J. Chem.* **2017**, *56*, 218-227.

[210] Jensen, K. F. Flow Chemistry: Microreactor Techonology Comes of Age. *AIChE* **2017**, *63*, 858-869.

[211] Wegner, J.; Ceylan, S.; Kirschning, A. *Adv. Synth. Catal.* **2012**, *354*, 17-57.

[212] Chow, S.; Liver, S.; Nelson, A. *Nat. Rev. Chem.* **2018**, *2*, 174–183.

[213] Gromski, P. S.; Henson, A. B.; Granda, J. M.; Cronin, L. *Nat. Rev. Chem.* **2019**, *3*, 119–128.

[214] Allen, C. L.; Leitch, D. C.; Anson, M. S.; Zajac, M. A. *Nat. Catal.* **2019**, *2*, 2–4.

[215] Milo, A. *Science* **2019**, *363*, 122–123.

[216] Krska, S. W.; DiRocco, D. A.; Dreher, S. D.; Shevlin, M. *Acc. Chem. Res.* **2017**, *50*, 2976–2985.

[217] Schmink, J. R.; Bellomo, A.; Berritt, S. *Aldrichimica Acta* **2017**, *46*, 71–80.

[218] Santanilla, A. B.; Regalado, E. L.; Pereira, T.; Shevlin, M.; Bateman, K.; Campeau, L.; Schneeweis, J.; Berritt, S.; Shi, Z.; Nantermet, P.; Liu, Y.; Helmy, R.; Welch, C. J.; Vachal, P.; Davies, I. W.; Cernak, T.; Dreher, S. D. *Science* **2015**, *347*, 443–448.

[219] Gesmundo, N. J.; Sauvagnat, B.; Curran, P. J.; Richards, M. P.; Andrews, C. L.; Dandliker, P. J.; Cernak, T. *Nature* **2018**, *557*, 228-232.

[220] Perera, D.; Tucker, J. W.; Brahmbhatt, S.; Helal, C. J.; Chong, A.; Farrell, W.; Richardson, P.; Sach, N. W. *Science* **2018**, *359*, 429–434.

[221] Wleklinski, M.; Loren, B. P.; Ferreira, C. R.; Jaman, Z.; Avramova, L.; Sobreira, T. J. P.; Thompson, D. H.; Cooks, R. G. *Chem. Sci.* **2018**, *9*, 1647–1653.

[222] Hwang, Y. J.; Coley, C. W.; Abolhasani, M.; Marzinzik, A. L.; Koch, G.; Spanka, C.; Lehmann, H.; Jensen, K. F. *Chem. Commun.* **2017**, *53*, 6649–6652.

[223] McAtee, R. C.; McClain, E. J.; Stephenson, C. R. J. *J. Trends Chem.* **2019**, *1*, 111–125.

[224] Bédard, A. C.; Adamo, A.; Aroh, K. C.; Russell, M. G. *Science* **2018**, *361*, 1220–1225.

[225] Douglas, J. J.; Sevrin, M. J.; Cole, K. P.; Stephenson, C. R. J. *Org. Process Res. Dev.* **2016**, *20*, 1148–1155.

[226] Shang, L.; Cheng, Y.; Zhao, Y. *Chem. Rev.* **2017**, *117*, 7964–8040.

[227] Neumann, M.; Zeitler, K. *Org. Lett.* **2012**, *14*, 2658–2661.

[228] Coley, C. W.; Abolhasani, M.; Lin, H.; Jensen, K. F. *Angew. Chem., Int. Ed.* **2017**, *56*, 9847–9850.

[229] Colmenares, J. C.; Varma, R. S.; Nair, V. *Chem. Soc. Rev.* **2017**, *46*, 6675–6686.

[230] Teh, S. Y.; Lin, R.; Hung, L. H.; Lee, A. P. *Lab Chip* **2008**, *8*, 198–220.

[231] Zhu, P.; Wang, L. *Lab Chip* **2017**, *17*, 34–75.

[232] Agresti, J. J.; Antipov, E.; Abate, A. R.; Ahn, K.; Rowan, A. C.; Baret, J.-C.; Marquez, M.; Klibanov, M.; Griffiths, A. D.; Weitz, D. A. *Proc. Natl. Acad. Sci. U. S. A.* **2010**, *107*, 4004-4009.

[233] Novak, R.; Zeng, Y.; Shuga, J.; Venugopalan, G.; Fletcher, D. A.; Smith, M. T.; Mathies, R. A. *Angew. Chem., Int. Ed.* **2011**, *50*, 390-395.

[234] Baret, J.-C.; Beck, Y.; Billas-Massobrio, I.; Moras, D.; Griffiths, A. D. *Chem. Biol.* **2010**, *17*, 528-536.

[235] Shim, J.-U.; Olguin, L. F.; Whyte, G.; Scott, D.; Babtie, A.; Abell, C.; Huck, W. T. S.; Hollfelder, F. *J. Am. Chem. Soc.* **2009**, *131*, 15251-15256.

[236] Joensson, H. N.; Samuels, M. L.; Brouzes, E. R.; Medkova, M.; Uhlen, M.; Link, D. R.; Andersson-Svahn, H. *Angew. Chem., Int. Ed.* **2009**, *48*, 2518-2521.

[237] Brouzes, E. R.; Medkova, M.; Savenelli, N.; Marran, D.; Twardowski, M.; Hutchinson, J. B.; Rothberg, J. M.; Link, D. R.; Perrimon, N.; Samuels, M. L. *Proc. Natl. Acad. Sci. U. S. A.* **2009**, *106*, 14195-14200.

[238] Clausell-Tormos, J.; Lieber, D.; Baret, J.-C.; El-Harrak, A.; Miller, O. J.; Frenz, L.; Blouwolff, J.; Humphry, K. J.; Koster, S.; Duan, H.; Holtze, C.; Weitz, D. A.; Griffiths, A. D.; Merten, C. A. *Chem. Biol.* **2008**, *15*, 427-437.

[239] Theberge, A. B.; Mayot, E.; El Harrak, A.; Kleinschmidt, F.; Huck, W. T. S.; Griffiths, A. D. *Lab Chip* **2012**, *12*, 1320-1326.

[240] Sun, S.; Slaney, T. R.; Kennedy, R. T. *Anal. Chem.* **2012**, *84*, 5794–5800.

[241] Sun, S.; Kennedy, R. T. *Anal. Chem.* **2014**, *86*, 9309–9314.

[242] Diefenbach, X. W.; Farasat, I.; Guetschow, E. D.; Welch, C. J.; Kennedy, R. T.; Sun, S.; Moore, J. C. *ACS Omega* **2018**, *3*, 1498–1508.

[243] Steyer, D. J.; Kennedy, R. T. *Anal. Chem.* **2019**, *91*, 1–12.

[244] Beulig, R. J.; Warias, R.; Heiland, J. J.; Ohla, S.; Zeitler, K.; Belder, D. *Lab Chip* **2017**, *17*, 1996–2002.

[245] Haidas, D.; Bachler, S.; Köhler, M.; Blank, L. M.; Zenobi, R.; Dittrich, P. S. *Anal. Chem.* **2019**, *91*, 2066–2073.

[246] Kelly, R. T.; Page, J. S.; Marginean, I.; Tang, K.; Smith, R. D. *Angew. Chemie - Int. Ed.* **2009**, *48*, 6832–6835.

[247] Wink, K.; Mahler, L.; Beulig, J. R.; Piendl, S. K.; Roth, M.; Belder, D. *Anal. Bioanal. Chem.* **2018**, *410*, 7679–7687.

[248] Beatty, J. W.; Douglas, J. J.; Cole, K. P.; Stephenson, C. R. J. *Nat. Commun.* **2015**, *6*, 7919–7925.

[249] Beatty, J. W.; Douglas, J. J.; Miller, R.; McAtee, R. C.; Cole, K. P.; Stephenson, C. R. J. *Chem* **2016**, *1*, 456–472.

[250] Monos, T. M.; McAtee, R. C.; Stephenson, C. R. J. *Science* **2018**, *361*, 1369–1373.

[251] Abolhasani, M.; Bruno, N. C.; Jensen, K. F. *Chem. Commun.* **2015**, *51*, 8916–8919.

[252] Hwang, Y. J.; Coley, C. W.; Abolhasani, M.; Marzinzik, A. L.; Koch, G.; Spanka, C.; Lehmann, H.; Jensen, K. F. *Chem. Commun.* **2017**, *53*, 6649–6652.

[253] Coley, C. W.; Abolhasani, M.; Lin, H.; Jensen, K. F. *Angew. Chemie - Int. Ed.* **2017**, *56*, 9847–9850.

[254] Dugan, C. E.; Cawthorn, W. P.; MacDougald, O. A.; Kennedy, R. T. *Anal. Bioanal. Chem.* **2014**, *406*, 4851–4859.

[255] Yoon, T. P.; Ischay, M. A.; Du, J. *Nat. Chem.* **2010**, *2*, 527-532.

[256] Lowry, M. S.; Bernhard, S. *Chem. Eur. J.* **2006**, *12*, 7970-7977.

[257] Narayanam, J. M. R.; Stephenson, C. R. J. *Chem. Soc. Rev.* **2011**, *40*, 102-113.

[258] Prier, C. K.; Rankic, D. A.; MacMillan, D. W. C. *Chem. Rev.* **2013**, *113*, 5322-5363.

[259] Fors, B. P.; Hawker, C. J. *Angew. Chem. Int. Ed.* **2012**, *8850-8853*.

[260] Xu, J.; Jung, K.; Atme, A.; Shanmugam, S.; Boyer, C. *J. Am. Chem. Soc*. **2014**, *136*, 5508.

[261] DeRosa, M. C.; Hodgson, D. J.; Enright, G. D.; Dawson, B.; Evans, C. E. B.; Crutchley, R. J. *J. Am. Chem. Soc.* **2004**, *126*, 7619-7626.

[262] Richter, M. M. *Chem. Rev.* **2004**, *104*, 3003-3036.

[263] *Photochemistry and Photophysics of Coordination Compounds I*; Balzani, V.; Campagna, S., Eds.; Topics in Current Chemistry 280; Springer: Berlin, Germany, 2007; 1-255.

[264]*Photochemistry and Photophysics of Coordination Compounds II*; Balzani, V.; Campagna, S., Eds.; Topics in Current Chemistry 281; Springer: Berlin, Germany, 2007; 1-327.

[265] Furst, L.; Narayanam, J. M. R.; Stephenson, C.R.J. *Angew. Chem., Int. Ed.* **2011**, *50*, 9655.

[266] Zhang, J.; Chen, J.; Zhang, X.; Lei, X. *J. Org. Chem.* **2014**, *79*, 10682-10688.

[267] Beatty, J. W.; Stephenson, C. R. J. *J. Am. Chem. Soc.* **2014**, *136*, 10270-10273.

[268] Nicewicz, D. A.; MacMillan, D. W. C. *Science* **2008,** *322,* 77-80.

[269] Zuo, Z.; Ahneman, D. T.; Chu, L.; Terrett, J. A.; Doyle, A. G.; MacMillan, D. W. C. *Science* **2014**, *345*, 437-440.

[270] Tellis, J. C.; Primer, D. N.; Molander, G. A. *Science* **2014**, *345*, 433-436.

[271] Hopkinson, M. N.; Sahoo, B.; Li, J-J.; Glorius, F. *Chem. Eur. J.* **2014**, *20*, 3874-3886.

[272] Dixon, I. M.; Collin, J-P.; Sauvage, J-P.; Flamigni, L.; Encinas, S.; Barigelletti, F. *Chem. Soc. Rev.* **2000**, *29*, 385-391.

[273] Costa, R. D.; Ortí, E.; Bolink, H. J.; Monti, F.; Accorsi, G.; Armaroli, N. *Angew. Chem. Int. Ed.* **2012**, *51*, 8178-8211.

[274] Slinker, J. D.; Gorodetsky, A. A.; Lowry, M. S.; Wang, J.; Parker, S.; Rohl, R.; Bernhard, S.; Malliaras, G. G. *J. Am. Chem. Soc.* **2004**, *126*, 2763-2767.

[275] Lowry, M. S.; Goldsmith, J. I.; Slinker, J. D.; Rohl, R.; Pascal, R. A.; Malliaras, G. G.; Bernhard, S. *Chem. Mater.* **2005**, *17*, 5712-5719.

[276] Flamigni, L.; Barbieri, A.; Sabatini, C.; Ventura, B.; Barigelletti, F. *Top. Curr. Chem.* 2007, 281, 143–203.

[277] King, K. A.; Watts, R. J. *J. Am. Chem. Soc.* **1986**, *109*, 1590-1591.

[278] In reality, the triplet emission state is an admixture of MLCT and LC transitions that have been estimated by time-resolved DFT calculations; however, photophysical trends are difficult to

predict *de novo* and the only definitive evidence for the photophysical properties of a complex can be established by the physical characterization of novel Ir(III) complexes.

[279] McGee, K. A.; Mann, K. R. *Inorg. Chem.* **2007**, *46*, 7800-7809.

[280] Sprouse, S.; King, K. A.; Spellane, P. J.; Watts, R. J. *J. Am. Chem. Soc.* **1984**, *106*, 6647-6653.

[281] Kappe, C. O. *Angew. Chem. Int. Ed.* **2004**, *43*, 6250-6284.

[282] Hoz, A de la.; Díaz-Ortiz, Á.; Moreno, A. ***Chem. Soc. Rev.*** **2005**, ***34***, 164-178.

[283] Gabriel, C.; Gabriel, S.; Grant, E. H.; Grant, E. H.; Halstead, B. S. J.; Mingos, D. M. P. *Chem. Soc. Rev.* **1998**, *27*, 213-224.

[284] Larhed, M.; Moberg, C.; Hallberg, A.; *Acc. Chem. Res.* **2002**, *25*, 717-727.

[285] Leadbeater, N. E., Schmink, J. R. and Hamlin, T. A. *Microwaves in Organic Synthesis*; Hoz, A. de la.; Loupy, A., 3rd ed.; Wiley-VCH Verlag GmbH & Co. KGaA, Weinheim, 2012; Vol 1

[286] This is mostly accepted as a general thermal effect of kinetics: Perreux, L; Loupy, A. *Tetrahedron,* **2001**, *57*, 9199-9223.

[287] de la Hoz, A; Diaz-Ortiz, A.; Moreno, A. *Chem. Soc. Rev.* **2005**, *34*, 164-178.

[288] Leadbeater, N. E. Microwave Heating and Continuous-Flow Processing as Tools for Metal-Catalyzed Couplings: Palladium-Catalyzed Suzuki–Miyaura, Heck, and Alkoxycarbonylation Reactions. In *Transition Metal-Catalyzed Couplings in Process Chemistry: Case Studies from the Pharmaceutical Industry*; Magano, J., Dunetz, J.R., Eds.; Wiley-VCH Verlag GmbH & Co. KGaA: Weinheim, 2003.

[289] Leadbeater, N. E. Organic synthesis using microwave heating. In *Comprehensive Organic Synthesis*; Knochel, P., Molander, G. A., Eds; Elsevier: Amsterdam, 2014.; Vol. 9, p 234-286.
[290] Hayes, B. L. *Microwave Synthesis: Chemistry at the Speed of Light*; CEM Publishing: Matthews, NC, 2002.

[291] Gottlieb, H. E.; Kotlyar, V.; Nudelman, A. *J. Org. Chem.* **1997**, *62*, 7512-7515.

[38] Singh, A.; Teegardin, K.; Kelly, M.; Prasad, K. S.; Krishnan, S.; Weaver, J. D. *Journal of Organometallic Chemistry* **2015**, *776*, 51-59.

[292] Jasti, R.; Bhattacharjee, J.; Neaton, J. B.; Bertozzi, C. R. *J. Am. Chem. Soc.* **2008**, *130*, 17646-17647.

[293] Hirst, E, S.; Jasti, R. *J. Org. Chem*. **2012**, *77*, 10473-10478.

[294] Darzi, E. R.; Sisto, T. J.; Jasti, R. *J. Org. Chem*. **2012**, *77*, 6624-6628.
[295] Leonhardt, E. J.; Jasti, R. *Nat. Rev. Chem.* **2019**, *3*, 672-686.

[296] Hines, D.; Darzi, E. R.; Jasti, R.; Kamat, P. *J. Phys. Chem. A.* **2014**, *118*, 1595-1600.

[297] Darzi, E. R.; Jasti, R. *Chem. Soc. Rev.* **2015**, *44*, 6401-6410.

[298] Golder, M. R.; Jasti, R. *Acc. Chem. Res.* **2015**, *48*, 557-566.

[299] Xu,Y.; von Delius, M. *Angew. Chem., Int. Ed.* **2020**, *59*, 559-573.

[300] Lovell, T. C.; Colwell, C. E.; Zakharov, L. N.; Jasti, R. *Chem. Sci.* **2019**,*10*, 3786-3790.

[301] White, B. M.; Zhao, Y.; Kawashima, T. E.; Branchaud, B. P.; Pluth, M. D.; Jasti, R. *ACS Cent. Sci.* **2018**, *4*, 1173-1178.

[302] Van Raden, J. M.; White, B. M.; Zakharov, L. N.; Jasti, R. *Angew. Chem. Int. Ed.* **2019**, *58*, 7341-7345.

[303] Van Raden, J. M.; Louie, S.; Zakharov, L. N.; Jasti, R. *J. Am. Chem. Soc.* **2017***, 139*, 2936-2939.

[304] Monos, T. M.; Sun A. C., McAtee, R. C.; Devery III, J. J.; Stephenson, C. R. J. *J. Org. Chem*. **2016**, *81*, 6988-6994.